Honda R&D

Technical Review



October 2004



Comment on the Cover

A variety of shapes from Honda, and shapes of dreams.
“Our Dream Road” can be made to stretch ahead without limit.
Let's all do our best heading into the future!



Wako R&D Center
Takeshi Koshiishi

Development of New Model LEGEND

Masahiro WATANABE* Masafumi TAKITA** Junichi FUKUDA*
Takefumi NAKAMURA** Yasunori OKU** Syoichi NEMOTO**

ABSTRACT

With the shrinking of the sedan market, the creation of new values for sedans is strongly demanded. Honda's luxury sedan, the LEGEND, is due for a full model change after an interval of nine years. The 2005 model year LEGEND has been developed with the aim of creating the ultimate luxury sedan brand of Honda and the attractive features expected of the luxury sedan class.

A good balance between excellent driving performance and fuel economy has been achieved with a lightweight and compact engine which has superb power performance, weight saving technologies, and SH-AWD to improve driving stability dramatically. The vehicle features the latest technologies such as iNVS and AFS, a driving support system to increase safety during night driving, and the latest safety equipment to reduce impact. The functional design of the spacious cabin, which appeals to the senses, and quietness in the cabin during driving present the driver and passengers with a relaxed and luxurious experience. These advanced technologies have been brought together in an ultimate sports sedan, the new LEGEND, which has new values and attractive features of " high quality as a luxury car " and "driving pleasure".

1. Introduction

Since the launch of its first generation as Honda's ultimate luxury sedan in 1985, the LEGEND has come to symbolize Honda's technological superiority. Recently, however, the Japanese sedan market has begun to shrink, and globally the production of flagship models in this class by major manufacturers has created an extremely competitive market situation. Nine years on from the launch of the third-generation model, the LEGEND therefore faced difficult prospects.

In designing a full model change for the fourth generation LEGEND, Honda therefore went back to basics in terms of what makes a driver's sedan. We have made an effort to produce a vehicle which fulfills expectations of a Honda product and offers a superb level of driving pleasure, and succeeded in providing a sports sedan with highly advanced features and possessing a level of appeal unprecedented in the class.

The fourth generation LEGEND brings together Honda's most advanced technologies, in particular a lightweight and compact but powerful engine, weight-saving technology throughout and SH-AWD to dramatically improve driving performance. The technologies employed in the new LEGEND offer new values and attractive features, combining the high quality of a luxury vehicle and unparalleled driving pleasure.

* Wako R&D Center
** Tochigi R&D Center

2. Concept and Development Goals

The new LEGEND aimed to provide executives with a vehicle in which every moment they spent is a pleasurable experience, which allows them to make essential trips anywhere at any time in comfort and peace of mind without consideration of the hour or the weather, and which is in addition simply a pleasure to drive.

To achieve these goals, the latest driver support technologies were employed to achieve top-in-class dynamic performance. The design of the vehicle is such that its distinction and superb performance are recognizable at a glance. In addition, development aims of the new LEGEND included the integration of cutting-edge safety and environmental technologies and the achievement of a superb quality of fit and finish.

After in-depth study of the competition with the top-class European luxury sedans as the benchmark in this class, the following three specific targets for dynamic performance of the new LEGEND were set:

(1) To achieve driving, cornering and stopping performance more advanced than that of European luxury sedans
(2) To realize the world's top level of luxury and comfort
(3) An original drive feeling for the LEGEND

3. Overview of the New LEGEND

In order to enable the realization of the goals, which are driving pleasure and a luxurious and comfortable cabin space as the concept of the new LEGEND, the specifications shown in Table 1 are adopted for the new LEGEND. In addition to the exterior styling of the vehicle shown in Fig. 1, the technologies and equipment discussed below have been employed to enable realization of these goals.



Fig. 1 Exterior styling of new LEGEND

Table 1 Comparison of vehicle specifications

	New Model	Previous Model
Overall length (mm)	4 915	4 995
Overall width (mm)	1 845	1 820
Overall height (mm)	1 450	1 435
Empty vehicle weight (kg)	1 760	1 690
Wheel base (mm)	2 800	2 910
Tire tread : front/rear (mm)	1 575/1 585	1 550/1 540
Tire size	235/50R17	215/60R16
Engine type	V6 SOHC VTEC	V6 SOHC
Engine displacement (l)	3.471	3.473
Power (kW/rpm)	221/6 200	158/5 200
Torque (N·m/rpm)	353/5 000	312/2 800
Transmission	5AT	4AT
Fuel capacity (l)	73	68
Minimum turning radius (m)	5.8	5.5
Riding capacity	5	5

3.1. Technologies for the Improvement of Dynamic Performance

(1) Power plant technologies: To realize superb driving performance, the new LEGEND employed a new compact and high-power 3.5L V6 engine, and is also provided with a newly developed 5-speed automatic transmission (5AT).
(2) Chassis technologies: The new LEGEND employed Super Handling All-Wheel Drive (SH-AWD). This new system enables independent control of the torque of all four wheels which increases both steering stability and the fidelity of the vehicle's cornering performance to the motion of the steering wheel, which dramatically improves driving performance. In addition, double wishbone suspension for the front wheels and multi-link suspension for the rear wheels have been adopted.
(3) Materials: Ensuring weight savings is vital to the achievement of a balance between dynamic performance and fuel economy. Aluminum materials to be made by a newly developed production process have been employed in chassis components, including the suspension arms and the subframe. And magnesium has been employed for the engine head cover, the propeller shaft has been formed from carbon composite (CFRP), and aluminum and high-strength steel sheets have been used to achieve weight savings in the body.
(4) Noise and vibration control technologies: To achieve a quiet and comfortable cabin, an anti-vibration rear subframe structure has been employed to improve vibration isolation and thus reduce the level of noise generated by vibration from the power plant and the road surface. New high-efficiency soundproofing materials have also been employed, and the use of active noise control to reduce the level of low-frequency noise has enabled the weight of the soundproofing to be reduced.

3.2. Environmental and Safety Technologies

(1) Driver support technologies: A Collision Mitigation Brake System (CMS) and HiDS have been employed to increase the driving safety of the new LEGEND. The

safety of night driving has also been a consideration, and the vehicle is fitted with a night vision system and Adaptive Front Lighting System (AFS).

(2) Collision safety technologies: The new LEGEND does not merely comply with the latest safety regulations, but employs Honda's proprietary crash compatible and pedestrian impact mitigation body technologies to achieve a top-in-class level of safety performance. The vehicle is fully equipped with advanced safety features, including side curtain airbags as standard.

(3) Environmental technologies: The employment of a high-precision A/F control system, among other measures, has enabled the new LEGEND to comply with 2005 exhaust emission standards. The vehicle also employs a wide range of other environmentally friendly measures and technologies: acrylic urethane is now used instead of PVC in the undercoat, non-toxic trivalent chromium has replaced hexavalent chromium as the plating material for nuts and bolts, and the purification performance of the catalyzer has been improved and the odor of sulfur reduced.

The next section will discuss target performance and the methods used in its achievement, in addition to offering an overview of the technical details and the performance of the most important of the technologies mentioned above.

4. Vehicle Performance and Main Technologies

4.1. Design

4.1.1. Packaging

The design concept for the new vehicle stressed high-density packaging to balance a level of compactness able to maximize dynamic performance with the comfort and spaciousness demanded of a luxury sedan.

Through the adoption of measures including lowering the floor to change the driving position and modification of the trunk hinge to reduce the rear overhang, the overall length of the vehicle has been reduced and cabin space has been increased against those of the previous model (Fig. 2).

The design of the instrument panel offers the driver ample space around the knees and in combination with careful design of the upper section of the door linings, offers users a sense of enfoldment and luxury. As a result of these painstaking designs, the cabin offers users just the right sense of being safely enfolded during sporty driving while providing a deep and relaxing sense of comfort when the vehicle is cruising.

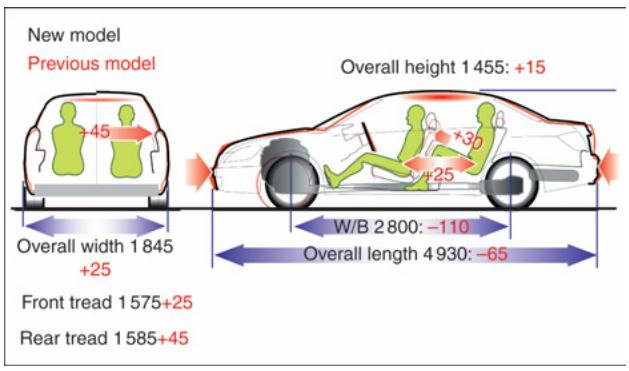


Fig. 2 Comparison of packaging design of new model and previous model

4.1.2. Exterior

"Emotional Ingot Design" was established as the concept for exterior design. This concept stressed a strong sense of integration that had at the same time a powerful emotional appeal (Fig. 3).

At the front of the vehicle, the sporty feel is expressed in the wide and low stance produced by the low hood and sharp grille.

Seen from the side, the vehicle's sporty framework gives it a powerful sense of integration, with the form flowing back in a single smooth motion from the low, sculpted hood to the cutaway rear deck. The side windows have also been made perfectly flush with the body to offer superb aerodynamic performance.

At the rear, the vehicle's wide stance, wide tires and flat twin silencers further express its sportiness. At the same time, production by aluminum blow molding gives the lid of the trunk a superb tautness, offering the elegance entirely appropriate to a luxury vehicle.

The integration, aerodynamics and wide stance of the new LEGEND's sporty framework and its details established in accordance with craftsmanship give the vehicle elegance which is suitable for a luxury vehicle. The superb integration of framework and detailing produces the embodiment of advanced luxury sedan design.



Fig. 3 Exterior design concept for new LEGEND

4.1.3. Interior

The interior design of the vehicle was based on the concept of "Sensuous Functionality," a functional design appealing to the senses, and aimed to bring together driving pleasure and a superbly comfortable, relaxing cabin space (Fig. 4).

The instrument panel is strongly slanted to produce an open form, and a new, organic surface treatment has been applied to the materials, resulting in a richly expressive design. Information systems, such as the navigation monitor, have been positioned to allow the driver to check the vehicle's status while driving with only minimal movement of the eyes. The superbly designed layout of the driving equipment, and the new technologies, including a multi-function controller, voice control system and paddle shifters, creates a space in which the driver can carry out all driving operations without changing his or her posture and can concentrate exclusively on driving.

The three large, independent, circular meters employed in the previous model have been further evolved for the new



Fig. 4 Interior design concept for new LEGEND

LEGEND, with a design that gives them a more three-dimensional feel and a sense of balance and sophistication.

The wood grain connecting the right and left and center panels respectively form an area of unified design. This new design sensibility offers not only structural power but also a condensed feel and a feel for the raw materials as a new value for sensuousness, and produced a superbly comfortable space.

The seats, increased in size and designed to hold their occupants more firmly, are soft and luxurious, thus contributing to the comfort and luxury of the overall cabin space.

4.2. Engine Performance

The concept for the new LEGEND power plant stressed driving performance and environmental performance in advance of its class. In order to realize this concept, the V6 SOHC-VTEC engine employed in the U.S. MDX was selected as the base engine for power train design, and the following basic performance targets were established:

(1) Top-in-class power performance
(2) Low emissions (75% less than stipulated in 2005 Japanese emissions standards)

4.2.1. Overview of engine and main specifications

Figure 5 shows a view of the engine. The power performance of the engine is shown in Fig. 6, and the main specifications in Table 2.

Both maximum power and maximum torque have been significantly increased against the engine of a previous model. This engine brought driving performance suitable for a luxury vehicle.



Fig. 5 View of V6 SOHC-VTEC engine

Table 2 Comparison of main engine specifications

	New Model	Previous Model
Engine type	60° V6 SOHC VTEC	90° V6 SOHC
Displacement	3471 (cc)	3473 (cc)
Compression ratio	11.0	9.6
Fuel	Premium	Premium
Max. power	221/6200 (kw/rpm)	158/5200 (kw/rpm)
Max. torque	353/5000 (N·m/rpm)	312/2800 (N·m/rpm)
Transmission	5AT	4AT
Fuel economy	8.6 (10-15mode)	8.7 (10-15mode)
Emission	J-SULEV ★★★★	J-LEV ★★

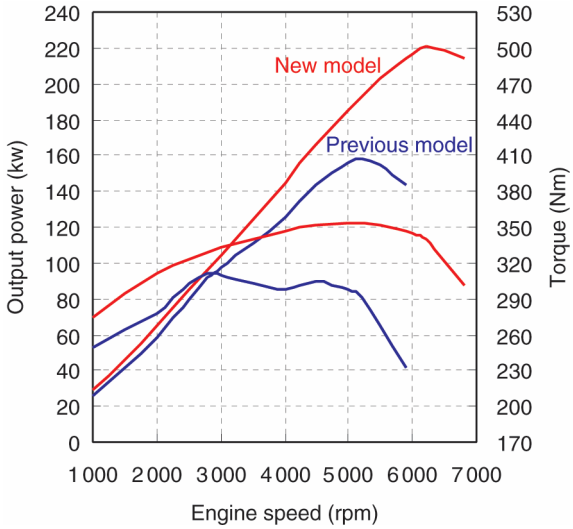


Fig. 6 Comparison of output performance of engine in new and previous models

4.2.2. Environmental performance

Figure 7 shows the configuration of the system employed to achieve the low emissions target. The engine is provided with an independent emission control system for each bank of cylinders. In addition, the employment of a high-precision A/F control system has resulted in the achievement of a 75% reduced emissions level, the 2005 Japanese standard, enabling the vehicle to take a four-star emissions rating in recognition of its superb environmental performance.

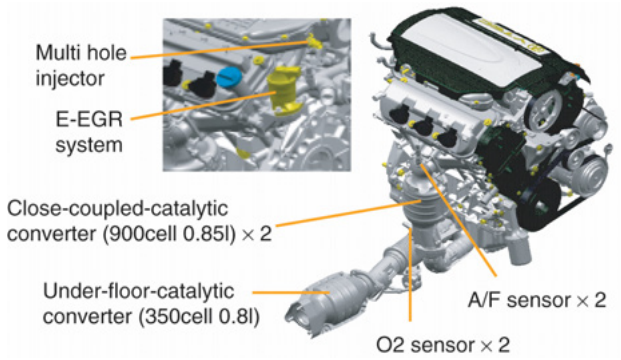


Fig. 7 Emission control system

4.3. Vehicle Performance

4.3.1. Collision safety performance

In terms of collision safety performance, the aim for the new LEGEND was to achieve the top level in collision safety evaluations carried out by the J-NCAP, the US-NCAP and the IIHS, as befits Honda's flagship model. To achieve this, a polygonal framework has been employed and its cross-section increased in size, the bending mode during collision has been controlled and the efficiency of restraint devices has been increased, reducing the deformation of the vehicle and improving occupant restraint performance and resulting in the achievement of a top-in-class level of collision safety performance.

The carbon fiber reinforced plastic (CFRP) propeller shaft was developed and employed for the new LEGEND. The CFRP tubes and the joints of the stabilizer shafts employed have been designed to collapse with the rearward motion of the engine in a collision, enabling collision energy to be absorbed.

The new LEGEND features Dual-Stage Front Airbags (SRS), front-side airbags with a passenger-side Occupant Position Detection System (OPDS), and a side curtain airbag system as standard safety equipment. Large side airbags have been employed to further increase the level of passenger protection.

The new LEGEND employs an Advanced Compatibility Engineering (ACE) body structure which represents a further advancement of Honda's proprietary G-force Control (G-CON) collision safety technology. The body effectively disperses and absorbs collision energy, and not only improves the self-protection of small vehicles, but also improves partner protection in large vehicles[1].

4.3.2. Overview of body

High-tensile strength steel was used in 50% of the steel sheets of the new LEGEND body, and part of the framework employs higher-strength 780 MPa class steel sheets which have been subjected to induction hardening. The employment of high-tensile steel sheets, in combination with high-efficiency joining of each section of the framework, has not only resulted in higher collision safety performance, but has also increased driving stability, improved NVH performance and reduced the weight of the vehicle. To achieve further weight savings, the external sheet of the hood[2], the front fender and the trunk have been formed from aluminum, as shown in Fig. 8. High-speed blow molding is used to produce the front fender and the trunk, enabling the achievement of a smooth sculptural form unattainable with the former press stamping. Aluminum is also employed in the front to rear bumper beam.

The efficient placement of high-tensile strength sheets

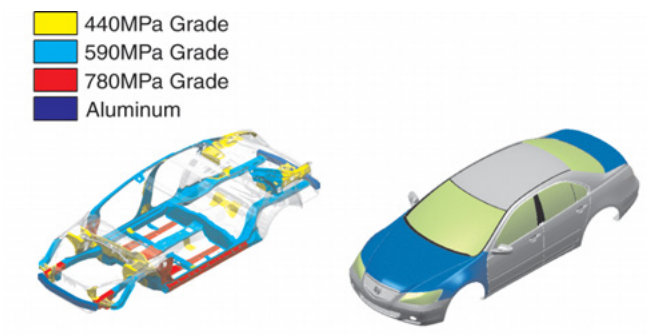


Fig. 8 Application of high-strength steel and aluminum in body construction

new model against the former model to only around 4%. It has also enabled weight reduction of components which are distant from the vehicle's center of gravity, thus reducing the inertial moment of the roll axis by approximately 5% despite the increase in the weight of the vehicle.

4.4. Advanced Technologies

In order to achieve the highest safety performance, in addition to improving visibility performance, the latest and most advanced technologies have been employed in the new LEGEND.

4.4.1. Intelligent Night Vision System

70% of pedestrian fatalities occur at night, and most of them are accidents involving pedestrians who are crossing the road or walking at the side of the road[3] when the vehicle is traveling on straight roads.

An Intelligent Night Vision System (iNVS) has been employed in the new LEGEND to reduce these accidents. This system processes stereo infrared images to enable it to detect the movements of pedestrians and judge the distance between the pedestrians and the vehicle. Together with a warning buzzer, a highlighted image of the pedestrian is shown on a head-up display (HUD) (Fig. 9). This system supports the driver in recognizing the presence of pedestrians approaching the road on which the vehicle is traveling at night[4].



Fig. 9 Example of HUD image

4.4.2. Adaptive Front Lighting System

The new LEGEND employs an Adaptive Front Lighting System (AFS) to further improve the driver's ability to locate pedestrians and to make it easier to judge the road situation at night. When the vehicle is cornering or traveling on a curve, the headlights on the inner wheel side turn in response to the steering angle and vehicle behavior. This illumination of AFS gives the driver better visibility during driving than the conventional front illumination (Fig. 10).

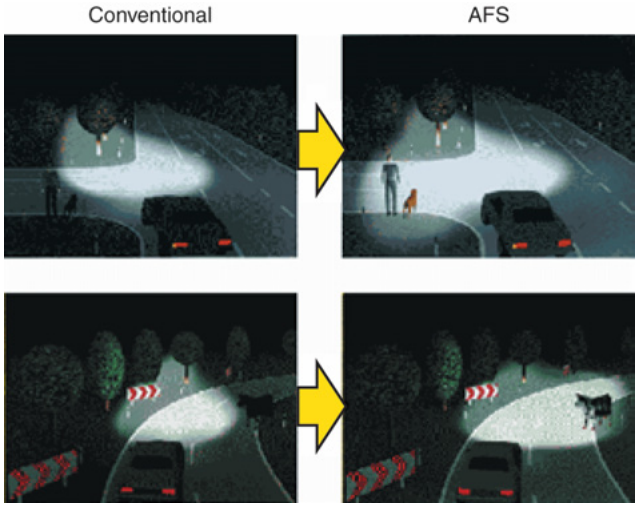


Fig. 10 Comparison of lighting performance

4.4.3. Collision Mitigation Brake System

The new LEGEND has been equipped with Honda's Collision Mitigation Brake System (CMS), already employed in the INSPIRE and other vehicles to help prevent rear-end collisions and mitigate injuries when collisions do occur.

4.4.4. HiDS

In the LEGEND equipped with HiDS, a newly developed pinion assist-type electronically controlled power steering system (EPS) was used. This EPS system employs a brushless motor to provide high-efficiency and high-power control. It has resulted in a reduction of steering wheel inertia relative to standard EPS vehicles and the achievement of a luxurious steering feel.

4.5. Steering Stability and Riding Comfort

The LEGEND aims to balance the achievement of luxurious driving at the top of the vehicle's class with high-performance driving, and to achieve overwhelming driving performance, that is, running, cornering and stopping, using application of handling improvement technology based on the newly developed SH-AWD system[5].

4.5.1. Suspension/subframe

Aluminum materials have been used throughout the suspension and the subframe, at both front and rear, to reduce weight at the same time as achieving high rigidity[6]. A double wishbone suspension system has been employed at the front of the vehicle, while an in-wheel multi-link system is used at the rear (Fig. 11).

The improvement of steering feel, roll feel and the responsiveness of the vehicle were important design aims. The front-rear roll axle has been designed to slope downwards from the rear to the front of the vehicle[7], which has improved responsiveness. With the theory of a three-link virtual arm[8], the length of the virtual arm and the positioning of the roll axis were decided with consideration of the reduction of jacking phenomenon (Fig. 12).

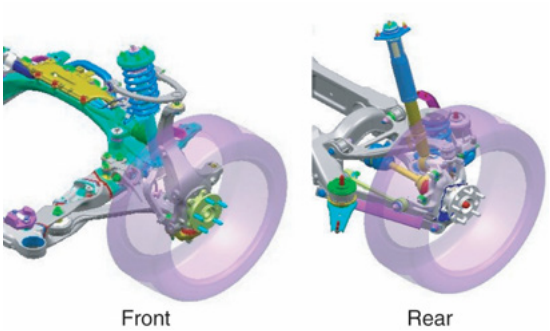


Fig. 11 View of suspension of new LEGEND

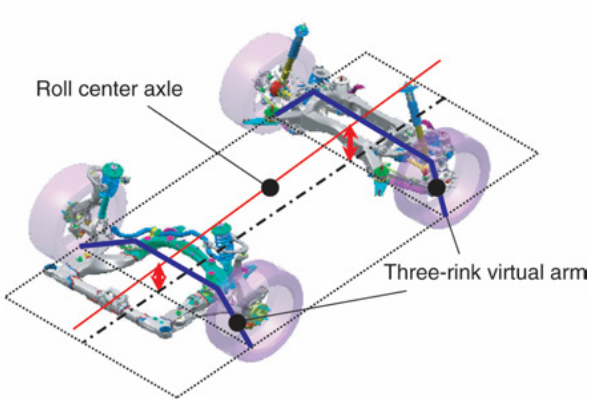


Fig. 12 Concept of suspension system

Correction of the locus inclination angle of the wheel centers[9] and increasing the size of the compliance bushing and the subframe mount bushing have reduced harshness, leading to increased riding comfort. In addition, low and wide positioning of the subframe mount has both increased steering stability and improved NVH performance.

4.5.2. Steering

Electronically controlled speed-responsive hydraulic power steering was employed. A motor torque assist control valve unit controlled by the ECU enables the system to apply the correct amount of assist in response to the speed of the vehicle, ensuring steerability from low to high speeds (Fig. 13).

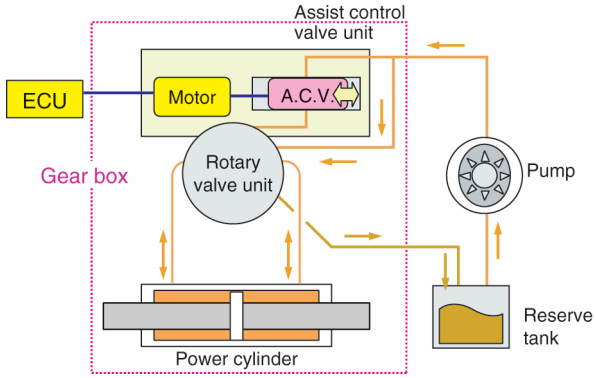


Fig. 13 System of ECPS system (Electronically controlled power steering)

4.5.3. Brakes

To achieve high levels of performance from the brakes while ensuring that they are lightweight and high-rigidity, high-diameter ventilated disks have been used in the front and rear brake system, aluminum opposed 4-pot calipers have been used in the front and aluminum body collet calipers in the rear (Fig. 14). In addition, ECU tuning (including provision with dedicated logic) has been carried out to match the performance of Vehicle Stability Assist (VSA) with that of SH-AWD.

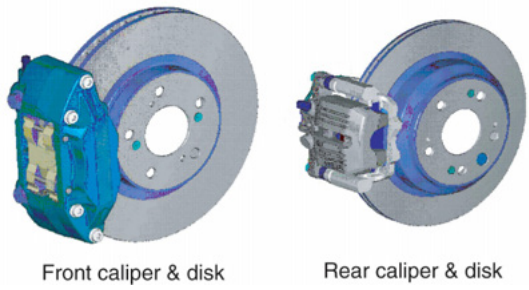


Fig. 14 Front & rear brakes

4.5.4. Aerodynamic performance

The new LEGEND demanded improvement of stability at high speeds, as expected of a luxury sporty vehicle, and for the front and rear lift balance to be fitted for the high stabilizing potential of SH-AWD. In order to satisfy these requirements, aerodynamic drag has been reduced through the technology of optimization of the body shape, such as flush surface side windows, and of the airflow around the

underfloor section by employment of large underfloor covers and rear defusers (Fig. 15).

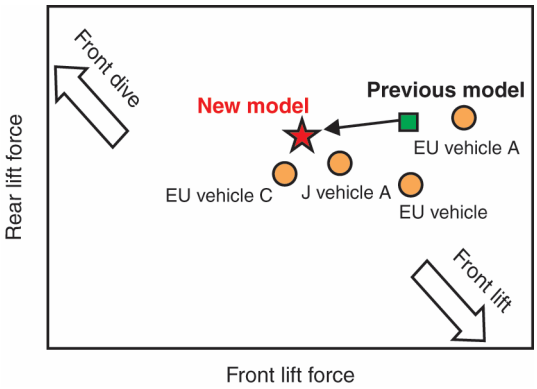


Fig. 15 Map of front & rear lift balance

4.6. Noise and Vibration

The employment of a high-power 221 kW engine, the SH-AWD system and large-diameter wide tires are detrimental to NVH performance. Against this background, the new LEGEND required the ambitious target of a level of engine noise and road noise suitable for a luxury vehicle. The following technologies gave the LEGEND the top level of cabin quietness, which equals and surpasses that of European competitors in this class.

4.6.1. Rear differential mount system

A sub-frame supported with rubber mountings can isolate the high frequency vibrations from differential gear box to body, however, there are vibration modes in which the sub-frame and the differential resonate at low frequencies. In such cases, these vibrations increase in amplitude and are transmitted to the body. A methodology to prevent resonance caused by vibration between differential and sub-frame is necessary. A sub-frame supported with rubber mountings is employed to reduce road noise; in addition, the new LEGEND employs the rear three-mount system shown in Fig. 16, with two mounting points at the front left and right and one mounting point at the rear left. This supporting system of the rear differential can control the pitching mode of the sub-frame, and thereby reduce the amplitude of vibration of the sub-frame.

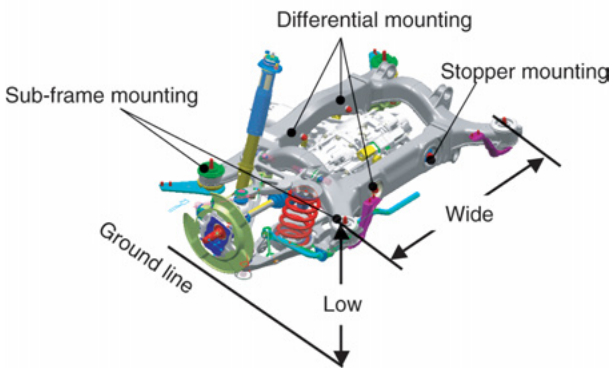


Fig. 16 Rear differential mounting system

4.6.2. Lightweight soundproofing package

The highly sound-absorbent but lightweight materials employed in the new LEGEND's soundproofing system have significantly reduced high-frequency noise, increasing the level of quietness of the vehicle.

Soundproofing has been employed throughout the interior, and includes a dash insulator, floor carpet, roof lining and trunk lining. The new soundproofing has increased the quietness of the vehicle while enabling the weight of the soundproofing system to be significantly reduced relative to that employed in the previous model (Fig. 17).

In order to design for acoustic sensitivity in the cabin, statistical energy analysis (SEA)[10], the latest method to study the configuration of soundproofing packages, was employed to enable the amount of sound insulation materials required as a result of the increased weight of the vehicle to be minimized.

As a result, an excellent balance has been achieved between weight savings and quietness, and the quietness of the new LEGEND excels that of the previous model despite the fact that its soundproofing package weighs only approximately 30% as much.

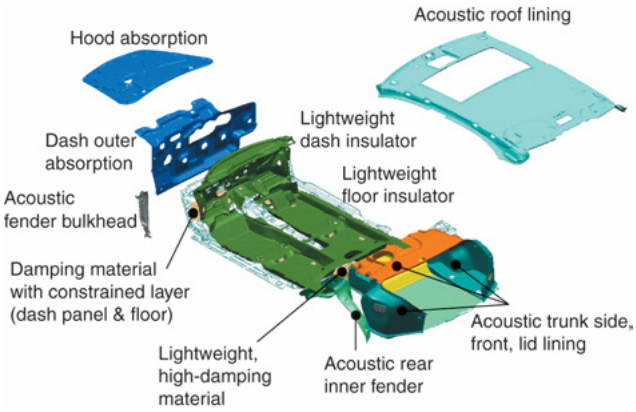


Fig. 17 Lightweight soundproofing materials

4.6.3. Exhaust system

The exhaust silencer (muffler) has been provided with variable exhaust valves to balance high flow with a high level of quietness. This enables engine power targets to be achieved while controlling exhaust noise and increasing cabin quietness at medium engine speeds using the minimum capacity of the exhaust silencer.

4.6.4. Active noise control

Active noise control (ANC) system has been employed in the new LEGEND to balance the level of quietness expected of a luxury vehicle with the achievement of the sportiness established as a goal for the new vehicle (Fig. 18). This has significantly reduced the large power level of low-frequency booming noise produced by resonance in the exhaust system, resulting in the achievement of both the target level of quietness and a linear sporty sound in the cabin.

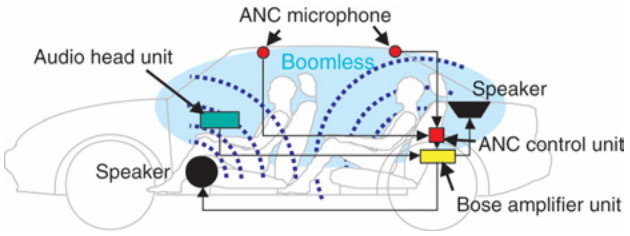


Fig. 18 Active noise control system

5. Conclusion

After an interval of nine years, the LEGEND has undergone a full model change with the new 2005 model. There are some of the world's finest vehicles in this luxury car class. In this class, the new LEGEND was required to create new value as an ultimate luxury vehicle, which other luxury vehicles do not have, and to create new attractive features as the LEGEND brand.

Among its many features, the new LEGEND is provided with an engine with superb dynamic performance, SH-AWD to dramatically improve driving stability, a range of weight saving technologies, advanced driver support technologies to increase safety, and ample safety equipment and body technologies that have enabled the vehicle to achieve the top results in the latest collision safety performance evaluations.

The new LEGEND is Honda's ultimate sports sedan, a vehicle possessing new values and attractive features and combining the quality of a luxury vehicle with driving pleasure. The 2005 LEGEND is worthy of taking its place as a part of Honda's ultimate luxury sedan brand.

This project succeeded with the generous assistance of many individuals from Honda and other companies. The authors wish to take this opportunity to thank all those who offered their assistance in the project.

References

(1) Yoshimoto, T., Taguchi, Y.: Innovative Body Structure for Compatibility, 2004 JSAE Annual Congress Proceedings, No. 45-04, p. 11-14 (2004)

(2) Hayashi, N., Ando, K., Kashiwagi, M.: Development of Aluminum Hood for 2005 Model Year LEGEND, Honda R&D Technical Review, Vol. 16, No. 2, p. 17-22

(3) Asanuma, N., Kawai, M., Takahashi, A., Tsuji, T.: Introduction of HONDA ASV-2 (Passenger cars), HONDA R&D Technical Review, Vol. 12, No. 2,p. 1-8

(4) Tsuji, T., Hattori, H., Watanabe, M., Nagaoka, N.: Development of Night Vision System (Collision avoidance system to the pedestrian), Honda R&D Technical Review, Vol. 13, No. 1, p. 151-158

(5) Kunii, R., Iwazaki, A., Atsumi, Y., Mori, A.: Development of SH-AWD (Super Handling-All Wheel Drive) System, Honda R&D Technical Review, Vol. 16, No. 2, p. 9-16

(6) Fukuchi, F., Yabane, T., Akiyama, H., Ogawa, T., Iwasaki, H., Hori, I.: Development of Aluminum Subframe Using Hot Bulging and Vacuum Die Casting, Honda R&D Technical Review, Vol. 16, No. 2, p. 23-30

(7) Higuchi, M., Taneda, K., Shibahata, Y., Minagawa, M.: A Theoretical Study of Influence of Roll on Vehicle Dynamics (First Report), Transactions of Society of Automotive Engineers of Japan, Vol. 33, No. 4, p. 121-126

(8) Teruo, M., Uemura, H.: On Development of Vehicle Dynamics by Means of a Digital Computer, SAE paper690233, p. 987-999 (1969)

(9) Ninomiya, J., Ninagawa, M., Orimoto, Y., Nakahara, J.: Measurement Technique of Force Transmitted from Road Surface to Tire during Actual Driving and Application, HONDA R&D Technical Review, Vol. 9, p. 148-155

(10) Misaji, K., Tada, H., Yamashita, T., Kokabu, S., Tanaka, H., Koshigoe, S.: Hybrid SEA Modeling Scheme for Analysis of High-Frequency Noise in Passenger Car, 2004 JSAE Annual Congress Proceedings, No. 72-04, p. 13-18 (2004)

■ Authors ■


Masahiro WATANABE


Masafumi TAKITA


Junichi FUKUDA


Takefumi NAKAMURA


Yasunori OKU


Syoichi NEMOTO

Development of SH-AWD (Super Handling-All Wheel Drive) System

Rikiya KUNII* Akihiro IWAZAKI*
Yoshihiro ATSUMI* Atsushi MORI*

ABSTRACT

In a world first, Honda has developed the SH-AWD (Super Handling-All Wheel Drive) system, enabling complete control of torque distribution to any wheel, front or rear, left or right.

A direct electromagnetic clutch in which solenoid attraction acts directly on the clutch was newly developed to enable the system to be realized. In addition, a 2-speed shift unit was developed to adjust differential revolutions in the clutch in order to enable the system to exert control under all conditions.

The use of this system in a vehicle provided incredible neutral steering and high vehicle stability by direct control of turning yaw moment through differential distribution of torque to the right and left wheels. The vehicle also experienced enhanced cornering limit performance by equalization of the load ratio between the wheels through differential distribution of torque to all four wheels.

1. Introduction

Recently, along with the increasingly high output of vehicles, there has arisen a tendency for a four-wheel drive train to be adopted instead of a two-wheel drive train. Conventional four-wheel drive trains have been devised in a variety of forms and put into practical application. Generally, a four-wheel drive train that places emphasis on vehicle maneuverability has low traction capability. Additionally, a four-wheel drive train that emphasizes traction is difficult to enhance cornering performance. In order to solve these issues, systems that electronically distribute the drive force between the front and rear wheels, and also systems that distribute the drive force between the left and right rear wheels, have been devised and put into practical application[1]. However, there was no known system that enabled both the front and rear wheel drive force and the left and right rear wheel drive force to be freely varied.

The results of analysis by β-Yaw Moment Diagram[2] indicated that direct control of yaw moment utilizing the difference in the lateral drive forces was effective for enhancing cornering performance and stability. This was verified in 1997 by means of an Active Torque Transfer System (ATTS)[3] mounted in a vehicle.

This paper describes the development of the SH-AWD system, the world's first four-wheel drive system that freely controls both the left to right distribution and front to rear drive forces, in order to increase the cornering performance and stability to the maximum limit. This system, which is based on the high drive performance of the four-wheel drive vehicle, employs direct control of yaw moment utilizing the difference in the left and right drive forces, in order to help minimize changes in the behavior of the vehicle when the accelerator pedal is pressed during cornering. In addition, the front and rear drive forces are distributed according to the engine torque and longitudinal acceleration, thus reducing tire slip when the accelerator is abruptly depressed.

A study was carried out with a view to adopt this system in the new LEGEND/ACURA RL, that was announced in the autumn of this year, to help reduce the necessity of carefully depressing the accelerator pedal and correcting the steering according to driving situations and road conditions, thereby reducing the burden on the driver. Accordingly, the development concept decided upon for the SH-AWD system was the realization of "neutral steering feel" turning characteristics that more accurately matched the intention of the driver.

2. Drive Force Control Theory

The maneuverability of a four-wheel drive vehicle is enhanced when a system that permits distribution of the drive

* Tochigi R&D Center

force between the rear wheels and also distribution of the drive force between the front and rear wheels is used. This is because such a system enables the yaw moment to be controlled directly and can also maintain a uniform load on each of the four wheels. This theory is explained below.

2.1. Effectiveness of Difference in Lateral Drive Force

2.1.1. Yaw moment control

The basic control logic is assigned by Eqs. (1) and (2). The left and right drive forces applied to the rear wheels is controlled according to both the longitudinal acceleration and the lateral acceleration, enabling changes in the behavior of the vehicle (understeering and oversteering) to be reduced both during acceleration and deceleration[4].

$$X_1 = \left(\frac{D_R}{2} + \frac{h}{tr} \cdot \frac{Y_G}{g} \right) \cdot \frac{W \cdot X_G}{g} \quad (1)$$

$$X_2 = \left(\frac{D_R}{2} - \frac{h}{tr} \cdot \frac{Y_G}{g} \right) \cdot \frac{W \cdot X_G}{g} \quad (2)$$

Where,

X_1 (X_2) : Drive force on the outside (inside) rear wheel
D_R : Rear wheel drive force distribution ratio
W : Weight of vehicle
Y_G : Lateral acceleration
X_G : Longitudinal acceleration
G : Acceleration of gravity
H : Height of center of gravity
Tr : Tread of rear tire

2.1.2. Reduction of the cornering force on the front wheels

While a vehicle is cornering, a yaw moment is applied to the vehicle, causing the cornering force on the front and rear wheels to change. Figure 1 shows a diagrammatic representation of this condition, and Eqs. (3) and (4) indicate the total cornering force on the front and rear wheels. The total cornering force on the front wheels is reduced in the amount M/l, and that on the rear wheels is increased in the amount M/l.

$$CF1 = \frac{b}{l} F - \frac{M}{l} \quad (3)$$

$$CF2 = \frac{a}{l} F + \frac{M}{l} \quad (4)$$

Where,

$CF1$ ($CF2$) : Front wheel (rear wheel) total cornering force
M : Yaw moment generated by the difference between the left and right drive forces
F : Centrifugal force

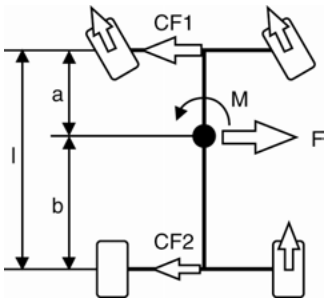


Fig. 1 Change of cornering force

2.1.3. Increase of cornering force

In a conventional drive system, the drive force on the left and right wheels is distributed evenly. As a result, tire friction is used as the main drive force, particularly on the inside wheel, hence only a small cornering force is generated.

By distributing a larger drive force to the outside wheel than the inside wheel when the vehicle is cornering, it is possible to generate a larger cornering force at the inside wheel as well.

The drive force during cornering and also the cornering force are indicated using a friction circle as below. Figure 2 (a) is applicable to a normal vehicle, and (b) to a vehicle that employs the SH-AWD system.

Figure 3 shows the cornering force versus torque distribution ratio on the inside and outside wheels. It can be seen that compared to an equal (50:50) distribution, the total cornering force on the left and right wheels increases as an increasing proportion of the drive force is applied to the outside wheel.

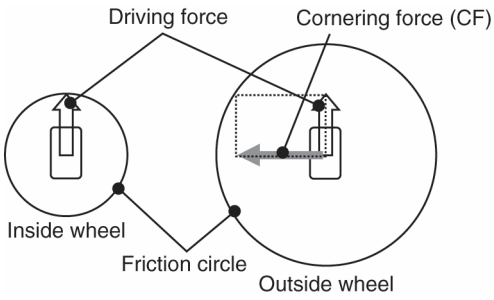


Fig. 2 (a) Tire force for conventional vehicle

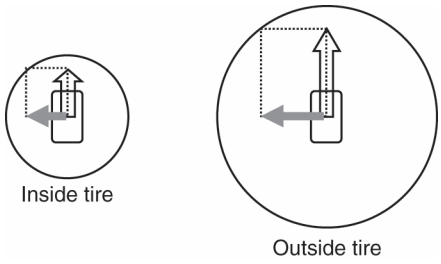


Fig. 2 (b) Tire force for SH-AWD

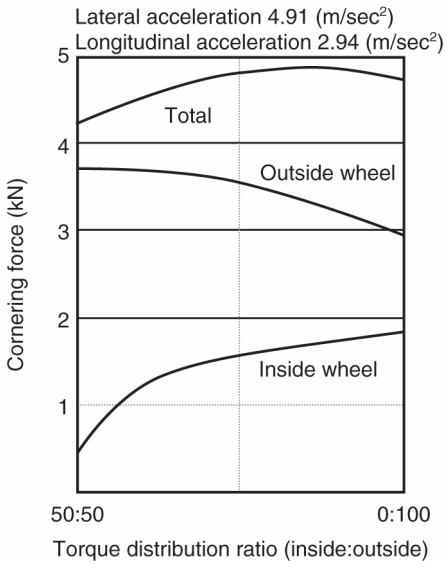


Fig. 3 Effect of torque distribution

2.2. Equalizing the Tire Load on the Four Wheels

The ground contact load and the force generated at the tires change according to the degree of acceleration and cornering. The tire load ratio is defined by Eq. (5) as the ratio of the generated force to the maximum force that can be generated.

$$\eta = \frac{\sqrt{F_x^2 + F_y^2}}{\mu \cdot W} \qquad (5)$$

Where,

H : Tire load ratio
F_x : Tire drive force
F_y : Tire side force
M : Road surface coefficient of friction
W : Tire ground contact load

Figure 4 shows the change of the tire load ratio with respect to the lateral acceleration. By equalizing the load ratio at the four wheels, it is possible to increase the lateral acceleration that can be generated, to the maximum limit, and thus enhance the cornering performance.

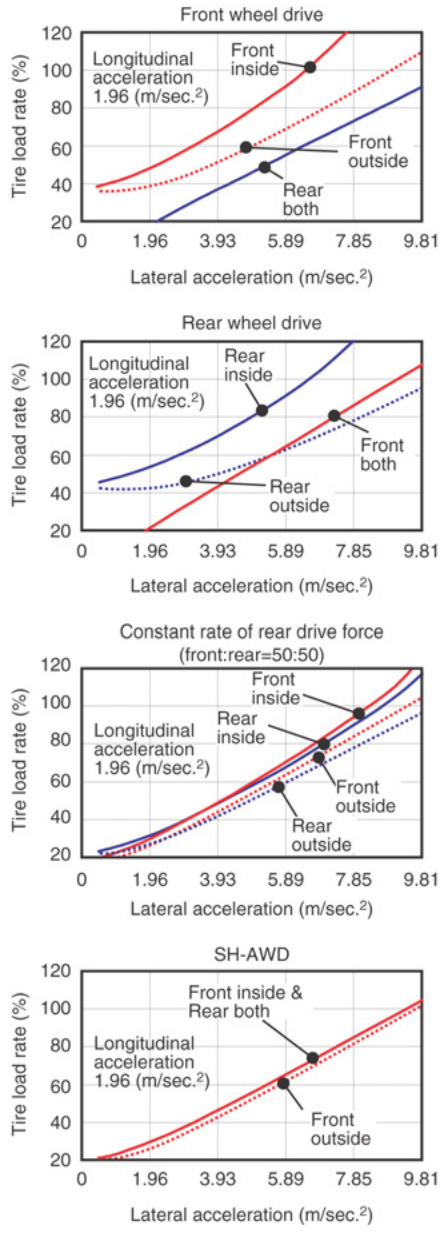


Fig. 4 Load rate of each wheel

3. SH-AWD System

The following describes the principle of this system and the control method used.

3.1. System Configuration

Figure 5 shows the configuration of the vehicle system. In this system, data from the various sensors is inputted to a dedicated ECU (SH-AWD ECU) from the other ECUs via CAN communication. When this dedicated ECU detects the intention of the driver and the driving situation, the rear drive unit distributes the drive force to the left and right, and increases the rotational speed to the rear wheels. The rear drive unit is located at the rear of the propeller shaft and is controlled by instructions from the dedicated ECU.

Figure 6 is a cross-sectional diagram of the rear drive unit.

This unit consists of a two-speed shift unit which increases the input speed from the propeller shaft when the vehicle is cornering, a hypoid gear which converts the input rotation from the two-speed shift unit into the rotational speed of the left and right wheels, and a pair of direct left and right electromagnetic clutches that accurately control and distribute the drive force.

By applying more drive torque to the outside rear wheel when the vehicle is accelerating during cornering, an inward yaw moment is generated, reducing understeering. In the rear drive unit, the outer clutch of the left and right clutches, mounted on the rear wheel axle, is pressed harder. This enables more drive force to be applied to the outside rear wheel. This is how the above mentioned condition is attained.

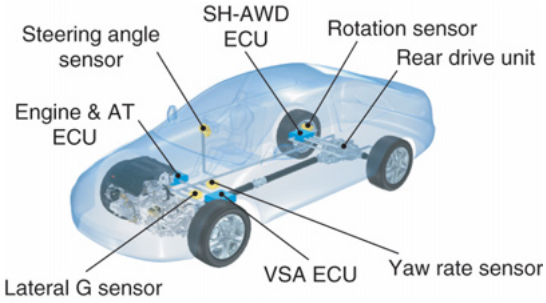


Fig. 5 System layout of SH-AWD system

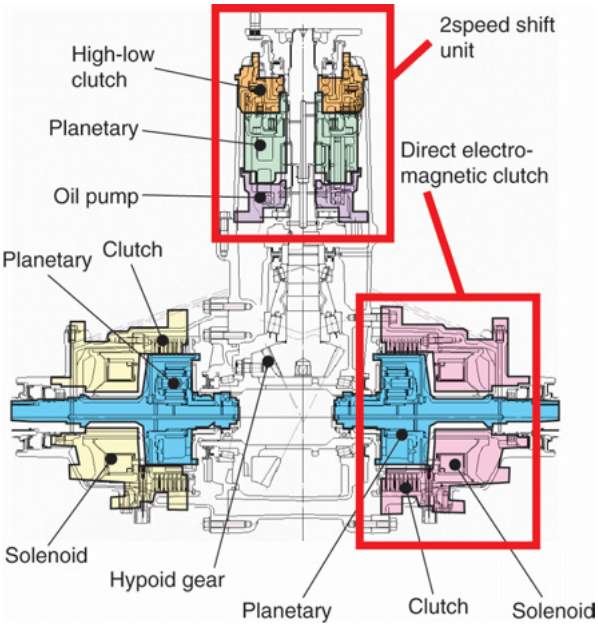


Fig. 6 Cross-section of rear drive unit

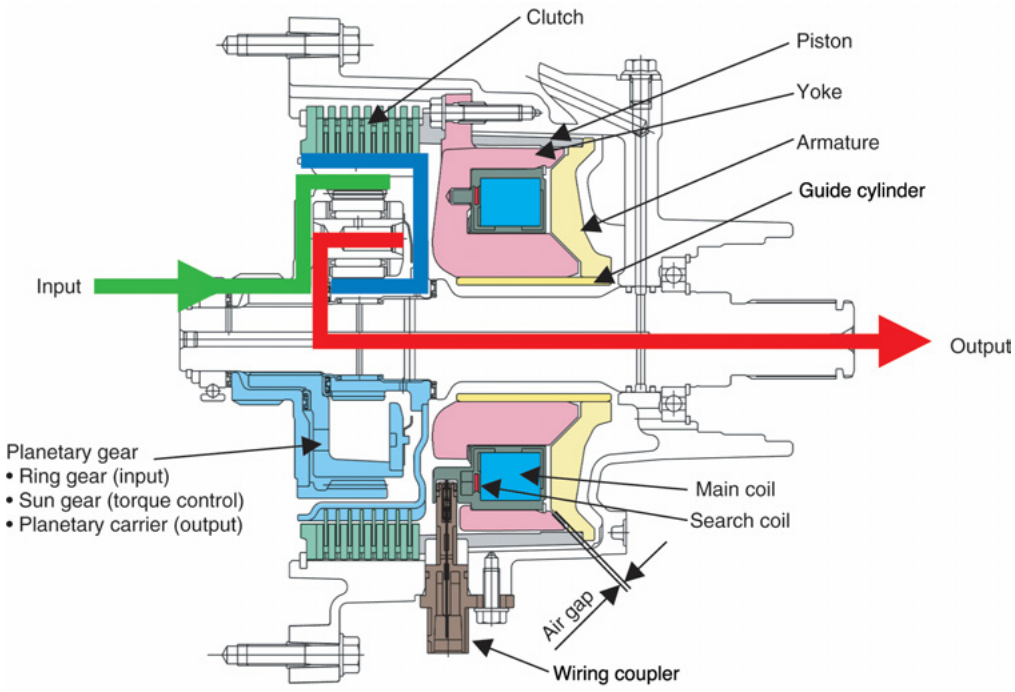


Fig. 7 Direct electromagnetic clutch section

3.2. Direct Electromagnetic Clutch

The electromagnetic clutch determines the drive force of the SH-AWD. It is required to have low hysteresis and linear torque characteristics. Therefore, the clutch is constructed in such a way that the transfer path of the attraction force is simplified. Also the attraction force generated by the electromagnetic solenoid acts directly on the clutch, thus minimizing elastic deformation.

3.2.1. Construction

Figure 7 shows the construction of the electromagnetic clutch. The magnetic circuit is formed by the armature and yoke. A low-hysteresis magnetic material was selected. The slider, which is press-fitted into the armature, centers the armature with respect to the yoke. It is made of non-magnetic material so that it does not form part of the magnetic circuit. A magnetic field is generated by energizing the electromagnetic coil fixed to the inside of the yoke. The yoke is subjected to a reactive force, created by the attraction force that acts across the air gap, because it is fixed to the side case. The attraction force generated at the armature acts directly on the clutch via the piston.

The torque from the propeller shaft is transmitted to the ring gear via the hypoid gear. The clutch is pressed by the armature via the piston, causing frictional force to be generated between the case and the sun gear. As a result, the torque input to the ring gear is boosted by the planetary gear set. The transmission torque of the clutch is multiplied by the planetary gear and outputted to the drive shaft via the planetary carrier. This torque amplifier enabled the electromagnetic clutch to be minimized in size.

The shape of the electromagnetic coil inside the search coil was selected so as to prevent ingress of lubricating oil. This was done by removing the fixing pin of the internal coil, during the resin molding process, in order to eliminate the resin boundary face. As a result, reliability was obtained, which ensures positive operation under the severe environment inside the rear drive unit.

3.2.2. Electromagnetic solenoid

The direct electromagnetic clutch was constructed so that the attraction force acted directly on the clutch. As a result, the air gap between the yoke and the armature changes due to the wear of the clutch, affecting the torque characteristics versus current. Figure 8 shows the empirical results of the torque characteristics versus the air gap for different magnetic circuit profiles (tapered and flat). By using a tapered magnetic circuit, stable torque characteristics with respect to changes in the air gap were obtained. It was also possible to obtain a higher attraction force over the range of the gap used.

Figure 9 shows the relationship between magnetic flux and torque. There is correlation between them, so it is possible to estimate the torque from the magnetic flux.

Here, in order to measure the magnetic flux, a method employing a search coil was developed. Concretely, this method detects the magnetic flux from the voltage generated in the search coil when the prescribed current is passed through the main coil. Figure 10 is a map that shows the relationship between the current, magnetic flux and torque.

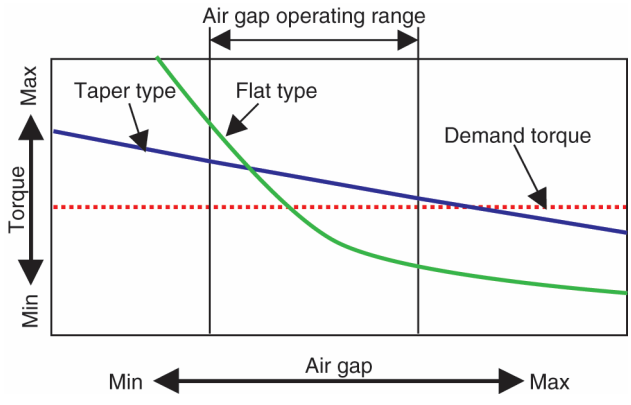


Fig. 8 Air gap-taper/flat torque characteristic

Based on the detected magnetic flux, the current that flows in response to the target torque is obtained from the above map. By correcting this current, it was possible to obtain correlation between the target torque and the actual torque for different air gaps. Figure 11 shows the test results when no correction was made, and Fig. 12 the results when correction was made.

3.2.3. Clutch

In order to fully control torque transmission, the clutch is continuously slip-controlled. The slip ratio is determined by the differential rotation of the front and rear wheels, so it is affected by the vehicle speed and the slip of the tires. If the friction characteristics are not stable, unpleasant vibration will occur.

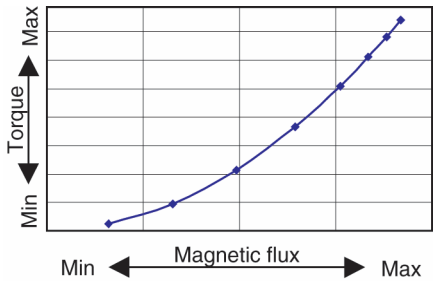


Fig. 9 Magnetic flux-torque characteristic

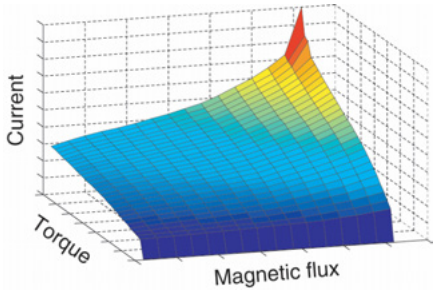


Fig. 10 Current-torque magnetic flux map

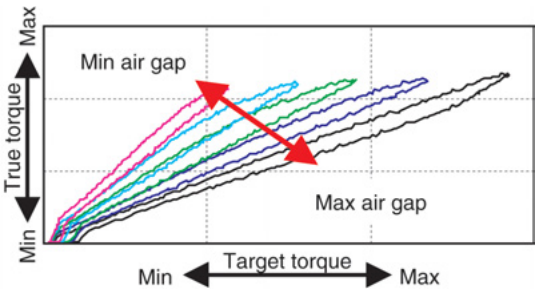


Fig. 11 Torque characteristic without magnetic flux correction

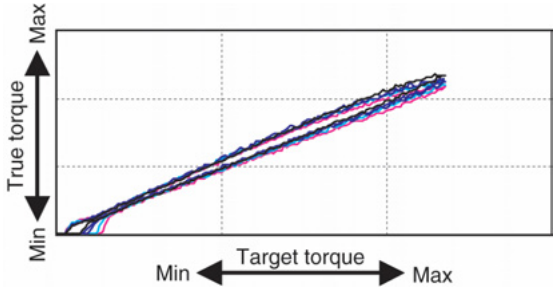


Fig. 12 Torque characteristic with magnetic flux correction

Also, as the clutch wears, the gap between the yoke and the armature will decrease until the yoke and armature strike each other, preventing an attraction force from being generated. If the air gap is made sufficiently large in order to prevent this, the torque capacity will fall, as can be seen from Fig. 8. Consequently, it is necessary that the clutch has stable friction characteristics and wear resistance.

The area where the surface pressure is low is advantageous for obtaining stable torque characteristics. For this reason, the previously mentioned torque amplifier was used to reduce the pressing load of the clutch, permitting the area where the surface pressure was lower than that of the AT and CVT to be used, as shown in Fig. 13.

Figure 14 shows the relationship between the absorbed energy and the clutch abrasion. The clutch abrasion is initially high, so an initial familiarity process was added to reduce initial abrasion.

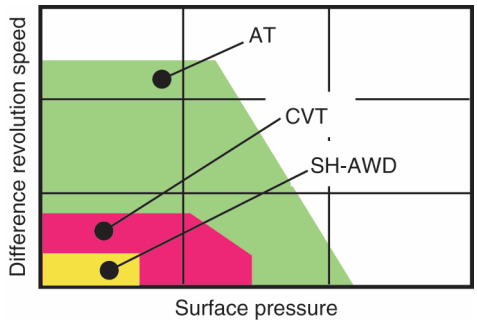


Fig. 13 Surface pressure image

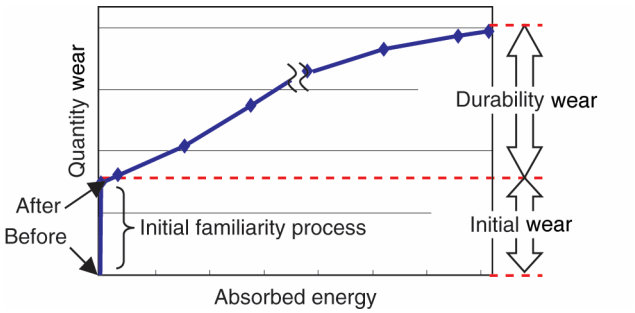


Fig. 14 Quantity of clutch wear

3.3. Principle of High Range

Figure 15 shows the trace line of the four wheels during cornering. The trace line of the outside rear wheel is outward of the average trace line of the front wheels. Figure 16 shows the ratio of the outside rear wheel velocity to the average velocity of the front wheels, versus the angle of front wheel. As soon as the vehicle corners, the outside rear wheel rotates faster than the average velocity of the front wheels. When the clutch is engaged in this condition, the outside rear wheel decelerates. In other words, resistance is generated with respect to the road. In order to avoid this, it is necessary to increase the speed of the propeller shaft and transmit this increase to the rear wheels. For this reason, it was decided to install a two-speed shift unit in all vehicles fitted with a SH-AWD system.

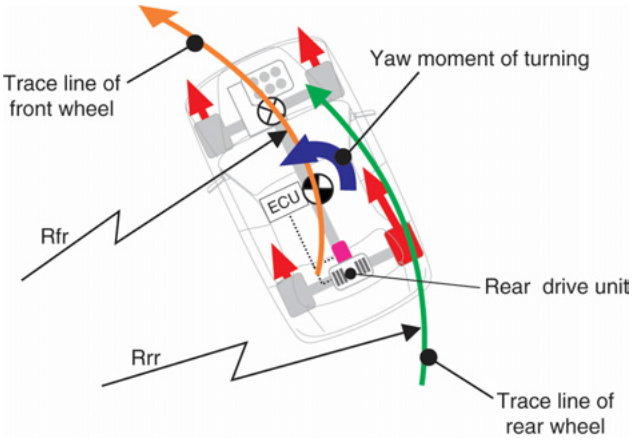


Fig. 15 Movement of vehicle in turning

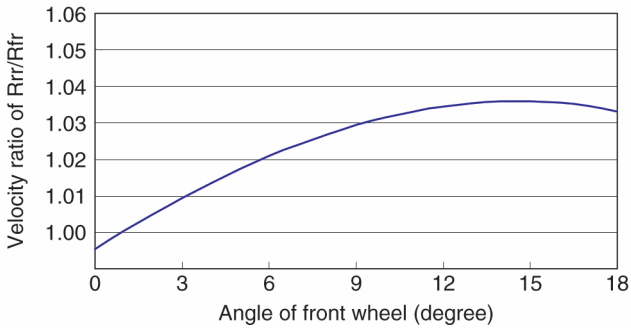


Fig. 16 Velocity ratio of rear to front wheel

3.4. Two-speed Shift Unit

It is necessary to reduce minimize the two speed shift unit size because it is installed under the bottom of the fuel tank and to ensure that there is adequate clearance above the ground. In order to realize this, the unit was designed so that the two clutches could be switched over with a single hydraulic actuator. A planetary gear, one-way clutch and a dedicated reversing clutch were also used.

3.4.1. Construction

Figure 17 is a cross-sectional diagram of the two-speed shift unit. The unit consists of a sun gear on the input shaft and a sun gear on the output shaft which have different numbers of teeth, a twin pinion consisting of a combination of two pinion gears which mesh with these sun gears, a planetary carrier which supports this twin pinion, a one-way clutch and low clutch which couple the planetary carrier to the input shaft, and a high clutch which couples the abovementioned carrier to the case.

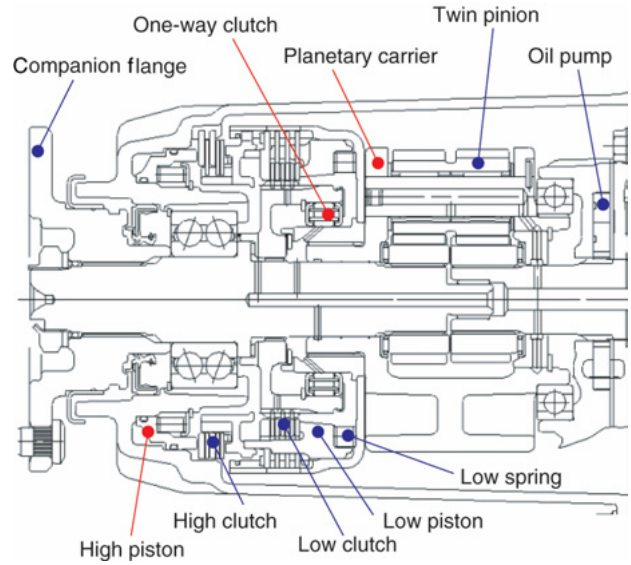


Fig. 17 Cross-section of 2speed shift unit

When the vehicle is moving forward, the low clutch is pressed to the low spring via the low piston, causing it to engage. As a result, the planetary carrier and input shaft rotate as one body in a low range state. The pinion gear does not revolve about its own axis, but instead revolves together with the carrier.

When the vehicle is cornering, the high piston, built into the case, generates a load by hydraulic pressure. As a result, the high clutch is pressed, causing it to engage, and also the low spring is compressed via the low piston, causing the low clutch to disengage. When the high clutch engages, the planetary carrier is fixed to the case, causing the pinion gear to stop revolving. Along with this, the pinion gears mesh with the sun gears on the input and output shafts, and rotation begins. The difference in the gear ratio at these two points results in a high range condition.

The one-way clutch was assembled in a manner such that the planetary carrier does not overtake the rotation of the input shaft when the vehicle is advancing. As a result, the carrier and the input shaft rotate as one body when the vehicle is accelerating in the forward direction. For this reason, the unit was constructed in such a way that it had a low range function, and did not prevent the carrier from being fixed when the vehicle was accelerating. The low range function, used when the vehicle is accelerating in the forward direction, is performed by the one-way clutch, which enables the size of the dedicated engine brake clutch intended for reversing and decelerating to be minimized.

3.4.2. Hydraulic control system

Figure 18 shows the hydraulic circuit diagram.

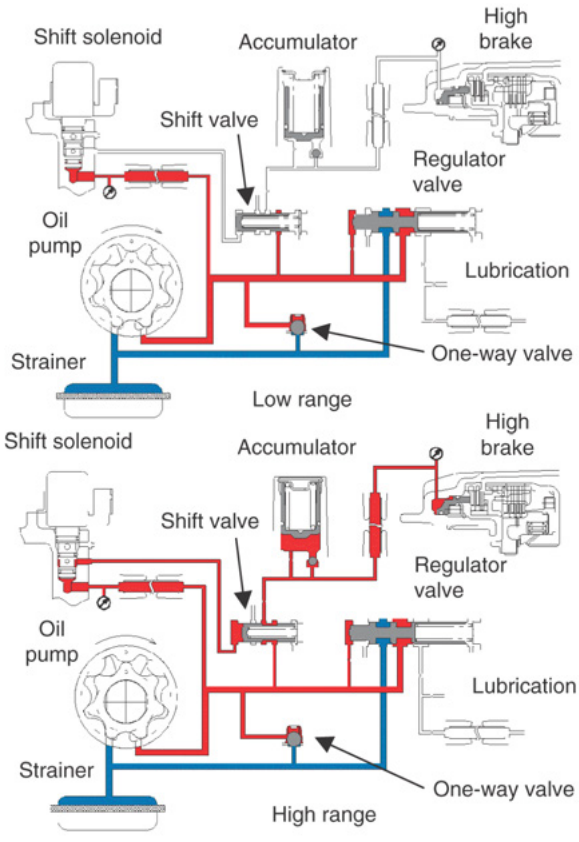


Fig. 18 Diagram of hydraulic circuit

This system consists of an oil pump that rotates together with the propeller shaft, a regulator valve that regulates the line pressure, a shift valve that switches between one clutch and the other, a solenoid that controls the shift valve, a hydraulic accumulator, and a one-way valve.

The oil that is discharged when the pressure is being regulated by the regulator valve was used as lubrication oil. Also, when the pressure of the lubrication oil reaches a certain level, the discharged oil is returned to the inlet port of the oil pump in order to protect the circuit, leveling the amount of lubrication oil and reducing the load on the oil pump.

The solenoid moves the shift valve based on instructions from the dedicated ECU, recirculating the line pressure to the clutch chamber, and controlling the discharge of residual oil in the clutch chamber.

The one-way valve recirculates the oil from the discharge port to the inlet port of the oil pump when the vehicle is reversing. This prevents a delay in response and also the occurrence of cavitation due to inclusion of air in the hydraulic circuit when the reverse-rotating oil pump is switched over to forward rotation. It also prevents the outflow of contaminants from the strainer due to reverse flow.

4. Vehicle Control System

4.1. Control Logic

Figure 19 shows the control flow chart for the SH-AWD. Emphasis was placed on the response of the system, and mainly feed-forward control was used. In feed-forward control, the control quantity is determined based on predetermined vehicle characteristics, which results in the possibility of the control accuracy being reduced by changes in the vehicle characteristics or changes in the environment, such as the road surface. For this reason, logic correction by feedback control was used.

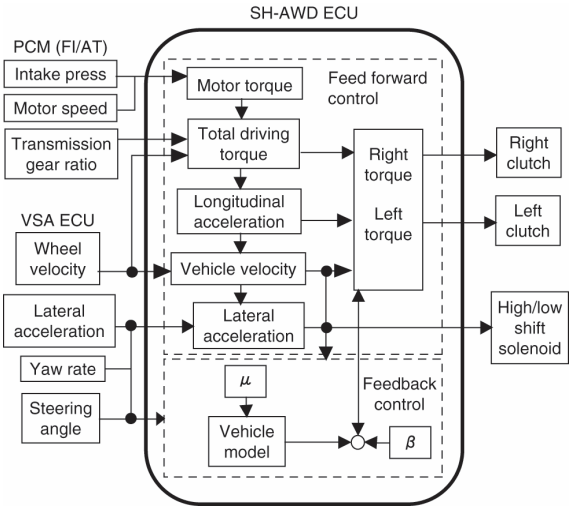


Fig. 19 Chart of control flow for SH-AWD system

4.2. Feed-forward Control

The control flow of feed-forward control is described below.

- The torque generated by the engine is estimated from the engine speed, manifold vacuum, and so on, referring to a preset torque map.
- The total drive torque on the axle is converted from the transmission gear ratio, the torque ratio of the torque converter, and so on.
- The front to rear wheel torque distribution ratio is set according to the driving situations such as running speed, transmission gear ratio, and throttle opening.
- The rear wheel torque is calculated from the total drive torque and front-rear wheel torque distribution ratio.
- The extent of cornering is calculated from the estimated lateral acceleration based on the average velocity of the rear wheels, steering angle, lateral acceleration sensor, and the yaw rate sensor.
- Each of the left and right rear wheel drive torques is calculated based on the extent of cornering.
- Each of the left and right rear wheel drive torques is output to the electromagnetic clutch as a current setting.

4.3. Feedback Control

The control flow of feedback control is described below.

- The vehicle body slip angle at the center of gravity is estimated based on a vehicle model.
- An estimated slip angle is compared to the slip angle threshold that corresponds to the extent of cornering. When the slip angle is judged to be large, output is corrected to reduce the difference between the left and right rear wheel torque values obtained by the feed-forward control.
- In addition, if no tendency for decreased slip angle is observed, a corrected output reduces the ratio of distribution torque on the rear wheels.

4.4. Two-speed Shift Unit Control

High range control is performed only when cornering. In order to judge cornering, the absolute value of the lateral acceleration estimated by feed-forward control is used. The method whereby the estimated lateral acceleration is used enables the cornering motion to be predicted from the driver's input. In this respect, it produces a better response compared to the case where the output from the lateral acceleration sensor is used.

Figure 20 shows the driving situation under which the front wheel average velocity and rear outside wheel velocity are equal when this system is in a low range condition, in terms of the relation between the vehicle velocity and the lateral acceleration. From Fig. 20, it can be seen that the value of the lateral acceleration requiring high range increases in proportion to the vehicle velocity. Consequently, a high range instruction is set to be output at the higher lateral acceleration value in the high velocity range.

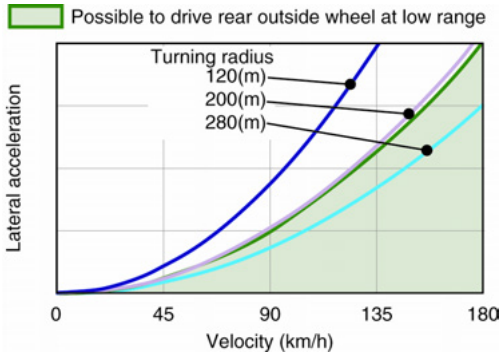


Fig. 20 Wheel speed relation at low range

5. Actual Vehicle Performance

The results of a running test carried out on a vehicle fitted with the SH-AWD are set out below. The vehicle was cornered and slalomed while accelerating. These examples illustrate the effectiveness of this system particularly well.

5.1. Acceleration Cornering Characteristics

A mechanical permanent four-wheel drive vehicle with a center differential that distributed the drive force evenly between the front and rear wheels was used as the comparison vehicle. Figure 21 shows the turning characteristics of the vehicle during acceleration. The vehicle was fully accelerated from a base circle cornering condition (steady state) in which the vehicle was moving at a very low fixed speed and a fixed steering angle, and the spread of the turning radius was evaluated in terms of the rate of change with respect to the base circle radius. It was found that a vehicle fitted with the SH-AWD produced a lower increase in turning radius and significantly less understeer compared to the comparison vehicle. In addition, the limit lateral acceleration at which cornering was possible increased significantly.

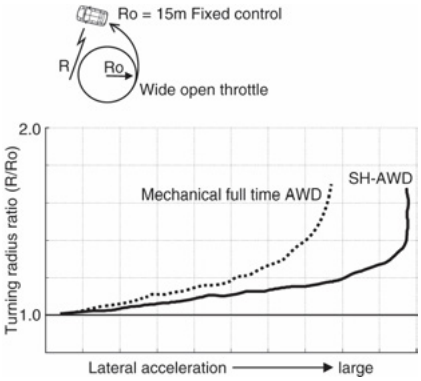


Fig. 21 Turning radius ratio against lateral acceleration

5.2. Slalom during Acceleration

The yaw rate response with respect to the steering angle when the vehicle was slalomed while abruptly accelerating was evaluated. Figure 22 shows the results for a front wheel drive vehicle, and Fig. 23 shows the results for a vehicle fitted with the SH-AWD. In the case of a front wheel drive vehicle, it was found that the yaw rate response worsened by continuous steering, and also the gain fell. In contrast, the vehicle fitted with the SH-AWD had better response, and also the divergence of the yaw rate was minimized due to the use of high gain. Thus both enhanced response and stability were achieved. (Shaded area of the figure)

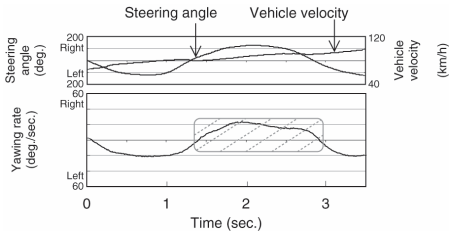


Fig. 22 Result of front wheel drive vehicle

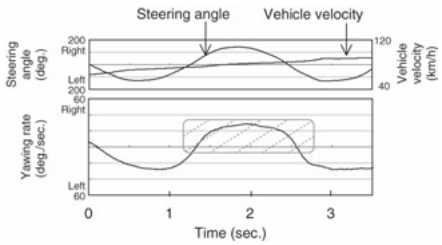


Fig. 23 Result of SH-AWD vehicle

6. Conclusion

By fully controlling the distribution of drive force between the front and rear wheels, and also the drive force of the left and right rear wheels, it was possible to achieve cornering performance that more accurately reproduced the steering operation, and also a high yaw rate response to the steering angle. As a result, a "neutral steering feel" was achieved in which the turning characteristics were a more accurate reproduction of the driver's intent.

Also, as a result of devising current correction control utilizing a direct electromagnetic clutch and search coil, it was found possible to control the drive force with higher accuracy. In addition, the use of a miniaturized two-speed shift unit enabled the unit to be readily installed under the vehicle, thus widening the range of cornering control.

In this SH-AWD development, many new developments were performed concerning each technological element individually. In this paper, an overall description of the system was given. In the future, the authors would like to obtain an opportunity to introduce each technological element independently.

Finally, the authors would like to express their heartfelt appreciation to the people who provided valuable assistance in the development of this system.

References

(1) Tanaka, S., Sawase, K., Takada, K., Sano, R., Okabe, T.: Development of Vehicle Cornering Control System Utilizing Driving/Braking Force Differences Between Right and Left Wheels, Mitsubishi Motors Technical Review, No. 9, p. 40-51 (1995)

(2) Shibahata, Y., Shimada, K., Tomari, T.: The Improve of Vehicle Maneuverability by Direct Yaw Control, Proceedings of the International Symposium on Advanced Vehicle Control, p. 452-457 (1992)

(3) Shibahata, Y., Kuriki, N., Kitamura, K., Honda, K., Wada, K., Kajiwara, H., Mori, A., Kuwahara, K., Ohkuma, S.: Development of Active Torque Transfer System, HONDA R&D Technical Review, Vol. 9, p. 70-79

(4) Shimada, K., Shibahata, Y.: Analysis of Vehicle Maneuverability by β-Yaw Moment Diagram, Transactions of Society of Automotive Engineers of Japan, No. 25, p. 122-127 (1994)

■ Authors ■


Rikiya KUNII


Akihiro IWAZAKI


Yoshihiro ATSUMI


Atsushi MORI

Development of Aluminum Hood for 2005 Model Year LEGEND

Noboru HAYASHI* Katsutoshi ANDO* Masakazu KASHIWAGI*

ABSTRACT

An aluminum hood was developed for the 2005 model year LEGEND in order to reduce cost while maintaining durability and performance requirements and help ensure pedestrian safety.

We focused on materials cost reduction for the aluminum hood skin sheet by reviewing its chemical composition and developing a 5000 series alloy produced with the continuous casting rolling method for the stiffener sheet.

Planning for general purpose processing specifications, a PVC-free acrylic acid resin system mastic sealer for steel and aluminum was applied for adhesion between the various components. Continuous multipoint self-piercing rivets were applied for the reduction of machining costs. The surface was treated with a surface conditioner that has a zinc phosphoric crystal as its main component. This allowed for the precise formation of a chemical conversion coating on the surface.

The frame structure of this developed hood was also optimized, enabling it to achieve the same performance in pedestrian safety as a conventional steel hood.

1. Introduction

The change to aluminum for external panels on vehicles to improve their dynamic performance and fuel consumption has yielded significant weight-reduction effects. Honda has therefore been applying aluminum hoods to the NSX, S2000, and INSIGHT. However, the application of aluminum sheet resulted in higher material costs than steel sheet, and lower spot weldability, so higher machining costs were an issue. Research was therefore conducted on cost reduction through lower material costs, use of general-purpose machining equipment, and so on. In addition, a hood was developed with an aluminum specification providing the pedestrian safety performance that has been included in every new model announced since the 1998 model year LIFE.

This report introduces these material technologies for aluminum sheet for hoods, adhesive bonding, surface treatment, and pedestrian safety compatibility.

2. Aluminum Hood Components

Figure 1 shows the materials and components of the aluminum hood on the 2005 model year LEGEND. A paint bake hardenable type 6000 series alloy with mechanical properties and formability equal to conventional alloys was used for the hood skin. A 5000 series alloy was used for the hood frame. A 5000 series alloy manufactured by the continuous casting rolling method was also used for the stiffener. PVC-free acrylic acid resin system mastic sealer was used to adhesively bond the hood skin and the hood frame. The hood frame and stiffeners were joined using self-piercing rivets. A surface conditioner with zinc phosphoric crystal as its main constituent was used for chemical treatment of the aluminum hood. The characteristics of the aluminum sheet that makes up the aluminum hood are shown in Table 1.

* Tochigi R&D Center

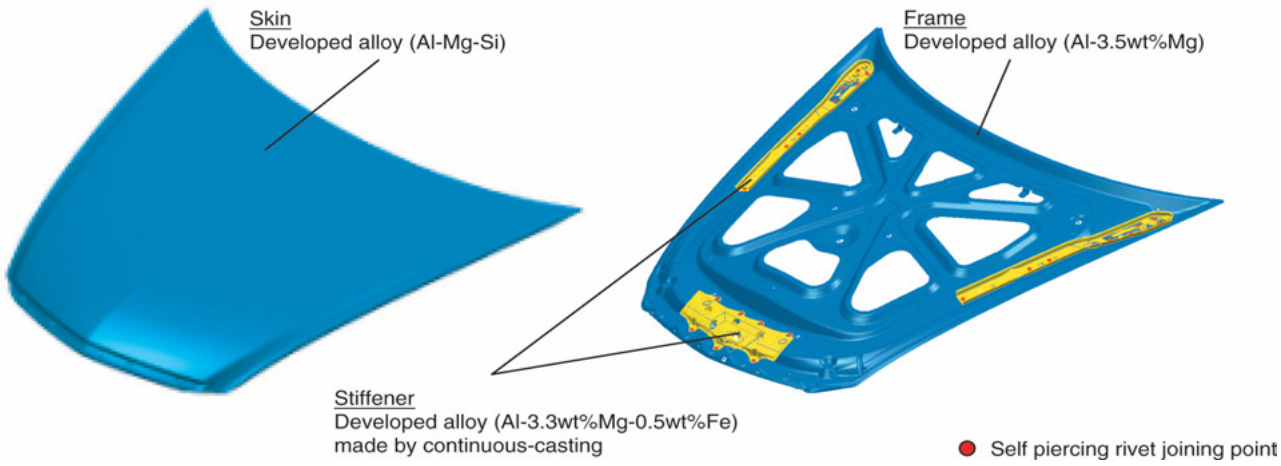


Fig. 1 Aluminum hood component

Table 1 Characteristics of aluminum hood materials

Parts	Yield stress (MPa)	Tensile stress (MPa)	Elongation (%)	Bake hard* (MPa)	Fatigue stress (MPa)	Bending
Hood skin	118	211	30	224	69	5% Stretch 0.5R
Hood frame	123	229	28	———	118	———
Stiffener	128	239	26	———	118	———

* Bake hard : Yield stress after 180°C_×_60min & non stretch

3. Hood Skin and Hood Frame Alloys

A heat treatable 6000 series alloy that was age hardened using the heat of the paint baking process was previously used for hood skin alloys in order to improve their dent resistance. For the developed hood skin alloys, less expensive aluminum ingots containing greater amounts of Cu impurities were used in order to lower the material costs. The Cu impurities in the hood skin alloys used previously were held down to 0.01 wt% or less because corrosion resistance diminished when Cu impurity content was higher. However, the use of improved surface treatment technology for the newly developed alloy made it possible to ensure equal corrosion resistance even when the Cu impurity content was higher. When the Cu impurities reach the 0.10 wt% level, however, a fibrous microstructure remains in the final sheet product because significant recrystallization does not take place after hot rolling. When a sheet has this type of structure, ridging marks (shown in Fig. 2) appear on the surface of the sheet. These marks degrade the appearance quality of the hood. Consequently, the content was kept below a maximum of 0.07 wt%. This level increased the allowable amount of Cu impurities present, and therefore made it possible to lower material costs. A 5000 series alloy with Al-3.5 wt% Mg content for better draw forming with low yield stress was used for the hood frame.

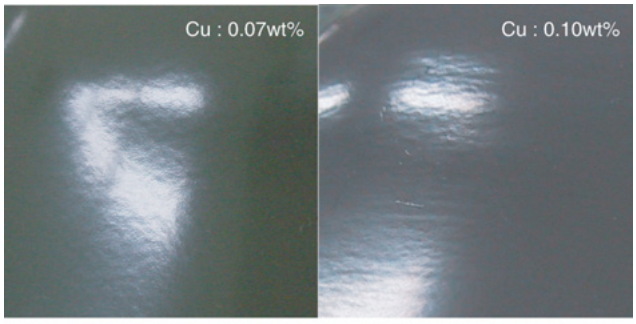


Fig. 2 Ridging mark

4. Stiffener Alloy

A 5000 series alloy manufactured by the continuous casting rolling method was used for the stiffener alloy. The continuous casting directed rolling method is unlike the conventional direct chill slab (DC) rolling method, which uses rolling to process large casting slabs into aluminum sheets, in that it continuously casts 6-mm thick aluminum plate directly from molten aluminum, and rolls it into a coil. In this method, the coil is then rolled to the final thickness to make the aluminum sheet. This method reduces the conventional 11 process steps in manufacturing aluminum sheet to 5 process steps, thereby lowering the material

Table 2 Characteristics of continuous casting alloy

Alloy type	Chemical composition			Mechanical property		
	Mg(wt%)	Fe(wt%)	Mn(wt%)	Yield stress (MPa)	Tensile stress (MPa)	Elongation (%)
A5052	2.6	0.30	0.01	86	198	25
High Fe/Mn	2.6	0.31	0.08	104	214	24
High Fe	2.3	0.39	0.00	82	209	27
High Mg	3.1	0.30	0.01	122	236	27

manufacturing cost. Because the solidification speed of the aluminum during continuous casting is also faster than with the DC method, it is possible to reduce the aluminum grain size as well as the Fe intermetallics within the aluminum matrix. This can affect the elongation of the final sheet product. Figure 3 shows the appearance of the Fe-type intermetallic compounds that crystallize in the alloy matrix of DC sheet and of continuous cast sheet alloys. The crystallized intermetallic compound is smaller in the continuous cast sheet than in the DC sheet. Figure 4 shows the crystallized grains in DC sheet and continuous cast sheet. The crystallized grains in the continuous cast sheet are significantly smaller than those in the DC sheet.

A study was made to determine whether these characteristics of the continuous casting rolling method would allow the use of less expensive ingots (containing more impurities), thus achieving a reduction in material costs. The study used continuous cast sheet based on the chemical composition of A5052 with varying amounts added of Mg, Fe, and Mn, which affect elongation. Table 2 shows the chemical composition and mechanical properties of the continuous cast sheet investigated. When larger amounts of Fe and Mn are present, more coarse Fe-Mn-type intermetallic compounds exist, as shown in Fig. 5(a), and these interfere with elongation. The result is that elongation is diminished. On the other hand, when more Fe was present but there was less Mn, then intermetallic compounds that interfere with elongation did not appear, as shown in Fig. 5(b). Only an extremely minute Fe-type intermetallic compound appeared in these cases, and there was no decrease in elongation. When the amount of Mg was increased, elongation improved as well. These results were used to develop an Al-Mg-Fe-type alloy that can use aluminum ingots containing greater amounts of impurities with a broader range of allowable Fe content, making it possible to reduce material costs.

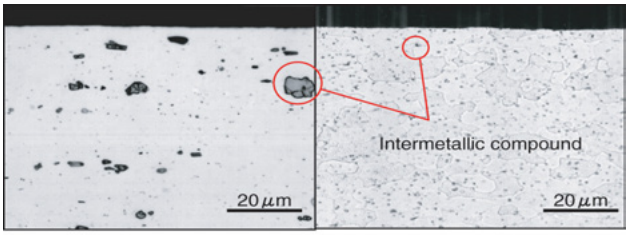


Fig. 3 Comparison of intermetalic compound

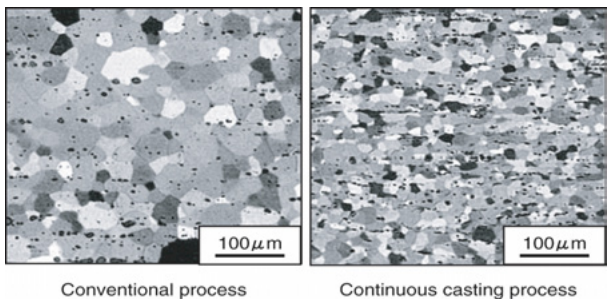
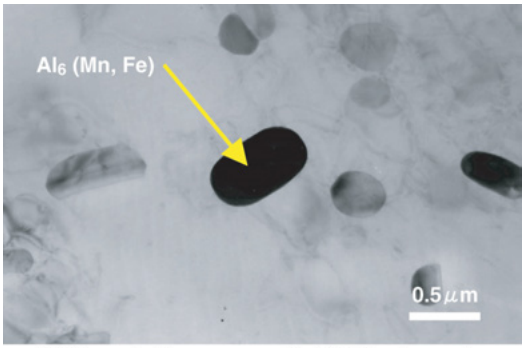
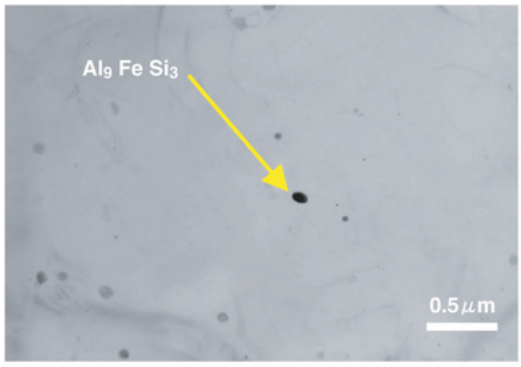


Fig. 4 Comparison of grain size



(a) Intermetallic compound in high Mn -type alloy



(b) Intermetallic compound in high Fe -type alloy

Fig. 5 Transmission electron microscopy photograph of intermetallic compound

5. Adhesive Bonding and Joints

A mastic sealer with acrylic resin as the main formulation that is capable of bonding both aluminum and steel was used for adhesive bonding of the various component parts. Devising new sealer application equipment capable of shared use enabled cost reduction.

Joints were made using self-piercing rivets, raising spot weldability (the number of joint points that can continuously maintain joint quality) performance and reducing the costs of production processing. The self-piercing rivets had a chrome-free coating applied as a rust inhibitor. Figure 6 shows a cross-section of the self-piercing rivet.

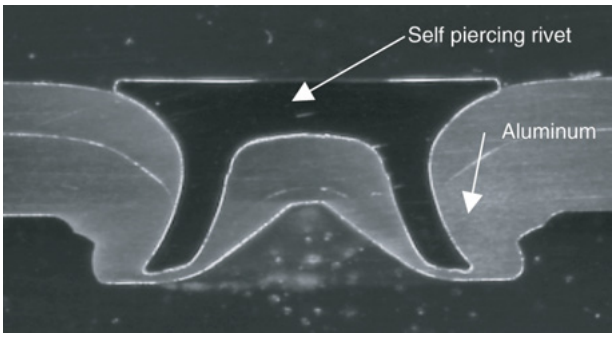


Fig. 6 Self piercing rivet cut model

6. Surface Treatment

Improvement was made to the surface conditioner that controls the formation of the chemical conversion coating during the surface treatment process. Specifically, the principal component of the surface conditioner was changed from Ti colloid to zinc phosphoric crystal in order to increase the crystallization rate of the chemical conversion coating. Figure 7 shows the change over time in the weight of the chemical conversion coating on an aluminum surface. Figure 8 shows a scanning electron microscope (SEM) photograph of the chemical conversion coating. These results indicate that improvement of the surface conditioner promoted the coating deposition reaction and gave the coating greater density. Figure 9 shows the results of filiform corrosion testing following coating. When a conventional surface conditioner is used, the newly developed hood skin with its high Cu impurity content has lower filiform corrosion resistance than a conventional hood skin with its lower Cu impurity content. When the improved surface conditioner is applied, however, it is possible even for the developed hood skin material to have corrosion resistance equal to that of the conventional skin.

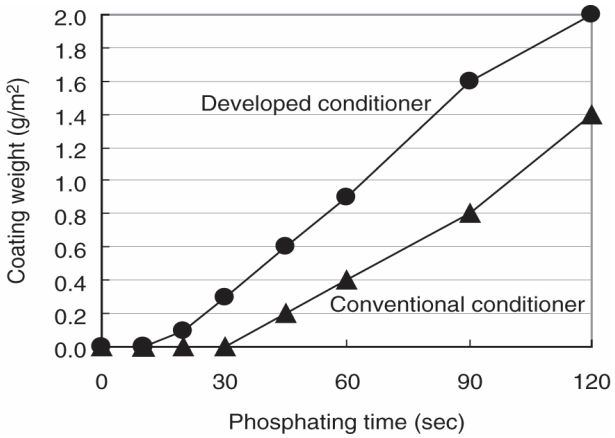


Fig. 7 Relationship between phosphating time and coating weight

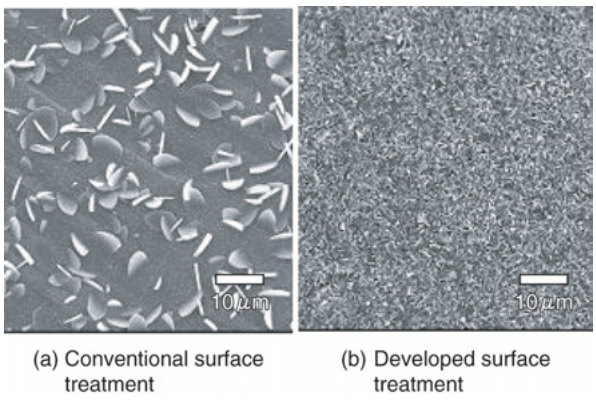


Fig. 8 Comparison of phosphoric acid zinc crystal on aluminum plate

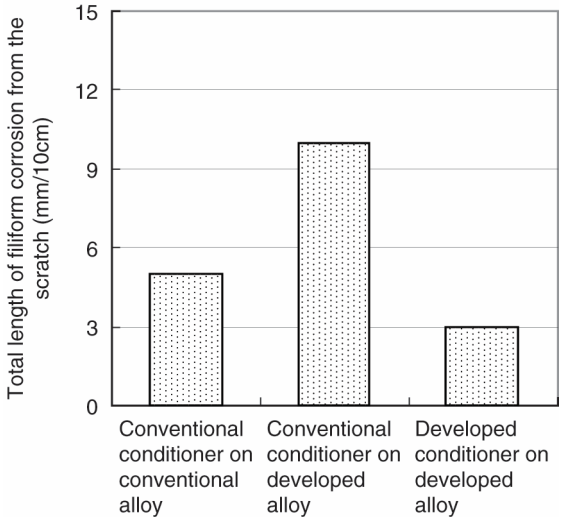


Fig. 9 Result of filiform corrosion test

7. Pedestrian Safety Technology

The deceleration characteristic of a headform impactor (shown as G_I, G_M, and G_B in Fig. 10) representing the collision of a pedestrian's head with the hood was controlled separately for the G_I region, where the hood mass plays a greater role, and the G_M region, where the hood stiffness plays a greater role. Figure 10 shows a comparison of an aluminum hood and a steel hood. In the case of the aluminum hood, G_I and G_M were lower while G_B tended to be higher. Therefore the following two measures were taken so that the hood would absorb the kinetic energy of the headform impactor as efficiently as the conventional hood:

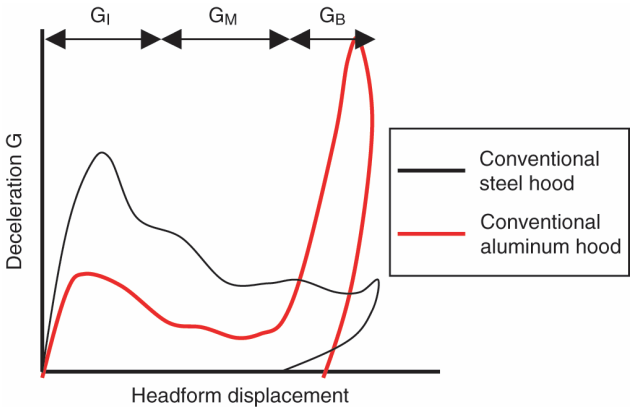


Fig. 10 Relationship between deceleration G and headform displacement

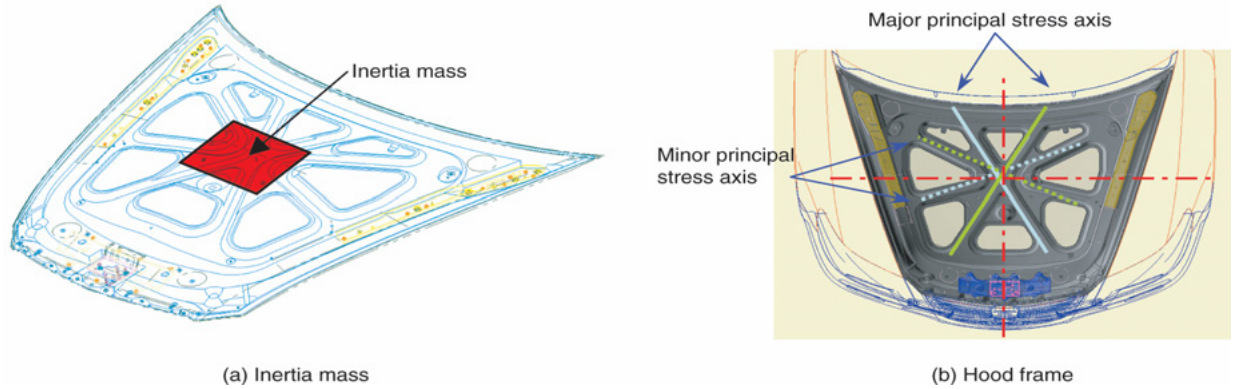


Fig. 11 Pedestrian head impact protection for 2005 model year LEGEND

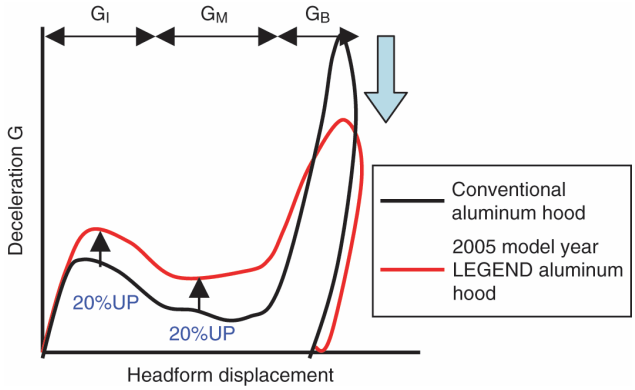


Fig. 12 Comparison of conventional hood and developed hood

(1) A polymer sheet was added to the hood center to increase inertial mass and therefore increase G_I (Fig. 11(a)).
(2) G_M was increased by increasing the hood stiffness (Fig. 11(b)). This was done by laying out the hood frame members so that the direction of the principal stress axis on the hood surface would coincide with frame members in the event of collision against a part of the hood with minimal clearance (clearance between the hood and the engine or intake manifold).

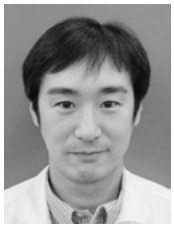
The above measures made it possible to increase G_I and G_M by 20%, and therefore to reduce G_B. Figure 12 shows the results.

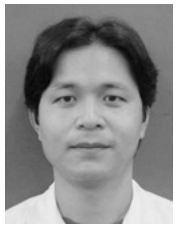
8. Conclusion

An aluminum hood that provides reduced material costs while maintaining durability and performance requirements and helps ensure pedestrian safety performance was developed for the 2005 model year LEGEND. The various technologies applied to this aluminum hood are summarized below:

(1) For the aluminum sheet alloy, the chemical composition of the hood skin alloy was given a higher Cu impurity content in order to reduce material costs. A continuous casting rolling method was used for the stiffener alloy. This shortened the sheet manufacturing process and broadened the range of allowable Fe impurity content, making it possible to reduce material costs.
(2) A mastic sealer that is capable of bonding both aluminum and steel was used as the adhesive. Allowing for shared use of general purpose equipment made it possible to reduce costs.
(3) Joints were made using self-piercing rivets with greater spot weldability, making it possible to reduce processing costs.
(4) A surface conditioner with zinc phosphoric crystal as the principal component was used for surface treatment. This made it possible to increase the crystallization rate of the chemical conversion coating. In this way even a hood skin material containing larger amounts of Cu impurities could provide corrosion resistance equal to conventional material. This made it possible to reduce material costs.
(5) For pedestrian safety, a polymer sheet for inertial mass was added to the aluminum hood and the hood frame structure was optimized. This allowed us to reduce the peak G caused by the impact of the engine parts through the hood.

■ Authors ■


Noboru HAYASHI


Katsutoshi ANDO


Masakazu KASHIWAGI

Development of Aluminum Subframe Using Hot Bulging and Vacuum Die Casting

Fumiaki FUKUCHI* Takanori YAHABA* Hiroshi AKIYAMA*
Tsutomu OGAWA* Haruyuki IWASAKI* Izuru HORI**

ABSTRACT

The world's first aluminum subframe that is composed of bulge-formed members and die cast members welded by MIG has been developed.

The bulging employed a newly developed hot process with superior formability together with an alloy developed for the hot process. The die casting employed a newly developed vacuum die casting process and alloy which has superior weldability. A method of MIG welding was established after the weldability of these new alloys was researched. The developed subframe achieved a 20% cost reduction and 10% weight reduction while keeping functional performance equal to or better than the company's conventional aluminum subframe.

1. Introduction

The achievement of weight savings in automobiles is becoming increasingly necessary in order to contribute to the preservation of the global environment and the conservation of energy resources, in addition to improving dynamic performance. To respond to this need, aluminum subframes which are 35% lighter than conventional steel subframes are already being employed in some models.

However, the aluminum subframes currently in use are assembled by MIG welding with brackets press-formed from aluminum sheets to cradles formed from aluminum pipes at room temperature. The total number of parts used is high and the weld lengths are long, putting limits on the cost reductions that can be achieved.

The aim of the research described in this paper was to reduce costs by integrating parts. Hot bulge forming and vacuum die casting were studied as methods of achieving the desired integration of parts, and materials were optimized for these new production processes. Hot bulge forming is a new bulging method which was developed to enable an increased degree of freedom in the formation of aluminum pipes. Research continued with study of the MIG welding performance of the materials produced using the new methods, resulting in the creation of welding technology.

2. Development Goals

The following development goals were established for the new subframe:

(1) Number of parts: 50% reduction against conventional subframe
(2) Welding length: 50% reduction against conventional subframe
(3) Weight: Equivalent to or lower than conventional aluminum subframe
(4) Cost: 20% reduction against conventional subframe

The project aimed to reduce the number of parts and the welding length by employing hot bulge forming for the members and vacuum die casting for the brackets and the members, enabling parts to be integrated. Figures 1 to 4 show the configuration of the parts of the new subframe, while Tables 1 and 2 show the methods applied in the production of each part.

The subframe supports the suspension and supplements the rigidity of the body, and was therefore required to display an equivalent level of strength and toughness within the suspension, and an equivalent level of impact absorption performance to the body. The positioning of the joints between parts was optimized to enable these requirements to be satisfied. In addition, the integration of parts has increased dimensional accuracy after welding.

* Tochigi R&D Center
** Honda Engineering Co., Ltd.

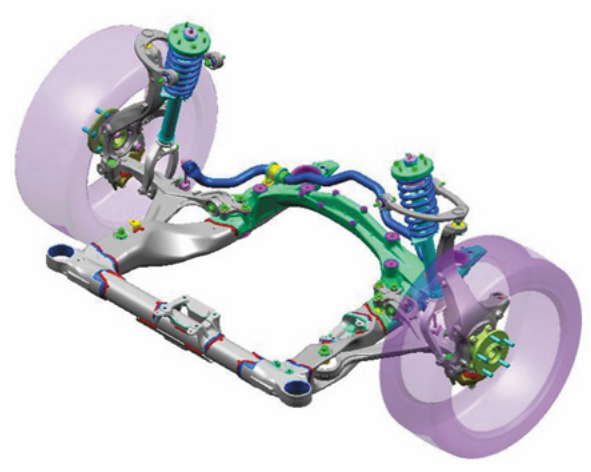


Fig. 1 Front chassis system

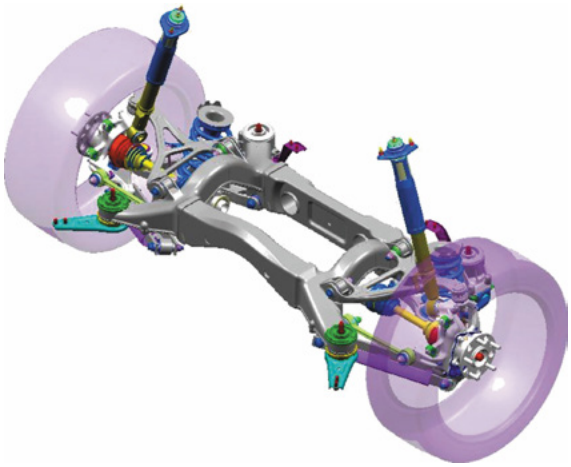


Fig. 2 Rear chassis system

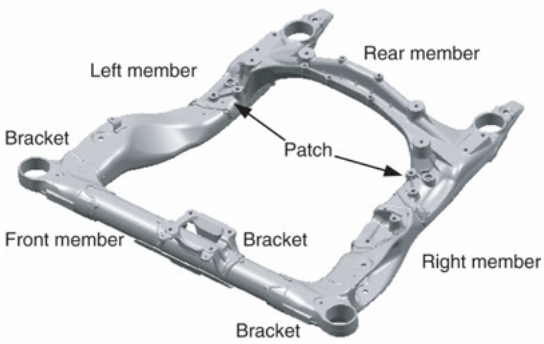


Fig. 3 Front subframe components

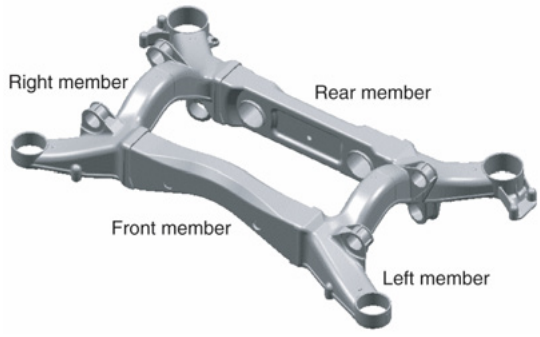


Fig. 4 Rear subframe components

Table 1 Application of process and alloy to front subframe components

Parts	Process	Alloy
Front member	Extrusion	Al-Mg
Rear member	Vacuum die casting	Al-Si-Mg
Left member Right member	Hot bulging	Al-Mg
Brackets	Squeeze die casting	AC4CH-T6
Patch	Stamping	A5052P-O

Table 2 Application of process and alloy to rear subframe components

Parts	Process	Alloy
Front member Rear member	Hot bulging	Al-Mg
Left member Right member	Vacuum die casting	Al-Si-Mg

Weight savings were achieved by increasing rigidity, optimizing the layout of the closed sections, and reducing thickness, chiefly in the structural parts. In particular, the employment of hot bulge forming enabled the sectional modulus of the bulge-formed members to be increased. In addition, the use of die casting enabled the thickness of the die cast members to be reduced and excess thickness to be eliminated.

3. Hot Bulge Technology

3.1. Issues in the Conventional Production Process

Bulge forming is a well established technique in the formation of pipes. The hydro-forming method, which uses liquid pressure in formation, is particularly widely used in the manufacture of subframes, and can be used with all materials. The adoption of this method enabled integrated formation of the cradles, which were formerly produced by welding a large number of pressed parts, considerably reducing the number of parts employed. However, because the conventional bulging process is a plastic forming process conducted at room temperature, in other words a cold process, the formability limit is comparatively low. The ratio of change of circular length (the ratio of the circular length of the original pipe to the circular length after formation) provides an index of formability, and in the case of conventional bulge forming is about 130%. This makes it difficult to achieve further integration of structural parts.

3.2. Development of a Hot Bulging Production Method

To solve this issue, the project focused on the characteristics of aluminum when heated in order to improve formability. As Fig. 5 shows, these studies demonstrated that when aluminum is heated to 510 °C, transformation resistance (pressure resistance) is reduced to 1/10 the figure the material displays at room temperature, and elongation is increased by a factor of six[(1) - (3)].

Exploitation of these characteristics by bulge forming while the pipe is heated (hot bulge) has increased the ratio of change of circular length to 190%, 1.5 times the ratio achieved using the conventional forming method. This has made it possible to form complex shapes and integrate parts.

In addition, the internal pressure during hot bulge formation is less than 1/100 that of hydro-forming, and this has enabled production facilities to be reduced in size.

In the hot bulge forming method, the change in dimension of the material during forming does not give an accurate indication of the thickness of the material after forming, and the reduction in thickness is particularly noticeable in parts with complex forms. To design hot bulge-formed parts, it is therefore necessary to predict the distribution of thickness after forming. A shape simulation technique was developed which takes into consideration the properties of aluminum when heated and the characteristics of the bulge forming process.

Because temperature and the velocity of strain have significant effects on the properties of aluminum, the parameters employed in the analysis were established on the basis of the results of tests of the properties of the material under temperature and strain conditions close to those experienced during actual forming. In addition, the boundary conditions and forming conditions with the most significant effect on the distribution of thickness were identified, and a database of measurements displaying excellent reproducibility was compiled. This research has enabled predictions of thickness accurate to within ±10%. Figures 6 and 7 show a comparison of the result of the prediction of thickness in a simulation and the distribution of thickness in a formed part.

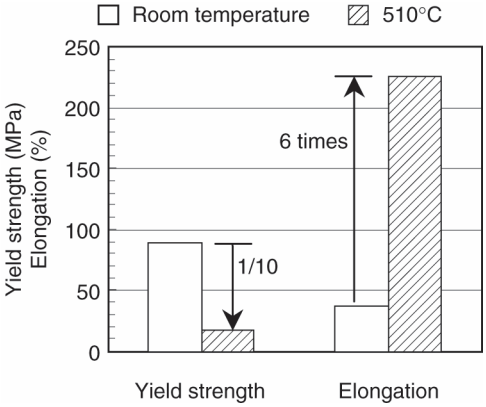


Fig. 5 Influence of bulging temperature on yield strength and elongation

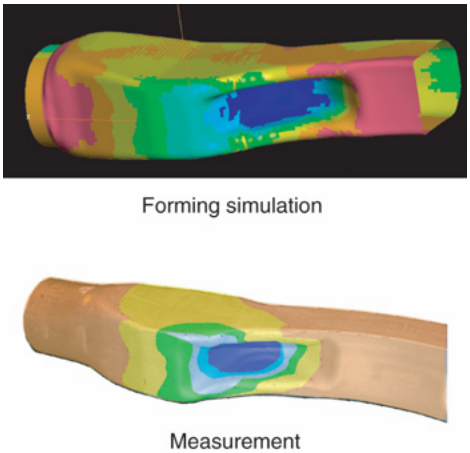


Fig.6 Comparison of thickness distributions by forming simulation and measurement

In addition, an axial inserting procedure has been added to the forming process. The resulting improvement in the flow of the material has been verified as having an effect on controlling the reduction in the thickness of the material following formation. As Fig. 8 shows, increasing the amount of insert replenishes the material and lowers the rate of reduction of thickness. The division of control of internal pressure and the insert stroke into multiple steps has enabled thickness targets to be achieved, in particular in complex shapes. Figure 9 shows the values employed in a simulation of the control program for internal pressure and insert during forming and the results of application of control.

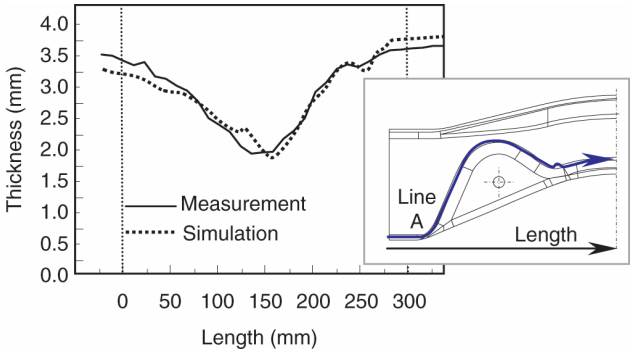


Fig. 7 Thickness distribution on line A

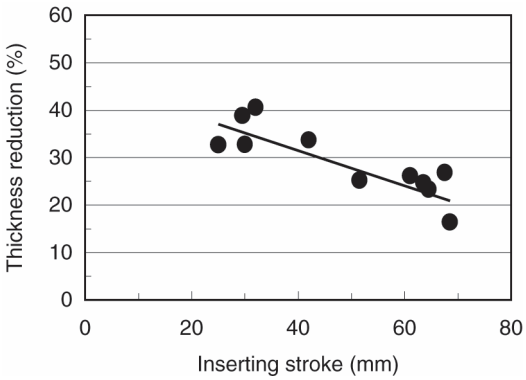


Fig. 8 Influence of inserting stroke

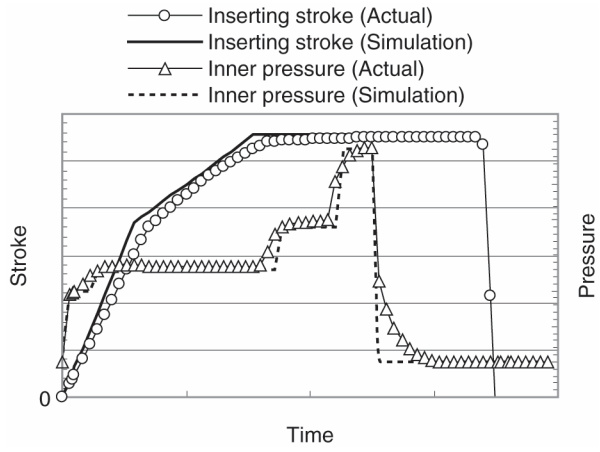


Fig. 9 Control of inserting stroke and inner pressure

3.3. Development of Material for Hot Forming Process

Because there was a possibility that grain growth (abnormal growth of crystal grains) and cavities which would cause material properties to decline might occur during forming if the former materials were employed in the hot bulge process, a new Al-Mg material was developed for use in hot forming.

Because residual stress from the process of formation of the original material and heat energy during heating causes recrystallization in the original material, grain growth is a difficult phenomenon to avoid in heat forming extended materials. In this project, Cr, which has been shown to be effective in grain fining[4], was added to the material to control grain growth. As Fig. 10 shows, grain growth has been controlled through the addition of the optimum amount of Cr. Conditions for the forming process were also studied to control grain growth. The temperature in forming has a significant effect on this phenomenon, as can be seen in Fig. 11, and the temperature at forming and the time taken in the process were therefore optimized.

Cavities are microscopic vacancies originating at the interfaces of intermetallic crystallization phases or triple grain boundary points in the matrix of the original material when it undergoes a large amount of forming process. The black points in the photograph of the aluminum microstructure shown in Fig. 12 are cavities. In studying a means to reduce the occurrence of cavities, the project first determined the upper limit for the cavity ratio (the ratio of the area of cavities to the total area of a surface used in measurements) at which satisfactory materials performance could still be ensured. Next, to enable the occurrence of cavities to be controlled, the relationship between the amount of Fe and Si added and the cavity ratio was clarified. As Fig. 13 shows, reducing the amount of Fe and Si reduces the intermetallic crystallization phases, consequently reducing the cavity ratio. This relationship was employed in establishing the acceptable range for the volume of Fe and Si components.

The techniques discussed above enabled the development of an Al-Mg alloy which displays identical properties to the conventional alloy even after hot forming.

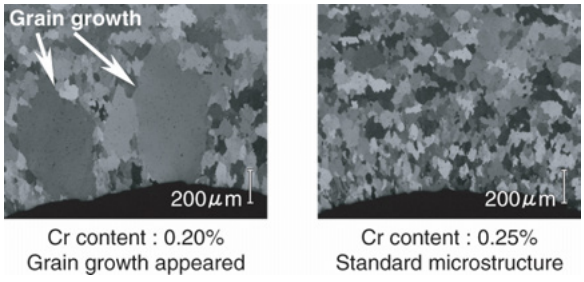


Fig. 10 Influence of Cr content on grain growth

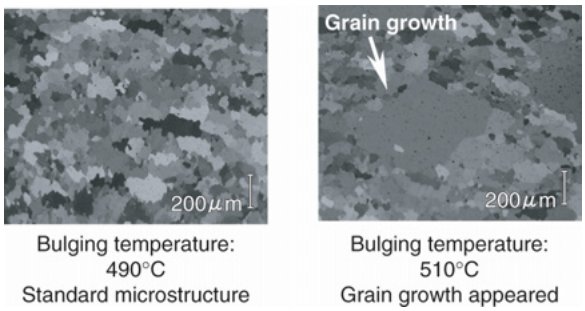


Fig. 11 Influence of hot bulging temperature

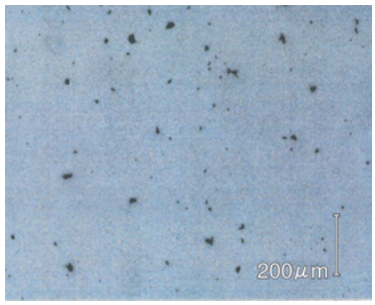


Fig. 12 Cavity in aluminum microstructure

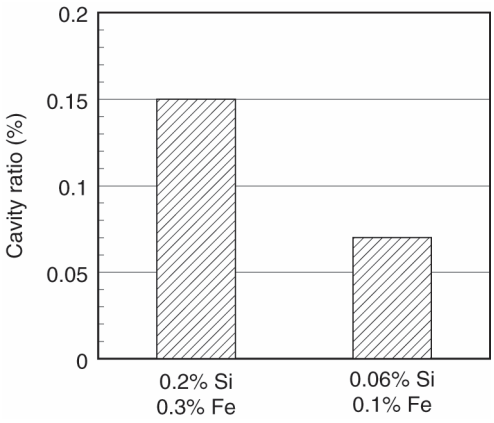


Fig. 13 Influence of Fe and Si content on cavity ratio

4. Vacuum Die Cast Technology

4.1. Issues of Conventional Production Method

The die is filled with molten metal instantaneously, and this makes it difficult to reduce the amount of casting defects such as oxide inclusions and blowhole occurring in the casting and ensure a level of die cast quality appropriate for use in an automotive subframe. In addition, gas is easily trapped in the mold, and the gas content of the casting is normally higher than 20 cm^3/100 gAl. For this reason, when the casting is welded, numerous blowholes occur in the welding bead, and ensuring welding strength is another issue. There are few examples of the use of die casts in a subframe, and even fewer examples of their use in a welded structure.

The following targets were established in this project in order to solve these issues:

(1) Achievement of a high level of casting quality, commensurate with use in an automotive subframe
(2) Development of a die cast alloy with excellent weldability

4.2. Achievement of Casting Quality

The project first studied optimization of mold patterns and casting conditions to enable improvement of casting quality. Figure 14 shows an example of the simulations of the flow of molten metal employed to analyze the effect of the position of the gate and overflow and changes in the casting conditions. Pattern A was predicted to trap a great deal of gas, while in pattern B the molten metal fills the mold uniformly, reducing the amount of trapped gas. The area of the gate was increased to enable filling of the die in a shorter time. In terms of casting conditions, the speed of injection of the metal into the mold has been increased (during high-speed injection, to more than twice the speed employed in the

former method) to fill the mold in a shorter time, and the temperature of the die has been controlled.

Next, to reduce the amount of gas in the castings, the volume of die lubricant and tip lubricant, which produce gas, has been reduced, and the pressure in the die was reduced to create a vacuum (vacuum die casting), as shown in Fig. 15.

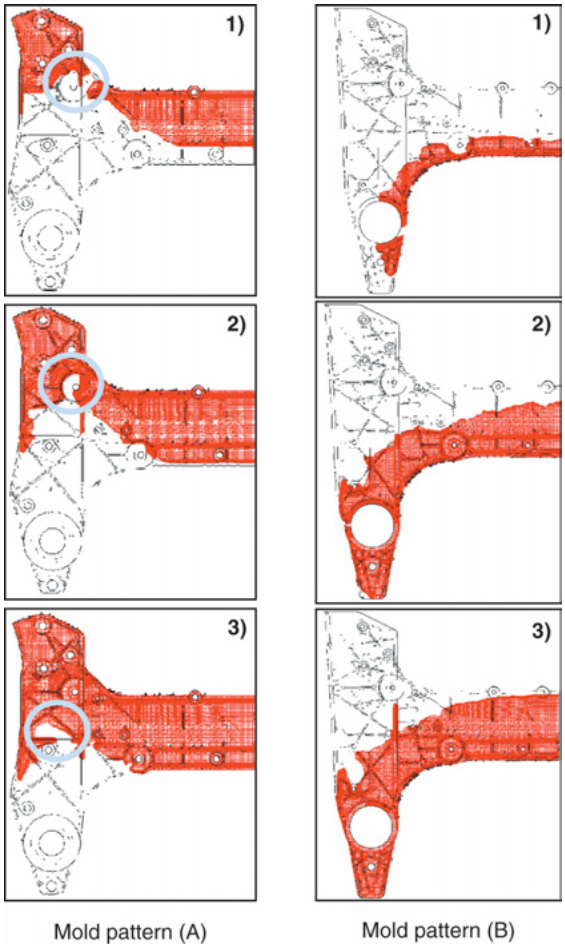


Fig. 14 Comparison of mold patterns by flow simulation of molten metal

Vacuum circuits have been positioned at several points, including the part of the die that is filled last, the most effective positioning for reducing the amount of trapped gas[5], and the internal pressure has been reduced to less than 5 kPa. Optimization of the timing of the pressure reduction has further reduced the amount of trapped gas, resulting in the achievement of a gas content of less than 3 cm^3/100 gAl as shown in Fig. 16. 85-90% of this gas is H_2, with the remainder made up of N_2 and other gases.

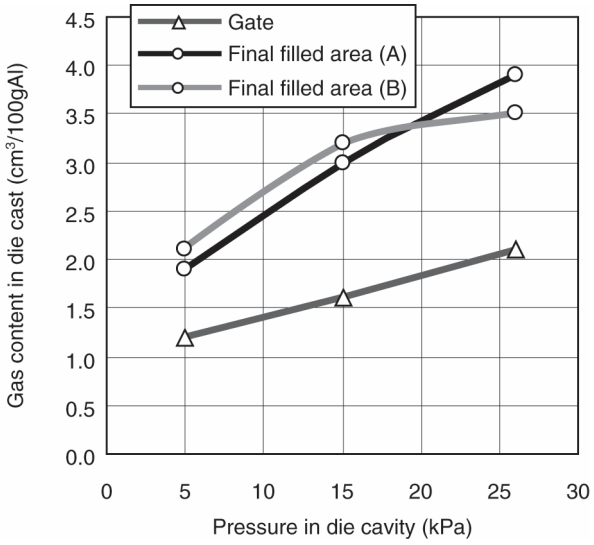


Fig. 16 Relation between pressure and gas content in die cast

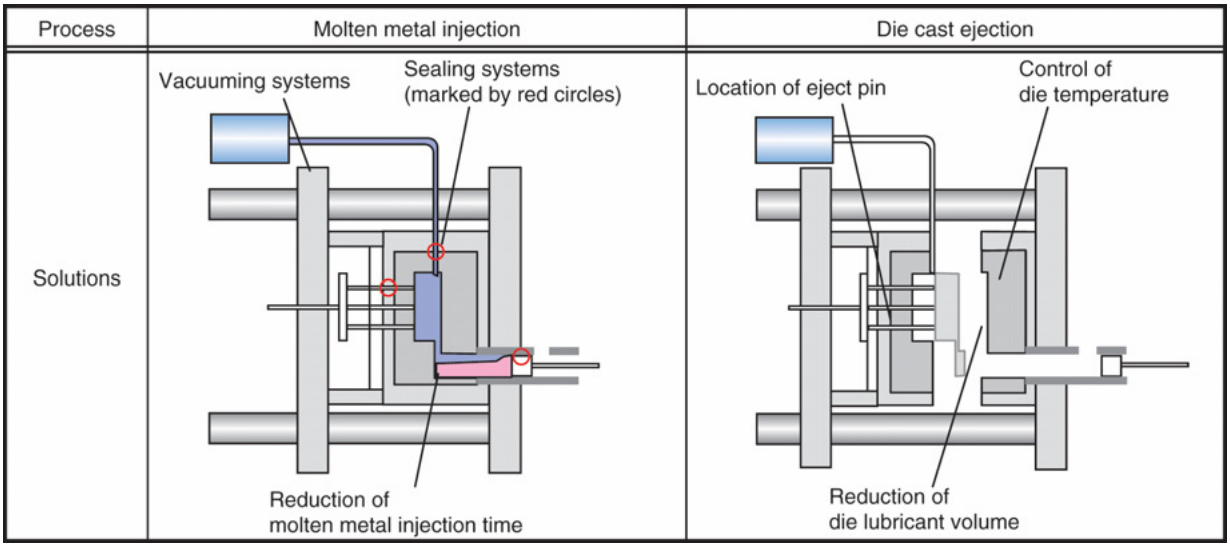


Fig. 15 Outline of solutions for vacuum die casting

4.3. Development of Die Cast Alloy

An Al-Si-Mg alloy is widely used in the casting of subframes. This alloy is strong and displays excellent castability. After a study of the required design properties of the material employed in the new subframe, this alloy was used as a base in the development of a new die casting alloy. T5 was adopted as the heat treatment, to eliminate the necessity of correcting the strain occurring in the application of the T6 solution treatment.

In establishing the composition of the new alloy, the effect of the amount of Si and Mg in the material was first studied. ASTM test pieces produced by a 200 ton die cast machine were used to evaluate the properties of the material, and the conditions employed in the T5 heat treatment were also investigated. Next, flat sheet test pieces were produced and the bead quality and joint strength after welding were studied to evaluate weldability. On the basis of the results of these tests, the basic composition was established based on an Al-Si hypoeutectic alloy, and the range of Mg content was set to enable design property targets to be satisfied. The Fe and Mn content was established through consideration of the anti-soldering performance of the material. Anti-soldering can normally be ensured with an Fe content of over 0.8 wt% and an Mn content of over 0.4 wt%[6),(7)]. The synergistic effect between Fe and Mn was considered in the design of the new alloy, and a range for these components has been established which ensures anti-soldering performance but does not affect toughness. Figure 17 shows the microstructure of the newly developed alloy. As this photograph shows, the Al-Si eutectic microstructure and the amount of precipitation of inter-Al-Mn-Si compounds has been reduced against the former alloy.

In terms of mechanical properties, as Fig. 18 shows, the new alloy shows an excellent balance of tensile strength, yield strength, elongation and impact value. The reduction of cold flaking in comparison to the former alloy has reduced the level of variations occurring in these properties.

5. Aluminum Welding Technology

In addition to the composition of the alloy and the quality of the materials, the quality of aluminum welding is significantly affected by all the elements of the welding process, including the filler metal employed. It is therefore necessary to establish optimum conditions for each material being welded.

This research project therefore clarified the welding characteristics of the materials formed using hot bulging and vacuum die casting, and established appropriate conditions for MIG welding.

5.1. Weldability of Hot Bulge-formed Material

Because extruded pipes are used in the hot bulging process, the study of weldability focused on the quality of the surface. The lubricants and high temperatures employed in this production method cause an oxide film more than 100 nm thick to form on the surface of the material. This surface film makes the welding arc unstable and prevents sufficient melting of the bead, and must therefore be cleaned.

Figure 19 shows the results of studies of film cleaning.

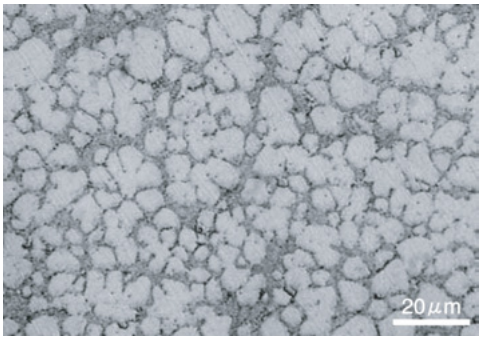


Fig. 17 Microstructure of developed alloy

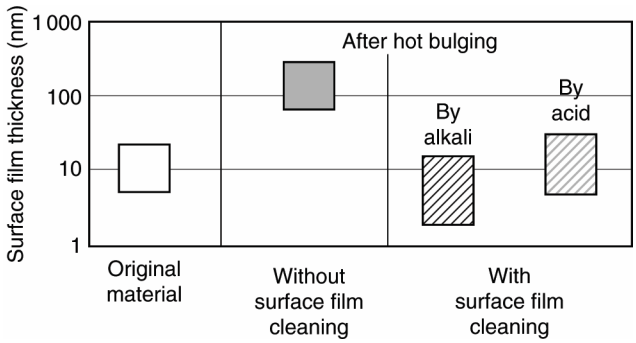


Fig. 19 Comparison of surface film thickness

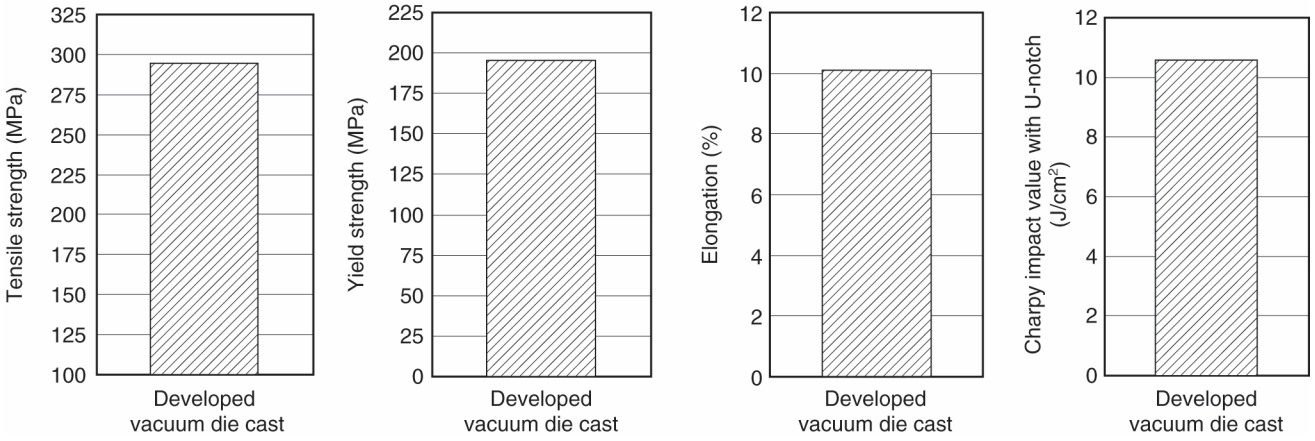


Fig. 18 Mechanical properties of developed vacuum die cast

These studies demonstrated that cleaning with alkali or acid reduced the thickness of the film to a level equivalent to that measured on the material before hot bulging.

Figure 20 shows the difference in welding quality with and without surface film cleaning. Removing the surface film and achieving a uniform state across the surface has stabilized the welding arc and increased the depth of melting of the bead.

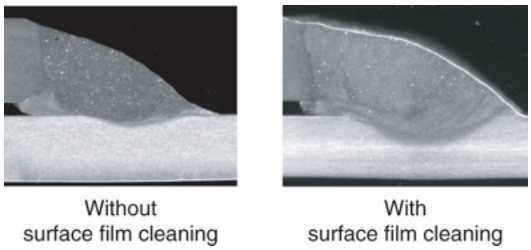


Fig. 20 Influence of surface film cleaning on welding quality

5.2. Weldability of Vacuum Die Cast Materials

As Fig. 21 shows, the gas content of the new vacuum die casts is less than 3 cm^3/100 gAl, an identical level to that previously measured in a thixo die casting[8]. The relationship between gas content and welding bead quality is shown in Fig. 22. At a content of 6 cm^3/100 gAl blowholes occur, and at 8 cm^3/100 gAl numerous blowholes occur in the upper part of the bead. Because these blowholes reduce the effective throat thickness of the joint strength and cause the quality of the join to decline, in MIG welding it is necessary to ensure a gas content of less than 3 cm^3/100 gAl. The use of the new die cast alloy reduces the occurrence of blowholes, and ensures excellent weld quality.

The results of measurements of the thickness of the surface film on the vacuum die cast using Auger electron spectroscopy showed a thickness of around 20 nm, with little effect on weldability.

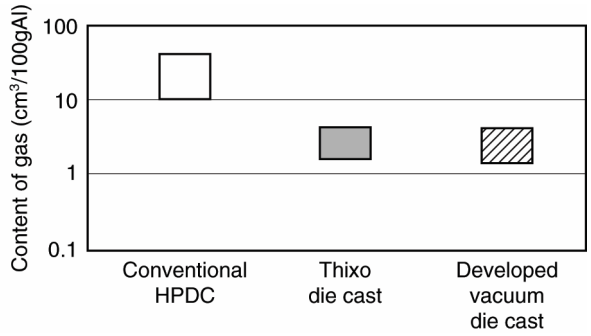


Fig. 21 Comparison of gas content

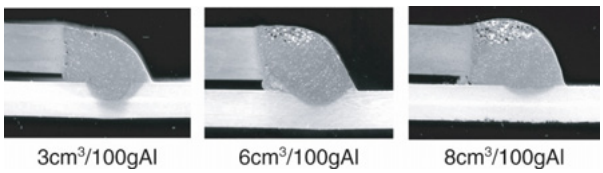


Fig. 22 Influence of gas content on blowhole

Welding conditions applicable to use with an automotive subframe were developed on the basis of these studies of the weldability of the newly developed materials. In addition, conditions were adjusted throughout the production process in order to ensure that these welding conditions could be achieved.

6. Conclusion

Hot bulge and vacuum die cast production techniques were developed as part of a project attempting to achieve cost reductions in aluminum subframes through the integration of parts. The following results have been achieved:

(1) A lightweight and low-cost hybrid aluminum structure has been produced by MIG welding bulge-formed members and vacuum die cast members.

(2) The development of a hot bulge process and an alloy for use in hot forming has enabled the achievement of a high degree of freedom in formation (1.5 times the ratio of transformation of circular length achieved with the former materials), making it possible to form complex shapes.

(3) The development of a vacuum die cast process and an Al-Si-Mg die cast alloy has enabled the production of weldable die cast parts with excellent and well-balanced mechanical properties.

(4) In MIG welding, the reduction of the thickness of the oxide film on the surface of the hot bulge-formed parts and the control of the gas content of the vacuum die cast parts to below 3 cm^3/100 gAl has ensured strength in the weld joints, and the conditions of welding have been optimized.

These developments have reduced the number of parts by 70%, welding length by 55%, weight by 10% and cost by 20% against conventional aluminum subframes.

The authors hope that this research will result in the wider application of aluminum subframes and therefore contribute to automotive weight savings.

References

(1) Ohwue, T., Takada, K., Saga, M., Kikuchi, M.: Deep drawability of 5000 series aluminum alloy sheets in warm working condition, Journal of Japan Institute of Light Metals, Vol. 50, No. 9, p. 451-455 (2000)

(2) Horiuchi, R.: Deformation and fracture in Aluminum alloys at elevated temperature, Journal of Japan Institute of Light Metals, Vol. 31, No. 6, p. 431-444 (1981)

(3) Sato, M., Fujimoto, K., Nakatani, Y., Shimizu, K.: Abnormal grain growth in Al-Mg (0-5%) alloys containing under 0.4% of Mn and Cr, Journal of Japan Institute of Light Metals, Vol. 20, No. 6, p. 278-282 (1970)

(4) Ohwue, T., Takada, K., Saga, M., Kikuchi, M.: Temperature and strain rate dependence of mechanical properties and square shell deep drawability of 5000 series aluminum alloy sheets in warm working condition, Journal of Japan Institute of Light Metals, Vol. 51, No. 8, p. 414-418 (2001)

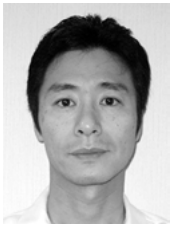
(5) Masuda, E., Itoh, I., Haraguchi, K.: Application of mold filling simulation to die-casting processes, Modelling of Casting, Welding & Advanced Solidification Processes 7, p. 747-754 (1995)

(6) Nishi, N., Kami, S.: Effects of Iron and Manganese Contents on Releasing Force of Aluminum Die Castings, Journal of Japan Foundry Engineering Society, Vol. 70, p. 648-654 (1998)

(7) Ito, T., Mochiduki, S., Hanada, A.: Reports of 47th Japan Institute of Light Metals Autumnal Meeting, p. 13 (1974)

(8) Saito, N., Nakamura, T., Otani, T., Kuroki, M., Masuda, E., Idegomori, T.: Development of Frame Joint Parts by Thixocasting, HONDA R&D Technical Review, Vol. 11, No. 2, p. 149-158

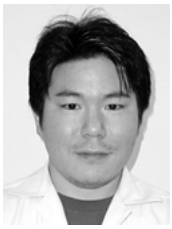
■ Authors ■


Fumiaki FUKUCHI


Takanori YAHABA


Hiroshi AKIYAMA


Tsutomu OGAWA


Haruyuki IWASAKI


Izuru HORI

Development of Peeling-less Casting Billet for Forged Aluminum Suspension Arm

Hiroshi AKIYAMA* Yushi AMAKI** Kiyotaka TOHMA**

ABSTRACT

Change to the use of aluminum material is being promoted in order to achieve the important goal of weight reduction. However, the high cost of this material means that weight reduction by this method is currently not progressing. Here we focused on the material cost, which occupies 59% of the manufacturing cost of forged aluminum suspension arms, and developed a new continuous casting technology which does not need peeling. This is called the peeling-less casting billet. To eliminate the peeling process, it was necessary to control material segregation and surface unevenness. Therefore the material content was adjusted (adding Ca) and direct cooling during casting was used, together with adiabatic mold casting and a graphite casting mold, and those problems were overcome. This developed technology eliminated the need for peeling, and in combination with reduced costs due to equipment depreciation, it reduced the cost of forging materials approximately 20%, thus realizing a reduction in cost compared to conventional forged aluminum suspension arms.

1. Introduction

In recent years, the weight of automobiles has been increasing because of the increase in comfort features and measures adopted for safety against collision. Moreover, improvements in fuel consumption are being demanded from the point of view of global environmental protection (reduction of CO_2 and NO_X emissions, etc.) and the need to reduce automobile weight is increasing year after year. Among these, the demand for reducing the weight of suspension, which contributes to better running performance of the car with enhanced riding comfort and handling stability, is especially high.

Honda promoted the use of aluminum suspensions for sports vehicles and fuel-efficient vehicles as shown in Fig. 1, and selected forging as the manufacturing method for the suspension arm, which requires high strength and toughness. However, high costs are incurred in forging which involves many processes, and it has not yet been used in mass-production vehicles. Thus, low cost aluminum forgings are in demand.



Fig. 1 Applied examples of forged aluminum suspension arms

* Honda R&D Americas, Inc.
** Tochigi R&D Center

2. Conventional Techniques and Development Goals

2.1. Cost Structure of Forged Aluminum Parts

Figure 2 shows the cost structure of forged aluminum parts. The percentage of material cost in the forging cost is high at 59%, of which 16% is the cost of peeling of the billet used for forging. Normally, peeling is performed to avoid macroscopic segregation of surface layer and unevenness of the surface because of solidification shrinkage, which occur during the cooling process.

Moreover, the extrusion billet, which does not require peeling, may also be considered as the forging material, but extrusion costs become higher than the peeling costs, leading to a large increase in the overall cost.

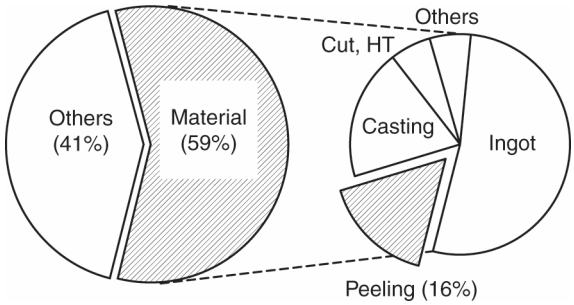


Fig. 2 Conventional cost composition of forged aluminum suspension arm

2.2. Issues in Conventional Techniques

Figure 3 shows the Direct Chill Casting (DC casting) method[1),(2)], which is a typical continuous casting method. The method consists of a two-stage cooling process. Molten aluminum in the mold forms a solidified shell because of the cooling of the water-cooled mold (primary cooling). Most of the residual part solidifies because of direct water-cooling from the lower part of the mold (secondary cooling). As shown in Fig. 4, this casting method causes unevenness on the billet surface because of solidification shrinkage that occurs with the cyclic two-stage cooling, and moreover, macroscopic segregation of the surface layer occurs. This may give rise to surface defects, reduction in strength, and reduction of resistance to corrosion of forging parts. Therefore, the billet surface is removed by the peeling process. Research for improvement of DC casting generally focused on minimizing the contact between the mold and the molten metal. That is, the focus was mainly on reduction of primary cooling capacity, and as shown in Fig. 5, hot top

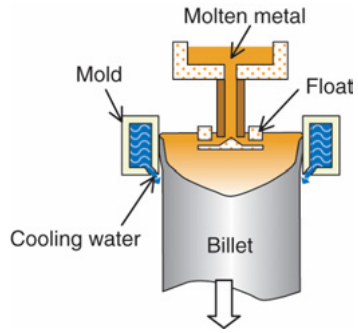


Fig. 3 Schematic of direct chill casting method

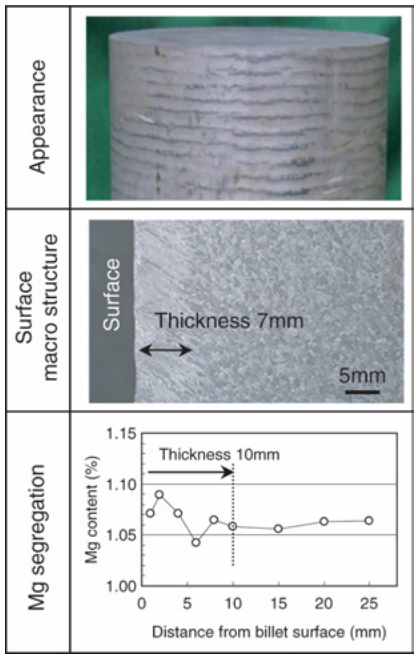


Fig. 4 Surface quality of direct chill casting billet

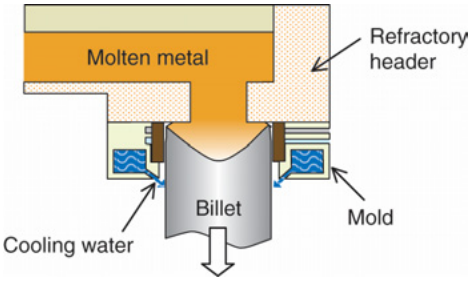


Fig. 5 Schematic of hot top casting method

casting[1),(3)] was considered as an improved casting method. However, even with this casting method, unevenness of billet surface and macroscopic segregation of the surface layer could not be eliminated, therefore peeling is being carried out.

2.3. Development Goals

The casting process using the method of cooling from the billet surface does not completely remove surface defects. The following items were considered for establishing a casting technique that would reduce the difficulties as far as possible:

(1) Avoiding two-stage cooling process (mold material and cooling process)
(2) Optimization of casting conditions (speed of casting and amount of cooling water)
(3) Strengthening the solidified shell of the uppermost layer (material composition)

The goal is to improve the quality of the billet surface, which becomes the forging material, to enable elimination of peeling work, and to reduce casting costs.

3. Peeling-less Casting Technique

3.1. Mold Material and Cooling Process

To eliminate the two-stage cooling in the conventional technique, heat insulating mold structure[4), (5)] in which the

mold does not have the cooling function was adopted. As shown in Fig. 6, while the refractory product is used in the mold holder, graphite was used as mold material because of its superior thermal conductivity to reduce the temperature gradient between molten metal and mold. Moreover, the benefit of the self-lubricating performance of graphite is that the molten aluminum can smoothly pass through the inner mold wall, thus improving the smoothness of the billet surface. Graphite reacts strongly with water vapor near the aluminum solidification temperature (casting temperature) of 700 °C. This affects the mold life. Therefore, graphite with its excellent oxidation-resistance was used.

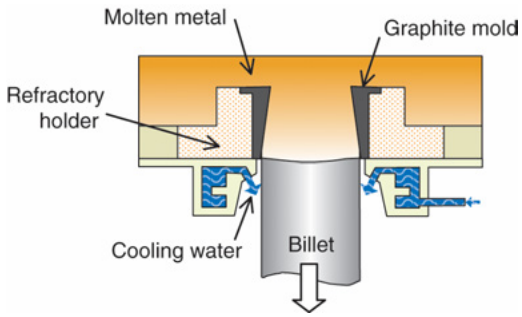


Fig. 6 Schematic of developed casting method

3.2. Casting Speed and Amount of Cooling Water

Because only direct water-cooling was used during casting, the effect of the cooling speed on the quality of billet became pronounced; therefore, improvement in the surface quality was attempted by controlling the casting speed and the amount of cooling water which dominate cooling speed. As shown in Fig. 7, optimization of casting speed and amount of cooling water made it possible to achieve the manufacturing conditions of billet with excellent surface quality.

Figure 8 shows the relationship between the casting speed and the quality of appearance of billet when the amount of cooling water is fixed. As the delay in the casting speed increases, longitudinal streaks and surface protrusions occur, and this reduces the quality. It is necessary to set the highest possible casting speed in the range where no leakage of molten metal occurs from the viewpoint of productivity.

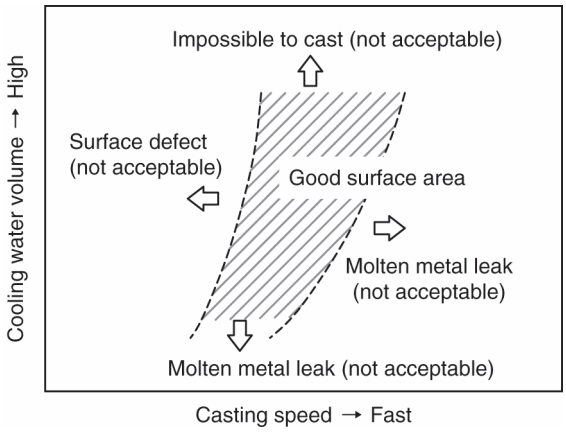


Fig. 7 Relationship between cooling speed and casting quality

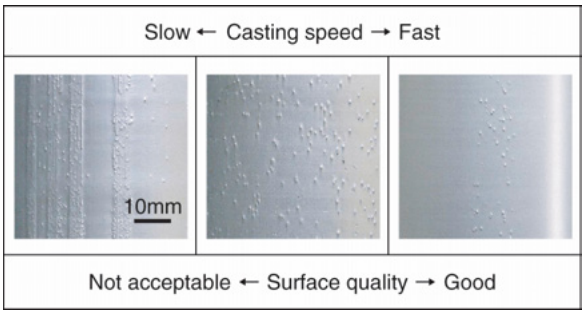


Fig. 8 Relationship between casting speed and casting quality

3.3. Material Composition

The goal to date has been to improve billet surface quality by setting the casting conditions and selecting the optimum mold material. However, surface protrusions have been noticed as shown in Fig. 8, and a smooth surface has not been achieved yet. As shown in Fig. 9, the solidified shell around the solidification boundary surface breaks and molten metal leakage occurs because of the friction force created when the mold comes in contact with the shell. By increasing the strength and ductility of the solidified shell, the protrusions were inhibited. Starting with Be[6),(7)], which creates an oxide film preferentially on the billet surface during solidification, attention was also paid to Sc, Ca and Sr[8)], which increase the surface tension of molten aluminum. These elements were added to the 6061 alloy, which is the base alloy, and the effectiveness in improving the surface quality of billet using the developed casting method was confirmed. As shown in Fig. 10, the effectiveness on elimination of surface protrusions by the addition of Be and Ca was confirmed, but the use of Be was shelved because of environmental concerns. Optimization of amount of Ca to be added to obtain the same effects was implemented, and the optimum amount to be added was set in the range of 50 ppm – 150 ppm. Figure 11 shows the billet surface quality for amount of Ca added.

Figure 12 shows the cross section of the Ca-added billet structure cast using the developed casting method. The thickness of the macro segregation layer obtained by conventional technology was 7 mm and the concentration segregation of Mg was 10 mm. In contrast, however, in the developed casting method, there was no macroscopic segregation layer, and there was an extremely thin microstructural layer of about 150 μm (hereafter referred to as "chilled layer"). Moreover, there was almost no segregation of Mg. The internal structure was also a very fine

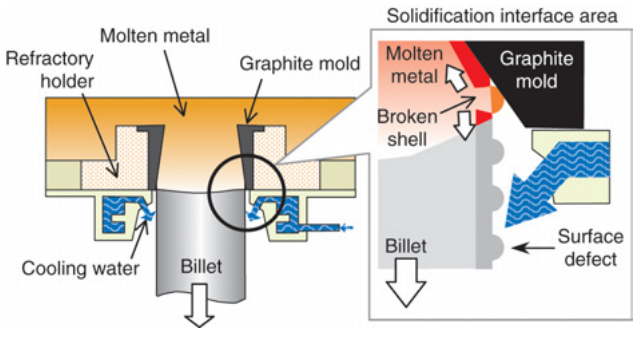


Fig. 9 Generating mechanism of surface defect

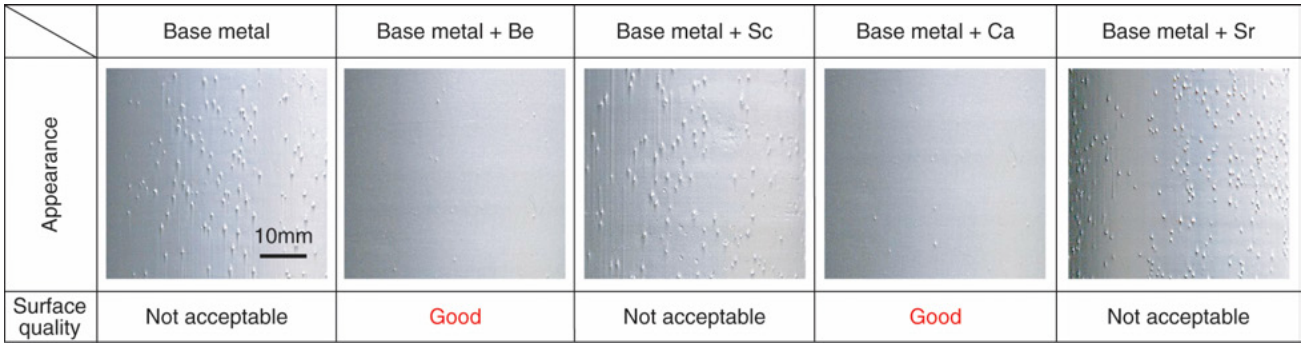


Fig. 10 Influence of additional element

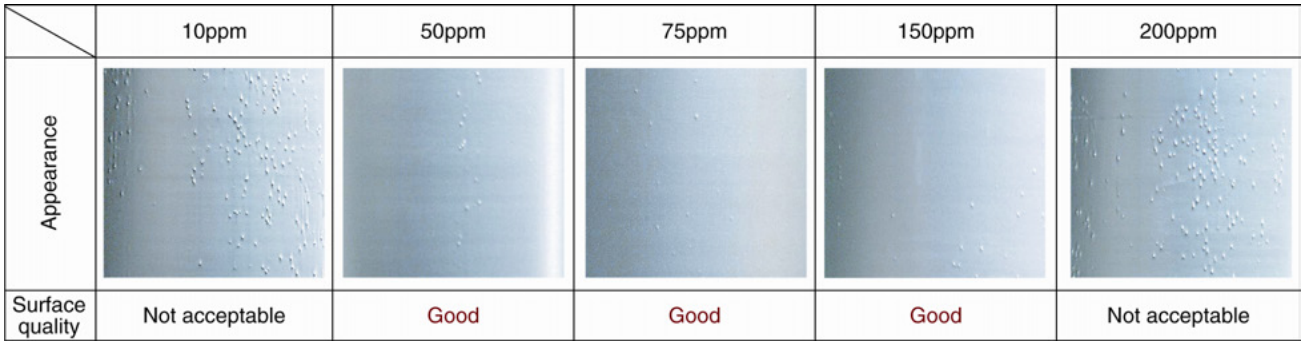


Fig. 11 Influence of Ca quantity to surface quality

macro structure formed because of quenching by direct water-cooling.

As mentioned above, use of the heat insulating mold, optimal setting of the casting conditions as well as addition of small quantity of Ca made it possible to produce a smooth billet surface and to restrict the non-uniformity of the structure to a minimum, enabling a peelingless cast billet to be obtained.

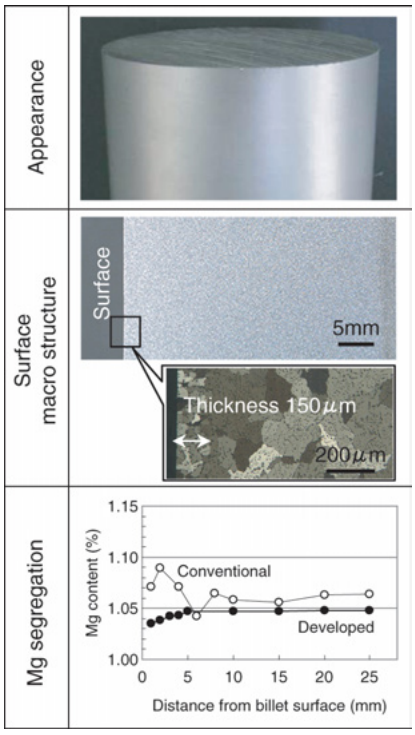


Fig. 12 Surface quality of developed billet

4. Mechanical Properties/ Characteristics of Parts

The effects of the residual chilled layer and addition of Ca on the peelingless cast billet used in the forged arm were confirmed.

4.1. Effects of Residual Chilled Layer

A chilled layer formed due to quenching when casting remains on the surface of the forging, if the billet is forged without performing peeling. To confirm this effect, hot flat forging at a tempering ratio of 80 % was implemented horizontally in the billet axial direction on the conventional and the developed materials, and the effect of the residual chilled layer was studied.

Figure 13 shows the mechanical properties of the test specimen cut from the flat forging. The strength and Charpy impact values were the same regardless of the existence of a chilled layer. However, from the data for damage probability P = 0.1, the fatigue strength improved by approximately 20 % compared to the conventional technology with no chilled layer. It is believed that a reinforcing effect was observed because the structure became microscopic due to the quenching action in the developed casting method and a chilled layer existed on the surface.

4.2. Effect of Adding Ca

Figure 14 shows the mechanical properties of the test specimens cut from inside the forged arm of the developed and the conventional materials. Generally, the Ca atoms in Al are considered to form compounds between metals by bonding with Si atoms, reduce the amount of Mg_2Si that contributes to the strength of the 6061 alloy, and reduces the strength[9]. However, in the range of addition of 50-150 ppm,

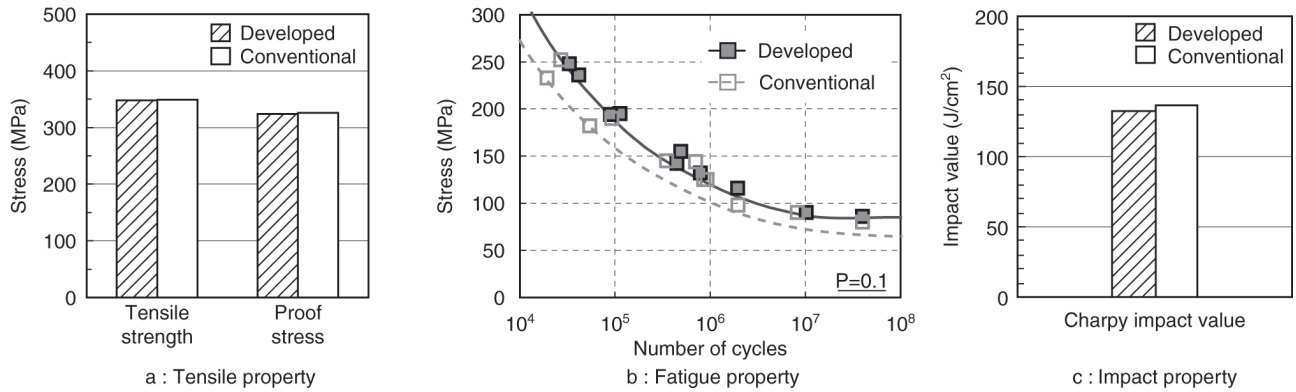


Fig. 13 Influence of residual chilled layer in flat forging

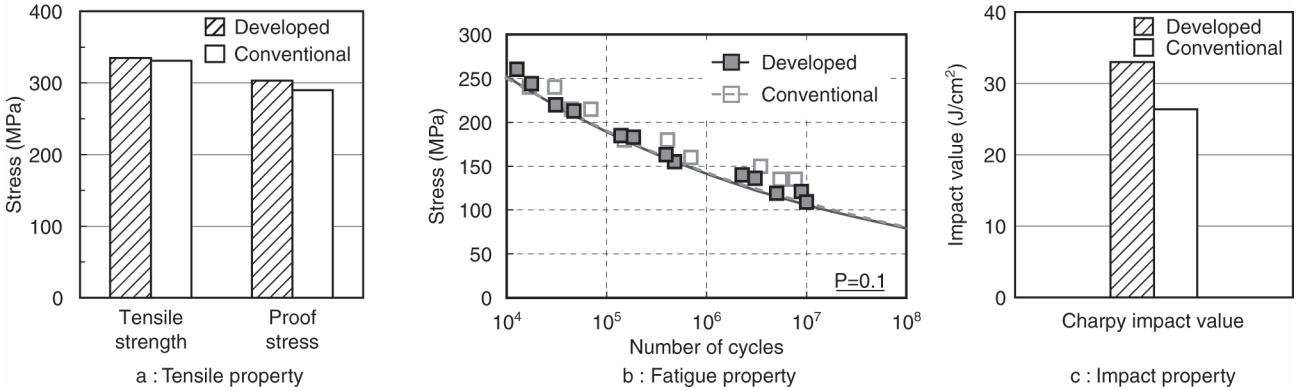


Fig. 14 Influence of Ca addition in forged arm

the value indicated was greater than the value when no Ca was added. In particular, the impact value in the developed casting method improved by 25 % compared to the conventional material. This is because of the effect of the microscopic structure due to the developed casting method.

As mentioned above, forged parts made by using peelingless cast billet showed excellent mechanical properties compared to conventional technology. Moreover, it was also confirmed that there were no concerns in the strength, durability, and corrosion resistance of the arm.

5. Practical Example

The developed technology enabled the elimination of the peeling process, which was necessary in the past. Elimination of the peeling process enabled a reduction of about 20 % of the material cost to be achieved because of elimination of straightening of casting billet and reduction in depreciation cost of equipment. Further, by application of the developed method to the mass production of the front lower arm in the 2005 year model LEGEND, we achieved a reduction in weight of approximately 43 % compared to the cast iron arm. Figure 15 shows the front suspension and Fig. 16 shows the front lower arm of the LEGEND.



Fig. 15 External view of front suspension



Fig. 16 Front lower arm

6. Conclusion

Research was carried out to develop a cast billet with excellent surface quality that does not require the peeling process, which was necessary in the past, for the manufacturing of aluminum forged suspension arms. The results of the research and development were as follows:

(1) A peelingless cast billet was developed by adding Ca, using a graphite mold, and optimizing the casting conditions.
(2) Compared to the conventional cast billet using the peeling process, it was possible to reduce the material portion of the forging cost by 20 %.

7. Acknowledgments

Finally, we would like to express our gratitude to Toyama Alloy Co., Ltd. and TFO Corporation for their cooperation relevant to this research and development.

References

(1) The Japan Institute of Light Metals: The Handbook of Advanced Aluminum Technology, p.334-343 (1996)

(2) Matsuo, M.: Continuous casting of aluminum, Journal of Japan Institute of Light Metals, Vol. 44, No. 9, p. 510-525 (1994)

(3) Schneider, W., Lossack, E.: Improvement of Billet Quality by Use of a Hot Top Mold with a Two Phase Lubrication, Light Metals, p. 763-768 (1987)

(4) Yamashita, T.: Characteristics of a vertical semi-continuous casting process using a heat insulating mould for a aluminum alloys, International Journal of CAST METALS RESEARCH, Vol. 9, No. 4,p. 241-247 (1996)

(5) Yamashita, T.: Solidification position and surface condition in aluminum billets produced by a vertical semi-continuous casting process using a heat insulating mold, Journal of Japan Institute of Light Metals, Vol. 46, No. 10, p. 494-499 (1996)

(6) Ushida, T., Yoshimura, O., Mashiyama, S.: The effect of small amount of beryllium on Al-Mg alloys, Journal of Japan Institute of Light Metals, Vol. 7, No. 6, p. 29-33 (1957)

(7) The Japan Institute of Light Metals: The Handbook of Advanced Aluminum Technology, p. 122 (1996)

(8) Nakae, H.: Wettability of liquid aluminum to non-metallic materials, Journal of Japan Institute of Light Metals, Vol. 39, No. 2, p. 136-146 (1989)

(9) Nemura, A., Ohno, T., Kamado, S., Kojima, Y., Masuda, R., Oosumi, K.: Effect of remained calcium on microstructure and various properties of 6061 aluminum alloy, Journal of Japan Institute of Light Metals, Vol. 46, No. 11, p. 576-581 (1996)

■ Authors ■



Hiroshi AKIYAMA



Yushi AMAKI



Kiyotaka TOHMA

Design and Development of HondaJet

Michimasa FUJINO*

ABSTRACT

Honda R&D has developed an advanced business jet. The HondaJet is an entry-level, light-weight, business jet featuring an extra large cabin, high fuel efficiency, and high cruise speed compared to existing small business jets. To achieve the performance goals, a natural-laminar-flow wing, a natural-laminar-flow fuselage nose, an over-the-wing engine-mount configuration, and other advanced technologies were developed. The wing is metal, having an integral machined skin to achieve a very smooth upper surface, which is required for natural laminar flow. The fuselage is made entirely of composites and the stiffened panels and the sandwich panels were co-cured integrally in an autoclave to reduce weight and cost. The advanced avionics system, which provides a high degree of integration for enhanced functionality and flight safety, was also installed in the cockpit. Several advanced technologies were employed for the HondaJet.

1. Introduction

Air transportation has seen an annual worldwide growth of 6.7% for the last 20 years, and the International Civil Aviation Organization (ICAO) estimates that it will continue growing at 5.3% per year for the coming 20 years. This represents a real increase with respect to the 3.3% growth predicted for the worldwide GDP during the same period. The market for business jets is expected to show the same trend; it averaged 8.1% growth during the last 20 years, and is projected to follow the course of GDP. There has been a renewed appreciation in recent years for the advantages of business jets over commercial travel (no waiting time at the ticket counter or for transfers to subsequent flights) and their safety (little exposure to hijackings or other terrorist acts). Interest in business jets has reached a pitch never before seen in the market.

However, business jets are expensive, both in the purchase prices for the aircraft themselves and in operating costs, and have remained well out of reach of the average air traveler. Even for charter usage, fares are higher than those for first-class commercial tickets. This has been the biggest obstacle to the popularization of these aircraft. If prices and operating expenses can be brought down to allow fares comparable with airline tickets, it will bring about a dramatic change in the business jet industry.

The above conditions were motivations for the development of the HondaJet, which Honda believes will become the paradigm for the next generation of business jets. This report will present the design and testing of this jet, in the fields of aerodynamics, aeroelasticity, structure and systems.

* Honda R&D Americas, Inc.

2. Overview of HondaJet and its Capabilities

Figure 1 shows an overall view of the twin-engine HondaJet. The power plant was developed by Honda. It is a highly efficient turbofan, designated HF-118. Each HF-118 develops a take-off thrust of 1 670 lb (7 428.5 N). It is a two-spool engine featuring Fully Automated Digital Engine Control (FADEC). The aircraft is a low-wing design with the engines mounted over the wing. The aircraft is 41.14 ft (12.5 m) long, has a wing span of 39.87 ft (12.2 m) and is 13.21 ft (4.1 m) high at the top of the T-tail. The design maximum take-off weight is about 9 200 lb (4 173 kg) and the maximum speed is about 420 kt (778 km/h) at 30 000 ft (9 100 m). This aircraft boasts about 10% greater speed and about 40% better fuel efficiency than other members of this class of business jets. The height inside the passenger cabin at the center aisle is 4.89 ft (1.49 m) and the length of the passenger cabin is 15.09 ft (4.6 m), offering a much larger passenger space than in other 4-seat planes. The passenger cabin is pressurized to 8.7 psi (60 kPa), to maintain 8 000 ft cabin altitude up to 44 000 ft.



Fig. 1 HondaJet

3. Aerodynamics

3.1. Wing

The aerodynamic design of the wing emphasized both good stall characteristics and minimum drag. A detail trade study was conducted to minimize both structural weight and induced drag. The study showed that the takeoff weight is minimized for a 1 100-nm-range aircraft when the wing geometric aspect ratio is 8.5 and a winglet having a height ratio of 9% is installed. An over-the-wing engine mount design was used for the HondaJet. This offers the advantages of minimum wave drag at high speed when the nacelle is in the optimized position and the maximum cabin volume[1]. Since this is not a commonly used configuration, however, the stall characteristics were carefully studied by theoretical analysis and low-speed wind tunnel tests. Figure 2 shows the stall pattern observed on the wing, engine installed, of a 1/6-scale model in a low-speed wind tunnel test. Stall is initiated around 55% semi-span and spreads forward along the central portion of the wing. Thus, there is adequate stall margin over the outboard portion of the wing. Also, stall did not occur at the wing root area, between the engine and the fuselage, even at angles initiating stall elsewhere on the wing. The over-the-wing engine configuration showed good stall characteristics. The low-speed wind tunnel tests showed similar results for the effect of the nacelle on lift characteristics; installation of the nacelle over the wing was proven not to disrupt the aerodynamic characteristics of the aircraft[2].

Conformal mapping[3] was used to develop a new natural laminar flow (NLF) airfoil designated SHM-1[4] in order to accomplish the high performance goals for the HondaJet. The shape of the SHM-1 and typical pressure contours are shown in Fig. 3. The pressure gradient on the upper surface is favorable to about 42% chord, followed by a concave pressure recovery. This represents a balance between maximum lift, pitching moment, and drag divergence. The pressure gradient along the lower surface is favorable to about 63% chord, reducing drag. The leading edge (LE) shape was designed to promote transition near the LE at high angles of attack (AOA) in order to minimize loss from the maximum lift coefficient due to surface roughness. The trailing edge shape on the upper surface was designed to cause a very steep pressure gradient, with the intent of inducing a small separation. The new concept in trailing edge design allowed a large reduction in the wing pitching moment at high speeds.

In addition to the wind tunnel tests of this airfoil at low and transonic speeds, a T-33 trainer (Fig. 4) was equipped

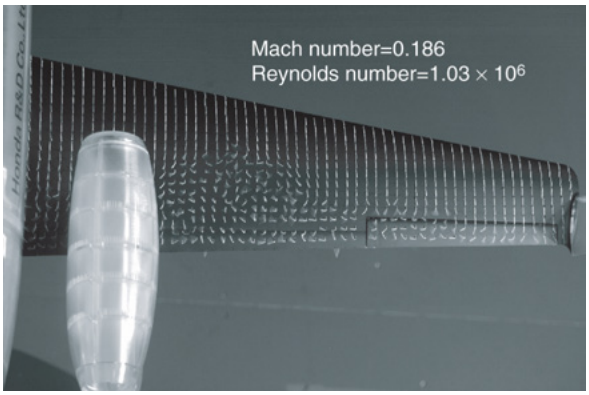


Fig. 2 Stall pattern

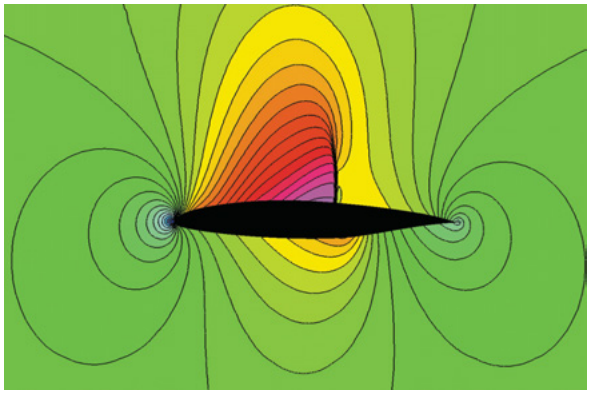


Fig. 3 SHM-1 airfoil shape and pressure contour

with a wing to confirm the performance of the airfoil at actual Reynolds numbers and Mach numbers. It was found to offer a low profile drag coefficient during cruise and clime, in addition to its high maximum lift coefficient and docile stall characteristics.



Fig. 4 T-33 aircraft modified for NLF flight test

3.2. Over-the-wing Engine Mount Configuration

The major design decision was that of engine location. Many technical parameters were examined in studies to compare the proposed over-the-wing engine mount configuration with that of the standard rear-fuselage engine mount. In general, locating the engine nacelles over the wing has potential to cause unfavorable aerodynamic interference and induces a strong shock wave, lowering the drag-divergence Mach number.

Theoretical studies were conducted using a three-dimensional Euler solver[5]; next, transonic wind tunnel tests were conducted in the Boeing Transonic Wind Tunnel to validate the theoretical predictions (Fig. 5). An optimum position for the nacelle relative to the wing was identified to minimize the shock wave, and drag divergence was found to occur at a Mach number higher than that for the clean-wing configuration. Favorable interference is obtained when the forward end of the nacelle is located near the position of the shock wave of a clean wing and the vertical distance between the wing upper surface and the nacelle lower surface is between one-third and one-half the maximum height of the nacelle above the upper wing surface; this results in a lower drag than the conventional rear-fuselage engine mount configuration[1].

The final configuration for this aircraft was determined by the above results. The over-the-wing engine mount configuration offers cruise performance superior to that of the rear-fuselage engine mount configuration and the largest cabin volume of any business jet in its class.

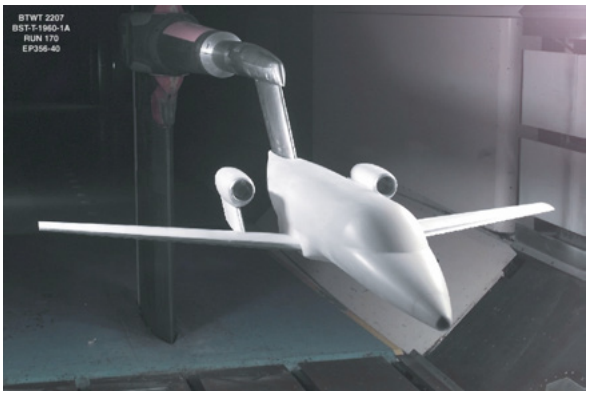


Fig. 5 Transonic wind tunnel test

3.3. Flaps

In addition to the required high-speed capabilities, in order to obtain the required stall speed, the aircraft employs a linkage-type, double-slotted 30% chord flap. The two-dimensional multiple-element panel code MCARFA[6] and the two-dimensional multiple-element Euler code MSES[7] were used to design the shapes, gaps, overlaps, and other characteristics of the vanes and flaps. These designs were then tested in the Honda low-speed wind tunnel using the 1/6-scale model and the 1/3-scale half-model (Fig. 6). The results of these tests at two Reynolds numbers were combined with the pressure-difference rule[8] to analyze the design, providing a quite accurate prediction of the maximum lift coefficient for this aircraft. The maximum lift coefficient was estimated to be about 2.5 in the full scale aircraft and the flap configuration was proven to meet the target stall speed.



Fig. 6 1/3-scale low-speed wind tunnel model

3.4. Engine Simulations

It is essential to minimize distortions in the flow into the engines above the wing during flight at high AOA. Low-speed powered-model wind tunnel tests were conducted using the 1/6-scale model (Fig. 7).

Forty total-pressure probes were installed on the plane of rotation of the fan to observe the flow pattern, and static pressure ports were drilled along the inlet duct to measure separation at the lip. The pitch and yaw of the fuselage, airspeed and engine fan speed were systematically varied and the combined effects of these on the complete distribution of pressure in the air inlet were studied. Four AOA (10°, 15°, 18° and 26°) and three yaw angles (–18°, 0° and 18°) were employed with a mass-flow ratio of 1.15, which corresponds to the condition of approach speed with required thrust. An example of the results is shown in Fig. 8.

The inlet total-pressure distortion was less than 0.1% up to the stall AOA of 15°, then within 2% from stall up to the 26°. Similar results were obtained from tests with mass-flow ratios of 0.65 and 2.15. The tests with the high mass-flow ratio of 2.15 showed low total-pressure distortion at all AOA; the tests with the low mass-flow ratio of 0.65, corresponding to the cruise condition, showed slightly higher distortion at AOA higher than stall. These results demonstrated that the distortion does not exceed the limits specified by engine requirements in the flight envelope.

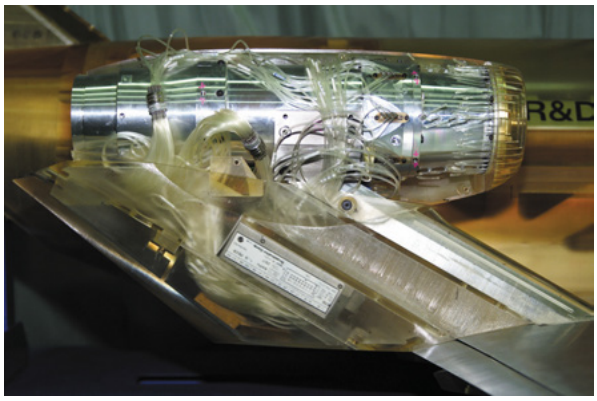


Fig. 7 1/6-scale engine simulator

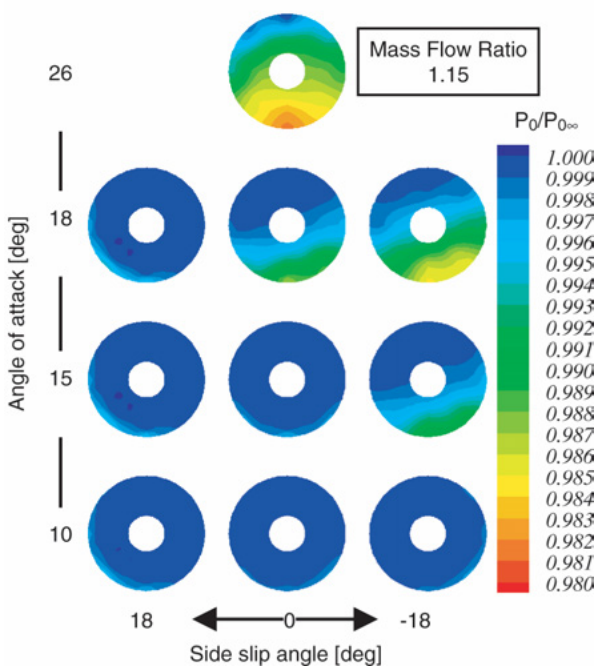


Fig.8 Pressure distribution pattern obtained from powered model test

3.5. Laminar Flow Nose

A new NLF nose shape was designed in order to reduce fuselage drag. A three-dimensional panel code and an integral boundary-layer method were used[9]. The exterior shape of the nose is designed both to maintain a favorable pressure gradient and to minimize crossflow, in order to maximize the length of the laminar flow region. A 1/3-scale model of the fuselage was constructed to verify this shape by testing in Honda's low-speed wind tunnel (Fig. 9). Infrared cameras were also used to visualize the flow on the nose at each AOA (Fig. 10).

The results show that extensive laminar flow is achieved at climb and cruise AOA. Since steps and gaps are detrimental to the achievement of NLF, various steps and gaps were installed on the nose to determine the critical sizes. A NLF nose reduces fuselage drag about 10% compare to that of a fuselage with a turbulent-flow nose (Fig. 10).



Fig. 9 1/3-scale fuselage model for NLF nose test

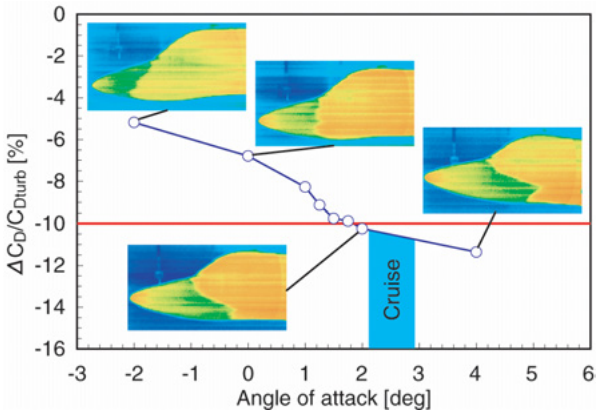


Fig. 10 Drag reduction of NLF nose

3.6. Low-speed Wind Tunnel Testing for Stability

Extensive, six-component force wind tunnel tests were conducted to obtain the aerodynamic characteristics and the stability derivatives. Two wind tunnels, the Honda low-speed wind tunnel (Fig. 11) and the University of Washington low-speed wind tunnel, were used. The stability derivatives obtained from these tests were used to simulate the aircraft flight characteristics using the Honda six-degree-of-freedom flight simulator (Fig. 12). It was verified that the flight characteristics satisfied the MIL-8785C and other standards.verified that the flight characteristics satisfied the MIL-8785C and other standards.

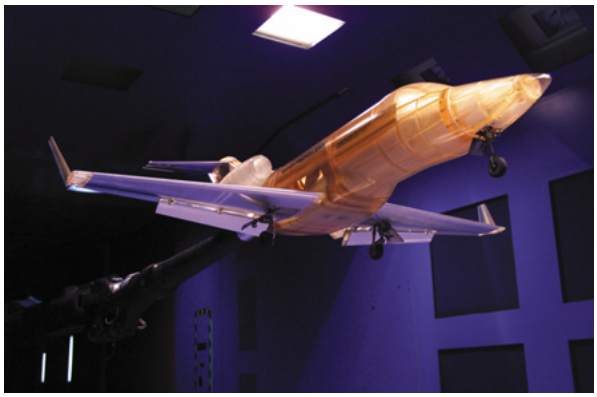


Fig. 11 1/6-scale wind tunnel



Fig. 12 Honda flight simulator(HNAFS)

4. Aeroelasticity

4.1. Over-the-wing Engine Configuration

Mounting the engines on the wing causes complex wing-flutter characteristics. The location of the engine mass, its relation to the wing, and the relation of the pylon stiffness to the wing stiffness are important for flutter characteristics. To investigate these characteristics, theoretical analyses were performed using the ERIN code and low-speed and transonic wind tunnel flutter tests were conducted at the Japan Aerospace Exploration Agency (JAXA) Transonic Flutter Wind Tunnel (Fig. 13).

For the over-the-wing engine mount configuration, the symmetric flutter mode occurred at a lower speed than the anti-symmetric flutter mode. It was also verified that the effects of the aerodynamic load and the interference due to the engine-nacelle installation over the wing are small at transonic speeds. The vibratory characteristics of the engine pylons were found to affect flutter characteristics. For example, the flutter speed was highest when the engine-pylon side-bending frequency is close to the uncoupled 1st wing-torsion frequency (about 0.9 – 1.0 times the uncoupled 1st wing-torsion frequency) and lowest when the engine-pylon pitching frequency is about 1.25 times the uncoupled 1st wing-bending frequency[10].

The wing stiffness and mass distribution were designed based on these results to satisfy the flutter-clearance requirements.

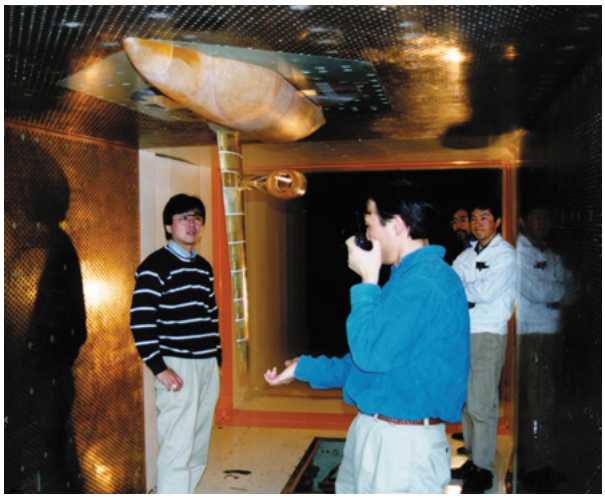


Fig. 13 Transonic wind tunnel flutter test at JAXA transonic wind tunnel

5. Structure

5.1. Wing

The wing is constructed in three sections, left outboard wing, center section, and right outboard wing (Fig. 14). Its structure consists of an aluminum spar and aluminum skin. The torque-box structure consists of three spars, ribs and skin with integrated stringers forming an integral fuel tank.

The skin of the upper surface, made of A7050 aluminum plate, is machined, integral panel to maintain the contour required for laminar flow. This configuration allows the most efficient distribution of material and the lowest number of parts.

The LE structure and the main torque-box structure are mated at 13.5% chord to reduce the disturbance to the laminar flow. The LE contains a piccolo tube (a tube with lines of holes) which directs hot engine bleed air against the inside surface of the LE skin for de-icing.

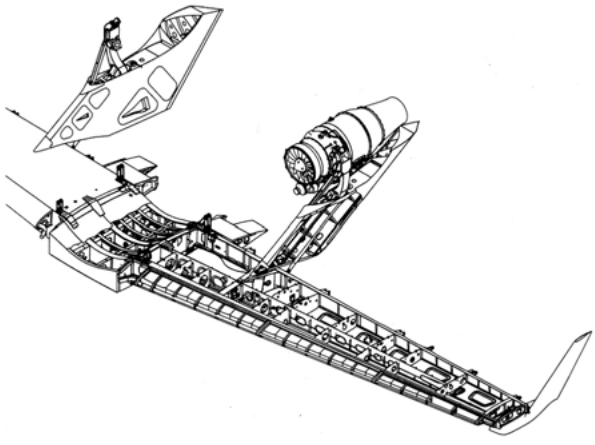


Fig. 14 Wing structure

The pylon structure is attached with four bolts to a reinforced, Y-shaped rib. The main landing gear is attached to the inboard side of the reinforced rib. The design introduces the heaviest loads on this aircraft structure into the same locations. The vertical loads from the wing are carried forward and aft into the fuselage main frame by four links, while the lateral loads are transmitted through V-shaped links left of those links. Forward-aft loads are transmitted to the fuselage by two thrust rods.

The wing structural design was substantiated by a proof test. The MTS Aero-90 test system was used with a total of 26 computer-controlled hydraulic actuators to simulate airloads, engine thrust and landing gear loads. Over 600 channels of data (strain, displacement, force, etc.) were measured during each test case. The actual number of cases studied, out of the 870 cases, was 10. These were pylon vertical load, pylon side load, flap load, Vc positive gust, Vc negative gust, right and left one-gear landing conditions, level landing with spin-up load, crabbed landing, and rudder maneuver.

Since the same wing structure used for proof tests will also be used for flight testing, the test loads were limited to 80% of the limit loads (Fig. 15). The measured strain, displacement, and reaction-force data were compared with those from a finite element analysis and the results were extrapolated to estimate the limit-load values.

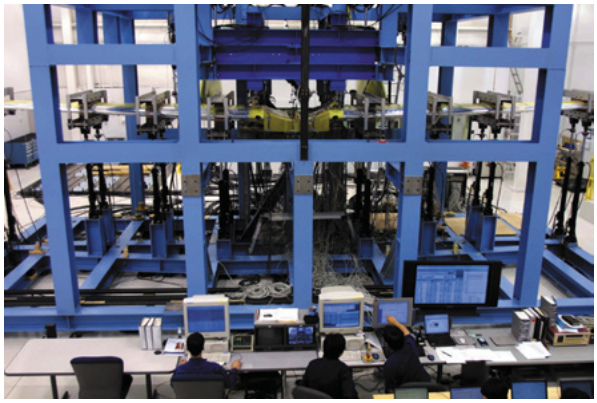


Fig. 15 Wing proof test

5.2. Fuselage

The fuselage structure is made of composites. The material is a 180 °C cure epoxy prepreg reinforced with carbon fiber. (The matrix is Cytec 5276-1 high-damage tolerance epoxy resin and the fiber is TOHO G30-500 high-strength, intermediate modulus fiber[11].)

As shown in Fig. 16, the cockpit and the tail section is a honeycomb sandwich construction to maintain the compound curves that are required for the laminar-flow nose. An integrally stiffened panel structure is employed for the constant cross section portion of the cabin, which maximizes the cabin volume. Identical frames and stringers are used for the constant section of the fuselage to simplify fabrication. The constant fuselage section can easily be stretched in future models.

A major feature of the fuselage is that the sandwich panel and the stiffened panel are co-cured integrally in an autoclave to reduce weight and cost. It was a technical challenge to cure the honeycomb sandwich structure under the pressure (0.6 MPa) required for the stiffened panel. The ends of the workpiece were stabilized in picture-frame jigs, which prevented crushing of the honeycomb core.

The windshields are shaped in compound curves for good aerodynamic characteristics. They are constructed of two plies (inner and outer) of stretched acrylic with a polyurethane interlayer, which has superior low-temperature ductility, a higher allowable operating temperature, and higher adhesive properties. The exterior surface of the outer acrylic ply and the interior surface of the inner acrylic ply are hard-coated for abrasion and chemical resistance. The windshield has an electric de-icing system. The windshield and its supporting structure are designed to withstand the impact of a 4-lb (1.8-kg) bird strike at Vc at sea level.

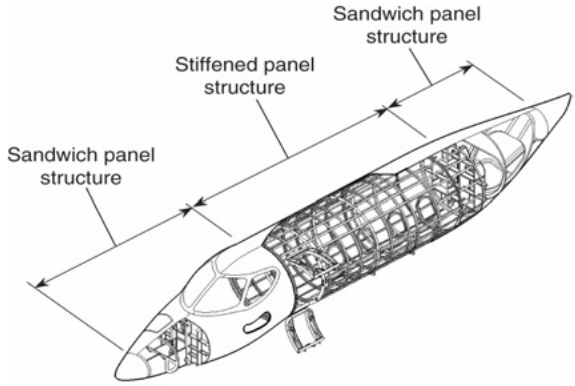


Fig. 16 Fuselage structure

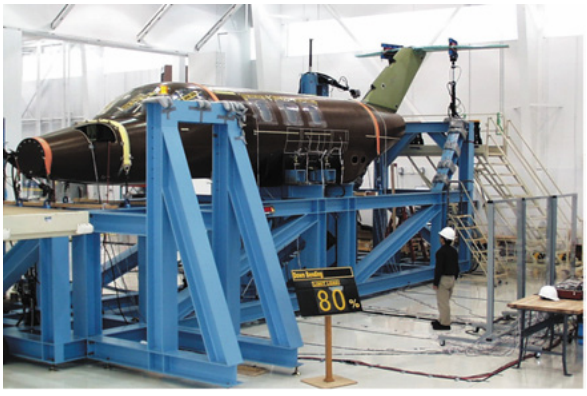


Fig. 17 Fuselage proof test

The fuselage structural design was substantiated by a proof test (Fig. 17). Six computer-controlled hydraulic actuators were used to simulate loads, including that from pressurization. A total of six load cases were observed: pressurization, positive gust, positive gust with pressurization, rudder maneuver, rudder maneuver with pressurization, and two-point landing. As in the wing structure tests, the same fuselage used for proof tests will also be used for flight testing, so the test loads were limited to 80% of the limit loads. The fuselage strength was verified by the same method as the wing strength.

6. Systems

6.1. Landing Gear

The landing gear is a typical tricycle configuration with a steerable nose wheel. The main gear is the trailing-link type (Fig. 18) and the retraction actuator is the side brace. The landing gear doors consist of three doors, inboard, middle and outboard. The inboard door is operated with its own hydraulic actuator and the middle and outboard doors are operated by the movement of the gear through a linkage with the landing gear strut. The wheel well is completely covered by the doors so that the wheels are unexposed to the airstream and minimizes drag during cruise. The side brace actuator is equipped with an internal down-lock mechanism; in an emergency, a dump-valve allows free-fall extension of the gear.

The main gear contains an anti-lock braking system; it was tested on a dynamo system to optimize brake control. The braking system is fully equipped with locked wheel protection, touch-down protection, and spin-up override.

The nose gear incorporates a shock-absorber strut (operating in the vertical direction). The drag brace actuator retracts the gear forward (Fig. 19). The doors are operated by a linkage with the gear as the gear is extended or retracted. The drag brace actuator is equipped with an internal down-lock mechanism. The nose gear features steer-by-wire through hydraulic actuators controlled by pulse-width modulation (PWM). There are two modes for the steering system: taxi mode, in which the steer-angle range is ±50°, and takeoff mode, in which the range is just ±10°. The nose gear also incorporates an accumulator for emergency control of steering in case of hydraulic pump failure.

Drop tests of the shock absorption characteristics of the gear were conducted using a weight to simulate aircraft mass (Fig. 20). The oleo shock absorber was found to satisfy the design objectives.

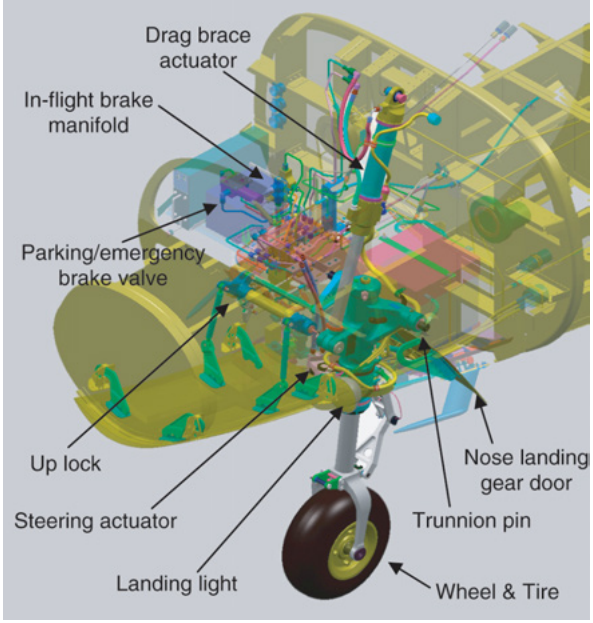


Fig. 19 Nose landing gear

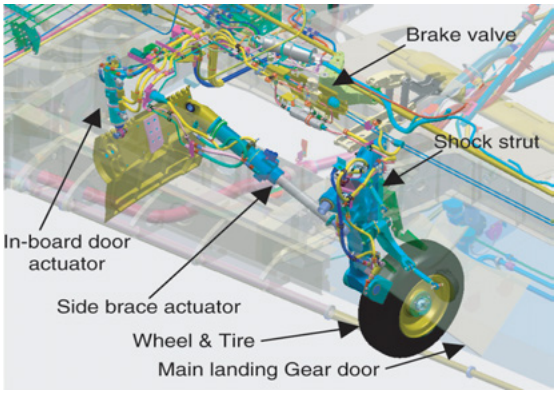


Fig. 18 Main landing gear

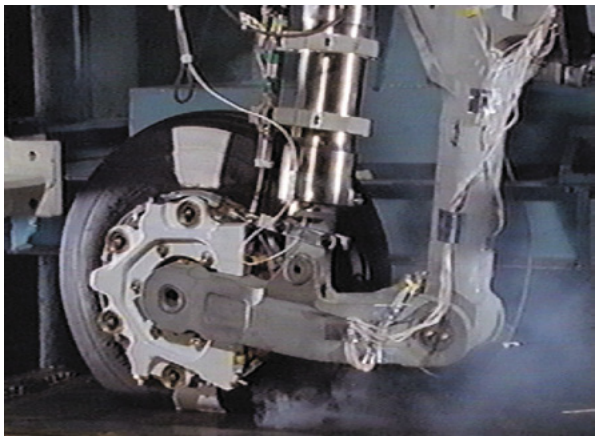


Fig. 20 Main landing gear drop test

6.2. Flaps

This aircraft employs a mechanically extended, linkage-type flap with a fixed vane. As shown in Fig. 21, there are two extended positions, 15.7° for takeoff and 50° for landing. The flaps are driven by two hydraulic actuators, one at the root of each wing, and are mechanically interconnected to prevent a split condition (differing extension angles between left and right sides).

A fatigue test was conducted under flight load conditions. Airloads were simulated using a hydraulically loaded whiffle tree, which allowed the flaps to move. The results indicated that the flap mechanism withstands the number of fatigue cycles required for the flight tests program.

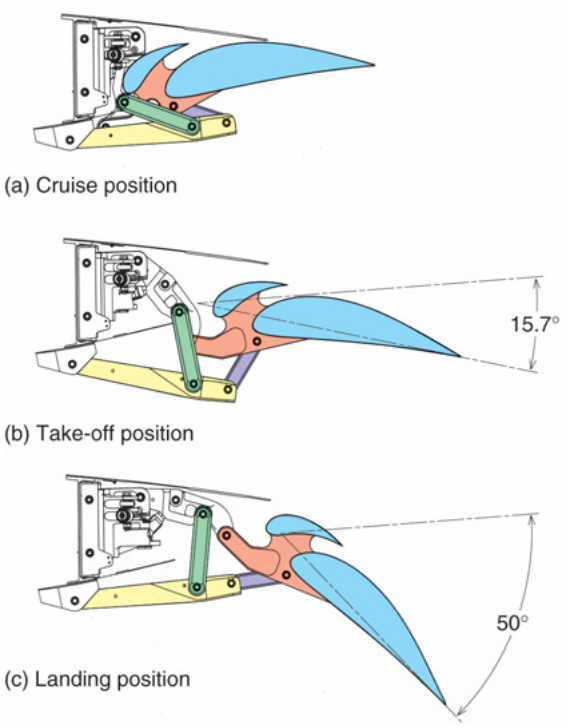


Fig. 21 Flap linkage mechanism

6.3. Fuel System

As shown in Fig. 22, the HondaJet has four fuel tanks, a carry-through tank, left-wing internal tank, right-wing internal tank, and rear-fuselage bladder tank.

Refueling is done through a single supply point on the right side of the rear fuselage. Fuel is transferred by two transfer pumps from the carry-through tank to the internal tanks in both wings. It is supplied to the right engine from the right-wing tank, and to the left engine from the left-wing tank, via collector tanks beneath each engine pylon. The primary pumps are ejector-type units and electric boost pumps are used during engine starting. A fuel transfer management unit (FTMU) maintains the fuel level in the wings, reducing mean wing root bending moment by about 12%. An automated cross-feed function system is also provided in order to allow both asymmetric thrust condition and correction of imbalance. The unusable fuel quantity was reduced to about 2% of total volume.

There are a total of 13 capacitance-type fuel sensors in the fuel system, three in the carry-through tank, four in each wing tank, and two in the bladder tank. They measure the amount of fuel with an accuracy of 2% + 1% of full-scale during any flight conditions within the aircraft's flight envelope.

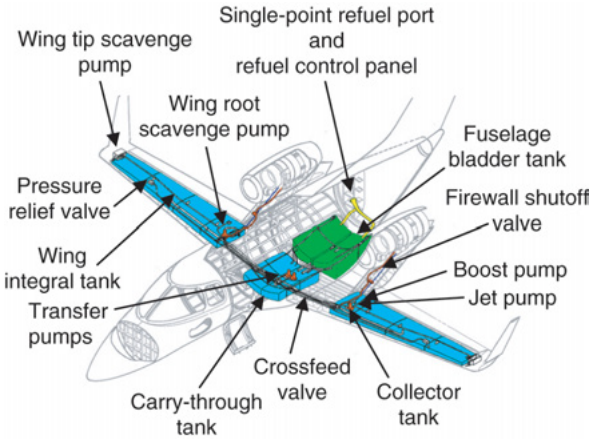


Fig. 22 Fuel system

6.4. Avionics

The HondaJet employs an all-glass flightdeck featuring modular design having open architecture. Figure 23 shows the cockpit. All data, such as aircraft attitude, air data, engine conditions, meteorological data, traffic conditions and geography, are digitally represented on two primary flight displays (PFD) and one multi-function display (MFD). The PFD contains an airspeed indicator, vertical-speed indicator, adjustable altimeter, direction indicator, pitch and bank indicator (artificial horizon), slip/skid indicator, dual NAV/COM and other functions. The MFD contains the EIDS (N1, ITT, N2, oil temperature, oil pressure), fuel flow, fuel quantity, generator current, GPS map, and other information.

Thus, the cockpit of the HondaJet incorporates highly integrated aircraft management capabilities for enhanced situational awareness, functionality, easy operation, redundancy, and flight safety.



Fig. 23 Cockpit

6.5. Other Systems

In order to maximize the volume of the cabin, the systems of the HondaJet were laid out as follows to make the most effective use of space in the nose compartment, wing-fuselage fairings, pylons and behind the rear bulkhead. The nose compartment contains the batteries, parking brake valves, the Attitude and Heading Reference System (AHRS), and other components. The wing-fuselage fairing holds Environmental Control System (ECS) tubing, heat exchangers, flow control valves, trim valves and other related equipment. In each pylon are fire control equipment and pre-coolers. In the aft section are the DC motor pumps (DCMP), reservers, accumulators, air conditioning, and related equipment. Figure 24 shows the locations of the systems. This new layout has allowed the designers to create an effective cabin volume which far exceeds that of other planes in this class.

7. Conclusion

Honda has developed and successfully flown a light, advanced business-class aircraft. It boasts many innovative features, including over-the-wing engine mount, natural laminar flow wings, natural laminar flow nose, and composite fuselage, which enable the HondaJet to offer a larger cabin volume, higher speed and greater fuel efficiency than any other jet in its class. The capabilities of this jet will be verified in extensive flight-testing. The author thanks everyone inside and outside Honda who have shared in this dream and contributed to its realization.

References

(1) Fujino, M., Kawamura, Y.: Wave-Drag Characteristics of an Over-the-Wing Nacelle Business-Jet Configuration, Journal of Aircraft, Vol. 40, No. 6, p. 1177-1184 (2003)

(2) Fujino, M.: Design and Development of the HondaJet, AIAA Paper 2003-2530 (2003)

(3) Eppler, R.: Airfoil Design and Data, Springer-Verlag, Berlin (1990)

(4) Fujino, M., et al.: Natural-Laminar-Airfoil Development for a Lightweight Business Jet, Journal of Aircraft, Vol. 40, No. 4, p. 609-615 (2003)

(5) Tidd, D.M., et al.: Application of an Efficient 3-D Multi-Grid Euler Method to Complete Aircraft Configurations, AIAA Paper 91-3236, AIAA 9th Applied Aerodynamics Conference (1991)

(6) Morgan, H.L.: High-Lift Flaps for Natural Laminar Flow Airfoils, Laminar Flow Aircraft Certification, NASA CP-2413, p. 31-65 (1986)

(7) Drela, M.: Design and Optimization Method for Multi-Element Airfoils, AIAA Paper 93-0969 (1993)

(8) Valarezo, W.O., Chin, V.D.: Maximum Lift Prediction for Multielement Wings, AIAA Paper 92-0401 (1992)

(9) Maskew, B.: Prediction of Subsonic Aerodynamic Characteristics: A Case for Low-Order Panel Methods, Journal of Aircraft, Vol. 19, No. 2 (1982)

(10) Fujino, M., et al.: Flutter Characteristics of an Over-the-wing Engine Mount Business-Jet Configuration, AIAA Paper 2003-1942 (2003)

(11) Matsui, N., Sato, K.: Research Work of the All-Composite Fuselage Structure for HondaJet , Honda R&D Technical Review, Vol. 16, No. 2

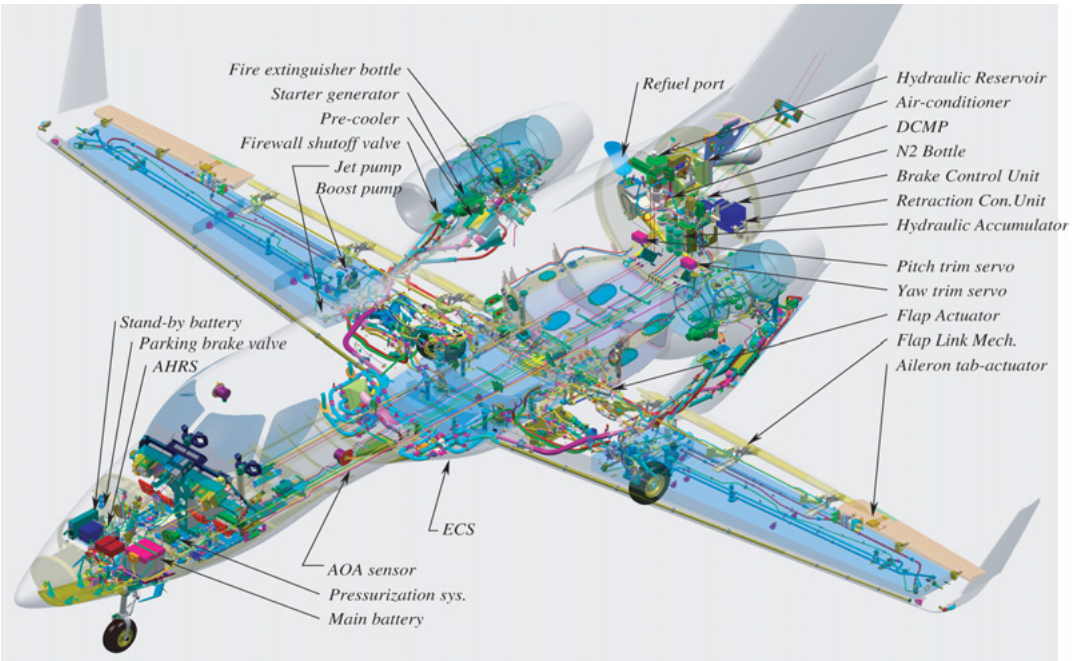


Fig. 24 System layout

■ Authors ■



Michimasa FUJINO

Research Work of the All-composite Fuselage Structure for HondaJet

Nobuo MATSUI* Keiichi SATO*

ABSTRACT

HondaJet utilizes an all-composite fuselage. The main feature of this fuselage structure is that the stiffened panel and the sandwich panel are co-cured integrally to reduce both weight and cost. Another key feature is that a buckling tolerance design is adopted for the skin. This means that shear buckling is allowed beyond 50% limit load. Several affordable process technologies were developed in the field of lay up and structural bonding. The material and structural tests were conducted applying the concept of "Building Block Approach" to prove safety of flight. First the design allowables of the materials were decided. Environmental, damage tolerance, and fatigue conditions were considered. Three major component tests were conducted.

1. Introduction

An important issue in the structures of aircraft is reducing weight. This has driven an increase in the use of composites in place of aluminum. Typically, a sandwich-panel structure is selected in the design of general aviation aircraft. Sandwich panel structure is effective in reducing the cost and development time due to a simple manufacturing process and a reduction in the number of molds and other manufacturing tools. However, the weight savings compared with conventional aluminum construction are not enough. In addition, there are difficulties with quality control and installation of some equipment.

The MH-02, an all-composite experimental aircraft developed by Honda, made its maiden flight in 1993[(1)]. Both its fuselage and wing were designed and successfully manufactured using sandwich panels. Later, a fuselage barrel was manufactured with co-cured stiffened panel structure with the objective of further reducing weight and evaluating the manufacturing process. This structure was indeed lighter, but it became clear that applying this method to components with three-dimensional contours would result in higher manufacturing costs.

This report describes the concepts and process technology behind the structural revisions accomplished in the lightweighting programs and cost-cutting measures of the HondaJet that achieved her first flight in December 2003[(2), (3)]. The procedures for assuring flight safety of the fuselage are also described.

2. Fuselage Structure

The fuselage of the HondaJet is constructed entirely of composites of carbon fiber reinforced plastics (below,

* Wako Research Center

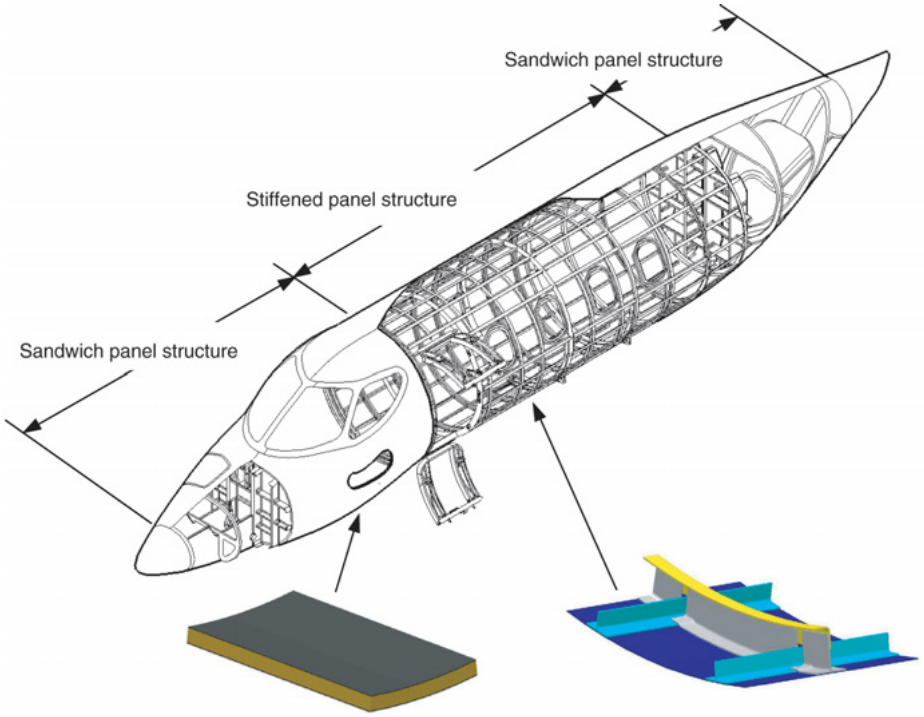


Fig. 1 Structural concept of all-composite fuselage

composite), with the exception of the windshields, the windows, and the metal fittings installed at locations subject to concentrated loads. The cabin is pressurized and has a clamshell type passenger door and a plug-type emergency exit. The design requirements are based on U. S. Federal Aviation Regulations (FAR) Part 23, a set of U. S. Federal Aviation Administration (FAA) standards for small aircraft.

The structural design was conducted to reduce weight and manufacturing costs while assuring adequate strength. Therefore, two structural configurations are used depending on shape: a stiffened panel structure and a sandwich panel structure (Fig. 1). Each panel type is assembled into the appropriate locations for curing in an autoclave as a large integrated whole as shown in Fig. 2. This co-curing process allows the fusing of multiple components into an integrated mass in a single cure step, without adhesives or fasteners. The structure of stiffened panel consists of a skin, stringers, and frames. While the structure of sandwich panel consists of a core material sandwiched between two sheets of skin. The stiffened panel structure, a typical construction for aircraft structures, is quite efficient from the structural view point and well suited for simple shapes such as the cylinder of an aircraft cabin. The sandwich panel structure, a very cost-efficient composite structure, is used for the three-dimensional contours of the nose, cockpit, and tail. In general, the curing pressure for sandwich panels is less than half of that for stiffened panels, which contain no honeycomb, to avoid collapsing the honeycomb core material. To realize this new concept structure, it was essential to cure the sandwich panels at the same pressures as the stiffened panels, so a new curing method was developed.

The second notable feature of this structure is that the buckling tolerant design was adopted for the skin of the stiffened panel beyond 50% of the limit load (the maximum possible load during flight). In decided contrast with other structures, aircraft structures, designed under severe weight requirements, are generally designed to allow some buckling.

In composite structures, however, few examples of buckling tolerant design exist. Therefore, shear buckling tests[4] were carried out on sub-components of stiffened panels to verify the post-buckling behavior and the final strength. From these results, a buckling tolerant design method for composite structure was established to select the numbers of skin laminations and fiber orientation necessary to meet design buckling conditions.



Fig. 2 Co- cured skin pane

The left and right skin panels are quite large, measuring 9.74 m in overall length, and are bonded to each other along the top and bottom single lap splices. This means that there are no splices running circumferentially except for the radome and the tail-cone splices. The cross sections for the stringers and the frames of the stiffened panels were designed in consideration of structural efficiency and the manufacturing process. Figure 3 shows those cross sections and the general configuration of intersections of them. The skin, stringers, and T-shaped frame members (white portion in the figure) making up the stiffened panels and the sandwich panels were integrally co-cured into a single, large skin panel. The L-section ring frames (yellow portion) and C-section ring frames (not shown), used where large concentrated loads were applied, were bonded at the same time that the left and right skin panels were bonded together. The height of the frame was limited to 45 mm to maximize available cabin space. Thus, the frame flange was laminated to preserve a modulus of elasticity of at least 80 000 MPa. The honeycomb thickness of the sandwich panels was set at 20 mm to provide the bending strength necessary to withstand cabin pressurization.

A trade study was conducted to compare weights of three fuselages for the reference model of a small business jet.

(1) Conventional aluminum structure (stiffened panel structure)
(2) Composite sandwich panel structure
(3) A new concept involving a sandwich panel and a stiffened panel structure

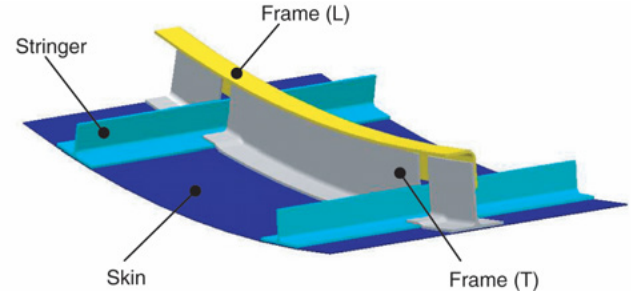


Fig. 3 Configuration of stiffened panel

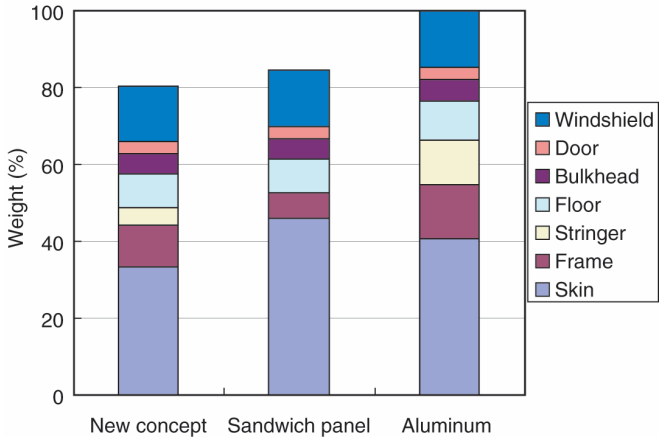


Fig. 4 Weight comparison of fuselage structures

The results of this study are shown in Fig. 4. The sandwich panel structure showed a reduction of 15% in weight over the conventional aluminum construction, and the new concept was predicted to show a reduction of about 20%.

3. Materials and Processes

3.1. Materials

The main material used for the fuselage structure was composite materials. The resin was a toughened epoxy type (Cytec 5276-1), cured at 180 °C and have high toughness and the capability to withstand hot-wet environments. The reinforced fibers were unidirectional and plain woven, high strength, and intermediate modulus carbon fiber (Toho G30-50). The raw material is sheet, called a "prepreg", and consists of a mixture of resin and fiber in a predetermined ratio. The components are designed with fiber-orientation angles and layup number of the prepreg (thickness) to satisfy the required characteristics. Once a component has been laid up on the mold, it is heated and pressurized in the autoclave to complete the forming and curing process. A honeycomb manufactured by Nomex was used as the core for the sandwich panels, and the core and skin were bonded with an epoxy film adhesive (3M FM300) that cures at 180 °C. Also, a resin film containing an expanded copper foil was laid on the outer surface to protect the skin from lightning damage.

3.2. Fabrication

To reduce labor-intensive operations from all phases of composite fabrication for the new concept structure, several new manufacturing processes were developed as follows:

- Press forming technique for pre-compaction parts with pre-laminate
- Step forming technique for joggle of pre-compaction parts
- Edge trimming technique for honeycomb with plugged freeze gel
- Fabrication technique for glass prepreg tool which considered thermal expansion
- Co-curing technique of stiffened panel and sandwich panel

3.2.1. Press forming technique for pre-compaction parts with pre-laminates

The stiffened panels in the fuselage were co-cured simultaneously with the skin, stringers, and frame into a single mass. The stringers of the stiffened panel were prepared by pre-compaction before co-curing. In general, composite parts are laminated layer by layer by hand lay-up, then vacuum bagged and heated. Labor costs of these processes are high. The process shown in Fig. 5 was developed to replace this. In this process, a wide, five-lamina sheet was fabricated in advance, and the machine-cut five layers were press-formed into the desired configuration. The pre-cut pieces were warmed at 90 °C, and the press-forming operation was carried out at 40 °C. This approach eliminated the inconvenience of single-layer lay-ups, vacuum bags, and heating in an oven. Required labor time has been cut to about one-fifth of the previous level.

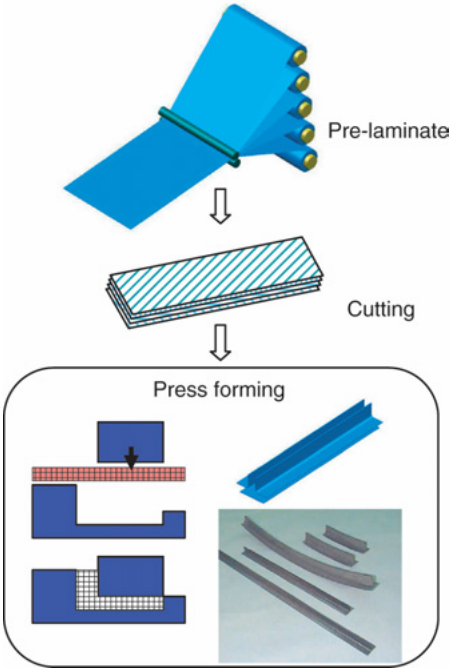


Fig. 5 Pre-laminate and press forming

3.2.2. Co-curing technique of stiffened panels and sandwich panels

Integrally co-cured composite structures are effective to reduce the number of parts and work load in manufacturing. Thus, it was necessary to combine the sandwich panels for the three-dimensional contours in an integral way with the stiffened panels for the cylindrical body (Fig. 6). The stiffened panels were formed under a high pressure (0.6 MPa) to assure quality and avoid interlaminar voids, but this pressure crushed the core of the sandwich panels. So usually, both configurations of panels could not be manufactured together. Potting compound is normally filled into the core to prevent collapse, but this increases weight. The method shown in Fig. 7 was developed to avoid these issues. Picture frame shaped plates 120 mm wide were placed around the edges of the honeycomb core to prevent slippage of the prepreg and stop collapse of the core. This approach allowed formation of an integrated, highly reliable skin panel without increasing weight.

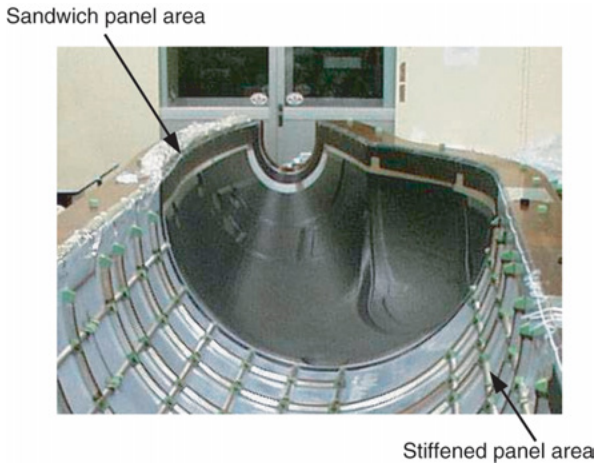


Fig. 6 Skin panel under fabrication

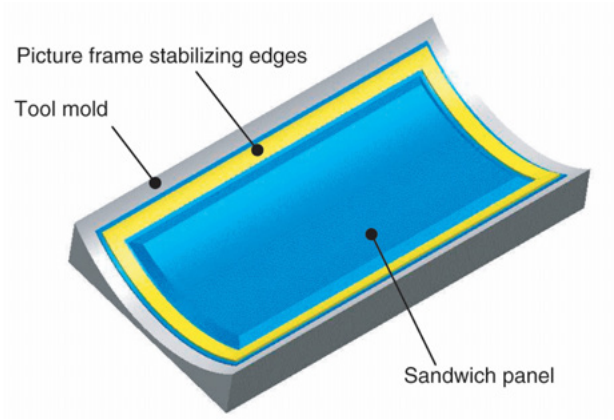


Fig. 7 Method to prevent core crash

3.3. Airframe Assembly

The primary structure of the fuselage was bonded with 120 °C cured epoxy film adhesive. The assembly method/jigs to keep the dimensional accuracy and contact pressure during bonding processes were developed. Figure 8 shows the fuselage assembly jig which was designed to keep accurate geometry of the fuselage and to maintain sufficient contact pressures during cure at 120 °C.

To address issues caused by different thermal expansion between the composite components and the steel jigs during the 120 °C curing process, the assembly jigs were designed to slide longitudinally. At the wing and fuselage joint, where relatively tight dimensional tolerances were called for, jigs were constructed of composite pipe to eliminate differential thermal expansion. These made it possible to hold, for example, a tolerance within 0.25 mm on a dimension of 1 360 mm between the two pins in critical metal fittings that fasten the wing to the fuselage.

Figures 9 and 10 show methods developed to ensure adequate contact pressure between adjoining components during the bonding process. The magnetic force of neodymium magnets were used at right and left skin bonded joint, and the hoop tension of composite bands were used at bonded ring frame assembly. These methods cut the labor time to one-third of that necessary for the same kind of procedure using clecos. Figure 11 shows the fuselage assembly.

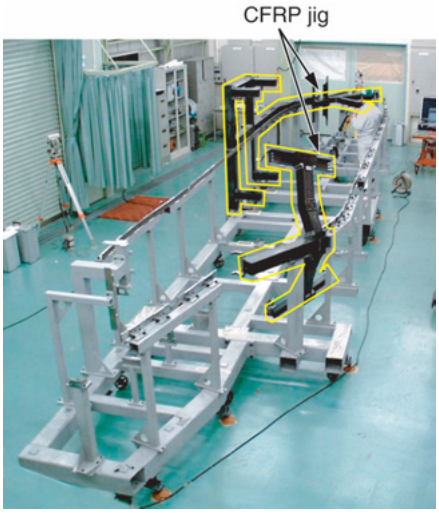


Fig. 8 CFRP/steel assembly jig

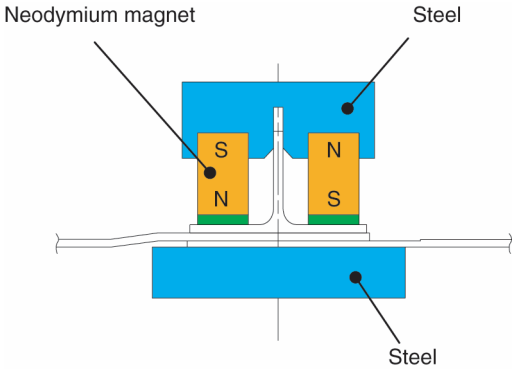


Fig. 9 Bonding method with neodymium magnet

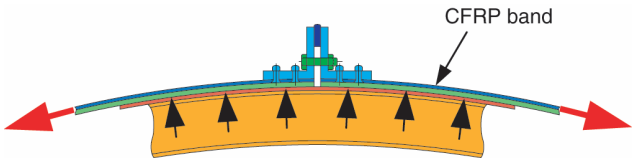


Fig. 10 Bonding method with CFRP band



Fig. 11 Fuselage assembly

4. Flight Safety Assurance

4.1. Procedure

HondaJet is an experimental aircraft, but the material and structural tests of the composite fuselage were conducted applying the concept of "Building Block Approach" based on FAA advisory circular AC20-107[5]. They comprised coupon, element, sub-component, and component tests. The purposes of these material and structural tests were to determine design allowables, to verify the accuracy of the FEA and other analyses, and finally to prove safety of flight for the composite fuselage. Furthermore, the full-scale proof test of the fuselage for flight was conducted to confirm the repeatability of the strain level to compare with component test results.

4.2. Design Allowables and Coupon Test

We considered "Damage tolerance", "Environmental condition (temperature and humidity)", and "No-growth damage under the fatigue" to determine material design allowables. A lot of data from coupon tests were obtained for these purposes. The coupon test specimens were subjected to impact damage, and the strength tests were conducted under hot-wet condition. Figure 12 shows the relationship between compressive failure strain and impact damage under hot-wet condition. The compressive design allowable was determined with these test data by considering barely visible impact damage and the worst environmental condition.

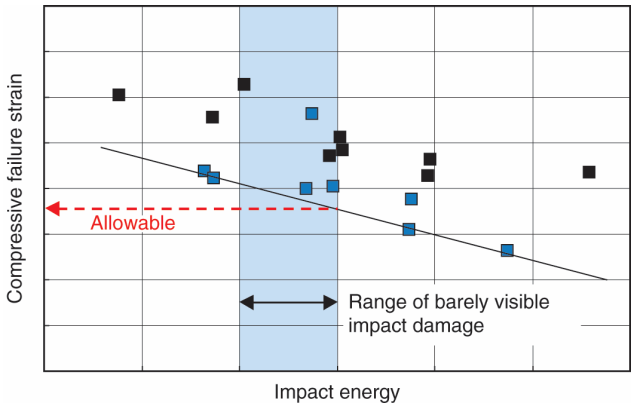


Fig. 12 Compression design allowable

4.3. Element Tests

The 17 strength-critical elements in the structure were selected and tested. The main objective in element tests is to verify the strength of already impact-damaged critical bonded joints in hot-wet environments. Other specific elements were tested such as cutouts in the heavily loaded frame web, skin joggles around the windshields, and transition area between sandwich panels and stiffened panels. The lightning protection system in the skin was also tested. The resin layer containing the expanded copper foil described above showed good protection capability with a minimal weight penalty.

4.4. Sub-component Tests

In the building block approach, before the component tests, which are the highest level, the following five essential structures were selected for testing at the sub-component level.

(1) Stiffened panel (tests for shear/compressive buckling, static strength)
(2) Stiffened panel with window (tests for shear buckling, static strength)
(3) Passenger door (tests for static strength, fatigue strength, fail safe strength)
(4) Wing and fuselage joint (tests for static strength, fatigue strength)
(5) Windshield (tests for static strength, fail safe strength)

All composite sub-components were subjected to barely visible impact damage to verify damage tolerance at critical points.

The shear buckling test of the stiffened panel was conducted to evaluate the post-buckling design and load carrying capacity after buckling (Fig. 13). The sub-components were 0.8 m squared curved panels with the same

structural detail and manufacturing process as the actual structure. The picture frame type jig to apply the shear load on the panel was designed to avoid warping due to curvature of the panel during the test.

Buckling load of finite element analysis (FEA) showed good agreement with the test result. The final strength shown by the panels was at least 4.5 times greater than their buckling load, and the failure mode was compressive failure of the skin. No clear delamination of the stiffener from the skin was observed until the collapse.

The objective of the passenger door sub-component test (Fig. 14) was to assure pressurization fatigue strength under three lifetimes, i. e., 60 000 cycles and air-tightness. The door was attached to a steel pressure vessel, and the pressure was cycled with a blower. Pressurization fatigue strength was confirmed for all components except the metal lugs connecting the upper and lower doors. The lugs were then re-designed, and fatigue strength was confirmed after additional element test.

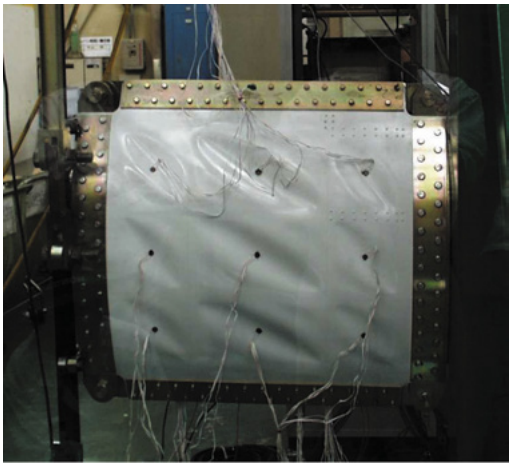


Fig. 13 Shear buckling test of stiffened panel

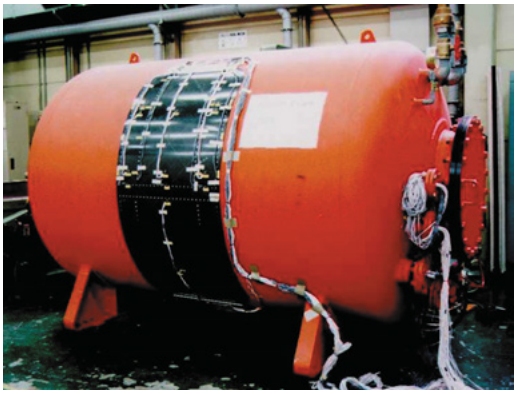


Fig. 14 Sub-component test of passenger door

4.5. Com ponent Tests

The objective of component tests was to prove the strength of the fuselage by full-size components. This corresponds to the top of the building block. The fuselage was divided into the three following components in consideration of manufacturing and testing facilities and the functions of the fuselage.

(1) Nose component (proof of nose landing gear attachment)
(2) Cabin component (proof of pressurized cabin for bearing flight loads and pressurized loads)
(3) Tail component (proof of vertical tail attachment)

Barely visible impact damage was applied to critical points of the components. The tests were carried out at standard room temperature conditions due to the limited test facilities. A knockdown factor was added to the test load to compensate for the expected decrease in strength of the components in hot-wet environments.

The nose component included the installation of a dummy nose landing gear attached to the front bulkhead. A hydraulic actuator applied three cases of landing loads through the dummy nose landing gear. The nose component carried these loads successfully.

The cabin component was the pressurized section between front and rear bulkheads of 5.8 m length including the passenger door, emergency exit, windshields, and windows. The main objectives of the cabin component test were to measure the strains, displacements, reaction forces, and skin buckling load to verify the accuracy of FEA, and to prove the static strength and three lives pressurized fatigue strength. The test procedure was as follows:

(1) Limit load test of four cases of flight and pressurized loads
(2) Pressurized fatigue test for three lifetimes (60 000 cycles of normal operating load) after impact damage in critical points of the composite
(3) Ultimate load test (1.5 times the limit load), residual strength (final strength) test

Five servo-controlled hydraulic actuators simulated flight loads and a blower applied pressurization (Fig. 15). Figure 16 shows buckling behavior under the limit load. Shear buckling occurred at the design target, 50% limit load, as shown in Fig. 17. Observation of strain revealed less than 10% error in the prediction by FEA. These tests also showed that the impact damages did not grow under three lives cyclic pressurized load. On the other hand, cracking occurred in a few fasteners, metal parts of the door, and the acrylic windshields. These were repaired or replaced during testing. The ultimate load test and residual strength test were carried out after the pressurized fatigue test.

The tail component was 2.6 m long with a dummy aluminum empennage. The main objectives of the tail component tests were to prove static strength of the fuselage to empennage joints. Front end of the component was clamped to the test frame, and loads were applied through the dummy empennage by six hydraulic actuators (Fig. 18). First, limit load tests were carried out at the critical three load cases. Because impermissible buckling occurred during some loading conditions near the empennage attachment, the affected locations were reinforced with laminate plate, and testing was continued to prove the strength of the component. This concluded the tail component test.

The necessary reinforcement during the component test was reflected in revisions to the design of the fuselage.



Fig. 15 Cabin component test



Fig. 16 Skin bucking at limit load

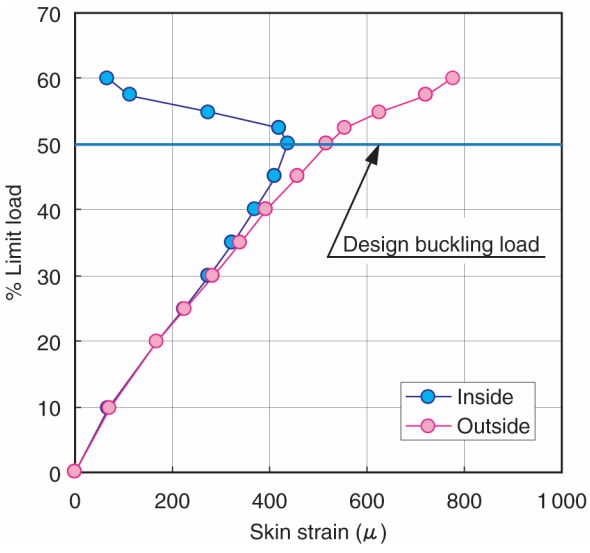


Fig. 17 Load vs. skin strain



Fig. 18 Tail component test

4.6. Proof Test

Proof test was carried out to confirm that the results of the three component tests would be reproduced in the entire fuselage used for the actual flight. The fuselage structure used for the test is used for the flight program so the test load was limited up to 80% limit load. Six load cases were selected: pressurization, positive gust, positive gust with pressurization, rudder maneuvers, rudder maneuvers with pressurization, and two-point landing. These were applied by the six actuators of MTS Aero90 system. It simulated design flight load as close as possible (Fig. 19), and the fuselage bore all load cases.

The strains, displacements, and reaction forces were measured at representative locations, and these results were compared with those from both component tests and FEA. The reproducibility of the component tests and validity of FEA were confirmed. The strain values extrapolated from strain observed at the critical points were also confirmed to be within design allowables.

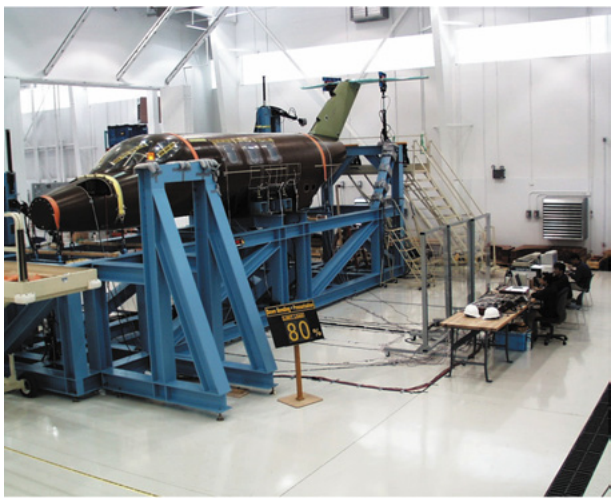


Fig. 19 Fuselage proof test

5. Conclusion

An all-composite fuselage was developed using a new concept involving the integral co-curing of assembled stiffened panel and sandwich panel. And the first flight was performed successfully. The following results were reported.

(1) The new structural concept and buckling tolerant design permitted the structure to be lightened by 20% in comparison to conventional aluminum structure.
(2) Newly developed process technology cut manufacturing costs in both fabrication of components and assembly with adhesives.
(3) Structural analyses and tests from the coupon level to the component level were carried out, in the same “building block approach” used for certification of an aircraft. Furthermore, the proof test of the fuselage for flight was conducted. As a result, safety of flight for the composite fuselage was proven.

References

(1) Nakayama, H., Bennett, G.: Introduction of the MH-02 Experimental Aircraft a Joint Research Program of MSU and Honda, Proc. AIAA/FAA/MSU 3rd Joint Symposium on General Aviation Systems (1994)

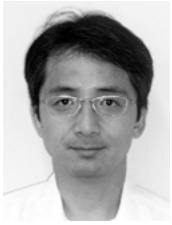
(2) Fujino, M.: Design and Development of the HondaJet, AIAA Paper 2003-2530 (2003)

(3) Matsui, N., Sato, K.: Research Work of the All-composite Fuselage Structure, SME Technical Paper, TP04PUB157 (2004)

(4) Sato, K., Kawabe, S.: An Experimental Investigation of Shear Buckling Behavior of Curved Stiffened Panels, Proc. 27th JSCM Composite Material Symposium, p. 165-166 (2002) (in Japanese)

(5) Federal Aviation Administration, AC 20-107A, Composite Aircraft Structure (1984)

■ Authors ■



Nobuo MATSUI



Keiichi SATO

Development of EM7000is Dual-voltage Inverter Generator

Masashi NAKAMURA* Shouhei KASAGI* Tadafumi HIROSE*
Yasuhiro SHINKAWA* Koichi ASAI* Kenji KAMIMURA*

ABSTRACT

Honda's current inverter generators have a maximum power output of 3kVA and are limited to single-voltage output. Dual-voltage output is essential when producing higher-power inverter generators, as the larger equipment connected to them requires either high current or high voltage. A new dual-voltage inverter has therefore been developed to meet these needs.

The dual-voltage inverter produces two voltages by connecting two inverters either in parallel or in series.

Sub-winding for each inverter unit power supply has not been employed in the alternator. Instead, only main windings have been used, and the power supplies have been built into each inverter unit, meaning that the system is composed of the output of the main winding. This has enabled the alternator to be reduced in size and increased in efficiency.

The completed generator is equipped with an integrated control unit. The centralization of control functions has enabled 2/3 of the electronic components to be eliminated and a liquid crystal monitor to be employed to display information.

Like Honda's previous inverter generators, the newly developed EM7000is employs an electronic governor. In combination with its shroud sound isolation duct structure, this enables the unit to run quietly with high fuel efficiency.

1. Introduction

Portable generators are used throughout the world for leisure, business, domestic applications, and also for emergency. In recent years, they have come into wide use as power sources for electronic equipment, such as computers, which require a high quality source of electric power. They are also required to be compact, lightweight, and easy to use. In order to meet the needs of such customers, a series of compact and lightweight inverter type generators, GENE21, which outputs high quality power and varies the engine speed according to the load was developed[(1) – (3)], and currently enjoys a very favorable reputation in the marketplace.

Recently, the proportion of electric power used in IT applications has increased greatly, and the need for a large output inverter type generators is increasing. The maximum output from GENE21 is 3 kVA, and all models output only a single voltage. In the case of a generator of 4 kVA or higher capacity, the equipment connected to the generator is also correspondingly large, hence large current and voltage are demanded. In other words, there is a need for a dual-voltage type generator that outputs two voltages, such as 120 V and 240 V, for example.

With the conventional synchronous generator, it is possible to obtain two outputs of identical phase by simply arranging the two output windings on the stator winding so that they are in the same phase. Connecting the two output windings in series results in a high-voltage output of 240 V, and connecting them in parallel enables a high-current output of 120 V to be obtained. In the case of the series 240 V output, it is also possible to simultaneously output 120 V between the neutral points. In this way, the conventional synchronous generator can readily provide a dual-voltage output.

This paper describes the issues to be solved in order to obtain a dual-voltage output from an inverter, and also newly developed technology. It also describes the contents of technology employed in the development of the EM7000is (name used in North America and applies to other generators

* Asakahigashi R&D Center

as well) dual-voltage inverter generator which is designed to be more compact than the conventional synchronous generator and generate less noise.

2. Technical Issues and Goals

2.1. Inverter

A study of a dual-voltage output type generator was made. As an example, a generator that has an output of 5 kVA and outputs two voltages, 120 V and 240 V is described.

First, a study of an inverter that outputs only one voltage, either 120 V or 240 V, was performed. The output was set to 5 kVA, and the component parts, mainly the power devices, were designed to pass a current of 42 A (5 kVA/120 V) and have a withstand voltage of 120 V in the case of a 120 V output, and were designed to pass a current of 21 A (5 kVA/240 V) and have a withstand voltage of 240 V in the case of a 240 V output. In the latter case, a withstand voltage of twice 120 V is necessary, however the required current carrying capacity is halved.

Next, a study of a single inverter unit that was capable of outputting two voltages of 120 V and 240 V was performed. The output was set to 5 kVA.

First, as (a), a study of the method in which the voltage is switched over by internal control was performed. In this case, the design current must be set to the higher value of the above, in other words to 42 A (5 kVA/120 V), and the design withstand voltage must be set to 240 V. Consequently, compared to the case of the voltage output of a generator that outputs only a single voltage, it is necessary to use power devices that have twice the current handling capacity and twice the withstand voltage even for the same 5 kVA, so it is difficult to make a compact and low cost design.

Also, as (b), a study was performed which involved the use of two 2.5 kVA inverters to produce two voltage outputs by switching them between series connection and parallel connection. In this case, the current is 21 A (2.5 kVA/120 V) and the withstand voltage is 120 V, so the power devices need only half the size. This enables the generator to be designed compactly and at low cost.

The foregoing is summarized in Table 1. For new specifications, (b) was adopted. However, it is necessary to accurately synchronize both inverter units. Therefore, dedicated communication lines were installed between the inverters, and signals were continuously exchanged between them, enabling them to be synchronized accurately with each other. Details are shown in 3.2.

2.2. Alternator

A study of an alternator was also performed.

The alternator for Table 1(a) requires both a large current and a high voltage, necessitating a substantial number of thick windings. This results in a large unit and also difficulty in making the windings.

In contrast, the alternator for Table 1(b) requires two separate systems, but can be made compact compared to (a). For new specifications, (b) was used in addition to the inverter. Details of the alternator are described later in 4.1.

Table 1 Comparison of dual-voltage inverter type

Devices	(a)	(b)
Specification	42A 240V	(21A 120V) × 2
Volume	2 :	1
Cost	High	Low
Adoption	–	○

2.3. Generator Control

The conventional synchronous generator consists of a large number of units including the ignition unit, timer unit for preventing the starter from double contact, auto throttle unit, battery charging unit, fuel cut solenoid drive unit with remote control interface, and oil alert unit. Also, a mechanical type auto-choke is used. In addition, an operating time integrating meter is being newly demanded, and with this configuration it is unavoidably necessary to install an expensive unit later.

Accordingly, this configuration was integrated and the entire generator was electronically controlled in order to reduce the number of components and realize a generator that could be used easily by the customer. Table 2 shows a system comparison. This unit is called a Generator Control Unit (GCU). By thus configuring the generator as a single unit, it was possible to reduce the number of components to 1/3, and also to add an electronically controlled choke for improved starting performance, as well as an information monitor (i-monitor) that functions as an hour meter, and so on. The detailed functions of the GCU are described later in section 6.

Table 2 Comparison of generator control systems

Function	Conventional system	New system	
Ignition system	Ignition unit + Ignition coil	GCU	+ Ignition coil
Automatic choke	Diaphragm vacuum pump		+ Stepping motor
Battery charge	Charge unit		–
Remote control	Interface		
Prevention of double contact of starter motor	Timer unit		
Oil alert	Oil alert unit		
Operating hours display	Total operating hours meter		
Fuel cut system	Power supply + Fuel cut solenoid		+ Inverter
Automatic throttle	Automatic throttle unit + solenoid	Inverter	
Number of parts	12	4	

Except for wire harness and mechanical links

2.4. Power Supply

A method of supplying power for controlling the two inverters and the GCU was studied.

First, the same sub-winding system as that of the conventional GENE21 series generator was studied. In this method, one dedicated winding corresponding to one tooth is used for the power supply of the inverter in the alternator, however the use of this winding in a large alternator results in

poor efficiency, so was abandoned.

Next, a transformer method was studied. The main winding was made the primary side, and the two power supplies for the inverter and also the power supply for the GCU were connected to the secondary side. This method makes for high efficiency, however the input frequency is low, so the transformer cannot be significantly reduced in size. In addition, it is difficult to obtain space to install the transformer in the completed generator. For these reasons, the transformer method was abandoned.

Next, a method was studied in which each of the inverter and GCU units generate their own power supplies from the main winding. For new specifications, this method was adopted. Table 3 shows a brief comparison between each method.

The necessary power supplies for the inverter consist of one positive and one negative power supply, and also three independent FET driver power supplies (H bridge construction, with common lower arm), so these were integrated in a 5-system Ringing Choke Converter (RCC) power supply configuration. This is shown in Fig. 1. Each inverter unit has this configuration, enabling the circuit configuration to be simplified.

Table 3 Comparison of power supply for inverter and GCU

	Sub-winding	Transformer	Built-in to each unit
Efficiency	750W loss	30W loss	30W loss
Volume	Increase volume of alternator	Another space for transformer	A little another space for each unit
Cost	High	Middle	Low
Adoption	–	–	○

Likewise, the power supply for the GCU was also obtained from the main winding. The generator is often used in a completely battery-less condition, and so ignition during recoil starting and the method of obtaining a power supply were important issues. In other words, it was necessary to obtain a power supply from a speed that was lower than that of the inverter. Details of the power supply for the GCU are described later in 6.2.

2.5. Packaging

The targets for the completed generator were 30% miniaturization and reduction of noise level to 7 dB (A)/7 m in the practical load region compared to the conventional synchronous generator. Miniaturization and noise reduction are conflicting requirements, and it is necessary to assess the extent to which both cooling performance and noise reduction can be realized.

One method of reducing noise is a sound isolation box method in which the entire generator is covered with an outer panel. Because this structure involves the use of an outer shell, the volume is increased by 10% as compared to the pipe frame structure (structure of the conventional generator), making it difficult to realize the volume reduction target of 30%.

To overcome this, the completed generator employed a shroud sound isolation duct structure in which the engine was fully covered. Figure 2 shows the shroud sound isolation duct structure.

As a result of using this structure, a 30% volume reduction and also a reduction of noise by 7 dB (A)/7 m in the practical load region compared to the conventional synchronous generator were attained. Details of the structure are described later in section 5.

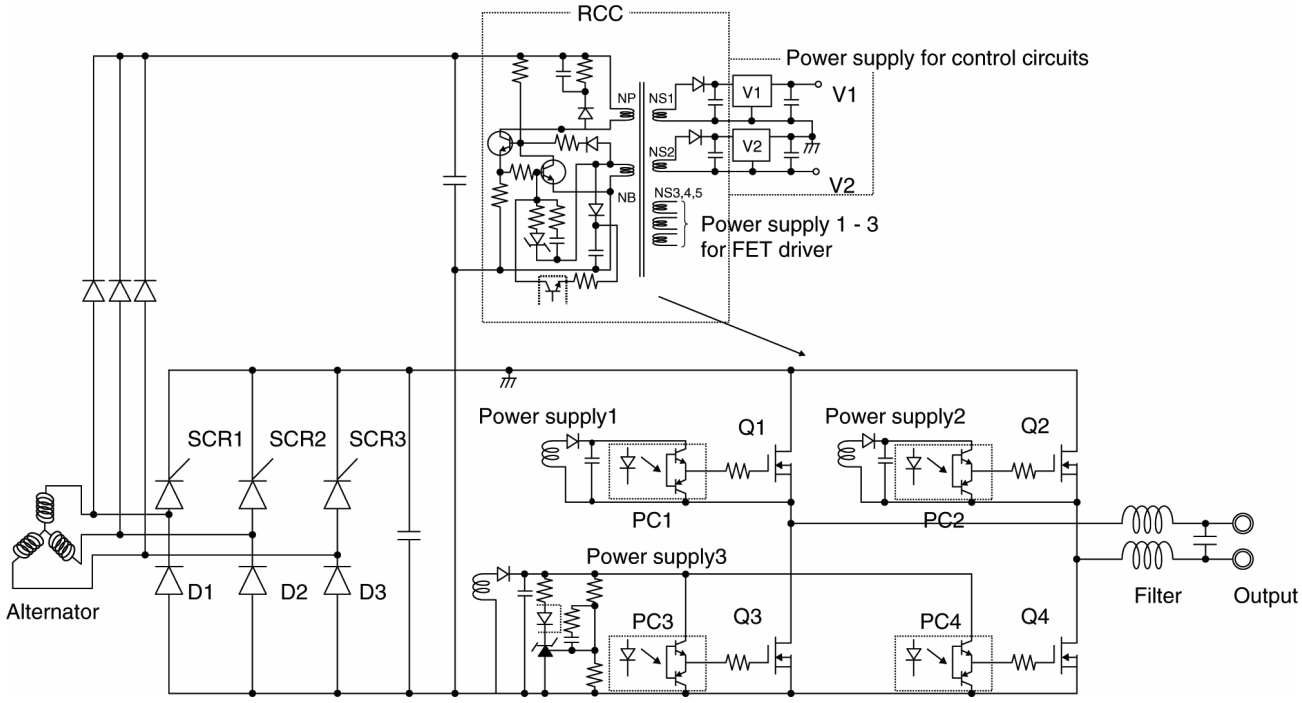


Fig. 1 Power supply system

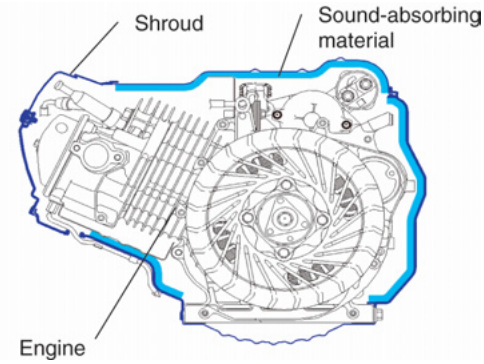


Fig. 2 Shroud sound isolation duct structure

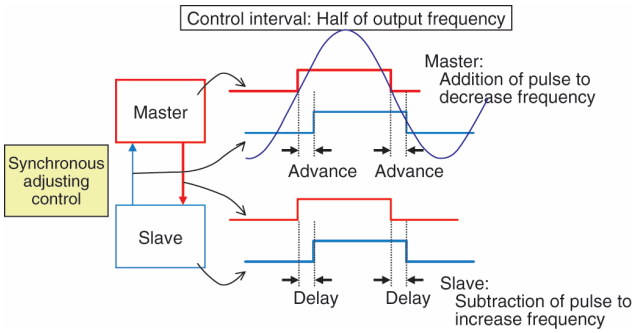


Fig. 4 Synchronous system of inverters

3. Dual-voltage Inverter

3.1. Configuration

The configuration of the dual-voltage inverter is shown in Fig. 3. As mentioned previously, this generator uses two inverters, called master and slave, respectively. When the two outputs are connected in parallel, a 120 V high-current output is obtained, and when they are connected in series, a 240 V single phase three-wire output is obtained. Switchover between series and parallel is done by a toggle switch. This connection method comprises a dual-voltage inverter that outputs two kinds of voltages. The phases of the two inverters must be identical to each other, so it is necessary to synchronize the inverters with each other.

3.2. Synchronization Method

Synchronization is realized by connecting mutually isolated dedicated communication lines between the two inverters. Figure 4 shows the actual control method employed.

Each of the master and slave inverters converts sine waves that it outputs itself, into square waves, and sends them to the opposite inverter. The square waves received from the opposite inverter are compared with the square waves output by the inverter itself. If an inverter judges that the phase of the waves that it outputs is advanced compared to that of the opposite inverter, it adds pulses to decrease the frequency of the sine waves that it outputs, while conversely if it judges that the frequency of the waves that it outputs is delayed compared to that of the opposite inverter, it subtracts pulses to increase the frequency of the sine waves that it outputs.

In this way, both the master and slave adjust their respective phases each half frequency, thus keeping in synchronism with each other. Because the communication lines are isolated from each other, the control operation keeps the inverters in synchronism without problem, for both series and parallel connections.

3.3. Reduction of Residual Harmonic

Like the GENE21 series, Pulse Width Modulation (PWM) is employed for the control system at the output stage. However, the carrier wave, in other words harmonics, remains in the output, and cannot be completely removed by filtering alone.

The dual-voltage inverter is connected as shown in Fig. 5. Here, the inverter was designed in such a way that the waveform of the slave is output 180° out of phase with that of the master, and when both outputs are connected to each other they are in phase. Consequently, the harmonics are connected in reverse phase to each other, enabling the residual harmonic to be significantly reduced. Figure 6 shows the case for an in-phase output. It can be seen that compared to this case, the residual harmonics have been reduced by roughly 6 V.

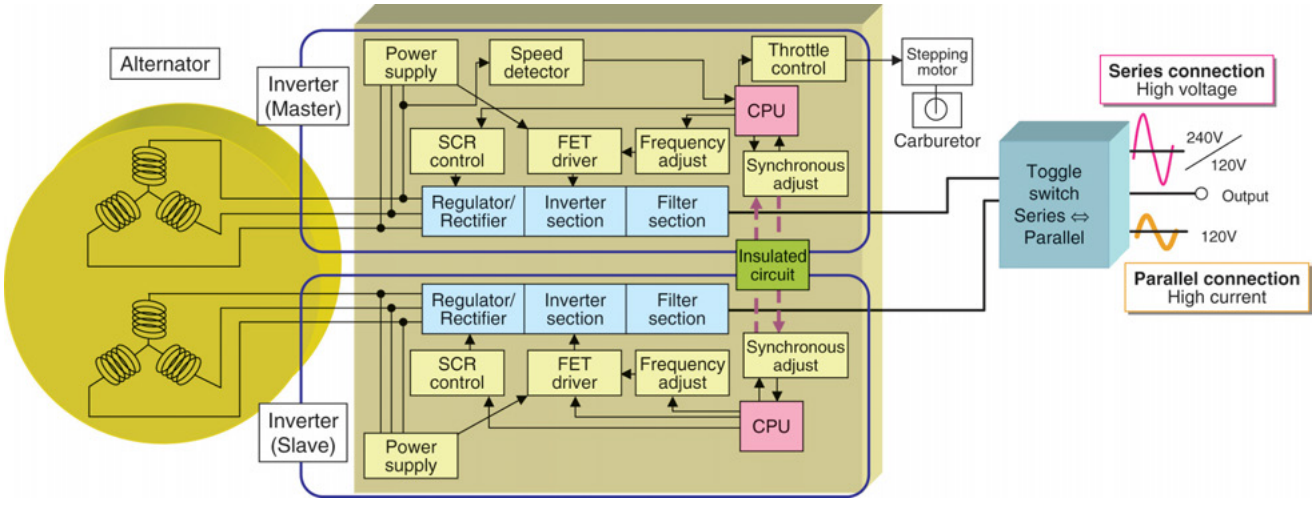


Fig. 3 Structure of dual voltage inverter system

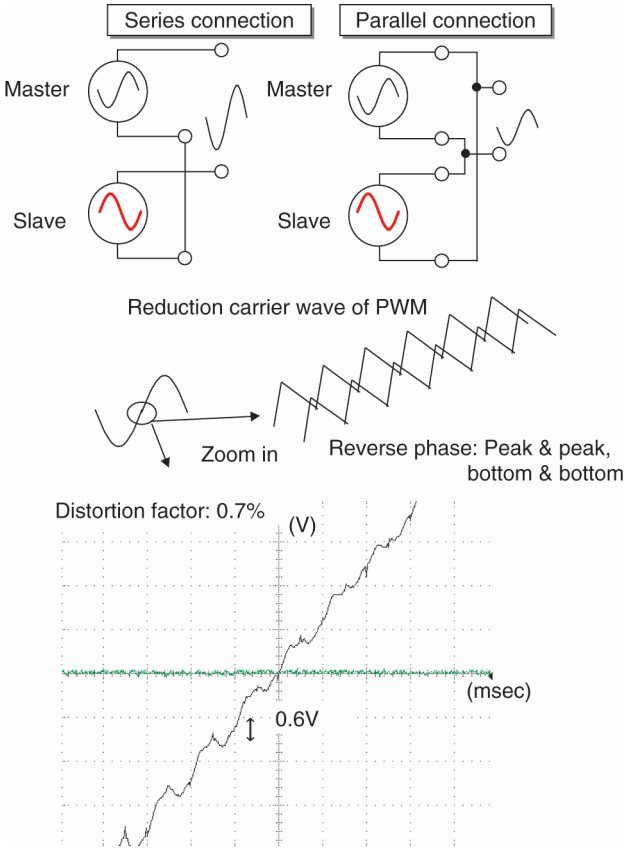


Fig. 5 Reverse connection method of master and slave

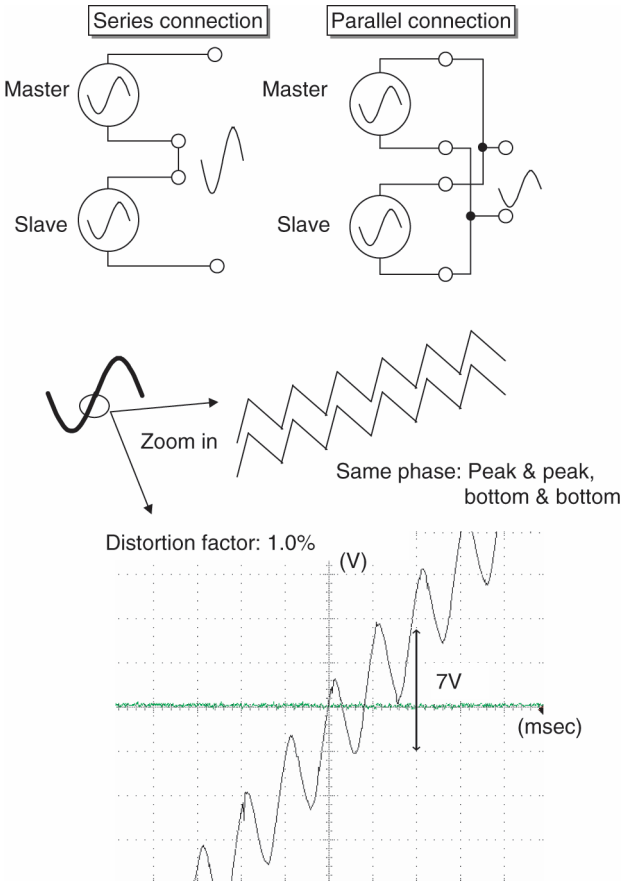


Fig. 6 General connection method of master and slave

4. Alternator

4.1. Structure

The EM7000is dual-voltage alternator was newly developed targeting compact size, high output, and high efficiency. Like the conventional GENE21 series, it is an outer rotor type high-speed multi-pole alternator. As shown in Fig. 7, the independent three-phase windings are configured as two systems. The stator has 30 teeth. Of these, 15 teeth each are used for the master and slave, respectively. There is no sub-winding for the control power supply of the inverter unit that existed in the conventional multi-pole alternator as mentioned previously. In other words, all of the teeth correspond to the main output windings.

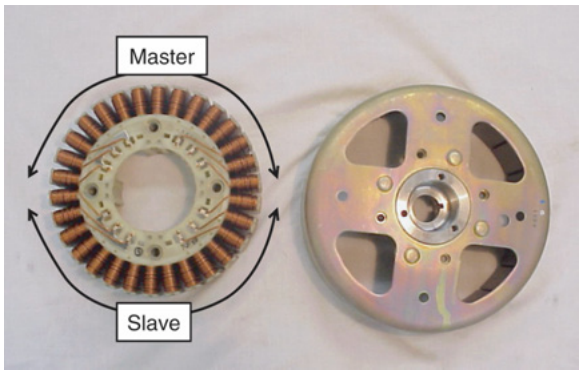


Fig. 7 Alternator for EM7000is

4.2. Comparison with Conventional Multi-pole Alternator

Because all of the teeth correspond to the main output, it was possible to realize a significant degree of miniaturization compared to the conventional multi-pole alternator, on a size-versus-output basis. Compared to the EU1000i, approximately 34% miniaturization was realized, and the output per tooth was increased roughly 5.2-fold. This is shown in Fig. 8.

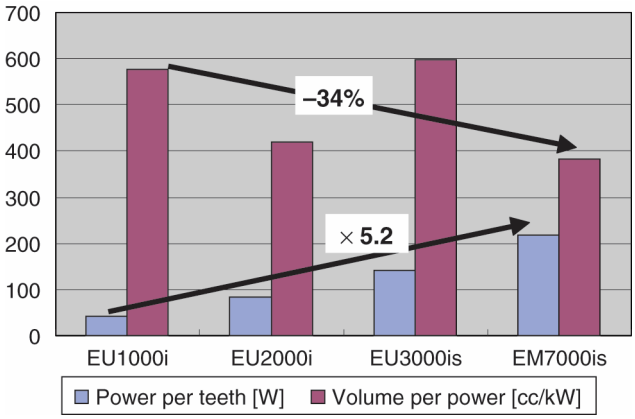


Fig. 8 Comparison of EM7000is with GENE21

5. Packaging

The structure of the completed EM7000is employed the optimum component layout and also a shroud sound isolation duct structure that fully covers the engine, in order to achieve reduced weight, compactness and cooling performance, while aiming for low noise. (Fig. 2)

5.1. Cooling Ability

As shown in Fig. 9, the various components of the generator were installed in a straight line in sequence from the inverter unit which produced the least heat, followed by the alternator, engine and muffler. The flow of the cooling air was made unidirectional, and the cooling air was made to flow in sequence from the components that generated only a small amount of heat, for improved cooling efficiency. As a result, whereas the conventional synchronous generator had two fans, one to cool the engine and the other to cool the alternator, this generator was able to combine these fans into one, resulting in reduced weight and size. In addition, the generator was constructed in such a way that the hot air emitted as a result of cooling of the engine was isolated from the other electrical equipment, in order to prevent the temperature in the vicinity of the electrical equipment covered by the shroud such as the ignition coil and self-starter motor from rising.

As shown in Figs. 10 and 11, the electrical equipment is partitioned from the engine cylinder by an upper bracket, forming a hot zone and a cool zone. This prevented the temperature of the electrical equipment from rising due to the flow of engine cooling air.

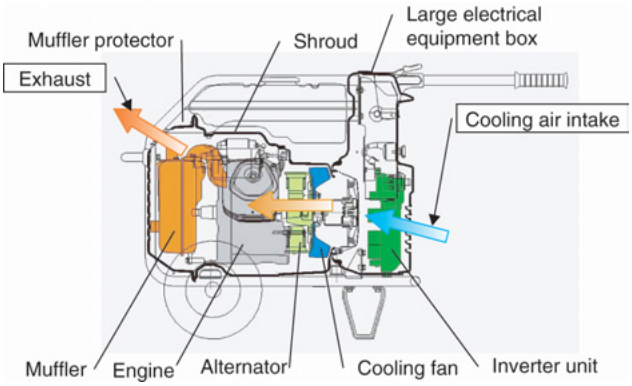


Fig. 9 Structure of complete generator

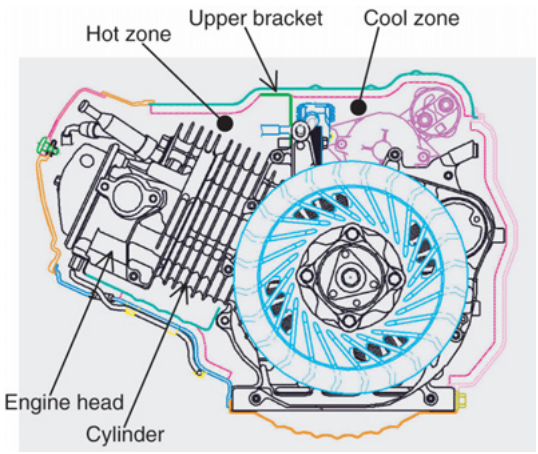


Fig. 10 Front view of engine

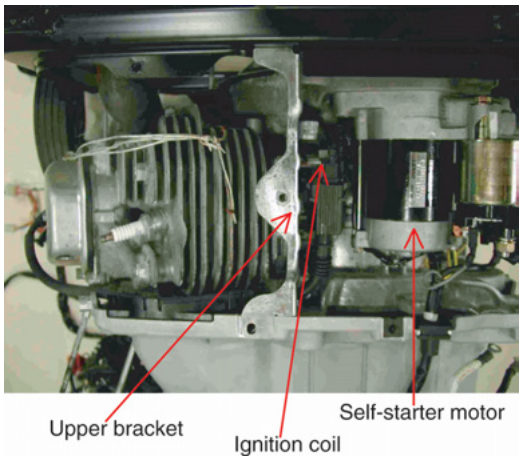


Fig. 11 Upper view of engine

5.2. Reduction of Noise and Fuel Consumption

The cooling mechanism shown in Fig. 9 was configured with the aim of simultaneously reducing noise emitted from the completed generator, which is a conflicting requirement. The large electrical equipment box which contains the inverter, control panel, and other electrical equipment, functions as a large intake chamber for the engine cooling air and the air cleaner. This was intended to reduce fan noise and air cleaner intake noise. The air exhaust section consisted of a large air exhaust chamber containing a long-tail large muffler, which was formed as a muffler protector. In addition, the entire engine was covered with a sound isolation shroud lined with soundproofing material (Fig. 2), aiming at reducing mechanical engine noise.

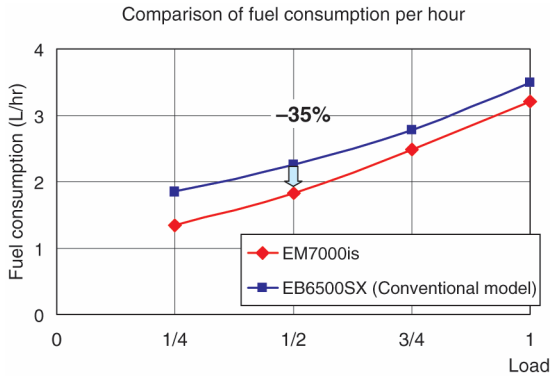


Fig. 12 Fuel consumption

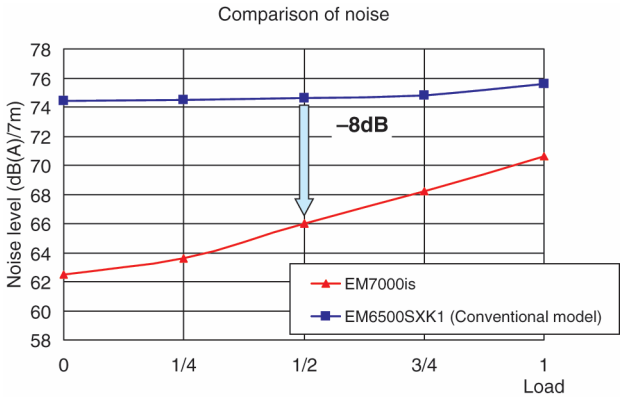


Fig. 13 Noise level

The employment of an electronic governor permitted the engine speed to be reduced in the practical load region, and also reduced both fuel consumption and noise. Compared to the conventional synchronous generator, the fuel consumption was reduced by about 35%, and noise was reduced by 8 dB (A) in the practical load region. The effectiveness in reducing fuel consumption is shown in Fig. 12, and the effectiveness in reducing noise is shown in Fig. 13. Note, however, that the effectiveness in reducing noise includes the noise reduction effectiveness of the completed generator cover.

5.3. Miniaturization and Weight Reduction

A U-shaped integrated pipe frame was employed, and a large plastic electrical equipment box was set at the front face corresponding to the open side of the frame. This is shown in Fig. 14.

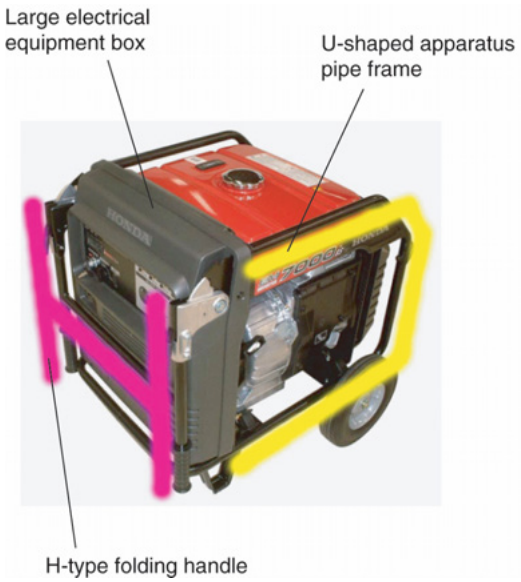


Fig. 14 Structure of a frame

A control valve type small MF battery (YTZ14S) was employed in a large electrical equipment box, instead of the large battery mounted on the outside of the frame of the conventional model.

This together with the use of a single fan mentioned above enabled the volume of the completed generator to be reduced by about 33% (when the handles are retracted) and the weight to be reduced by about 20%, compared to the conventional synchronous generator.

6. Generator Overall Control System

The EM7000is employed a system Generator Control Unit (GCU) that performs overall control of the completed generator. This enabled the number of electrical equipment to be reduced to about 1/3, and also realized a generator that is easy to use.

6.1. System Configuration

Figure 15 shows the configuration of the overall system. The system mainly performs the following kinds of control.

(1) Ignition timing control
(2) Choke control
(3) Starter control
(4) i-monitor and self-diagnosis
(5) Inverter communication and monitoring
(6) Reduction of after-burn when the engine is stopped
(7) Remote control interface

6.2. Power Supply

As mentioned above, there is no power supply sub-winding because the power supply is installed inside the unit.

Because it is necessary to maintain a high voltage for the main output voltage, it is not possible to use the shorting type thyristor regulator that is normally used. Also, this type of pipe frame generator is often used in a completely battery-less condition, so the full-transistor ignitor for recoil starting and also the power supply were major issues.

Accordingly, the power supply shown in Fig. 16 was developed and incorporated in the generator. The

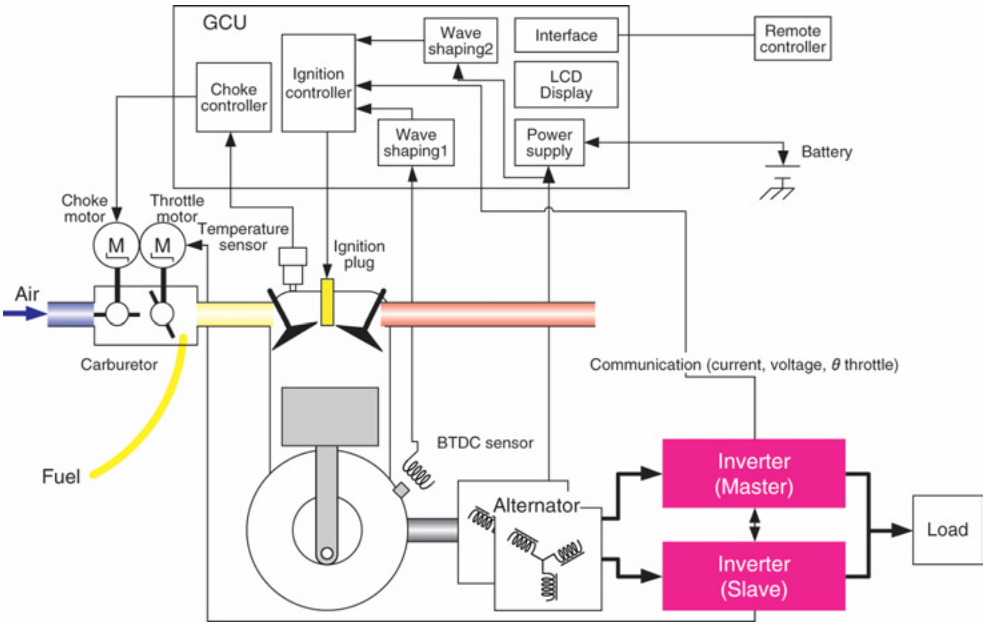


Fig. 15 Structure of GCU

specifications of this power supply are shown in Table 4.

Figure 17 shows the input versus output characteristics of this power supply during startup. Both outputs start to be generated at 125 rpm, and the system starts up, however in this speed region, the effect of kick-back during startup is large, so ignition is prevented from occurring below 180 rpm. The voltage of 5 V is obtained by voltage-dropping from the 15 V output using a 3-terminal regulator. The voltage boosting action of the 15 V system takes place to about 200 rpm, and that of the 17 V system to about 250 rpm.

Table 4 Specification of power supply

Input voltage	DC 10 - 400V
Output voltage 1	DC 15V ± 0.5V
Output current 1	MAX 2A
Output voltage 2	DC 17V ± 1V
Output current 2	MAX 0.8A

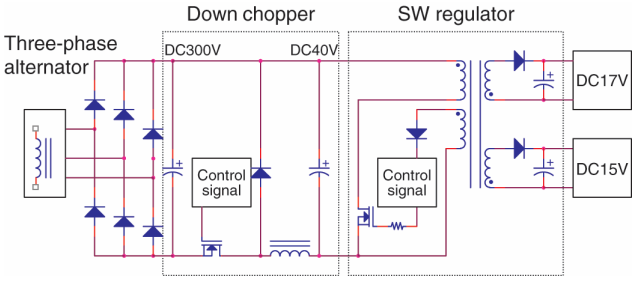


Fig. 16 Schematic diagram of power supply

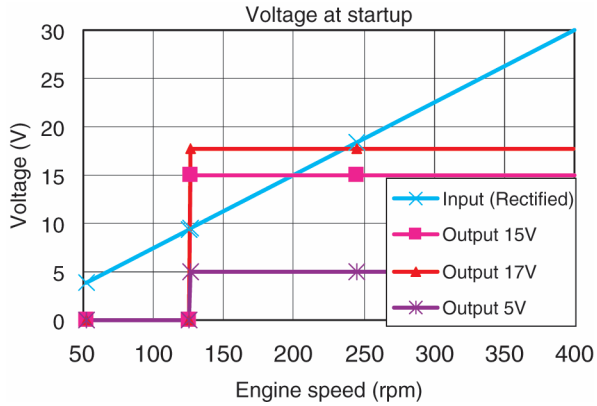


Fig. 17 Voltage of startup

6.3. Ignition System

A general-purpose product is often used in a battery-less condition, so the ignition method generally employs a transistorized magneto or a CDI which consumes relatively little power. In the case of this generator, however, the way became clear to obtaining power supply capacity for recoil starting, so a simple full-transistor ignitor method was used. A full-transistor ignitor method necessitates energization period control, so a crank angle sensor is necessary in addition to a TDC sensor. In this system, a 10-pulse/revolution pulse which is obtained by rectifying the alternator waveform is used instead of a crank angle sensor, rendering the crank angle sensor unnecessary. The timing for this is shown in Fig. 18.

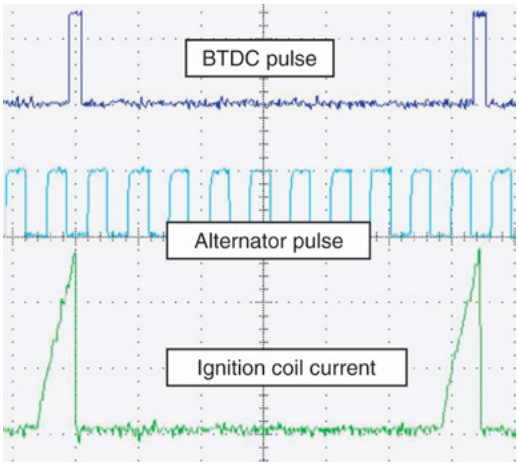


Fig. 18 Timing chart of ignition

6.4. Choke Control

Figure 19 shows the carburetor of this generator. On the left is the governor stepping motor, and on the right is the choke opening control stepping motor. The specifications of both of these motors are identical. Detection of the warm-up condition of the engine is done by using the cooling water temperature in the case of a fuel injection type water-cooled engine. In the case of an air-cooled engine, there are reported cases concerning motorcycles in which the temperature of the engine oil is used[4]. Both types employ injection period control in which the engine temperature is detected continuously, and combustion is regulated according to the temperature at that time. Although the engine of this generator is an air-cooled type, it does not have an oil circuit around the head, like the case of a motorcycle. Lubrication is performed only inside the crankcase, so it was not possible to use oil temperature to measure the engine temperature. For this reason, it was decided to install a thermistor on the head to directly detect the temperature of the head.

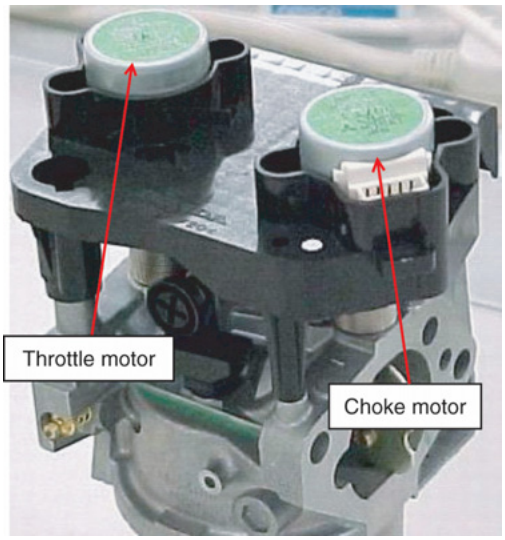


Fig. 19 Carburetor

6.5. i-monitor

Figure 20 shows the GCU. The liquid crystal display repeatedly displays the contents of Table 5 in the numbered sequence when the button at the right side of the display window is pressed. This is called an i-monitor. The default is an hour-meter display, which displays the data once every hour. However, internal integration is performed at 1-minute intervals so as to reduce the integration error.

If an error occurs in the system, a red LED flashes and an error code appears on the LCD display, as shown in Fig. 20. The display shown here is an example in which the engine temperature sensor is abnormal. The monitor communicates continuously with the master and slave inverters, and if an error occurs on the inverter side, the GCU immediately executes fail-safe action such as stopping the engine.

Table 5 i-Monitor display

	Mode	Unit
1	Total operating hours	hour (1 hour)
2	Power output	VA (50VA)
3	Engine speed	rpm (10rpm)
4	Battery voltage	V (0.1V)



Fig. 20 GCU

6.6. After-burn Reduction Control

When the temperature inside the muffler is high, and the ignition is stopped by turning OFF the engine switch, raw gas inside the muffler sometimes burns in a rush after the engine stops. This is called after-burn. A conventional generator has a solenoid valve beneath the carburetor for cutting off the supply of fuel the instant that ignition stops, thus preventing after-burn. As shown in Fig. 21, in this generator, after the engine switch is turned OFF, ignition is continued until the engine speed falls to the designated value or below, and is stopped once the engine speed falls below the value, reducing blow-out of raw gas. This, together with the fact that the cooling performance of the muffler is improved, enables after-burn to be reduced.

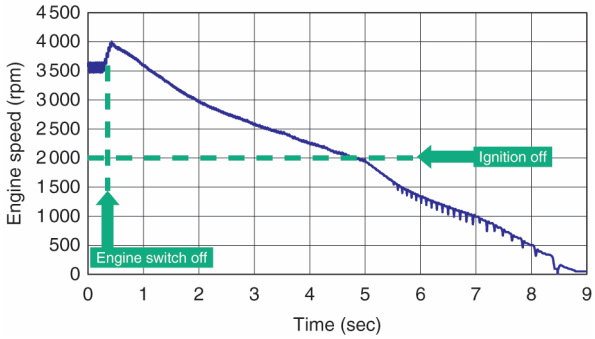


Fig. 21 Engine-stop control and engine speed

7. Completed Generator

The EM7000is generator that employs the technologies introduced above is shown in Fig. 22, and a specification comparison is shown in Table 6.

Table 6 Specification of EM7000is

			EM7000is
Engine	Displacement (cm^3)		389
	Speed (rpm)		∗ 2 400 - 3 600
			☆ 3 300 - 3 600
	Operating noise level (dB(A)at7m)		69
Generator	Type		Multi-pole field rotary
	Excitation method		Magneto
	Voltage regulation method		※ PWM
	AC voltage (V)		120/240
	AC frequency (Hz)		60
	Max. AC output		6 500
	Rated AC output		5 500
	Voltage variation rate	Momentary	10% max.
		Stability	6% max.
	Frequency variation rate	Momentary	1% max.
		Stability	1% max.
	Waveform distortion		5% max.
	Generating efficiency		85%
Dimensions	Dimensions L × W × H (mm)		1 155 × 670 × 710
	Dry weight (kg)		95

∗ : Eco SW ON ※ PWM = Pulse width modulation
☆ : Eco SW OFF



Fig. 22 EM7000is

8. Conclusion

The EM7000is, a dual-voltage inverter generator that has a larger output than the GENE21 series, was developed.

(1) Two inverters were used, and two kinds of voltages were obtained by connecting these inverters in series or parallel. Also, a control system that accurately synchronizes these inverters was developed.
(2) A power supply was incorporated in each unit, realizing a compact, highly efficient alternator that produces a high output.
(3) The completed generator employs a shroud sound isolation duct structure that completely covers the engine. As a result, a 30% volume reduction compared to the conventional synchronous generator and also a reduction of noise to 8 dB (A)/7 m in the practical load region were attained.
(4) The use of a GCU enabled the number of electrical components to be reduced to 1/3 of that of a conventional synchronous generator, and also realized an information display with self-diagnostic function.

References

(1) Tanaka, Y., Kouchi, T., Ito, K., Nakamura, M.: Development of Lightweight and Compact Portable Generators - GENE21 Series, HONDA R&D Technical Review, Vol. 11, No. 2, p. 15-22

(2) Kouchi, T., Shimizu, M., Hirose, T., Sugimoto, Y.: Development of Lightweight, Compact Sine Wave Inverter-Equipped EU16i Generator, Honda R&D Technical Review, Vol. 13, No. 2, p. 35-42

(3) Fujii, S., Shimizu, M., Nakamura, M.: Development of Sine Wave Inverter Generating System, HONDA R&D Technical Review Vol. 8, p. 59-66

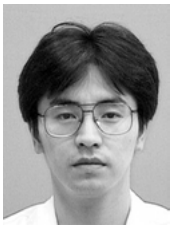
(4) Tamaki, K., Kokubu, S., Akamatsu, S.: Control Device of Electronically Controlled Fuel Injection System of Air-cooled Engine for Small Motorcycle, Honda R&D Technical Review, Vol. 16, No. 1, p. 145-152

■ Authors ■


Masashi NAKAMURA


Shouhei KASAGI


Tadahumi HIROSE


Yasuhiro SHINKAWA


Koichi ASAI


Kenji KAMIMURA

Development of 4-stroke Engine for Small Motorcycles with Low Fuel Consumption and High Performance for Use in Brazil

Yuichi TAWARADA* Takashi KANBE* Yukihiro YASUDA*
Hiroyuki YABE* Hidemi YOKOYAMA*

ABSTRACT

A 4-stroke, 150 cm^3 engine that satisfied the low fuel consumption and drivability goals was developed for the Brazilian market. To decrease the fuel consumption compared to the previous model, a tumble-port, and leaner air-fuel ratio were used to obtain a quick burning engine. In order to decrease the engine friction, a thin oil ring and a cam follower with a roller bearing was employed. Engine output at low and middle engine speed was enhanced and a high gear ratio was used to reduce the fuel consumption at the same vehicle speed. As a result, compared to the former 125 cm^3 models, the fuel economy at ECE-40 mode was enhanced by 18% despite increasing displacement to 150 cm^3. The maximum output was increased by 18%, while the output at low and middle engine speeds was enhanced by 37%. A EURO-2 emissions level was obtained without any devices such as secondary air induction. In addition, vibration was decreased with a primary balancer.

1. Introduction

In recent small motorcycle engines, reduction of fuel consumption and reduction of CO_2 emissions has become an important issue in consideration of the global environment. In Brazil, where 4-stroke engines are mainly used for motorcycles, further improvements in fuel economy are being demanded. Furthermore, the infrastructure, including expressways, is being built, and improvements of driving performance for traveling comfortably are expected.

Recently, an air-cooled 4-stroke 150 cm^3 engine has been developed for the Brazilian market. This engine features top fuel economy and power in a 125 to 150 cm^3 displacement class and also low emissions and low vibration. The concept of the previous model, which has been popular in Brazil for many years, has been maintained. This paper describes the technology employed in this engine.

2. Development Goals

The development targets were based on the viewpoints of global energy conservation and environmental protection and the needs of the Brazilian market.

(1) Reduced fuel consumption: Low fuel consumption that enables the user to readily see the difference between the new model and the previous model and also other manufacturers' models.
(2) Improved engine performance: Good performance in the

* Asaka R&D Center

middle engine speed range, and improved cruising performance on expressways.
(3) Environmental protection: Realization of emission performance equivalent to the EURO-2 regulation level, though this type of engine is subject to the EURO-1 regulations. (The EURO-1 regulation values are CO/HC/NOx = 13/3/0.3 g/km, and the EURO-2 regulation values are CO/HC/NOx = 5.5/1.2/0.3 g/km.)
(4) Reduced vibration: Realization of pleasant high-speed cruising with reduced vibration due to the application of a primary balancer

3. Outline and Major Specifications of Engine

Figure 1 shows a cutaway model of the newly developed engine, and Table 1 shows the major specifications of the engine. The engine is an OHC 2-valve air-cooled single-cylinder 4-stroke engine, which has a cylinder inclination of 15° to the front. It was developed for the Brazilian market and is designed to run on a general gasoline-ethanol mixture. The main differences from the previous model are as follows.
(1) The displacement was increased from 124.1 cm^3 of the previous model to 149.2 cm^3.
(2) The bore × stroke was increased from the previous value of 56.5 × 49.5 (S/B = 0.88) to 57.3 × 57.8 (S/B = 1.01).
(3) The valve drive method was changed from the OHV method, which used a push rod, to a chain driven OHC.
(4) The included valve angle was reduced from 55° to 49°.
(5) The intake valve diameter was left unchanged at 30 mm, and the exhaust valve diameter was increased from 25 mm to 26 mm.
(6) An oil jet was added to the underside of the piston.
(7) A primary balancer was installed.



Fig. 1 Cutaway model of developed engine

4. Technology for Improving Engine Output, Fuel Economy and Emission

4.1. Engine Output

Figure 2 shows the engine performance curves. The output per unit displacement is the same, compared to the previous model, but the maximum output has been improved by 18%. Also, the output in the targeted middle engine speed range was improved by 37%. A higher torque compared to that of the previous model was obtained over the entire engine speed range including the low speed range, and the maximum torque was improved by 24%.

4.2. Tumble Port

Generally, when the mixture-flow in the cylinder is strengthened[1] in order to realize rapid combustion and the ability to run on a leaner mixture for improving fuel economy, the steady-flow performance of the port decreases. However, in order to realize both good fuel economy and

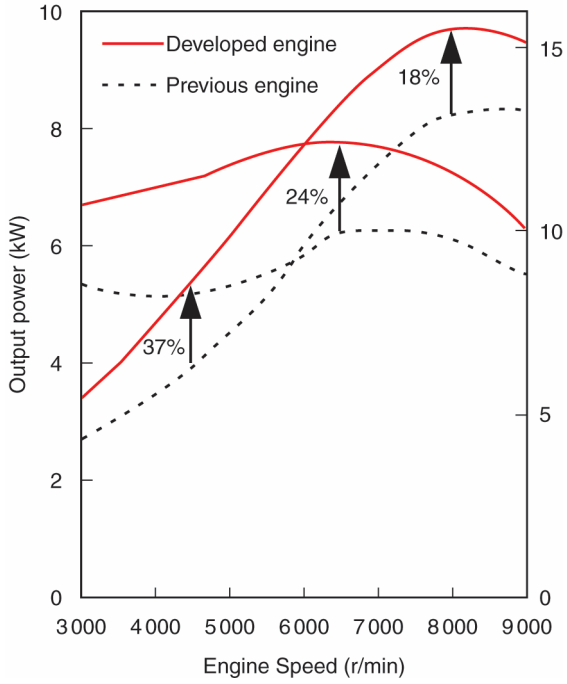


Fig. 2 Output engine performance

Table 1 Major specifications of engines

Items		Developed engine	Previous engine
Engine type		4-stroke, single-cylinder	4-stroke, single-cylinder
Displacement	(cm^3)	149.2	124.1
Bore × Stroke	(mm)	57.3 × 57.8	56.5 × 49.5
Compression ratio		9.5	9.2
Valve train		SOHC 2-valves	SOHC 2-valves
Valve diameter	(mm)	IN 30, EX 26	IN 30, EX 25
Included valve angle	(deg)	49	55
Balancer shaft		Applied	–
Transmission		5 speed constant mesh	5 speed constant mesh

power performance, it is necessary to secure high steady-flow performance at the port while generating a mixture-flow. In order to satisfy both of these requirements, a tumble port of the type shown in Fig. 3 was used as the intake port to optimize the tumble and thereby realize both tumble intensity and steady-flow performance. Figure 4 shows the shape of the intake port of the developed engine.

In order to predict and satisfy both the tumble intensity and steady-flow performance of the intake port, CFD simulation of port steady-flow was performed from an early stage of development, and the tumble was optimized. In the case of the developed engine, a study was performed with the aim of raising the tumble ratio as far as possible while maintaining the same steady-flow performance as that of the conventional port shape. Figure 5 shows the simulation results. It was found that the intake port adopted produced an increase in the blow-off flow velocity. The blow-off flow is passing through the upper part of the intake valve and flowing into the cylinder along the cylinder wall face, and becomes the cause[2] of generation of tumble. At the intake port in which the tumble ratio and the steady-flow performance were optimized based on the simulation, it was possible to make the effective valve-opening area (Z) of the intake port the same as that of the previous model, as shown in Fig. 6. The percentage of fluctuations in combustion for constant speed running at 60 Km/h is shown in Fig. 7. By using a tumble intake port, it enables a leaner setting of two points on an air-fuel mixture compared to that of the previous model.

Also, in order to cope with rapid combustion, the crankshaft support rigidity was improved by using a roller bearing for the right journal bearing, as shown in Fig. 8. In the developed engine, the use of rapid combustion results in a maximum pressure increase rate ($dp/d\theta$) of 1.6 times compared with the previous model. Increase of engine noises was a concern, but the noise on rider's ears was reduced by 70% by using roller bearings compared with the ball bearing model.

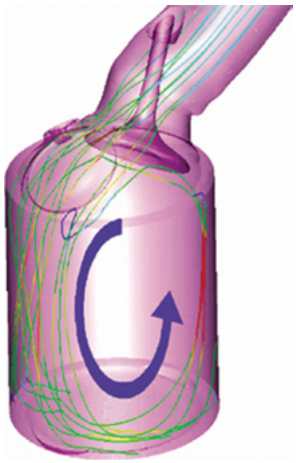


Fig. 3 Tumble flow

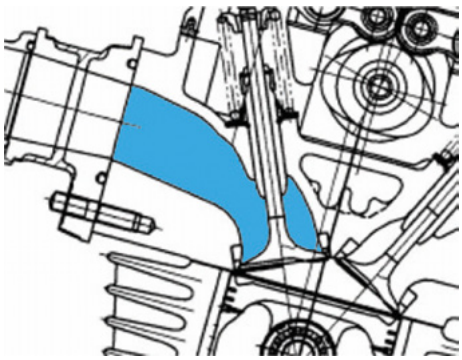


Fig. 4 Shape of intake port

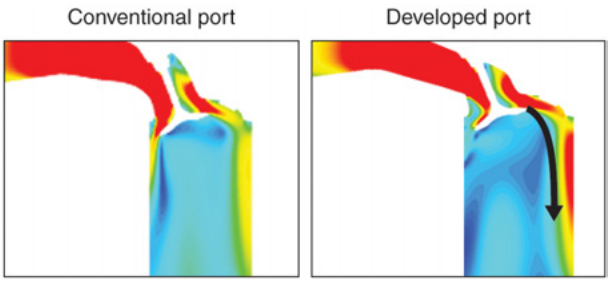


Fig. 5 Simulation result of intake port

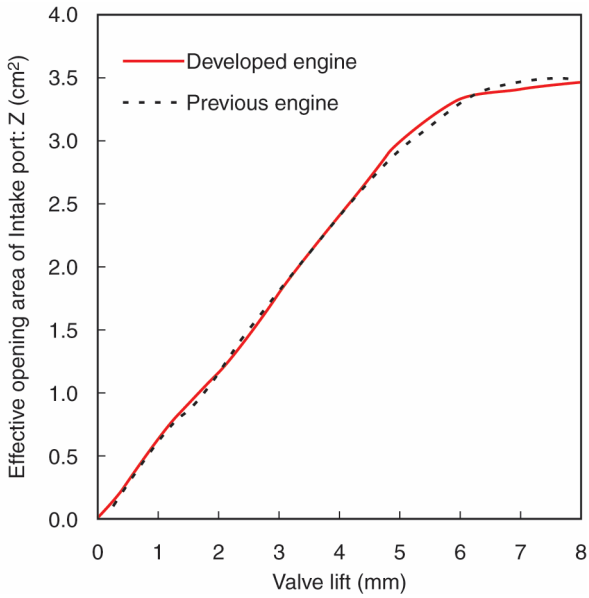


Fig. 6 Comparison of effective valve-opening area of intake port

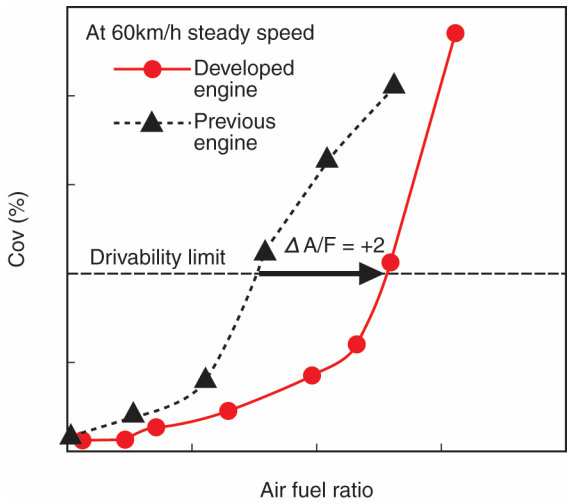


Fig. 7 COV(IMEP) at 60km/h steady speed

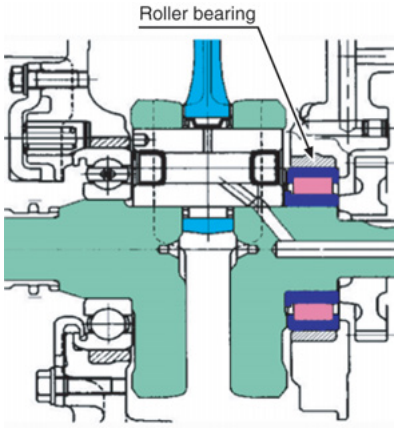


Fig. 8 Section drawing of main bearing

4.3. Compact Combustion Chamber

The bore was increased from 56.5 mm to 57.3 mm, and the valve included angle was reduced from 55° to 49° to permit a more compact combustion chamber. The combustion chamber as shown in Fig. 9 was designed by making the cylinder head hemispherical and also by making the dent on piston head like a cavity. As a result, the S/V ratio was improved by 8% compared to that of the previous model, despite the increase in the bore.

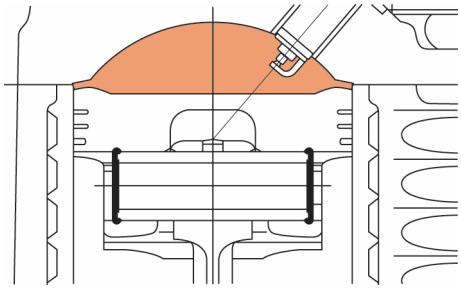


Fig. 9 Spherical combustion chamber

4.4. Improved Cooling Performance

In order to improve the anti-knocking performance of the engine, a T-shaped air jacket with cooling fins that branched toward the plug seat and also toward the rear of engine was employed. Figure 10 shows the cross-sectional diagram of the air jacket.

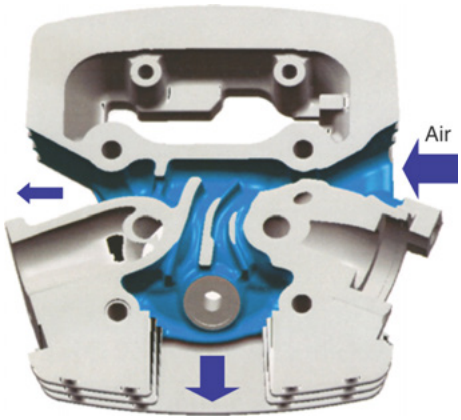


Fig. 10 Air jacket section view

Also, in order to actively oil-cool the back of the piston crown, a dedicated oil jet was arranged in the proximity of the journal, as shown in Fig. 11, in addition to the conventional oil spray from the big end thrust face of connecting rod. As a result, the maximum temperature of the piston was reduced by 10 °C.

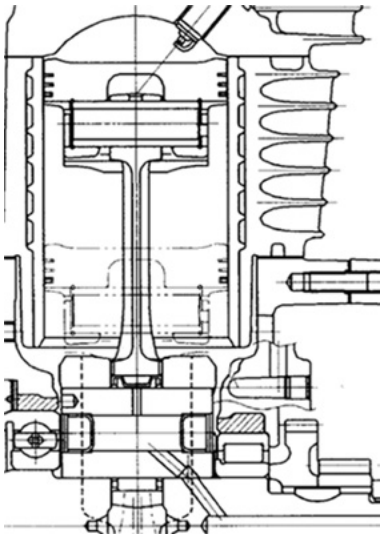


Fig. 11 Oil jet to piston

4.5. Offset Cylinder

In order to reduce friction due to pressure on the piston side in the low and middle engine speed range, an offset cylinder structure was used. As shown in Fig. 12, the center of the cylinder was offset 4 mm to the exhaust port from the center of crankshaft.

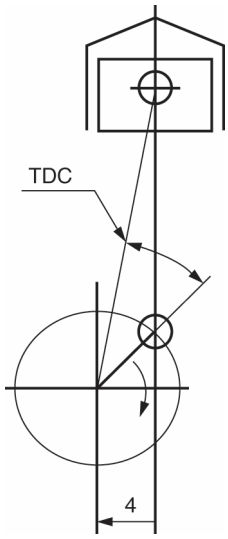


Fig. 12 Offset cylinder

4.6. Valve Drive System

In order to realize good fuel economy and power, the camshaft drive train system was changed from OHV to OHC. The OHV system of the previous model was used in the Brazilian market over a long period of time. The OHC system reduces friction and the equivalent mass of the valve train. Also, a rocker arm[3] having a roller follower was employed in order to reduce the sliding resistance between the rocker arm and the cam profile face.

4.7. Reduction of Friction and Mass of the Piston

As shown in Fig. 13, the entire surface of the piston was tin-plated and also the piston skirt was striated[3] in order to reduce the friction of the piston. Furthermore, in order to reduce the sliding resistance of the piston rings, the thickness of the oil ring was reduced from 2.0 mm of the previous model to 1.5 mm, resulting in a reduction of oil ring tension of 15% compared to that of the previous model. In addition, the overall height of the piston was shortened 3.3 mm and the profile was changed in order to reduce the mass of the piston. As a result, the bore was widened from 56.5 mm to 57.3 mm, but the complete piston assembly mass (mass of the piston with piston rings and piston pins) was reduced by 4%.

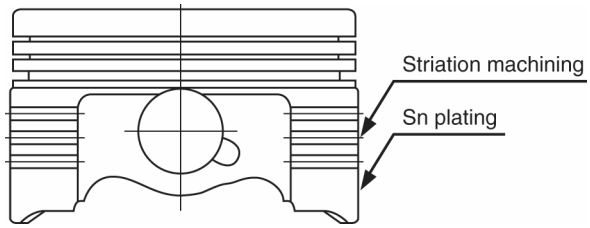


Fig. 13 Developed piston

4.8. Reduction of Fuel Consumption at the Same Vehicle Speed due to the Change in the Reduction Gear Ratio

In order to reduce friction by lowering the engine speed for the same vehicle speed, the low and middle engine speed characteristics were enhanced by increasing displacement and adopting a longer stroke. In addition, the reduction gear ratio was set on the low side, resulting in a 17% reduction of fuel consumption for 60 km/h steady speed running. Figure 14 shows the BSFC for 60 km/h steady speed running.

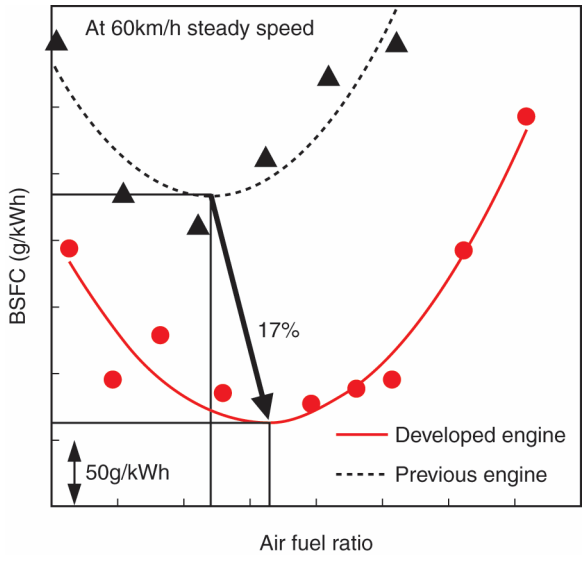


Fig. 14 BSFC at 60 km/h steady speed

5. Effectiveness of Fuel Economy Improvement and Emission Reduction

5.1. Effectiveness of Combustion Improvement

As a result of the combustion improvement mentioned in the previous chapter, the Pmi was improved by up to about 10% compared to that of the previous model, as shown in Fig. 15.

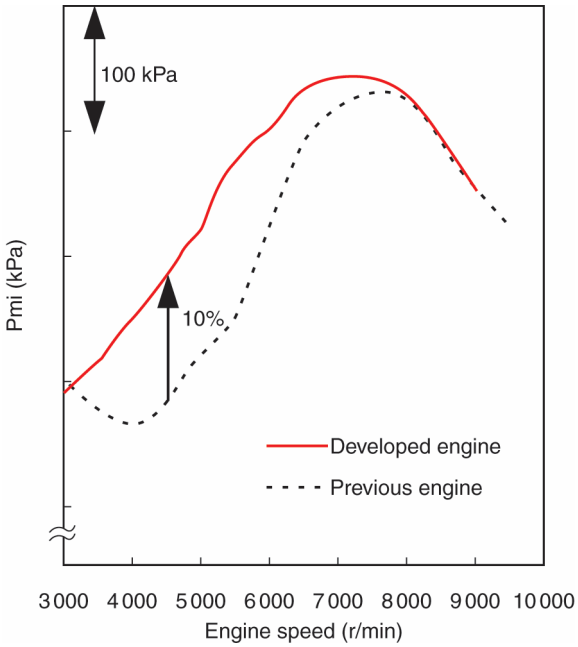


Fig. 15 Result of Pmi

5.2. Effectiveness of Friction Reduction

As a result of the adoption of friction reduction technology mentioned in the previous chapter, the Pmf in the middle engine speed range was reduced by 13% compared to that of the previous model, as shown in Fig. 16.

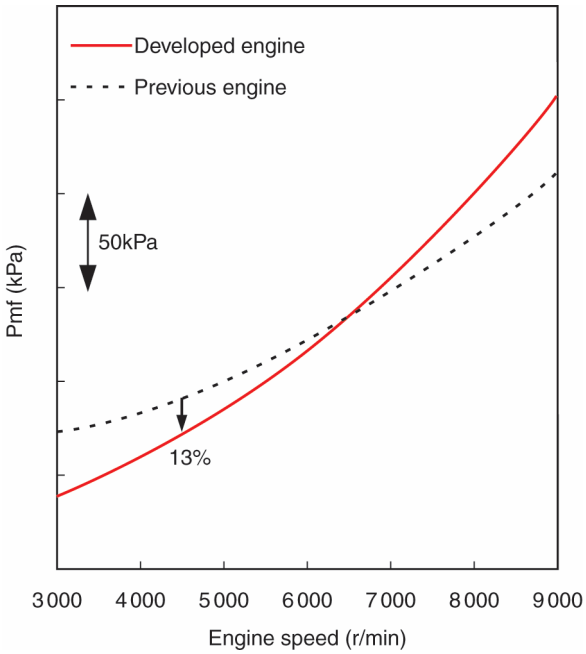


Fig. 16 Result of Pmf

5.3. Effectiveness of Fuel Economy Improvement and Emission Reduction

As a result of combustion improvement, friction reduction of each part, and the change of the reduction gear ratio due to improved engine output at low and middle engine speeds, the fuel consumption in the ECE-40 mode was improved by 18% compared to the previous model. Figure 17 shows the measured value of the fuel consumption in the ECE-40 mode. As shown in Fig. 18, the emissions decreased to the EURO-2 regulation level without applying a secondary air induction system or a three-way catalyst.

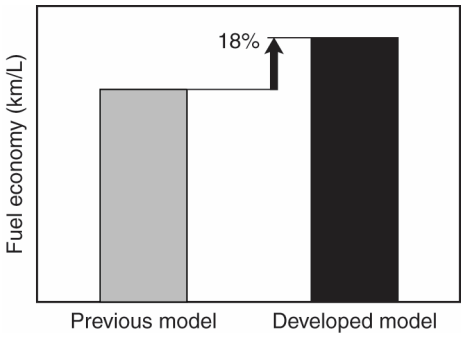


Fig. 17 Result of fuel economy in ECE-40 mode

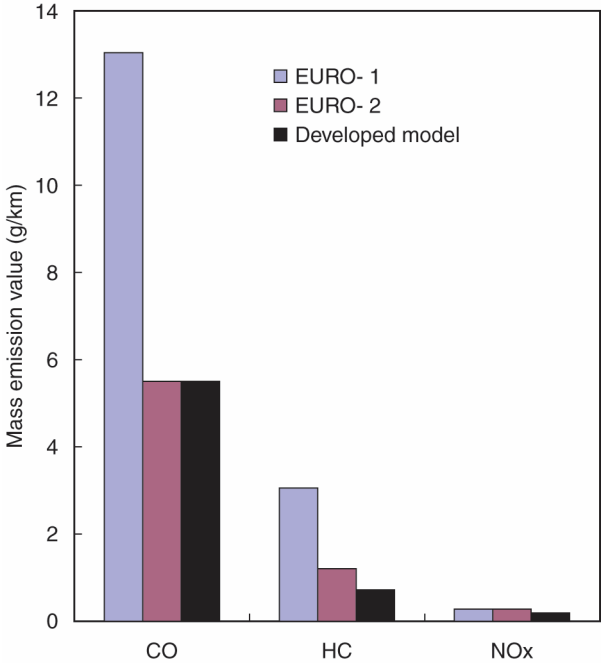


Fig. 18 Result of mass emission

6. Vibration Reduction Technology

6.1. Primary Balancer

Along with the increase in displacement, the primary balancer shown in Fig. 19 was used as a method of reducing engine vibration. As a result, the primary engine vibration of the frame head pipe was reduced about 1/2 that of the previous model.

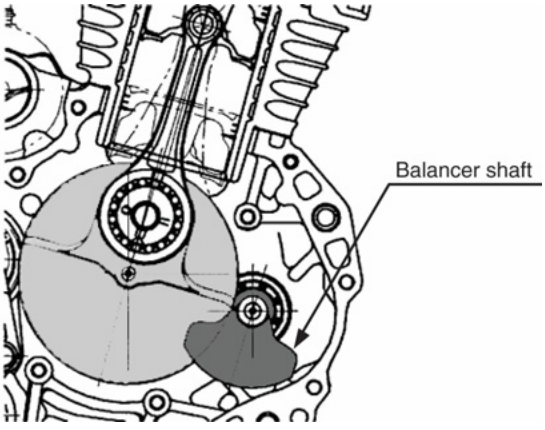


Fig. 19 Side view of balancer shaft

7. Conclusion

The combustion improvement, friction reduction, and vibration reduction technology led to the following results with the newly developed air-cooled 4-stroke 150 cm^3 engine.

(1) The fuel economy in the ECE-40 mode was improved by 18% compared to that of the previous model.
(2) The output per unit displacement was the same as that of the previous model, and the maximum output was improved by 18%. The output in the middle engine speed range which is the target range was improved by 37%.
(3) The emission decreased to the EURO-2 regulation level without applying special devices.
(4) The use of a primary balancer realized the lowest level of riding vibration for this class of motorcycle.

References

(1) Nakajima, Y., Muranaka, S.: Chapter 2, Nenpi no Koujo, Kaitei Jidousha Gasorin Enjin, Tokyo, Sankaido (2001) (in Japanese)

(2) Hayashi, A., Takabayashi, T., Sakurahara, K., Endo, T.: Development of Lean-burn Engine for "ACCORD/TORNEO", HONDA R&D Technical Review, Vol. 10, p. 49-57

(3) Sawamura, Y., Saito, N., Sakamoto, B., Kobayashi, H., Hirose, Y.: Development of a 4-stroke Engine for Small Motorcycle with Low Fuel Consumption and Low Emission for Thailand, Honda R&D Technical Review, Vol. 15, No. 1, p. 77-82

■ Authors ■


Yuichi TAWARADA


Takashi KANBE


Yukihiro YASUDA


Hiroyuki YABE


Hidemi YOKOYAMA

Optimization of Combustion Chamber for 2.0L Direct-Injection Gasoline Engine

Shinya ABE* Naohiro ISHIKAWA*
Naoaki TAKEDA* Shigeru AKIMOTO*

ABSTRACT

A center injection system in which a high-pressure fuel injector is located in the center of the combustion chamber has been employed in a direct-injection engine, significantly improving fuel economy and emissions performance in the direct injection stratified charge (DISC) range. Ensuring the stable formation of a combustible mixture around the spark plug at the appropriate time is the most important element in achieving stable combustion in the DISC range. During the development of the engine, a variety of methods were used to measure mixture distribution, including visualization using Laser Induced Fluorescence (LIF) and infrared absorption analysis to measure the air-fuel ratio around the spark plug, and CFD simulations were conducted to analyze mixture distribution and in-cylinder flow, enabling analysis and evaluation of the combustion process. These analyses enabled the design of an original piston cavity form with reference to the fuel spray characteristics of the center-positioned high-pressure injector. This has ensured the stable formation and maintenance of a compact combustible mixture around the spark plug, enabling the achievement of a high lean combustion limit in stratified combustion and significantly reducing fuel consumption.

1. Introduction

Increasing concern over global environmental issues have led to demands for improved automotive fuel economy and decreased automotive emissions. The achievement of stratified charge combustion through in-cylinder direct injection is effective as a means of increasing the fuel economy of spark ignition internal-combustion engines, and automotive manufacturers have developed and marketed direct injection engines in a variety of forms[(1)-(3)]. Honda has continued in this direction with the development of the first 2.0L i-VTEC I direct injection engine. The combustion method employed in this engine uses an original center injection system to enable the achievement of ultra-lean stratified charge combustion, previously considered difficult in a direct injection gasoline engine, achieving a balance between increased fuel economy and reduced exhaust emissions. The stable supply of a combustible mixture to the area around the spark plug is of the greatest importance to the achievement of stratified charge combustion, and the clarification of the process of formation of the mixture is important in enabling it. This paper will discuss the optimization of the cavity form through analyses of the effect on the mixture formation process generated by changes to parameters such as the fuel spray characteristics and the combustion chamber appropriate to use in a center injection system.

* Tochigi R&D Center

2. Overview of Engine / Specifications

Table 1 shows the main specifications of the newly developed K20B engine. Figure 1 shows the combustion chamber form. The major issues in achieving ultra-lean stratified charge combustion are ensuring the formation and maintenance of a combustible mixture and fast burn after sparking. The aim established for the new engine was to employ a center injection layout and, by means of the fuel spray characteristics[4] (Table 1) achieved by the use of a high-penetration injector and the spray flow achieved by a deep-bowl type cavity piston, to stably form and maintain a combustible mixture around the spark plug. A further aim was the achievement of fast burn by means of the swirl generated by the closure of one valve by the VTEC mechanism after sparking. The selection of an appropriate cavity form was very important in realizing this concept. The parameters with the most significant effect on the achievement of stable combustion through enabling the formation of a combustible mixture around the spark plug are the slope angle of the bottom of the cavity, the cavity volume ratio (ratio of cavity volume to total combustion chamber volume), and the deflection angle of the cavity. The research project discussed in this paper sought to define and optimize[5],[6] the parameters of a cavity form enabling the achievement of a high lean combustion limit in stratified charge combustion and a good balance between load and engine speed. Figure 2 shows the form of the piston cavity.

Table 1 Engine specifications

Engine code	K20B
Cylinder configuration	In-line 4-cylinder
Bore × Stroke (mm)	86 × 86
Displacement (cm^3)	1 998
Compression ratio	10:1
Valvetrain	DOHC VTEC
Number of valves	4 per cylinder
Fuel injection pressure (MPa)	8 – 10.5
Fuel spray angle (deg)	25
Penetration (mm)	73 (1msec after start of injection)
Fuel spray particle size (μm)	11.4 (Sauter mean diameter) at 10MPa fuel pressure

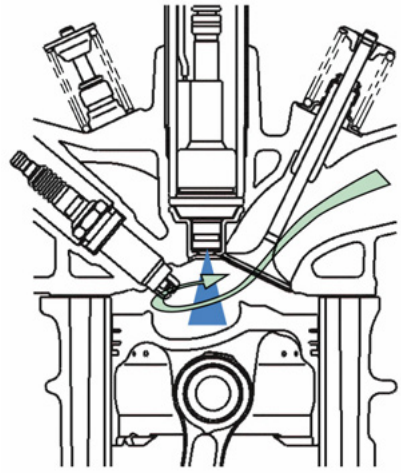


Fig. 1 Combustion chamber configuration

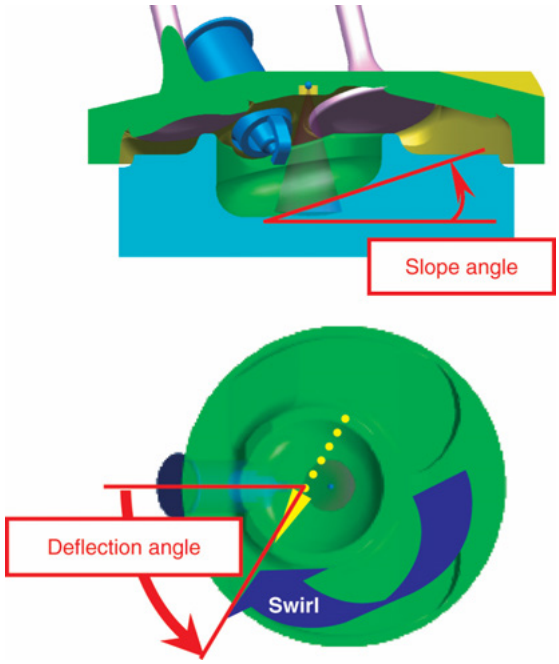


Fig. 2 Form of piston cavity

3. Optimization of Cavity Form

3.1. Visualization of Mixture Distribution and Correlation with Simulation

The large number of parameters in tests with actual equipment made them difficult to employ in defining the required parameters in the optimization of the cavity form. Analyses employing simulations were effective in restricting the parameters. As the first stage of simulation analysis in this project, the results of visualization tests of in-cylinder mixture distribution using LIF were compared and correlated with the results of CFD simulations. Visualization tests employed a single-cylinder engine set up for visualization and observed the in-cylinder mixture distribution at sparking in stratified charge combustion. Figure 3 shows a diagram of the test equipment for LIF visualization. An excimer laser with a 1 mm sheet was employed as the excitation light source, and an image intensifier and CCD camera were used to photograph the fluorescence of a 3-pentanone additive in fuel through the observation window.

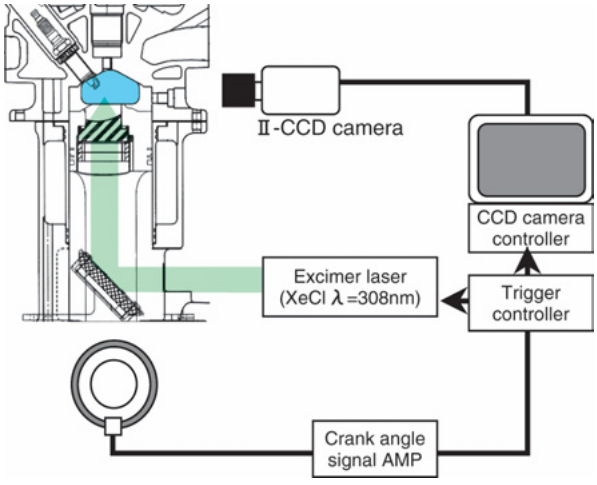


Fig. 3 LIF system for fuel distribution visualization

Figure 4 compares the mixture distribution results for visualization at an engine speed of 1 500 rpm, an indicated mean effective pressures (IMEP) of 267 kPa, and an ignition timing of 40° BTDC with the results of a simulation for the same conditions. The visualization results show that at an injection timing of 40° BTDC, the mixture is most concentrated around the spark plug between 15° and 20° BTDC, and stratified with equivalence ratio of 1.0 or more.

There is a good correlation between the form of the mixture distribution around the spark plug and the extent and density of the distribution of the mixture opposite the spark plug in the results of visualization of compression stroke towards top dead center and the CFD simulation results. The correlation between the visualization, towards top dead center, and CFD simulation demonstrated that simulation could be used as a tool in designing the form of the piston cavity.

3.2. Analysis of In-cylinder Flow and Mixture Distribution

In the next stage of research, simulations were used to analyze the in-cylinder flows and mixture distribution produced by different combustion chamber forms.

3.2.1. Comparison of results for in-cylinder flow

Table 2 shows the cavity volume ratio, slope angle and deflection angle for two different cavity forms, designated type A and B.

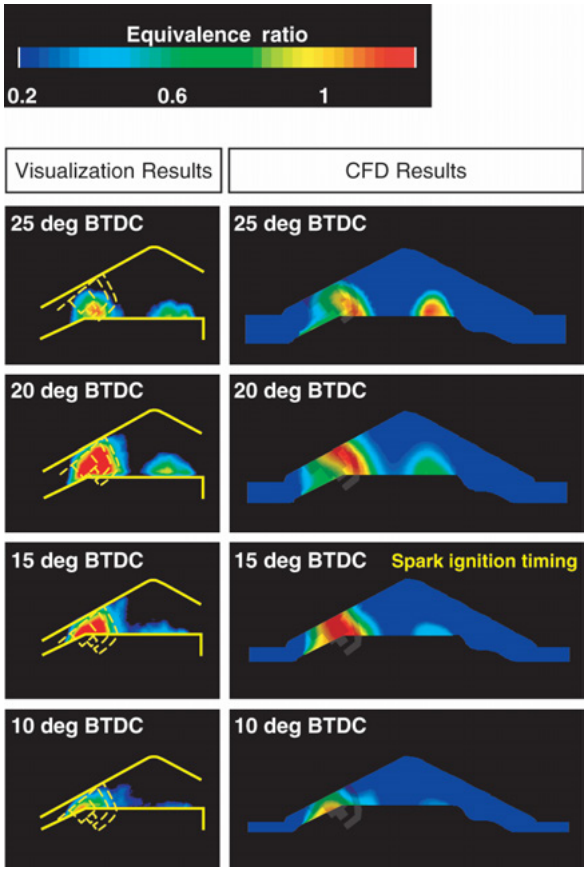


Fig. 4 Comparison of mixture distributions in CFD simulations and measurements

Figure 5 compares simulation results of in-cylinder flow in cavity A and B at 1 500 rpm, an IMEP of 267 kPa and an injection timing of 40° BTDC. The results of a vertical cross-

Table 2 Cavity pattern A, B

Type	Cavity volume ratio (%)	Slope angle (deg)	Deflection angle (deg)
A	28.9	10	60
B	26.4	15	30

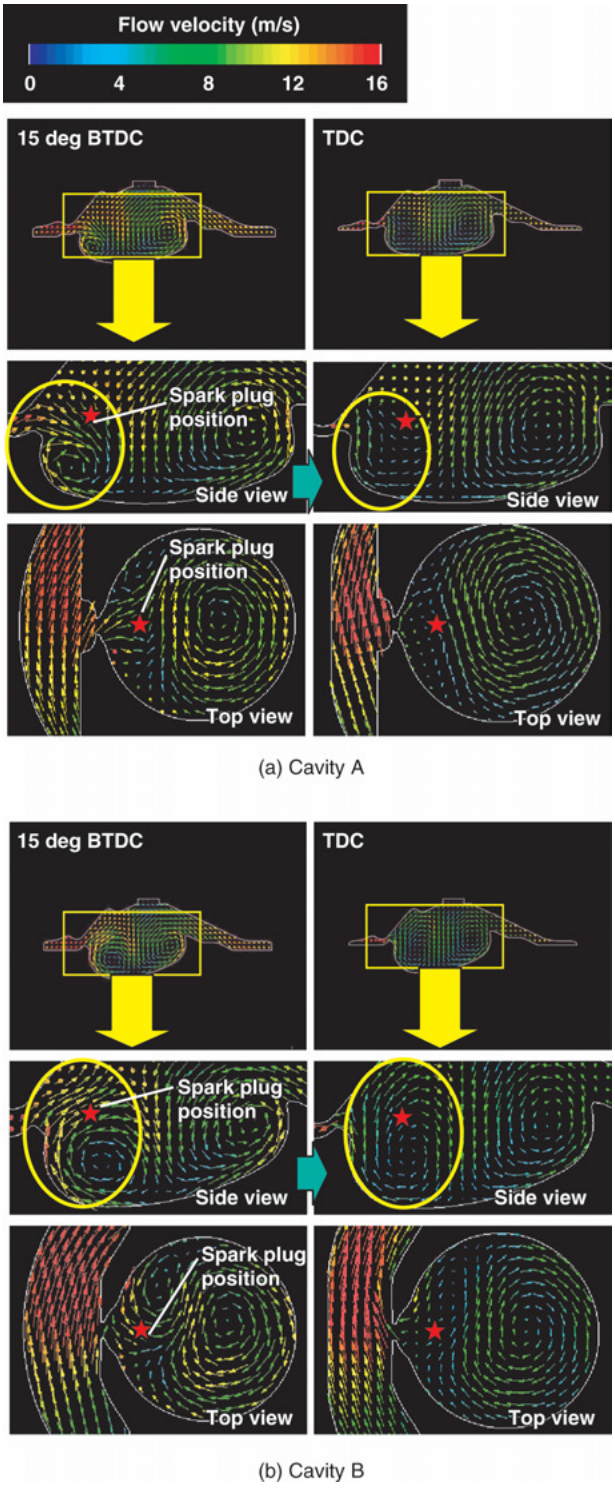


Fig. 5 CFD results for flow velocity in piston cavity

section of the combustion chamber show that at 15° BTDC, the vertical vortex forming under the spark plug in cavity B extends further in the vertical direction and has a greater amount of velocity components than the vortex in cavity A. A flow of air from outside the cavity towards the spark position can be observed in cavity A, but this is absent in cavity B. In horizontal cross-section results the direction of the vectors also shows a strong flow from the bottom of the cavity in the direction of the spark plug, and there is no inflow of air towards the inside of the cavity. By contrast, there is an inflow of air from outside the cavity in cavity A. This difference is produced by the strength and size of the vertical vortex forming under the spark plug in the cavities. In cavity B there is no air inflow from outside until top dead center, this enables the formation of a large vortex extending in the direction of the spark plug, and the vortex is maintained until top dead center. This indicates that cavity B enables the stable supply and maintenance of the mixture around the spark plug. In both cavities swirl produced a large vortex, indicating that the swirl flow produced throughout the cylinder by VTEC is transmitted to the cavity and maintained there. This in-cylinder swirl flow could be expected to enable fast burn after sparking.

3.2.2. Comparison of results for mixture distribution

Figure 6 shows a comparison of a simulation of the mixture distribution in cavity A and B at 1 500 rpm, an IMEP of 267 kPa and an injection timing of 40° BTDC. The results for a vertical cross-section of the combustion chamber show that in cavity B at 15° BTDC a stratified mixture with an equivalence ratio of 1.0 or more forms under the spark plug, and the high-density section extends towards the plug. The results obtained in the simulations of in-cylinder flow indicate that this is because the fuel spray is concentrated and carried towards the spark plug by the vertical vortex. In addition, in cavity B the growth of the stratified mixture is maintained until top dead center, and covers a wider area. This is because there is no air inflow into the inside from outside the cavity. In cavity A, the stratified area under the spark plug is divided in two. This phenomenon is generated by the inflow of air into the inside from outside the cavity.

The density of the mixture is also lean. This is because the velocity components of the vertical vortex are small, and do not generate a flow able to concentrate and form the mixture. The results from a horizontal cross-section of the combustion chamber show that in cavity B a mixture with an equivalence ratio corresponding to 1.0 or more formed around the spark plug and was maintained until top dead center. In cavity A the rich mixture was concentrated more on the upstream of the swirl than the spark position, and only a lean mixture was present around the spark plug. This is because the flow of air from outside the cavity limited the advance of the combustible mixture to the area around the spark plug. The results of these simulations showed that the deflection angle of the cavity has an effect on the size and strength of the vertical vortex, and the cavity volume ratio has an effect on the concentration of the mixture. The results also show that in cavity B a very rich mixture is present around the spark plug, and the mixture is maintained well.

Figure 7 shows a comparison of the lean combustion limit for cavity A and B against amount of restriction of the throttle under the same load in DISC operation at 1 500 rpm. Opening the throttle and increasing the volume of air throughout the cylinder does not cause any rapid increase in indicated specific fuel consumption (ISFC) or variation of combustion in cavity B, and they remain stable up to an air-fuel ratio of around 80. This demonstrates that the stratification and maintenance of a combustible mixture is possible in the cavity despite the high volume of air flowing into the cylinder when the throttle is opened. By contrast, in cavity A, ISFC reaches its minimum at an intake manifold pressure of –20 kPa, and there are rapid increases in ISFC and variation of combustion as the throttle is opened. This indicates that mixture cannot be maintained in the cavity, and mixture around the spark plug is made lean by air inflow into

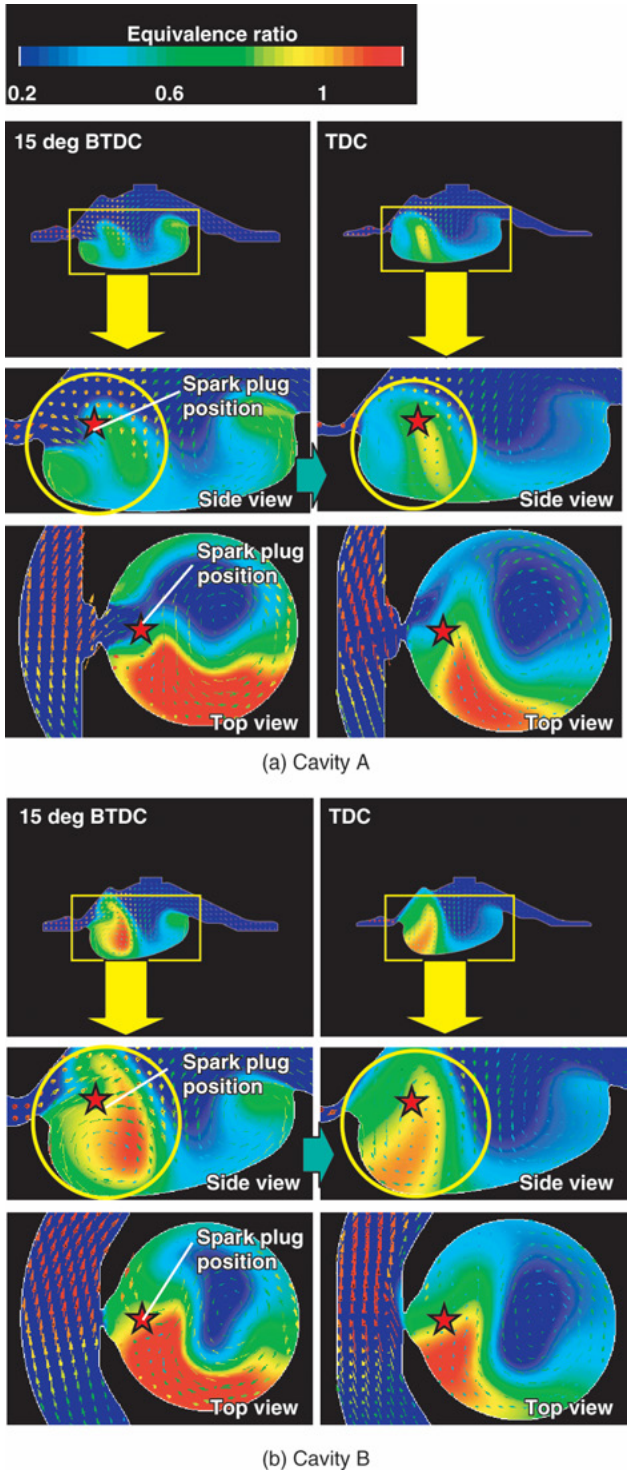


Fig. 6 CFD results for stratified mixture formation in piston cavity

the cavity. In addition, there are significant differences between the absolute values of ISFC, air-fuel ratio and variation of combustion in cavity A and B at identical intake manifold pressures. These results corresponded well with the results of simulations showing the effect of the presence or absence of a flow of air into the cavity due to the strength of the vertical vortex on in-cylinder flow and the mixture distribution.

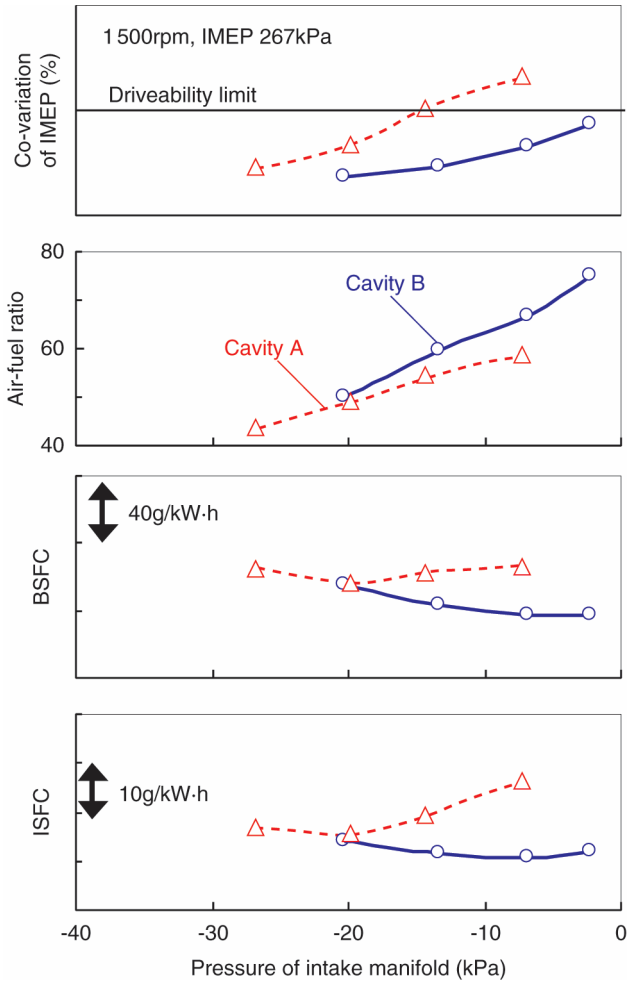


Fig. 7 Influence of pressure of intake manifold on combustion characteristics and lean combustion limit

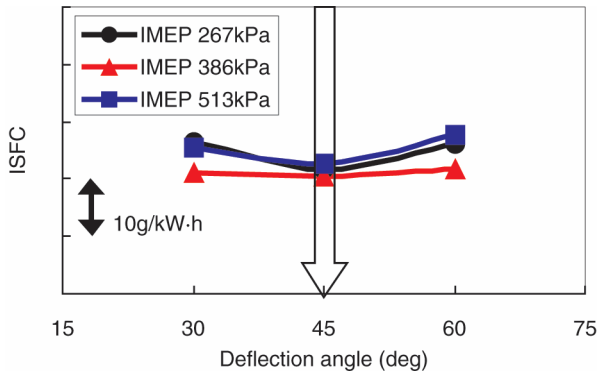


Fig. 8 Influence of deflection angle on ISFC

The results of analyses of the mixture using simulations and of measurements of lean combustion limit in engine tests described above showed that cavity B enabled the formation of a mixture with a higher lean combustion limit than cavity A, would significantly reduce BSFC by reducing pumping loss, and also demonstrated little variation of combustion.

The slope angle and volume ratio of cavity B were therefore adopted as the specifications of the new cavity, while performance tests were carried out using different deflection angles to optimize this parameter. Figure 8 shows ISFC for different deflection angles at an engine speed of 1 500 rpm and IMEP of 267, 386 and 513 kPa.

The effect of the difference in deflection angles was apparent at low loads and high loads. A deflection angle of 45° was judged most suitable in terms of swirl strength, and produced the best results for ISFC. This resulted in the adoption of the cavity specifications shown in Table 3.

Table 3 Optimized cavity specifications

Cavity volume ratio (%)	Slope angle (deg)	Deflection angle (deg)
26.4	**15**	**45**

4. Air-fuel Ratio Around Spark Plug

Infrared absorption method was used to conduct measurements of the air-fuel ratio around the spark plug during stratified charge combustion for the optimized cavity form[7),(8)], enabling the process of mixture formation and its level of stability to be studied. Figure 9 shows the setup of the measurement equipment. Infrared light with a wavelength of 3.392 μm generated by a He-Ne laser was directed by optic fiber to the measurement area at the spark plug. Having passed the measurement area, where it was absorbed and attenuated by the gasoline, the light was directed by another optic fiber to the detection area, where its transmissivity was measured. Figure 10 shows the configuration of the measuring probe.

Measurements were conducted under conditions of an engine speed of 1 500 rpm, an IMEP of 270 kPa, a mean air-fuel ratio of 45 and a fixed ignition timing of 15° BTDC. Figure 11 shows average results over 100 cycles for air-fuel

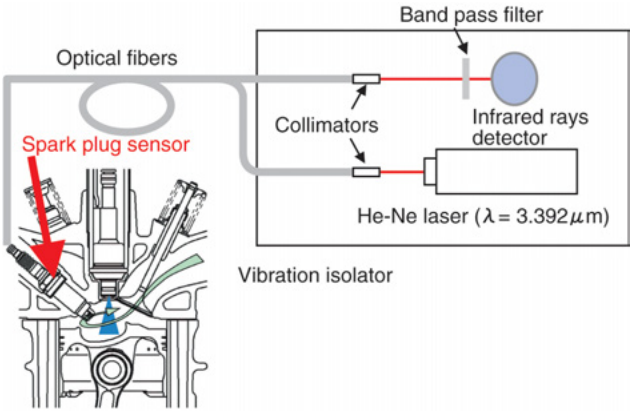


Fig. 9 Experimental setup for concentration measurement in direct injection engine

ratio around the spark plug and their standard deviation for injection timings of 30°, 40° and 50° BTDC. For all the injection timings, the air-fuel ratio at the spark plug was stoichiometric at approximately 20° after the end of injection, after which it became richer until it reached a figure of around 10, and the mixture was maintained at this air-fuel ratio for a specific period of time. With respect to the air-fuel ratio around the spark plug at ignition timing, a combustible mixture did not form around the spark plug with an injection timing of 30°, but there was no significant difference observed for timings of 40° and 50°, with ratios of around 10 for each. Figure 12 shows the variation of air-fuel ratio and combustion for each of the injection timings. A correlation can be observed between variation of air-fuel ratio and combustion at ignition timing, with air-fuel ratio most stable and the minimum variation of combustion at a timing of 40°. Figure 13 shows the relationship between the air-fuel ratio around the spark plug at ignition timing and ignition delay (the period from sparking to a mass fraction burned of 10%). Here also an injection timing of 40° shows the least ignition delay and the most rapid combustion, and this timing was therefore adopted as optimum.

Figure 14 shows the effect of different injection timings on combustion in engine tests at identical engine speeds and loads. The optimum ignition timing to minimize ISFC was employed in each case. These results show that the employment of a piston cavity form ensuring a high level of maintainability of the mixture and a center injection system have enabled the achievement of stable combustion across a broad range of injection timings from 20° to 50° BTDC. ISFC is at its minimum between 40° and 50°, and the results of performance tests have indicated that 40° is the optimum timing from the perspective of NOx and HC emissions and variation of combustion. Infrared absorption method and performance tests have indicated that the piston cavity specifications developed in this research have realized initially established aims for mixture formation, and enable the achievement of a high lean combustion limit and significantly improved fuel economy.

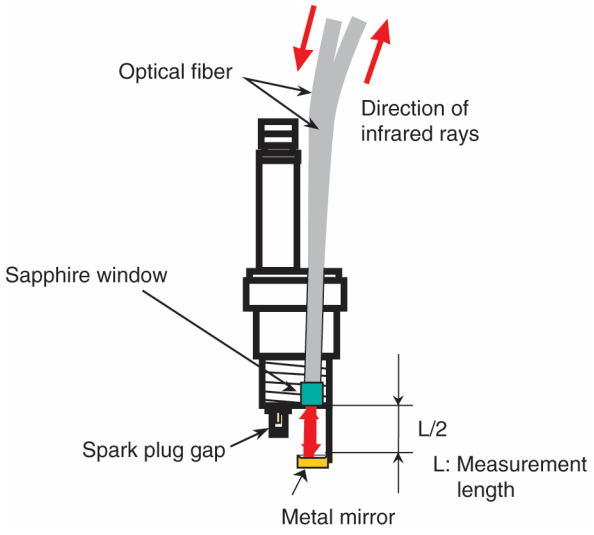


Fig. 10 Schematic of measuring probe

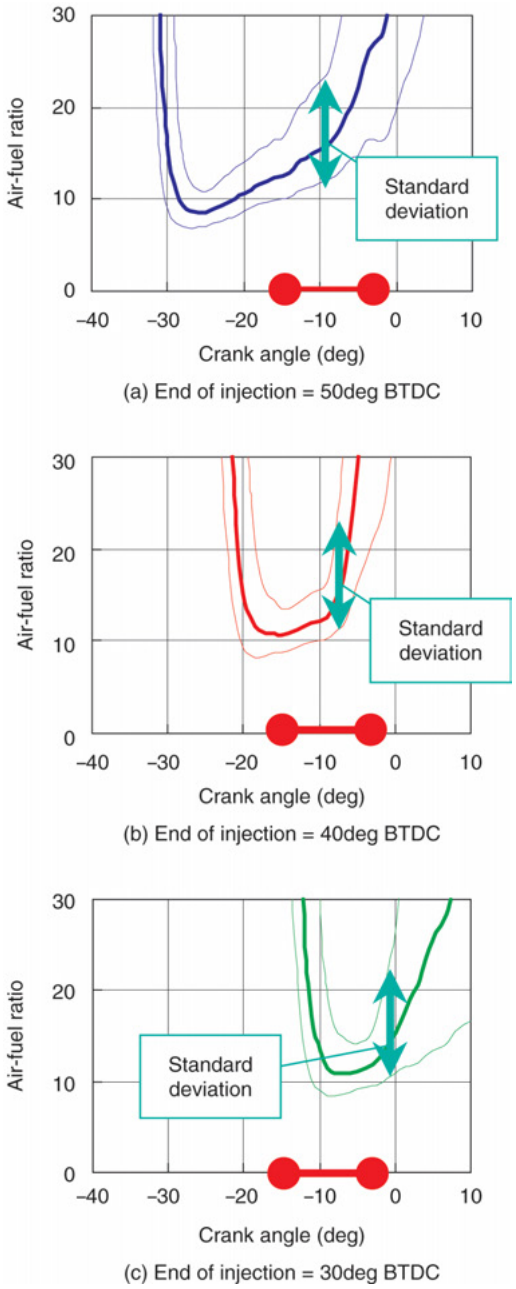


Fig. 11 Air-fuel ratio at spark plug

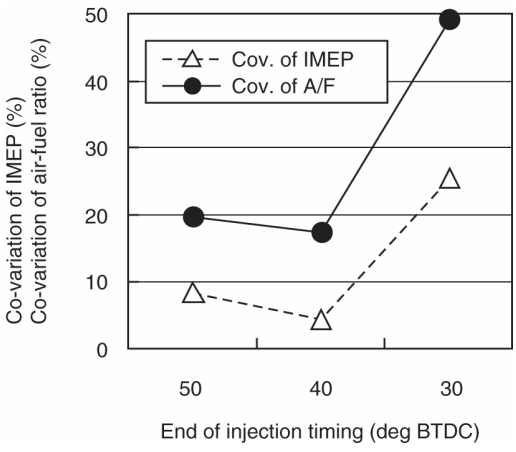


Fig. 12 Influence of injection timing on coefficient of variation in air-fuel ratio at spark plug and coefficient of variation in IMEP

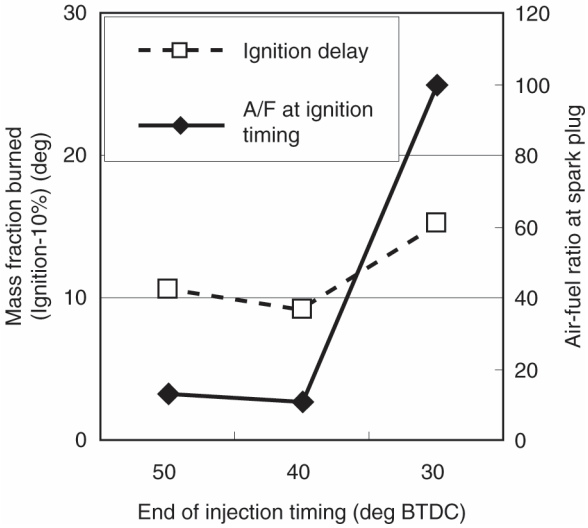


Fig. 13 Influence of injection timing on air-fuel ratio at spark plug and ignition delay

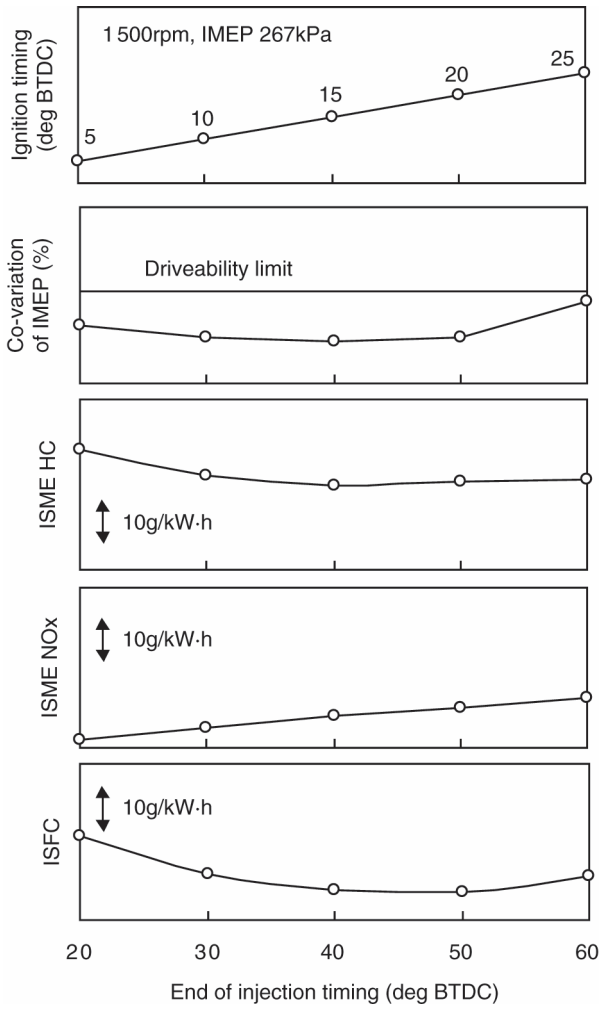


Fig. 14 Influence of injection timing on combustion characteristics

5. Conclusion

Analyses of in-cylinder flow and mixture distribution, infrared absorption method of the air-fuel ratio around the spark plug and the results of engine tests conducted to enable the optimization of the form of the piston cavity have produced the following conclusions:

(1) Optimization of the slope angle, volume ratio and deflection angle of the piston cavity has enabled the generation of a strong vertical vortex in the cavity by a center injection system with a high-penetration spray, resulting in excellent concentration and maintenance of the mixture around the spark plug.

(2) The optimized cavity records its best figures for ISFC at an air-fuel ratio of around 70 and has a high lean combustion limit, with variations of combustion remaining within the range allowing stable combustion up to an air-fuel ratio of 80, resulting in significant reduction of BSFC.

(3) CFD simulations showed that differences in cavity specifications produced differences in in-cylinder flow and mixture distribution, and correlated well with the results of engine tests.

(4) Infrared absorption method of air-fuel ratio around the spark plug and the results of performance tests showed that the optimized cavity specification enabled rapid stratification and stable maintenance of the mixture around the spark plug, and enabled stable combustion for a wide range of injection timings.

References

(1) Koike, M., Saito, A., Sawada, D., Ishikawa, Y.: A New Concept Direct Injection SI Gasoline Engine, JSAE Annual Congress Proceedings, No. 69-99, JSAE9939596

(2) Kanda, M., Shimizu, R., Kobayashi, T., Matsushita, S., Koike, M., Saito, A.: New Concept of a Direct Injection SI Gasoline Engine, JSAE Annual Congress Proceedings, No. 69-99, JSAE9939604

(3) Abe, S., Sasaki, K., Baika, T., Nakashima, T., Fujishiro, O.: Combustion Analysis of a New L4 Direct Injection SI Gasoline Engine, JSAE Annual Congress Proceedings, No. 78-00, JSAE20005524

(4) Goto, H., Hirose, K., Saitoh, M., Matsumoto, S., Iitaka, S., Takashiba, K.: Development of High-pressure Fuel System for Direct Injection Gasoline Engine, Honda R&D Technical Review, Vol. 16, No. 1, p. 47-54

(5) Kohda, Y., Suganami, T., Kobayashi, H., Ogawa, K.: Development of High-performance and Low-emission Direct Injection Gasoline Engine, Honda R&D Technical Review, Vol. 16, No. 1, p. 39-46

(6) Kohda, Y., Goto, H., Kobayashi, H., Horie, K.: Development of Low-fuel economy and Low-emission Direct Injection Gasoline Engine, JSAE Annual Congress Proceedings, No. 19-04, JSAE20045178

(7) Nishiyama, A., Kawahara, N., Tomita, E., Fujiwara, M., Ishikawa, N., Kamei, K., Nagashima, K.: In-Situ Fuel Concentration Measurement near Spark Plug by 3.392 μm Infrared Absorption Method-Application to a Port Injected Lean-Burn Engine, SAE Paper 2004-01-1353

(8) Yamaguchi, K., Kakuho, A., Fukuda, T., Urushihara, T., Itoh, T.: A Study of Air-Fuel Mixture Formation in Direct Injection SI Engine, JSAE Annual Congress Proceedings, No. 77-01, JSAE20005524

■ Authors ■



Shinya ABE



Naohiro ISHIKAWA



Naoaki TAKEDA



Shigeru AKIMOTO

Development of New Compact 4-speed Automatic Transmission for Honda LIFE

Yoshiharu UCHIDA* Osahide MIYAMOTO* Tetsuya OTANI*
Tetsurou MARUYAMA* Kazuaki SAKAI* Seiji TANIMOTO*

ABSTRACT

A new electronically controlled 4-speed automatic transmission has been developed for use in next-generation compact class vehicles and employed in the new Honda LIFE. In addition to new fourth gear shift and lock-up mechanisms, the new AT features a parallel triple-shaft structure with a flat torque converter and a case with no side cover. The control system components are also concentrated. These have made the unit more compact, the shortest in its class at 334 mm in overall length. The employment of Active Lock-up II to provide lock-up control has significantly increased the lock-up control area with no loss of drivability. In combination with the addition of a fourth gear and the reduction of friction by 30%, this expansion of the control area has contributed significantly to improved fuel economy.

In addition, the employment of clutch hydraulic pressure direct control using a linear solenoid, center positioning of idler gear trains on each shaft, and climbing and descending control, among a variety of other technologies, has resulted in a smooth and very stable shift feeling, superb quietness, and improved drivability.

1. Introduction

Honda re-entered the small passenger vehicle market with the 1986 model TODAY's Hondamatic with overdrive. During the 1988 full model change, a parallel dual shaft type hydraulic control 3-speed automatic transmission (3AT hereafter) was established. Since then, the 3AT has been adopted for this class of vehicle, but in response to the need for greater environmental protection and conservation of natural resources in recent years, and to realize the development concept for the 2004 LIFE full model change, an electronically controlled 4-speed automatic transmission has been developed. This electronically controlled 4-speed automatic transmission (new 4AT hereafter) was completely developed anew from the platform for the next generation of compact class vehicles.

This paper reports on the major technologies adopted for the new 4AT.

2. Development Goals

In the development of this new 4AT as the AT for the next generation of compact class vehicles, the development targets were "compact", "improved fuel economy", and "commercial appeal beyond the vehicle's class". The following three items were set as development goals in order to achieve these targets.

(1) Compact AT both in total length and longitudinal length, to achieve both high level of collision safety performance and a more spacious cabin.

* Tochigi R&D Center

(2) Achievement of a friction level equivalent to the 3AT and expansion of the lock-up control area to achieve a class leading level of fuel economy performance.
(3) Achievement of quietness and shift quality equivalent to the small vehicle class to achieve a comfortable driving performance, including on expressways and suburban roads.

3. Basic Specifications and Basic Structure

Figure 1 shows the main cross-section of the new 4AT, and Table 1 gives the main transmission specifications.

As shown in Fig. 1, the new 4AT is a parallel, triple-shaft 4AT with one-way clutch in 1st gear. The structure is such that the 3rd gear train and the idler gear train are common.

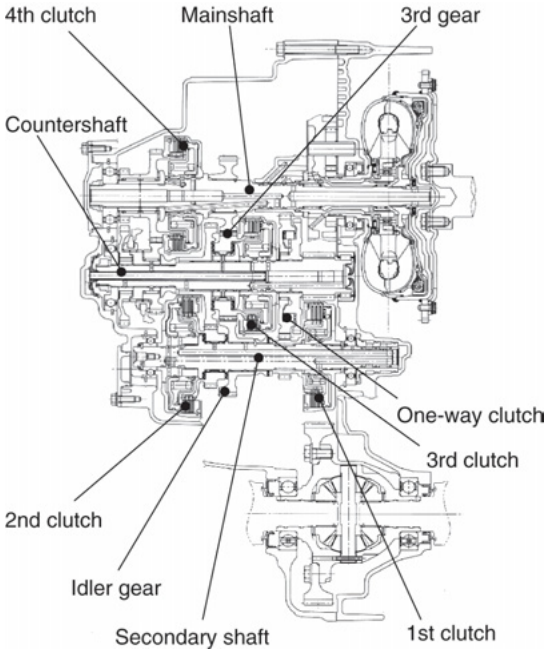


Fig. 1 Cross-section view of newly developed 4AT

Table 1 Transmission specifications

		Newly developed 4AT		Previous 3AT	
Engine specifications	Displacement (Type)	660cm³ (NA)	660cm³ (Turbo)	660cm³ (NA)	660cm³ (Turbo)
Dimensions (mm)	Overall length	334	334	328	347
Axis center distance (mm)	M/shaft ~ C/shaft	80	80	77	77
	C/shaft ~ S/shaft	80	80	–	–
	C/shaft ~ Differential	110	110	110	110
Torque converter	Diameter of flow path	ϕ190	ϕ190	–	–
	Lock-up clutch	Yes	Yes	–	–
Overall gear ratio	1st	15.282	13.448	15.341	13.975
	2nd	8.487	7.702	8.047	7.654
	3rd	5.358	4.938	4.940	4.483
	4th	4.068	3.488	–	–
	Rvs	9.997	8.792	10.873	10.873

Note: M/shaft: mainshaft, C/shaft: countershaft, S/shaft: secondary shaft

In addition, as will be explained in section 4.3.1, on the assumption of the adoption of a lock-up mechanism using in natural aspiration spec engines (NA engines hereafter), the structure and control system based on the assumption were all adopted in variation. This enables the new transmission to be compatible with anything from a 660 cm^3 NA engine to a 660 cm^3 engine with turbocharger, while maintaining the basic structure as it is.

4. Major Technologies and Results

4.1. Compact Structure

Towards the goal of being more compact, a parallel, triple shaft layout was adopted to balance compactness with enhanced gear noise quietness. As will be explained in section 4.4.3, the structure is such that an idler gear train that is common with the 3rd gear train is placed in the center of each shaft.

To shorten the total length, a flat type of torque converter was established, and the case has no side cover. Moreover, in order to shorten longitudinal length, the layout is such that the differential axis is located under the engine center. In combination with these measures, the control system was concentrated, as explained in section 4.4.1.

4.1.1. Squashed torque converter

In order to actualize the new 4AT "compact" target, it was necessary to place the torque converter torus section and the lock-up mechanism within a limited space, so a vital issue was flattening the torque converter.

It is known that squashing the torus section creates a separation phenomenon of internal circulation oil and causes a drop in torque ratio and capacity factor, leading to affect start-off performance, fuel economy, and cooling performance[(1)].

To address these issues, a method for optimizing design parameters independently developed based on the one-dimensional angular momentum theory[(2)], and a three-dimensional CFD according to standard k – ε model[(3)] were adopted to optimize the pump and turbine blades.

Figure 2 shows the results of turbulence energy calculations, for a conventional torque converter with a flattening rate of 92% and for the newly developed torque converter with a flattening rate of 81%. As shown in Fig. 2, the distribution of turbulence energy that expresses the size of hydraulic loss of the newly developed torque converter is confirmed as equivalent to that of the conventional unit.

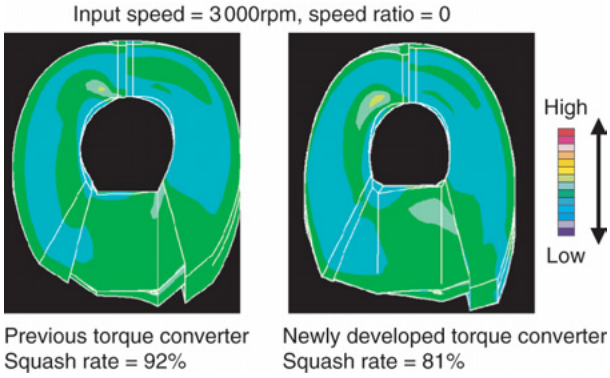


Fig. 2 Results of calculation of kinematic turbulence energy

By employing the methods above, the width of flow path is 6 mm less than the conventional unit as shown in Fig. 3, and at the same time, the performance achieves a high stall torque ratio of 2.5, which is equivalent to the conventional unit. Furthermore, in the range with speed ratio of 0.3 to 0.7, torque ratio characteristics better than the conventional unit were achieved.

4.1.2. Structure of case without a side cover

(1) Shortening total length

The total AT length must be no more than 350 mm so that it can be fitted in the engine room of the new model LIFE.

Using a conventional structure with an ordinary side cover would mean that, if the fastening rigidity and membrane rigidity required were to be ensured, the length would exceed the target. It is also predicted that the stress occurring between the shaft support bearing housings would exceed the strength target.

Therefore, a structure was adopted, as shown in Fig. 4, which gives the side cover functions to the transmission case and eliminates the side cover itself. As a result, it was possible to achieve the total length target, and even in the stress areas noted above it was possible to reduce the stress by 52% against the initial forecast by ensuring the section area in the areas concerned and rigidity in the surrounding areas. Figure 5 shows the results of CAE analysis of the transmission case.

(2) Reduction in longitudinal length

In order to achieve the new model Honda LIFE's long room package, a layout was adopted such that the differential axis is placed under the engine center to shorten longitudinal length.

With this layout, as shown in Fig. 6, the direction of the final gear reaction force is in the forward direction, which is contrary to the conventional downward direction. However, the input on the transmission case membrane was an issue.

With the new 4AT, ensuring case membrane rigidity was a challenge due to the location of the Automatic Transmission Fluid (ATF) strainer. Therefore, as shown in Fig. 7, a center bolt type was adopted, placing the bolt and dowel pin in the vector of the reaction force of the final gear. These measures enabled the stress to be received in front of the ATF strainer and the later case walls to be made only to the thickness necessary for die-casting.

As a result, it was possible to shorten the longitudinal length of the power train without an increase in weight.

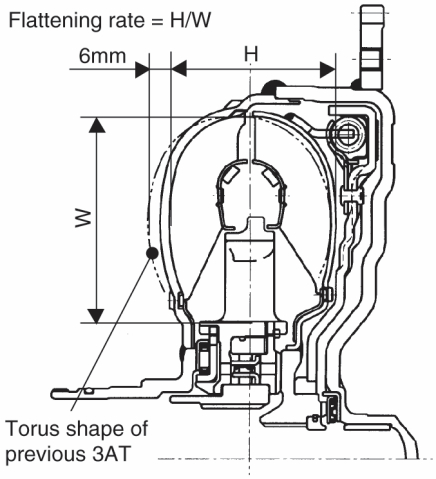


Fig. 3 Cross-section view of newly developed torque converter

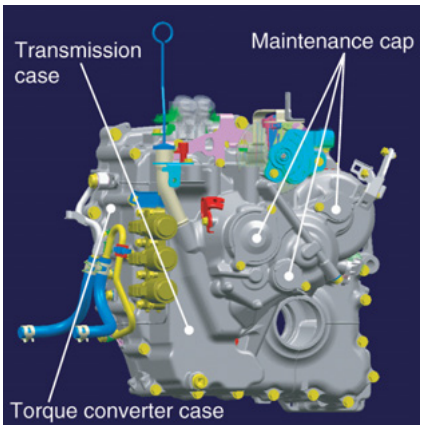


Fig. 4 Newly developed 4AT with side cover-less housing

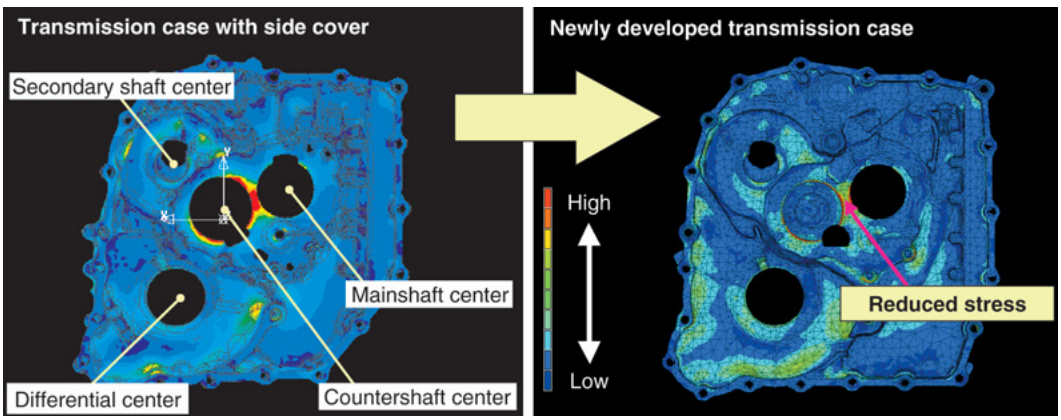


Fig. 5 Results of CAE analysis of newly developed transmission case

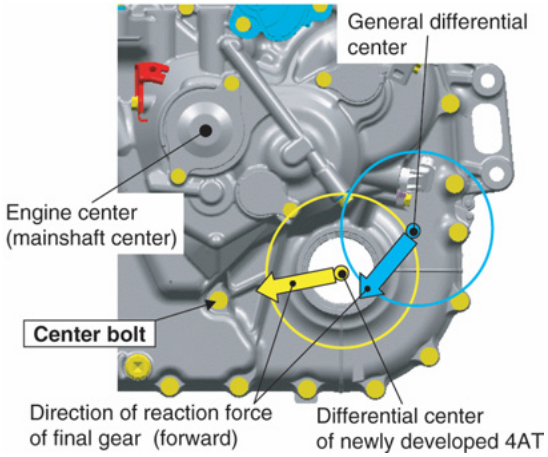


Fig. 6 Direction of reaction force

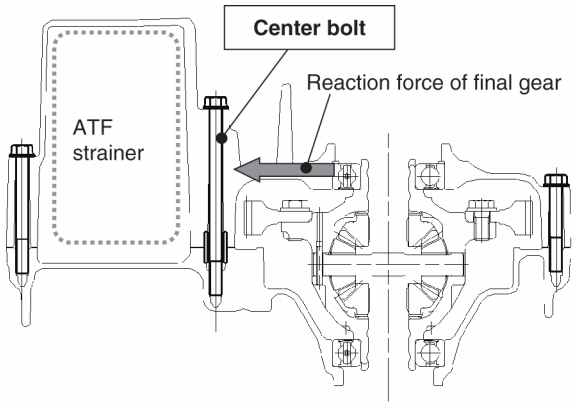


Fig. 7 C enter bolt layout

Through the measures outlined above, the total length is 334 mm even while adding new elements and the longitudinal length of the power train, including engine and AT, is 480 mm. Both of these are the shortest in this class.

4.2. Friction Reduction

In the mini-compact car class, the use of high engine speeds is frequent, so friction reduction greatly contributes to improved fuel economy. The new 4AT was therefore developed with a target of achieving the same friction level as 3AT in order to achieve the best-in-class fuel economy.

4.2.1. Reduction in oil pump loss

Because electronic devices for electronic control are added with the new 4AT, the required oil pump capacity is greater than the 3AT and oil pump loss is also greater. Therefore, in order to prevent a drop in hydraulic pressure in high temperatures at low engine speeds, where any insufficient capacity is most noticeable, the diameter of the control valves were reduced, aluminum valves were adopted, and enhancements were made to surface pressure distribution when the valve body bolts were fastened. These measures enabled the increase in capacity over that of the 3AT to be kept to no more than 15%.

Moreover, the addition of a machined groove to the oil pump drive gear side and the optimization of the machining width of the relief groove for the grinding process enabled a mechanical loss reduction of 10%.

4.2.2. Reduction in differential churning loss

Differential churning loss was reduced by limiting the amount of oil between the AT case and the differential case and final driven gear to an appropriate amount.

First, the AT case bottom volume was increased, as shown in Fig. 8, reducing the oil level height without causing a drop in the oil pump aeration limit. Furthermore, the clearances were optimized between torque converter case and differential case, and between final driven gear and torque converter case.

This resulted in a reduction of 13% in differential churning loss.

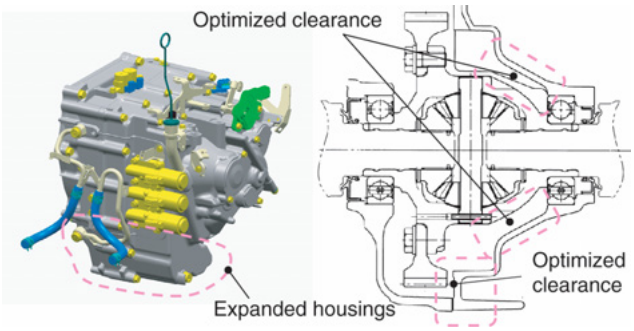


Fig. 8 Optimized area

4.2.3. Reduction in clutch drag

For each clutch pack, in order to reduce the lubrication oil shearing force caused by the friction plates, the target was to enhance emission performance as much as possible, while maintaining the oil retention function. To this end, conventional methods such as tuning the lubricant emission path were utilized and drag was reduced.

Next, with the new 4AT's 2/3/4 gear clutch for the NA engine, a new shape was adopted for the friction material grooves of the friction plates. This was applied in combination with the waved clutch plate. As a result, it was possible to further enhance the lubricant emission performance, and to reduce drag to no more than half of what it had been. The difference in friction with the new groove design is shown in Fig. 9.

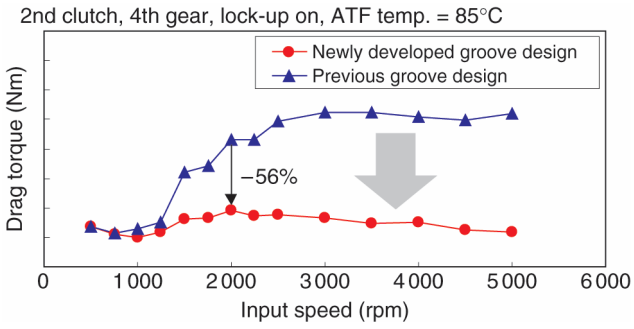


Fig. 9 Drag torque comparison

By reducing the oil pump loss, differential churning loss, and clutch drag, friction was reduced by 30%, and a 3AT level of friction was achieved with this new 4AT. Figure 10 shows the results of friction analysis of each element, before and after the countermeasures were taken.

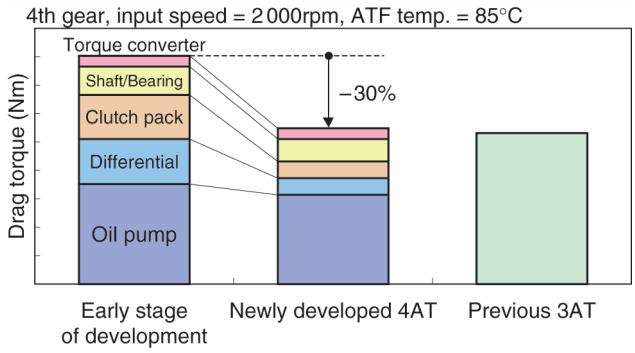


Fig. 10 Results of friction factor measurement

4.3. Driving Performance and Fuel Economy Performance

4.3.1. Addition of fourth gear and lock-up

Figure 11 shows the results of a fuel consumption simulation for the new 4AT carried out at the concept stage. As shown in the figure, greatly improved fuel economy performance cannot be expected simply by making it a 4AT. To achieve the fuel economy target, application of a lock-up mechanism was necessary.

Therefore, assuming adoption of a lock-up clutch for each variation and aiming to achieve both fuel economy improvement and advanced drivability, the Active Lock-up II was adopted[(4)].

At the same time as adopting this system, a long torsion damper was adopted in the lock-up clutch, enabling engine torque fluctuation to be damped. Due to this torque fluctuation damping effect and to this system's highly accurate feedback control using linear solenoid, the lower limit speeds in the cruising range and in the lock-up possible range during acceleration were lowered, enabling the lock-up operation to be carried out from 2nd gear, 12 km/h or faster. As a result, in comparison with the lock-up control area adopted conventionally in this class, it was possible to greatly extend that control area, particularly in the low and medium speed ranges.

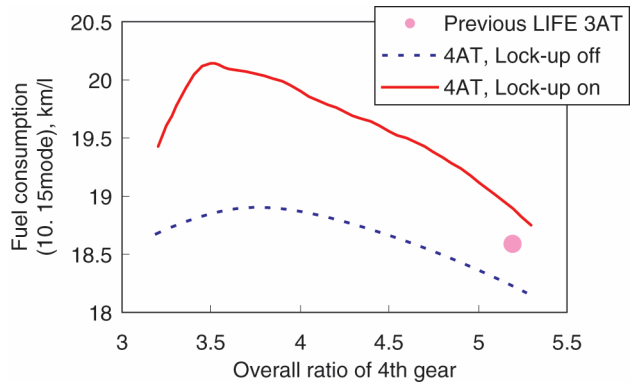


Fig. 11 Results of fuel consumption simulation

4.3.2. Setting the gear ratio

In setting gear ratios, the target was to achieve both improved fuel economy with the new 4AT for the NA engine and drivability in 4th gear. Therefore, the 4th gear ratio was set giving full consideration to cruising performance at 100 km/h, including climbing slopes on an expressway. As for the 1st gear ratio, it was set with emphasis on start-off and gradability, while close ratios were set between 2nd, 3rd, and 4th gears considering fuel economy improvements with lock-up. A comparison of the new 4AT gear ratios established against the 3AT, is shown in Table 1.

Through the fuel economy improvement countermeasures, including lock-up control, gear ratio setting, and friction reduction, a 7% fuel economy improvement in the Japanese 10.15 fuel consumption mode in comparison with the 3AT was achieved.

4.4. Enhanced Commercial Appeal

4.4.1. Shift quality

One aim with the new 4AT was to achieve a smooth and highly responsive shift feeling that would be acceptable even in the small vehicle class. The control system to achieve this target must be compact together with the lock-up control system requiring high accuracy. Therefore, a direct control system for clutch hydraulic pressure[(4)], which has been used in Honda's high-class vehicles, was adopted with partial modifications added.

As a result of these modifications, in comparison with Honda's conventional system, it was possible to eliminate two ON/OFF solenoid valves, one ATF temperature sensor, and two hydraulic pressure switches. This created a concentrated control system unit. With these measures, it was possible to apply direct control and Active Lock-up II to the new 4AT, while maintaining its compactness. Table 2 shows the results of a comparison with other control systems.

This control system is one that directly controls clutch pressure using linear solenoids, and the control logic is composed of the following two controls.

(1) Clutch transient response control that stably carries out clutch preparation in response to clutch and oil path status.

(2) Torque-based control that calculates clutch standard pressure during shifting by estimating torque input into the AT and coefficient of friction of friction plate.

Table 2 Comparison of control systems

	Newly Developed 4AT	Honda LIFE/DUNK Previous 3AT	Honda STEP WAGON 4AT
Clutch control	**Direct control**	Indirect control	Direct control
Lock-up control	**Active lock-up Ⅱ**	–	Active lock-up Ⅱ
Number of control valves	**15**	15	14
Number of one-way clutches	**1**	1	0
Number of on /off solenoids	**2**	0	4
Number of linear solenoids	**3**	0	3
Number of ATF temp. sensors	**0**	0	1
Number of pressure switches	**0**	0	2

In the torque-based control, a setting method called G-design[4] was adopted. It determines body G changes during shifting. Figure 12 is a concept diagram, showing up-shift.

Together with the adoption of this shift control system, a hydraulic centrifugal cancel mechanism was adopted for the 2nd, 3rd, and 4th gear clutch. These greatly enhanced clutch pressure control accuracy and quality stability, achieving a smooth, highly responsive shift feeling, and high gearshift responsiveness.

4.4.2. Control in climbing and descending conditions

When making mini-compact cars, which have small engine torque absolute values, into a 4AT it was expected that shifting becomes frequent due to insufficiencies in surplus driving force when climbing a slope, and insufficiencies in engine braking when descending slopes also becomes noticeable. Therefore, control in climbing and descending conditions was adopted in all variation. This has rarely been adopted in mini-compact cars; it is the first time it has been adopted in a mini-compact car fitted with an NA engine.

In response to the load generated by climbing and descending a slope, the PROgressive Shift schedule Management TEChnology (PROSMATEC) selects the optimum gear from among 2nd, 3rd, and 4th. This technology minimizes unnecessary shifting on ascending roads, and assists with engine braking on descending roads, enabling drivability that goes beyond the mini-compact car class to be achieved.

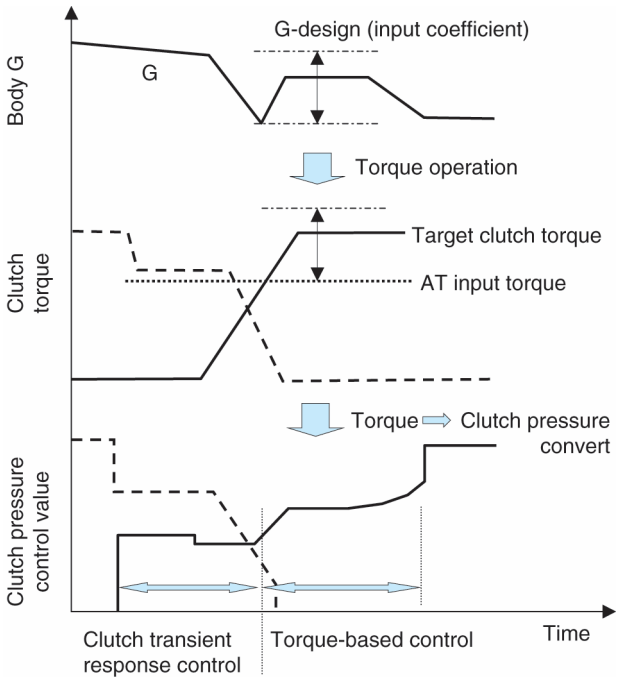


Fig. 12 Overview of new control logic (up-shift)

4.4.3. Noise and vibration (NV) commercial appeal

The new 4AT has a parallel, triple-shaft structure, adopting a layout whereby 1st and 2nd gears are driven through the idler gear. The conventional structure, with an idler gear train placed on each shaft end, is subject to shaft deflection due to driving force fluctuations. In order to prevent worsening of gear noise due to gear misalignment, the structure had to have the increased tooth width and adopt bearings to limit gear misalignment. Therefore, use of a conventional structure would be the issue for making a compact new 4AT.

For the new 4AT, an idler gear train with multiplex meshing was placed at the center of each shaft of the parallel, triple shaft structure. Due to this, as shown in Fig. 13, the shaft deflection effect was minimized and gear misalignment was reduced. The target compact size was achieved, while gear engagement accuracy during input load fluctuations was enhanced.

At the same time, each gear's basic specifications were set, greatly enhancing total contact ratio in comparison with the 3AT. In addition, rib placement was optimized through CAE analysis, and case rigidity fully maintained. This minimized the generation of radiated noise due to case resonance.

As shown in Fig. 14, this resulted in a noise reduction of at least 4 dB in both acceleration and deceleration for AT unit 3rd gear noise.

Moreover, the benefits of a 4AT and the adoption of lock-up across a wide operation range reduced engine speed when driving, and have contributed to vehicle quietness in both the practical use range and in the high speed cruise range.

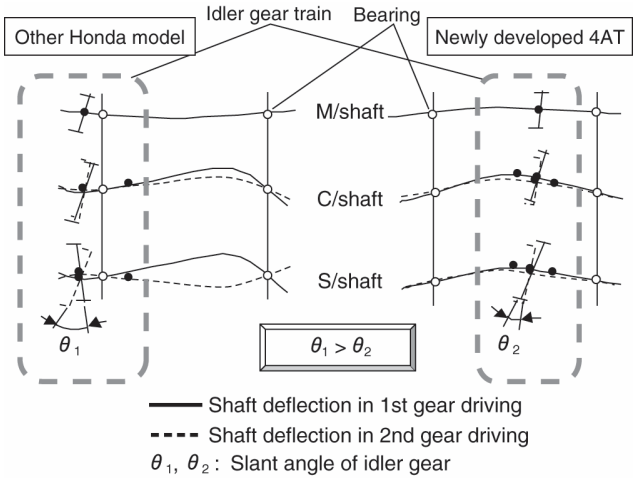


Fig. 13 Comparison of idler gear train

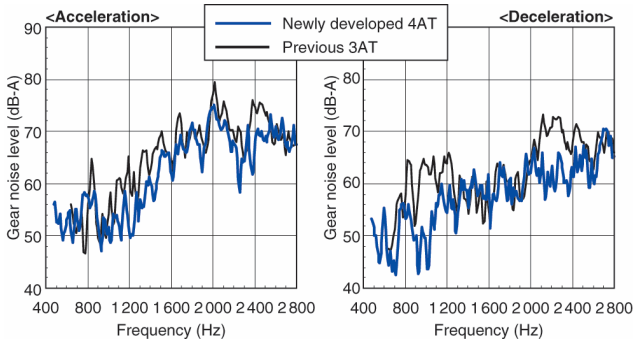


Fig. 14 3rd gear noise

5. Conclusion

In looking towards the next-generation compact class vehicle, the following results were obtained when a completely new 4AT was developed from the platform and installed in the new model Honda LIFE.

(1) With the adoption of a parallel, triple shaft type structure, case components, flat torque converter, and differential axis placed under the engine center, both the total length and longitudinal length were reduced to best-in-class, at 334 mm and 480 mm respectively.
(2) As a result of reducing oil pump loss, clutch pack drag, and differential churning loss, a friction value equivalent to 3AT was achieved, even though the 4th gear was added.
(3) Adopting the Active Lock-up II in the lock up control area enabled lock-up control to be made from 2nd gear, 12 km/h. This, combined with the effects of a 4AT and friction reduction, achieved a 7% fuel economy improvement in the Japanese 10.15 fuel consumption mode.
(4) With the adoption of a direct control system for clutch hydraulic pressure and a hydraulic centrifugal cancel mechanism, a highly responsive and high-level shift quality was actualized. In addition, drivability was enhanced with the application of the PROSMATEC.
(5) As a result of placing the idler gear train in the center of each shaft and enhancing total contact ratio, combined with the adoption of a 4AT and highly practical lock-up mechanism, high level NV commercial appeal at the top of the mini-compact car class was achieved.

References

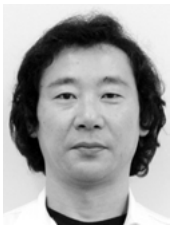
(1) Ejiri, E., et al.: Influence of the Flatness Ratio of a Torque Converter on Hydrodynamic Performance, Transactions of The Japan Society of Mechanical Engineers, Series B, Vol. 64, No. 623, p. 151-156 (1998-7)

(2) Abe, H., Miyoi, N., Yamashita, T., Shirakigawa, K.: Practical Simulation Method by Compensating the Outlet Flow Angle of a Stator, JSAE Annual Congress Proceedings, No. 951, p. 121-124 (1995)

(3) Abe, H., Maruyama, T., et al.: Development of an Ultra Flat Torque Converter by Applying Three-dimensional Computational Fluid Dynamics, Honda R&D Technical Review, Vol. 13, No. 1, p. 75-80 (2001)

(4) Kato, S., Miyamoto, O., Saitoh, Y., Tokuda, M., Hotta, T., Sunada, S.: Development of One-way Clutch-less 5-speed Automatic Transmission, JSAE Annual Congress Proceedings, No. 29-01, p. 13-18 (2001)

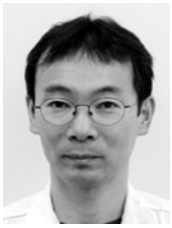
■ Authors ■


Yoshiharu UCHIDA


Osahide MIYAMOTO


Tetsuya OTANI


Tetsurou MARUYAMA


Kazuaki SAKAI


Seiji TANIMOTO

Development of CVT for 2004 Model Odyssey

Yoichi SATO* Junji URANO* Akihito OHASHI*
Shinji SAKUMA* Masaaki YAMAGUCHI*

ABSTRACT

A 2.4L class CVT has been newly developed for the 2004 Odyssey to provide superior automotive fuel economy and a high level of driving pleasure. In addition to a torque converter, a first for a Honda CVT, the new CVT includes among its features lock-up control operating from immediately after start-off, a high-efficiency oil pump with a delivery switching mechanism, technologies enabling overall length to be reduced, a simple hydraulic circuit capable of optimizing pulley pressure, an ECU to realize excellent driving performance, and a three-part case. With a maximum transmitted torque of 218 Nm at 385 mm in length and weighing 95.3 kg the new CVT records 7.5-11% higher transmission efficiency than competitors' CVTs in the same class. The new CVT has enabled optimization of shift control, balancing fuel economy with sporty driving performance.

1. Introduction

Automotive fuel economy performance has become an extremely important issue as global concern over energy resources and the environment has increased. At the same time, manufacturers are required to increase the level of driving pleasure of their vehicles, which remains the basis of commercial appeal. As part of its response to these widespread social demands, Honda has employed CVTs offering superb fuel economy in its vehicle range since 1996. These CVTs have been consistently modified through the Civic, Logo and Insight ranges; significant modifications were made to enable the development of a new 1.5L class CVT able to satisfy demands for fuel economy and driving pleasure for use in the 2002 Fit.

This paper will discuss the technologies employed in the development of a new 2.4L class CVT offering both superb fuel economy and a high level of driving pleasure as part of the full model change of the Odyssey.

* Tochigi R&D Center

2. Development Goals

The following goals were established to enable the development of a 2.4L class CVT offering top-of-class fuel economy and running performance:

(1) Use of torque converter to provide smooth and powerful start-off
(2) Operation of lock-up clutch control from directly after start-off to minimize slip loss
(3) Significantly increased transmission efficiency
(4) Optimum shift control balancing fuel economy with sporty driving performance

3. Basic Layout and Main Specifications

Figures 1 and 2, respectively, show a cross-section and an external view of the CVT developed for the new Odyssey. Table 1 shows the major specifications of the CVT.

The basic layout of the CVT features a torque converter

as part of the startoff mechanism (a first for a Honda CVT), a vane pump including a delivery switching mechanism to increase the efficiency of the drive system, a stator shaft with built-in oil channels to enable overall length to be reduced, a hydraulic pressure sensor which constantly monitors driven pulley pressure to increase efficiency, sharing of linear solenoid functions to make the structure of the control circuits more efficient, and the simplest possible three-part structure for the case.

These technologies have enabled the required specifications to be realized, with a maximum transmitted torque of 218 Nm at an overall length of 385 mm and a total weight of 95.3 kg.

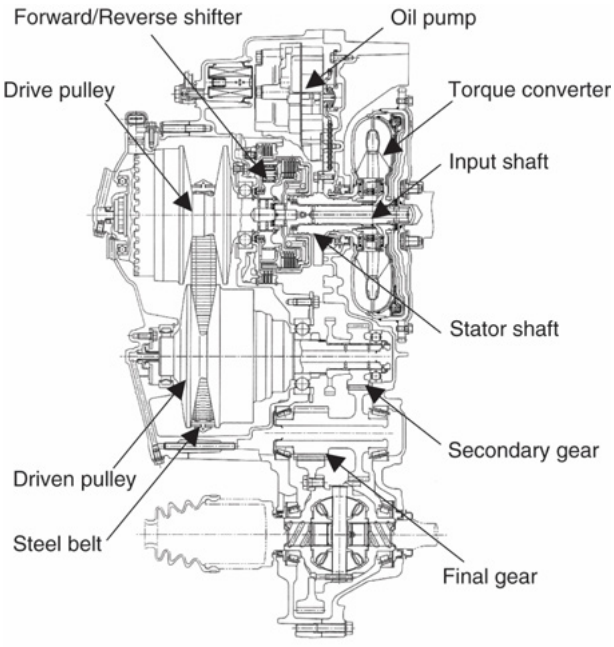


Fig. 1 Main section of CVT

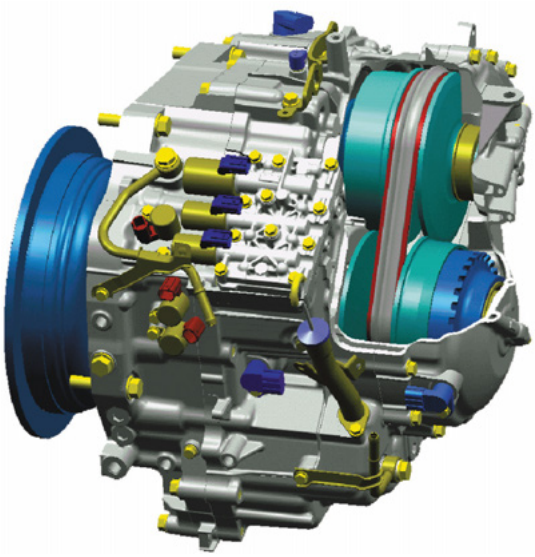


Fig. 2 View of CVT for Odyssey

Table 1 CVT specifications

		2004 Model Odyssey
Engine specifications	Type	2.4L 4VLV
	Max. power (kW/rpm)	118/5 500
	Max. torque (Nm/rpm)	218/4 500
Ratio	LOW	2.470
	OD	0.450
	Secondary	1.514
	Final	3.350
	Reverse	1.735
Dimension	Overall length (mm)	385
	Pulley axis length (mm)	170
	Weight (kg)	95.3 (Wet)

4. Main Technologies

4.1. Torque Converter

The employment of a torque converter in the startoff system enables the system to provide a smooth acceleration feeling at start-off, combining peak acceleration and continuous acceleration, as shown in Fig. 3.

4.2. Vane Oil Pump with Delivery Switching Mechanism

A high-efficiency oil pump has been developed to reduce the required oil pump drive torque. Inclusion of a delivery switching mechanism with the pump enabled a reduction in pump driving torque while guaranteeing the high oil pressure required for 2.4L engine torque loads and ensuring the required oil supply at low engine speeds.

4.2.1. Basic configuration

The former gear-driven oil pump has been replaced with a pressure balance-type vane oil pump to ensure stable high oil pressure and sufficient oil supply from low to high temperatures.

In addition, the oil pressure control valves have been built into the body and base making up the oil pump to make the unit more compact.

Figure 4 shows the basic configuration of the vane pump and the position of the valves.

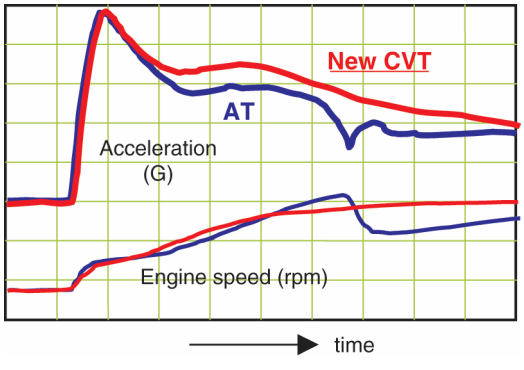


Fig. 3 Start-off acceleration characteristic

4.2.2. Delivery switching mechanism

The oil pump employs a delivery switching mechanism to effectively exploit the characteristics of a pressure balance-type vane pump in which two chambers take in and deliver oil with every revolution.

In driving modes in which the oil pump would supply excess oil, the pump switches from two-chamber delivery (full delivery) to one chamber delivery (half delivery). Signal pressure controlled by a separate ON/OFF solenoid operates a pump shift valve to switch delivery mode.

Figure 5 shows the oil delivery paths in full delivery and half delivery modes.

This system has enabled the drive torque for the pump to be reduced, thus increasing the transmission efficiency of the CVT.

Figure 6 shows the difference in pump drive torque for full delivery and half delivery modes.

4.2.3. Vane guide mechanism

The oil pump used in a CVT is required to produce the necessary oil pressure for control as soon as the engine is started.

In a vane pump, the resistance of the vane to movement is normally increased by the viscosity of the oil between the rotor and the vane when the engine is started at low temperatures, and oil pressure response therefore declines. A vane guide, as shown in Fig. 7, has been employed in the new pump to prevent this from occurring, enabling oil pressure response to satisfy CVT performance requirements even when the engine is started at low temperatures.

4.3. High Torque Response

4.3.1. Metal pushing belt

A 30 mm metal pushing belt manufactured by Van Doorne's Transmissie b.v. has been employed in the CVT to ensure a maximum transmitted torque of 218 Nm. The shift ratio range used for the belt is approximately 5.5. Figure 8 shows a comparison of the dimensions of the 24 mm belt employed in the Civic and the 30 mm belt employed in the new Odyssey.

4.3.2. Responses to increased hydraulic pressure

To achieve high torque output in the new CVT, the maximum pulley pressure has been increased to 5.4 MPa from the maximum pressure of 3.5 MPa in the former CVT. Ensuring strength and resistance to deformation in the control valve bodies became a concern with this increased pressure, and FEM analysis was therefore employed to optimize the shape of the high-pressure oil channels and the bolt pitch in the valve bodies.

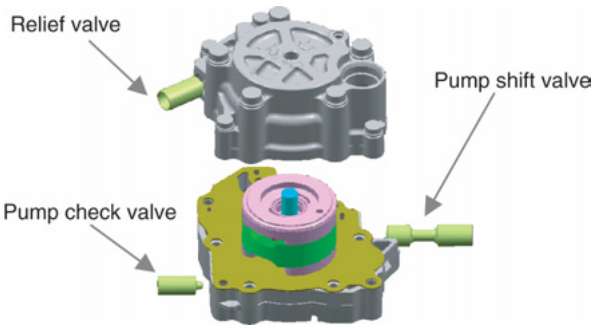


Fig. 4 Layout of pump and valves

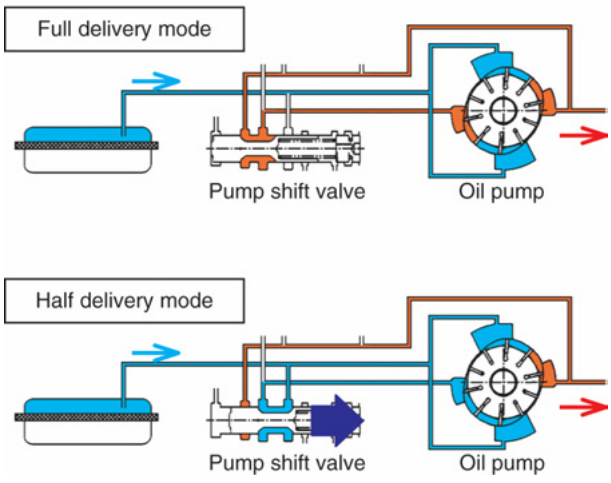


Fig. 5 Delivery modes of pump

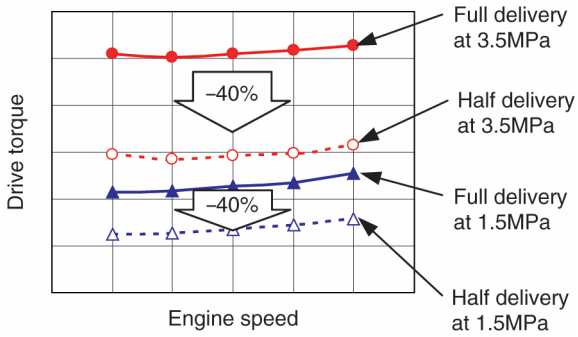


Fig. 6 Drive torque of pump

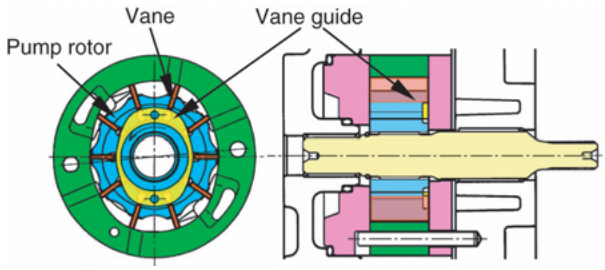


Fig. 7 Vane guide

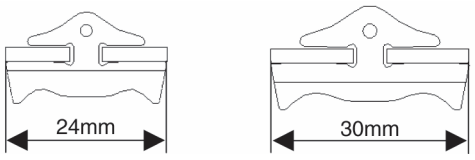


Fig. 8 Comparison of CVT belt size

The results of FEM analysis are shown in Fig. 9.

4.3.3. Case strength

FEM was also used in stress analyses and analyses of pressure distribution on the contact faces of the case in order to optimize the shape of each section as a response to the high transmitted torque of the CVT.

Examples of the results of stress analysis are shown in Fig. 10 and of analysis of contact face pressure distribution in Fig. 11.

Particular considerations in the optimization of the shapes employed in the case were ensuring the strength of the supports for the bearings around the final gear system and guaranteeing contact pressure between mating faces in sections in which it was impossible to use linear shapes between the bolts when coupling with the engine.

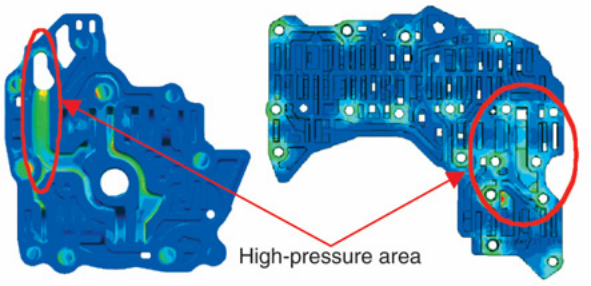


Fig. 9 Valve body stress analysis with FEM

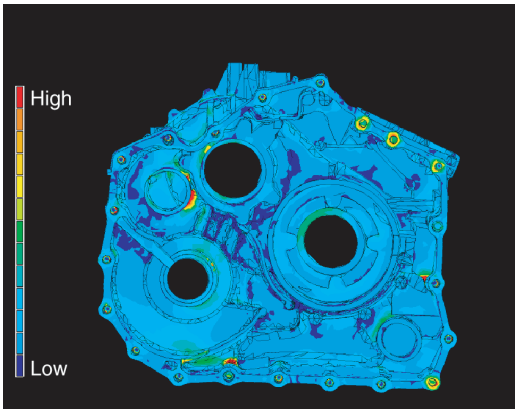


Fig. 10 Stress contour

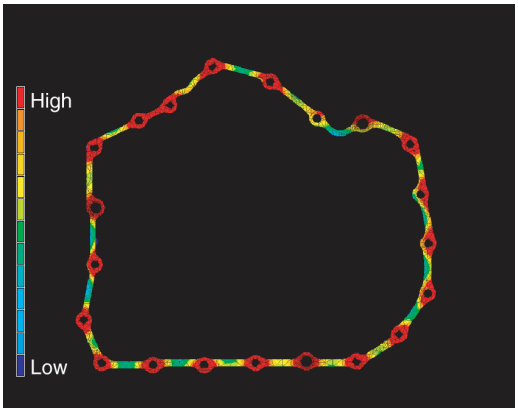


Fig. 11 Contact pressure

4.3.4. Pulley stiffness

FEM stress and deformation analyses of the four V-surfaces on the fixed and movable sides of the drive and driven pulleys were conducted to enable shapes to be optimized with consideration of a balance of stiffness between the four surfaces. The balance of stiffness was taken into consideration to minimize belt misalignment between the drive and driven pulleys and in particular to prevent contact between the metal belt rings and the pulley V-surfaces at high speeds and high loads.

Figure 12 shows the results of FEM analysis of pulley deformation. The amount of deformation shown here was used in analyses of the frequency of contact between the rings and pulley V-surfaces and the rings and elements during operation, with consideration of the trajectory of the belt.

4.4. Technologies to Reduce Overall Length

Development focused on elements in the drive pulley shafts to reduce overall length. This section discusses the main technologies employed and their effect in reducing the length of the CVT.

4.4.1. Stator shaft

Oil channels have been employed in the stator shaft to enable it to guide oil from the oil pump to the input shaft, and to supply oil to other components such as the torque converter. This has reduced overall length by approximately 25 mm against a conventional automatic transmission (in-house comparison).

4.4.2. Bearings

Length was further reduced by not directly clamping the drive pulley shaft support bearings to the drive pulley shaft. As shown in Fig. 13, the nuts connecting the pulley cover to the pulley shaft and the bearings are positioned in the same plane, reducing the overall length of the CVT by approximately 10 mm, which is equivalent to the width of the bearings.

4.4.3. Input shaft

The input shaft and the forward clutch can be coupled by a variety of methods, including spline clamping. In the new

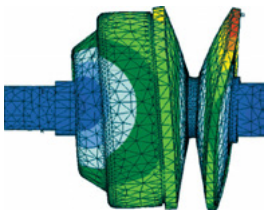


Fig. 12 FEM pulley deformation

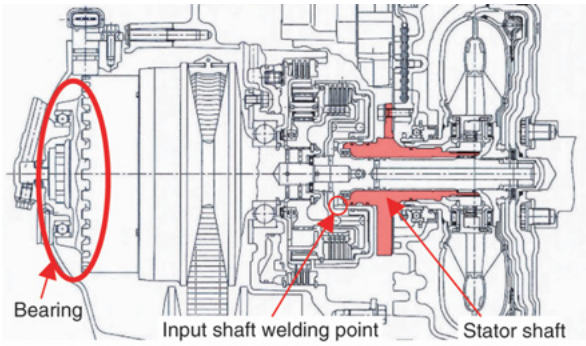


Fig. 13 Layout of drive pulley shaft

CVT they have been welded to reduce overall length. The welding point is shown in Fig. 13. This method of coupling has reduced the length of the unit by approximately 10 mm compared to spline clamping. The integration of the two components has also reduced the number of components employed.

4.5. Increasing Efficiency

4.5.1. Oil pressure sensor

An oil pressure sensor has been employed in the hydraulic pressure control system to provide constant monitoring, enabling self-learning control of hydraulic pressure as determined by the ECU in response to operating conditions and CVT operating hydraulic pressure through feedback of measurements. The use of the sensor has reduced the incidence of excess oil pressure and also enabled oil pump drive torque and belt friction to be reduced against the previous model.

Figure 14 shows the control logic of the oil pressure sensor.

4.5.2. Drive pulley double piston

The former single drive pulley piston has been replaced by a double piston, increasing the area of the piston receiving pressure while the external diameter remains the same. This has reduced the pulley control pressure when the vehicle is cruising, thus reducing the oil pump drive torque during cruise.

Figure 15 shows the area of the single and the double pistons on which pulley pressure acts, and a cutaway view of the piston mechanism.

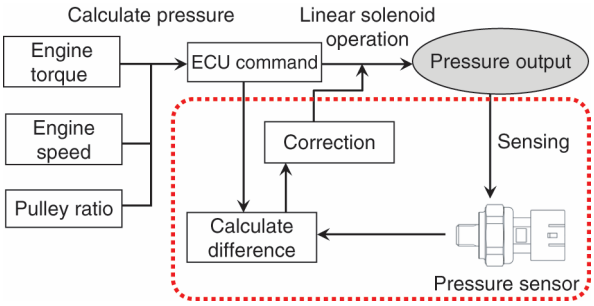


Fig. 14 Control program of pressure sensor

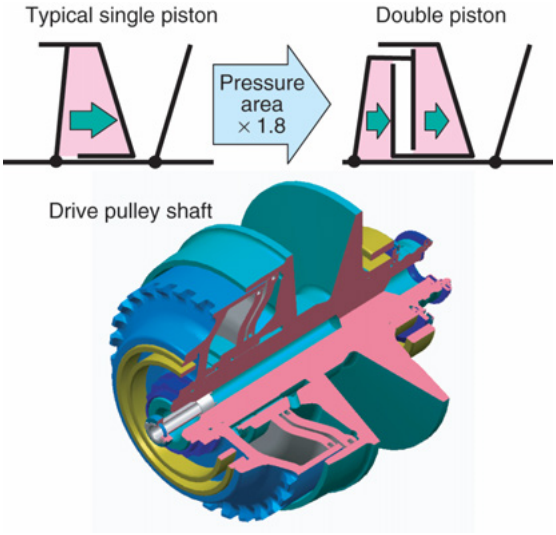


Fig. 15 Double piston mechanism

4.5.3. Reduction of drag resistance of reverse brake

When a vehicle is moving forward, the oil between the reverse brake disc and plate generates constant viscous dragging resistance. This resistance has been reduced in the Odyssey through the employment of a wave disc with a number of wave-like undulations on the circumference.

Figure 16 shows the relationship between drag resistance and engine speed.

4.5.4. Reduction of oil agitation resistance

Because the drive pulley is positioned in the lower section of the CVT, the accumulation of oil in the belt housing would significantly increase agitation resistance. A discharge hole enabling high-efficiency discharge of the oil accumulated in the belt housing after lubrication of the belt and bearings has therefore been employed.

In addition, ribs have been positioned to enable high-efficiency return of the gear and bearing lubricating oil and the oil discharged from the control system to the oil pan, in order to use less oil to maintain the required level to prevent aeration when the vehicle is stopping, starting off, or turning.

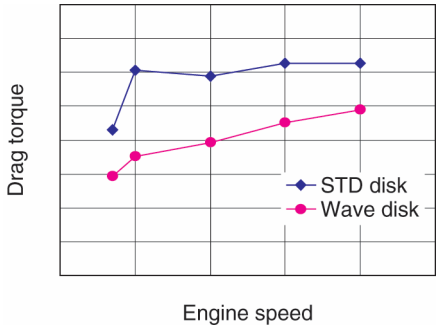


Fig. 16 Drag torque of reverse brake

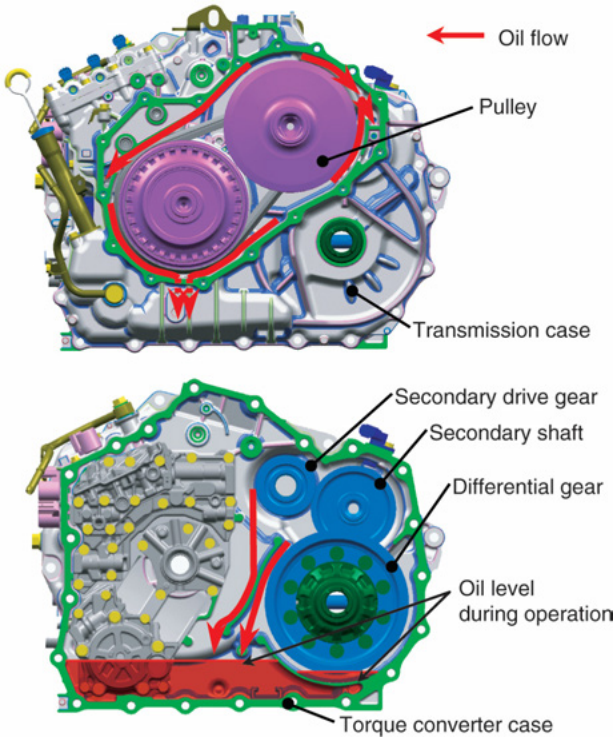


Fig. 17 Oil flow inside case

Figure 17 shows the oil flow inside the transmission.

The employment of the technologies described above has reduced friction torque and increased transmission efficiency by 6%, to a level 7.5 - 11% higher than competitors' CVTs in the same class, as shown in Fig. 18.

4.6. Hydraulic Control System

A direct control system has been employed for the pulley hydraulic control circuit, in which two linear solenoids separately control drive and driven pulley pressure. The employment of a double piston for the drive pulley in the CVT has significantly reduced drive pulley pressure. This eliminates the need for a pulley line pressure control valve, enabling the pulley hydraulic control circuit to be simplified.

In addition, a single solenoid valve is employed for forward and reverse clutch control when the system is in gear and lock-up clutch control. Forward and reverse clutch control and lock-up clutch control are divided into four modes, in gear mode, startoff mode, cruising mode and deceleration mode. Two ON/OFF solenoids enable switching between the modes. This has reduced the shift shock when the vehicle is put in gear, ensured lock-up controllability during startoff and cruising, and enabled control to be applied to protect the belt during deceleration using a single linear solenoid valve, while reducing costs and increasing the efficiency of the space layout.

The hydraulic control system is shown in Fig. 19.

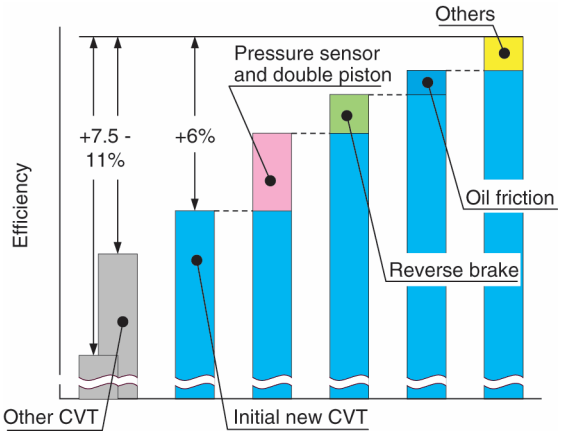


Fig. 18 Transmission efficiency at 60km/h cruise

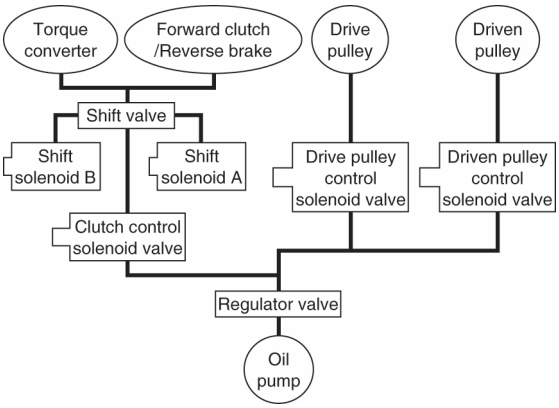


Fig. 19 Hydraulic circuit

4.7. ECU Control System

4.7.1. Lock-up clutch control

Employing a torque converter provided with a lock-up clutch as a startoff device can heighten the appeal of a vehicle by increasing startoff torque against a conventional start clutch, but slip loss at startoff decreases efficiency.

In the new CVT, the range of operation of the lock-up clutch has been extended to vehicle startoff, minimizing slip loss and increasing efficiency.

Figure 20 shows the operating range of the lock-up clutch.

At vehicle speeds close to 0 km/h the lock-up clutch is not engaged, and maximum use has been made of the torque amplification of the torque converter in order to increase the appeal of start-off performance. The moment an operating range is reached in which the torque amplification ratio of the torque converter drops, the lock-up clutch engages and provides control coordinated with the throttle opening angle. At low opening angles, clutch capacity rises rapidly, in order to minimize slip loss, while at high opening angles it rises slowly, in order to prioritize power performance.

Figure 21 shows the slip rate characteristic of the lock-up clutch against vehicle velocity at startoff for low and high throttle opening angles.

As discussed above, the characteristics of the torque converter have been exploited to ensure commercially appealing startoff performance, and optimization of lock-up clutch control has increased efficiency at startoff.

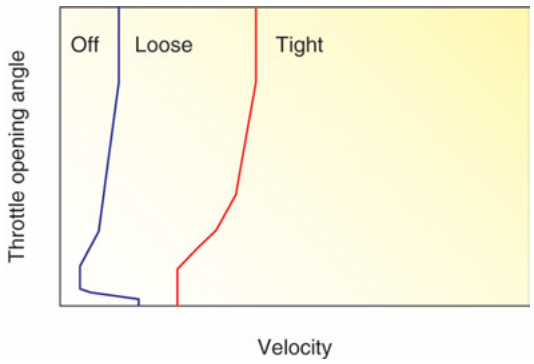


Fig. 20 Lock-up clutch map

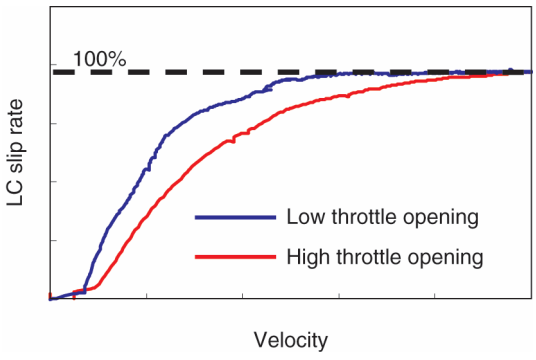


Fig. 21 Lock-up clutch slip rate characteristic

4.7.2. Shift control

The shift control in the new CVT has been optimized for a variety of different driving modes, and represents a new advance in shift control technology.

The following are employed as criteria in determining the driving mode:

- Vehicle velocity
- Throttle opening angle history
- Cornering G (lateral acceleration) history

Switching control between three shift schedules (D1/D2/S shift schedules) and cornering G shift control is applied on the basis of these criteria.

(1) D1 shift schedule

This shift schedule prioritizes fuel economy, and is engaged at low throttle opening angles. In this schedule engine speed is limited and engine torque is the main power source.

(2) D2 shift schedule

This schedule engages when the frequency of medium throttle opening angles increases. Engine speed is higher in D2 than in D1, and the schedule offers superior acceleration performance.

(3) S (Sports) shift schedule

The S shift schedule engages when the frequency of high throttle opening angles increases. Engine speed is higher than D2, and the schedule provides acceleration and engine/brake performance appropriate to sporty driving. Figure 22 shows an image of switching between shift schedules, and Fig. 23 shows a comparison of D1, D2 and S. The schedules offer different shift characteristics at identical throttle opening angles.

(4) Cornering G shift control

Cornering G shift control uses cornering G history to determine whether the vehicle is on a winding road. When the control goes into operation, it effectively maintains a high engine speed.

(5) Effect of switching between shift schedules

Figures 24 to 26 show the results of measurements of the relationship between vehicle velocity and engine speed in a variety of driving modes.

Figure 24 shows the results of measurements conducted during city and highway driving. These driving modes employ the D1 shift schedule, and the measurements indicate that engine speeds remain low.

Figure 25 shows the results of measurements taken during uphill and downhill driving. In this driving mode, D2 and uphill/downhill shift schedules are engaged. This driving mode uses higher engine speeds than city driving, offering the user a smooth drive feeling despite the fact that the vehicle is proceeding up or downhill.

Figure 26 shows the results of measurements taken during driving on winding roads and circuits. This driving mode uses S and cornering G shift schedules, enabling even higher engine speeds to be maintained. These shift schedules ensure a superb drive feeling even as the vehicle is operating in difficult running conditions.

The automatic switching between shift schedules according to driving mode described above has enabled the achievement of a balance of fuel economy and driving performance in D range driving without the need for the driver to touch the shift lever.

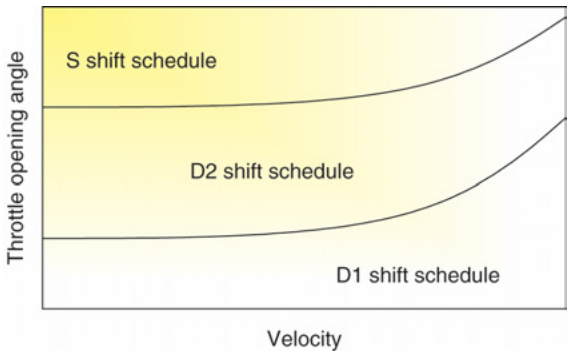


Fig. 22 Switching between shift schedules

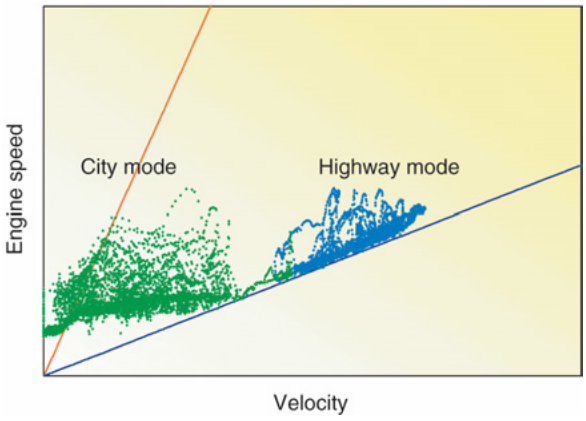


Fig. 24 City and highway mode

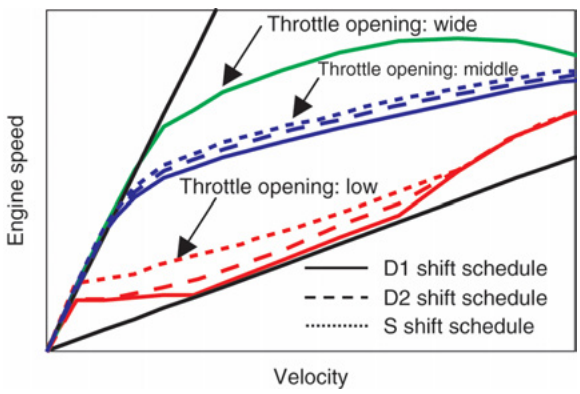


Fig. 23 D1, D2 and S shift schedules

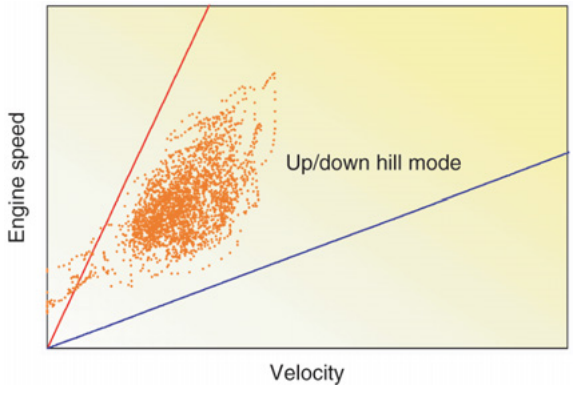


Fig. 25 Uphill and downhill

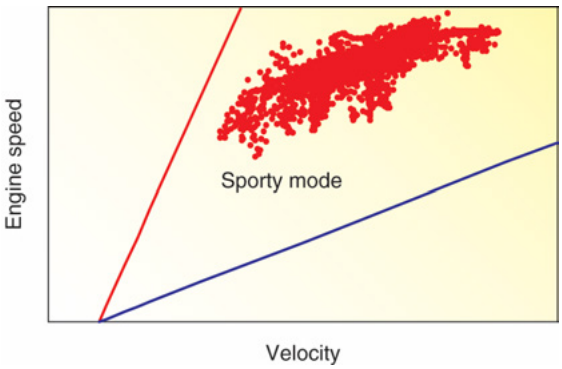


Fig. 26 Sporty mode

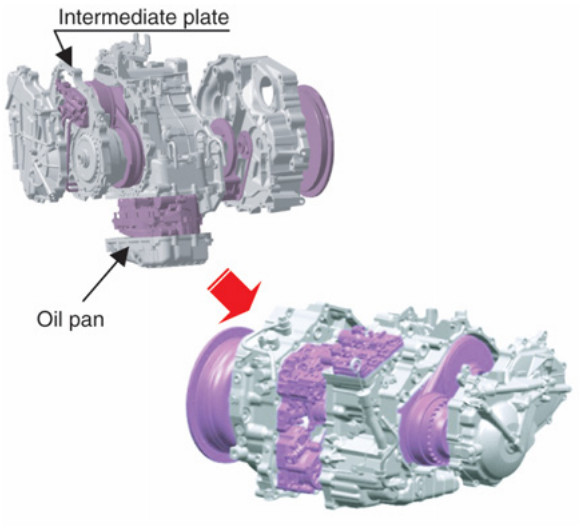


Fig. 27 Transmission consists of three cases

4.8. Three-part Case Structure

The new CVT case has been simplified in comparison to the former case, which was made up of five parts. The oil pan-less structure of the case used in the Fit was adopted and further developed to eliminate the intermediate plate, resulting in a three-part case structure.

Figure 27 shows a comparison of the conventional and the newly developed CVTs. The conventional CVT employed a start clutch and required an intermediate plate to enable positioning of a forward and reverse drive switching mechanism and to support the pulley shaft. The use of a torque converter in the new CVT enabled the positioning of the forward and reverse drive switching mechanism and the pulley oil chamber to be changed, contributing to the realization of a three-part case configuration.

The new configuration has reduced the number of mating faces in the case, increasing the rigidity of the CVT. In addition, it has been possible to both shorten and reduce the number of the bolts employed in the case, which has contributed to weight savings.

5. Conclusion

The development of a new 2.4L class CVT employed the following technologies:

(1) Lock-up clutch control optimization technology to extend the range of operation of lock-up clutch control to directly after start-off in order to minimize slip loss while enabling the characteristics of the torque converter to be maximized to increase commercial appeal
(2) Technologies to significantly increase the transmission efficiency of the CVT (7.5% - 11% higher than competitors' CVTs)
(3) Automatic shift schedule switching technology to enable a balance between fuel economy and sporty driving performance

References

(1) Ota, S., Kunii, H., Sumi, M., Fujimoto, S., Yamaguchi, T.: Development of a Compact CVT for the Hybrid Car - Insight, HONDA R&D Technical Review, Vol. 12, No. 2, p. 61-70

(2) Sumi, M., Fujimoto, S.: Development of a Compact CVT for Hybrid Automobiles, Automotive Technology, Vol. 54, No. 4, p. 48-54 (2000)

(3) Sumi, M., Kunii, H., Fujimoto, S., Ichijo, S., Hasegawa, T., Fukushima, Y.: Development of a New Compact CVT for the Fit, Honda R&D Technical Review, Vol. 14, No. 1, p. 67-76

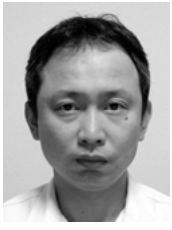
(4) Saito, T., Okano, T.: Application of Metal Pushing V-Belt Stress Simulation with CVT Pulley Stiffness, Honda R&D Technical Review, Vol. 14, No. 1, p. 191-196

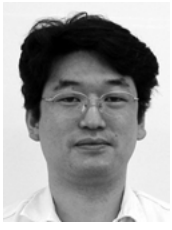
■ Authors ■


Yoichi SATO


Junji URANO


Akihito OHASHI


Shinji SAKUMA


Masaaki YAMAGUCHI

Development of Metal Pushing V-belt for Continuously Variable Transmission for 2L Class Vehicle

Tooru YAGASAKI* Hideaki AOYAMA* Motonori OHNUKI*
Yoshinari OKADA* Ryuhei KATAOKA*

ABSTRACT

Honda presently mass produces a metal pushing V-belt to enable a compact CVT layout in a 1.5L class vehicle. The project discussed in this paper is based on the technologies developed for mass production of the 1.5L class belt. It furthermore employed dynamic analysis of slack string elements and study of ATF extreme pressure lubricant oil films using measurements of electrical resistance, resulting in the development of a metal pushing V-belt enabling a compact CVT layout in a 2L class vehicle.

The size of CVTs has conventionally been determined by the pitch radius of the V-belt. To increase the torque capacity of the CVT, it was formerly necessary to increase the pitch radius of the belt in order to reduce the belt load. In the newly designed belt reduction of the pitch radius has enabled the distance between the shafts to be reduced, hence reducing the size of the CVT. The newly developed belt achieves a maximum transmitted power of 150 kW with 170 mm between the shafts, and enables a more compact CVT layout.

1. Introduction

The main method of increasing the torque capacity of continuously variable transmissions, using metal pushing belts, is to increase the distance between the shafts of the drive and the driven pulleys. As in other automatic transmissions, the strength is increased by increasing the size of the mechanical elements. Due to the fact that almost no technical reports have been published, which include examples of analyses of the dynamic behavior of metal belts, limits are applied to the maximum rotational speed of the belt to ensure dynamic strength based on empirical observation.

On the basis of the technological knowledge and experience gained in the mass production of a metal belt for a 1.5L class CVT[(1)-(4)], the authors conducted dynamic analyses and studied the properties of the extreme-pressure lubricant oil films (oil film, hereafter) in automatic transmission fluid (ATF) on the various components of metal belts, enabling the development of an original Honda metal pushing belt. This paper discusses the newly developed technologies employed in the belt.

2. Development Concept

It is necessary to increase the speed ratio range to achieve a balance between improved fuel economy and adequate start torque in a CVT. It is desirable to reduce the pitch radius of the metal belt to ensure the required speed ratio range, but there is a limit to the extent to which the minimum pitch radius can be reduced to ensure that belt fatigue life is maintained. The distance between the shafts must be extended to increase the torque capacity of the CVT, but this results in an increase in the size of the transmission. In addition, the pulley thrust exerted on the metal belt by the pulleys also increases, making the maintenance of an oil film necessary to prevent wear in the sections of the belt making contact with the pulleys.

* Tochigi R&D Center

Therefore, to increase the torque capacity of the CVT while making the unit more compact it was necessary to employ a belt configuration enabling the belt pitch radius to be minimized, to increase fatigue life by reducing the load on the elements and rings, and to design the belt with consideration of the characteristics of the oil film in each section.

Figure 1 shows a diagram of alternative designs for increasing the torque capacity of the CVT which have identical speed ratio ranges. As the diagram shows, to make the CVT more compact, it is necessary to reduce the distance between the shafts. However, the pitch radius is reduced as a result, and this makes ensuring the fatigue strength of the rings in the metal belt an issue.

Figure 2 shows a plot of maximum transmitted power against distance between shafts for an existing CVT. This graph shows that maximum transmitted power increases with increasing distance between the shafts, increasing the size of the CVT. The issue, therefore, is to reduce the distance between the shafts.

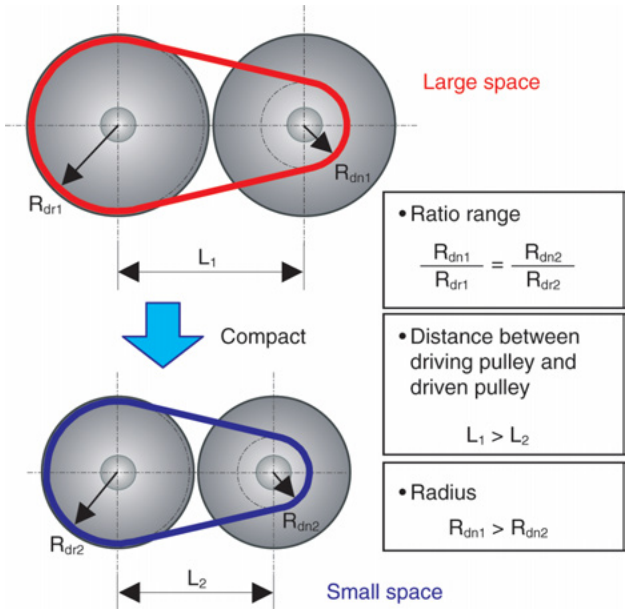


Fig. 1 Structure of CVT with same ratio range

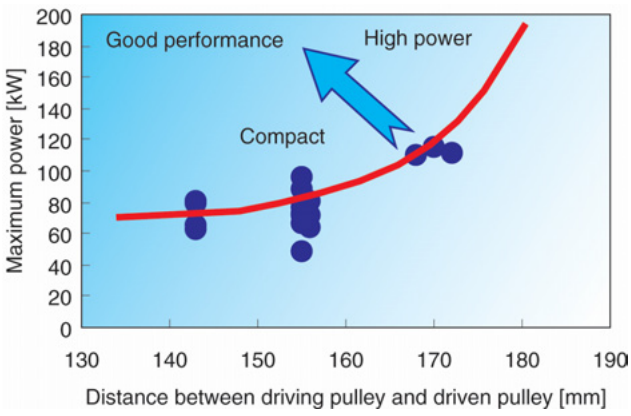


Fig. 2 Maximum power and distance between driving pulley and driven pulley

The following development concept was established on the basis of the above considerations:

(1) Clarification of the dynamic load on each component of the belt through study of the dynamic behavior of the slack strings of the belt.
(2) Optimization of the shape of each component of the belt with consideration of dynamic load.
(3) Guarantee of safety factor through clarification of element fatigue limit load.
(4) Ensuring of wear resistance by verifying the condition of the oil film on each component of the belt.
(5) Reduction of cost through employment of new production process.

3. Structure of Metal Pushing Belt

3.1. Structure of Metal Pushing V-Belt and Component Nomenclature

Metal pushing V-belts are composed of several hundred elements and two rows of multiple layered rings (Fig. 3).

Figure 4 shows the nomenclature applied to each component of the belt.

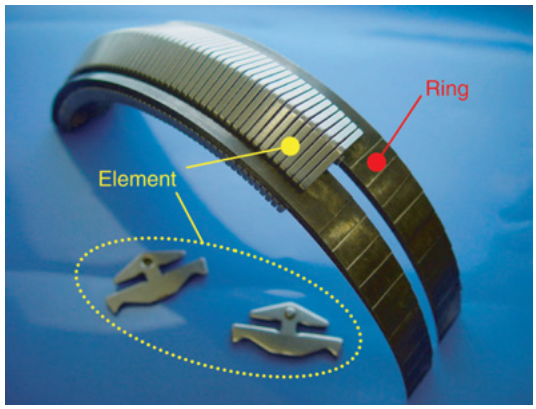


Fig. 3 Metal pushing V-belt

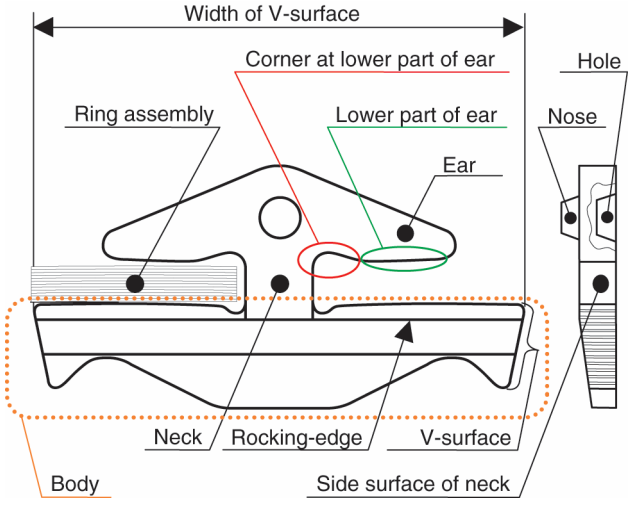


Fig. 4 Configuration of elements and ring assembly

4. Optimization of Element Shape

4.1. Element and Pulley

Measurement of the actual forces of the slack strings in the belt has to the present been considered difficult, but dynamic analyses were conducted in this study to clarify the forces acting on the belt.

4.1.1. Dynamic analysis of elements near exit of driven pulley

Figures 5 and 6 show the results of dynamic analysis of the belt.

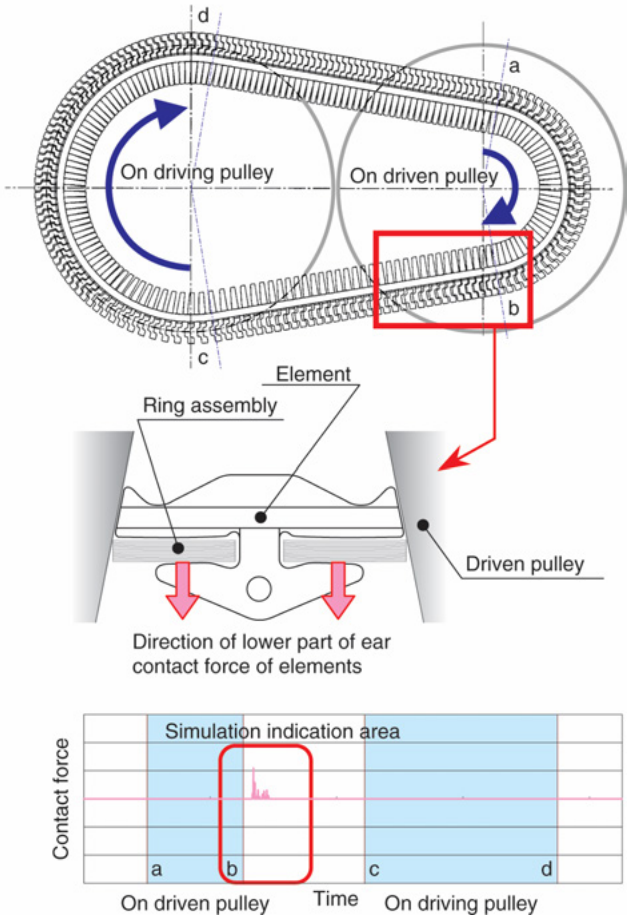


Fig. 5 Lower part of ear contact force of elements

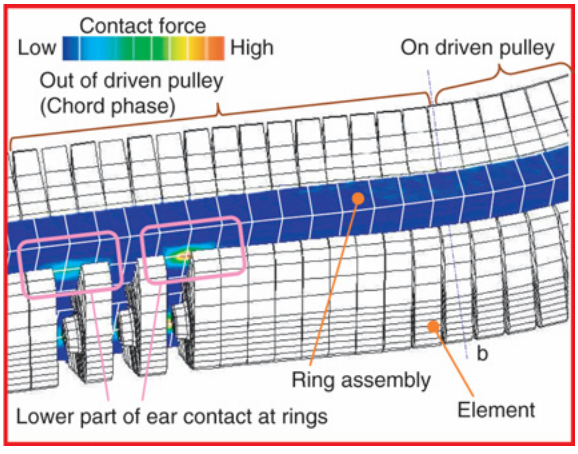


Fig. 6 Lower part of ear contact force of rings

In Fig. 5, entrance to and exit from the driven pulley are marked a and b respectively, and entrance to and exit from the driving pulley are marked c and d respectively. The slack strings correspond to the area between b and c. Figure 5 shows the load on the lower part of the ear. The load is generated as the elements move from the exit of the driven pulley to the slack string section. Figure 6 magnifies the area around the driven pulley exit, and shows the contact between the ring assembly and the lower part of the ear. Contact between the lower part of the ear and the ring assembly occurs as the elements proceed from rotary motion to linear motion.

4.1.2. Optimization of shape of sections of the ear

A structural analysis was conducted to determine the stress generated on the element by the load input from the lower part of the ear. This analysis showed that stress was concentrated in the corner of the lower part of the ear. As shown in Fig. 7, by making the corner a compound radius the stress was able to be reduced without increasing the weight of the elements. Figure 8 shows the results of a structural analysis of the load acting on the slack string section of the belt. Modification of the corner of the lower part of the ear from the former simple radius to a compound radius has reduced stress by approximately 40%.

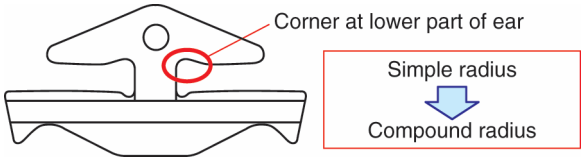


Fig. 7 Configuration at lower part of ear

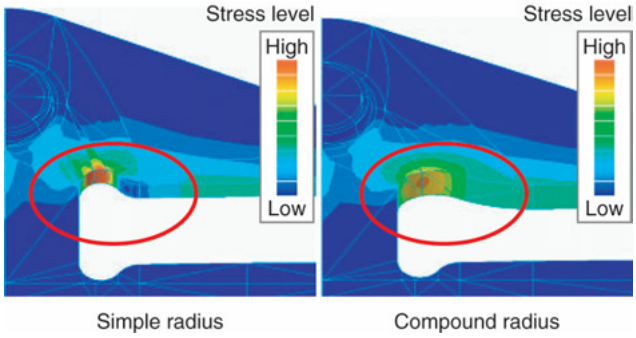


Fig. 8 Corner stresses at lower part of ear

5. Evaluation of Oil Film

The increase of torque capacity to a level appropriate for a 2.0L class CVT required higher wear resistance in the metal belt and pulleys than was required for a 1.5L class CVT. There is an infinitesimal amount of slip between the pulleys and the belt, yet the formation of films by the extreme-pressure lubricants in the ATF ensures wear resistance. It is therefore essential to evaluate the condition of the film. In this study, electrical resistance was used to measure the microscopic slip velocity in an actual belt as a method of evaluating the film. Figure 9 shows a schematic diagram of the circuit used to measure electrical resistance. A pin with a tip of compound radius is pressed onto a test piece corresponding to the pulley or the rings and made to slide. A

fixed voltage is impressed between the pin and the test piece, and the separated voltage which is generated against the resistance between the two surfaces is registered as a film between the surfaces making contact. If no film is formed voltage is recorded as zero, but when a film is formed the voltage reading varies according to the condition of the film.

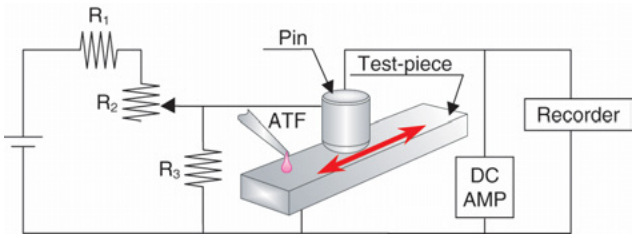


Fig. 9 Circuit for measurement of electrical resistance

5.1. Between the Elements and the Pulley

5.1.1. Relative velocity of elements and pulley

Figure 10 shows a schematic view of measurements of relative slip velocity between the elements and the pulley. A sensor to measure the velocity of the elements and a displacement meter to measure the pitch radius of the metal belt were mounted at the driven pulley to record measurements in a range of angles between 0° and 150° from their position of placement. The relative velocity of the elements and the pulley was determined from the difference between the velocity of the metal belt and the velocity of the pulley at the positions at which the belt wraps around the pulley.

Figure 11 shows the relationship between the wrap angle of the belt on the driven pulley and the pitch radius of the belt at a ratio of 0.5. It is apparent that the pitch radius of the belt decreases between the entrance to and the exit from the driven pulley. Elastic deformation of the elements on the pulley and deformation of the pulley strongly influence this change in the pitch radius of the belt on the driven pulley.

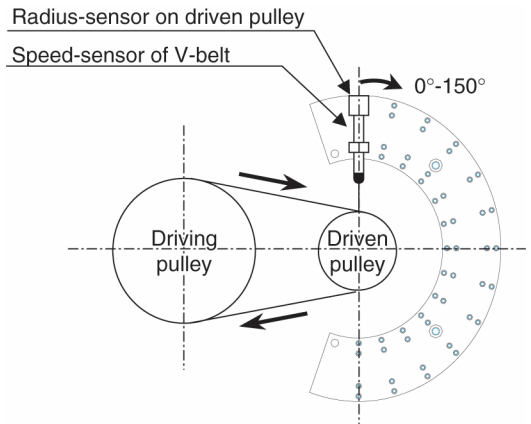


Fig. 10 Schematic view of measurement of sliding velocity on driven pulley

Figure 12 shows the results of calculations of the relative velocity at a tangential direction between the elements and the pulley. The relative slip velocity between the elements and the pulley is approximately zero at the entrance to the driven pulley, then steadily increases between the entrance and the exit, and is at its maximum at the exit from the pulley. This maximum relative slip velocity was used as the relative velocity for evaluation in oil film tests.

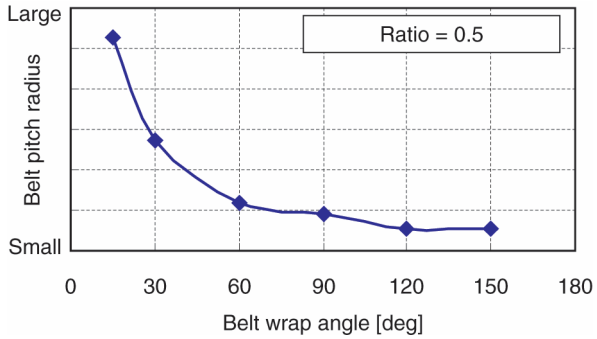


Fig. 11 Variations in belt pitch radius with respect to belt wrap angle

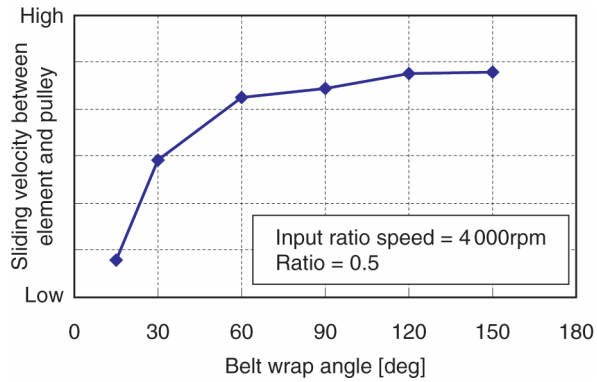


Fig. 12 Sliding velocity with respect to belt wrap angle

5.1.2. Evaluations of oil films formed by different ATF extreme-pressure lubricants

Measurements of electrical resistance were used to determine the conditions of maintenance of different ATF oil films with respect to Hertzian contact pressure and relative velocity between the elements and the pulley in conditions of actual use. A sulfur-phosphorous extreme-pressure lubricant was added in ATF1, while a sulfur extreme-pressure lubricant was added in ATF2. The results of oil film measurements for these two ATFs are shown in Figs. 13 and 14.

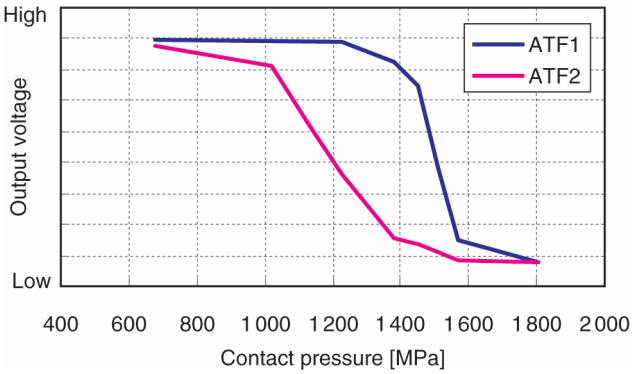


Fig. 13 ATF oil film conditions with respect to contact pressure

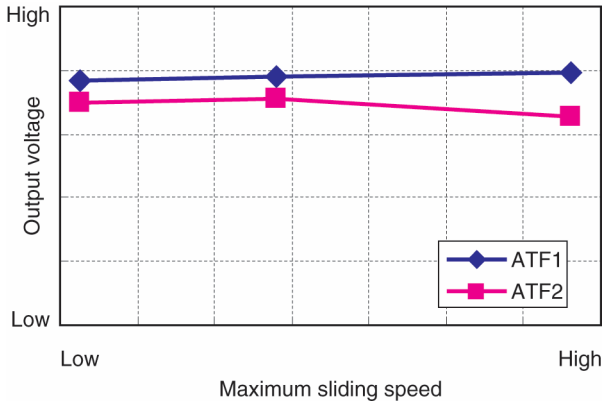


Fig. 14 Relationship between oil film conditions and maximum sliding speed

Figure 13 shows the results of oil film measurements with changes in contact pressure. Both the ATFs maintained stable film characteristics at low and medium contact pressures, but at high contact pressures ATF1 recorded a higher separated voltage as pressure increased; indicating superior maintenance of the film. Figure 14 shows the results of measurements with changes in relative velocity. As relative velocity increases ATF1 maintains fixed characteristics, but ATF2 shows a slight performance decline.

5.2. Elements and Rings

As shown in Fig. 15, a mesh is applied to the inner surface of the rings. The shape of the mesh has an effect on the lubrication performance of the rings.

Figure 16 shows changes in the condition of the oil film with changes in the contact ratio of the mesh. These results demonstrate that a superior oil film is achieved with a lower contact ratio. The shape of the mesh was optimized on this basis.

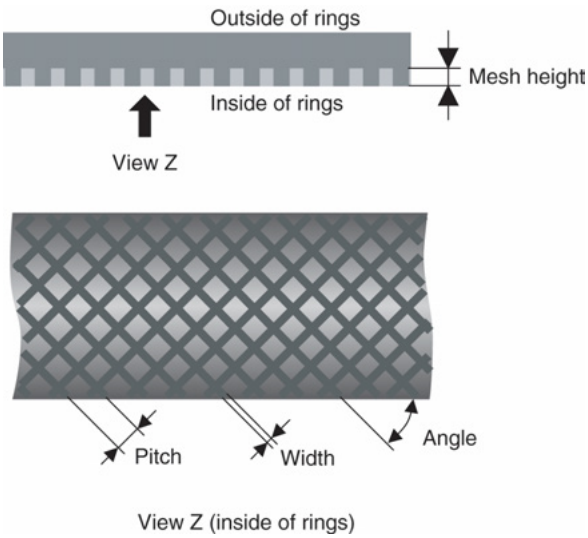


Fig. 15 Configuration of ring mesh

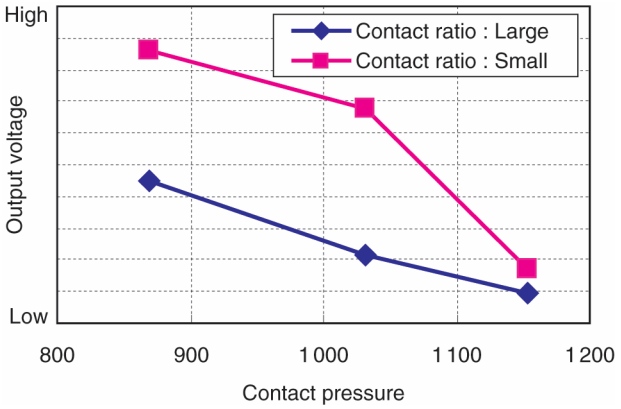


Fig. 16 Oil film conditions at differences of contact ratio

6. Cost Reduction

Increasing the size of the rings should necessarily increase costs, but cost reductions have been achieved by applying a new method to produce the ring edge.

6.1. Method of Polishing Ring Edge

The rounded form shown in Fig. 17 is desirable for the ring edge to reduce the load generated when the side of the element neck makes contact with the pulley V-surface.

The ring edge was previously formed by using a grindstone to cut a drum-shaped cylinder of metal into rings of a set size and then barrel polishing the rings, as shown in Fig. 18. The increased diameter of the rings required in a metal pushing V-belt for a 2L class CVT would lengthen the time required for processing, hence increasing costs.

A new manufacturing method using a plastic brush treated with abrasive powder was therefore developed to reduce the time required for manufacturing.

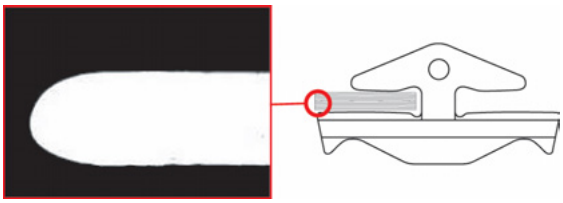


Fig. 17 Profile of ring edge

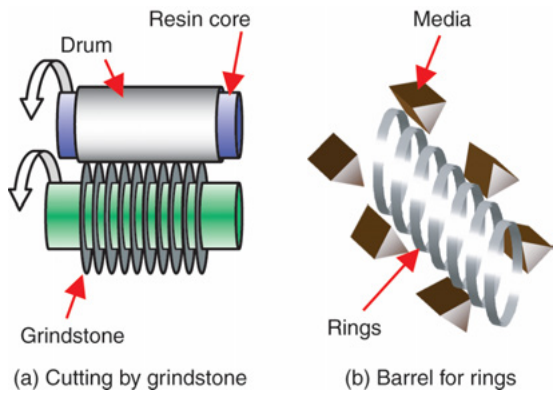


Fig. 18 Manufacturing method of former rings

Figure 19 shows a diagram of the new method employing the brush. After cutting, the rings are clamped to a turntable which rotates automatically. The brush, attached to a brush head, also rotates, polishing the ring edges. This new manufacturing method has significantly reduced costs over the previous method.

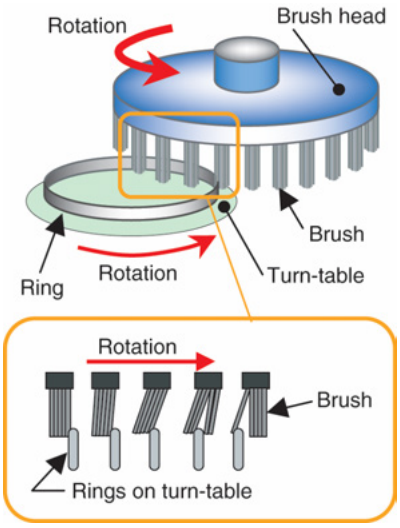


Fig. 19 Ring edge brushing method

7. Verification of Fatigue Strength

7.1. Elements

7.1.1. Element ear

Unit damage tests and damage tests in a functioning CVT were carried out on the element ears to verify the results of the dynamic analysis of the elements. These tests demonstrated the effectiveness of the compound radius shape.

Figure 20 shows the form and fracture face of a fracture occurring in an element during durability test in a functioning CVT. The fracture can be judged as occurring due to forces input from the lower part of the ear, which corresponds well with the results of dynamic analyses.

Figure 21 shows the results of unit strength tests for the element ears. The arrows in the figure represent elements in which no fracture occurred during the cycle concerned. The tests confirmed the greater strength of the compound radius shape than the simple radius shape, and verified that they demonstrated the required safety factor with respect to the loads occurring in a functioning CVT.

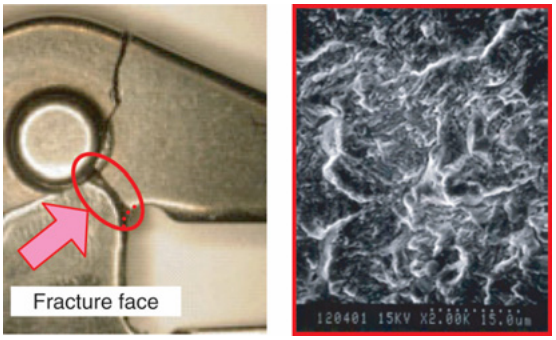


Fig. 20 Damaged element and SEM photograph of fracture face

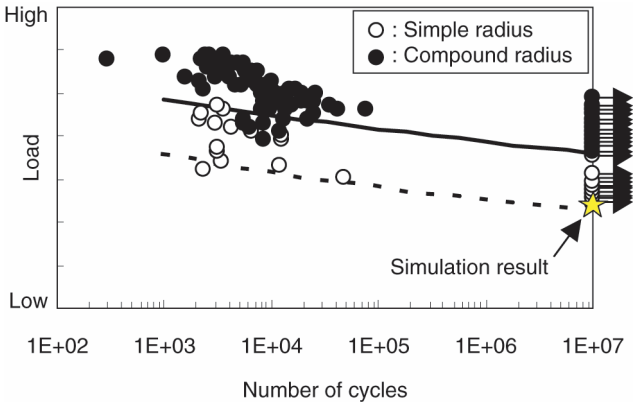


Fig. 21 Comparison of fatigue behavior in simple radius element and compound radius element

7.1.2. Giga-cycle fatigue strength of element materials[5]

To the present, unit strength tests on elements have not been conducted past 10^7 cycles on the premise that a fatigue limit exists. Ultrasonic fatigue tests were conducted on element materials to verify the existence of this fatigue limit. Figure 22 shows the results of giga-cycle fatigue tests. In these tests the element material did not fracture from inclusions at high cycles, but fractures always originated at the surface. These results verified the existence of a fatigue limit for the element materials. Figure 23 shows an outline of the equipment employed in the ultrasonic fatigue tests. A piezo electric element is used as the excitation source, and the test piece resonates as the amplitude of vibration is increased.

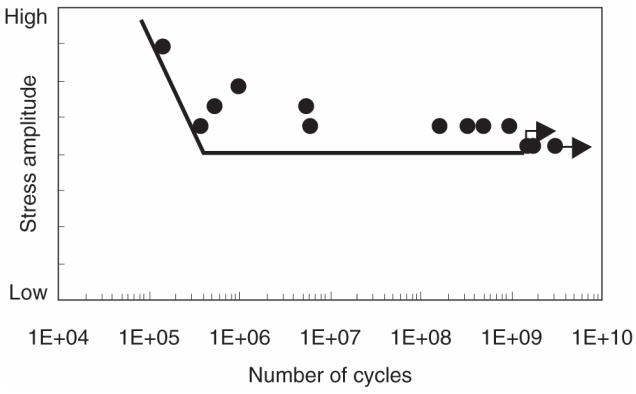


Fig. 22 S-N diagram by ultrasonic fatigue test

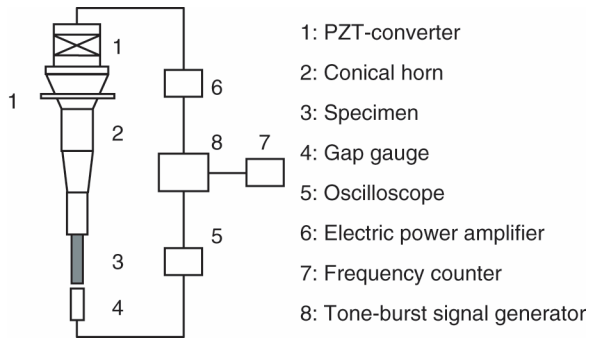


Fig. 23 Block diagram of ultrasonic fatigue test

7.2. Ring

Ring fatigue tests were conducted to determine whether the new manufacturing method for the ring edges had any effect on durability.

Figure 24 shows the results of unit fatigue tests on the rings. The results show that there is no difference in strength between rings produced using the previous method and the new method.

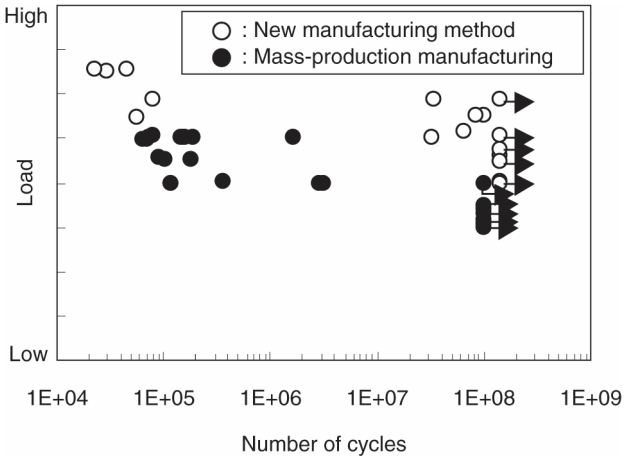


Fig. 24 Comparison of fatigue behavior in rings produced by mass production method and new manufacturing method

8. Maximum Transmitted Power

The reduced minimum pitch distance of the belt resulting from the reduction of the distance between the shafts necessitated high durability in the metal pushing belt. Figure 25 shows the maximum transmitted power of the CVT based on the results of durability tests. The development project conducted for the 2L class CVT metal pushing belt has succeeded in increasing the power of the CVT while making the unit more compact.

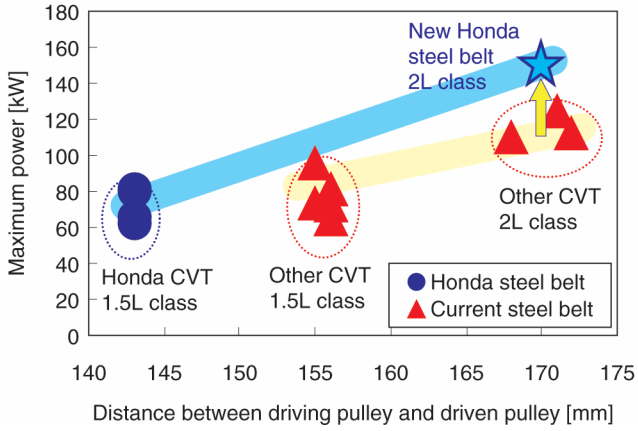


Fig. 25 Potential of newly developed V-belt

9. Conclusion

The following are the most significant details of the development project for a 2.0L class CVT metal pushing V-belt:

(1) Dynamic analysis of the metal pushing V-belt showed that the contact between the lower section of the element ear and the laminated rings at the exit of the driven pulley generates significant stress on the corner of the lower section of the ear.

(2) Application of a compound radius shape for the corner of the lower section of the element ear reduced the stress on the ear with no increase in weight.

(3) Tests showed that at high cycles inclusions in the element material did not affect the durability of the element, and confirmed the existence of a fatigue limit.

(4) Evaluation of ATF extreme-pressure oil films using measurements of electrical resistance clarified the effect of differences in the composition of the ATF fluid and the mesh ratio, and enabled the optimization of the form of the mesh.

(5) The employment of a new manufacturing method which uses a plastic brush treated with abrasive powder to form the edges of the rings has enabled production costs to be reduced while maintaining an equivalent level of strength and durability to that of rings produced by the previous method.

Items (1)-(5) above have enabled the minimum pitch radius of the metal belt to be reduced; thus, increasing the compactness of the CVT. In the future the authors wish to pursue further evolutions with more theoretical investigation of the forms of the components of the belts and the development of groundbreaking manufacturing technologies.

References

(1) Yagasaki, T., Aoyama, H., Toshihiro, S., Ishii, K., Okada, Y., Arikawa, M.: Development of Metal Pushing V-Belt for Continuously Variable Transmission, Honda R&D Technical Review, Vol. 14, No. 1, p. 181-190

(2) Ishii, H., Yagasaki, T., Akagi, H.: Evaluation of giga-cycle fatigue properties of some maraging steels by intermittent ultrasonic fatigue testing, Proceedings of the International Conference on Fatigue in the Very High Cycle Regime, p. 89-96 (2001)

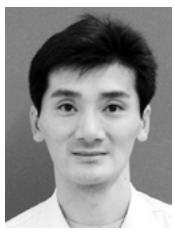
(3) Evaluation method for inclusions in maraging steel, Japan Patent P3345367

(4) Process for producing maragingsteel, United States Patent US 6, 309, 474 B1

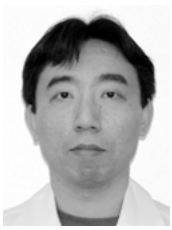
(5) Yagasaki, T., Kanehara, S.: Development of Metal Pushing V-belt for Continuously Variable Transmission, FISITA 2004 World Automotive Congress Barcelona, F2004F384 (2004)

■ Authors ■


Tooru YAGASAKI


Hideaki AOYAMA


Motonori OHNUKI


Yoshinari OKADA


Ryuhei KATAOKA

Optimization Method for Reduction of Transmission Housing Weight

Yuji OGATA* Satoru SUZUKI* Yasutomo IIJIMA*

ABSTRACT

An optimization method has been developed as a tool to contribute to the design of lightweight and high-rigidity automotive transmission housings. The method is divided into topology optimization and shape optimization and can be applied at any of three different stages depending on the maturity of the design. The application of topology optimization from the framework conception stage in the design of an actual automotive transmission enabled rigidity targets to be met with a reduction in weight of 10%. Study of the generation of stress in the optimized shapes predicted by the method indicated that the placement of ribs along the paths of transmission of bearing load to increase rigidity was highly efficient.

1. Introduction

Due to recent heightened concerns toward protection of the global environment and conservation of resources, demands are mounting to reduce weight and size in the development of automotive transmissions.

The transmission housing accounts for a high proportion of the overall transmission weight, and as such is a part with great need of weight reduction.

The housing rigidity and strength could be predicted in the design stage using conventional analysis technology[(1)], but the input load transmission routes are complex and there are many design parameters that must be taken into account, so the calculation model size increased and prediction calculations took time. Therefore, numerous designs had to be investigated separately during the short development period, which made it difficult to obtain a shape that satisfied the weight reduction targets.

The topology optimization functions of commercially available finite element analysis applications are nearing the practical level that would enable application to obtaining lightweight product shapes. However, while there have been reports of topology optimization theory[(2) - (5)] and application to simple shapes such as beam shapes[(6)] and pressed parts[(7), (8)], there are no cases yet of application to complex shapes such as transmission housings.

Therefore, this research applied both topology optimization and shape optimization methods to transmission housing design, and realized a reduction in weight while still taking into account rigidity. These details are reported below.

2. Method of Setting Conditions for Application of Topology Optimization to Transmission Housings

When applying topology optimization, it is necessary to set the load conditions, limiting conditions (design parameter tolerance range), and the optimization subject space.

Methods of setting the conditions for applying topology optimization to transmission housings were investigated for these three items.

2.1. Load Setting Method

The engine torque is transmitted as a load (hereafter, bearing load) through the gears and shaft to the bearings that support these parts and then to the housing.

* Tochigi R&D Center

In the topology optimization calculations, it is extremely difficult to calculate the bearing load in a practical time by modeling all parts that transmit the engine torque and creating a calculation model that also takes into account torque transmission due to gear teeth contact.

Therefore, the newly developed method created two-dimensional elastic elements in the direction of the bearing load, and set the load at the bearing center-point which is the terminus of these two-dimensional elastic elements. (Fig. 1)

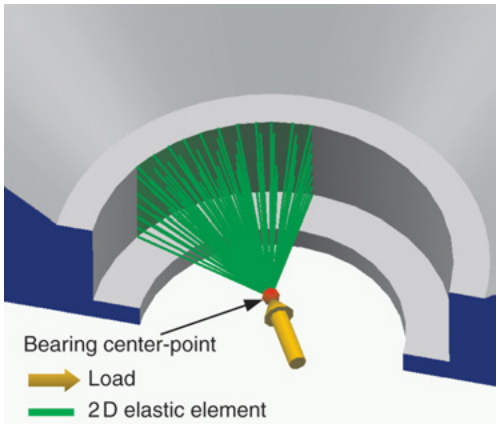


Fig. 1 Definition of load

2.2. Limiting Condition Setting Method

When evaluating the housing rigidity, it is important to determine the degree of bearing center-point displacement caused by the bearing load from the no-load condition[(1)].

Therefore, keeping bearing center-point displacement within a certain target value was set as a limiting condition. (Fig. 2)

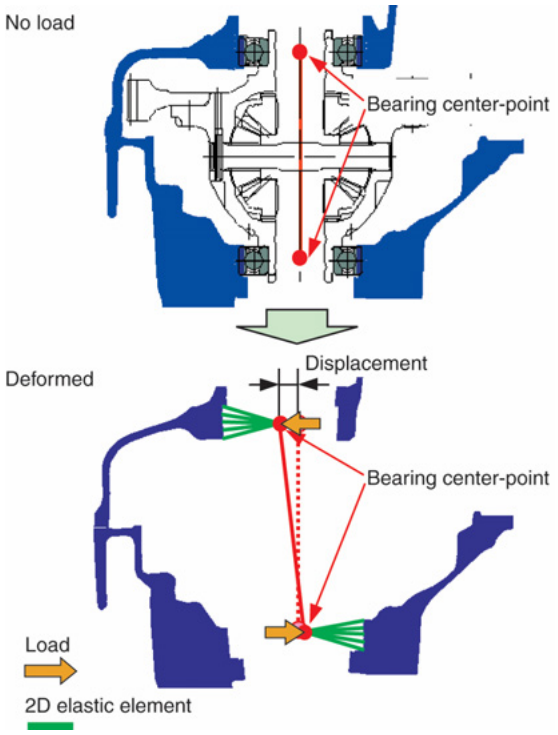


Fig. 2 Displacement of bearing center-point as limiting condition for design responses

2.3. Optimization Subject Space Setting Method

If the design space that is the subject of optimization has a large spatial volume to be set, the number of meshes increases. These calculations may not be possible due to the limitations of current computer resources, so the space to be set must be narrowed down to some extent.

The stress produced on the transmission housing by the bearing load is not uniform, and has local concentrations. Therefore, static analysis was performed and the design space was set (Fig. 5) with the focus on portions where high stress is produced (Fig. 3) and portions with high displacement (Fig. 4).

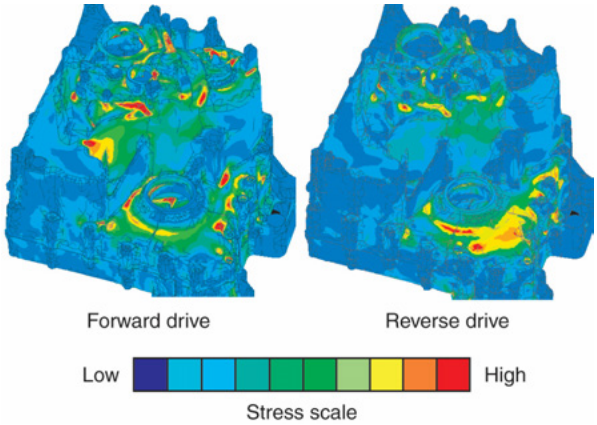


Fig. 3 Example of static analysis : stress

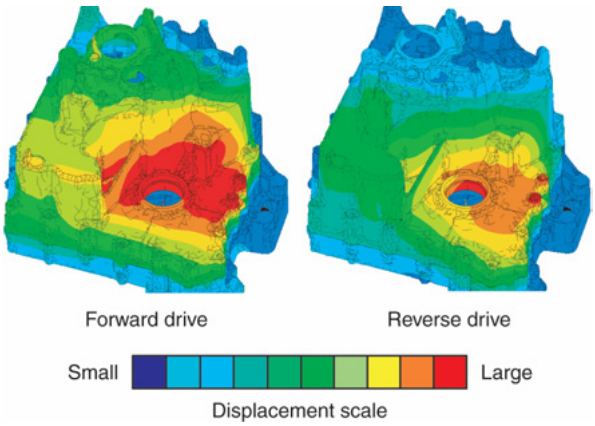


Fig. 4 Example of static analysis : displacement

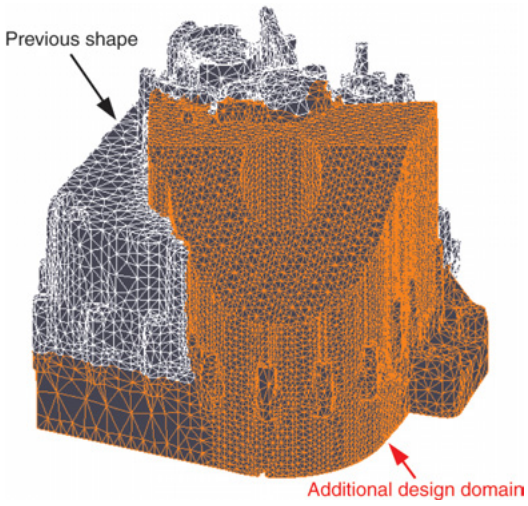


Fig. 5 Defining design domain

3. Method of Applying Optimization to Transmission Housings

3.1. Housing Design Process Using Optimization

In the early design stages there is generally a high degree of usable space freedom, and this degree of space freedom then decreases thereafter as the specifications mature. This means that the weight reduction effects of optimization are higher in the early design stages and lower in later design stages.

Therefore, a design process is needed to determine the most appropriate optimization method according to the maturity of the design. Design stages were classified into the following three stages, and optimization methods were investigated for each stage.

(1) The framework concept stage with a high degree of freedom during early development
(2) The stage where investigating the housing external rib shapes
(3) The stage where only minor modifications are made to the rib thickness and height, etc.

3.1.1. Topology optimization in the framework concept stage

This is the shaft placement, main section and housing joint surface layout stage. In this stage the stiffeners needed to withstand the bearing load (Fig. 7) could be predicted by setting the maximum usable space as the design domain that is the subject of optimization (Fig. 6), and applying topology optimization.

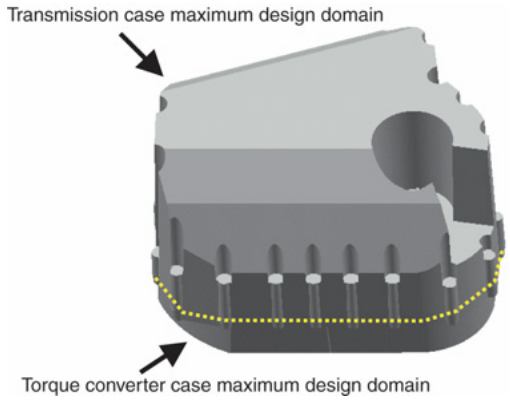


Fig. 6 Maximum design domain in early design stage

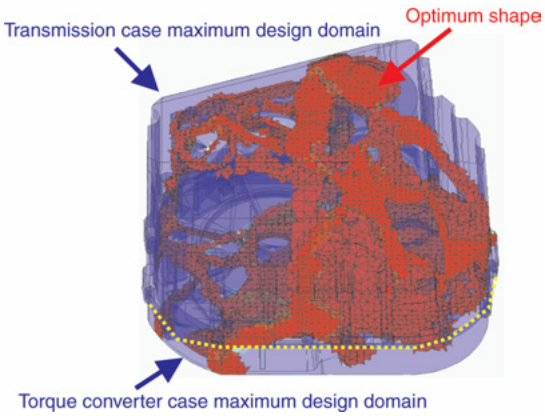


Fig. 7 Result of topology optimization using maximum design domain

In the framework concept stage, the gears, shaft, oil pressure control unit and other internal parts are designed in parallel with the housing layout work, so the housing internal layout is matured to allow effective use of the stiffeners predicted by topology optimization.

3.1.2. Topology optimization for investigating the housing external rib shapes

In the stage where the internal parts layout has been for the most part established, the main design work is to investigate the housing external rib shapes.

In this stage, as mentioned in section 2, attention was focused on the stress and displacement conditions, and the space that avoids interference between the frame and mounting brackets inside the engine room and other items outside the housing was set as the design domain for applying topology optimization. At this time modeling was performed with the housing internal wall shape as a non-design domain that was not subject to optimization in order to consider the stiffness of the walls (the fixed thickness portion that covers the entire housing to seal in the lubricating oil). (Fig. 8) In addition, transmission housings are manufactured using the die casting process, so the draw direction was also specified.

This made it possible to predict the rib shapes that can be applied to the 3D drawing (three-dimensional model used to create the official drawings). (Fig. 9)

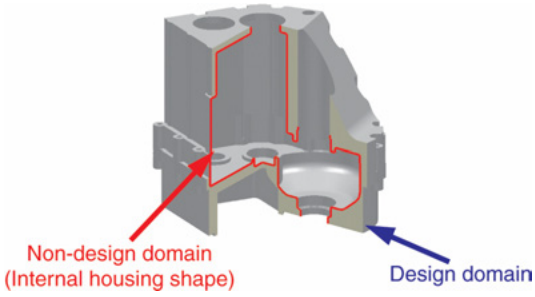


Fig. 8 Defining domain in external housing rib shape optimization phase

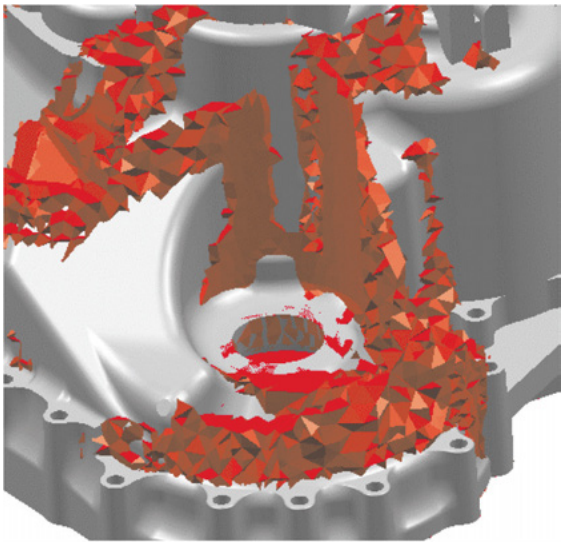


Fig. 9 3D drawing with optimum shape

3.1.3. Shape optimization when making minor modifications to the rib thickness and height, etc.

The shape predicted by topology optimization is displayed using meshes as the minimum unit. Given the limitations of current computer resources, it is necessary to create mesh of a certain size or larger. This means that topology optimization cannot predict a smooth shape (Fig. 9), which makes it difficult to accurately reflect the shape to the 3D drawing.

When performing weight reduction in stages with a high design maturity, the main design work consists of making minor modifications to the rib thickness and height, etc. For this reason, the shape predicted by optimization must have high dimensional accuracy. Therefore, shape optimization was applied to predict the optimum shape by morphing the mesh. The obtained results are expressed as the amount of change in the dimension values, which made it possible to accurately reflect the shape to the 3D drawing. (Fig. 10)

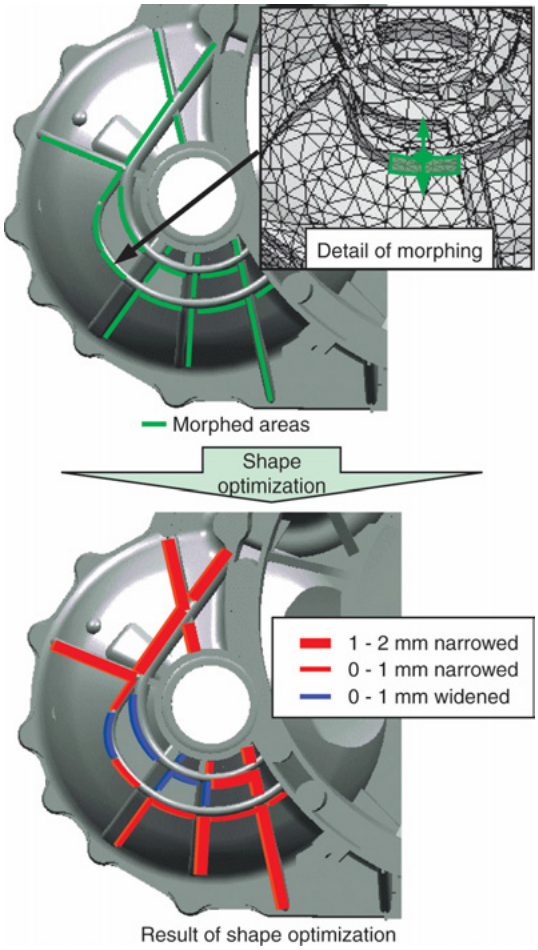


Fig. 10 Morphing and result of shape optimization

4. Application Effects

4.1. Confirmation of Weight Reduction Effects and Verification of Rigidity

The newly developed method was applied to a horizontal automatic transmission in order to reduce the weight.

Topology optimization was applied from the housing framework concept stage, and resulted in a 10% reduction in weight when the most efficient stiffener layout space could be obtained.

In addition, the weight reduction effects were also confirmed to decrease in later development stages with a low degree of design freedom when optimization was applied from the housing external rib shape definition stage to the rib thickness and height modification stage. (Fig. 11)

In addition, the displacement amount of the bearing center-point was calculated for four different types of transmission housings using analysis technology that takes into account housing joint surface contact and friction[1] in order to verify the stiffness of the shape predicted by optimization. These results are shown in Fig. 12, and confirm that the stiffness is the same as the shapes before applying optimization.

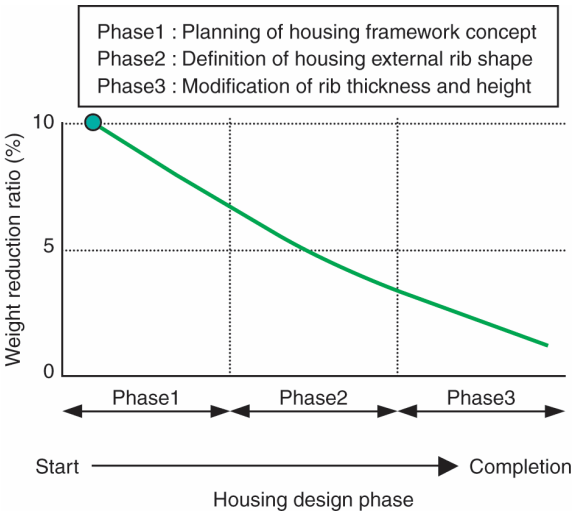


Fig. 11 Reduction of housing weight by optimization

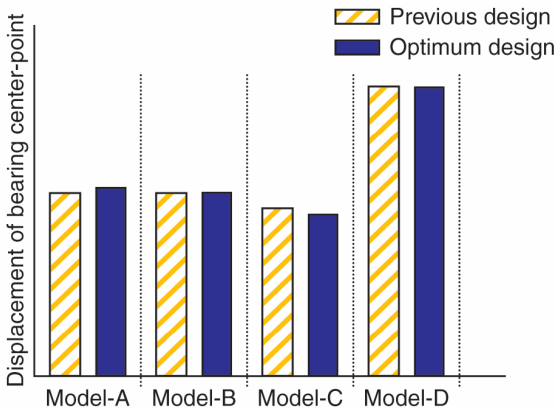


Fig. 12 Example of stiffness calculation

4.2. Study of Optimized Shapes

Static analysis was performed on the shapes before and after optimization and the stress distributions were calculated to confirm whether the shapes predicted by optimization were efficient with regards to the bearing load transmission routes.

The differential bearing load is dominant for overall transmission deformation[1], so the shape of the housing part that supports the differential bearing was studied.

Figure 13 shows that stress generation along the ribs is not uniform for the transmission case shape before optimization, indicating that this is not an efficient shape.

In contrast to this, stress is generated evenly along the ribs for the optimized shape, thus confirming that the stiffeners have been efficiently designed along the bearing load transmission routes.

In addition, Fig. 14 shows that stress generation is also not uniform for the torque-converter case shape before optimization, and that there are some portions that are not functioning as stiffeners.

In contrast to this, stress is generated along the ribs and there is low stress on the walls for the optimized shape, thus confirming that this is an efficient shape.

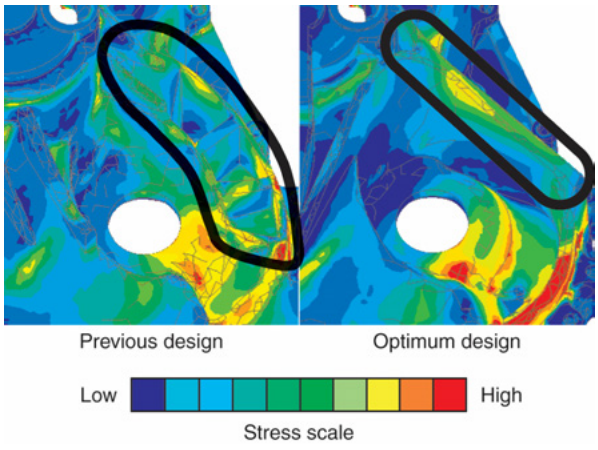


Fig. 13 Example of static analysis of transmission case

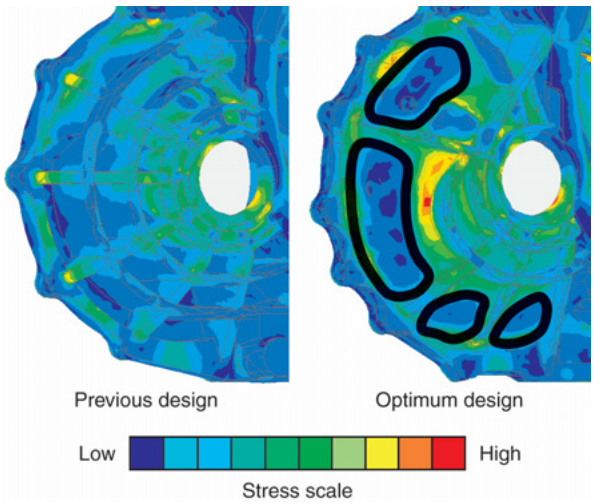


Fig. 14 Example of static analysis of torque converter case

5. Conclusion

Topology optimization and shape optimization methods were applied to transmission housing design, and the following results were obtained.

(1) The stages for applying optimization were classified into three stages according to the maturity of the design, and a design method that makes selective use of topology optimization and shape optimization methods as appropriate was established in order to design lightweight and high-rigidity automotive transmission housings.

(2) Applying topology optimization from the housing framework concept stage resulted in a 10% reduction in weight while still meeting the target rigidity values.

(3) Shapes predicted by optimization were studied from the viewpoint of the stress generation conditions, and it was confirmed that the ribs placed as stiffeners along the bearing load transmission routes were efficiently designed.

References

(1) Hiraoka, M., Tomita, K., Suzuki, S., Iijima, Y., Sasahara, C.: Development of Stiffness Analysis Technology for Transmission Housing, Honda R&D Technical Review, Vol. 14, No. 2, p. 115-122

(2) Fujii, D., Suzuki, K., Ohtsubo, H.: Topology optimization of structures using the voxel finite element method, Transactions of JSCES, Paper No. 20000010

(3) Nakanishi, Y.: Structual Optimization under Topological Constraint Represented by Homology Groups, Japan Society of Mechanical Engineers, (Vol. A) Vol. 69, No. 687, p. 86-92 (2003)

(4) Kim, W, Y., Nakahara, T., Okuma, M.: An Evolutionary Optimization Method for Designing the Three-Dimensional Structures, Transactions of JSCES, Paper No. 20020019

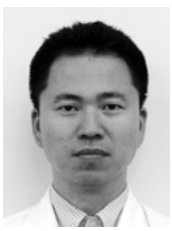
(5) Yuge, Y., Ejima, S., Abe, J.: Design of Structural for Crashworthiness Using Three Dimensional Topology Optimization, Japan Society of Mechanical Engineers, (Vol. A) Vol. 69, No. 687, p. 93-100 (2003)

(6) Nishiwaki, S.: Structural Optimization Based on Discrete Elements, R&D Review of Toyota CRDL, Vol. 37, No. 1, p. 17-24 (2002)

(7) Hayakawa, K.: Status and Future of Computer Simulation, DENSO Technical Review, Vol. 5, No.1, p. 9-15 (2000)

(8) Yoshimura, M., Nishiwaki, S., Izui, K.: A Cross-sectional Shape Initial Design Method for Automotive Frame Structure Using Generi Algorithms, Japan Society of Mechanical Engineers, (Vol. C) Vol. 70, No. 689, p. 235-242 (2004)

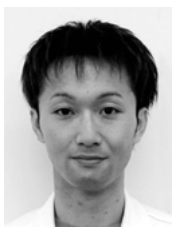
■ Authors ■



Yuji OGATA



Satoru SUZUKI



Yasutomo IIJIMA

Development of Side Curtain Airbags with Rollover Sensor

Naotoshi TAKEMURA* Osamu TAKAHATA*
Shigeo TOBARU* Yoshimasa EGUCHI*

ABSTRACT

Fatalities in rollover accidents have recently been increasing in the US. In particular, 60% of fatalities in SUVs are related to rollover accidents. In addition, 62% of occupants who die in rollover accidents involving all passenger vehicles are either partially or completely ejected from the vehicle. To help address this issue, a side curtain airbag system has been developed that enhances occupant safety in rollover accidents. When a rollover sensor detects the possibility of the vehicle rolling, the side curtain airbags are deployed, covering the greater part of the side windows and thus reducing the possibility of occupant ejection.

1. Introduction

1.1. Rollover Accidents

In the U.S., fatalities that occurred in rollover accidents are on the increase. The total number of fatalities that occurred in rollover accidents in 2002 for all passenger vehicles including light truck vehicles (LTV) such as sports utility vehicles (SUV), pickup trucks and vans, and passenger cars was 10 626, which is an increase of 4.9% compared to 2001. In regard to SUVs, the number of rollover accidents increased by 9.8% (Fig. 1).

The proportion of accidents involving bodily injuries occurring in rollover accidents was about 5% each in the case of passenger cars and vans, and about 10% and 13% for pickup trucks and SUV, respectively. The proportion of accidents involving fatalities occurring in rollover accidents was 24% for passenger cars, 33% for vans, 46% for pickup trucks, and 61% for SUV (Fig. 2)[(1) - (3)].

The fatalities that occurred during rollover accidents for all passenger vehicles were primarily caused by the occupants being ejected from the vehicle. While the wearing of seat belts is the most effective method of helping prevent occupants from being ejected from a vehicle, the National Highway Traffic Safety Administration (NHTSA) of the U.S. Department of Transportation, in 1988, also commenced research into ways of improving the side window glass, such as by using laminate glazing called Advanced Glazing, to help reduce the incidence of occupant ejection. However, rulemaking was abandoned in 2002 partly owing to design restrictions, and instead research and development pertaining to an overall evaluation of the ejection mitigation performance of Advanced Glazing and side curtain airbags were commenced[(4) - (6)].

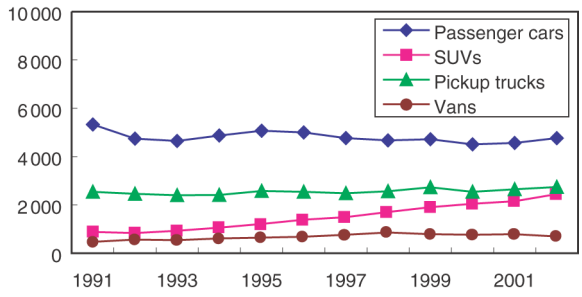


Fig. 1 Occupant fatalities in rollover accidents by year and type of vehicle

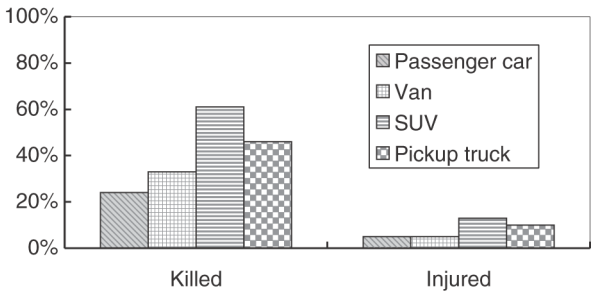


Fig. 2 Percentage of fatalities and injuries in rollover accidents by type of vehicle

* Tochigi R&D Center

Table 1 Seat belt use and vehicle ejection in rollover fatalities

	Not ejected	Totally ejected	Partially ejected	Total
Belt used	14272	771	1382	16425
Belt not used	22089	49017	9328	80434
Total	36361	49788	10710	96859

Source: FARS 1991-2001

1.2. Ejection from a Vehicle Due to a Rollover Accident

62% of occupants who die in a rollover accident for all passenger vehicles are either partially or completely ejected from the vehicle. In fatal rollover accidents for all passenger vehicles in which the occupant was not wearing a seat belt, 73% of the unbelted occupants were either partially or completely ejected from the vehicle. Also, 83% of occupants killed in rollover accidents for all passenger vehicles were not wearing a seat belt. On the other hand, in fatal rollover accidents for all passenger vehicles in which the occupant was wearing a seat belt, only 13% of the belted occupants were ejected from the vehicle (Table 1).

Reportedly, in most cases in which an occupant wearing a seat belt was ejected from the vehicle in a rollover accident, the occupant was ejected through the side window glass. Also, at least half of the occupants who were not wearing seat belts were ejected through the side window glass (Fig. 3).

Regarding the probability of injury in a rollover according to the Abbreviate Injury Scale (AIS) classification, when the occupant remained in the vehicle the occupant was either uninjured or sustained only minor injuries in 71% of the rollover accidents, and sustained serious injuries or worse in 13% of the rollover accidents. In contrast, when the occupant was either partially or completely ejected, and the injury probability distribution was the same, the occupant was either uninjured or sustained only minor injuries in about 30% of the rollover accidents, and sustained serious injuries or worse in about 50% of the rollover accidents (Fig. 4).

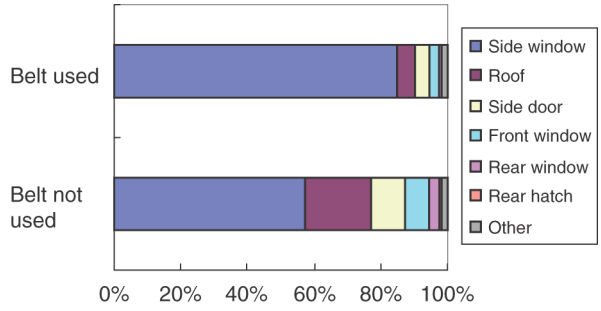


Fig. 3 Ejection path of occupant
Source: NASS CDS 1993-2001

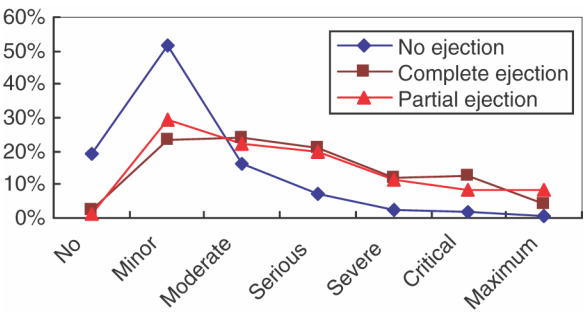


Fig. 4 Likelihood of injury in rollover by AIS Source: NASS/CDS 1988-2001

2. Side Curtain Airbag System

2.1. Side Curtain Airbag

In the conventional side curtain airbag system, when the side impact sensor detects a collision of sufficient magnitude with the side of the vehicle, the side curtain airbag, housed in the roof rail on the inside of the vehicle, deploys to cover the side window as shown in Fig. 5, thus providing protection for the head of the occupants from external objects and the pillars. The system developed here possesses this side impact occupant protection function, and in addition detects the possibility of the vehicle rolling causing the side curtain airbags to deploy as well. In this way, it functions as a supplemental restraint system for the seatbelt, thus helping reduce the possibility of the occupant ejection from the side window of the vehicle and helping increase the possibility of the occupant remaining inside the vehicle.

2.2. Rollover Sensor

A rollover sensor was developed in order to detect the possibility of a rollover of the vehicle and cause the side curtain airbags to deploy. Like the front crash sensor and side impact sensor, the rollover sensor constitutes a sub-system of the airbag control system (Fig. 6).



Fig. 5 Deployed front airbags, side airbag and side curtain airbag

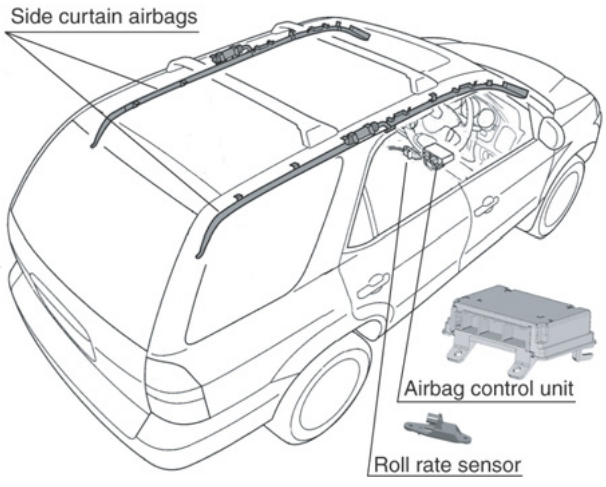


Fig. 6 Layout of side curtain airbags and rollover sensor system

2.2.1. Sensor system configuration

The rollover sensor system consists of an airbag control unit and a roll rate sensor.

The airbag control unit contains one horizontal direction accelerometer and one vertical direction accelerometer (sensors G_y and G_z), a microprocessor, an ignition control circuit, a circuit for communicating with the roll rate sensor, and a power supply circuit.

The roll rate sensor digitizes the analog voltage output from the gyro sensor by means of an analog-to-digital converter (ADC), and sends the resulting data serially to the airbag control unit.

(1) Accelerometer

Acceleration is measured using a Micro Electro-Mechanical System (MEMS) accelerometer made by silicon micro-fabrication, which has excellent impact resistance and reliability and is extremely compact. By utilizing semiconductor manufacturing technology, a fine structure consisting of the sensor element supported by springs is formed on the surface of a silicon chip by etching. The displacement of the sensor element due to acceleration is detected as a change in electrostatic capacitance. An analog signal processing circuit incorporated in the same semiconductor chip outputs a voltage proportional to the acceleration.

(2) Roll angular velocity meter

For measuring the roll angular velocity as well, a MEMS vibration gyro sensor was used, which, like the accelerometer, has excellent impact resistance and reliability, and is extremely compact. This sensor uses the same principle of operation as that of the MEMS accelerometer, and detects the displacement of a resonator due to Coriolis force (Fig. 8). A pair of resonators are driven in opposite phases, and the differential output is used to remove the in-phase acceleration component, permitting accurate measurement of angular velocity even in the case of a large impact due to a collision, for example. The resonator drive circuit and signal processing circuit are also contained in the same chip, realizing a compact gyro sensor (Fig. 9)[7].

(3) Microprocessor

The roll angular velocity and roll angle of the vehicle are computed from the signal output from the roll rate sensor. The analog voltage output from the accelerometer is converted into a digital signal by a built-in ADC.

These signals are processed by a pre-programmed rollover judgment algorithm, and a rollover judgment is made.

In order to raise the system reliability with respect to a breakdown of the roll rate sensor, two independent rollover judgment sections are used, namely a main judgment section that primarily uses the output from the roll rate sensor and a safe judgment section which uses the output from the accelerometer. Each of these sections sends a rollover judgment signal to the ignition control circuit.

(4) Ignition control circuit

When the rollover judgment signals are sent simultaneously from the main judgment section and the safe judgment section in the microprocessor to the ignition control circuit, current flows to the squib (ignition circuit) of the side curtain airbag inflator (gas generator), causing the airbag to deploy.

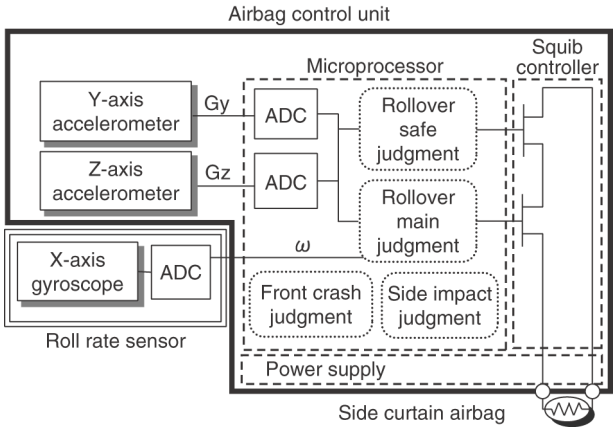


Fig. 7 System diagram of rollover sensor

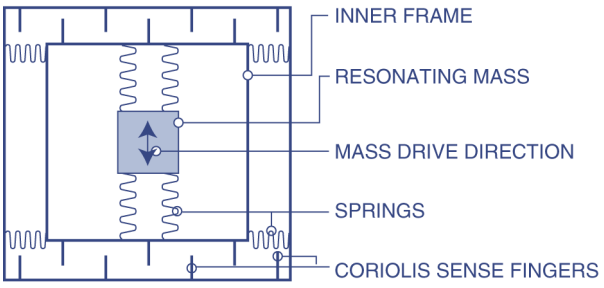


Fig. 8 Schematic of mechanical structure of gyro

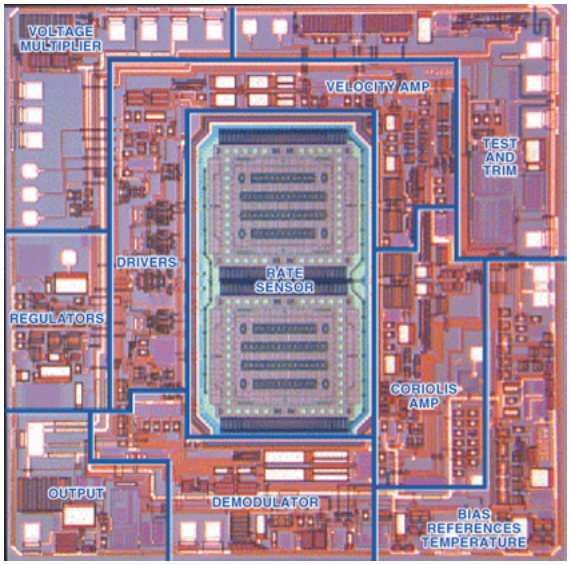


Fig. 9 Photograph of gyro die, highlighting integration of mechanical rate sensor and signal conditioning electronics

2.2.2. Rollover judgment algorithm

(1) Main judgment section algorithm

A rollover is primarily defined as the case where a vehicle tilts at least 90 degrees. When the center of gravity of the vehicle reaches the perpendicular line passing through the center of rotation, that is, the maximum stable angle, the vehicle will roll over under gravity.

Also, if the vehicle has sufficient angular velocity for it to reach the maximum stable angle, it will roll over even without the application of an external force. This dynamic rollover limit is the basis of vehicle rollover judgment.

When the vehicle is considered to be a rigid pendulum as shown in Fig. 10, the dynamic rollover judgment is expressed by Eq. (1). A rollover judgment is made according to whether or not the total rotational energy consisting of the sum of the potential energy $E(\theta)$ and the rotational kinetic energy $E(\omega)$ exceeds the minimum energy (MgR) necessary for reaching the maximum stable angle.

$$E(\theta) + E(\omega) \geq MgR \quad (1)$$
$$E(\theta) = MgR \sin(\theta + \theta o)$$
$$E(\omega) = 1/2 \cdot I\omega^2$$

θo : Initial inclination of C.G.
θ : Roll angle of vehicle
g : Gravity acceleration
R : Rotational radius
I : Inertia moment of O-axis

Figure 11(a) shows the result of expressing Eq. (1) as a graph of ω versus θ. If the threshold is exceeded on the graph, it is judged that there is a high possibility of rollover occurring. Normally, a vehicle rolls over when a sustained external force is generated, causing the rotational energy to increase. For this reason, it is possible to make a rollover judgment more quickly by predicting the increase in rotational energy due to an external force that may conceivably be applied in the future, from the change in angular velocity ($\Delta\omega$) and the deceleration. This is expressed mathematically by Eq. (2). Figure 11(b) shows a 3-dimensional diagrammatic representation of this equation. An actual vehicle differs from a pendulum in that it has a suspension mechanism. Consequently, this was taken into account in the determination of the threshold.

$$E(\omega) + E(\theta) \geq \text{Threshold} - E(\Delta\omega, G_y, G_z) \quad (2)$$

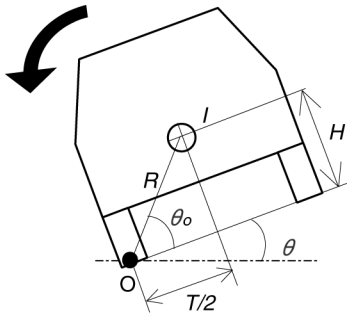


Fig. 10 Vehicle rigid model

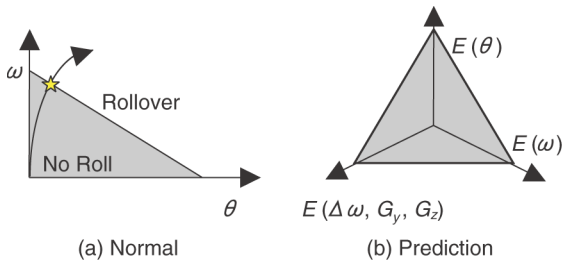


Fig. 11 Rollover main judgement threshold

(2) Safe judgment section algorithm

The safe judgment section of the algorithm uses the values G_y and G_z.

When a rollover phenomenon occurs, abrupt motion occurs in the horizontal or vertical directions in addition to rotary motion, and compared to when the vehicle is running normally, a large acceleration is detected. This is utilized for making a safe judgment.

3. Conclusion

As a supplemental restraint system for the seatbelt, a side curtain airbag system with rollover sensor was developed in order to help increase the occupant safety in rollover accidents.

When the rollover sensor detects a situation that can conceivably lead to the occurrence of vehicle rollover, the side curtain air bags deploy, covering most of the side windows. As a result, the possibility of the occupant ejection from the vehicle is reduced and the possibility of the occupant remaining inside the vehicle is increased.

This system was installed on the 2004 model Acura MDX, and is scheduled to be installed progressively on future models.

Acknowledgments

The authors would like to take this opportunity to thank the persons concerned in Autoliv Inc. and TRW Automotive LLC for their kind cooperation in this development, and also Analog Devices, Inc. for kindly providing photographs and illustration of gyro sensors.

References

(1) National Center for Statistics and Analysis Traffic Safety Facts 2002: A Compilation of Motor Vehicle Crash Data from the Fatality Analysis Reporting System and General Estimates System DOT HS 809 620, p. 80-81

(2) National Center for Statistics and Analysis: Motor Vehicle Traffic Crash Fatality and Injury Estimates for 2002, 2002 Annual Assessment

(3) Deutermann, W.: Characteristics of Fatal Rollover Crashes, Technical Report DOT HS 809 438

(4) Summers, S., Harper C.: Ejection Mitigation Using Advanced Glazing, A Status Report, November 1995, Old Docket Number 95-41-GR

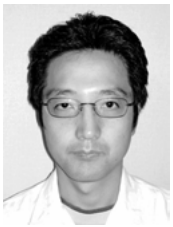
(5) Willke, D., Summers, S., Wang, J., Lee,J., Partyka, S., Duffy, S.: Ejection Mitigation Using Advanced Glazing Status Report II, Docket Number NHTSA-1996-1782-21

(6) Willke, D., Summers, S., Wang, J., Lee, J., Harper, C., Partyka, S., Duffy, S.: Ejection Mitigation Using Advanced Glazing Final Report, Docket Number NHTSA-1996-1782-22

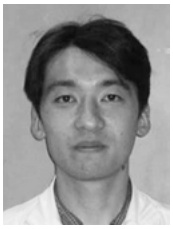
(7) Analog Devices, Inc.: http://www.analog.com/library/analogDialogue/archives/37-03/gyro.html

■ Authors ■


Naotoshi TAKEMURA


Osamu TAKAHATA


Shigeo TOBARU


Yoshimasa EGUCHI

Development of Honda Precrash Safety Technology

Koichi KAMIJI* Kenji KODAKA* Hiroshi AKABA*

ABSTRACT

In the field of collision safety, conspicuous progress has been made in recent years in occupant restraint devices. Collision avoidance and injury mitigation technologies are also developing rapidly. Various proposals have been made for next-generation systems combining collision avoidance technologies with injury mitigation and occupant restraint technologies. This paper introduces a first step in this direction, the Honda precrash safety technology employed in the Inspire.

1. Introduction

In the field of collision safety technology, significant progress has been made in recent years in occupant restraint devices. Collision avoidance and injury mitigation technologies are also evolving rapidly. A variety of proposals have been made for next-generation systems combining collision avoidance technologies with injury mitigation and occupant restraint technologies.

The companies involved in the Advanced Safety Vehicle (ASV) project, conducted since 1991 under the auspices of the Ministry of Land, Infrastructure and Transport, have proposed various collision avoidance systems employing external sensing technologies such as radar, in addition to injury mitigation systems. Collision avoidance systems that help predict a collision with a vehicle ahead by means of external sensors and automatically applied the brakes have been discussed from Phase I of the ASV project, but further maturation of concepts and technologies was necessary before such systems could be put on the market. The Honda Precrash Safety Technology employed in the INSPIRE represents a first step in the direction of practical application of these technologies. This paper discusses the technologies employed in the Collision Mitigation braking System (CMS) and the E-pretensioner System that make up the new Honda system.

* Tochigi R&D Center

2. Background to System Development

A high percentage, amounting to approximately 30%, of traffic accident fatalities are caused by rear-end collisions[1), 2)] (Fig. 1). The majority of these accidents occur at low to medium speeds, and most are caused by inattention,

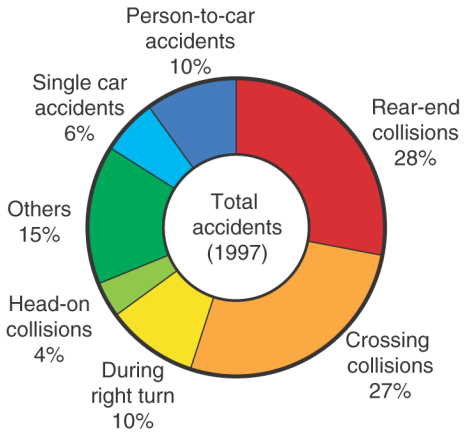


Fig. 1 Breakdown of accident type

especially forward inattention. Approximately 90% of these accidents occur on straight roads. The majority, 87%, are rear-end collisions with a stationary vehicle (Figs. 2-5). The representative scenario is therefore a collision occurring at a low to medium speed on a straight road due to delay in the driver recognizing the presence of a vehicle ahead as a result of looking to the side, etc.

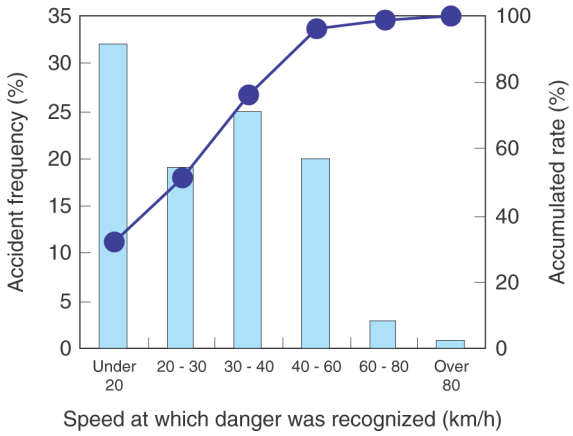


Fig. 2 Frequency of rear-end collisions and accumulated rate in relation to speed at which danger was recognized

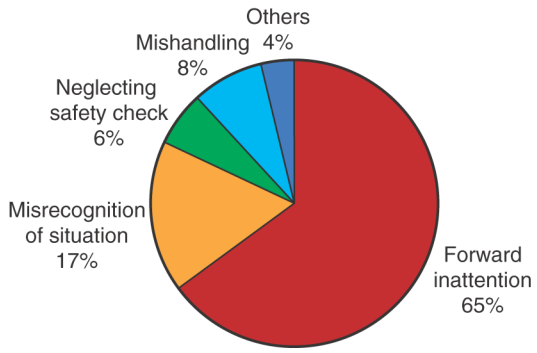


Fig. 3 Cause of rear-end collisions

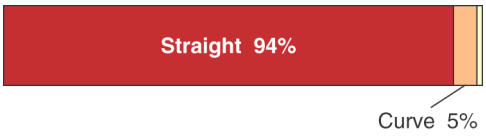


Fig. 4 Road condition at time of accident

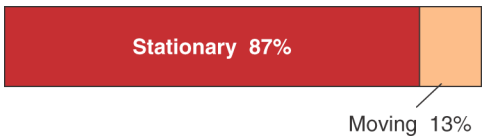


Fig. 5 Status of vehicle ahead at time of accident

3. System Concept and Predicted Effectiveness

The results of studying the conditions in which rear-end collisions occur determined the focus of the research on trying to reduce the number of accidents caused by the driver's inattention. This would be achieved through the creation of a system that supported the driver's maneuvers to help avoid a collision. In this, the role of warnings provided to the driver would be important, and the project therefore studied the effectiveness of the system, the timing of warnings and the driver's reaction time, from the perspective of the relationship between the length of the period of inattention to the road and the occurrence of collisions.

3.1. Study of System Effectiveness from Perspective of Length of Period of Inattention

Simulations were employed to determine the exact nature of driver inattention resulting in rear collisions. The simulations assumed conditions in which the vehicle in front braked when the driver of the following vehicle was momentarily inattentive to the road. Headway time between the vehicles was 1.5 seconds, and the braking speed of the leading vehicle when the driver of the following vehicle was distracted from the road was set at 0.3 G. After the period of momentary inattention the driver of the following vehicle returns their attention to the road, recognizes the situation, makes a judgment, and applies the brakes. The driver's reaction time (from returning attention to the road to applying the brakes) was 1.3 seconds, and the braking speed was 0.8 G. The effect of varying the length of the driver's period of inattention to the road under these conditions was compared.

The results of these simulations are shown in Fig. 6. The horizontal axis shows the speed of the following vehicle and the vertical axis shows the relative velocity at the time of the collision. As the results show, under the conditions of the simulation collisions occur at low to medium speeds, but at high speeds collisions are avoided by the driver's application of the brakes. This indicates that an extended period of inattention to the road is not an often seen factor in the occurrence of rear-end collisions: at low to medium speeds even momentary inattention can result in a collision.

Eye cameras were used to take measurements to determine the length of periods of forward inattention under normal driving conditions. Figure 7 shows the results of these measurements. These results show that normal operations such as using the car stereo or checking the meters require periods of momentary inattention of 1-2 seconds.

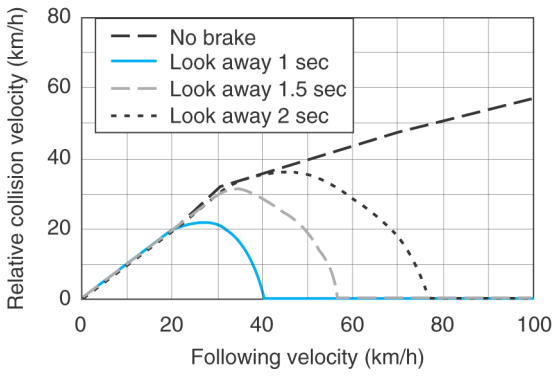


Fig. 6 Simulated collision velocity

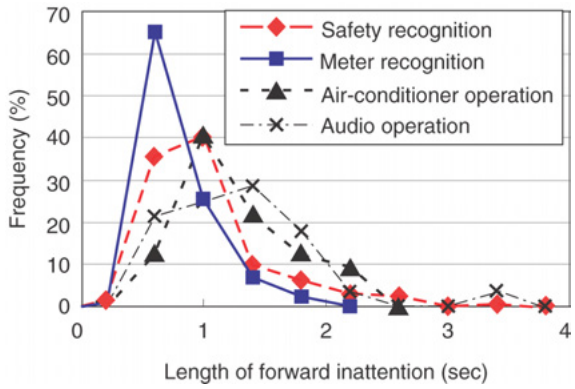


Fig. 7 Length of forward inattention

Simulations were next conducted to compare the effectiveness of the CMS with the provision of warnings only. An average figure of one second from warning to application of the brakes obtained from a driving simulator was employed as the driver's reaction time in the simulations. Braking speed for the automatic emergency application of the brakes was set at 0.6 G. The simulations assumed conditions in which the driver of the leading vehicle applies the brakes at 0.3 G with 1.5 seconds headway time between the vehicles. At this time the system in the subject vehicle goes into operation, and the driver of the vehicle applies the brakes at 0.8 G one second after the warning is provided. The results of these simulations are shown in Fig. 8. The horizontal axis shows the speed of the following vehicle, and the vertical axis shows the relative velocity at the time of collision. The results show that collisions were avoided at low to medium speeds, and the velocity at the time of collision was reduced at high speeds. These results indicate that, while headway and the speed of the following vehicle remain factors, it is possible to help prevent rear-end collisions occurring due to momentary inattention at low to medium speeds.

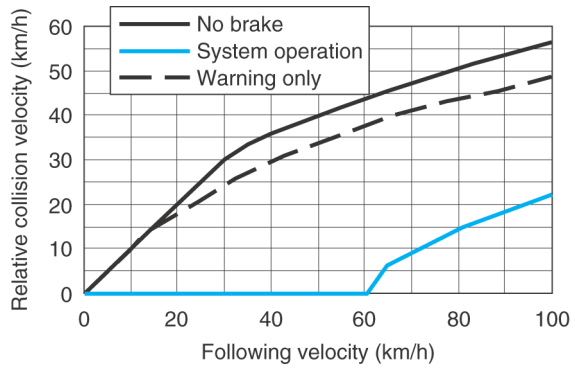


Fig. 8 Effect of CMS system (by simulation)

3.2. Study of Timing of Warnings

A system to support collision avoidance maneuvers that utilizes warnings must provide warnings at a timing enabling the driver to make a judgment and maneuver the vehicle to avoid the accident. A driving simulator was therefore used to study reaction time to warnings. In the tests, reaction times to warnings provided when the vehicle in front braked as the driver of the subject vehicle looked away from the road were measured. Results showed that reaction times of between 0.6 and 1.4 seconds were required. The timing of the provision of warnings would therefore have to take this range of reaction times into account.

However, if the timing of warnings was increased there was a possibility that warnings would be provided when there was no danger of collision, and if the timing was delayed, there was a possibility that there would not be a sufficient margin of time for the driver to make a judgment and commence maneuvers to try to avoid the collision. Therefore, in both cases there was a possibility that warnings would not be sufficiently effective.

3.3. System to Support Collision Avoidance Maneuvers

On the basis of the results of the studies conducted to this stage, the development aim was established as the creation of a system to support the driver's maneuvers to avoid accidents which would be effective in high risk situations but which would not interfere with the operation of the vehicle under normal driving conditions. A system was proposed that, in addition to sounding a buzzer, would automatically apply the brakes and tighten the seatbelts to provide a tactile warning to the driver when there was a high possibility of collision. The concept stressed the timing of warnings to interfere with the driver as little as possible, and the automatic operation of the brakes to compensate for delays in judgment and the commencement of collision avoidance maneuvers. In addition, when a collision was unavoidable, the seatbelts would be automatically tightened before impact to increase their effectiveness.

Honda has termed the braking system which combines these various functions the Collision Mitigation braking System (CMS), and the seatbelt system is termed the E-Pretensioner System.

4. System Configuration

4.1. System Overview

The newly developed system is made up of the CMS and the E-Pretensioner System. Figure 9 shows the system configuration.

The system is made up of a radar unit to monitor vehicles in front, yaw rate and wheel sensors to monitor the status of the subject vehicle, a hydraulic actuator for automatic operation of the brakes, an electric seatbelt retractor to tighten the seatbelts, a warning display and an electronic control unit (ECU).

The radar system employs millimeter-wave radar[3], which functions effectively in a broad range of climatic conditions. This system has a measurement range of approximately 100 m, and is able to detect a vehicle 3 seconds ahead at a relative velocity of 100 km/h. The horizontal detection angle of 16° enables the system to detect vehicles on straight roads and gentle curves.

Figure 10 shows the configuration of the electric seatbelt retractor. In addition to the standard ELR mechanism, this retractor is provided with a pyrotechnic pretensioner and a load limiter. Positioned in parallel to these units are a DC motor and a transmission mechanism to transmit motor torque to the ELR shaft. A clutch mechanism separates the ELR mechanism and the motor torque transmission mechanism when the seatbelt is extended and retracted under normal driving conditions. The electric seatbelt retractor has three operating patterns: warning of approach, retraction control and lock release control.

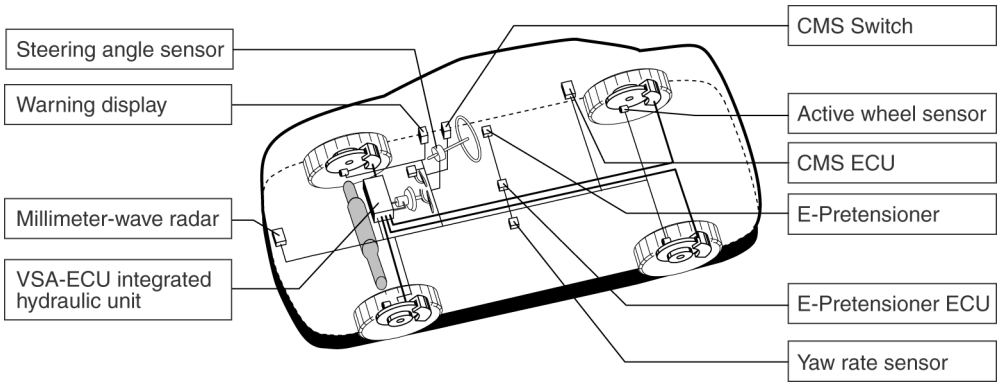


Fig. 9 System configuration

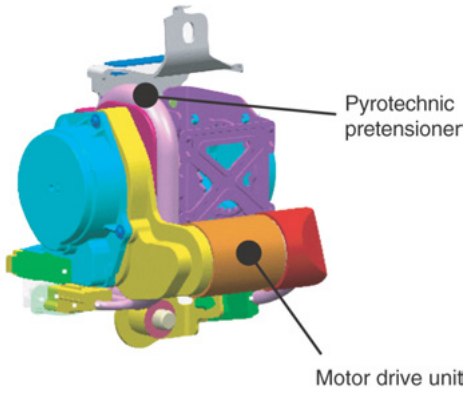


Fig. 10 Retractor with electric pretensioner

Figure 11 shows the basic control flow. A vehicle in front is detected by the radar, and the trajectory of the subject vehicle is estimated from its current status. The system judges the danger of collision and whether or not the collision is avoidable through steering maneuvers. If this is judged difficult, the automatic braking system and the seatbelt retractor go into operation.

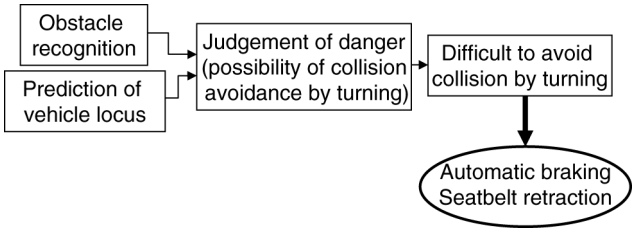
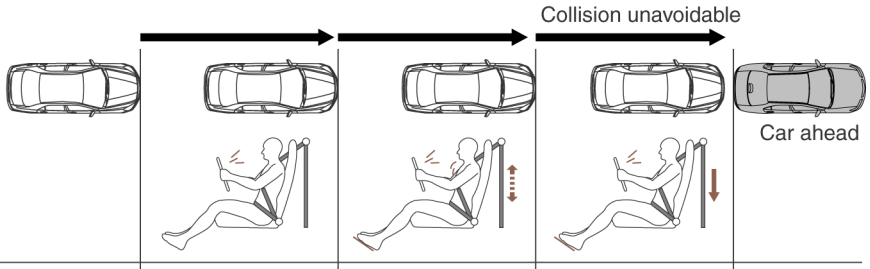


Fig. 11 Block diagram of basic control

4.2. Operating Modes

To ensure that the driver is aware of the warning, in addition to sounding a buzzer, the system lightly applies the brakes and gently retracts the seatbelts to provide a tactile warning. These functions are termed the warning brake and seatbelt warning functions respectively. A braking strength of 0.1-0.2 G was determined from tests as appropriate for the warning brake function. In the case of the seatbelt warning function, tests enabled the establishment of a retraction force and operating pattern that would provide a clear warning to the occupants of the vehicle but which would not interfere with vehicle operation. These functions not only increase the effectiveness of the warnings, but also reduce the delay in the commencement of avoidance maneuvers by the driver.



Audio & visual warnings	Buzzer display	Buzzer display	Buzzer display	
CMS		Light braking	Strong braking	
E-pretensioner		Light seatbelt retraction	Strong seatbelt retraction	

Fig. 12 System operation

The strength of emergency braking was established on the assumption of avoidance of a collision through a combination of braking and steering maneuvers, and with consideration of maneuverability and changes in the driver's posture during automatic application of the brakes. In addition, when the driver applies the brakes, that braking force is added to the automatic emergency braking force. Maximum braking force is therefore produced through a combination of the automatic operation of the system and the driver's application of the brakes.

When emergency braking is applied, the operating pattern for the electric seatbelt retractor switches to approach warning retraction control. In this case also, the retraction force is set at a level which will not interfere with the driver's operation of the vehicle. After a fixed period of time has elapsed from the completion of operation of the three seatbelt retraction modes, if the system judges from the brake signal and vehicle speed data that the retraction can be released, lock release control is engaged. The electric seatbelt retractor operates in response to the radar system, and also in response to emergency braking immediately before collision. The series of operations is shown in Fig. 12.

5. Confirmation of System Functioning in Vehicle Tests

Vehicle tests were conducted to confirm the functioning and effectiveness of the CMS and the E-Pretensioner System.

5.1. CMS

The effectiveness of the CMS in reducing the speed of the vehicle at impact with a stationary forward object was measured in vehicle tests. In these tests an obstacle resembling a vehicle was positioned directly in front of the test vehicle. The test vehicle was driven at the obstacle, and its speed at the time of the collision was measured. Tests were conducted with operation of the CMS and with operation of the warning system only, and results were compared. In both cases, the driver applied the brakes one second after the warning was provided. Figure 13 shows the test results. The horizontal axis shows the relative velocity of the subject vehicle, and the vertical axis shows the velocity at the time of the collision. As Fig. 13 indicates, collision was avoided at low to medium speeds, and the vehicle velocity at impact was reduced at high speeds. As Fig. 2 showed, the majority of rear-end collisions occur at low to medium speeds, and this system can therefore be predicted to be effective in reducing the incidence of these collisions. Despite the fact that the reaction time of the driver in applying the brakes was identical, the speed reduction at impact was lower in tests conducted with a warning only than when the automatic braking system was in operation.

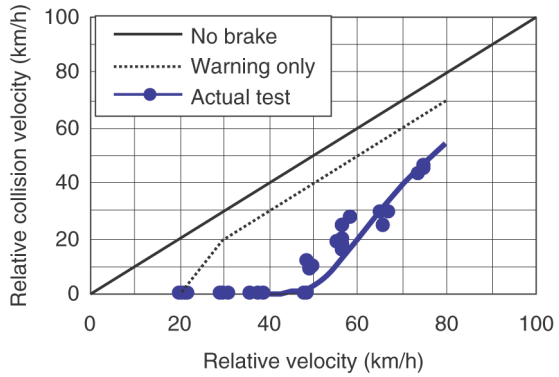


Fig. 13 Effect of CMS system (by actual test)

5.2. E-Pretensioner System

Vehicle tests were also conducted to confirm the effectiveness of the E-Pretensioner System in improving occupant restraint. In these tests the focus was the degree of the forward movement of the vehicle occupants during emergency braking, front barrier crash performance and offset barrier crash performance.

5.2.1. Degree of forward movement during operation of brakes before collision

Vehicle tests were conducted to confirm the effectiveness of the E-Pretensioner System in reducing the degree of the forward movement of the vehicle occupants during emergency braking.

In the tests, emergency braking was applied before collision, and the degree of the forward movement of the vehicle occupants due to deceleration was measured with and without operation of the E-Pretensioner System. Results were compared for occupants of three different sizes (AM 95 percentile, AM 50 percentile and AF 5 percentile) under identical test conditions, as shown in Fig. 14. In all cases, the operation of the E-Pretensioner System reduced the degree of forward motion. This effect is due to the difference in operation between the E-pretensioners and standard seatbelt retractors. In standard seatbelt retractors, the ELR lock mechanism is set to operate at a higher rate of deceleration than that occurring during emergency braking, while the E-pretensioner retracts the seatbelt from the commencement of braking, further reducing slack in the belt.

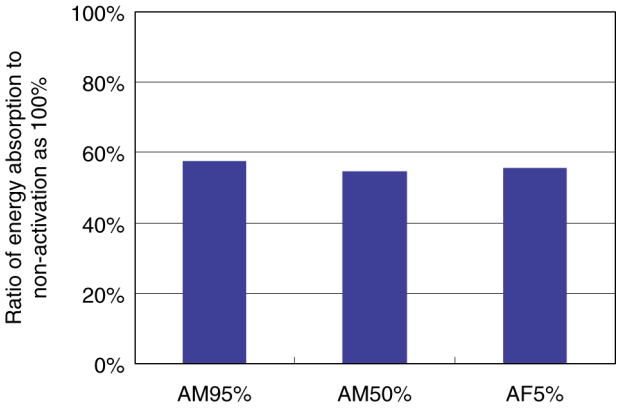


Fig. 14 Comparison of head displacement at 1G braking

5.2.2. Initial restraint performance in front collision

Figure 15 shows the results of the tests of occupant restraint performance with and without operation of the E-Pretensioner System. The tests measured the amount of energy absorbed by AM 50 percentile, AM 95 percentile and AF 5 percentile occupants at the initial stage of a front collision at 55 km/h. Results showed improved initial restraint performance for AM 50 percentile and AF 5 percentile occupants.

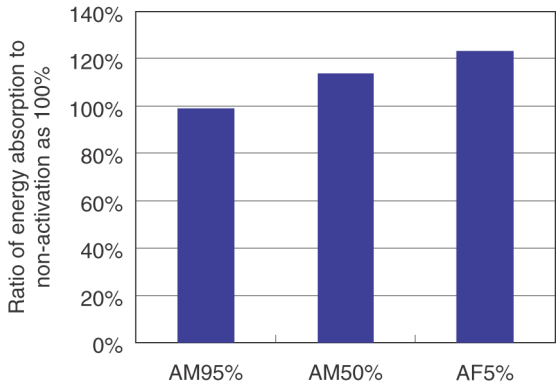


Fig. 15 Comparison of energy absorption in frontal barrier crash

5.2.3. Initial restraint performance in offset barrier crash

Occupant restraint performance with and without the operation of the E-pretensioners was compared at braking speeds corresponding to an offset barrier crash. Tests were carried out under the abovementioned conditions, and the initial energy absorption for an AM 50 percentile occupant were compared. The results of these tests are shown in Fig. 16, and confirm that the operation of the E-pretensioner also improves initial restraint performance in offset barrier crashes.

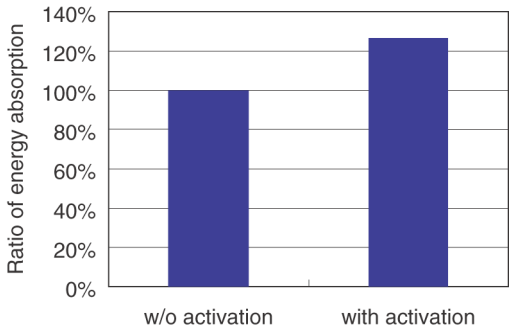


Fig. 16 Comparison of energy absorption in offset barrier crash

6. Conclusion

A Collision Mitigation braking System (CMS) combining external sensing technology employing millimeter-wave radar with automatic braking has been developed. This system will be effective in helping reduce injuries occurring in rear-end collisions. The system has been designed to support the driver's collision avoidance maneuvers while not interfering with the driver's operation of the vehicle.

The CMS can be expected to be effective in helping reduce the number of rear-end collisions occurring at low to medium speeds, at which the majority of these accidents have been shown to occur. This effectiveness has been increased through combination with an E-Pretensioner System that increases occupant restraint performance and provides the driver with tactile warning of an impending collision through the seatbelt.

Honda has combined these technologies and employed them in an actual vehicle as the Honda Precrash Safety System.

References

(1) Institute for Traffic Accident Research and Data Analysis (ITARDA): Traffic statistics 1997

(2) Signal: Signal, No. 296 (1997)

(3) Fujita. Y., et. al.: Radar Brake System, JSAE Congress Proceedings, No. 186, 9437845 (1994)

■ Authors ■



Koichi KAMIJI



Kenji KODAKA



Hiroshi AKABA

Countermeasures against Noise and Vibration in Direct Injection Diesel Engine

Masao HIRUMA* Shigeji NONAKA* Yuji KATOU*
Yoshihiro NOGUCHI* Hajime IGAMI**

ABSTRACT

The newly developed 2.2L 4-cylinder diesel engine for the new ACCORD marketed in Europe employs numerous noise and vibration reduction technologies. 2nd-order vibration balancers and other technologies have been used to reduce engine noise and vibration, and optimization of pilot injection has reduced combustion noise. In addition, a principal axis of inertia type engine mounting system with torque rods has been employed, and soundproof performance of the complete vehicle has been improved.

The new ACCORD using this new engine is powerful yet achieves the high quality cabin sound and low vibration levels, and has been extremely well received in the European market.

1. Introduction

Concerns for environmental issues are growing world wide, but Europe has been especially concerned about global warming. Currently Europe is striving to reduce CO_2 emissions and has developed a large market focused on diesel engines, as they provide high performance.

Now Honda has developed a new turbo charged diesel engine (intelligent- Common Rail Turbocharged Direct injection: hereafter i-CTDi). Figure 1 shows an external view of the engine.

The i-CTDi engine incorporates a variable geometry turbocharger and a DOHC four-valve direct injection system. In order to increase the fuel injection pressure, the latest 1 600-bar common rail control system is applied. Through these applications, both high output power and high fuel economy are achieved, and this engine has conformed to the Euro-IV regulations at an early stage[(1)].

However, the increases in power output and the fuel injection pressure cause more engine vibration and combustion noise which affect the quietness of a vehicle[(2) - (4)].

In order to solve these issues, the focus was given to the following items to develop countermeasures against noise and vibration.

(1) Reduction of engine noise and vibration
(2) Reduction of combustion noise
(3) Improvement of the engine mount system
(4) Improvement in soundproof performance of the vehicle



Fig. 1 External view of i-CTDi engine

* Tochigi R&D Center
** Honda R&D Americas, Inc.

This report discusses the reduction of engine noise and vibration through the application of a 2nd order vibration balancer, the reduction in combustion noise through the optimization of pilot injection, the application of a principal axis of inertia type mounting system with torque rods and improvements in soundproof performance of the vehicle.

2. Reduction of Engine Noise and Vibration

Compared to a gasoline engine, the diesel engine produces increased inertial forces and the combustion-induced vibrations which typically result in high NVH levels of the complete vehicle. The following actions are taken to resolve this issue for the i-CTDi engine.

2.1. 2nd Order Vibration Balancer

Increased inertial forces cause 2nd order vibration to increase, therefore a 2nd order vibration balancer system is employed to reduce 2nd order vibration. The system is driven by the crankshaft using a single strand roller chain which, as shown in Fig. 2, is placed inside of the oil pan. By employing this device, the power plant vibration is reduced, leading to significant reduction of the booming noise level in a cabin.

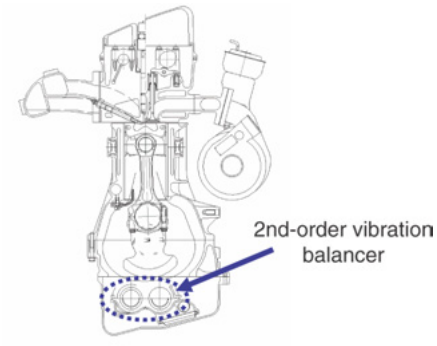


Fig. 2 Cross-section of engine

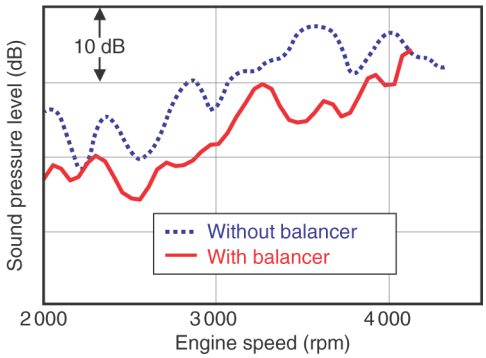


Fig. 3 Cabin booming noise

2.2. Top Acoustic Cover

Since high frequency noise such as high-pressure injector and combustion noise from the common rail system deteriorate a vehicle's marketability considerably, an acoustic cover is employed. As shown in Fig. 4, by optimizing the rib shape of the cover, the placement of the acoustic material, and the attachment points and characteristics of the isolating rubber, the noise level measured above the engine is reduced by 5 dB, as shown in Fig. 5.

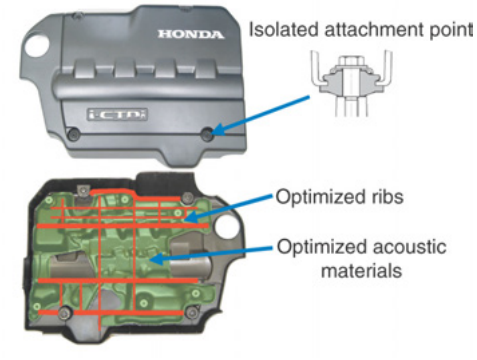


Fig. 4 Engine top acoustic cover

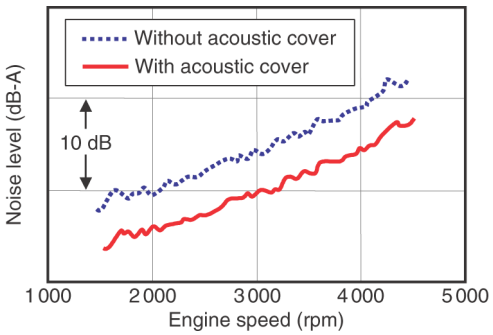


Fig. 5 Engine noise

2.3. Cylinder Block

A closed deck type aluminum block cast with cast iron sleeves is used for the cylinder block to realize a compact and lightweight structure that is able to withstand high combustion pressures[5]. As shown in Fig. 6, the dimensions of all sections (shape of cylinder block surface and journal thickness etc.) are optimized through a CAE study using the lower block of a gasoline engine as a reference.

In addition, the aluminum holder for the 2nd order balancer system is attached to the main bearing support in such a way to increase the total stiffness. High rigidity is achieved, as shown in Fig. 7.

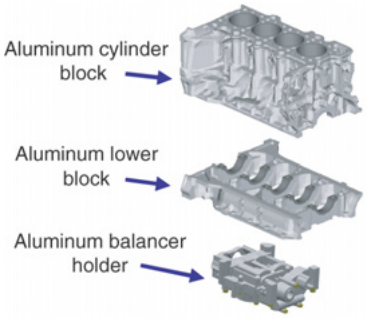


Fig. 6 Cylinder block and balancer holder

By CAE study on the surface of the cylinder block ribs, a reduction in noise emission is shown. Figure 8 shows the structural finite element model used for study as well as the rib placement employed. The structural attenuation of the cylinder block is shown in Fig. 9. Compared with competitors' blocks, including those made out of cast iron for

similar engine displacement, this engine block has superior attenuation.

Another characteristic of the cylinder block is that it is positioned offset from the center line of the crankshaft. As shown in Fig. 10, the crank center is offset to the thrust side of the bore center. The results of a CAE study on piston impact energy (Fig. 11) show that the impact force is mitigated in the direction of thrust.

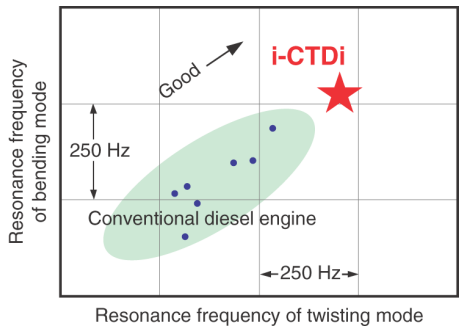


Fig. 7 Cylinder block dynamic characteristics

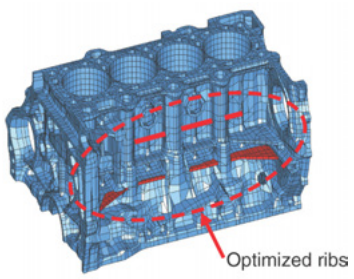


Fig. 8 FEM Model for optimizing ribs

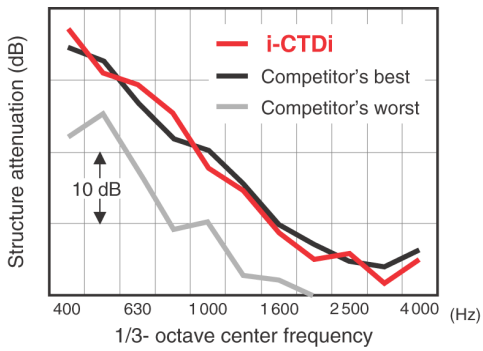


Fig. 9 Structural attenuation

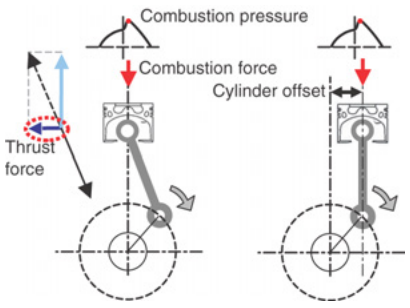


Fig. 10 Cylinder offset structure

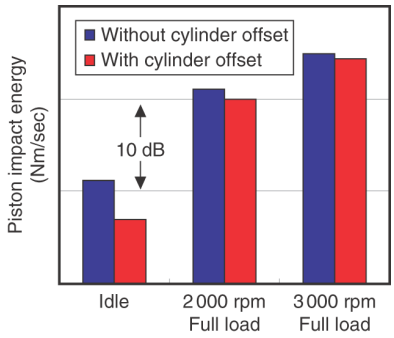


Fig. 11 Calculated piston impact energy

3. Reduction of Combustion Noise

By using the benefit of fuel injection control of the common rail system[2] - [4], pilot injection is employed in a large area. Figure 12 shows a conceptual diagram of the pilot injection.

Adjusting the process between pilot injection and main injection smoothes out the ignition of the main injection and reduces the characteristic diesel combustion by preventing rapid combustion. Figure 13 shows the effects of the pilot injection on the combustion pressure and combustion speed.

In addition, the settings of the amount of fuel released and timing of the pilot injection were adjusted for all types of environmental conditions. As a result, as shown in Fig. 14, lower combustion noise compared to existing diesel engines is realized.

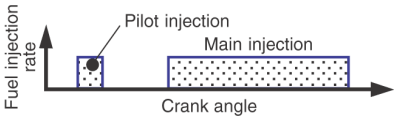


Fig. 12 Conceptual diagram of pilot injection

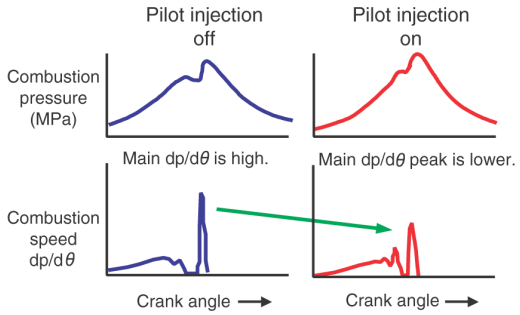


Fig. 13 Effect of pilot injection

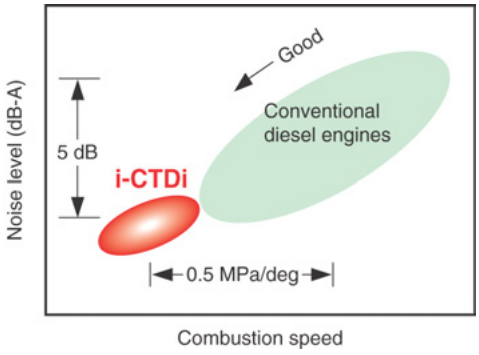


Fig. 14 Combustion noise

4. Improvement of Engine Mount System

In case of the diesel engine, the effect of combustion is large while idling and at engine speeds lower than 3 000 rpm during acceleration. 2nd order vibration is much worse, resulting in increased booming noise and steering vibration, compared to a gasoline engine[4].

In order to efficiently control 2nd order vibration components, the i-CTDi includes the main mount placed on the principal axis of inertia and a mount system that has a torque rods placed in the upper and lower parts of the engine to react to the drive torque as shown in Fig. 15.

Due to the torque rods placed on the upper and lower parts of the engine, the torque fluctuation input is changed to the horizontal direction from the vertical direction, as in the stopper mount type, used in conventional Honda gasoline engine types (hereafter: conventional types), as shown in Fig. 16. As shown in Fig. 17, the body noise transfer function is reduced by 3 to 5 dB.

Figure 18 shows the benefit of this system for cabin noise compared to conventional types. A booming noise reduction of 3 to 5 dB in the 3 000 rpm region is achieved.

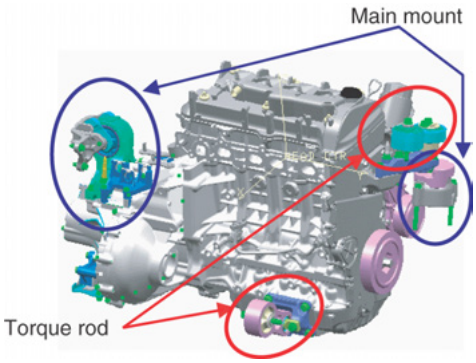


Fig. 15 Principal axis of inertia type mounting system with torque rods

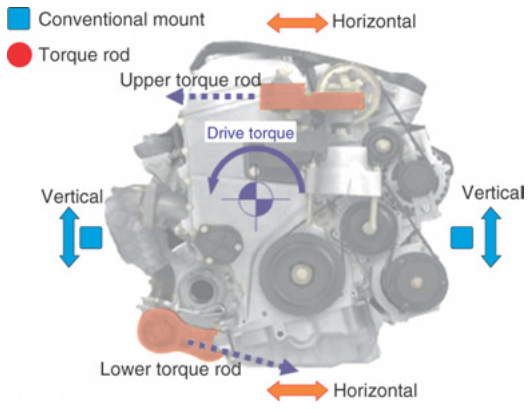


Fig. 16 Direction of principal input force

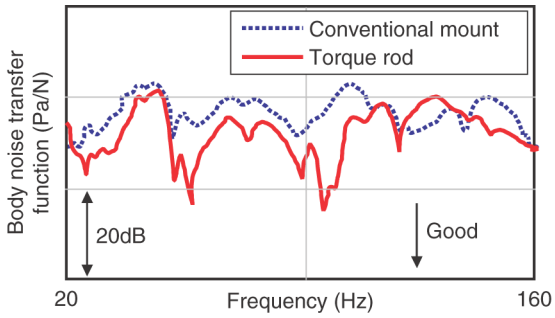


Fig. 17 Body noise transfer function

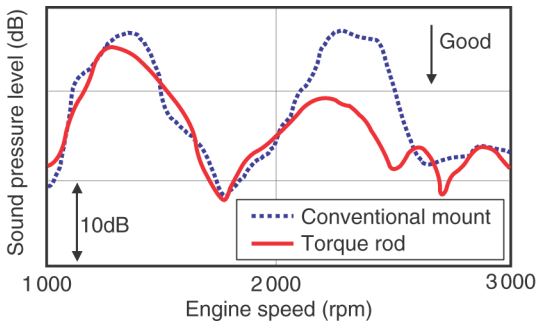


Fig. 18 Booming noise level

In general, the two important characteristics of the torque rod mount system are: 1) the installation angle of the torque rod under its operation, and 2) maintaining the engine mount rigidity in the vertical direction which has a large effect on riding comfort.

For this system, the installation angle of the torque rod, as shown in Fig. 16, is set in the normal direction to the operating drive torque. In addition, as shown in Fig. 19, the transmission lower mount on the lower end of the transmission is newly added.

Through improving the installation angle of the torque rod and adding the transmission lower mount, rotational rigidity under driving torque is assured, as shown in Fig. 20. Also, through employing a transmission lower mount, adequate rigidity in the vertical direction has been provided. Through these countermeasures, a level of riding comfort comparable to the European competitors' vehicles is achieved.

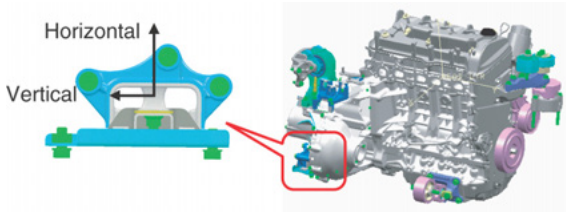


Fig. 19 Transmission lower mount

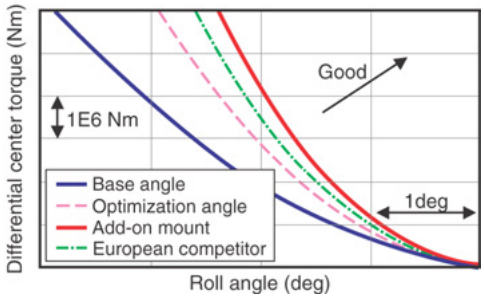


Fig. 20 Comparison of rotational stiffness

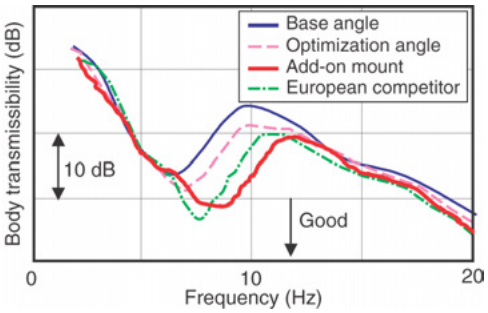


Fig. 21 Body transmissibility

Figure 21 shows the results of the vibration bench test for evaluating the riding comfort performance. Note, as the transmission lower mount is mounted on the sub frame, which has double vibration prevention measures, the deterioration due to noise and vibration is kept to a minimum.

5. Improvement in Soundproof Performance of Vehicle

In addition to the countermeasures for the power plant described above, improvements in vehicle soundproof performance were also investigated.

For optimizing soundproof materials, investigation was performed utilizing the panel contribution analysis method. As a result, it was found that the dashboard and floor are areas where soundproof materials should be effectively applied, as shown in Fig. 22.

The main countermeasures for the dashboard and surrounds are the following

(1) Through changing the harness grommet structure, between the engine room and the cabin, from the current single layer construction to a hollow double-layer construction, this soundproof performance was improved.

A structural diagram for the grommet is shown in Fig. 23.

(2) A cover was added to the lower part of the instrument panel so the instrument panel was given as an overall box

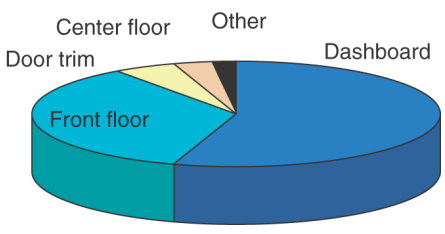


Fig. 22 Contribution analysis of panel

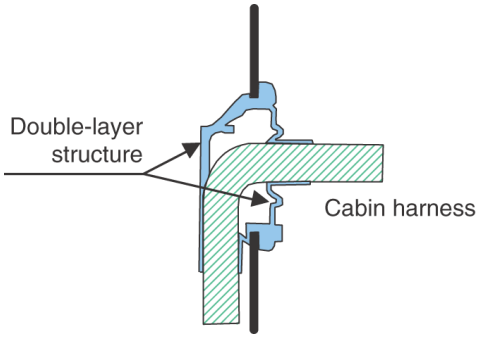


Fig. 23 Structure of cabin harness grommet

type structure. Moreover, on surface of inside instrument panel, acoustic material with improving performance (+25% compared to current materials) is applied to improve soundproof performance. As a result, acoustic material weight was reduced 60% compared to current material.

In addition, materials with high acoustic performance were also used for a floor carpet. Therefore, the soundproof performance of a vehicle was greatly improved compared to before applying the countermeasures as shown in Fig. 24.

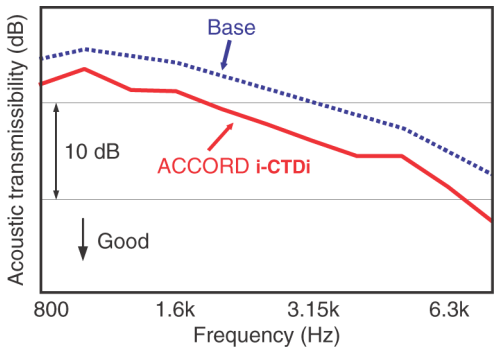


Fig. 24 Soundproof performance of completed vehicle

6. Cabin Noise of Complete Vehicle

As a result of the employment of noise and vibration reduction technologies discussed above, the new EU Accord, equipped with the i-CTDi engine, achieves quiet cabin noise levels as shown in Fig. 25.

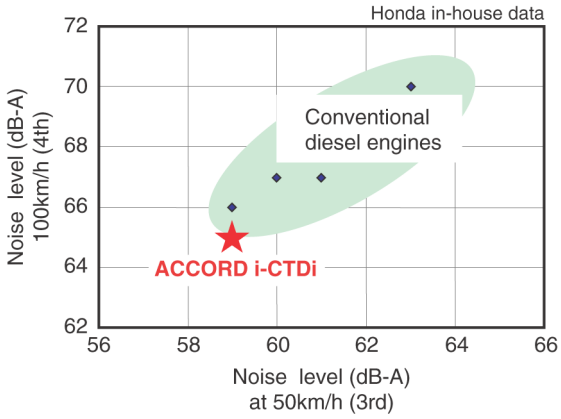


Fig. 25 Interior noise

7. Conclusion

The newly developed 2.2L 4-cylinder diesel engine for the new ACCORD marketed in Europe employed the following noise and vibration reduction technologies. This enabled the new ACCORD to be powerful yet achieves the high quality cabin sound and low vibration levels, associated with a luxury vehicle.

(1) Reduction of engine noise and vibration
The engine noise and vibration was reduced by increasing the rigidity of the cylinder block, employing a lower block structure, offsetting the cylinders, application of a top acoustic cover, and a 2nd order vibration balancer.

(2) Reduction of combustion noise
The use of a pilot injection reduces combustion noise by smoothing out the ignition of the main injection and by preventing rapid combustion.

(3) Improvement of engine mount system
In order to efficiently control 2nd order vibration components, a principal axis of inertia type mounting system with torque rods is employed, and the mount characteristics and installation angle of the torque rod are optimized. This leads us to the realization of a vehicle where noise and vibration is reduced and where the riding comfort is comparable to that of European competitors' vehicles.

(4) Improvement in soundproof performance of vehicle
The soundproof performance of a vehicle was greatly improved by changing the structure of the harness grommet and utilizing acoustic materials with excellent performance of noise absorption.

References

(1) Abe, T., Nagahiro, K., Aoki, T., Minami, H., Kikuchi, M., Hosogai, S.: Development of New 2.2-liter Turbocharged Diesel Engine for the EURO-IV Standards, SAE Paper 2004-01-1316 (2004)

(2) Tawata, K., Fujii, M., Hirano, T.: Noise Reduction of Small Direct Injection Diesel Engine with Common-rail System, 1999 JSAE Annual Congress Proceedings, No. 70-99, p. 13-16 (1999)

(3) Usuda, S., Otsuka, M., Nagata, M.: Noise and Vibration Reduction of Newly Developed 3.0 litter Direct Injection Diesel Engine, 2001 JSAE Annual Congress Proceedings, No. 45-01, p. 5-8 (2001)

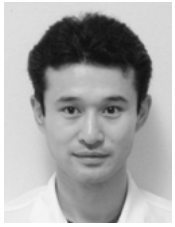
(4) Hiruma, M., Nonaka, S., Katou, Y., Igami, H.: Countermeasure against Noise and Vibration of Direct Injection Diesel Engine for New Honda Accord, FISITA Paper, F2004F417 (2004)

(5) Yamazaki, M., Takai, A., Murakami, O., Tanikawa, H., Ito, O., Yasuda, K.: Development of a High-Strength Aluminum Cylinder Block for Diesel Engine Employing a New Production Process, FISITA Paper, F2004A063 (2004)

■ Authors ■


Masao HIRUMA


Shigeji NONAKA


Yuji KATOU


Yoshihiro NOGUCHI


Hajime IGAMI

Research into New Emission Control Techniques for Motorcycles to Achieve EURO-3 Emission Regulation

Shunji AKAMATSU* Tomoya KONO* Mamoru URAKI*
Hiroaki MIYATA* Ryutaro YAMAZAKI*

ABSTRACT

The EURO-3 emission regulation will be enforced in Europe in the year 2006. To meet the regulation, emission reduction technologies were developed using a motorcycle with a liquid-cooled, four-cylinder, 1 100 cm^3 engine. In order to reduce HC during the cold-start cycle the catalyst was activated early by means of combining an Idle Air Control Valve System (IACV) with ignition retard and atomization of fuel spray. In order to reduce NOx during the extra-urban driving cycle, the number of cells and capacity of the three-way catalyst were optimized. However, the increase of catalyst capacity caused increase of exhaust resistance, and reduced engine power. In order to solve this problem, location of the catalyst was optimized. By these measures, the EURO-3 regulation value was sufficiently attained without detriment to the engine power and drivability.

1. Introduction

In recent years, as concern for environmental issues grows, demands for reduction in emissions from motorcycles have increased. New emissions regulations are being implemented in various countries throughout the world. For example, in Europe, which is a main market for large motorcycles, the Euro-3 emission regulation is scheduled for implementation in 2006. In addition, cold-start mode and high-speed mode are added in the measurement modes of the regulation. Hence it is difficult to meet the regulation for motorcycles.

For exhaust emission reduction on large motorcycles combinations of three-way catalysts, O_2 feedback and secondary air induction systems are commonly used. However, demand for favorable drivability is also a requirement of the engines for high-speed high-output motorcycles, therefore having a strong demand of both high-output and low emissions. This paper describes research of the emissions reduction system that satisfies the Euro-3 regulation based on the CBR1100XX.

2. Euro-3 Regulations and Issues

Regulations of motorcycle emissions are being strengthened especially in Europe and Asia. It is in these areas that their percentage of contribution to atmospheric pollution cannot be ignored. Included in the Euro-3 regulation are several items where the regulation has been strengthened with new policies for reduction of motorcycle emissions. Figure 1 shows the measurement mode for the Euro-3 regulation while Table 1 compares the regulation

* Asaka R&D Center

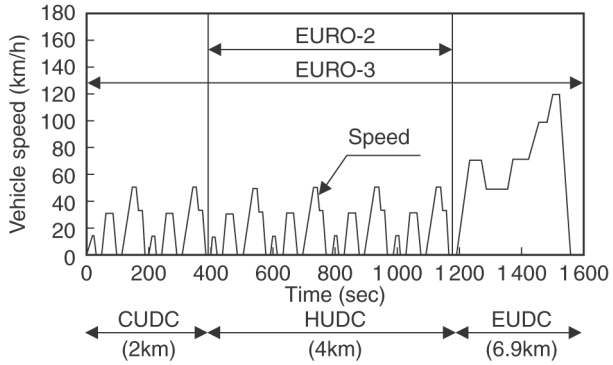


Fig. 1 Federal test procedure

Table 1 EURO-3 emission standards

(Displacement ≧ 150cm^3)

Standards	CO (g/km)	THC (g/km)	NOx (g/km)
EURO-2	5.5	1.0	0.3
EURO-3	2.0	0.3	0.15

values with those of Euro-2. In comparison with the Euro-2 regulation, the changes and requested performance for the Euro-3 regulation is given below.

(1) Due to cold start and sampling requirements, in addition to improvements in the purification rate of the catalyst, early activation for CO and HC cleanup are required.
(2) Due to the addition of the high-speed mode (EUDC), which causes an increase in NOx emissions, an improvement in the catalyst purification rate for NOx is required.
(3) Due to the addition of 30 000 km durability requirements, long-term stability of the entire emissions reduction system is required.

3. Technical Method for Reducing Emissions

In conjunction with the research of technology needed to meet Euro-3, the exhaust emissions performance of a mass production motorcycle that meets Euro-2 was retested. Figure 2 shows the exhaust measurement results when Euro-3 were divided into 3 intervals[(1)]. The first-interval is the first 2 cycles after startup and called Cold-Urban-Driving-Cycle (CUDC). The second-interval is 4 cycles and called the Hot-Urban-Driving-Cycle (HUDC), as same as the current ECE40-01. The third-interval is the additional high-speed mode called the Extra-Urban-Driving-Cycle (EUDC). The amount of exhaust shown in the first-interval (CUDC) shows a condition where the catalyst is not sufficiently active and therefore it is not providing an adequate purification rate. In order to rectify this issue, technology for reducing engine out emissions and to provide early activation of the catalyst need to be worked on. The second-interval (HUDC) shows a condition where the catalyst is sufficiently active but as the regulation is more stringent, further reduction in emissions is required. The third-interval (EUDC) is a new, high-speed mode and NOx emissions have greatly increased during the acceleration to 120 km/h.

As a result, in order to meet Euro-3 regulation, development focused on the issues of reducing HC emissions during cold start and NOx emissions during high-speed mode.

4. Test Vehicle

A mass production liquid-cooled in-line 4-cylinder motorcycle with a displacement of 1 100 cm^3 was used for testing. The main specifications are shown in Table 2. An electronically controlled fuel injection system is used for fuel supply and O_2 sensors are used for feedback control. The system is shown in Fig. 3. A pintle type injector is used for fuel injection.

A metal substrate three-way catalyst and secondary air induction system are used for the exhaust cleanup system. Due to not having enough space, the catalyst cannot be mounted beneath the exhaust manifold. Therefore, it is mounted on the rear of the exhaust pipe as shown in Fig. 4.

Table 2 Specifications of test engine

Items	Specifications
Cooling system	Liquid-cooled
Cylinder configuration	In-line 4-cylinder
Bore × Stroke (mm)	79 × 58
Displacement (cm^3)	1 137
Compression ratio	11.0 : 1
Valve train	DOHC

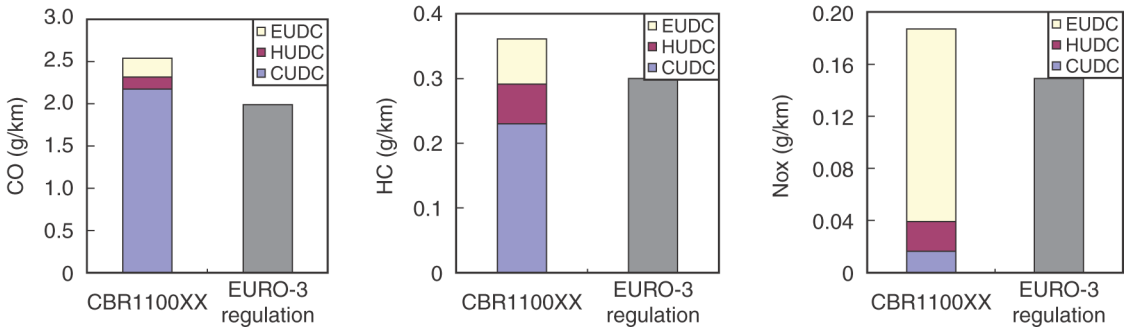


Fig. 2 CBR1100XX emissions by EURO-3 mode

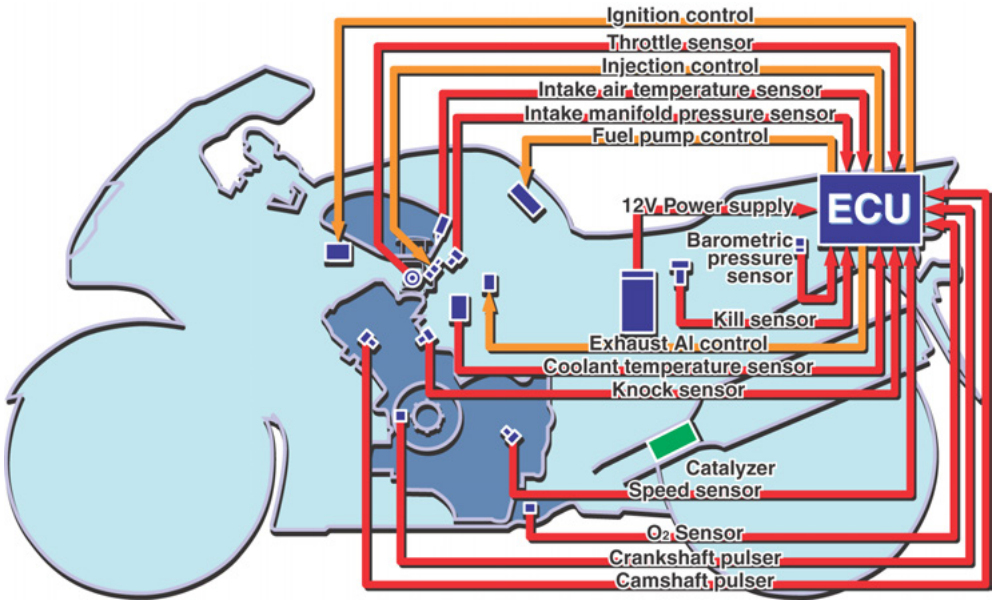


Fig. 3 Diagram of PGM-FI system

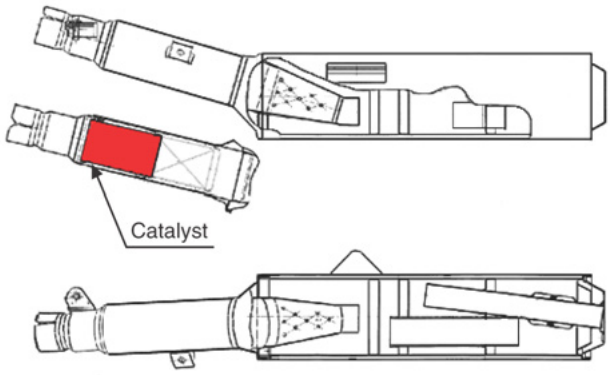


Fig. 4 Catalyst location

5. Emission Reduction Technology

Various emissions reduction technologies have been developed for automobiles; however, the technologies that can be adapted to large motorcycles with high-speed, high-output engines are extremely limited. For example, in order to activate the catalyst early, catalysts are placed beneath the exhaust manifold in many automobile applications[(2)]; however, due to difficulties of layout and the effect on their output characteristics, it is difficult to apply this to motorcycles. Therefore, this research focused on technology that can be applied to motorcycles.

5.1. Reduction of HC Emissions at Cold Start

There are several approaches to reduce the HC emissions at cold start. This report will describe the method of reducing HC emissions using improved atomization of fuel spray by the injector, and the method of obtaining early activation of catalyst by increasing intake air volume using an Idle Air Control Valve (IACV) and by increasing exhaust temperature by retarding ignition timing.

5.1.1. Atomizing injector

Improved atomization of the injected fuel spray and its effect for reduction of engine out HC emissions were investigated. The specifications of the injector used for the test are shown in Table 3.

The 12-hole tapered nozzle injector used for this test provided much better atomization as compared to the pintle type. Through utilizing this atomizing injector, a reduction in HC emissions prior to catalyst early activation as well as during deceleration has been realized. A 20% reduction in HC emissions compared to conventional levels has been obtained. The results are shown in Fig. 5.

Table 3 Specifications of test injectors

	Developed injector	Base injector
Nozzle	Taper nozzle	Pintle nozzle
Number of nozzle	12	1
Static injection quanlity	252mm³/st	258mm³/st
SMD	80μm	120μm

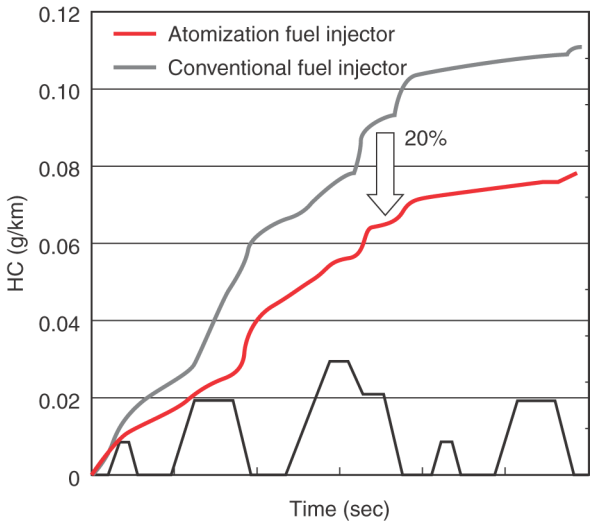


Fig. 5 HC reduction by atomized injector

5.1.2. Early activation of the catalyst

In order to reduce HC emissions during CUDC mode, a prompt increase in the temperature of the catalyst leading to early activation is effective. However, it is difficult to both simply move the catalyst closer to the exhaust valve and maintain output. For this test, the ignition timing was retarded in order to increase the temperature of the exhaust. However, when ignition timing is retarded, intake air volume becomes insufficient and idle engine speed decreases. Therefore, the IACV controlled by the ECU to provide optimum airflow was used to correct for the amount of air.

Figure 6 shows the results of ignition timing, catalyst temperature, and reduction in HC emissions in this test. By retarding the ignition timing, the time the catalyst takes to reach activation temperature (300 °C) was reduced by 70 seconds. HC emissions were reduced by 30% at 300 seconds.

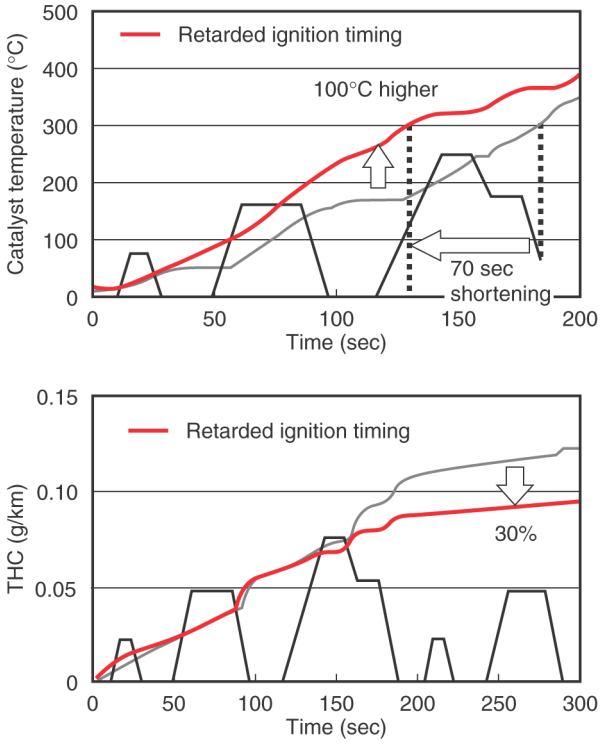


Fig. 6 Effect of quick warm-up system

5.2. NOx Reduction for High-speed Mode

The EUDC mode drive cycle is within the O_2 feedback area for this test motorcycle and the air-fuel ratio is set to a stoichiometric air-fuel ratio that enables the three-way catalyst to provide efficient exhaust cleanup performance. For this test, optimization of the number of cells and the volume of the catalyst and optimal tuning of the air-fuel ratio were performed for NOx reduction for the EUDC mode.

5.2.1. Selection of catalyst

In general, large volume catalysts have the ability to reduce emissions. However, due to limited space on motorcycles, the size of catalysts and places they can be mounted are limited. The number of cells and amount of precious metals were used as parameters to confirm reduction of the three components CO, HC and NOx in this test and the specification for the catalyst was defined. Figure 7 shows the test results for increasing the number of cells in the catalyst while holding its volume constant. When using more cells than were used in the base catalyst, each of the three components was found to be reduced. However, if more than 600 cpsi were used, conditions actually got worse. The back pressure in the muffler was considered along with these results and it was decided to use 300 cpsi. The measurement results for the amount of emissions when using the same catalyst volume while increasing the amount of precious metals are shown in Fig. 8. Increasing the amount of precious metal reduces CO and HC emissions. However, it causes NOx emissions to increase. Increase in the amount of precious metals increases cost. However, due to the purification rate requirements, the amount used has been doubled compared with the base catalyst. The final specification for the catalyst is shown in Table 4.

Table 4 Specifications of test catalyst

Items	Specifications
Cell density	300 cpsi
Catalyst layer thickness	50μm
Diameter of carrier	80 mm
Length of carrier	90 mm
Precious metal	Platinum, Rhodium

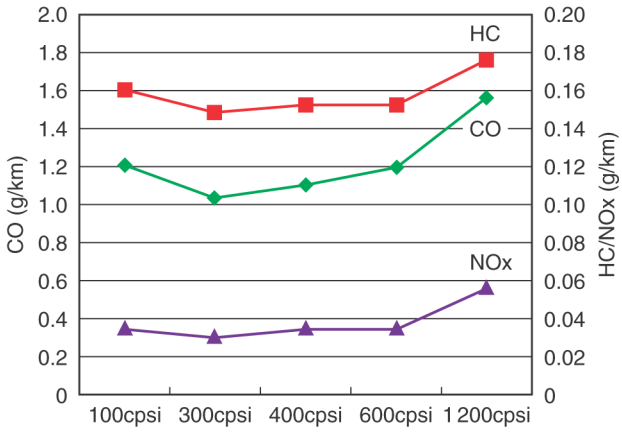


Fig. 7 Emission results from different number of cells

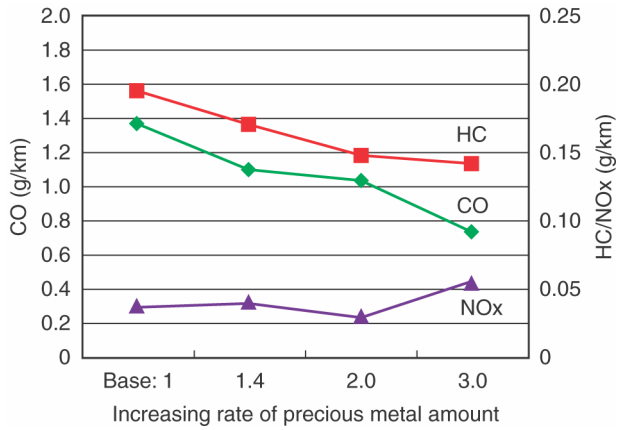


Fig. 8 Emission results from different amount of precious metal

5.2.2 recise control of the air-fuel ratio

It is said that the purification rate of all three components using a three-way catalyst is best when using a stoichiometric air-fuel ratio. For this test, in place of the O_2 sensor, a UEGO sensor was used and the air fuel ratio providing minimum emissions density at all loads was determined during the emissions drive cycle tests. The purification rate based on air-fuel ratio was compared for the current emissions drive cycle with a maximum speed of 50 km/h and for the new EUDC mode with a maximum speed of 120 km/h.

The results are shown in Fig. 9. The air-fuel ratio that provides the minimum emissions density has moved into the rich area as the drive cycle changed to high load. It follows that through adjusting the air-fuel ratio, it was possible to reduce emissions.

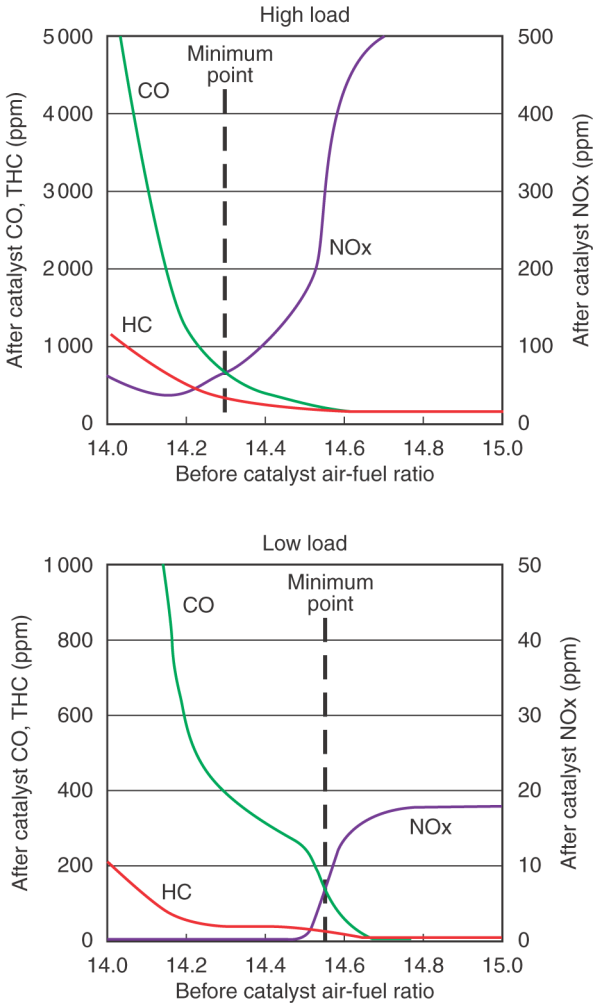


Fig. 9 Reforming gas ratio by different air-fuel ratio

5.3. Effect on Power

Concerning the reduction in output associated with the increase in catalyst volume, Fig. 10 shows the results of confirmation based on peak power, back pressure and number of cells. When the number of cells in the catalyst is increased, the back pressure also increases leading to a reduction in power. Taking into the consideration the requirements of maintaining high power for a super sports type motorcycle, the specifications as shown in Table 4 were chosen.

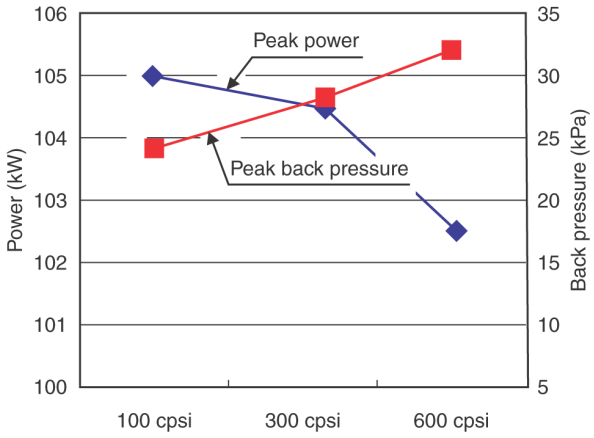


Fig. 10 Back pressure of catalyst

6. Test Results

6.1. Emissions

The measurement results for Euro-3 emissions taken on the test motorcycle are shown separately for CUDC, HUDC, and EUDC in Fig. 11.

(1) In the CUDC mode, HC emissions were reduced by 73% compared to the base.

(2) In the EUDC mode, NOx emissions during high speed driving were reduced by 97% compared to the base.

These results enabled the system to pass the Euro-3 emissions regulation.

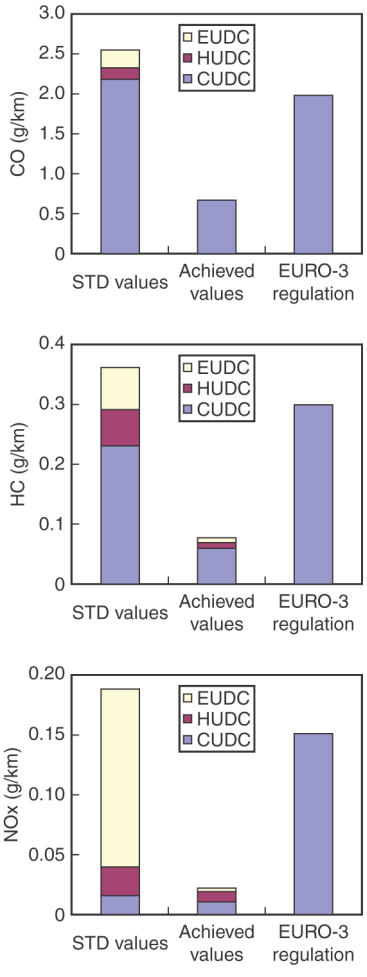


Fig. 11 Exhaust mass emission

6.2. Power Output

Though the number of cells in the catalyst was increased, the power output performance remained the same as the base model. Figure 12 shows the power output performance curve.

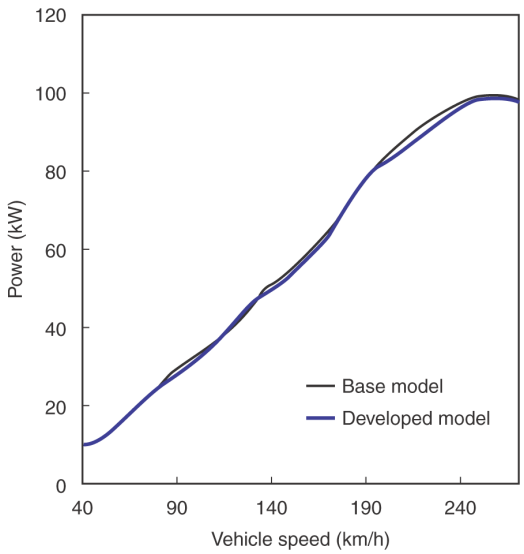


Fig. 12 Power output

6.3. Durability

The 30 000 km durability test, established in the regulation, was performed. Figure 13 shows the change in emission values and it can be seen that even after the durability test, the regulations are met without difficulty.

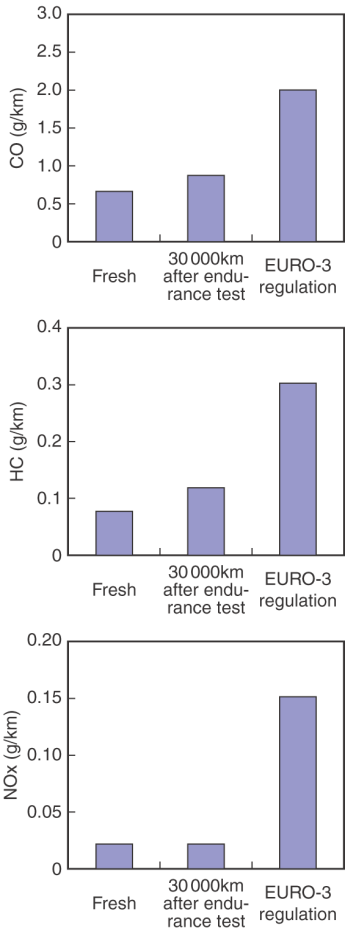


Fig. 13 Durability performance of emission reduction system

7. Conclusion

Increasing the performance of the after treatment system for the exhaust gas has enabled the same engine specifications to meet the Euro-3 regulations, while maintaining the same power output and drivability.

(1) Increase in exhaust temperature by retarding ignition timing was effective for reducing HC emissions at cold start.
(2) The purification capability of the catalyst was used to its fullest by controlling the target air-fuel ratio during feedback control to meet driving requirements for reduction of NOx during high-speed mode.
(3) Increase of the number of catalyst cells has enabled the purification rate of the catalyst to increase, while maintaining power output.

References

(1) Kitagawa, H., Mibe, T., Okamatsu, K., Yasui, Y.: Super Ultra Low Emission System for ACCORD SULEV, HONDA R&D Technical Review, Vol. 12, No. 2, p. 37-44

(2) Matsuki, M., Ohura, H., Watanabe, K., Kinoshita, Y.: Development of a 1.5L Lean-burn Engine for the 2001 Civic, HONDA R&D Technical Review, Vol. 12, No. 2, p. 29-36

■ Authors ■


Shunji AKAMATSU


Tomoya KONO


Mamoru URAKI


Hiroaki MIYATA


Ryutaro YAMAZAKI

Research on Combustion Switching Control for Direct Injection Gasoline Engine

Ken OGAWA* Isao KOMORIYA* Hiroshi TAGAMI*
Yutaka KOHDA* Masahiro TAKEUCHI* Yuji FUJIKI*

ABSTRACT

Honda has developed its first-ever i-VTEC I direct injection gasoline engine employing a center injection system in which a high-pressure fuel injector is located at the center of the combustion chamber. Direct injection enables stratified charge combustion to be employed, and the new center injection engine demonstrates significantly improved fuel economy and emissions performance in the range of vehicle operation in which this type of combustion is used. The authors studied methods of switching between direct-injection stratified charge (DISC) and pre-mixed combustion in order to utilize DISC. The two forms of combustion employed in the new direct-injection engine differ in terms of combustion limits in relation to recirculated exhaust gas and air-fuel ratio. This causes the torque difference which is a specific issue in direct injection gasoline engines. The authors resolved this issue through the application of two technologies. Fuel injection during the intake stroke and the compression stroke has improved the combustion limit. When combustion is stable, the appropriate quantity of fuel to be supplied is determined from the required torque.

1. Introduction

Due to the increasing concern with the issue of global warming in recent years, it has been seen that the automotive industry has strived to develop high fuel economy and low emissions power plants. In particular, significant research and development efforts have been made to investigate various forms of direct injection gasoline engine as a means of improving the fuel economy of spark ignition internal combustion engines[1]-[3]. Direct injection gasoline engines display low pumping loss and heat loss during DISC combustion. These characteristics result in high thermal efficiency, low intake air temperature during homogeneous charge combustion, superior resistance to knocking and a high charging efficiency. While direct injection gasoline engines possess a number of advantages, however, the difficulty of controlling the mixture makes the achievement of stratified charge combustion across the entire operating range a challenge in these engines.

For this reason, direct injection engines employ both stratified charge combustion and homogeneous charge combustion depending on operating conditions[4]. At the same torque, the engine control parameters (spark timing, etc.) necessary for optimum fuel economy differ for these two forms of combustion. This makes a method of preventing torque fluctuations essential when switching between stratified charge and homogeneous charge combustion.

The research discussed in this paper attempted to develop a method of misfire prevention and a method of calculating the appropriate quantity of fuel to be injected to prevent the driver from experiencing any fluctuation in torque when a direct injection gasoline engine switches between combustion states.

* Tochigi R&D Center

Table 1 Engine specifications

Engine code		K20B
Cylinder configuration		In-line 4-cylinder
Bore × Stroke (mm)		86 × 86
Displacement (cm³)		1 998
Compression ratio		10:1
Valve train		DOHC VTEC
Number of valves		4 per cylinder
Valve diameter (mm)	In.	34
	Ex.	28
Fuel supply system		Programmed fuel injection
Fuel supply pressure (MPa)		8 - 10.5
Fuel		Regular (91RON)
Max. power (kW/rpm)		115 / 6 300
Max. torque (N·m/rpm)		188 / 4 600

2. Engine Specifications and System Configuration

2.1. Overview of Engine and Main Specifications

Table 1 shows the specifications of the test engine and Fig. 1 shows the configuration of the combustion chamber. The formation and maintenance of the mixture by the spray flow produced by the centrally positioned high-penetration injector and the deep bowl-type piston cavity, and the achievement of rapid combustion by the swirl induced by closing one valve by the VTEC mechanism, enable ultra-lean stratified charge combustion[5].

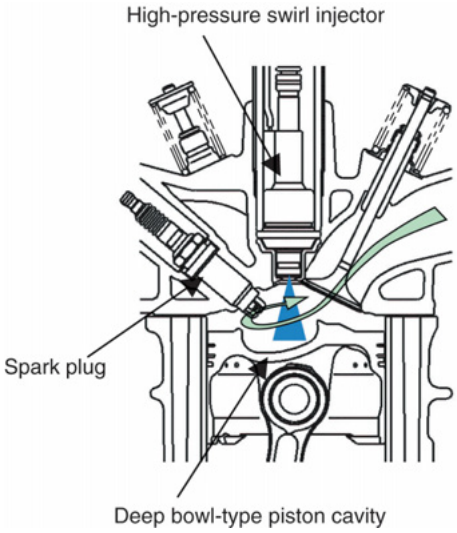


Fig. 1 Combustion chamber configuration

2.2. System Configuration and Outline of Control Methods

Figure 2 shows the configuration of the test engine control system. The characteristics of this test system are as follows:

(1) The system employs an air flow meter to enable accurate calculation of air intake during stratified charge combustion operation, etc., even when EGR is high; the required amount of fuel is calculated on the basis of the results for the amount of intake air.

(2) An electronically controlled throttle valve able to converge on the target opening angle in a short period is used to enable employment of both stratified charge and homogeneous charge combustion to meet the demand for different amount of intake air.

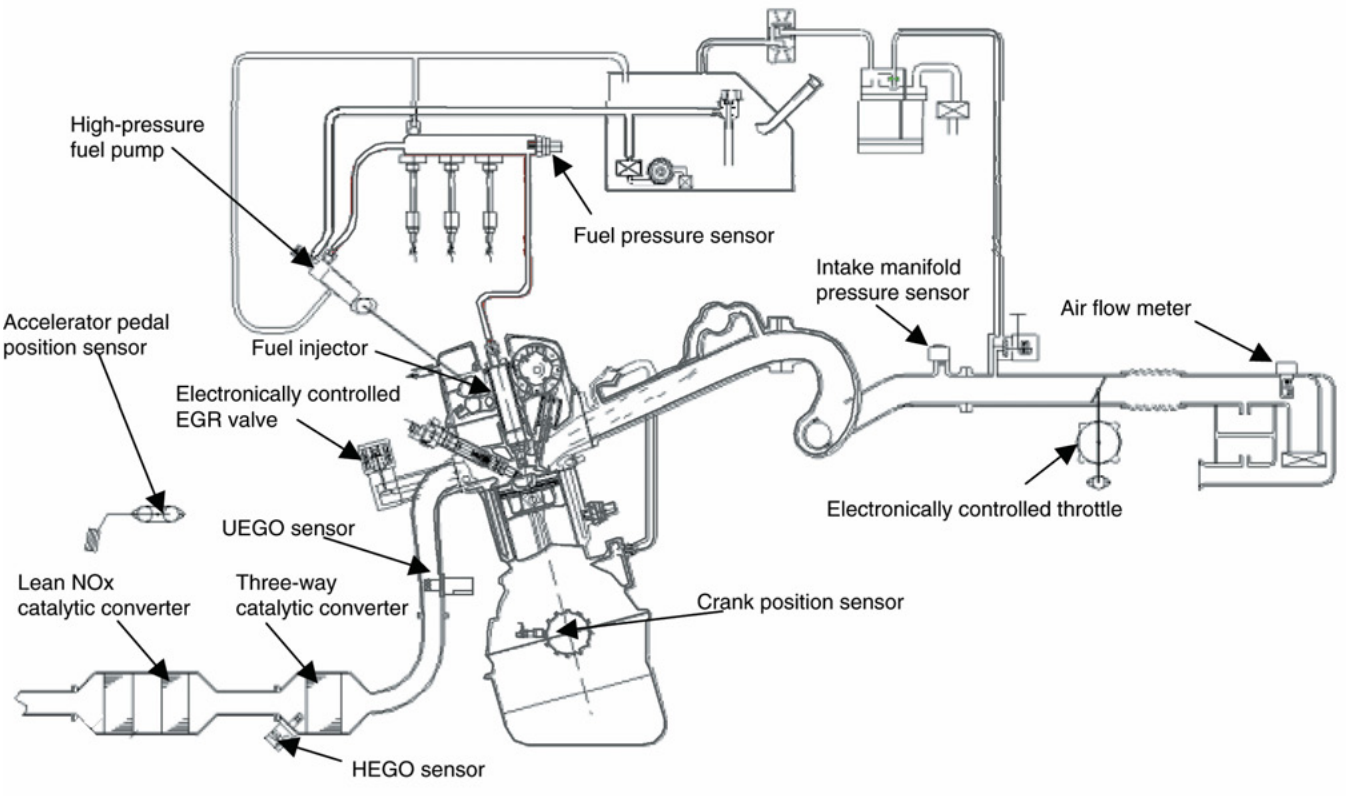


Fig. 2 System configuration

(3) In a direct injection gasoline engine, the EGR ratio makes a significant contribution to drivability, exhaust emissions and fuel economy[6]. In this system, the widely used step motor EGR valve has therefore been replaced by a linear solenoid EGR valve which is five times more responsive (Fig. 3) in order to accelerate convergence on the required EGR ratio. Figure 4 compares the response times of the linear solenoid and step motor EGR valves.

(4) The exhaust system is composed of –A universal exhaust gas oxygen (UEGO) sensor to enable air-fuel ratio feedback to be conducted during stratified charge operation in addition to homogeneous charge operation in order to maintain optimum drivability, fuel consumption and engine-out exhaust emissions;–A three-way catalyst for purification during operation at stoichiometric air-fuel ratios and HC purification during operation at lean air-fuel ratios;–A heated gas oxygen (HEGO) sensor to improve purification performance during stoichiometric operation; –A NOx absorption reduction type three-way catalyst for NOx purification during lean operation.

(5) Fuel pressure control is provided by a spill valve which adjusts the amount of fuel supplied by the single-plunger high-pressure pump driven by the exhaust cam. The basic amount of control to be applied by the spill valve is calculated on a spill valve operating map from engine speed and the amount of fuel supplied by the injector, and modified on the basis of feedback from the output of a fuel pressure sensor positioned on the fuel delivery pipe[7].

(6) Because the required engine parameters differ in stratified charge combustion, it is impossible to decide engine load using amount of air and intake pipe pressure, which are widely used for this purpose in port injection systems. The new system employs an accelerator pedal sensor to enable the amount of torque demanded by the driver to be calculated, and control parameters (type of combustion, amount of EGR lift, etc.) are decided on the basis of the demanded torque and engine speed.

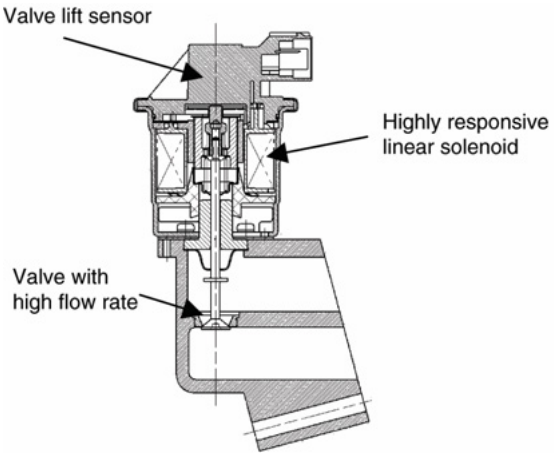


Fig. 3 Newly developed EGR valve

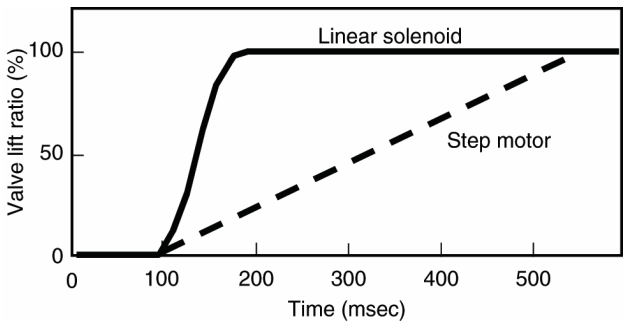


Fig. 4 Comparison of response times of linear solenoid EGR valve and step motor EGR valve

3. Combustion Switching Control

3.1. Why Combustion Switching Is Necessary

Figure 5 compares plots of brake specific fuel consumption (BSFC) against load in the test engine for DISC and homogeneous charge combustion at a stoichiometric air-fuel ratio. Significant fuel consumption improvements are offered by DISC in the low load area, but these benefits decline with increasing load, and above a certain load DISC does not offer any improvement over homogeneous charge combustion at a stoichiometric air-fuel ratio. This occurs because as load increases, the effect of improved pumping loss diminishes. It is therefore necessary to switch between DISC and homogeneous charge combustion according to engine load in order to optimize fuel consumption.

3.2. Combustion Switching Control: Targets and Issues

Fuel injection during both the intake and compression strokes is known as a method of forming weakly stratified mixture, preventing over-rich air-fuel ratios while ensuring stable combustion with lean mixture until a load has been reached at which lean combustion is possible for homogeneous charge[6]. This method has the benefit of ensuring stable combustion, but also makes it possible that operation at a lean air-fuel ratio will continue until a specified load is reached, creating concerns about an increase in exhaust emissions. The aim of this research project was to modify the operating parameters at combustion switching to ensure that there was no increase in emissions and no fluctuation in torque.

Figure 6 shows the behavior of control parameters at combustion switching. The figure indicates that high values are required for throttle opening and EGR lift during stratified charge combustion, while low values are required during homogeneous charge combustion. With the command for combustion switching, the command values for these parameters change, but there is a period of dead time during

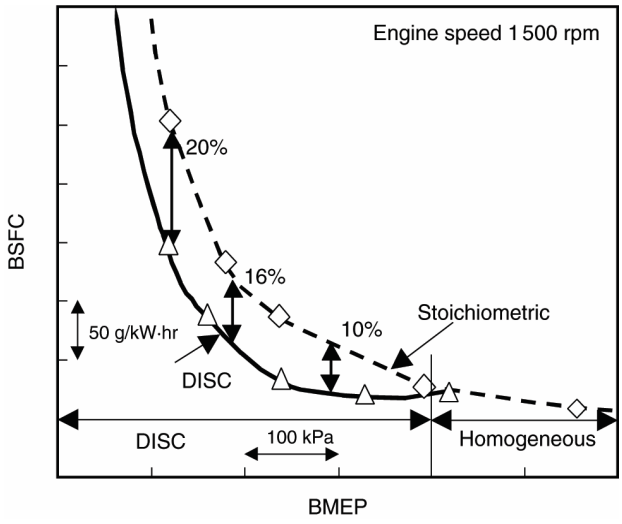


Fig. 5 Comparison of BSFC

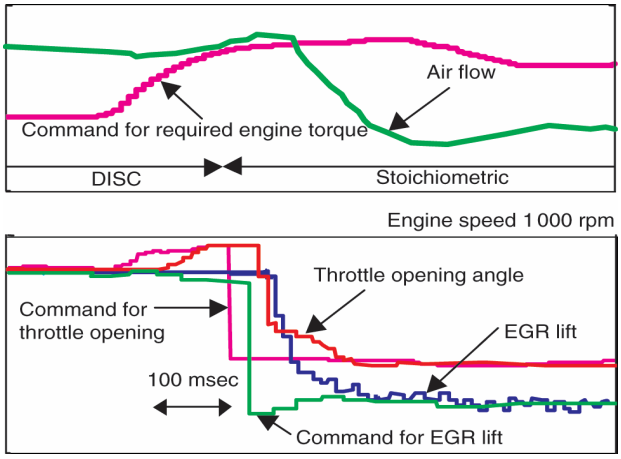


Fig. 6 Characteristics of engine control parameters during combustion switching

which actual throttle opening angle and actual EGR lift do not correspond to command values. The parameters show a first-order delay characteristic in reaching command values. This indicated that there were two challenges for combustion switching control in the period between the application of the command and the parameters converging on command values, when both EGR ratio and the amount of intake air are high: to prevent misfires during homogeneous charge combustion due to excess EGR, and to prevent a rapid generation of torque through the excess supply of fuel due to the supply of too much air.

3.3. Prevention of Misfire

To achieve equivalent torque to that supplied by stratified charge combustion during homogeneous charge combustion directly after switching, when the throttle valve opening and EGR lift retain the values they have for stratified charge combustion, the air-fuel ratio must be increased. However, if a high amount of EGR is introduced during homogeneous charge combustion at a lean air-fuel ratio, misfires occur.

A system of double injection, during the intake stroke and the compression stroke, is therefore employed to ensure that a combustible mixture is present around the spark plug at sparking even when a high EGR ratio is used. As Fig. 7 shows, injection timing control has three phases: compression stroke injection (late injection in the figure), in which fuel is injected late in the compression stroke for DISC combustion at low loads, intake stroke injection (early injection in the figure), in which fuel is injected early in the intake stroke for homogeneous mixture combustion at high loads, and double injection, in which fuel is injected both late in the compression stroke and early in the intake stroke to prevent misfires at combustion switching.

Figure 8 shows the comparison of combustion characteristic against EGR ratio at the same engine speed, load and air-fuel ratio for early injection and double injection. The employment of two injection timings has ensured stable homogeneous charge combustion with a low rate of fluctuation even at EGR ratios which cause misfires, and combustion is stable over a wider range of operating conditions. This indicates that late injection in the compression stroke ensures a combustible air-fuel ratio around the spark plug. Double injection is conducted until the response time for the EGR valve has elapsed and the equivalent ratio calculated from the amount of fuel required to achieve a stoichiometric air-fuel ratio (as calculated from the air intake) and the amount of fuel actually injected has become higher than a specified figure. This has ensured accurate misfire prevention.

3.4. Method to Calculate Fuel Amount for Injection

In this control system, the amount of fuel for injection is determined on the basis of air intake as measured by an air flow meter. This causes certain issues to arise at combustion switching. For example, when switching from stratified charge combustion to homogeneous charge combustion, the high amount of air which has been required for stratified charge combustion leads to the injection of an excess amount of fuel for the required torque until the throttle opening angle reaches the command angle. This causes torque to increase too rapidly. To prevent this, a limit is applied to the amount of fuel for injection as calculated on the basis of the amount of intake air. The limit value for the current amount of fuel required is calculated from the required torque and the amount of fuel for injection directly before combustion switching and the current required torque.

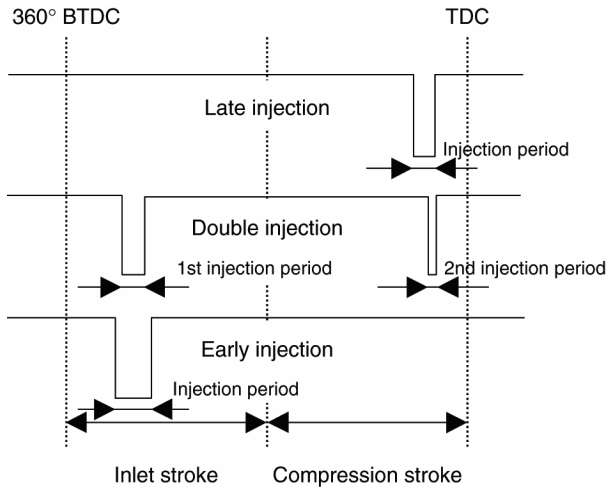


Fig. 7 Injection timing control

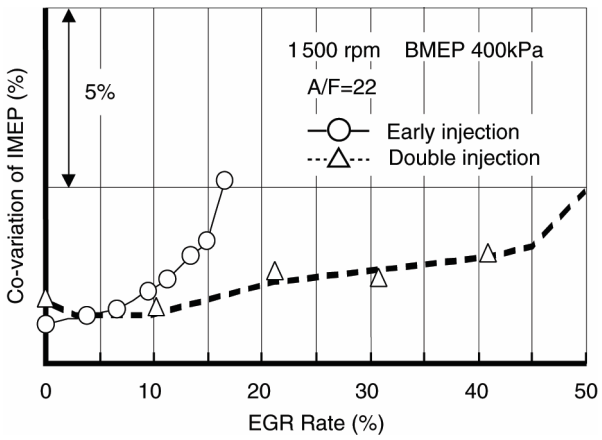


Fig. 8 Comparison of EGR characteristic for early injection and double injection

The application of this type of control requires an understanding of the relationship between torque and the amount of fuel injected. The measurement results, as shown in Fig. 9, indicated that the relationship between brake mean effective pressure (BMEP) and injection period could be expressed as a linear equation. The limit on the amount of required fuel is calculated using the equation below. The limit ceases to be applied when the limit value and the amount of fuel for injection calculated on the basis of the amount of air intake become equivalent, preventing sudden changes in the amount of fuel injected. The equation for calculation of the fuel limit value is as follows:

$$T_{lmt} = \{T_{in} + (\Delta T_{req} / \Delta P_m) \times (P_m - P_{min})\} \times (1 \pm K_{cmb})$$

T_{lmt} : Limit value for amount of fuel for injection
$\Delta T_{req} / \Delta P_m$: Amount of change in injection period against BMEP
T_{in} : Required injection period at moment of switching
P_m : Current torque demand from driver
P_{min} : Torque demand from driver at moment of switching
K_{cmb} : Correction for combustion efficiency

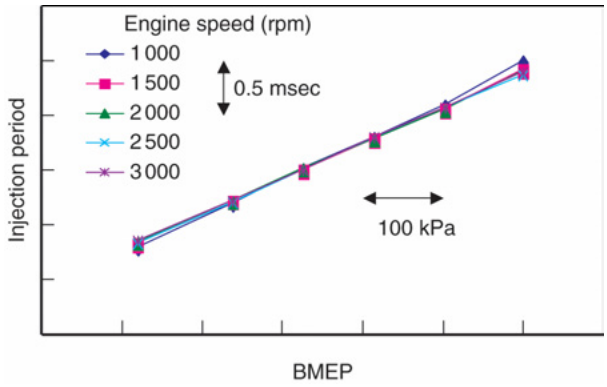


Fig. 9 Relationship of BMEP and injuction period

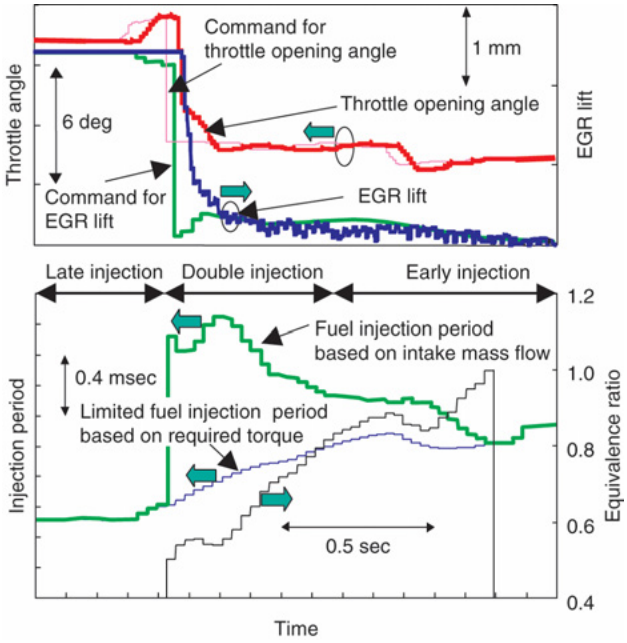


Fig. 10 Schematic diagram of transient condition

4. Engine Test Results

Figure 10 shows the behavior of engine control parameters when switching control is applied.

Double injection is no longer applied when a specified equivalent ratio is reached after EGR lift converges on the command value.

The results in the figure also indicate that the limit applied to the amount of fuel for injection has prevented any sudden increases in fuel supply, and has ensured that fuel supply changes smoothly, and in accordance with requirements based on the amount of air intake.

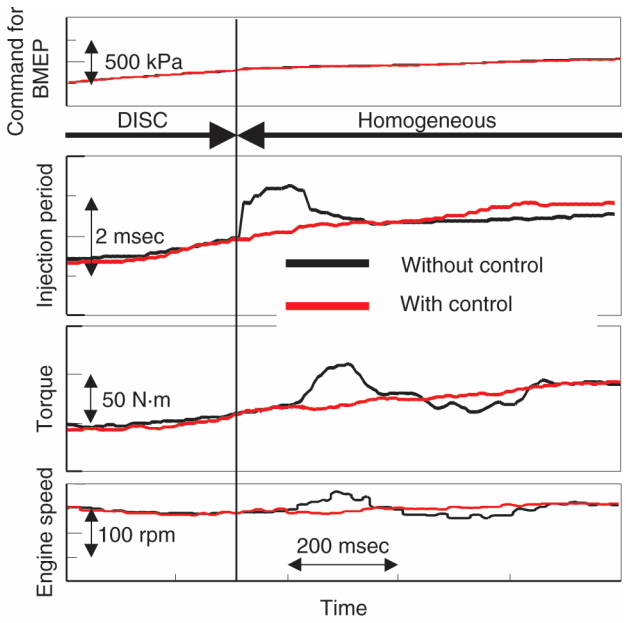


Fig. 11 Effect of combusion switching control on transient torque behavior

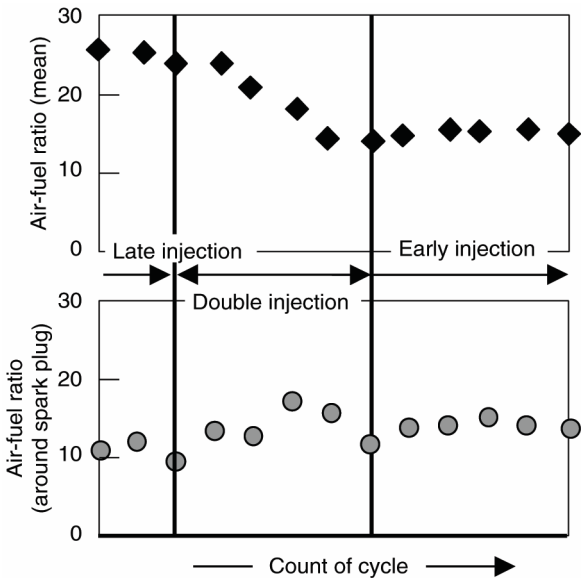


Fig. 12 Characteristics of air-fuel ratio around spark plug

Figure 11 demonstrates the effect of combustion switching control by means of changes in torque behavior. The use of combustion switching control has eliminated sudden changes in torque and in engine speed caused by the change of the combustion mode, and has ensured that combustion switching is carried out without shock and smoothly follows changes in torque demand.

Figure 12 shows the measurement results of air-fuel ratio around the plug and mean air-fuel ratio per cycle, using infrared absorption before and after switching. It is clear that the air-fuel ratio around the plug is controlled to a combustible level when combustion mode is switched, and that double injection in the intake and compression strokes has been effective in preventing misfiring. In addition, a combustible mixture is maintained around the spark plug during stratified charge combustion even when the mean air-fuel ratio is lean, and during homogeneous charge combustion the mean air-fuel ratio and the air-fuel ratio around the spark plug are equivalent.

5. Conclusions

Various control methods have been explored in this work to ensure smooth transition from stratified charge combustion to homogeneous charge combustion. The major conclusions can be summarized as follows:

(1) The employment of double injection in the intake and compression strokes prevents misfires during combustion switching when the EGR ratio is still high.
(2) The calculation of a limit value for the amount of fuel supplied based on the required torque and the amount of fuel supplied directly before combustion switching and the current required torque, and the employment of this value as a control parameter, prevents sudden changes in the amount of fuel supplied during combustion switching.
(3) A control system composed of early, late and double injection timing control and fuel supply limit control enables smooth combustion switching in a direct injection gasoline engine with no negative effects on emissions performance.

References

(1) Kume, et al.: Combustion Control Technologies for Direct Injection SI Engines, Proceedings of JSAE, No. 961, 9631948

(2) Kuma, T., Iwamoto, Y., Iida, K., Murakami, M., Akishino, K., Ando, H.: Combustion Control Technologies for Direct Injection SI Engine, SAE Paper 960600

(3) Noda, T., Iriya Y., Naito, K., Mitsumoto, H., Iiyama, A.: Air-fuel Mixture and Power Performance of Direct-injection Gasoline Engines, Proceedings of JSAE, No. 976, 9740307 (1997)

(4) Harada, J., Tomita, T., Mizuno, H., Mashiki, Z., Ito, Y.: Development of Direct Injection Gasoline Engine, SAE Paper 970540

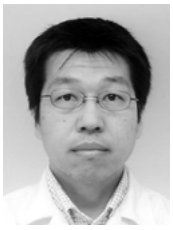
(5) Koda, Y., Suganami, T., Kobayashi, H., Ogawa, K.: Development of High-performance and Low-emission Direct Injection Gasoline Engine, Honda Technical Review, Vol. 16, No. 1, p. 39-46

(6) Masuki, et al.: Development of D-4 Engine, Toyota Technical Review Vol. 47, No. 2, p. 33-37, Nov. (1997)

(7) Goto, H., Hirose, K., Saitoh, M., Matsumoto, S., Iitaka, S., Takashiba, K.: Development of High-pressure Fuel System for Direct Injection Gasoline Engine, Honda Technical Review, Vol. 16, No. 1, p. 47-54

■ Authors ■


Ken OGAWA


Isao KOMORIYA


Hiroshi TAGAMI


Yutaka KOHDA


Masahiro TAKEUCHI


Yuji FUJIKI

Combustion Technologies for Euro IV-compliant Direct Injection Diesel Engine

Tomohiro KANDA* Shinichi KOBAYASHI*
Ryuta MATSUI* Hiroshi SONO*

ABSTRACT

In fall 2003, Honda introduced a passenger vehicle diesel engine to the European market. During the development of this engine, research was conducted on combustion technologies to reduce fuel consumption, combustion noise and emissions.

By adopting pilot injection while also advancing the start of main combustion event, fuel consumption and combustion noise are both lowered, but emissions performance was not improved. Dispersion of the air-fuel mixture and the extension of the appropriate period for dispersion ensured a lean local air-fuel ratio which resolved the emissions issue.

The use of these combustion technologies has enabled fuel consumption and engine out emissions to be reduced with no increase in combustion noise. Fitted in a 1 590 kg equivalent inertia class vehicle in combination with the catalyst, the vehicle satisfied the 2005 European diesel exhaust emissions standards (EURO IV), and achieved a low fuel consumption of 5.4L / 100 km and superb quietness.

1. Introduction

The high speed direct injection (HSDI) diesel engine has become widely accepted throughout the European market as it offers low fuel consumption and substantial low speed torque. Furthermore, combustion noise has been reduced with a series of recent technical developments. The amount of market share HSDI's claim is increasing year by year, and is expected to approach 50% by the year 2010. Exhaust emission systems have improved in accordance with the passing of more stringent regulations; however, as further improvements in emissions are required, developments in both after-treatment systems[(1)－(4)] as well as improvements in combustion[(5)－(11)] are being pursued. Unfortunately, many developments in these areas lead to a reduction in fuel economy.

In the development of this engine, low fuel consumption, the hallmark of a diesel engine's value, was dramatically improved. Additionally, the improvement in combustion has enabled a reduction in both combustion noise and engine emissions.

2. Experimental Equipment

2.1. Test Engine

The main specifications of the Accord i-CTDi diesel engine[(12)] used for testing are shown in Table 1.

* Tochigi R&D Center

Table 1 Main specifications of Accord i-CTDi diesel engine

Cylinder configuration	Inline 4
Displacement volume	2 200cm^3
Bore × Stroke	85.0mm × 97.1mm
Compression ratio	16.7
Fuel injection equipment	Common rail (Max. pressure 160MPa)
Nozzle type	Micro mini-sack
Turbocharger	With variable nozzle
Swirl control valve	Continuously variable
EGR valve	Electric control
EGR cooler	Without bypass valve

2.2. In-Cylinder Visualization Apparatus and 3D CFD Code

As can been seen in Fig. 1, in-cylinder fuel spray and luminous flame were observed from directly above the cylinder head using an endoscope as a visualization apparatus. Also, using an Image Intensifier (I.I.) the visualization was amplified 3 000 times to observe non-luminous flame and high temperature areas. In addition, 3D CFD was utilized to estimate the behavior of the fuel spray as well as the air-fuel mixture.

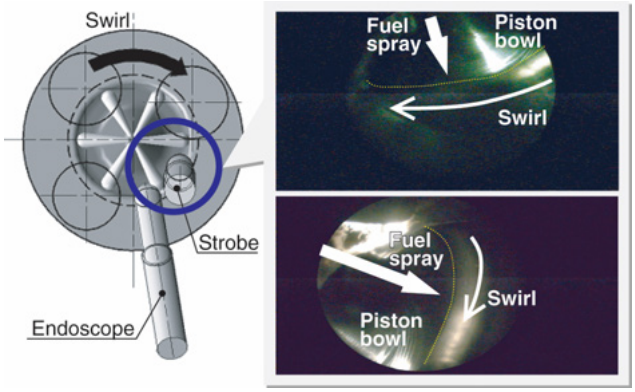


Fig. 1 Experimental setup for observation manuscript

3. Combustion Improvement Concepts

3.1. Pilot Injection Improves Fuel Economy and Reduces Combustion Noise

Figure 2 shows the relationship between brake specific fuel consumption (BSFC) and the maximum rate of in-cylinder pressure increase (dP/d θ_{max}) when amount of fuel, EGR ratio (%), and main injection timing are varied. The relationship between BSFC and NOx is given in Fig. 3. BSFC is greatly affected by the start of combustion event, and reaches a minimum at a prescribed start of combustion event. This prescribed start of combustion event is defined as θ_{min_bsfc} in this paper.

When pilot injection is not used, dP/dθ_{max} is high at θ_{min_bsfc} and combustion noise deteriorates. Therefore, injection timing in current diesel engines is retarded from θ_{min_bsfc}.

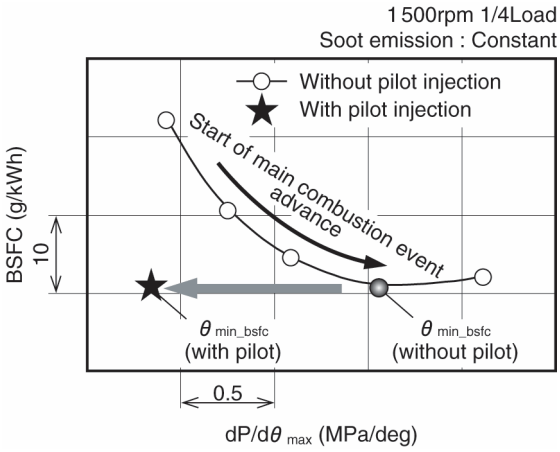


Fig. 2 Effect of pilot injection on dP / dθ_{max} and BSFC

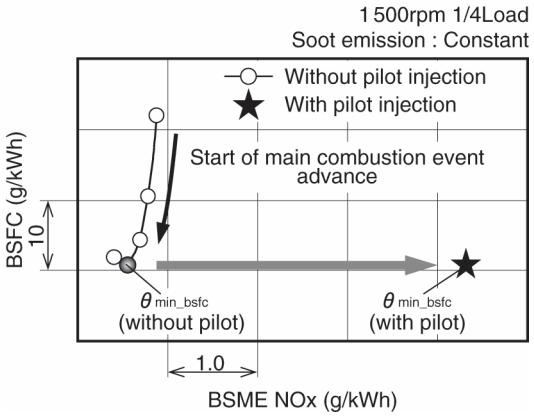


Fig. 3 Effect of pilot injection on NOx and BSFC

The ★ shows the BSFC, dP/dθ_{max}, and NOx for the case where pilot injection was utilized and the main injection timing was adjusted to allow the start of combustion timing to be θ_{min_bsfc}. The dP/dθ_{max} improves at an equivalent BSFC compared to the case where pilot injection is not used; however, while the insoluble organic fraction (soot) is constant, the amount of NOx greatly increases.

As explained above, it was found that the employment of pilot injection and the setting of start of combustion event to θ_{min_bsfc} enables simultaneous achievement of lowered combustion noise and fuel consumption. The issue concerning how to reduce emissions is discussed below.

3.2. Reduced Emissions from Promoted Dispersion of Air-fuel Mixture

The effect of the nozzle cone angle in relation to the piston bowl on emissions was investigated.

Figure 4 shows the shape of the piston bowl and the specifications of the nozzle used in testing. The shape of the piston bowl effectively utilizes the penetration ability of the spray that strikes the wall of the bowl, and promotes the mixing of air with the fuel spray. Concerning the nozzle specifications, a micro-sac nozzle was used because its variability in the fuel spray for each hole is small and it minimizes the amount of fuel dribbling from the sack volume. Sufficient nozzle hole area to enable full power output was ensured.

Figure 5 shows the NOx emissions for cases where the nozzle cone angle was set to be 7 degrees wider and for the

case where it was set to be 10 degrees narrower than the nozzle cone angle α, for the same level of soot generation. As a result, NOx is minimized by using the cone angle α.

In order to analyze this phenomenon, in-cylinder visualization as well as a simulation were performed. The simulation results of the air-fuel mixture behavior for each cone angle, are shown in Fig. 6. Also, the results of visualization for the cone angle α and that of α –10 degrees are shown in Fig. 7.

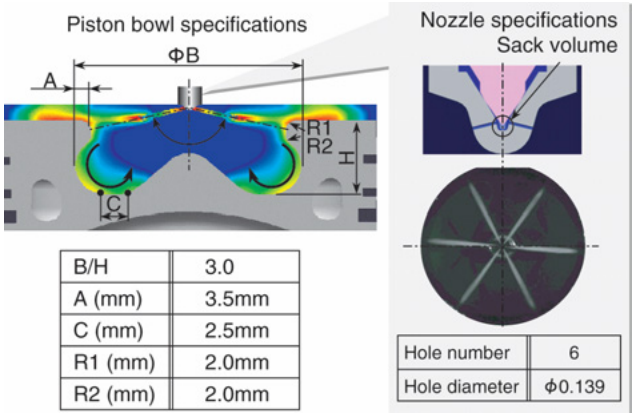


Fig. 4 Specifications of piston bowl and nozzle

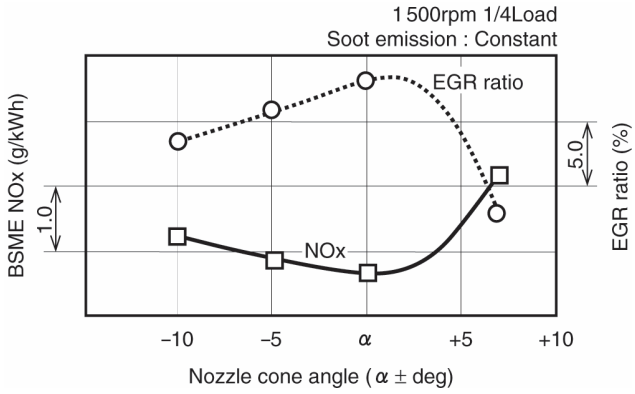


Fig. 5 Effect of nozzle cone angle on NOx

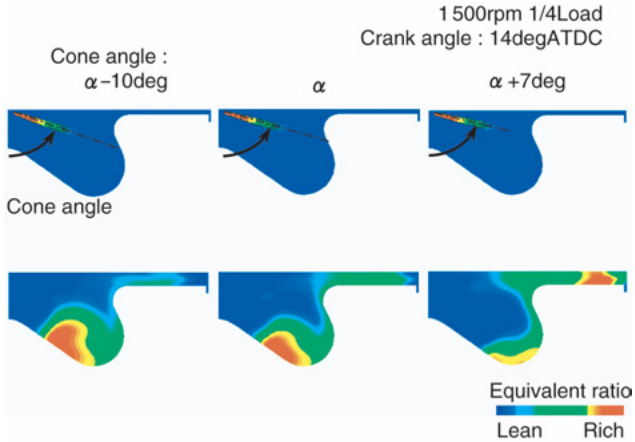


Fig. 6 Effect of nozzle cone angle on mixture distribution

From the simulation results in Fig. 6, it was found that most of the injected fuel spray stays inside the piston bowl for the α –10 degrees case. For the cone angle α, when the spray strikes the wall of the piston bowl it flows out of the bowl and lastly for the α +7 degrees case, the ratio of released air-fuel mixture greatly increases. In other words, an excessively narrow nozzle cone angle leads to the formation of an over rich mixture inside the bowl. Also, an excessively wide nozzle cone angle leads to the formation of an over rich mixture outside the piston bowl. After all, the cone angle α leads to the best distribution of air-fuel mixture inside and outside of the bowl. Therefore, it is considered that this enables increasing the amount of EGR, which leads to a reduction in NOx.

The in-cylinder visualization results in Fig. 7 show the generation of a dark luminous flame that includes a quantity of soot inside the bowl for the case of α –10 degrees. These results can be explained by the combustion of a rich mixture inside the bowl.

In comparison, for the case of the cone angle α, the luminous flame is released outside the bowl, leaving the flame brightness higher inside the bowl. Also, as the heat release ratio is more active, it is considered that the air/fuel ratio of the mixture inside the bowl becomes leaner through the flow of air-fuel mixture leaving the bowl and the mixture inside the bowl becomes more favorable.

It is normally considered that forcing combustion to take place inside the bowl reduces emissions and is therefore better; however, from the results of this test, it was found that to achieve a balanced mixture both inside and outside the bowl through the discharge of fuel spray is more effective for reducing emissions.

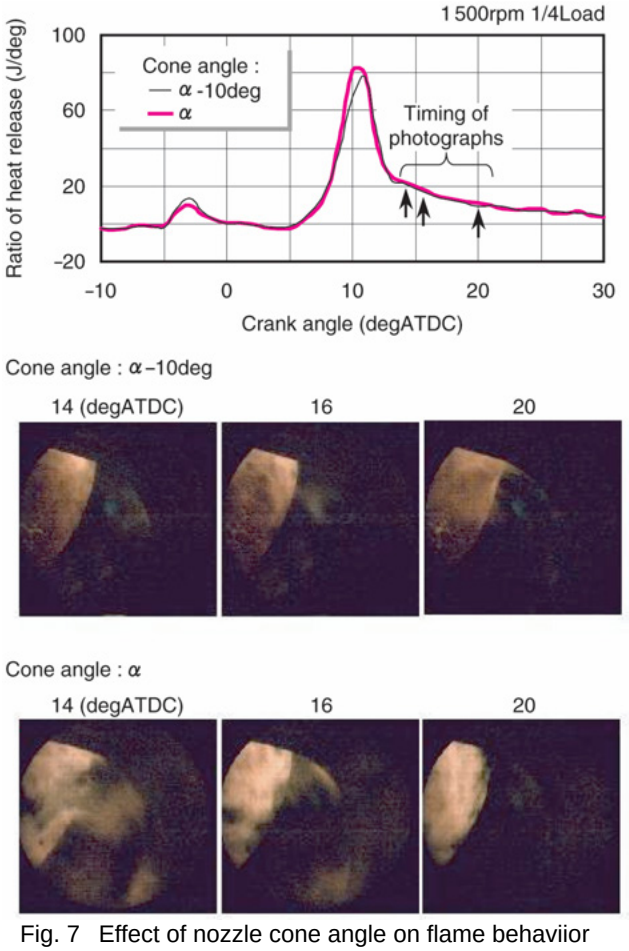


Fig. 7 Effect of nozzle cone angle on flame behaviior (CCD camera)

3.3. Reduced Emissions from Increased Dispersion Period of Air-fuel Mixture

In order to reduce NOx with a constant level of soot through increasing the amount of EGR, it is necessary to reduce the amount of fuel spray injected after the start of main combustion event. Therefore, as can be seen in Fig. 8, an indicator of the amount of fuel injected after the start of main combustion has been defined as θ_{eoi_soc}.

Figure 9 shows the relationship between θ_{eoi_soc} and NOx emissions, while varying the EGR ratio, the pilot injected amount, and the injection timing for the pilot as well as the main injections, under the condition of constant soot level. From these results, a shorter θ_{eoi_soc} enables increasing the EGR ratio and therefore NOx is reduced.

Figure 10 shows the relationship between the pilot heat release ratio (ratio of heat generated by pilot combustion and total heat generation) and $dP/d\theta_{max}$ for the same experiment.

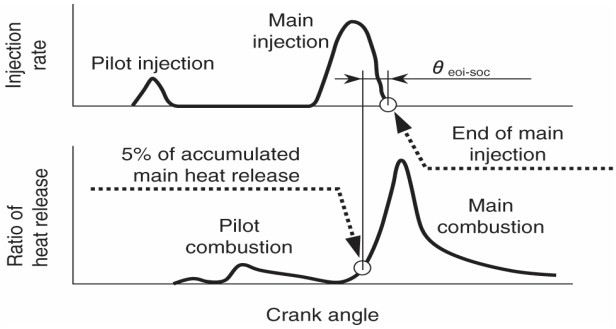


Fig. 8 Definition of θ_{eoi_soc}

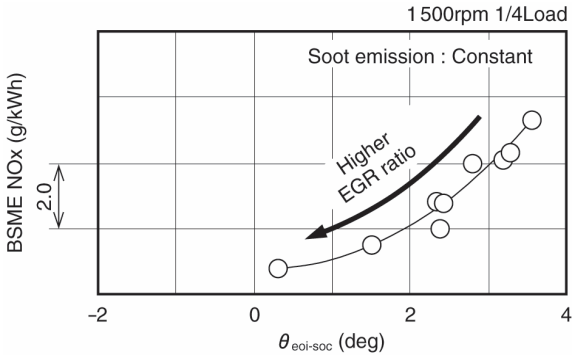


Fig. 9 Effect of θ_{eoi_soc} on NOx

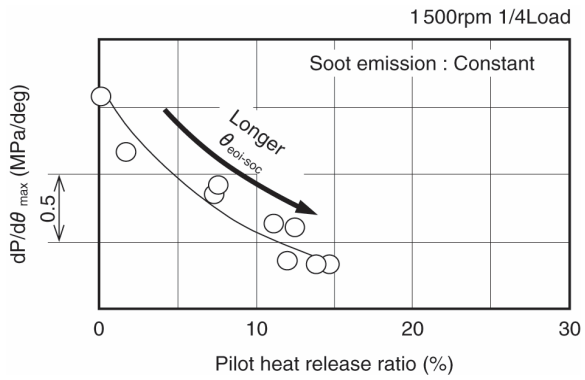


Fig. 10 Effect of pilot heat release ratio on dP/d θ_{max}

When the pilot heat release ratio is increased, $dP/d\theta_{max}$ does decrease, however, θ_{eoi_soc} is lengthened. In other words the pilot heat release ratio and θ_{eoi_soc} are inversely proportional.

It was considered that in order to shorten θ_{eoi_soc} in conjunction with an increase in the pilot heat release ratio, a reduction in the in-cylinder temperature would be effective. Therefore, with the combinations of compression ratio and EGR cooling shown in Table 2, testing was performed with changes made to the pilot injection amount and injection timing. In order to maintain fuel economy, the main injection timing was adjusted so that a constant start of main combustion event was maintained. In addition, the EGR ratio was adjusted to maintain a constant soot level.

Figure 11 shows the test results. Smaller compression ratios and higher efficiency of the EGR cooler lead to shorter θ_{eoi_soc} for the same pilot heat release ratio. As a result, as can be seen in Fig. 12, NOx was reduced for a constant $dP/d\theta_{max}$.

In order to analyze the phenomenon described above, combustion visualization tests and simulations were performed for a case where the compression ratio was 18.0 with an EGR cooler efficiency of 39% and a case with a compression ratio of 16.7 with an EGR cooler efficiency of 50%. EGR and injection timing were adjusted so that the soot and $dP/d\theta_{max}$ would be equal for each of the cases.

Table 2 Compression ratio and EGR cooler efficiency

NO.	Compression ratio	EGR cooler efficiency (%)
1	18.0	39
2	16.7	50
3	15.5	50
4	14.5	50

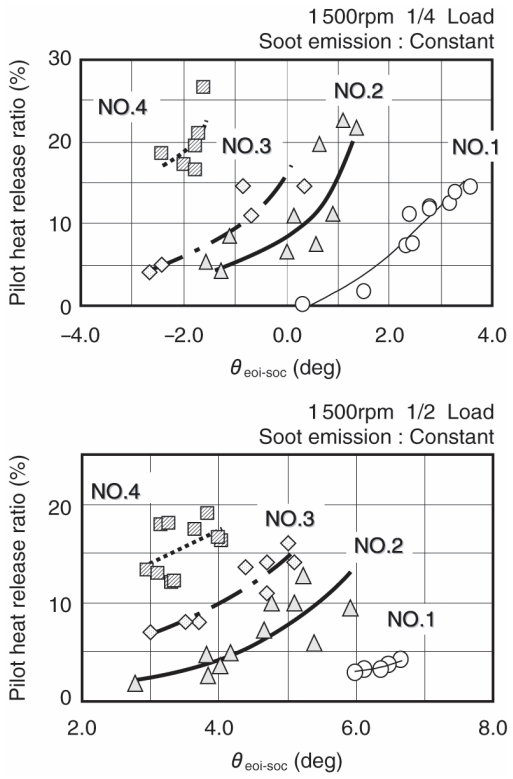


Fig. 11 Effect of compression ratio and EGR cooler efficiency

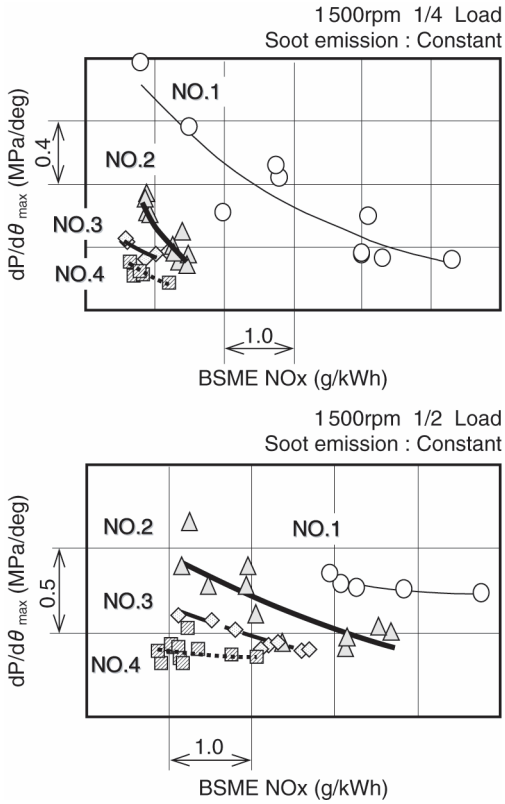


Fig. 12 Effect of compression ratio and EGR cooler efficiency on NOx and dP/dθ_{max}

The observation results using a CCD camera for both cases are shown in Figs. 13(a) and 14(a). The observation results of equipping the CCD camera with an I.I. are shown in Figs. 13(b) and 14(b). Also, the simulation results of the spray behavior are shown in Figs. 13(c) and 14(c).

For the case where the compression ratio is 18.0 with an EGR cooler efficiency of 39%, the pilot spray is ignited near the walls of the combustion chamber and combustion is occurring accompanied with a slight amount of luminous flame. From the photograph of the pilot combustion taken using I.I., active non-luminous combustion directed from the walls to the center of the combustion chamber can be seen. The main fuel spray directed towards the piston bowl wall is ignited before coming into contact with the walls of the piston bowl and was surrounded by luminous flames. This is considered due to the speeding up of the ignition of the main fuel spray as it was injected into the high temperature environment of the cylinder generated from the pilot combustion.

In comparison, for the case of a compression ratio of 16.7 with an EGR cooler efficiency of 50%, a weak non-luminous combustion is seen near the combustion chamber walls after the pilot spray struck the wall and a luminous flame during the main combustion is seen only after the main spray is completely finished. This phenomenon is considered to be due to low temperature combustion of the pilot spray near the walls, there was an increase in the delay in ignition of the main fuel spray.

It is considered that this suppresses the generation of soot, enabling an increase in the EGR ratio, therefore reducing NOx. In addition, it is estimated that because the

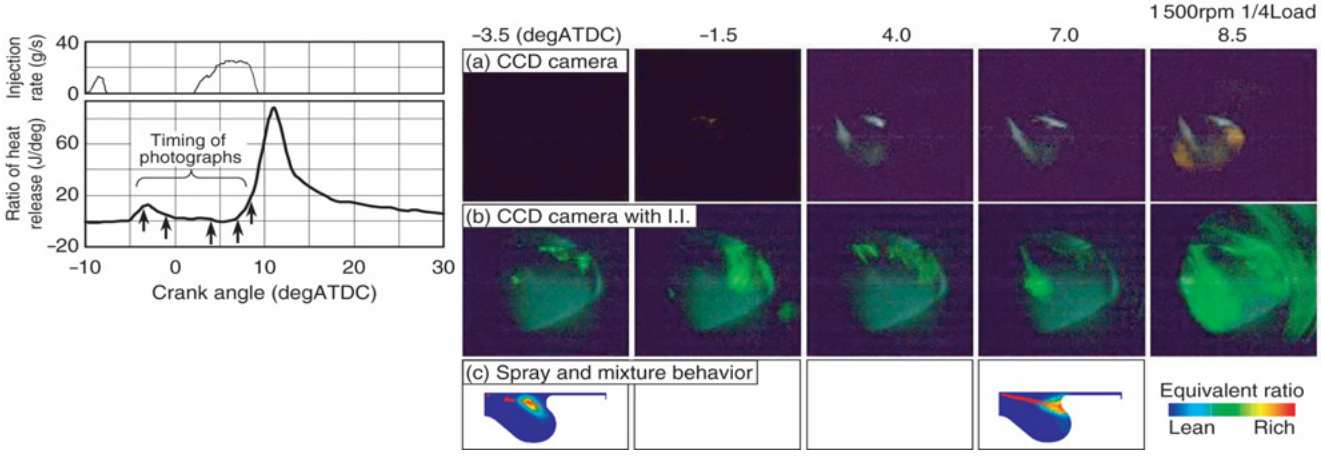


Fig. 13 ε18.0 flame behavior (CCD camera only and CCD camera with I.I.)

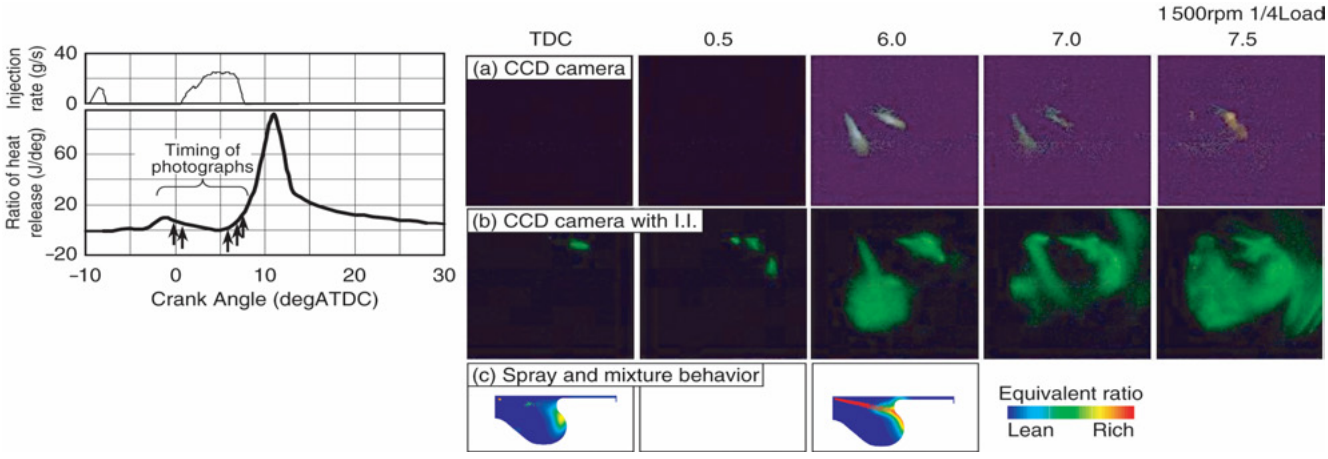


Fig. 14 ε16.7 flame behavior (CCD camera only and CCD camera with I.I.)

leading edge of the main fuel spray was ignited and the flame spread upstream, very rapid combustion was suppressed, enabling $dP/d\theta_{max}$ to be maintained.

It was found that it was possible to reduce NOx without causing $dP/d\theta_{max}$ to deteriorate through increasing the efficiency of the EGR cooler and reducing the compression ratio. However, because excessive reduction in the compression ratio increases the generation of white smoke, HC and CO while the engine is cold, as well as reducing fuel economy, the compression ratio for this engine was set at 16.7.

4. Performance of the New Engine

The main specifications of the engine were set according to the results as discussed in the previous section and are shown in Table 1. Figure 15 shows the full load performance of this engine. Also, Figs. 16 and 17 show fuel economy, combustion noise, and emissions performance at partial load. A Modern European diesel engine was used as a reference for comparison. The results show that this engine has a similar level of combustion noise while fuel consumption and emissions have been reduced.

This engine is being used in the European Accord starting last fall. Fuel economy, emission, and power output performance are shown in Figs. 18 and 19. In addition to the reduction in emissions described so far, the after-treatment system mounted under floor and directly beneath the engine has enabled this engine to meet 2005 European diesel exhaust emissions standards. And at the same time, while it belongs to 1 590 kg equivalent inertia weight class, it has achieved the fuel economy of a C category vehicle, 5.4L/100 km.

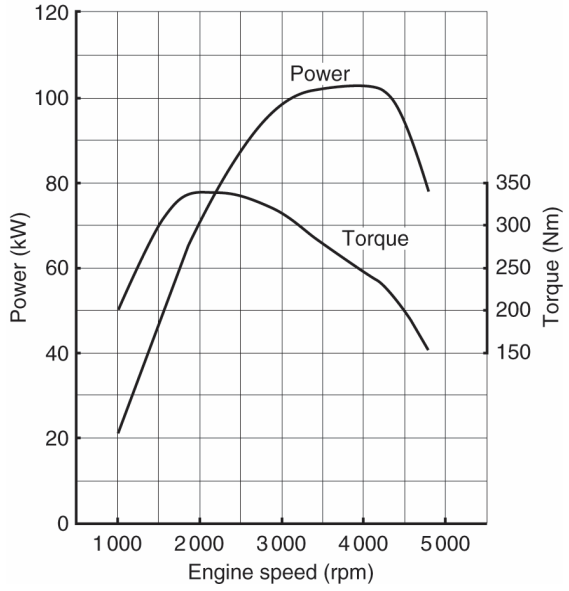


Fig. 15 Full load performance

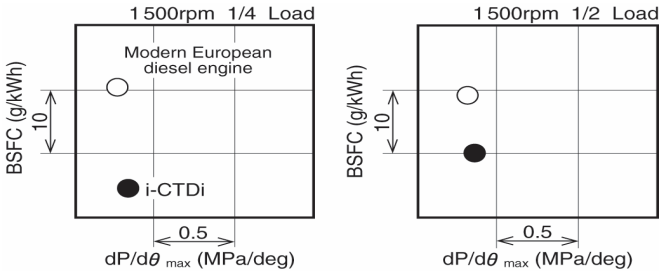


Fig. 16 BSFC and $dP/d\theta_{max}$ under partial load

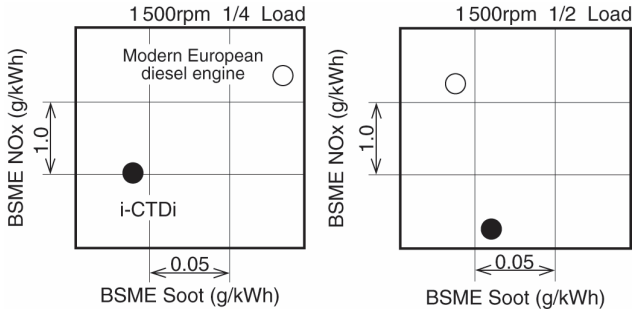


Fig. 17 NOx and soot under partial load

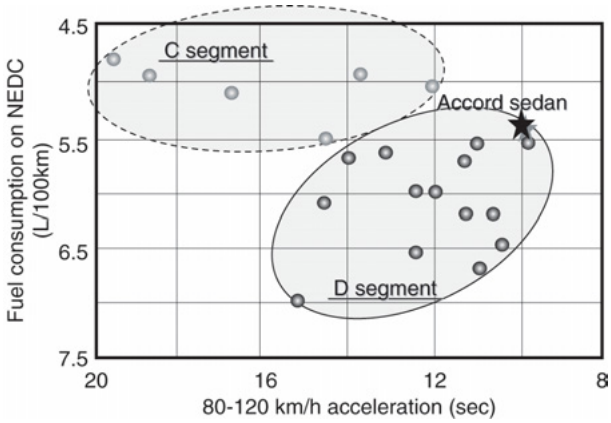


Fig. 18 Fuel consumption and performance of Accord sedan

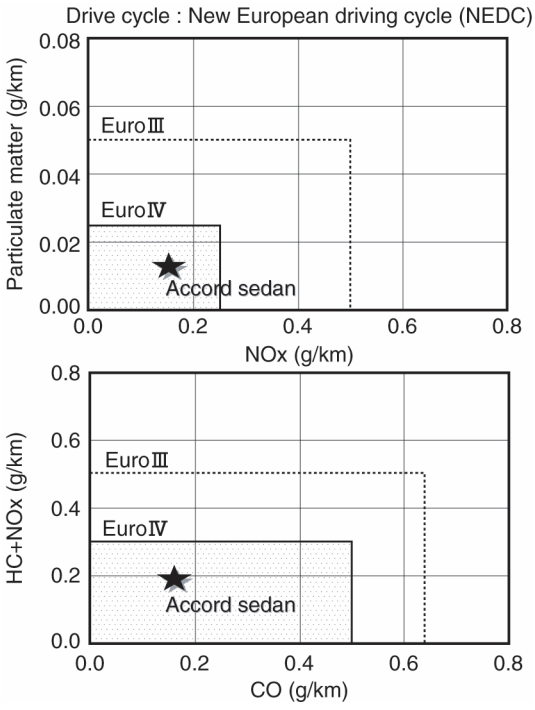


Fig. 19 Accord sedan emissions

5. Conclusion

With the prerequisites of low fuel consumption and low combustion noise, technology that meets the 2005 European emissions standards was developed. The items learned through this development are summarized below.

(1) Utilization of pilot injection and advancement of start of main combustion event enables both low fuel consumption and low combustion noise. The deterioration in generation of soot in conjunction with this can be reduced through the acceleration of the dispersion of the air-fuel mixture.
(2) Acceleration of the dispersion of the air-fuel mixture
  (a) Through dispersing an appropriate amount of fuel spray out of the piston bowl, a lean local air-fuel ratio is ensured, therefore generation of soot is reduced. As a result, it is possible to increase EGR enabling a reduction in NOx for an equivalent level of soot.
  (b) The reduction of $\theta_{\text{eoi-soc}}$ enables an increase EGR ratio, resulting in a reduction of NOx for an equivalent level of soot.
  (c) Increasing the pilot heat release ratio results in lowering $dP/d\theta_{max}$. However, because θeoi-soc gets longer, the amount of NOx for an equivalent level of soot increases.
  (d) In order to both shorten $\theta_{\text{eoi-soc}}$ and increase the pilot heat release ratio, reduction of the compression ratio and cooling of EGR is effective.
(3) This combustion technology is being utilized in the i-CTDi diesel engine that is used for the European Accord. While it belongs to a 1 590 kg equivalent inertia weight class vehicle, it meets the 2005 European emissions standards, and has achieved low combustion noise and a fuel economy of 5.4L/100 km.

References

(1) Quigley, M., Seguelong, T.: Series Application of a Diesel Particulate Filter with a Ceria-based Fuel-Borne Catalyst, SAE paper 2002-01-0436

(2) Nakatani, K., Hirota, S., Takeshima, S., Itoh, K., Dohmae, K.: Simultaneous PM and NOx Reduction System for Diesel Engines, SAE paper 2002-01-0957

(3) McDonald, J., Bunker, B.: Testing of the Toyota Avensis DPNR at U.S. EPA-NVFEL, SAE paper 2002-01-2877

(4) Walker, A. P., et al.: An Integrated SCR and Continuously Regenerative Trap System to Meet Future NOx and PM Legislation, SAE paper 2000-01-0188

(5) Kimura, S., Aoki, O., Kitahara, Y., Aiyoshizaw, E.: Ultra-Clean Combustion Technology Combining a Low-Temperature and Premixed Concept for Meeting Future Emission Standards, SAE paper 2001-1-0200

(6) Hasegawa, R., Yanagihara, H.: HCCI Combustion in Diesel Engine, SAE paper 2003-01-0745

(7) Akihama, K., Takatori, Y., Inagaki, K.: Mechanism of the Smokeless Rich Diesel Combustion by Reducing Temperature, SAE paper 2001-01-0655

(8) Shimazaki, N., Akagawa, H., Tsujimura, K.: An Experimental Study of Premixed Lean Diesel Combustion, SAE paper 1999-01-0181

(9) Takeda, Y., et al.: Emission Characteristics of Premixed Lean Diesel Combustion with Extremely Early Staged Fuel Injection, SAE paper 961163

(10) Walter, B., Gatellier, B.: Development of the High Power NADITM Concept Using Dual Mode Diesel Combustion to Achieve Zero NOx and Particulate Emissions, SAE paper 2002-01-1744

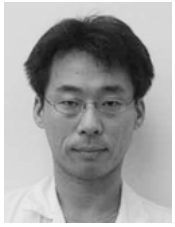
(11) Nandha, K. P., Abraham, J.: Dependence of Fuel-Air Mixing Characteristics on Injection Timing in an Early-Injection Diesel Engine, SAE paper 2002-01-0944

(12) Kanda, T., Sono, H., et al.: Study on Euro Ⅳ Combustion Technologies for Direct Injection Diesel Engine, SAE paper 2004-01-0113

■ Authors ■


Tomohiro KANDA


Shinichi KOBAYASHI


Ryuta MATSUI


Hiroshi SONO

Accurate Engine Speed Control Using Sliding Mode Algorithm

Yuji YASUI* Kanako SHIMOJO*
Mitsunobu SAITO* Hiroshi TAMAGAWA*

ABSTRACT

Accurate engine speed control has been required to improve the shift quality of automatic transmissions. However, engine dynamics dramatically change with engine load and with engine aging. Therefore, conventional controls such as PID control cause large overshoots and therefore cannot ensure accurate controllability. A control composed of a sliding-mode controller and an adaptive disturbance observer was designed and applied to engine speed control to address these issues. The new control had high robustness against changes in engine dynamics and excellent ability to suppress overshoot. In addition, it provided accurate and rapid engine speed control under all engine conditions.

1. Introduction

Accurate and rapid engine speed control is increasingly required to improve the shift quality of automatic transmissions. However, engine dynamics dramatically change with engine load and with engine aging. Variations between similar engines will produce different engine dynamics also. Therefore, engine speed control requires robustness against these changes.

However, most conventional engine speed control has been open loop control using tables and maps or PID control. Figure 1 shows the results of engine speed control using PI control. Here, the engine speed N_e overshoots the target value N_{er} by a significant margin. This indicates that conventional control cannot achieve sufficient controllability.

On the other hand, sliding mode control[1], which is a type of robust control, has been applied to engines[2, 3] and other devices[4] in recent years.

Therefore, a new control method composed of a sliding-mode controller (SMC) and an adaptive disturbance observer was designed, and applied to engine speed control in this research.

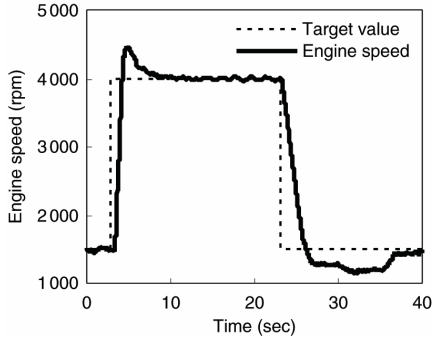


Fig. 1 Step response result using PI controller

* Tochigi R&D Center

2. Engine Speed Control Challenges

Table 1 shows the specifications of the prototype engine used for the vehicle tests, and Fig. 2 shows the throttle angle T_h used to regulate the engine speed N_e to each N_{er} value. This figure shows a correlation between N_e and T_h in accordance with the electrical load level and the engine warm-up condition, but the T_h needed to regulate each N_{er} varies widely. For example, when T_h is around 8 degrees, N_e is approximately 4 000 rpm at a low electrical load, or approximately 3 000 rpm at a high electrical load.

This means that conventional open loop control may cause a significant steady-state error depending on the load conditions. A control method using scheduled maps and tables according to the engine load and warm-up condition can also be employed, but it cannot compensate for steady-state error caused by the engine torque characteristic changes from aging and variation between similar engines.

On the other hand, when PID control and adaptive sliding mode control[2], which are types of closed loop controls, are applied to engine speed control, the steady-state error of N_e from N_{er} can be compensated.

However, each of these methods uses an integrator to suppress the steady-state error, so overshoot occurs as shown in Fig. 1.

Table 1 Specifications of experimental power train

Engine	In-line 3, 1.0 liter, SOHC
Air device	Electrical controlled throttle
Transmission	6-speed automated manual transmission

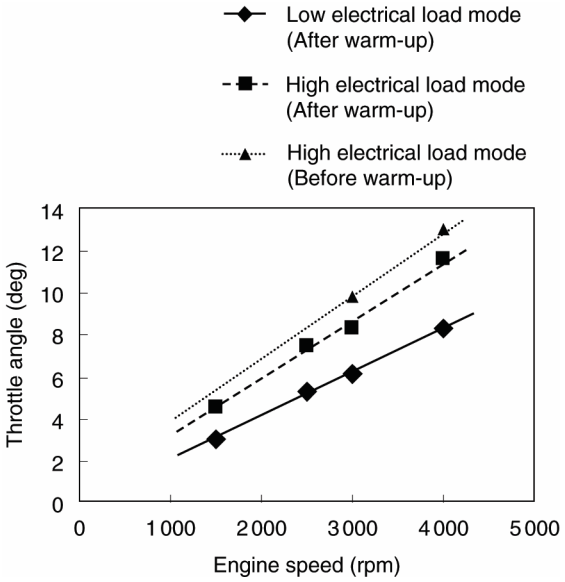


Fig. 2 Correlation of throttle angle with engine speed under several load conditions

3. Approach

A control system that can compensate for steady-state error caused by changes in engine dynamics due to aging condition and variation, while at the same time suppressing overshoot, was constructed as follows.

First, the engine dynamics from T_h to N_e were modeled not by using maps and tables, but by focusing on frequency characteristics and using a discrete-time auto-regressive exogenous (ARX) model[5].

Next, the adaptive sliding mode control input was calculated as the sum of the three inputs of the equivalent control input U_{eq}, reaching law input U_{rch} and adaptive law input U_{adp} as shown in Fig. 3. Here, U_{eq} is calculated based on N_e and N_{er}, and U_{rch} and U_{adp} are calculated as the proportional element and integral element, respectively, of the switching function σ which is calculated according to the error between N_e and N_{er}. In addition, U_{adp} functions to compensate for changes in the engine dynamics, but since U_{adp} is the integral element of σ, it is also a cause of N_e overshoot relative to N_{er}.

Therefore, this research eliminated U_{adp} from the sliding-mode controller in Fig. 3 and added an adaptive disturbance observer in its place that calculates the estimated disturbance value (c_1) based on N_e and the control input. In addition, the U_{eq} calculation formula was changed to include c_1 in order to compensate for changes in the engine dynamics. Figure 4 shows the configuration of this new sliding-mode controller, and the details are described below.

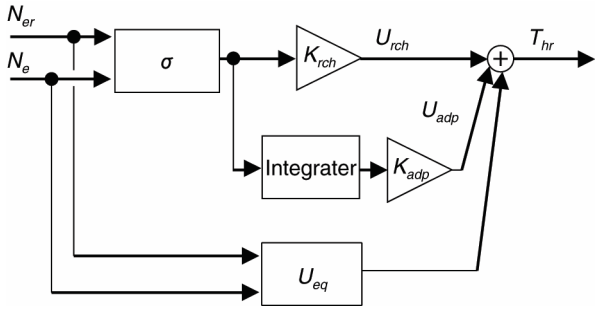


Fig.3 Sliding-mode controller with adaptive law input

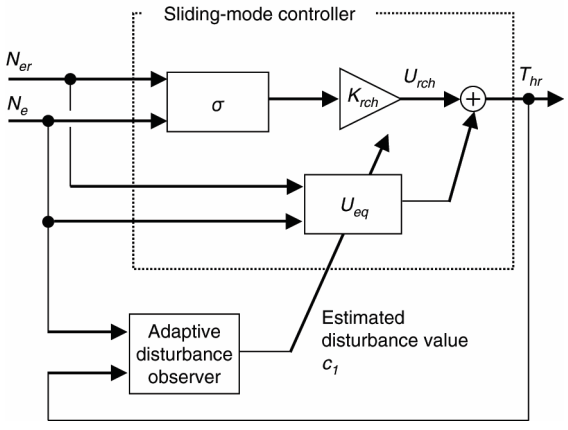


Fig.4 Sliding-mode controller with adaptive disturbance observer

4. Controller Design

4.1. Modeling of the Engine

Figure 5 shows the N_e response characteristics relative to changes in T_h, in other words the engine frequency characteristics, at 1 500, 2 000, and 3 000 rpm. As shown in this figure, the engine frequency characteristics indicate low-pass characteristics, the gains of which are decreased at frequencies above 1.0 Hz. The gains of the frequency characteristics at passband frequencies are increased according to increases of N_e.

Based on these observations, the engine was modeled using the following equation.

$$N_e(k+1) = a_1 N_e(k) + a_2 N_e(k-1) + b_1 T_{hr}(k) + b_2 T_{hr}(k-1) \quad (1)$$

a_1, a_2, b_1, b_2 : Model parameters
T_{hr} : Throttle target value
k : Control time

Figure 6 shows the frequency characteristics of the engine and the model using the model parameters shown in Table 2 at 1 500 rpm. This shows that the model is able to accurately express the low-pass characteristics of the controlled object.

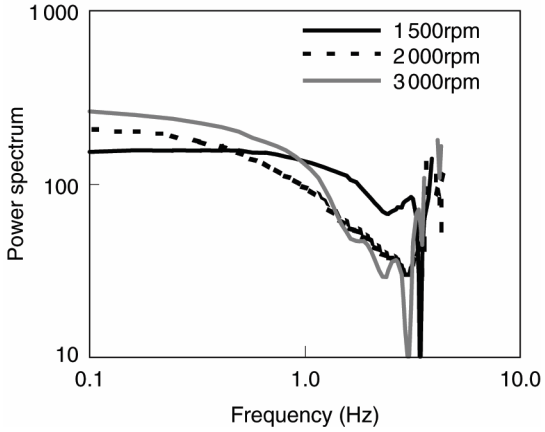


Fig. 5 Frequency characteristics under several engine speed conditions

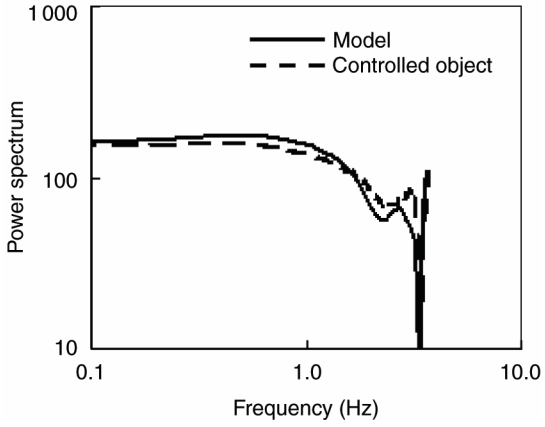


Fig. 6 Frequency characteristics comparison between model and controlled object at 1 500 rpm

Table 2 Model parameters of controlled object model at 1 500rpm

a_1	a_2	b_1	b_2
1.83	-0.84	34.53	-31.84

4.2. Adaptive Disturbance Observer

As N_{eh} is defined as the estimated value of N_e by Eq. (2), which was obtained by shifting Eq. (1) to the previous control time-step and adding c_1, the adaptive disturbance observer estimates c_1 to minimize the difference between N_{eh} and N_e.

$$N_{eh}(k) = a_1 N_e(k-1) + a_2 N_e(k-2) + b_1 T_{hr}(k-1) + b_2 T_{hr}(k-2) + c_1(k-1) \quad (2)$$

c_1 : Estimated disturbance value

Here, c_1 is estimated as shown in the equation below using the fixed gain method that is used by adaptive control [6].

$$c_1(k) = c_1(k-1) + \frac{P}{1+P} e_{dov}(k)$$
$$e_{dov}(k) = N_e(k) - N_{eh}(k) \quad (3)$$

P: Estimated gain

4.3. Sliding Mode Controller

When using an adaptive disturbance observer, the control input T_{hr} of the sliding-mode controller is calculated as the sum of the two inputs U_{eq} and U_{rch} as follows.

$$T_{hr}(k) = U_{eq}(k) + U_{rch}(k) \quad (4)$$

At this time, by defining σ and the error E_{ne} as shown in Eqs. (5) and (6), U_{rch} can be calculated using Eq. (7).

$$\sigma(k) = E_{ne}(k) + SE_{ne}(k-1) \quad (5)$$

$$E_{ne}(k) = N_e(k) - N_{er}(k) \quad (6)$$

S: Switching function setting parameter

$$U_{rch}(k) = \frac{-K_{rch}}{b_1} \sigma(k) \quad (7)$$

K_{rch}: Reaching law gain

In addition, U_{eq} is defined as the input that restricts the combination of the errors $E_{ne}(k)$ and $E_{ne}(k-1)$ (hereafter, the "state") onto the line indicated by $\sigma = 0$, in other words, the switching line. Therefore, U_{eq} can be obtained as shown in Eq. (9) by substituting the left side of the conditional formula shown in Eq. (8) into Eq. (2) and solving for T_{hr}.

$$\sigma(k+1) = \sigma(k) \tag{8}$$

$$\begin{aligned} U_{eq}(k) = \frac{1}{b_1} \{ & (1 - S - a_1)N_e(k) \\ & + (S - a_2)N_e(k-1) \\ & + N_{er}(k+1) \\ & + (S - 1)N_{er}(k) \\ & - SN_{er}(k-1) \\ & - b_2 T_{hr}(k-1)\} \\ & - c_1(k)\} \end{aligned} \tag{9}$$

Here, the U_{eq} obtained using Eq. (9) adds the final term c_1 which serves to compensate for disturbance to the U_{eq} when also using U_{adp}, as shown in Fig. 3.

5. Simulation Results

A virtual engine was created by substituting the model parameters shown in Table 2 into the block diagram shown in Fig. 7 in order to simulate and compare the disturbance suppression performance of SMC using U_{adp} and SMC using an adaptive disturbance observer. Disturbance d_1 which estimates the variation and aging-induced changes in the engine torque characteristics, and disturbance d_2 which estimates the electrical load and other factors were applied to this virtual engine as shown in Fig. 8. In addition, N_{er} was set at 2 000 rpm in the simulation.

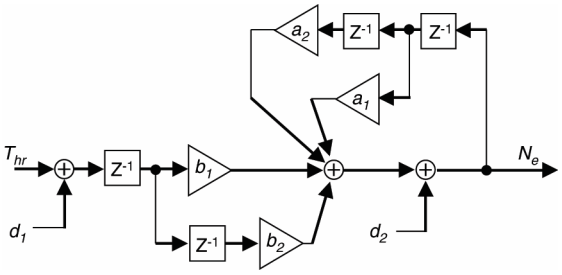


Fig. 7 Controlled object model for comparison between conventional and newly designed sliding-mode controller

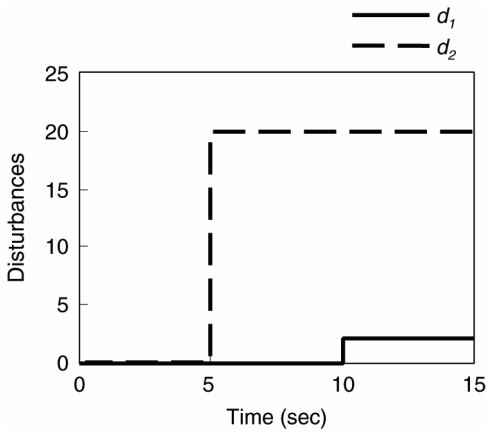


Fig. 8 Disturbances inputted to controlled object model

The simulation results showed that when U_{adp} was used, the integral characteristics of U_{adp} produced both oscillatory converging behavior and significant overshoot in response to both d_1 and d_2 as shown in Fig. 9.

On the other hand, when an adaptive disturbance observer was used, slight overshoot occurred in response to d_2, but the settling time after the disturbance was about half that when using U_{adp}, and there was also no oscillatory behavior, as shown in Fig. 10.

These results indicate that the SMC using an adaptive disturbance observer provides superior overshoot suppression capability and a faster response.

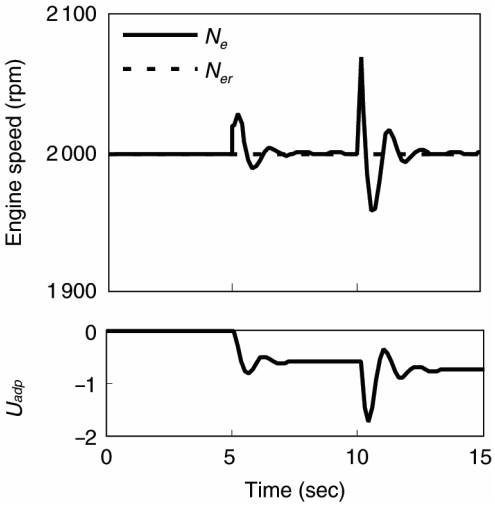


Fig. 9 Simulation results for sliding-mode controller with U_{adp}

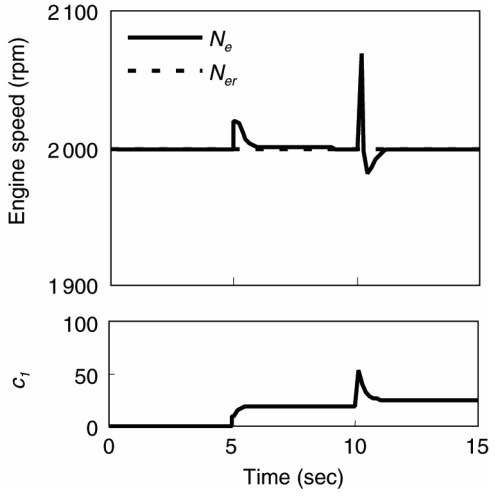


Fig. 10 Simulation results for sliding-mode controller with adaptive disturbance observer

6. Test Results

6.1. Comparison of Step Response

The step responses for PID control, SMC using the adaptive law input, and SMC using an adaptive disturbance observer were compared using the engine described in Table 1. Figure 11 shows the results.

These results show that the SMC using an adaptive disturbance observer provides superior overshoot suppression capability compared to the other controls that have integral elements.

6.2. Robustness against Engine Warm-up Conditions

Figure 12 compares the N_e step responses obtained by the SMC using an adaptive disturbance observer under the conditions before warm-up (immediately after engine startup), and after warm-up.

These results show that the SMC using an adaptive disturbance observer exhibits a stable target value tracking response regardless of the warm-up conditions.

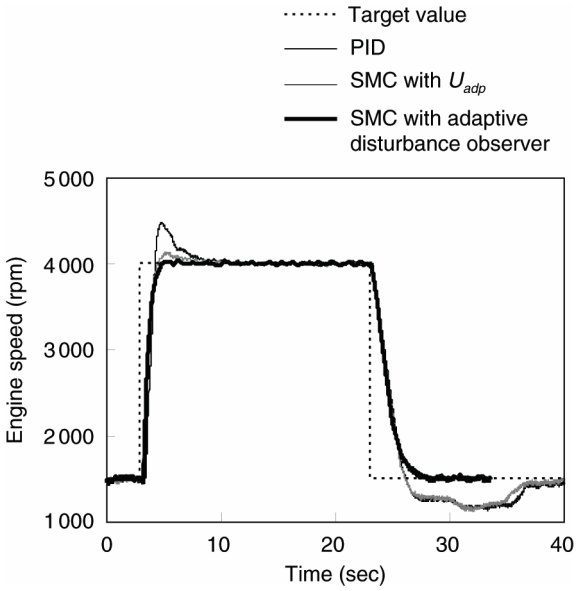


Fig. 11 Step responses controlled by PID, SMC, with U_{adp} and SMC with adaptive disturbace observer

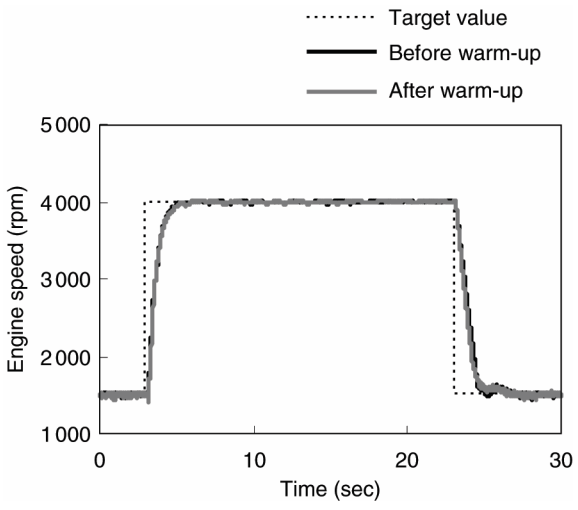


Fig. 12 Step responses before and after warm-up

6.3. Robustness against Engine Torque Characteristic Error

Figure 13 shows the control results when errors of +50%, 0%, and –50% are applied to the throttle angle in order to evaluate the robustness of the SMC using an adaptive disturbance observer against engine torque characteristic error. In addition, the control results for the SMC using U_{adp} with a throttle angle error of 0% are also shown.

Even when an error of –50% was applied, the SMC using an adaptive disturbance observer realized a settling time equivalent to that for the SMC using U_{adp} with 0% error, and also exhibited a smaller overshoot than the SMC using U_{adp} when an error of +50% was applied.

This confirms that the SMC using an adaptive disturbance observer has superior robustness.

7. Conclusion

Sliding mode control using an adaptive disturbance observer was applied to engine speed control, and the following results were obtained:

(1) Overshoot was dramatically reduced compared to controls that have integral elements for compensating steady-state error.
(2) Stable controllability was realized that is independent of the engine warm-up state.
(3) Robustness against engine variation and aging-induced changes in the engine torque characteristics was dramatically enhanced.

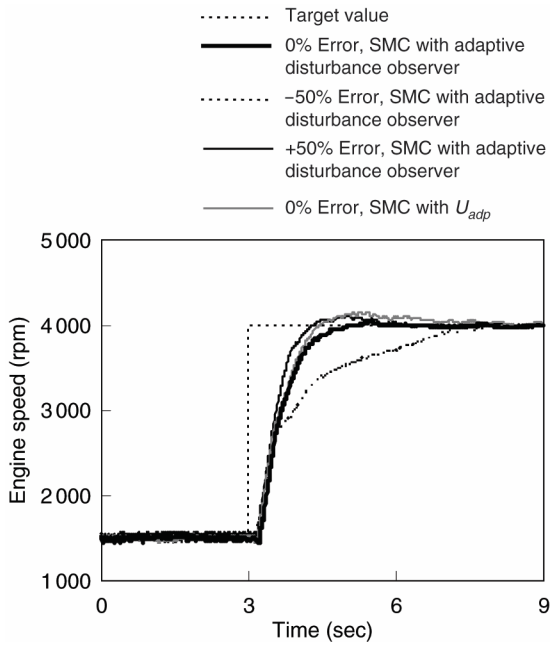


Fig. 13 Robustness against engine torque error

References

(1) Nonami, K., Tian, H.: Sliding Mode Control, Corona Publishing Co., Ltd., p. 263 (1994)

(2) Yasui, Y., Akazaki, S., Ueno, M., Iwaki, Y.: Secondary O2 Feedback Using Prediction and Identification Sliding Mode Control, SAE Paper 2000-01-0936 (2000)

(3) Kajitani, M., Nonami, K.: High Performance Idle Speed Control Applying the Sliding Mode Control With H Robust Hyperplane, SAE Paper 2001-01-0263 (2001)

(4) Hashimoto, E., Ishiguro, T., Yasui, Y., Akazaki, S.: High Reliability Electronic Throttle System , SAE Paper 2003-01-0708 (2003)

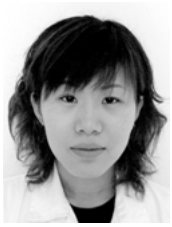
(5) Adachi, S.: Yuza no Tame no Shisutemu Doutei Riron, Corona Publishing Co., Ltd., p. 222 (1993) (in Japanese)

(6) Terao, M., Kanai, K.: Robasuto Tekiou Seigyo Nyumon, Ohm Publishing Co., Ltd., p. 187(1989) (in Japanese)

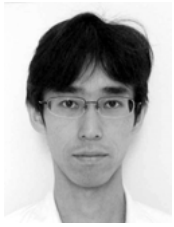
■ Authors ■



Yuji YASUI



Kanako SHIMOJO



Mitsunobu SAITO



Hiroshi TAMAGAWA

Damper Control Using a Sliding Mode Algorithm

Kanako SHIMOJO* Yuji YASUI*
Eijiro SHIMABUKURO* Yoshihisa IWAKI*

ABSTRACT

Sliding mode algorithms are highly responsive and robust, leading to their use in air-fuel ratio and device control systems. Altering the switching line gradient enables their ability to suppress disturbance to be freely set. However, to date no applied research has been conducted to verify these characteristics. In the research presented in this paper, the ability of a sliding mode algorithm to suppress disturbance was lowered to enable the construction of a high-compliance servo control system used for shift control in an automated manual transmission where compliance control is required during shifting. The sliding mode algorithm was employed in position control to ensure contact between the sleeve and the synchronizer ring and force control to enable the synchronization of the main shaft and counter-shaft through sleeve force. The compliance established between the sleeve and the synchronizer ring by this means has enabled the previously required mechanical buffer to be eliminated, and shift time has been reduced to 350msec. In addition, stabilizing sleeve force has suppressed bouncing and stoppage of the sleeve and failure of the synchronizer ring during shifting.

1. Introduction

Sliding mode control[1] (SMC) is highly responsive and robust, and has been used for air-fuel ratio control[2), (3)], device control[4], and other systems. In addition, SMC has the ability to freely set the disturbance suppression characteristic of the system by altering the gradient, V_{POLE}, of the switching function. However, no applied research had previously been conducted on this ability. This research focused on this characteristic, by way of a controller to dampen impacts (damper control) and to lower the disturbance suppression characteristic by altering V_{POLE}.

Figure 1 shows an outline of the variable-speed gear[5), (6)] used as the controlled object in this research. The shift rod is driven by the motor, and shifting is performed by coupling the sleeve to the next gear via the fork. In automated manual

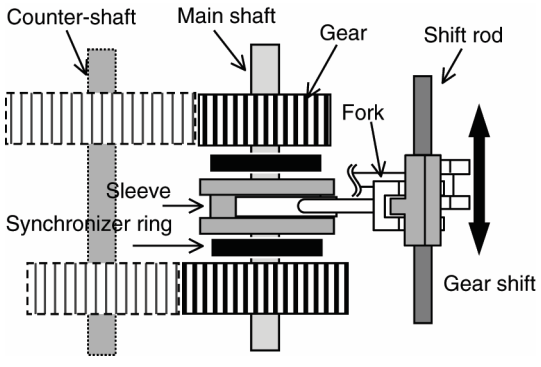


Fig. 1 Outline of AMT mechanism

* Tochigi R&D Center

transmissions (AMT), the sleeve contacts the synchronizer ring in the shortest time possible during shifting, then a certain pressing force is applied to the synchronizer ring to synchronize the revolution of the main shaft and counter-shaft. Often when the sleeve contacts the synchronizer ring the sleeve bounces off the synchronizer ring, or the sleeve is pressed into the gear by an excessive impact force before synchronizing with the synchronizer ring. Different methods have been used to counter this, such as reducing the variation at the target position to lower the sleeve movement speed just before contact between the synchronizer ring and the sleeve, or recently by adding a damper system to mechanically dampen the impact force. However, the former method increased the shifting time and the latter one resulted in a more complex system of additional weight and size.

This research applied SMC to AMT in order to shorten the shifting time without the use of a mechanical damper system that was formerly considered necessary. In addition, this also suppressed bouncing and stoppage of the sleeve and prevented failure of the synchronizer ring when shifting gears.

2. Features of Sliding Mode Control

In SMC, the deviation E(k) is defined as the difference between actual position P(k) and target value of controlled object P_{cmd} (k) in Eq. (1), and the switching function σ(k) by Eq. (2).

$$E(k) = P(k) - P_{cmd}(k) \tag{1}$$

$$\sigma(k) = E(k) + V_{POLE}E(k-1) \tag{2}$$

Figure 2 shows the phase plane that has E(k) and E(k-1) as the respective coordinate axes. The straight line indicates that the switching function σ is zero, which is called the switching line on the phase plane (see Fig. 2).

SMC restrains the combination of E (k) and E (k–1) (the deviation state) to the switching line, and then the deviation state converges toward the origin of the phase plane along the switching line. In other words, the deviation E(k) converges to zero. The switching line is expressed by Eq. (3) as the relationship between E(k) and E(k-1), and V_{POLE} is set within the range in Eq. (4).

$$E(k) = -V_{POLE}E(k-1) \tag{3}$$

$$-1 < V_{POLE} < 0 \tag{4}$$

Therefore, when the deviation state reaches the switching line after the reaching mode (see Fig. 2), it then converges towards the origin of the phase plane over time. This behavior on the switching line is called sliding mode (see Fig. 2), and the convergence speed of the deviation state toward the origin can be set by V_{POLE}.

As an example of this, Fig. 3 shows the change in the disturbance suppression characteristic according to V_{POLE} when step disturbance is applied. The convergence speed of the deviation increases as V_{POLE} approaches 0, and decreases as V_{POLE} approaches –1. This indicates that the compliance can be set by the gradient of the switching line, V_{POLE}.

In this research, the disturbance suppression characteristic is lowered to allow the construction of a high-compliance servo system, and SMC is applied to the shift control of AMT which requires damper control during shifting. This attempt aimed to perform the damping operation in a short period of time without the use of a mechanical damper system. Consequently, V_{POLE} is set to a small value in order to lower the disturbance suppression characteristic when the sleeve contacts with the synchronizer ring. This makes it possible to electrically provide compliance between the sleeve and the synchronizer ring. These details are described below.

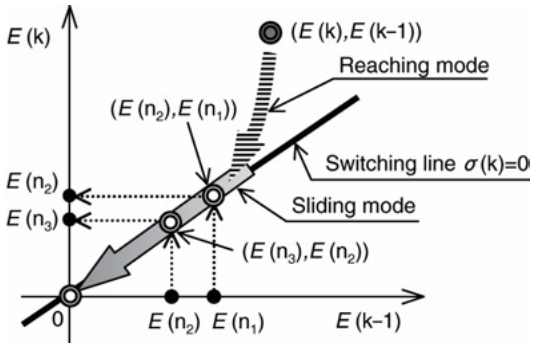


Fig. 2 Sliding mode

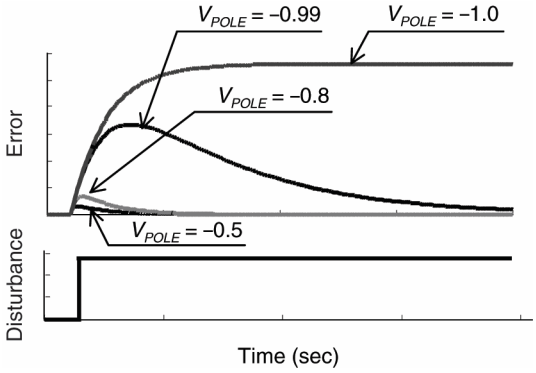


Fig. 3 Effect of changed V_{POLE}

3. Modeling the Shift Mechanism

Figure 4 shows the contact behavior between the sleeve and the synchronizer ring modeled as a collision between an inertial system and a spring-mass system. Here the synchronizer ring is viewed as a spring-mass system having a high stiffness K_{sc}, the motor, fork and other elements are viewed as the inertial system J_m.

Equation (5) is an equation of motion for inertial system J_m which takes into account the reaction force F_{sc} from the synchronizer ring and the back electromotive force.

$$J_m \dot{\omega} = \frac{K_m(V_{in} - K_m'\omega)}{R_m} - R_{sc} F_{sc} \tag{5}$$

J_m : Mass of motor, sleeve, fork and shift rod
V_{in} : Input voltage
ω : Revolution speed of motor
K_m : Torque constant
K_m' : Back electromotive force constant
R_m : Transformation coefficient of torque
R_{sc} : Gear ratio of revolution angle of motor and inertial system

On the other hand, the relationship between the revolution speed ω and revolution angle θ of the motor and the sleeve position P_{sc} is obtained by Eq. (6).

$$\begin{cases} P_{sc} = R_{sc}\theta \\ \dot{P}_{sc} = R_{sc}\dot{\theta} = R_{sc}\omega \quad \therefore \ \omega = \dfrac{\dot{P}_{sc}}{R_{sc}} \\ \ddot{P}_{sc} = R_{sc}\dot{\omega} \quad \therefore \ \dot{\omega} = \dfrac{\ddot{P}_{sc}}{R_{sc}} \end{cases} \tag{6}$$

By substituting Eq. (6) into Eq. (5) and rearranging, a continuous-time model is expressed by Eq. (7).

$$\ddot{P}_{sc} = \frac{-K_m K_m'}{J_m R_m}\dot{P}_{sc} + \frac{K_m R_{sc}}{J_m R_m} V_{in} - \frac{R_{sc}^2 R_m}{J_m R_m} F_{sc} \tag{7}$$

In order to express Eq. (7) as a discrete-time model, the state variable P_{sc} is expressed as shown in Eq. (8).

$$x_1 = P_{sc}, \ x_2 = \frac{dx_1}{dt}\dot{P}_{sc}, \ \frac{dx_2}{dt} = \ddot{P}_{sc} \tag{8}$$

Equation (8) was then substituted into Eq. (7). Here, with the sampling period defined as T, the continuous-time model in Eq. (7) is transformed by Euler approximation as shown in Eq. (9).

$$\begin{aligned} x_1(k+1) = &\left(2 - \frac{K_m K_m'}{J_m R_m}T\right)x_1(k) - \left(1 - \frac{K_m K_m'}{J_m R_m}T\right)x_1(k-1) \\ &+ \frac{K_m R_{sc}}{J_m R_m}T^2 V_{in}(k) - \frac{R_{sc}^2}{J_m}T^2 F_{sc} \end{aligned} \tag{9}$$

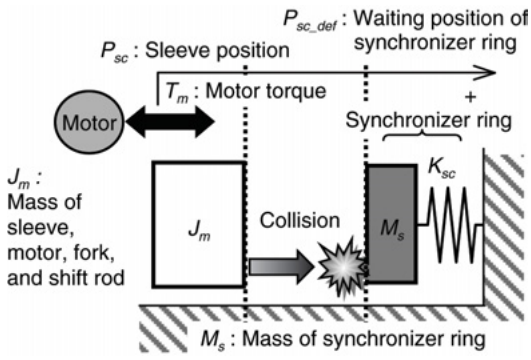


Fig. 4 Modeling of shift mechanism

Therefore, the discrete-time model is expressed as the Auto-Regressive with eXgeneous (ARX) model[7] shown in Eq. (10).

$$P_{sc}(k+1) = a_1 P_{sc}(k) + a_2 P_{sc}(k-1) + b_1 V_{in}(k) + d \tag{10}$$

$$\begin{cases} a_1 = 2 - \dfrac{K_m K_m'}{J_m R_m}T, \ a_2 = -1 + \dfrac{K_m K_m'}{J_m R_m}T, \\ b_1 = \dfrac{K_m R_{sc}}{J_m R_m}T^2, \ d = \dfrac{R_{sc}^2}{J_m}T^2 F_{sc} \end{cases} \tag{11}$$

The model parameters a_1, a_2, and b_1 in Eq. (11) are identified by the least squares method based on the input voltage V_{in} (V) and the sleeve position P_{sc} (mm) data.

4. Control Design

4.1. Control Requirements

The control requirements for the motorized AMT shift actuator are as follows:

(1) Tracking performance to the target value
(2) Prevention of sleeve bounce, stoppage, and collision
(3) Synchronization of main shaft and counter-shaft revolutions

4.2. Control System Configuration

The synchronizer ring control system is comprised of a V_{POLE} scheduler block, a target value calculation block and a compliance controller as shown in Fig. 5.

4.3. Mode Judgment

The sleeve behavior during shifting is classified into the following modes:

MODE1: Shift command - Synchronizer ring waiting position
MODE2: Contact with synchronizer ring - Synchronization of main shaft and counter-shaft revolutions
MODE3: Engagement after synchronization - End of shifting operation

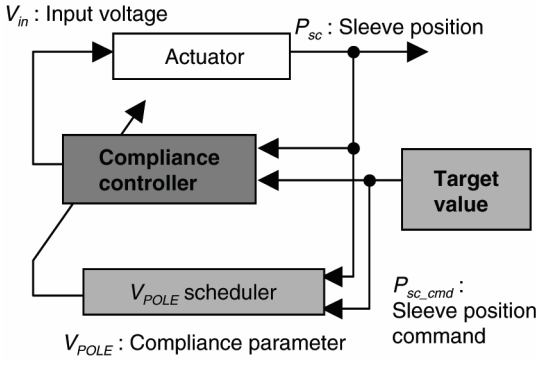


Fig. 5 Block diagram of compliance controller

The mode judgment conditions are given by the sleeve position. However, when shifting from MODE1 to MODE2, P_{sc} variation DP_{sc} is used for the mode judgment shown in Eq. (12).

$$DP_{sc}(k) = P_{sc}(k) - P_{sc}(k-1) \tag{12}$$

When the value DP_{sc_wv} obtained by wavelet transformation of Eq. (12) exceeds the MODE2 judgment threshold value W_{mode2}, the system judges that revolution synchronization has started and shifts to MODE2. The mode judgment conditions for each mode are as follows.

MODE1: $P_{sc} < P_{sc\_def}$
MODE2: $P_{sc} > P_{sc\_def}$ and $DP_{sc\_wv} < W_{mode2}$
MODE3: $P_{sc} > P_{sc\_mode3}$

DP_{sc_wv} : Wavelet transformed value of DP_{sc}
W_{mode2} : MODE2 judgment threshold value
P_{sc_mode3} : MODE3 judgment threshold value (sleeve position)

Wavelet transformation is used to block frequency components of the Nyquist frequency or higher, and to amplify and output the low-frequency component gain. This is an effective filtering method for extracting the low-frequency range behavior of controlled objects with high levels of backlash and friction, such as transmissions. The wavelet transform algorithm is comprised as shown in Fig. 6, and performs filtering by repeating the process of half band low-pass filter G and the data decimation processing two times.

4.4. Sliding Mode Controller

4.4.1. V_{POLE} setting

As shown in Fig. 7, V_{POLE} is set to a large value (< 0) to enhance the tracking performance of the actual position P_{sc} to the target value P_{sc_cmd} and to raise the disturbance suppression characteristic until the sleeve contacts the synchronizer ring.

In addition, when the sleeve reaches the synchronizer ring waiting position P_{sc_def}, V_{POLE} is set to a value near –1 to lower the disturbance suppression characteristic in preparation for contact with the synchronizer ring and protect the synchronizer ring. Therefore, V_{POLE} is set as follows in each mode.

MODE1: Large V_{POLE}: High convergence speed

MODE2: Small V_{POLE}: High impact damping ability

MODE3: Large V_{POLE}: High convergence speed

4.4.2. Derivation of the control inputs

The control input V_{in} of the sliding mode controller is obtained by Eq. (13). V_{in} is expressed as the sum of the three inputs of the equivalent control input U_{eq}, reaching law input U_{rch}, and adaptive law input U_{adp}.

$$V_{in}(k) = U_{eq}(k) + U_{rch}(k) + U_{adp}(k) \tag{13}$$

The equivalent control input U_{eq} is used to restrict the deviation state to the switching line. Strictly speaking, U_{eq} holds the deviation state at an arbitrary position on the phase plane.

U_{eq} is calculated as a value that satisfies Eq. (14).

$$\sigma(k+1) = \sigma(k) \tag{14}$$

Here, $\sigma(k)$ is the switching function, and is defined by Eq. (16) using the deviation $E_{sc}(k)$ obtained from the actual sleeve position and the sleeve position target value in Eq. (15).

$$E_{sc}(k) = P_{sc}(k) - P_{sc\_cmd}(k) \tag{15}$$

$$\sigma(k) = E_{sc}(k) + V_{POLE}E_{sc}(k-1) \tag{16}$$

Substituting Eq. (10), (15) and (16) into Eq. (14) and rearranging, U_{eq} is obtained as shown in Eq. (17).

$$\begin{aligned} U_{eq}(k) = \frac{1}{b_1}\{&(1 - V_{POLE} - a_1)P_{sc}(k) + (V_{POLE} - a_2)P_{sc}(k-1) \\ &+ P_{sc\_cmd}(k+1) + (V_{POLE} - 1)P_{sc\_cmd}(k) \\ &- V_{POLE}P_{sc\_cmd}(k-1)\} \end{aligned} \tag{17}$$

The reaching law input U_{rch} is used to converge the deviation state toward the switching line and is expressed by Eq. (18).

$$U_{rch}(k) = -\frac{K_{rch}}{b_1}\sigma(k) \tag{18}$$

K_{rch}: Reaching law gain

The adaptive law input U_{adp} is used to suppress modeling error and disturbance, and to place the state onto the switching line. U_{adp} is expressed by Eq. (19).

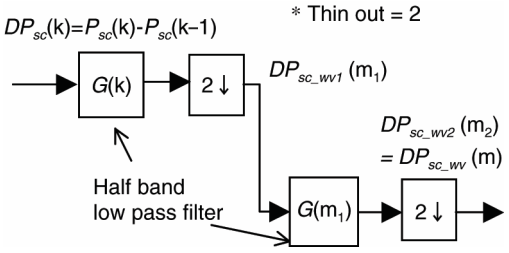


Fig. 6 Wavelet transform algorithm

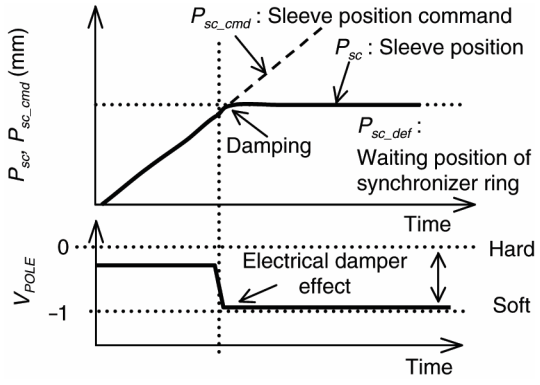


Fig. 7 Compliance effect

$$U_{adp}(k) = -\frac{K_{adp}}{b_1}\sum_{i=0}^{k}\sigma(i) \tag{19}$$

K_{adp}: Adaptive law gain

4.5. Calculation of the Target Values

The ramped path that is temporarily held at the synchronizer ring balk position shown in Fig. 8 is used as the target value. At this time, the balk position is set to the maximum design tolerance value, but the variation of the actual balk position causes the variance of the sleeve pressing force during revolution synchronization.

Therefore, when the sleeve exceeds P_{sc_def} and stops at the target value hold portion shown in Fig. 9, SMC displaces P_{sc_cmd} to the addition target value U_{fb_cmd} by voltage feedback in order to stabilize the pressing force.

Equations (20) to (24) show equations of voltage feedback.

$$U_{fb}(k) = U_{fb\_ini}(k) + U_{rch\_ufb}(k) + U_{adp\_ufb}(k) \tag{20}$$

$$U_{rch\_ufb}(k) = -K_{rch\_ufb}\,\sigma_{ufb}(k) \tag{21}$$

$$U_{adp\_ufb}(k) = -K_{adp\_ufb}\sum_{i=0}^{k}\sigma_{ufb}(i) \tag{22}$$

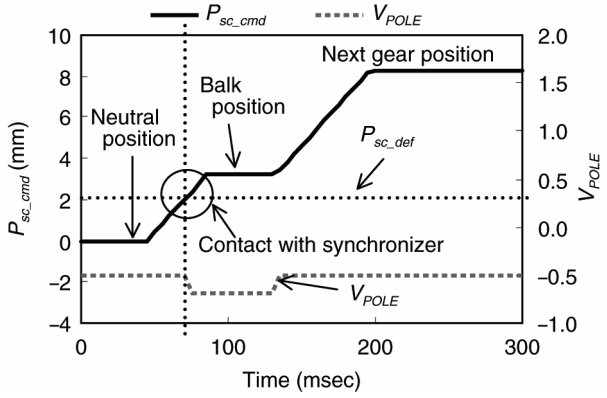


Fig. 8 Time series data for target value

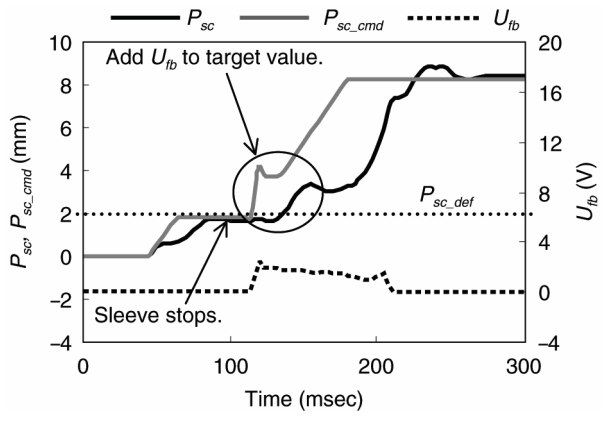


Fig. 9 Altaration of target value by voltage feedback

$$\sigma_{ufb}(k) = E_{ufb}(k) + V_{POLE\_ufb}E_{ufb}(k-1) \tag{23}$$

$$E_{ufb}(k) = V_{in\_ave}(k) - U_{fb\_cmd} \tag{24}$$

U_{fb_ini}(k) : Voltage feedback initial value
V_{in_ave}(k) : Input voltage moving average value
U_{fb_cmd} : Voltage addition target value

5. Vehicle Test Results

5.1. Effects of Varying V_{POLE}

Figure 10 shows the test results when there is no target value hold portion, V_{POLE} is constant at –0.45, and mode judgment is not performed. Figure 10 shows the behavior when shifting from the previous gear position through the neutral position to the next gear position. The sleeve advances at a constant speed near the synchronizer ring waiting position P_{sc_def}, which causes the synchronizer ring and the sleeve to collide and the elastic deformation of the synchronizer ring. If too great of an impact force is applied, the sleeve may be pushed into the gear without synchronizing or may bounce back to the engagement dog.

Figure 11 shows the results when there is no target value hold portion, but mode judgment is performed and V_{POLE} is varied.

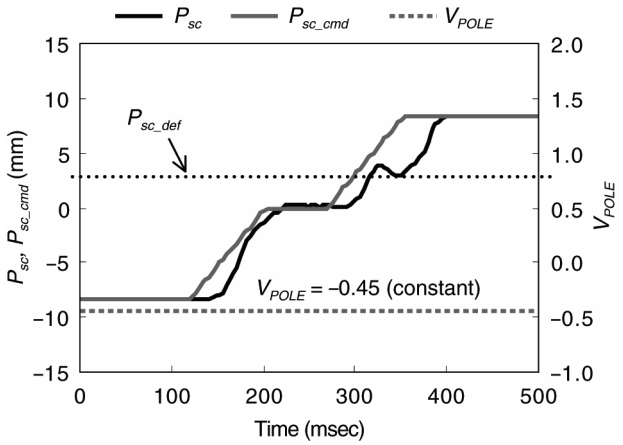


Fig. 10 Test results for constant V_{POLE}

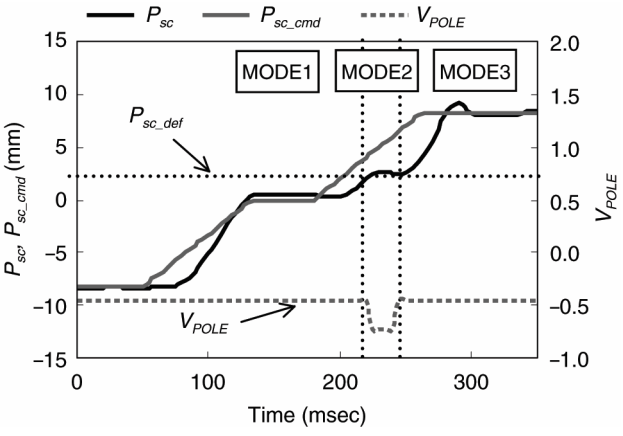


Fig. 11 Test results for variable V_{POLE}

The above-mentioned mode judgment conditions are applied as the V_{POLE} switching conditions. When the sleeve position P_{sc} *moves* to the synchronizer ring waiting position P_{sc_def} and the sleeve position variation DP_{sc} satisfies the MODE2 conditions, V_{POLE} changes from –0.45 to –0.75 to enhance the compliance. As a result, sleeve bouncing such as that shown in Fig. 10 does not occur.

5.2. Effects of the Target Value Calculation Block

Figure 12 shows the results of adding a target value calculation block to prevent sleeve stoppage due to insufficient pressing force toward the synchronizer ring. When the sleeve exceeds the synchronizer ring resting position P_{sc_def} but stops even though the mode shifts from MODE2 to MODE3, the control input V_{in}(k) is increased by voltage feedback. As a result, the sleeve is pressed slowly to the next gear position by the stabilized pressing force. In addition, gear shifting is performed in the short time of 350 msec.

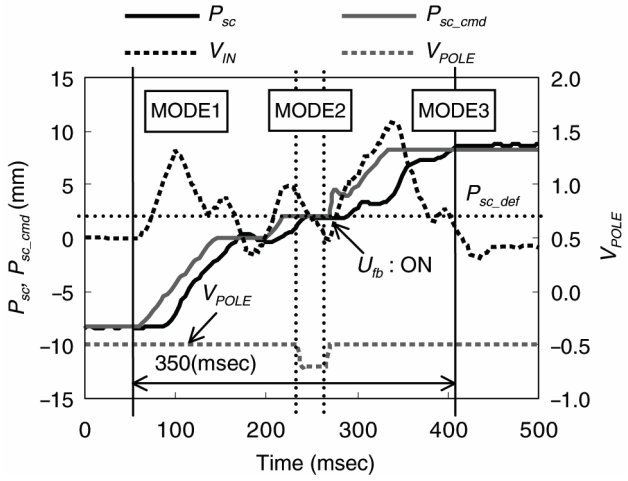


Fig. 12 Test results of for alteration of target value

6. Conclusion

Lowering the disturbance suppression characteristic by altering the SMC switching function gradient V_{POLE} was applied to damper control. This realized the following results for AMT which was the controlled object.

(1) Gear shifting could be performed in a short time (350 msec) without the use of a mechanical damper system by providing compliance between the sleeve and the synchronizer ring.

(2) The sleeve pressing force during shifting was stabilized by increasing the input voltage by voltage feedback when the sleeve stopped, which made it possible to suppress bouncing and stoppage of the sleeve and prevent failure of the synchronizer ring when shifting gears.

References

(1) Nonami, K., Tian, H.: Sliding Mode Control, Corona Publishing Co., Ltd., p. 263 (1994)

(2) Yasui, Y., Akazaki, S., Ueno, M., Iwaki, Y.: Secondary O2 Feedback Using Prediction and Identification Sliding Mode Control, SAE paper 2000-01-0936 (2000)

(3) Ueno, M., Akazaki, S., Yasui, Y., Iwaki, Y.: A Quick Warm-up System during Engine Start-up Period Using Adaptive Control of Intake Air and Ignition Timing, SAE paper 2000-01-0551 (2000)

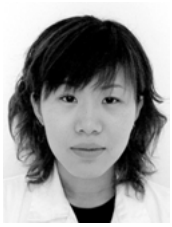
(4) Hashimoto, E., Ishiguro, T., Yasui, Y., Akazaki, S. : High Reliability Electronic Throttle System, SAE paper 2003-01-0708 (2003)

(5) Sakurai, I.: Jidou Hensokuki no Riron to Jissai, Tetsudo-Nipponsha Co., Ltd., p. 341 (1980) (in Japanese)

(6) Ishihara, T.: Douryoku Dentatsu Souchi, Sankaido Publishing Co., Ltd., p. 399 (1980) (in Japanese)

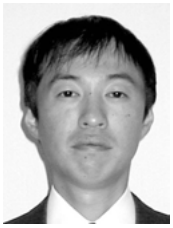
(7) Adachi, S.: Yuza no Tame no Shisutemu Doutei Riron, Corona Publishing Co., Ltd., p. 222 (1993)

■ Authors ■


Kanako SHIMOJO


Yuji YASUI


Eijiro SHIMABUKURO


Yoshihisa IWAKI

Study on Variable Valve Timing System Using Electromagnetic Mechanism

Chihaya SUGIMOTO* Atsushi UMEMOTO* Yasuo SHIMIZU*

ABSTRACT

The elimination of the throttle has recently attracted attention as a means of improving fuel economy through the reduction of pumping loss. The research described in this paper concerns fuel economy, noise, vibration performance and wide-open throttle performance in an engine equipped with an electromagnetic variable valve timing mechanism. This mechanism enables the throttle to be eliminated.

A high-efficiency mechanism equipped with a low voltage drive method from considerations of practical use and constant voltage opening and closing control that has realized short and stable valve contact speed were developed. In comparison with a conventional cam-driven valvetrain, this new valve mechanism has achieved a simulation-based improvement of 7% in fuel economy in the 10.15 mode and a roughly 20% increase in torque at low to mid engine speeds through optimization of valve timing and scavenging effectiveness. In addition, the combination of compact type-integrated hydraulic tappet, dual over-excitation constant voltage control and resin engine cover, has enabled the engine to record the same noise level when idling as an engine with a conventional valvetrain.

1. Introduction

Many attempts are being made to reduce pumping losses in a 4-stroke engine by eliminating the throttle to improve the fuel economy of the engine. Methods of doing this include an inlet air regulation method in which the inlet valve opening and closing timings are varied[(1)-(6)], a hydraulic drive valve method in which hydraulic pressure between the cam and inlet valve is released during the valve lift and the inlet valve closing timing is changed[(7)], and a mass-produced mechanical method employing an intermediate lever and an eccentric camshaft in which the valve lift is varied by changing the contact part of the operating curve between the base of the intermediate lever and the roller follower. However, these methods necessitated an increase in the number of parts due to environmental compatibility and the complexity of the mechanism. In order to overcome this issue, research was carried out concerning the mechanism and control of an electromagnetic valve that was simple and whose valve timing had a high degree of freedom resulting in improved engine performance.

* Tochigi R&D Center

2. Basic Principle and Operating Mode of an Electromagnetic Valve

As shown in Fig. 1, the basic principle of operation of an electromagnetic valve is free vibration of a spring and a kinetic system. The friction and structural attenuation parts

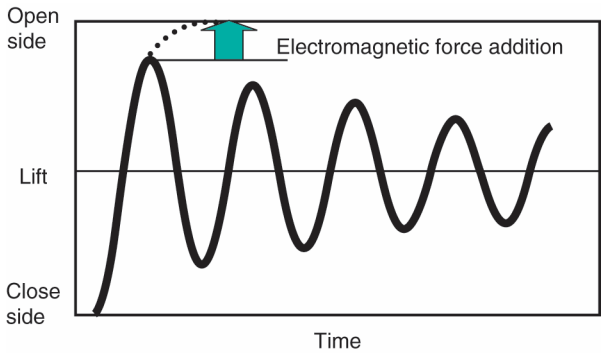


Fig. 1 Basic principle of electromagnetic valve

are drawn in and held by an electromagnet. As shown in Fig. 2, compared to the conventional valve profile the behavior of an electromagnetic valve is controlled by the timing of energization of the electromagnet, and the lift time is constant irrespective of the rotational speed. Consequently, the profile with respect to the crank angle is a rectangular wave in the low to mid range speed, enabling the volumetric efficiency to be increased. Also, the valve open and close timing can be made fully variable, aiming to optimize the intake and exhaust pulsations and reducing pumping loss.

Figure 3 shows the operating mode. In the initial state (center part of the diagram), there is equilibrium between the upper and lower springs, so the valve and armature are stationary at a point midway along the valve lift. When the signal for putting the engine into an operating condition is sent, electric current flows alternately through the upper and lower coils at a fixed period, causing the armature to be drawn in while vibrating, until the valve is fully closed (left part of the diagram). After this, the valve operates continuously (right part of the diagram), and when the signal for putting the engine into a deactivated condition is sent, all valves cease operation at once, and return to the neutral position (center part of the diagram).

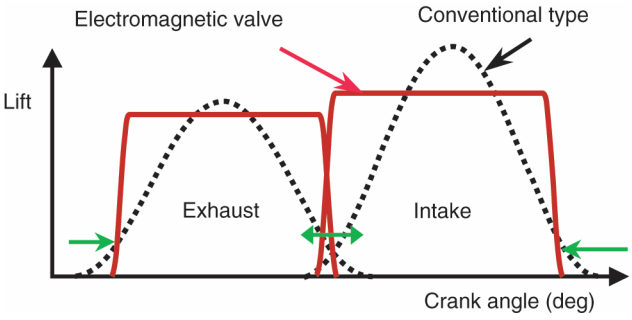


Fig. 2 Comparison of electromagnetic valve profile and conventional valvetrain profile

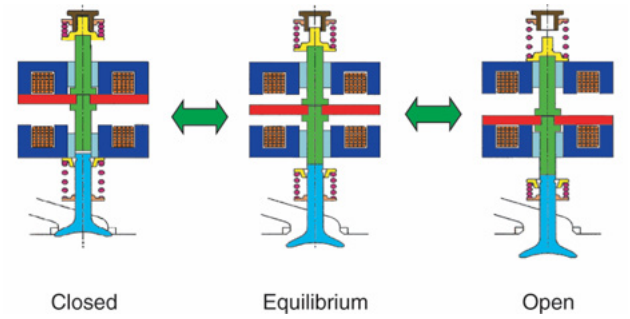


Fig. 3 Motion of electromagnetic valve

3. Outline of Structure and System

Figure 4 and Table 1 show the main structure and specifications of the electromagnetic valve used in this research, and Fig. 5 shows the system.

Concerning the structure, shafts which are supported by springs above and below are fixed to square-shaped armature disks. At the end of the upper shaft is a lift sensor, and between the lower shaft and the valve is a compact-type integrated hydraulic tappet which is used as a valve buffer mechanism. In consideration of wear and thermal expansion of each part, there is a separation mechanism which ensures that the valve makes contact first and then the armature is drawn in on the fully closed side. This is equivalent to the tappet clearance in the conventional cam-driven valvetrain. In order to minimize the effect of pressure inside the cylinder, the spring load on the exhaust side is made higher than that on the intake side. The yoke is made of laminated silicon steel sheets in order to reduce eddy current loss and reduce

Table 1 Valvetrain specifications

Valve diameter (IN/EX) (mm)	30/24
Valve lift (IN/EX) (mm)	7/6
IN maximum spring force (N)	480
EX maximum spring force (N)	550

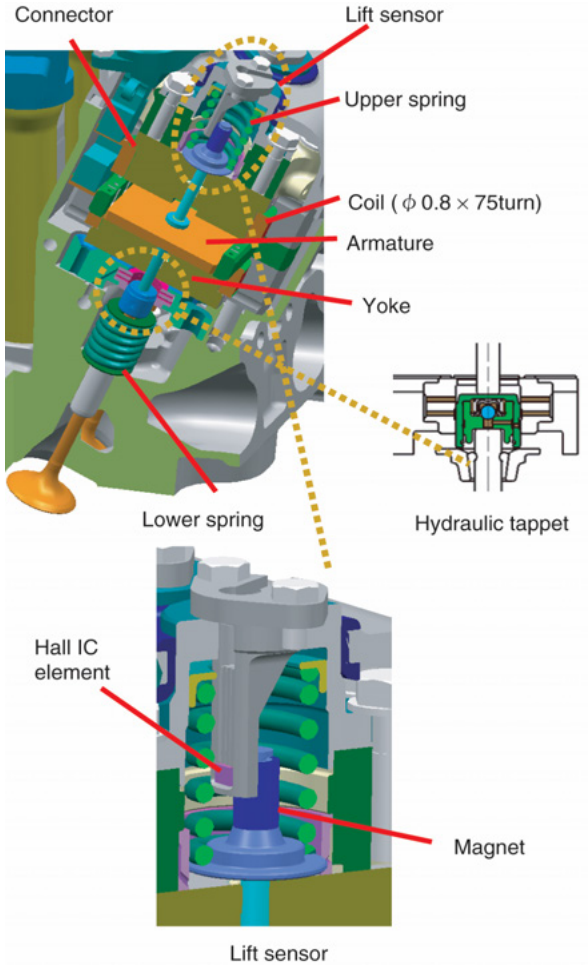


Fig. 4 Structure and hydraulic tappet and lift sensor

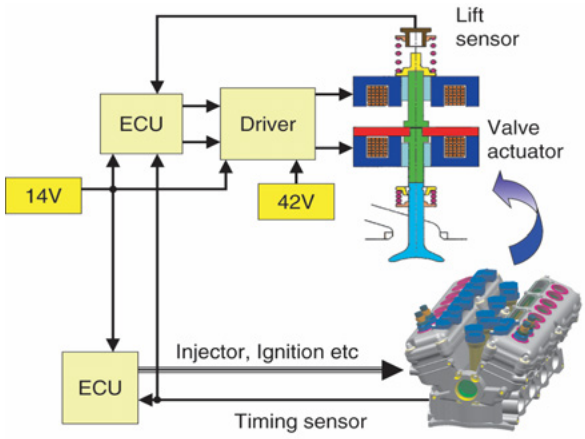


Fig. 5 Electromagnetic valve management system

cost. It contains a resin bobbin around which is wound a coil. The electromagnetic valve system shares only the timing sensor. The ECU and driver are dedicated parts which have been added to the existing ECU. Each valve is driven by a low voltage of 42 V in consideration of mounting in an actual engine, and is controlled independently of the others by a signal from the lift sensor.

4. Study of High Efficiency by Simulation

When the amount of intake air is controlled by using variable valve timing in order to eliminate the throttle and improve fuel economy, the electric power consumption performance exerts a large effect on the fuel economy. Generally, methods used to reduce the consumption of electric power include improved attraction force by means of increased magnetic path area, reduced leakage magnetic flux, improved material characteristics, reduced eddy current loss by means of lamination, and coil cooling.

The B (magnetic flux density) - H (magnetic field) characteristics of the silicon steel used in this research are shown in Fig. 6. It can be seen that the magnetic flux density is saturated in places where the magnetic field is strong. Based on this fact, static magnetic field simulation was used to analyze the attraction force. In the simulation of the electric and mechanical compound, the mechanism of the actual behavior of the electromagnetic valve in which the application of a voltage causes current to flow, generating magnetic flux, which in turn causes the armature to be drawn in, was analyzed. Eddy current loss generated by an abrupt change in the magnetic flux when the armature is drawn in was also analyzed, several patterns were calculated, enabling a low power consumption laminated structure and drive method to be devised.

Figure 7 shows a comparison between the attraction force simulation and the measured results when the displacement distance is minute. Although there are differences in saturated areas, good accuracy is obtained.

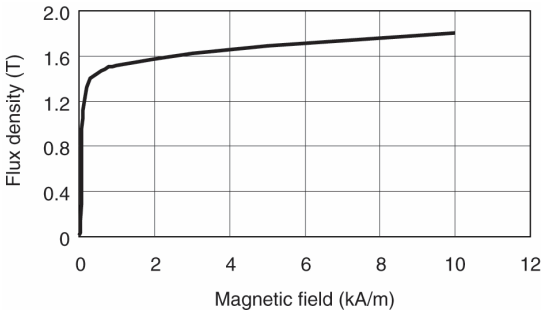


Fig. 6 Magnetic flux and magnetic field characteristics

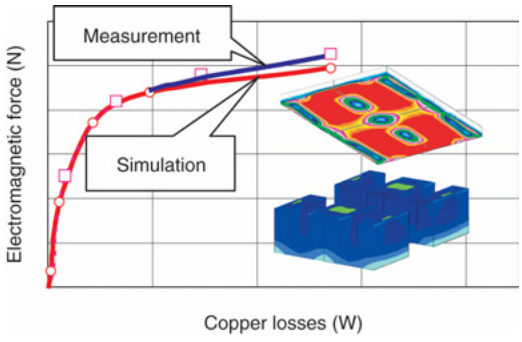


Fig. 7 Static magnetic field simulation

Figure 8 shows the transformer model for the electrical and mechanical compound simulation, and the results of simulation. Equations (1), (3) and (4) apply to the circuit on the left side, and Eq. (2) applies to the circuit on the right side. Both the self induction and mutual inductance are factors of time. This is because the B-H characteristics are non-linear, the magnetic permeability varies, and also the magnetic resistance changes along with the displacement of the armature. Consequently, not only the product of L_1 and $\frac{dI_1}{dt}$, but also the product of I_1 and $\frac{dL_1}{dt}$ contribute to the generation of an induced electromotive force accompanying current I_1.

During the lifting operation, the attraction force does not rise immediately, even when the current rises, but exhibits abrupt characteristics when the distance between the armature and coil becomes minute. Also, it can be seen that eddy current loss occurs when the magnetic flux changes abruptly, and does not occur when the armature is held.

$$V_1 = R_1 I_1 + L_1 \frac{dI_1}{dt} + \frac{dL_1}{dt} I_1 + M \frac{dI_2}{dt} + \frac{dM}{dt} I_2 \tag{1}$$

$$0 = R_2 I_2 + L_2 \frac{dI_2}{dt} + \frac{dL_2}{dt} I_2 + M \frac{dI_1}{dt} + \frac{dM}{dt} I_1 \tag{2}$$

$$L_1 = \frac{N_1^2 A}{\frac{1}{\mu} + \frac{2x}{\mu_0}} \tag{3}$$

$$\frac{dL_1}{dt} = -\frac{N_1^2 A}{\left\{\frac{l}{\mu} - \frac{2x}{\mu_0}\right\}^2} \left\{\frac{1}{\mu_0} \times \frac{d\mu}{dB} \times \frac{dB}{dt} + \frac{2}{\mu_0} \times \frac{dx}{dt}\right\} \tag{4}$$

M in the above equation is the mutual inductance, μ is the magnetic permeability of the magnetic material, μ_0 is the magnetic permeability of air, l is the effective length of the magnetic path, A is the effective cross-sectional area of the magnetic path, N is the number of coil turns, and x is the armature lift.

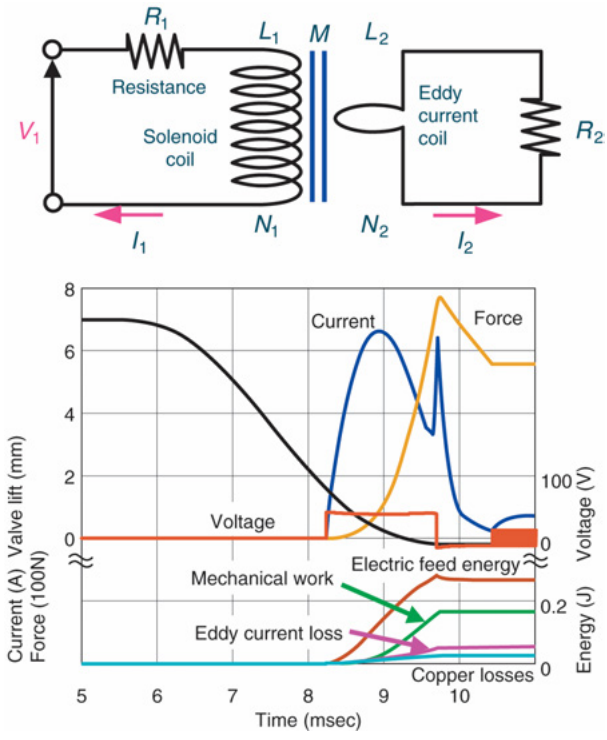


Fig. 8 Electric/mechanical compound simulation

5. Power Consumption Performance

Based on the above simulation results, a 4-cylinder engine on which were mounted electromagnetic valves having a high efficiency laminated structure was fabricated, and the power consumption between the coil terminals was measured using the actual engine. The results of measurement are shown in Fig. 9. A performance of about 150 W was attained at 1 500 rpm when one each of the inlet and exhaust valves were deactivated, and a performance of about 300 W, equivalent to slipper-type valvetrain, was obtained for 16-valve operation.

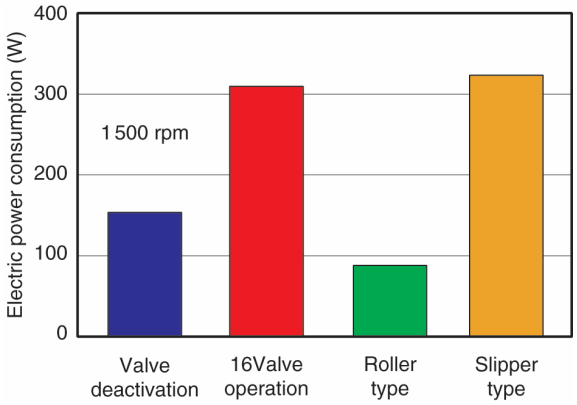


Fig. 9 Comparison of electric power consumption

6. Control System

Figure 10 shows the basic principle of control. During valve lift, constant voltage control takes place, and when the valve is in a held state, constant current control takes place. In the case of the more generally known constant current control, if the valve is subjected to an external disturbance such as friction while lifting, the attained distance of free vibration will be small, and changes in the inductance of the actuator will be more sluggish, causing current to flow more readily. However, because the current is constant, the voltage is reduced, causing the attraction force to be reduced. In contrast, constant voltage control is used in this system, so the current increases, causing the attraction force to increase, thus enabling stable behavior to be realized. The constant voltage control method used controls the energization timing based on a comparison of the actual displacement of each valve detected by the lift sensor with the target value. Energization start control is intended to realize both stable operation of the valve and reduction of contact speed.

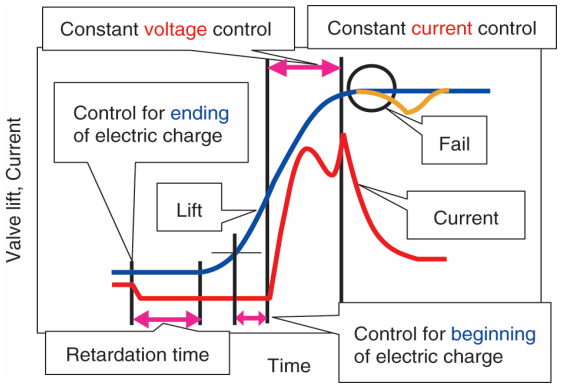


Fig. 10 Control principle

Because the contact speed is determined by the energization start timing, this method measures the valve displacement time, compares it with the target value, and determines the energization start timing of the next cycle.

Energization end control is used to determine the valve timing using the energization end timing. For this reason, it corrects random variations in the delay time caused by the effect of residual magnetic flux, and measures the period from the end of energization to a lift of 1 mm in order to correct the delay time for the next cycle. In addition, this control system uses a contact judgment detection system. When a failure occurs and the valve reaches the neutral position, the engine performance is largely affected, so the armature is attracted to the closed valve side or the open valve side depending upon the timing of the occurrence of the failure.

7. Noise and Vibration Characteristics

A conventional valvetrain mechanism has a buffer curve to control impact noise generated when the valve makes contact and also durability. However, an electromagnetic valve has no buffer curve, and its attraction force characteristics become increasingly abrupt with decreasing distance between the armature and the coil. For this reason, impact noise when the valve and armature make contact becomes a concern.

The contribution of the valvetrain noise to mechanical noise is highest when the engine is idling, so an evaluation of proximity noise above the cylinder head during idling was carried out in a simple anechoic chamber. The results are shown in Fig. 11. The sound pressure level of the electromagnetic valve was about 19 dB worse than that of the conventional cam-driven valvetrain.

In contrast, as shown in Figs. 12 and 13, by employing dual overexcitation for constant voltage overexcitation control, the abrupt attraction force characteristics in the vicinity of contact were reduced, and the armature contact speed was reduced from 0.45 to 0.1 m/sec, causing the impact acceleration on the yoke to be reduced to no more than 1/4. In addition, by using compact-type integrated hydraulic tappet shown in Figs. 14 and 15, it was possible to obtain a reduction of 15 dB, and also by using a resin engine cover and reduced idling speed to obtain the same noise reduction performance as a conventional cam-driven valvetrain.

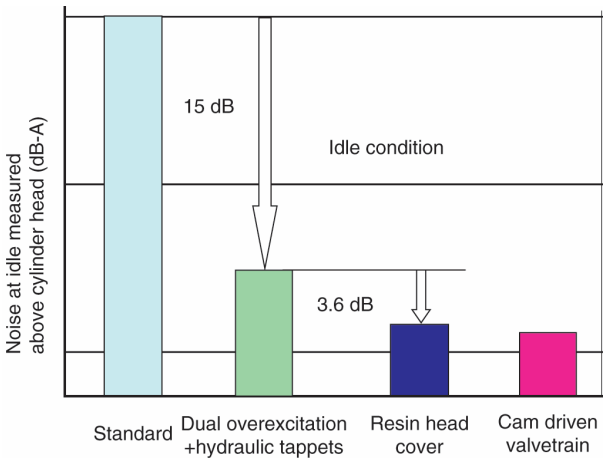


Fig. 11 Controlling methods, structural difference and effects

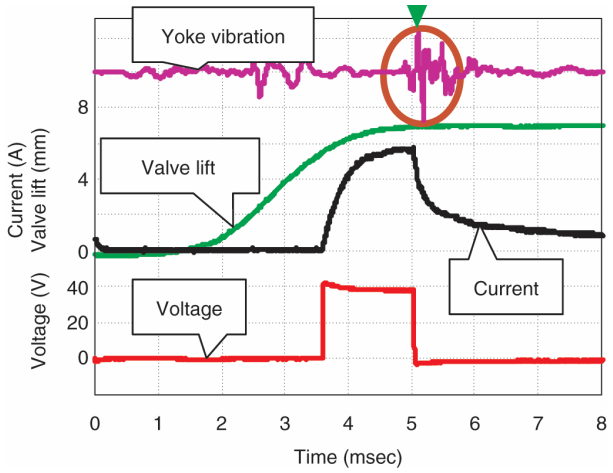


Fig. 12 Overexcitation control under constant voltage condition

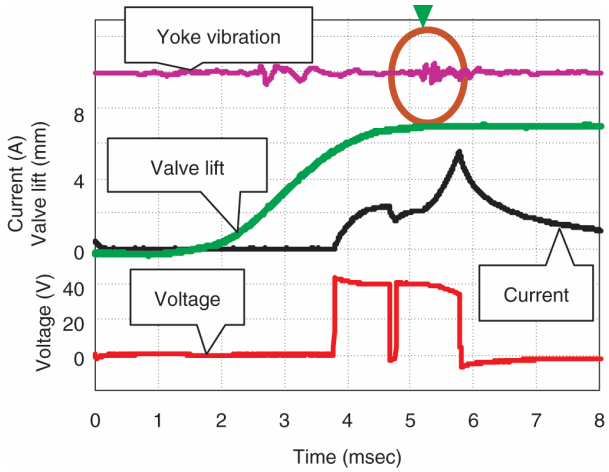


Fig. 13 Dual overexcitation control under constant voltage condition

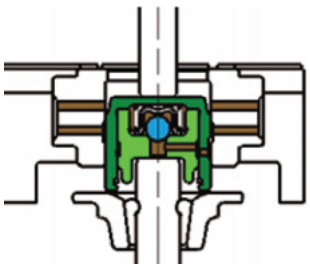


Fig. 14 Hydraulic tappet

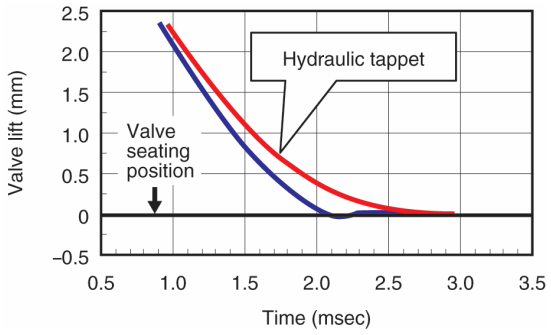


Fig. 15 Hydraulic tappet effect

8. Performance of Actual Engine

Table 2 shows the specifications of the engine used in the performance test, and Fig. 16 shows the results of the actual engine fuel economy performance. It was confirmed that the use of variable valve timing permits the throttle to be eliminated, and the BSFC including electric power consumption was improved by 10% compared to the conventional cam-driven valvetrain owing to delayed intake valve close timing. Figure 17 shows the corresponding PV curves. It can be seen that pumping loss has been reduced as a result of delayed closing. (Output power 2.9 kW at 1 500 rpm, one each of the inlet and exhaust valves deactivated)

In addition, 10.15 mode fuel economy simulation analysis was performed, the simulation result yields a 7% improvement in fuel economy.

Table 2 Test engine specifications

Bore × stroke (mm)	75 × 90
Displacement (cm^3)	1 590
Bore spacing (mm)	84
Valve lift (IN/EX) (mm)	7/6
Valve train type	Electromagnetic valve train

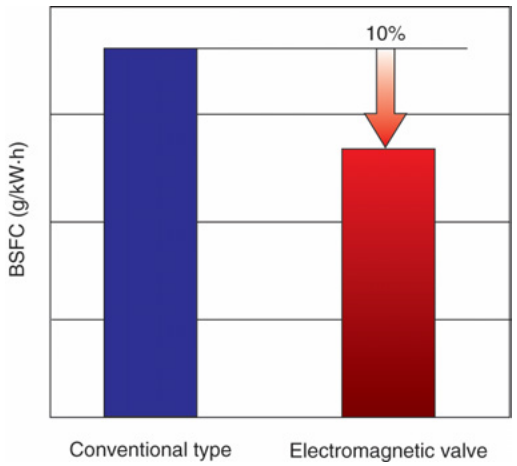


Fig. 16 Comparison of fuel consumption values

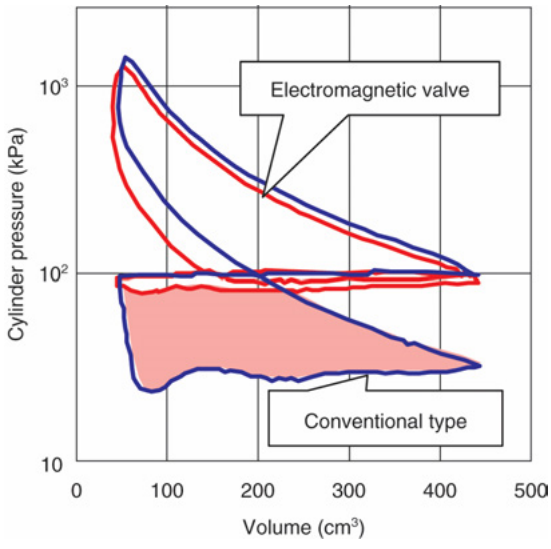


Fig. 17 Pumping loss reduction

Figure 18 shows the actual engine wide-open throttle performance. By setting the closing timing of the intake valve to the bottom dead center, the actual stroke volume was increased, and in addition the improved volumetric efficiency resulting from scavenging utilizing intake and exhaust pulsations realized a torque improvement of about 20% in the low to mid range speeds.

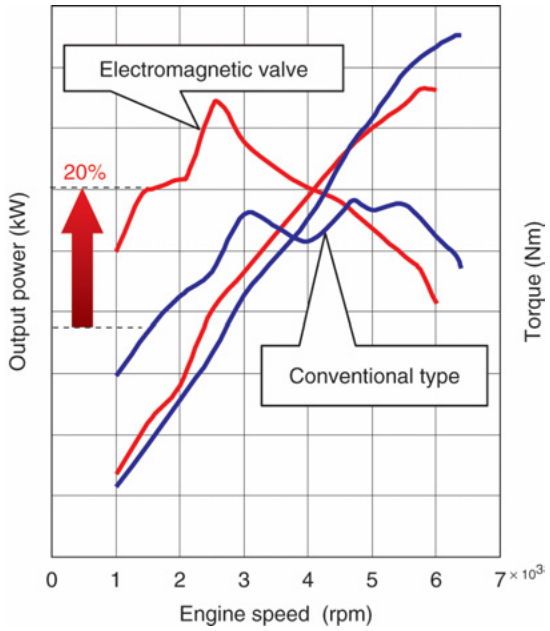


Fig. 18 Wide-open throttle performance

9. Conclusion

A high efficiency electromagnetic valve mechanism driven by a practical low voltage (42 V) was developed, and the following results were obtained.

(1) By using the electromagnetic valve to eliminate the throttle, a 10% improvement of BSFC (Output power 2.9 kW at 1 500 rpm) compared to the conventional valvetrain was obtained, and also a 7% improvement was obtained by 10.15 mode fuel economy simulation.
(2) By utilizing the optimum valve timing and scavenging effect, a torque improvement of roughly 20% was obtained in the low to mid range speeds.
(3) By using a combination of energization start control and end control, stable valve behavior and low contact speed were attained.
(4) By using a compact-type integrated hydraulic tappet, dual overexcitation constant voltage control, and a resin engine cover, the noise reduction performance obtained during idling was equivalent to that of a cam-driven valvetrain.
(5) By combining a static magnetic field simulation and an electrical and mechanical compound simulation of a transformer model, the mechanisms of eddy current loss in operating condition, copper loss, mechanical work, applied energy were analyzed.

References

(1) Tuttle, J.: Controlling Engine Load by Means of Late Intake Valve Closing, SAE Paper 800794

(2) Tuttle, J.: Controlling Engine Load by Means of Early Intake Valve Closing, SAE Paper 820408

(3) Gray, C.: A Review of variable engine valve timing, SAE Paper 880386

(4) Nuccio, P.: Variable Valve Timing as a Means to Control Engine Load, FISITA 82071

(5) Lenz, H.: Initial test result of an electro-hydraulic variable-valve actuation system of a firing test, SAE Paper 890678

(6) Suzuki, J.: Study of improving Fuel Economy by Early Intake Valve Closing Concept, Transaction of the SAE of JAPAN, No. 24 (1982)

(7) Urata, Y.: A Study of Vehicle Equipped with Non-Throttling S. I. Engine with Early Intake Valve Closing Mechanism, SAE Paper 930820

■ Authors ■


Chihaya SUGIMOTO


Atsushi UMEMOTO


Yasuo SHIMIZU

Development of Positive Crankcase Ventilation System for Four-stroke Engine Used in Small Motorcycles

Ryuji MORIYAMA* Yuki MURAOKA* Kazuo FUJIHARA*

ABSTRACT

In a motorcycle engine blow-by gas is generally introduced into the intake system, including the air cleaner, to decrease blow-by emissions inside the crankcase. There was concern in the aforementioned system that some running conditions might shorten the oil change interval. Those phenomena were caused by mixing of water and gasoline in the blow-by gas into the engine oil. In order to control the phenomena, a new positive ventilation system of the crankcase was developed. In the new system fresh air is introduced into the crankcase by pressure fluctuations in the crankcase. The introduction of fresh air ventilates the crankcase. Comparing to the previous system, the developed Positive Crankcase Ventilation system has decreased the density of water and gasoline contained in the engine oil by 73% and 42% respectively.

1. Introduction

Most scooters with a displacement of 50 cm^3 sold in Japan until 1999 were equipped with two-stroke engines. In 1999, Honda released the scooter equipped with a water-cooled four-stroke 50 cm^3 displacement engine for the first time in Japan. The purpose was reducing emissions and improving fuel consumption. This scooter is used mainly as a means of daily transportation. Under some running conditions, water and gasoline components contained in the blow-by gas mix with the engine oil, which results in a shortened oil change interval[(1)].

The authors have developed a new positive crankcase ventilation system (PCV system) for the single-cylinder engines of small motorcycles in order to inhibit the mixing of these components and lengthen the time between oil changes. The system, unlike the conventional PCV system, has a one-way valve and a solenoid valve. This system was employed in the Smart Dio Z4 scooter released in Japan in February 2004. Figure 1 shows an external view of this scooter.



Fig. 1 External view of Smart Dio Z4

* Asaka R&D Center

2. Engine Specifications

Table 1 shows the specifications of the four-stroke water-cooled engine mounted in the scooter released in February 2004. The radiator is located on the right side of the crankcase, and cooled by a fan attached to the crankshaft. The water pump is driven from the cam shaft via a magnet coupling, and the oil separator is located on the cylinder head. The fuel supply system uses the first fuel injection (FI) system in this category.

Table 1. Specifications of test engine

Engine type	4-stroke, 1 cylinder
Valve train	OHC 4-valve
Displacement (cm^3)	49.9
Bore × Stroke (mm)	38.0 × 44.0
Compression ratio	12
Cooling system	Liquid cooled
Lubricating system	Wet sump
Fuel supply system	Fuel injection
Power train	Belt converter

3. Mechanism of Water and Gasoline Components Mixing in the Engine Oil

When the engine temperature is low, the product of combustion, water and unburnt gasoline adhere to the cylinder walls in liquid form. This liquid enters the crankcase through the gaps between the cylinder, piston rings and piston. Also, the unburnt gasoline and water contained in the blow-by gas are cooled and condense inside the crankcase. In this manner, liquid gasoline and water blend into the engine oil. Figure 2 shows a model of this mechanism[2].

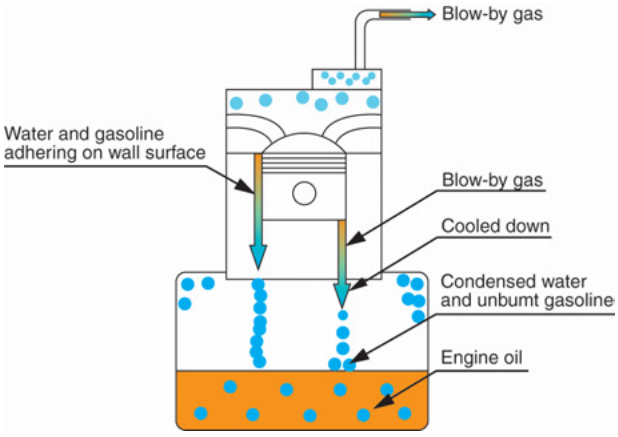


Fig.2 Generating mechanism of blending into oil

4. PCV System

4.1. System Outline

The PCV system introduces fresh air into the crankcase. Since the introduced fresh air dilutes the water and gasoline in the blow-by gas and the dew point is lowered, condensation becomes less likely. Furthermore, fresh air has an effect of vaporizing the liquid gasoline and water. The system, therefore, will be capable of discharging water and gasoline from the crankcase into the air intake system of the engine.

Figure 3 shows an outline of the Honda PCV system used in automobiles [3]. This fresh air flow is generated by the negative pressure of the inlet manifold. A PCV valve is provided to control the flow in order to stabilize the idling performance at a small throttle angle. At a wide throttle angle there is much blow-by gas and the inlet pipe has a low negative pressure, so the blow-by gas also flows backwards from the fresh air line. Therefore, oil separators are needed in the locations where the fresh-air line and the PCV valve are attached. However, this conventional system cannot be used in small motorcycles for the following reasons.

(1) Since the amount of air intake at idling is extremely small, it is impossible to control such an amount of air intake with the PCV valve and to achieve adequate idling performance.
(2) Since most motorcycles have one cylinder and one throttle body, negative pressure in the inlet pipe is relatively low compared with automobiles so that a sufficient amount of fresh air will not flow.
(3) Gas-liquid separator systems must be installed for both the case and head for the system. It is difficult to locate these components on compact engines for small motorcycles.

Therefore, the authors devised a method not to return the blow-by gas to the inlet pipe.

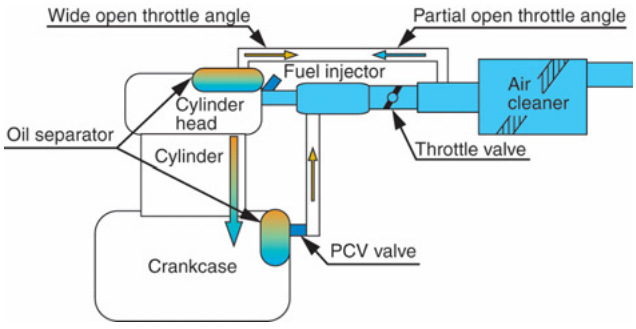


Fig. 3 PCV system for automobiles

4.2. PCV System with Two One-way Valves (Specification 1)

The blow-by gas in a motorcycle is normally returned to an air cleaner to prevent air pollution by the blow-by gas. In case of a scooter, an oil separator is located on the cylinder head due to layout restrictions, and the blow-by gas is returned from the oil separator outlet to the clean side of the air cleaner (Fig. 4). In addition to this system, a reciprocating type pump was formed utilizing the pressure fluctuation inside the crankcase by using two reed-valve type one-way valves (Fig. 5). One reed- valve type one-way valve was installed in the conventional tube that leads the blow-by gas to the air cleaner. This one-way valve is oriented to flow from

the cylinder to the air cleaner. The other one-way valve was installed in a new tube leading from the air cleaner to the crankcase. This one-way valve is oriented to flow from the air cleaner to the crankcase.

Installing this system produced the flow rate characteristics shown in Fig. 6. The return gas flow rate was higher at low vehicle speeds, and in particular the fresh air flow rate was about six times the blow-by gas flow rate at a vehicle speed of 5 km/h.

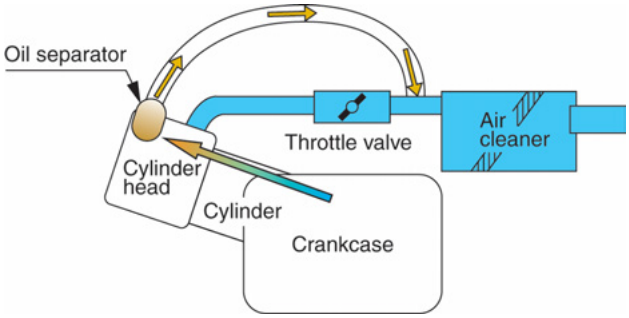


Fig. 4 Conventional blow-by return system

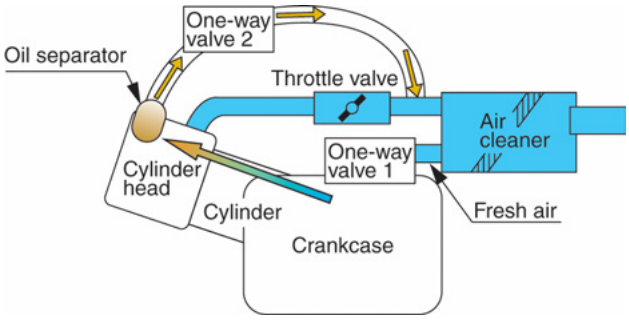


Fig. 5 Spec. 1: PCV system with two one-way valves

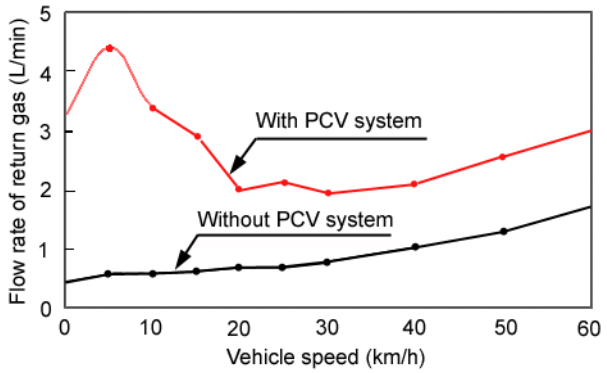


Fig. 6 Return gas characteristics in Spec. 1

- Fresh air:
  Air taken into the crankcase from the air cleaner by the PCV system
- Return gas:
  Gas returned from the crankcase to the air cleaner
- Flow rate of return gas:
  Fresh air flow rate + Engine blow-by gas flow rate

4.3. PCV System with a Single One-way Valve (Specification 2)

With Specification 1 there was a concern that the pressure inside the crankcase might rise to abnormal levels if the one-way valve oriented towards the air cleaner becomes blocked due to oil degradation or water freezing. Therefore, the one-way valve 1 flowing toward the air cleaner as shown in Fig. 5 was removed. There was a concern that removing this one-way valve would cause the flow rate to drop, but roughly the same flow rate was ensured by reviewing the characteristics of the piping and the one-way valve (Fig. 7). Figure 8 shows the pressure in each part.

When the piston moves from the bottom dead center to the top dead center, the pressure inside the crankcase becomes lower than the pressure inside the air cleaner (A in Fig. 8). This pressure difference causes the one-way valve to open and lead fresh air to the crankcase. At the same time, the pressure inside the oil separator on the cylinder head also becomes lower than the pressure inside the air cleaner, which produces a flow from the air cleaner to the oil separator (B in Fig. 8). Then, when the piston moves from the top dead center to the bottom dead center, the pressure inside the crankcase becomes higher than the pressure inside the air cleaner (C in Fig. 8). This pressure difference causes the one-way valve to close and sends the return gas which consists of blended blow-by gas and fresh air through the oil separator to the connecting tube. In this manner, fresh air is led into the crankcase by operating the one-way valve using the pressure fluctuation inside the crankcase.

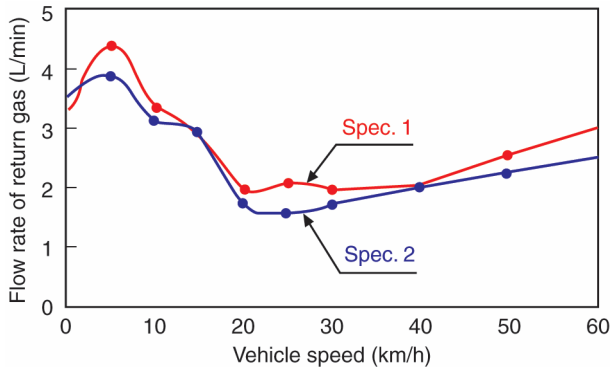


Fig. 7 Flow rate of return gas in Spec. 2

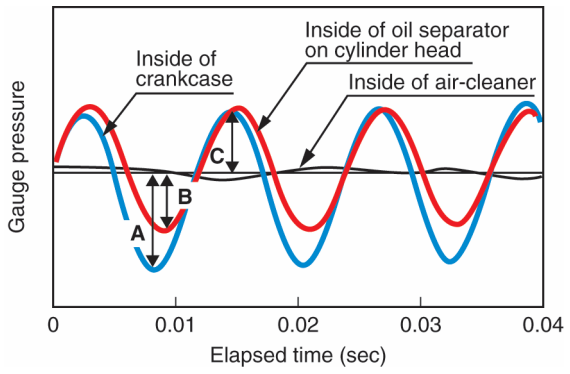


Fig. 8 Pressure fluctuation at 20km/h of behicle speed

4.4. Specification with a Single One-way Valve and a Solenoid Valve (Specification 3)

The fresh air must be controlled to improve separation of the oil in the return gas in the high engine revolution range, and to enhance the idling performance in the low revolution, low load range in the vicinity of idling. Therefore, a solenoid valve was added to Specification 2 as Specification 3. This solenoid valve is map controlled by the ECU. The basic control consists of turning the PCV system off when the engine is idling, and turning it on when running starts (Fig. 9). The PCV system is also turned off at the high revolution side to improve the oil separation performance.

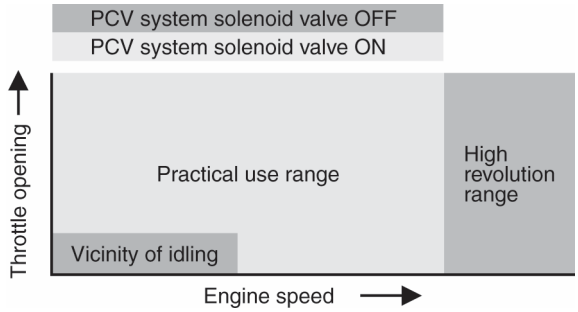


Fig. 9 Solenoid valve control map

5. PCV System Specifications for the Smart Dio Z4

Figure 10 shows the PCV system based on Specification 3 which was employed in the Smart Dio Z4. The PCV system reed valve type one-way valve is located on top of the crankcase, and the solenoid valve is located between the reed valve and the air cleaner. The return gas flow rate was set to the flow rate characteristics shown in Fig. 11 based on the oil separation performance and the reduction effects of water and gasoline in the engine oil. The maximum fresh air flow was approximately 6.5 times that of the blow-by gas. The flow rate characteristics were controlled by the plate thickness and lift amount of the reed valve. The flow rate of the return gas from the engine to the air cleaner was greatly increased by the PCV system in this manner, so it was necessary to enhance the gas-liquid separation capability of the oil separator. This was done by providing a labyrinth structure under the cylinder head cover. It was also confirmed that fresh air flows from the air cleaner at the reed valve location on the fresh air line side, so an oil separator is not needed in this location.

The concentration of CO in the exhaust gas while cruising was measured at the flow rate characteristics shown in Fig. 11. The results showed that the concentration of CO in the exhaust gas was slightly higher for the specification with the PCV system than without the PCV system due to the effects of the HC in the return gas (Fig. 12). The CO value in the mass emissions in ECE40 mode was also about 6% higher. However, this increase can be eliminated by setting the system in consideration of this increase.

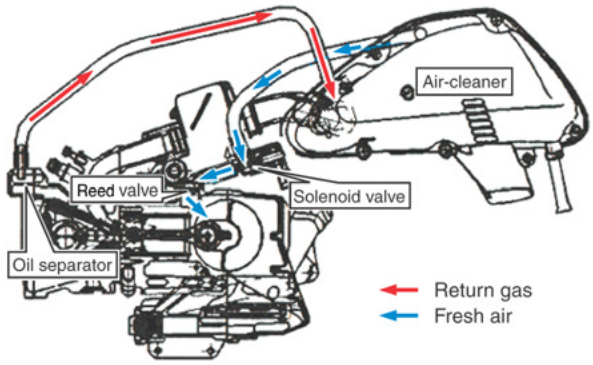


Fig. 10 PCV system for Smart Dio Z4

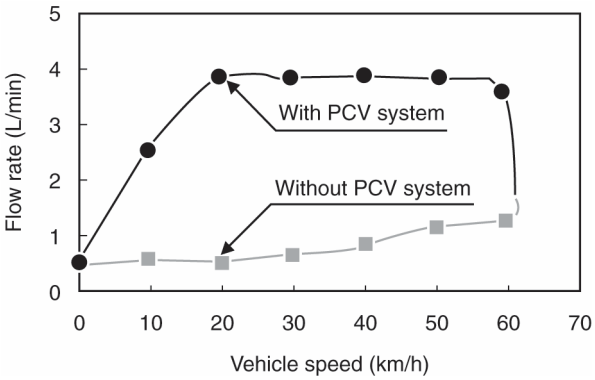


Fig. 11 Flow rate of return gas of Smart Dio Z4

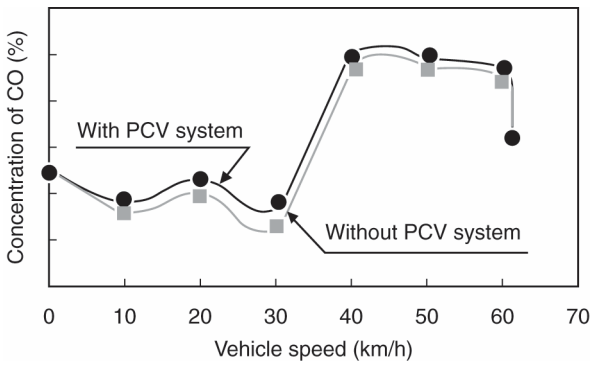


Fig. 12 Concentration of CO in exhaust gas

5.1. Confirmation of Water Content and Gasoline Content Reduction Effects by Vehicle Tests

5.1.1. Test conditions

The test mode was low-speed short-distance running. The running distance was 2 km per cycle, and 40 cycles were performed.

5.1.2. Climatic conditions

The environmental conditions were a temperature of 0 to 7 °C and relative humidity of 43 to 88%. (Fig. 13)

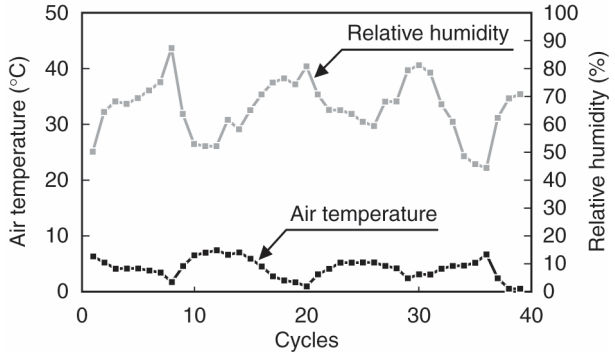


Fig. 13 Climatic conditions for running test

5.2. Test Results

The effects of the PCV system were evaluated by simultaneously running the vehicles equipped with and without the PCV system. The results showed that the gasoline concentration was reduced by 42% and the water concentration by 73% compared to the vehicle without the PCV system (Fig. 14).

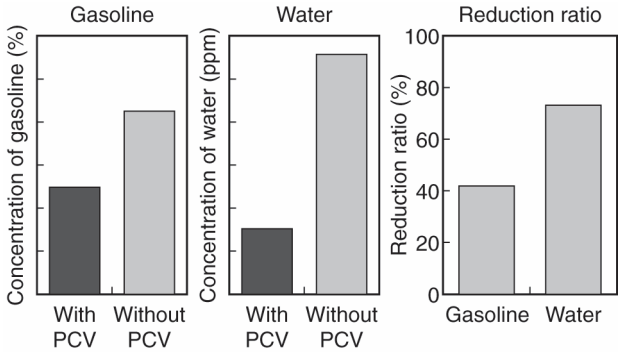


Fig. 14 Test results of runnnung test

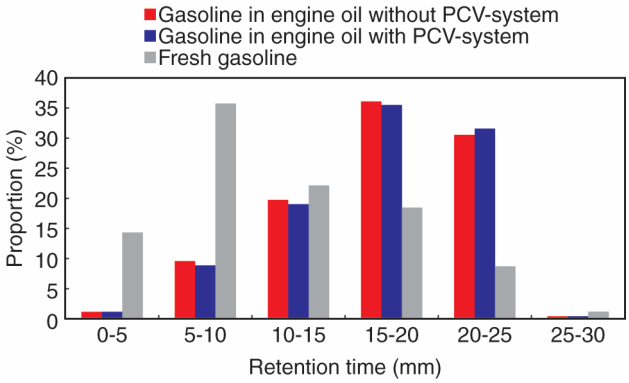


Fig. 16 Proportion of gasoline component after running test

The gasoline components contained in the engine oil after 40 cycles of these vehicle running tests were analyzed using gas chromatography. Figure 15 shows the results. The gasoline components in the oil for the vehicle with the PCV system were less than those for the vehicle without the PCV system. This included all components from low boiling point with a small retention time (RT) to high boiling point components with a large RT. This is due to the effects of the PCV system. Figure 16 compares the proportions of these gasoline components, and shows that the proportions are roughly the same both with and without the PCV system. In addition, the gasoline in the engine oil has less low boiling point components and more high boiling point components than fresh gasoline. This reason is thought to be that the low boiling components vaporize and burn easily inside the combustion chamber, and that even if these components enter the crankcase, most are returned to the air cleaner as blow-by gas.

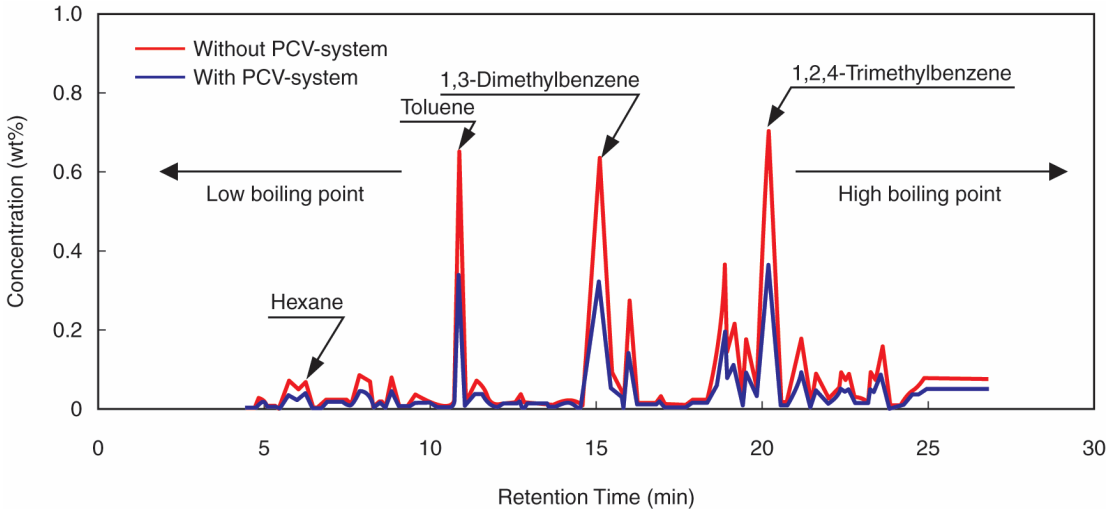


Fig. 15 Gasoline components in engine oil of running test

6. Conclusion

(1) Water and gasoline accumulate in the engine oil as a result of repeated short-distance running at low temperatures. This gasoline in the engine oil has less low boiling point components and more high boiling point components than fresh gasoline.
(2) Using the newly developed PCV system in a compact four-stroke water-cooled engine with a displacement of 50 cm^3 reduced the concentration of water by 73% and gasoline by 42% in the engine oil, respectively.

Acknowledgement

The authors wish to express their deep thanks to all related parties at Idemitsu Kosan Co., Ltd. for their cooperation in promoting this research and development.

References

(1) Ishikawa, M.: The Crankcase Emission Control System of Automotive Engine, ENGINE THECHNOLOGY, Vol. 3, No. 6 (in Japanese)

(2) Murakami, H., Aihara, H.: Analysis of Mechanism Intermixing Combustion Products in Engine Oil, Transactions of The Japan Society of Mechanical Engineers (Edition B), Vol. 55, No. 519 (1989)

(3) Schwartz, S.E., Smolenski, D.J.: Development of an Automatic Engine Oil-Change Indicator System, SAE Paper 870403 (1987)

■ Authors ■



Ryuji MORIYAMA



Yuki MURAOKA



Kazuo FUJIHARA

Development of ILSAC GF-4 0W-20 Gasoline Engine Oil

Takayuki SATO* Syouji KAWAUCHI*

ABSTRACT

This paper describes the development of a 0W-20 engine oil designed to meet the ILSAC GF-4 engine oil standard beginning on July 31st, 2004.

The GF-4 engine oil standard stipulates upper limits for phosphorus and sulfur content in oil to prevent poisoning of exhaust system components. The new standard has also generated concerns that the reformulated oil will accelerate wear of engine parts. Each additive in the newly developed oil has been selected to improve anti-wear performance. In addition, the contribution of kinematic viscosity and HTHS viscosity to engine motoring friction has been verified, and the molecular weight of the viscosity index improver has been optimized to achieve GF-4's the higher fuel economy requirement.

The newly developed engine oil was evaluated in GF-4 standard tests and was confirmed to meet GF-4 performance.

1. Introduction

The demand to cut down the environmental impact of automobiles has increased in recent years. Engine oil must be optimized to minimize this impact. Generally, environmentally friendly engine components can only be applied at the factory. This is not the case with engine oil. With advanced engine oils, additional environmental benefits can be achieved in existing engines. Honda has focused on reducing the environmental impacts of its engines through improvements in fuel economy. Honda has achieved this in part by developing engine oils that enhance engine fuel economy performance[1),2)].

In 1994, US automobile manufacturers (GM, Ford and Daimler-Chrysler) and the Japan Automobile Manufacturers Association (JAMA) started the International Lubricant Standardization and Approval Committee (ILSAC). The objective of ILSAC is to maintain the quality of oil in the marketplace and improve oil's effect on engine fuel economy and performance. As shown in Fig. 1, ILSAC standards have been revised synchronously with the US emission and fuel economy regulations.

The US Environmental Protection Agency (EPA) has issued guidelines related to the performance of engine oil. The new ILSAC approved GF-4 engine oil standards introduction begins July 31, 2004, and is applicable to 2005-model year vehicles[3)]. The most important changes in the new GF-4 standards in comparison to the current GF-3 standards are the improvement of catalyst compatibility by strengthening the element content standards for phosphorous and sulfur in engine oil, high temperature oxidation stability, and fuel efficiency[4)]. Honda has developed an engine oil that meets the new standards.

Model Year			94	95	96	97	98	99	00	01	02	03	04	05	06	07
US regulation	Emission	Federal	Maskie Act				Tier1 100k mile			LEV 100k mile			Tier2 120k mile			
		California	LEV1 100k mile										LEV2 120k mile			
	CAFE	LDV	27.5mpg													
		LDT	20.7mpg											21.0	21.6	22.2
Engine oil standard	ILSAC		GF-1				GF-2				GF-3			**GF-4**		
	API		SH				SJ				SL			SM		
	Catalyst compatibility	Phospho-rus	0.12%max				0.10%max							0.06%min 0.08%max		
		Sulfur	Not required											0.5%max*1 0.7%max*2		
	High temp. oxidation	Test	Sequence III-E								Sequence III-F			Sequence III-G		
		W.P.D*3 Min. limit	Not required								4.0P			3.5P		
		Viscosity increase	375%max at 64hrs				64hrs max to 375%				275%max at 80hrs			150%max at 120hrs		
	Fuel efficiency	Test	Sequence VI				Sequence VI-A				Sequence VI-B					
		Min. limit*4	2.7%				1.4%*5 Not required*6				2.0%*5 1.7%*6			2.3%*5 2.0%*6		

*1; 0W-20, 5W-20, 0W-30, 5W-30
*2; 10W-30
*3; Weighted Piston Deposit (Merit rating)
*4; 0W-20, 5W-20
*5; after 16hrs aging
*6; after 96hrs aging

Fig. 1 US emissions/FE regulations and engine oil standards

* Tochigi R&D Center

2. Development Goals

The two points below were the main development goals of the new GF-4 compliant engine oil.

(1) Compliance with standards for Phosphorous content (More than 0.06%, less than 0.08%) and Sulfur content (Less than 0.5%)

(2) Improvement of fuel economy performance

Phosphorous and sulfur are elements included in additives used in engine oil. The upper and lower limits according to the standards restrict the type, and content of the additives. Figure 2 shows the limits of sulfur and phosphorus allowed in the GF-3 and GF-4 standards. Figure 2 also shows the North American market average values for phosphorous and sulfur content under the GF-3 standard.

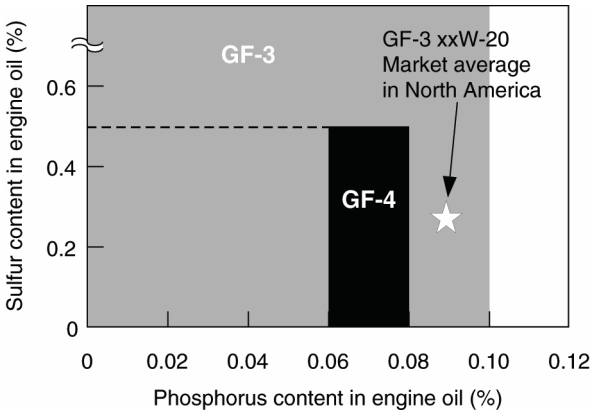


Fig. 2 Standard limits and xxW-20 market average for phosphorus and sulfur content in engine oil

The GF-4 standards place more importance on phosphorous content than sulfur content. In this development, the appropriate phosphorous content and sulfur content in engine oil were studied, and the improvement of the fuel economy performance of engine oil was investigated.

3. Study of Engine Oil Specifications

Base oil (B/O), detergent inhibitors (DI) and viscosity index improvers (VII) were selected to satisfy fundamental performance requirements of engine oil. The fundamental performance requirements include friction reduction, cooling, sealing, anti-rust, detergency and power transmission characteristics. Each of these items were studied individually.

3.1. Base Oil

American Petroleum Institute (API) categorizes base oil into five groups (Table 1)[5]. Group I to III are mineral oils obtained by the distillation and refining of crude oil, while Group IV and V are synthetic oils. Mineral oils are further sub-divided according to the proportions of sulfur content, saturates, and viscosity index. In the past Honda has used Group III oil. Group III oil was also investigated during this development.

Table 1 API base oil interchange guidelines

Base oil category	Sulfur [%]		Saturate [%]	Viscosity index
Gr.I	0.03 <	and/or	< 90	80 to 120
Gr.II	≤ 0.03	and	90 ≤	80 to 120
Gr.III	≤ 0.03	and	90 ≤	120 ≤
Gr.IV	All polyalphaolefins (PAOs)			
Gr.V	All others not included in Gr.I,II,III or IV			

3.2. Detergent Inhibitors

Various additives are used in engine oil to satisfy fundamental performance requirements. Table 2 shows the functions, typical chemicals, phosphorous, and sulfur content (if existing) of various kinds of additives. Compared to sulfur, phosphorous is limited to a few kinds of engine oil additives, extreme pressure agents, and in oxidation inhibitors. Currently, phosphorous-type extreme pressure agents are almost never used. Organometallic compound zinc dithiophosphate (ZnDTP) is used in practically all engine oils as an extreme pressure agent because of its performance and availability. ZnDTP also has the property of anti-oxidation, and is a prominent additive. Reducing the phosphorous content to meet the new GF-4 standards requires nothing but reducing the ZnDTP content. Thus, it is necessary to find the method to compensate the reduced ZnDTP.

Table 2 Typical engine oil additives

Additive	Function	Typical chemicals	Phos -phorus	Sulfur
Extreme pressure agents	Anti-wear Anti-seizure	Organometallic compound type (Zinc dithiophoshate)	✓	✓
		Sulfur type		
		Phosphorus type	✓	
		Chlorine type		
Oxidation inhibitors	Chain reaction stop	Phenol type		
		Amine type		
	Peroxide decomposition	Organometallic compound type (Zinc dithiophoshate)	✓	✓
		Sulfur type		✓
Detergent -dispersant additives	Detergency	Sulfonate type		✓
		Salicylate type		
		Phenate type		
	Sludge dispersancy	Amin type		
		Imide type		
Friction modifiers	Friction reduction	Organometallic type		✓
		Ester type		
Viscosity index improvers	Viscosity adjustment	Polymethacrylate		
		Olefine copolymer		
Carrier oils	Solvent of additives	Mineral oil		✓
Others				

The effects of ZnDTP content, specifically anti-wear performance were investigated. Also the effects of phosphorous content in the current GF-3 engine oil on the cam wear of valve train were studied by carrying out a test with and without molybdenum dithiocarbonate (MoDTC), which is a friction modifier (FM). The results of the test are shown in Fig. 3 and the test conditions in Table 3.

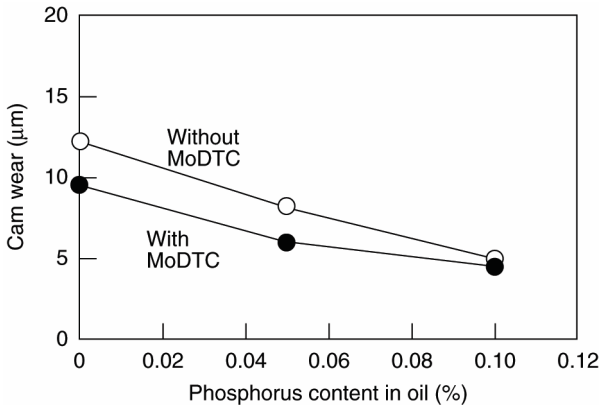


Fig. 3 Cam wear level in Honda valve train wear test

Table 3 Valve train wear test conditions

Engine	L4, 2.2L, MPI
Valve train	SOHC, 4valve, Slide-type
Engine speed [rpm]	2000 / 0
Oil temperature [°C]	90 - 95 / 20 - 30
Water temperature [°C]	80 - 90 / 15 - 25
Test duration [cycle]	300

ZnDTP prevents wear and seizure by generating a phosphate film formed by the chemical reaction between its decomposition product and the metallic surface[6]. When MoDTC is added, it is assumed that MoS_2 is formed on the rubbing surface due to the decomposition of ZnDTP and itself. As a result, friction reduction and anti-wear/anti-seizure performance become more effective[7, 8]. Although the wear due to the reduction of ZnDTP can be prevented to a certain extent using MoDTC, the amount of wear increased. However, for a treatment in which MoDTC is added, it was estimated that a performance equivalent to or better than the current performance could be obtained within the range of acceptable levels of phosphorous contents of GF-4 by making more effective use of MoDTC. On the other hand, detergent-dispersant additives, particularly ashless dispersant, reacts with ZnDTP and also affects the generation of MoS_2. In this development, optimization of the detergent-dispersant additives increases the generation of MoS_2 on the rubbing surface, and attempts to prevent wear and to reduce friction. The Schwingung Reibung Verschleis (SRV) test was carried out[9, 10] on the current GF-3 oil and a study oil obtained by changing its detergent-dispersant additives. The test conditions are shown in Table 4.

The binding energy of molybdenum compound on the surface of the disk specimen was measured using X-ray photoelectron spectrometer (XPS). The results of comparison of the measured results are shown in Fig. 4[11].

The binding energy of MoS_2 (229eV) was confirmed to be stronger than that of oil with GF-3 specifications because of the optimization of the detergent-dispersant additives. The MoS_2 molecules generated on the surface are estimated to have increased.

Table 4 SRV test conditions

Pin	Diameter [mm]	15
	Length [mm]	22
	Material	DIN 100Cr6
Disk	Diameter [mm]	24
	Thickness [mm]	6.9
	Material	DIN 100Cr6
Temperature [°C]		80
Load [N]		200
Frequency [Hz]		50
Sliding distance [mm]		1.0
Test duration [min]		20

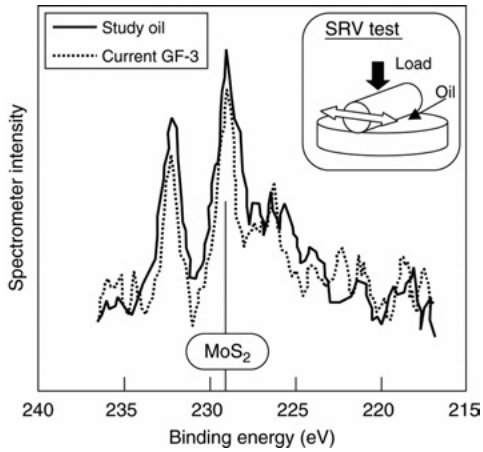


Fig. 4 XPS analysis in SRV test

3.3. Viscosity Index Improvers

Engine friction may be broadly classified into frictional resistances, pumping, and stirring resistance under reciprocating sliding condition. The former is affected to a large extent by high temperature high shear (HTHS) viscosity, while the latter is affected to a large extent by kinematic viscosity. To study the fuel economy of the engine oil, the effects of HTHS and kinematic viscosity on the engine friction were verified. Engine friction was taken as the friction during motoring, and three engine speeds most often used at actual driving condition were selected. Table 5 shows the test engine specifications.

Table 5 Test engine specifications

Engine	L4, 2.0L, MPI
Bore × Stroke [mm]	86.0 × 86.0
Valve train	DOHC, 4valve Roller-type rocker-arm Chain-driven
Compression ratio	9.7

The contribution of each kind of viscosity to the overall engine friction is as shown in Fig. 5. At temperatures below 80 °C, the effect of kinematic viscosity increased, while at temperatures above 80 °C, that of the HTHS viscosity increased. It is evident from the above that a moderate balance between the HTHS viscosity and kinematic viscosity is necessary to reduce the engine friction effectively. With HTHS viscosity constant (2.6 mPa•s) at 150 °C, the molecular weight of viscosity index improver was varied and the HTHS viscosity and kinematic viscosity at 60 °C, 80 °C and 100 °C were examined. As shown in Fig. 6, each viscosity characteristic has an opposite tendency to the molecular weight of viscosity index improver. Thus, the molecular weight with which the optimum viscosity setting can be obtained was selected.

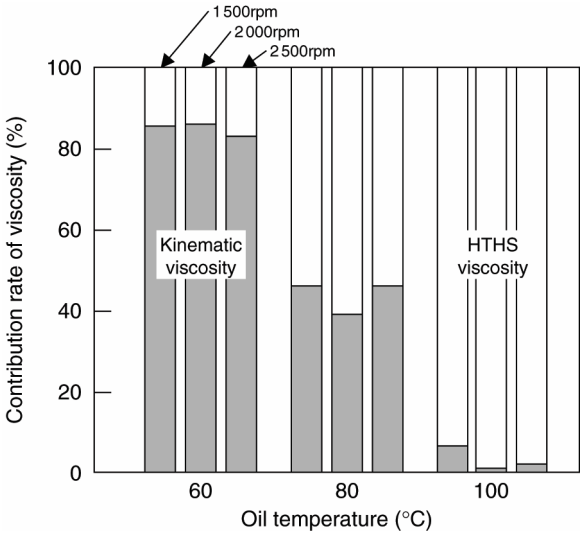


Fig. 5 Contribution of viscosity to engine motoring friction

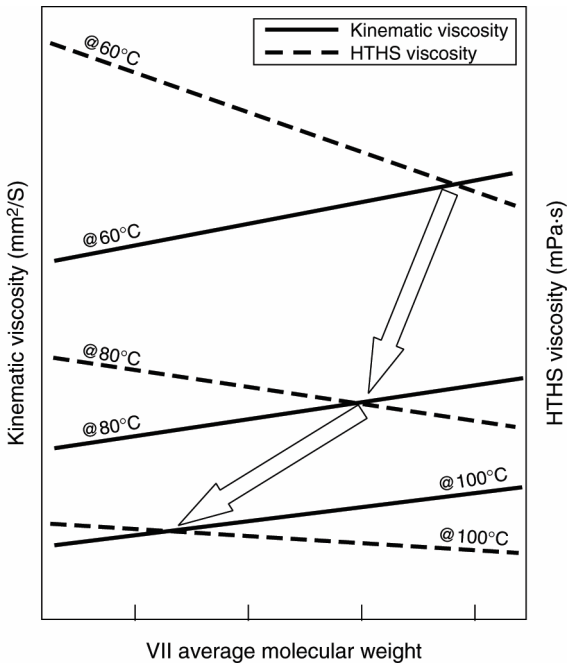


Fig. 6 Viscosity characteristic by VII molecular weight

4. Results Confirming the Performance

From the results of the study above, the test oil (prototype GF-4 oil) was experimentally blended and its performance was confirmed. The oil specifications are shown in Table 6. As reduction in phosphorous content concerns high temperature oxidation stability, anti-wear and fuel economy performance, these confirmed results are described below.

Table 6 Properties of test engine oil

		Current GF-3 oil	Prototype GF-4 oil
Formulation (DI)		A	B
Base oil		Gr.III	Gr.III
Viscosity grade		0W-20	0W-20
Kinematic viscosity [mm²/s]	40 [°C]	34.8	33.4
	100 [°C]	7.85	8.02
HTHS viscosity [mPa·s]	150 [°C]	2.6	2.6
Phosphorus [%]		0.10	0.08
Sulfur [%]		0.30	0.25
Viscosity index improver		PMA-A	PMA-B
Friction modifier		MoDTC-A	MoDTC-B

4.1. High Temperature Oxidation Stability

The high temperature oxidation stability of test oils was evaluated by the Indiana Stirring Oxidation Test (ISOT). Figure 7 shows the test results and Table 7 the test conditions of the current GF-3 oil and the prototype GF-4 oil. It is clear that the prototype GF-4 oil prevents the viscosity increase due to high temperature oxidation compared to the current GF-3 oil.

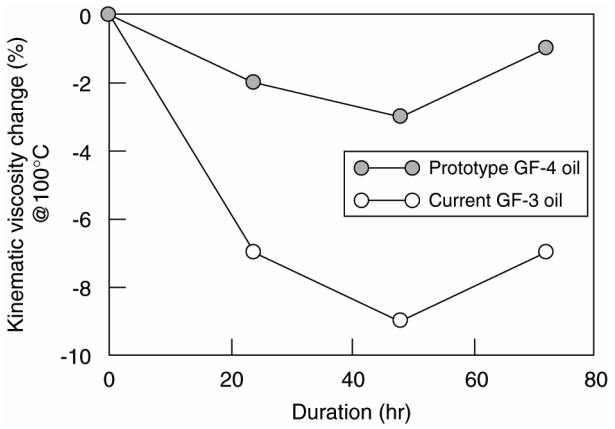


Fig. 7 Kinematic viscosity change in ISOT

Table 7 ISOT test conditions

Method	Based on JIS K 2514		
Oil volume [ml]	250		
Oil temperature [°C]	175		
Catalyst	Copper and Iron		
Test duration [hr]	24	48	72

4.2. Anti-wear Performance

Valve train wear test in the Honda engine described earlier and Sequence IV-A valve train wear test (ASTM D 6891) specified in the GF-4 standards were used to evaluate the anti-wear performance. The results of the valve train wear test using the Honda engine are shown in Fig. 8. The test conditions are the same as those in Table 3. The Sequence IV-A valve train wear test results are shown in Fig. 9 and the test conditions are given in Table 8. In all tests, prototype GF-4 oil showed better results in comparison to the current GF-3 oil.

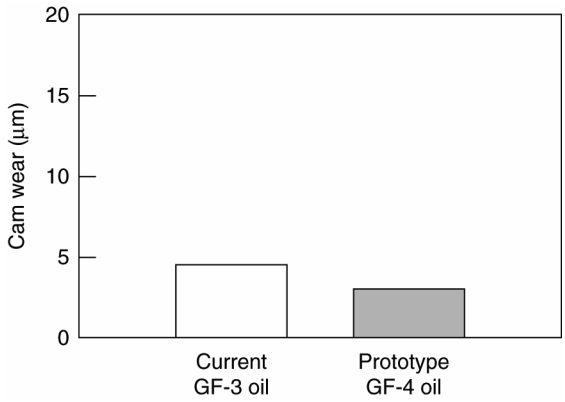


Fig. 8 Comparison of cam wear level in Honda valve train wear test

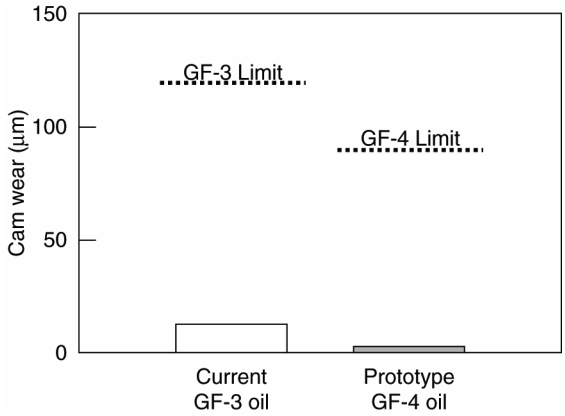


Fig. 9 Comparison of cam wear in Sequence IV-A

Table 8 Sequence IV-A test conditions

Engine	Nissan KA24E, L4, 2.4L	
Stage	I	II
Stage duration [min]	50	10
Engine speed [rpm]	800	1 500
Engine torque [N·m]	25	25
Oil temperature [°C]	50	60
Water temperature [°C]	50	55
Test duration [cycle]	100	

4.3. Fuel Economy Performance

Figure 10 shows the results of 10.15-mode fuel economy test in a vehicle equipped with a typical Honda engine. The specifications of the vehicle are given in Table 9. Figure 11 shows the fuel economy improvement (FEI) by the Sequence VI-B fuel economy test (ASTM D 6837) specified in the GF-4 standards. The conditions of the test are given in Table 10. In these tests, fuel economy was confirmed to improve in the prototype GF-4 oil over the current GF-3 oil. Also the prototype GF-4 oil met the FEI standards in the 0W-20 category of GF-4.

Table 9 Japanese 10.15 mode test conditions

Engine	L4, 2.0L, MPI
Valve train	DOHC, 4valve, Roller-type
Vehicle	Domestic production model
Test mode	Japanese 10.15

Table 10 Sequence VI-B test conditions

Engine	Ford modular, V8, 4.6L	
Aging stage	I	II
Stage duration [hr]	16	80
Engine speed [rpm]	1 500	2 250
Engine power [kW]	15.39	23.10
Oil temperature [°C]	125	135
Water temperature [°C]	105	105

Test stage	1	2	3	4	5
Engine speed [rpm]	1 500	800	800	1 500	1 500
Engine power [kW]	15.39	2.18	2.18	15.39	15.39
Oil temperature [°C]	125	105	70	70	45
Water temperature [°C]	105	95	60	60	45

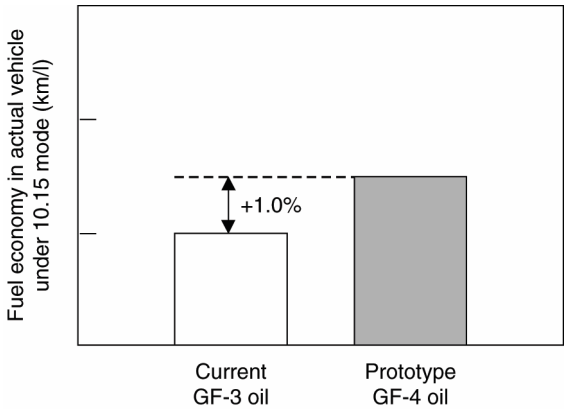


Fig. 10 Fuel economy improvement in Japanese 10.15 mode test

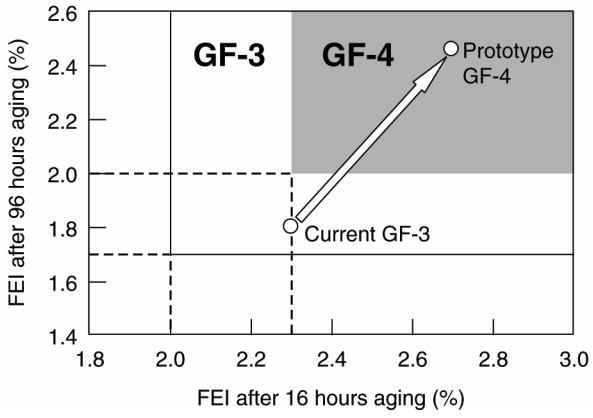


Fig. 11 Fuel economy improvement in Sequence VI-B

5. Conclusion

The researchers arrived at the following conclusions through the development of 0W-20 fuel economy gasoline engine oil conforming to the new GF-4 standards:

(1) By selecting MoDTC and detergent-dispersant appropriately to compensate for extreme pressure agent ZnDTP, wear could be prevented.
(2) The contribution of kinematic viscosity and HTHS viscosity on engine friction varies with the temperature. It was found that optimizing the molecular weight of viscosity index improver was an effective method to reduce friction.
(3) The prototype oil blended based on this knowledge met the GF-4 standards and improved the actual fuel economy by 1%.

References

(1) Tanaka, H., et al.: The Effect of 0W-20 Low Viscosity Engine Oil on Fuel Economy, SAE 1999-01-3468 (1999)

(2) Sato, T.: Development of fuel economy engines and fuel economy engine oils in Honda, IDEMITSU TRIBO REVIEW, No. 26, p. 2-5 (2003)

(3) Environmental Protection Agency: Vehicle programs and compliance guidance letters, CCD-04-07 (LDV/LDT/MDPV/HDV), http://www.epa.gov/otaq/cert/dearmfr/ccd0407.pdf

(4) Yaguchi, A.: Gasoline Engine Oil Standard ILSAC GF-4, ENEOS Technical Review, Vol. 46, No. 1, p. 26-32 (2004)

(5) American Petroleum Institute : Technical Bulletin 15th Edition of API 1509, APPENDIX E, (2002)

(6) Nihon junkatsugakkai: Hyoumensonshou, Kaiteiban Junkatsu Handbook, Tokyo, Yokendo, p. 81-82 (1987)

(7) Miyashita, A., et al.: Lubricity Mechanism of Organo-Molybdenum-Compound, Proceedings of the International Tribology Conference, Nagasaki, p. 15-20 (2000)

(8) Muraki, M., Wada, H.: Frictional Properties of Organo Molybdenum Compounds in Presence of ZnDTP under Sliding Condition (Part 1), Tribologist, Vol. 38, No. 10, p. 919-926 (1993)

(9) Hoshino, H., et al.: Fuel Efficiency of SAE 5W-20 friction Modified Gasoline Engine Oil, SAE 982506 (1998)

(10) Sagawa, T., et al.: Development of 0W-20 ILSAC GF-3 Gasoline Engine Oil, SAE 2002-01-1636 (2002)

(11) Tohyama, M., et al.: Low Friction Gasoline Engine Oil - Effects of Lower Viscosity and Friction Modifiers-, Toyota Central R&D Labs., Inc. Technical Review, Vol. 32, No. 4, p. 35-43 (1997)

■ Authors ■



Takayuki SATO



Syouji KAWAUCHI

Research on Method of Evaluation of Energy in Gas Generators Using Variable Volume Tank Pressure Measurement Device

Daiei TONOOKA* Takeshi KAI* Yoshihiko MORITA*

ABSTRACT

To date, fixed volume tank pressure measurement devices have been employed in the evaluation of the performance of the gas generators (inflators) used in airbags, etc. However, these measurement devices are limited in accurately gauging inflator characteristics as the volume changes. This research project therefore built a variable volume tank pressure measurement device [(3)] to enable measurement data to be obtained as internal volume changes with increasing tank pressure. This device was used in tests, and measured values were input into a predictive equation to define an index (inflator work) for the evaluation of inflator performance. The new measurement device has made it possible to evaluate energy in an inflator and has enabled the development of a new performance evaluation index (inflator work) and method.

1. Introduction

Fixed volume tank pressure measurement is one of the methods for evaluating the performance of the gas generator used in air bags, etc. This method of measurement has been employed, because it facilitates the manufacturing control of inflators.

J. T. Wang reports that knowing only the tank pressure curve (pressure measurement results obtained by fixed volume tank pressure measurement) is insufficient to determine the capability of an airbag [(1)]. Many other performance evaluation methods of the inflator are being studied[(1),(2)]. However, these evaluation methods mainly use the fixed volume tank pressure measurement device and not only are the theoretical and experimental equations complex, but also the measurement method is not simple. Therefore, it is not widely used as a method for evaluating the performance of the inflator.

Therefore, the work obtained due to the variation in the volume of the tank was focused on, and it was considered that a method for evaluating the inflator performance can be constructed based on this work. As a result, a variable volume tank pressure measurement device[(3)] with built-in flat disk piston capable of sliding within the tank was devised.

This research attempts to define the performance evaluation index of the inflator by substituting the pressure difference and the volume difference obtained as a result of the sliding of the internal piston accompanying the increase in tank pressure in this device, into the predictive equation based on the Energy Conservation Law.

Based on this assumption, the variable volume tank pressure measurement device was manufactured.

2. Definition of Measured Value Symbols

Figure 1 shows the conceptual drawing of the variable volume tank pressure measurement device. Measured value symbols are defined as shown below.

* Tochigi R&D Center

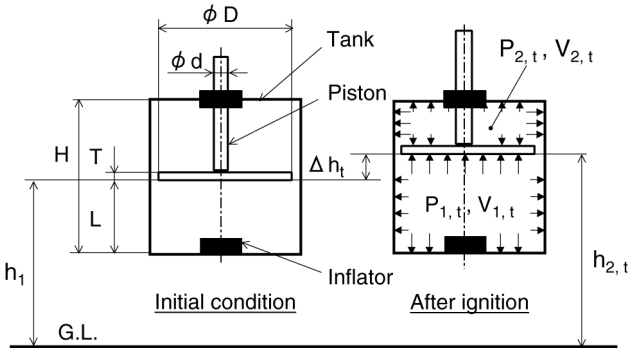


Fig. 1 Conceptual drawing of variable volume tank pressure measurement device

D : Flat disk diameter (m) of flat disk piston
d : Shaft diameter (m) of flat disk piston
T : Thickness of flat disk (m) of flat disk piston
m : Mass (kg) of flat disk piston
H : Overall internal height of tank (m)
$P_{1,t}$: Pressure in tank (Pa) on the lower side of disk surface of flat disk piston (hereafter referred to as "lower side of disk surface")
$P_{2,t}$: Pressure in tank (Pa) on the upper side of disk surface of flat disk piston (hereafter referred to as "upper side of disk surface")
$P_{1,0}$: Atmospheric pressure (Pa) in tank on the lower side of disk surface
$P_{2,0}$: Atmospheric pressure (Pa) in tank on the upper side of disk surface
$\Delta P_{1,t}$: Pressure difference (Pa) in tank on the lower side of disk surface
$\Delta P_{2,t}$: Pressure difference (Pa) in tank on the upper side of disk surface
$V_{1,t}$: Volume (m^3) of tank on the lower side of disk surface
$V_{2,t}$: Volume (m^3) of tank on the upper side of disk surface
$\Delta V_{1,t}$: Volume difference (m^3) in tank on the lower side of disk surface
$\Delta V_{2,t}$: Volume difference (m^3) in tank on the upper side of disk surface
h_1 : Height (m) from the ground line to the lower side of disk surface at the initial position of flat disk piston
$h_{2,t}$: Height (m) from the ground line to the lower side of disk surface after sliding of flat disk piston
Δh_t : Height difference (m)
Δt : Time difference (s)
L : Height (m) from the bottom surface in tank to the lower side of disk surface
Δw_t : Flat disk piston local work (J)
W_t : Flat disk piston total work (J)
Δw_t^* : Inflator local work (J)
W^*_t : Inflator total work (J)
$\Delta w^*_{\kappa,t}$: Inflator local work (J) applying ratio of specific heat κ
$W^*_{\kappa,t}$: Inflator total work (J) applying ratio of specific heat κ

The subscript t in the symbols used in the equations mentioned above shows the measurement values that vary with time.

3. Predictive Equation for Variable Volume Tank Pressure Measurement Device

3.1. Flat Disk Piston Work

Here, flat disk piston work is defined as the work generated by the sliding of the flat disk piston due to the increase in pressure in the tank when gas is generated by the inflator. If the heat issued and received in the system in Fig. 1 is ignored, the flat disk piston local work can be determined from the external work created by the system and the combination of the increased energy inside the system (Energy Conservation Law). The time integration of the flat disk piston local work is the total work of the flat disk piston.

$$\Delta w_t = P_{1,t}\cdot\Delta V_{1,t} - P_{2,t}\cdot\Delta V_{2,t} - mg\cdot\Delta h_t + \frac{1}{2}m\cdot\left(\frac{\Delta h_t}{\Delta t}\right)^2 \quad (1)$$

$$\sum_{t=0}^{N}\Delta w_t = W_t = \sum_{t=0}^{N}\left\{P_{1,t}\cdot\Delta V_{1,t} - P_{2,t}\cdot\Delta V_{2,t} - mg\cdot\Delta h_t + \frac{1}{2}m\cdot\left(\frac{\Delta h_t}{\Delta t}\right)^2\right\} \quad (2)$$

3.2. Inflator Work

The inflator work is assigned by dispersion of Eq. (1).

$$\begin{aligned}\Delta w_t = {} & P_{1,0}\cdot\Delta V_{1,0} + \left(\Delta P_{1,1}\cdot\Delta V_{1,1} + \Delta P_{1,2}\cdot\Delta V_{1,2} + \cdots + \Delta P_{1,t}\cdot\Delta V_{1,t}\right) \\ & - P_{2,0}\cdot\Delta V_{2,0} - \left(\Delta P_{2,1}\cdot\Delta V_{2,1} + \Delta P_{2,2}\cdot\Delta V_{2,2} + \cdots + \Delta P_{2,t}\cdot\Delta V_{2,t}\right) \\ & - mg\cdot\Delta h_t + \frac{1}{2}m\cdot\left(\frac{\Delta h_t}{\Delta t}\right)^2\end{aligned} \quad (3)$$

Every member that forms the second and fourth member in Eq. (3) is the inflator local work. The inflator local work is defined as the amount of energy that expresses the phenomenon of the generation of gas generated by the inflator per unit time.

Assuming that the gas generated from the inflator is ideal gas, the inflator local work can be defined as shown in the following equation.

$$\Delta P_{1,t}\cdot\Delta V_{1,t} \approx \Delta P_{2,t}\cdot\Delta V_{2,t} \quad (4)$$

By applying the conditions assumed in Eq. (4), a general equation for the total work and the inflator local work was formulated. The total inflator work is the measured value that expresses the total amount of energy that can be assigned by the inflator to a restraint device until a specific time stage.

$$\Delta w_t^* = \Delta P_{2,t}\cdot\Delta V_{2,t} \quad (5)$$

$$\sum_{t=0}^{N}\Delta w_t^* = W_t^* = \sum_{t=0}^{N}\left(\Delta P_{2,t}\cdot\Delta V_{2,t}\right) \quad (6)$$

The reason for formulating a general equation for inflator work using the term on the right side of Eq. (4) is to reduce the compressibility effects of the air that exists in the tank.

If the ratio of specific heat κ is applied to Eqs. (5) and (6),

$$\Delta w_{\kappa,t}^* = \Delta P_{2,t}\cdot\Delta V_{2,t}^{\kappa} \quad (7)$$

$$\sum_{t=0}^{N}\Delta w_{\kappa,t}^* = W_{\kappa,t}^* = \sum_{t=0}^{N}\left(\Delta P_{2,t}\cdot\Delta V_{2,t}^{\kappa}\right) \quad (8)$$

then Eqs. (7) and (8) are used to compare inflators with different gas components.

The predictive equations assigned in Eqs. (5) to (8) are the equation of state of gas consisting of pressure difference and volume difference obtained by the sliding of the flat disk piston.

4. Variable Volume Tank Pressure Measurement Device

Figures 2 and 3 show the conceptual drawing and photo of the variable volume tank pressure measurement device. The variable volume tank pressure measurement device consists mainly of the cylindrical tank and the flat disk piston.

The inflator is positioned on the bottom surface of the tank and at the center of the tank in the normal direction.

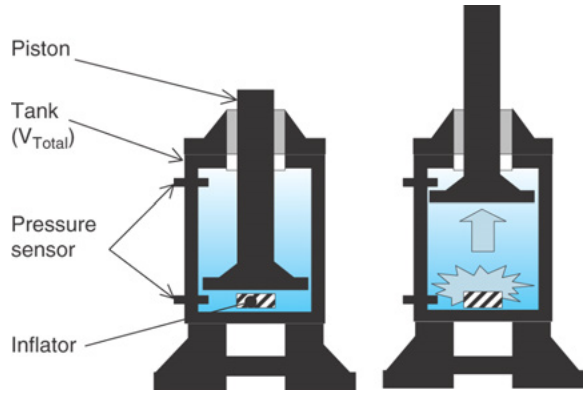


Fig. 2 Structure of variable volume tank pressure measurement device

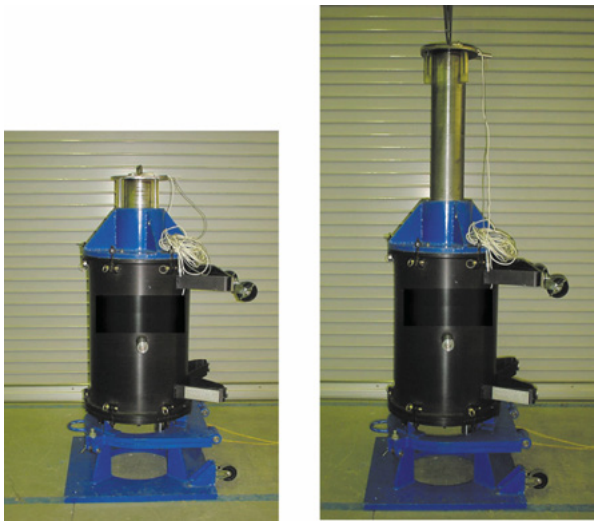


Fig. 3 Picture of variable volume tank pressure measurement device

5. Experiment

5.1. Overview of the Variable Volume Tank Pressure Measurement Device

The total tank volume V_{Total} of the variable volume tank pressure measurement device used in the experiment was taken as 0.054 [m^3].

5.2. Experimental Conditions

5.2.1. Measurement method

The measurement of pressure on the upper and lower sides of the disk surface in the variable volume tank pressure measurement device was performed using two pressure sensors installed on the outer surface of the cylindrical tank at arbitrary positions in the normal direction. The position of installation of the pressure sensor was arbitrary, because the flat disk piston built in the tank is considered to slide while maintaining equilibrium between the pressures on the upper and lower side of disk surfaces.

The change in the volume of the variable volume tank pressure measurement device was calculated from the slide displacement of the flat disk piston.

5.2.2. Inflator used in the experiment and the experimental conditions

1) Dual ignition pyrotechnic inflator

- Simultaneous ignition (First and second stages 0 (ms))
- Delay ignition (First stage 0 (ms), second stages 20 (ms))
- Delay ignition (First stage 0 (ms), second stage 40 (ms))

The settings of 20 and 40 (ms) for the experimental conditions in the delay ignition are optional settings used for validating the gas generation phenomenon.

2) Single ignition pyrotechnic inflator

- The experiment was performed thrice for inflators with the same inflator specifications.

6. Validation and Observations of Experimental Results

6.1. Validation of Experimental Results

Figures 4 to 7 show the measurement results of internal pressure in the variable volume tank pressure measurement device. The vertical axis shows the pressure on the upper and lower side of disk surface in the tank and the horizontal axis shows the time from ignition of inflator.

All the measurement results in Figs. 4 to 7 show that the curves in the graph of pressures on the upper and lower sides of disk surface of the variable volume tank are in equilibrium. (Enveloped area in the figure.) This proves that the time integrated value of the pressure differences in the upper and lower side of disk surface is in equilibrium even when the inflator specifications and experimental conditions vary. Thus, the conditions assumed in the internal pressure equilibrium equation (4) proposed in this report were confirmed. Moreover, the validity of the manufactured variable volume tank pressure measurement device was also confirmed.

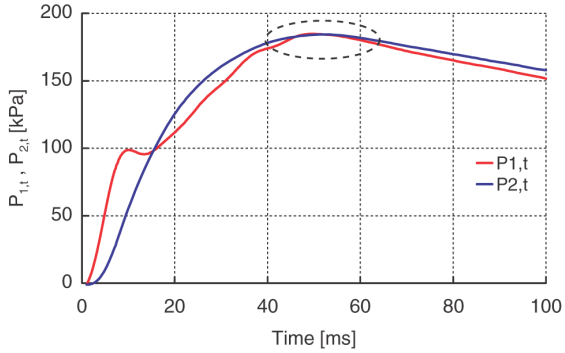


Fig. 4 Tank pressure (dual ignition pyrotechnic inflator, 0ms)

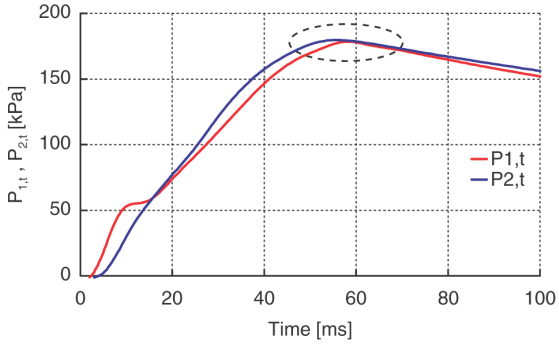


Fig. 5 Tank pressure
(dual ignition pyrotechnic inflator, 20ms delay)

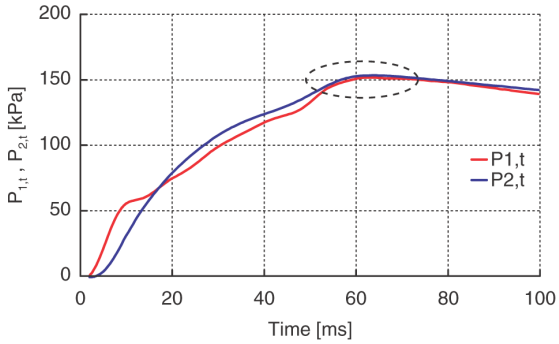


Fig. 6 Tank pressure
(dual ignition pyrotechnic inflator, 40ms delay)

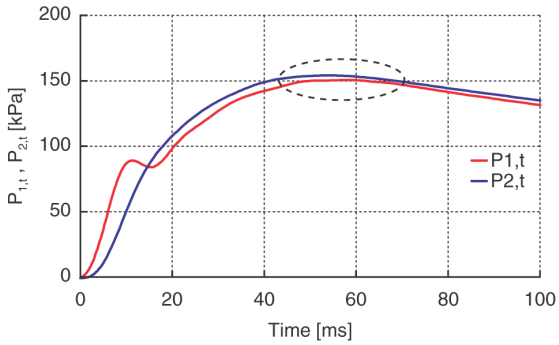


Fig. 7 Tank pressure
(single ignition pyrotechnic inflator)

6.2. Considerations

The inflator local work and the total work can be determined by substituting the pressure difference derived from internal pressure measurement results of the variable volume tank pressure measurement device and the volume difference, into predictive equation (5) and (6), or (7) and (8).

6.2.1. Dual ignition pyrotechnic inflator

Figures 8 and 9 show the calculation results of the inflator work. The vertical axis shows inflator work and the horizontal axis shows the time from ignition of inflator. The following can be understood from the results:

(1) The graph for the local inflator work in simultaneous ignition is curved and the slope of time of local inflator work is higher than 20 and 40 ms in the secondary stage delay ignition.

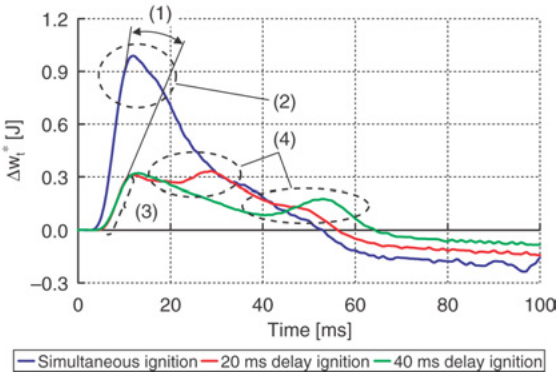


Fig. 8 Local inflator work
(dual ignition pyrotechnic inflator)

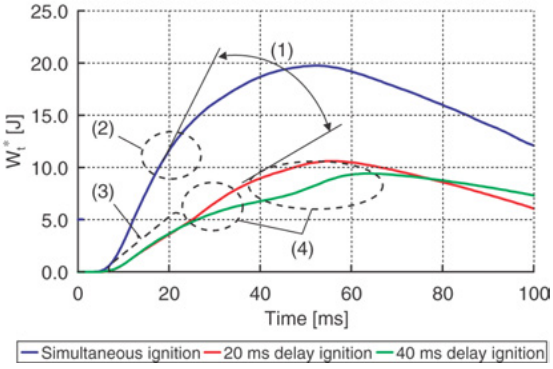


Fig. 9 Total inflator work
(dual ignition pyrotechnic inflator)

(2) The local inflator work in simultaneous ignition deteriorates at stages earlier than the secondary stage delay ignition.

(3) The curve in the local inflator work graph at 20 and 40 ms of secondary stage delay ignition is consistent until it reaches the vicinity of the secondary stage delay ignition time.

(4) The increase in the local inflator work graph at 20 and 40 ms of secondary stage delay ignition can be seen from the vicinity of the secondary stage delay ignition time.

These considerations are similar also for the total inflator work shown in Fig. 9.

6.2.2. Single ignition pyrotechnic inflator

Figures 10 and 11 show the calculation results of local inflator work when the experiments for single ignition were performed thrice and simultaneous ignition of dual ignition pyrotechnic inflators. The following can be understood from the results:

(1) From the time slope and its maximum value for local inflator work and the curve of the graph, it can be seen that the dispersion of the inflator gas generation phenomenon was low when the predictive equation proposed in this paper was used.

(2) The differences in the local inflator work can be expressed by comparing the calculation results for the single and dual ignition pyrotechnic inflators.

These considerations are similar also for the total inflator work shown in Fig. 11.

From the results for single and dual ignition pyrotechnic inflators mentioned earlier, it can be said that inflator work is

the amount of energy that expresses the gas generation phenomenon and the energy characteristics.

Consequently, the variable volume tank pressure measurement device with which this inflator work can be obtained is a measurement device that enables validation of the appropriate inflator performance evaluation index.

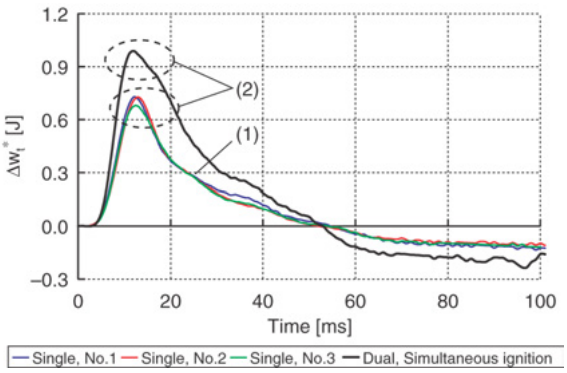


Fig. 10 Local inflator work
(single and dual ignition pyrotechnic inflators)

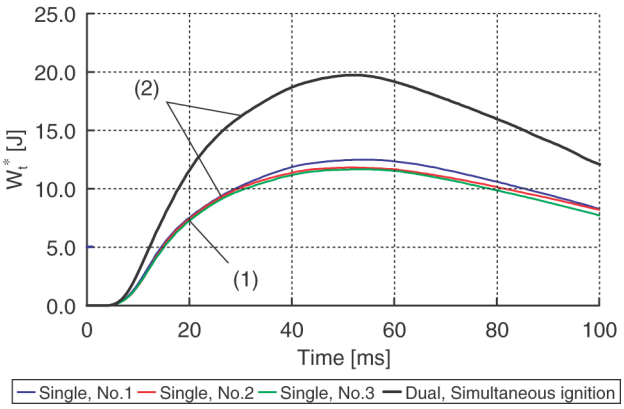


Fig. 11 Total inflator work
(single and dual ignition pyrotechnic inflators)

7. Conclusion

The goal of this research was to construct a method for evaluating the energy of the inflator considering the variable volume, for which a variable volume tank pressure measurement device with a built-in flat disk piston sliding in the tank was designed.

The inflator performance evaluation index was obtained from experiments using this device.

Henceforth, our endeavor will be to verify that this method of energy evaluation of the inflator can also express gas temperature and temperature conditions of the laboratory.

Acknowledgments

We would like to express our heartfelt gratitude to everybody at Autoliv Japan for their assistance in this research.

References

(1) Wang, J. T.: Are Tank Pressure Curves Sufficient Discriminate Airbag Inflators, SAE Paper 910808

(2) Hussey, B., Rink, M. L.: Predictive Techniques for Airbag Inflator Exit Properties, SAE Paper 950344,

(3) JP, Patent Application No. 2004-175413

■ Authors ■


Daiei TONOOKA


Takeshi KAI


Yoshihiko MORITA

Development of 590 and 780MPa Grade High-ductility Steel Sheets

Takahiro TANAE* Katsuyoshi KANEKO**

ABSTRACT

A high-ductility TRIP steel sheet has been developed to achieve weight savings in automotive bodies. When TRIP steel is deformed by stamping, etc., the transformation of the retained austenite distributed in its matrix structure into martensite controls the strain concentration. This gives the material higher formability than the conventional steels. However, TRIP steel sheets contain a higher amount of Si than the conventional steel sheets, and this can cause the coating quality of the material during hot-dip galvanealing and the ability of cold rolled sheets to accept coatings to decline. A TRIP steel displaying the required strength and formability while possessing identical coating quality and e-coating performance to conventional steels has therefore been developed by optimizing the amount of C, Si and Mn, the main constituent elements of the steel, adding an element which controls Si concentration to sheets for hot-dip galvanealed (GA steel sheet) and removing the concentrated Si surface layer of non-galvanealed sheets for cold rolling (CR steel sheet). As a result, it has been possible to achieve an identical level of formability in 590 MPa and 780 MPa class steel sheets when compared to 440 MPa and 590 MPa class conventional high strength steel sheets (HSS) respectively. In addition, the new steel possesses identical energy absorption characteristics to the conventional HSS but is 10% lighter, enabling weight per vehicle to be reduced by more than 10 kg when the new sheets are applied.

1. Introduction

Auto manufacturers are increasingly tending to use high strength steel sheets (HSS), in particular steels of tensile strengths of 590 MPa and above, in body framework parts in order to achieve weight reductions while complying with requirements for improved collision safety performance. These requirements continue to grow more stringent every year[(1)]. To maximize the weight reduction benefits of HSS, they must be applied to as many parts as possible. However, formability declines as tensile strength increases, and this places limits on the specific parts for which HSS can be used.

In our attempt to achieve significant weight reductions, the authors focused on TRIP steel, which possesses a higher level of strength and formability than the conventional steels while continuing to meet the coating and spot welding performance requirements for automotive materials.

This paper discusses the characteristics of the newly developed steels in comparison to the conventional steels, with a focus on coating quality, e-coating performance, formability and energy absorption properties.

* Tochigi R&D Center
** Honda R&D Europe (UK)

2. Development Goals

In terms of the relationship between strength and formability in steel sheets, tensile strength and elongation are normally in the relationship shown in Fig. 1. Higher elongation means superior formability: in the graph, the higher a sheet registers in the upper right, the better its characteristics.

At the time this development project was commenced, the 2001 model year CIVIC applied the greatest proportion of HSS in the framework. HSS, mainly solid solution strengthened 440 MPa class and precipitation hardened 590 MPa class, represented 57% of the weight of the framework[2]. The development project established the goal of replacing the 440 MPa and 590 MPa HSS with steels of a strength one rank higher, 590 MPa and 780 MPa HSS respectively. The goal was to improve the mechanical properties of the steels in order to achieve an equivalent level of formability in a 590 MPa HSS to a 440 MPa HSS, and in a 780 MPa HSS to a 590 MPa HSS.

The project investigated the use of 980 MPa HSS, but the achievement of this level of tensile strength in a TRIP steel increases the amount of carbon required in the composition to more than 0.30 mass%, generating difficulties with spot welding, among other issues, which would potentially limit the range of parts for which the steel could be used. Other than TRIP steels, cold rolled dual phase 980 MPa HSS is already in use and can also be considered, but it does not possess sufficient formability, once again placing restrictions on its use. It was therefore judged that the maximum weight reduction benefits would be achieved by establishing the targets for tensile strength at 590 MPa and 780 MPa.

Yield strength was another mechanical property of the steel which was considered. Having determined the parameters for weight reduction benefits, studies were conducted to ensure that the new steel would possess equivalent collapse strength to the conventional solid solution strengthened 440 MPa and precipitation hardened 590 MPa steels. The properties shown in Table 1 were established as targets on the basis of these studies.

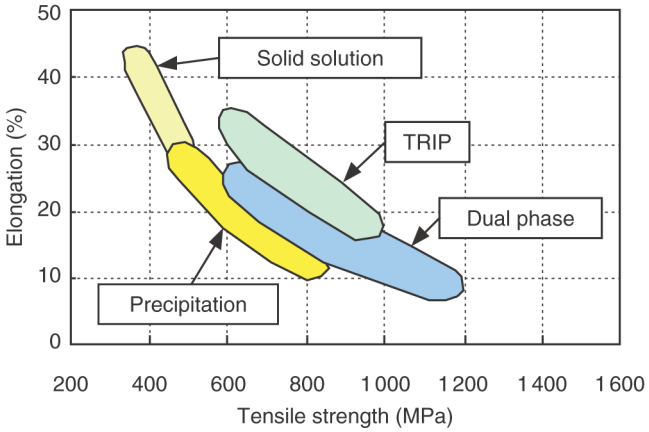


Fig. 1 TS-EL balance of high-strength steel

In addition to the mechanical properties discussed above, GA steel sheets for automotive use require good coating performance and GA and CR sheets require good e-coating and spot welding performance. The development goal established here was to achieve performance in these areas equivalent to that displayed by conventional HSS sheets.

Table 1 Target for mechanical properties of TRIP steel

Grade	YS(MPa)	TS(MPa)	El(%)
GA 590TRIP	360 min.	590 min	32 aim
GA 780TRIP	400 min.	780 min.	25 aim
CR 780TRIP	400 min.	780 min.	27 aim

3. Specifications of Steels

3.1. Principle of the TRIP Effect

This section will provide a basic introduction to the properties of TRIP steels which were considered in determining the specifications of the new steels. TRIP is an abbreviation of transformation induced plasticity. This phenomenon originates in the construction of the microstructure. An example of this microstructure is shown in Fig. 2. As the photograph shows, the microstructure is characterized by the dispersion of metastable retained austenite in volume fractions from a few % up to around 15% in the matrix structure, which is composed of ferrite, etc. When the retained austenite receives a deforming strain, as for instance when the material is pressed, it is transformed into martensite. The martensite is in a hard phase, and the sections which have undergone transformation are therefore relatively stronger than the sections which have not. As a result, the deforming strain is transmitted to the relatively weaker, untransformed sections. The repetition of this phenomenon prevents the strain from concentrating in one area, which could be the point of origin of breakage, thus increasing the ductility of the material. Ensuring that the steel contains this metastable retained austenite is therefore the major consideration in the manufacture of TRIP steels.

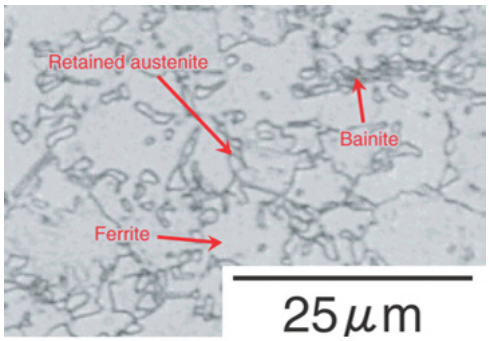


Fig. 2 Microstructure of TRIP steel

3.2. Study of Basic Components of Steels

Like other steel sheets, the required properties of TRIP steels are generally achieved through appropriate composition of the material and the application of heat treatments. Figure 3 shows an outline of the heat treatment used for TRIP steels. Almost all steel sheets contain carbon, and in the case of TRIP steels it is desirable to concentrate this carbon as much as possible in austenite, in order to ensure that metastable retained austenite is obtained[3]. The most important factors in achieving this are the cooling and overaging processes. During cooling a ferrite phase precipitates from the austenite. Because the solubility of carbon in ferrite is low, as ferrite precipitates carbon concentrates in the austenite. As the steel is aged at

temperatures of 400-500 °C, carbon is further concentrated in the process of bainitic transformation. As a result the austenite, which is stable at high temperatures, remains in a semi-stable state up to room temperature. The most important component of the steel in this process is Si. Si is one of the elements making up ferrite, and does not exist in solid solution in cementite, and it therefore retards pearlite transformation during the cooling process, thus promoting the concentration of carbon which occurs with its precipitation from ferrite[4]. This provides a base for the further concentration of carbon in the overaging process which the steel undergoes after cooling. In addition, the fact that Si exists in solid solution in ferrite contributes to strength. Al is known to function in the same way as Si[4]. Mn is another important element in TRIP steels. Mn is one of the elements which makes up austenite, and therefore contributes to the formation of the retained austenite in the steel, and also contributes to strength by being present in the ferrite in solid solution. Therefore, in addition to carbon, the most basic component of all steel sheets, the important components of TRIP steels are Si or Al, which contribute to the formation of retained austenite and increase strength by being present in ferrite in a solid solution, and Mn, which is a component which makes up austenite and enables the strength of the material to be regulated. In this research project, a basic composition of C-Si-Mn system was selected as providing an excellent balance between strength and ductility.

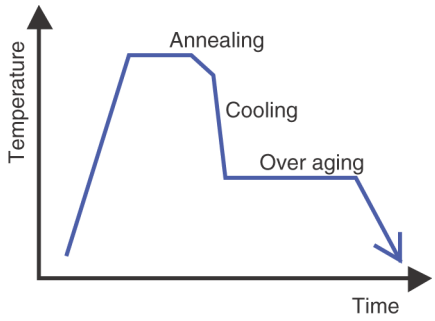


Fig. 3 Heat treatment diagram

3.3. GA TRIP Steel

After selection of C-Si-Mn system as the basic composition of the new steel, the specifications of the steel and the production process were optimized to balance excellent coating performance on GA sheets with the achievement of the required mechanical properties.

3.3.1. Causes of decline in coating performance

Si plays an important part in the achievement of the required properties in TRIP steel, but it also has a negative effect on coating performance in the hot dip galvanizing process. This is because in the annealing process during production, Si concentrates on the surface layer of the steel sheet as compound oxides with Mn[5),(6)]. The continuous galvanizing line (CGL) used in the production of GA sheets generally includes the processes shown in Fig. 4. Of these, the major purpose of the annealing process is to achieve the desired mechanical properties in the TRIP steel, but at the same time it is also used to adjust the surface condition of the steel to ensure successful hot dip galvanizing. In the annealing process, the steel sheets are first heated in a non-oxidizing furnace, which burns off residues of the rolling oil used in cold rolling remaining on the surface at the same time as forming a thin iron oxide layer. The sheets are then placed in a mixed nitrogen-hydrogen reducing atmosphere to remove the oxide layer and activate the surface. These treatments enable a good coating to be achieved in galvanizing, the next process. However, Si and Mn form oxides more easily than Fe does, and oxidation can therefore proceed even in an atmosphere which is reducing for steel. The concentration of Si and Mn on the surface as compound oxides causes wettability and adhesion between the galvanizing solution and the steel sheet to decline, and can lead to defects in the coating, including tiny areas in which the coating has failed.

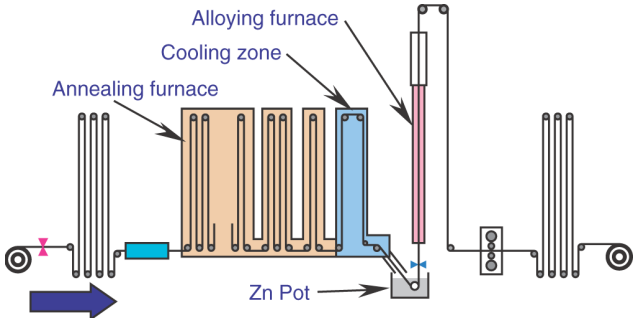


Fig. 4 CGL process flow

3.3.2. Coating quality and mechanical properties

Another issue in the manufacture of GA TRIP steel sheets is the achievement of a balance of coating quality and mechanical properties. After galvanization, GA steel sheets are subjected to an alloying heat treatment, as shown in Fig. 4. In this process the substrate steel and the surface coating of zinc diffuse into each other, forming a steel-zinc alloy, otherwise known as GA steel. In the manufacture of GA TRIP steels, the alloying heat treatment process shown in Fig. 3 doubles as the overaging. Therefore, the fact that the optimum temperatures used in the two treatments differ generates certain issues. Figure 5 shows this in schematic form. The optimum temperature for the alloying heat treatment is 500-550 °C. Below this, alloying is affected and sufficient coating quality for a GA steel cannot be obtained. The optimum temperature for the overaging process is lower at 400-500 °C; if the temperature goes above this range, the retained austenite breaks down and the ductility declines. This means that in order to balance coating quality and

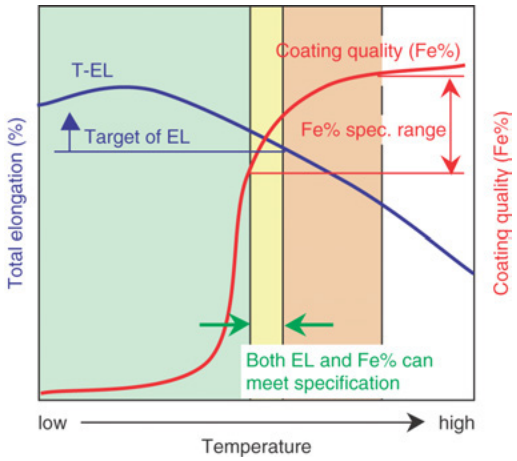


Fig. 5 Relationship between elongation and coating quality

mechanical properties, the range of temperatures which can be used is narrow.

3.3.3. Specifications and method of manufacture of GA TRIP steel

This section will discuss how the issues outlined above were resolved. With respect to the decline in coating quality, optimization of the thickness of the oxidizing layer formed in the non-oxidizing furnace in the annealing process enabled the concentration of Si and Mn on the surface in the following reducing process to be controlled to a certain extent[6]. In addition, elements have been added to the basic composition of C-Si-Mn system to control the concentration of Si and Mn on the surface of the steel sheet. Figure 6 shows a photograph of a cross-section of the coating layer achieved as a result. The coating layer is not inferior to that achieved on the conventional GA steel and no reduction in adhesion can be observed. The measures adopted can therefore be judged successful in controlling the reduction in coating performance caused by Si and Mn. The mechanism of this effect may be considered as follows:

The elements added to the composition were selected on the basis of oxidizing less readily than Fe, and a steel oxide layer therefore forms when the material is heated in the production process or placed in the non-oxidizing furnace during annealing, causing the added elements to concentrate on the surface. This is believed to have the same effect as the formation of a layer on the steel sheet surface which controls the concentration of Si and Mn.

To achieve a balance between coating quality and mechanical properties, the concentration of Al in the zinc bath was controlled to enable the temperature used for the alloying process which follows galvanization to be lowered close to the optimum temperature to ensure the desired mechanical properties.

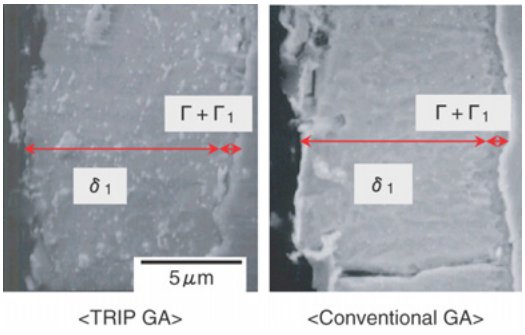


Fig. 6 Comparison of coating layer (TRIP and conventional)

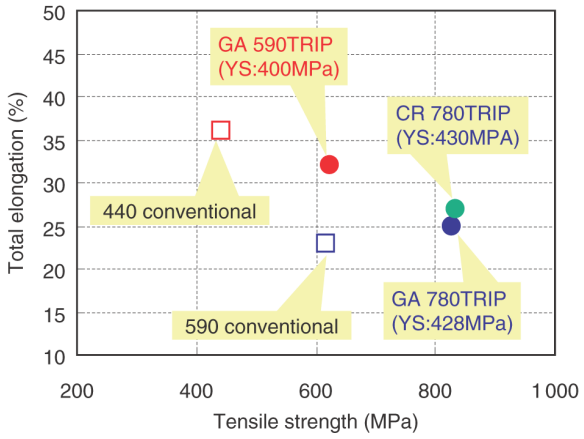


Fig. 7 Comparison of TS-EL balance

The mechanical properties of the steel were tested after the measures described above had been implemented. As Fig. 7 shows, the results of these tests indicated that the steel sheet satisfied requirements for a GA steel sheet, and target values for strength and total elongation have been achieved.

3.4. CR TRIP Steel

With a basic composition of C-Si-Mn system, materials specifications and the production process were optimized to achieve good e-coating performance and the required mechanical performance for CR TRIP steel.

3.4.1. Causes of decline in e-coating performance

In addition to its effect on e-coating performance in GA steels, Si has a negative effect on e-coating performance in CR TRIP steels. As in the case of GA TRIP steels, the mechanism of this effect is the concentration of Si and Mn on the surface during annealing, but it is particularly related to the concentration of Si. Figure 8 shows the distribution of elements on the surface of a CR TRIP steel sheet from the initial stages of development, and a marked concentration of Si can be observed. Figure 9 shows the results of hot salt water dipping tests conducted to determine the quality of the chemical conversion film forming when the sheet undergoes phosphate treatment and the level of adhesion of the e-coat. There are a large number of gaps and irregularities in the chemical conversion film, and the width of peeling in the hot salt water dipping tests was more than two times the standard figure. E-coating performance was therefore judged as inadequate.

3.4.2. Material specifications and production process for CR TRIP steel

In order to improve the e-coat performance of the CR TRIP steel, the project first attempted to modify the conditions of the phosphate treatment to improve etching and increase the mass of the film. However, despite the fact that the chemical conversion film showed a slight improvement in quality, no improvement was observed in the adhesion of the e-coat. The following methods were therefore adopted to remove the concentration of Si on the steel surface:

(1) Reduction of the amount of Si in the steel: The concentration of Si on the surface of the steel was controlled by reducing the amount of Si in the steel while ensuring that sufficient Si was added to achieve the required mechanical properties.
(2) Capture of the Si on the surface in an oxide scale layer and removal of the layer by descaling.

Other methods were tested, including strengthening the pickling, using surface grinding, pickling and alkali cleaning after the annealing process. But their effectiveness could not be verified. The addition of elements to control the concentration of Si on the surface of the steel which proved effective in the case of GA steels was ruled out from considerations of increases in materials costs.

Figure 10 shows the results of measurements of the distribution of elements on the surface of the steel after the measures described above were implemented. It is clear that there has been a significant reduction in the concentration of Si compared with the results shown in Fig. 8. The results of tests on the quality of the chemical conversion film and resistance to hot salt water conducted on the steel after the measures were implemented are shown in Fig. 11. No gaps or irregularities can be observed in the film, and peel width is also within standard values. The results of corrosion resistance tests conducted after e-coating also met the standards, and the e-coat can be judged as satisfying automotive performance requirements.

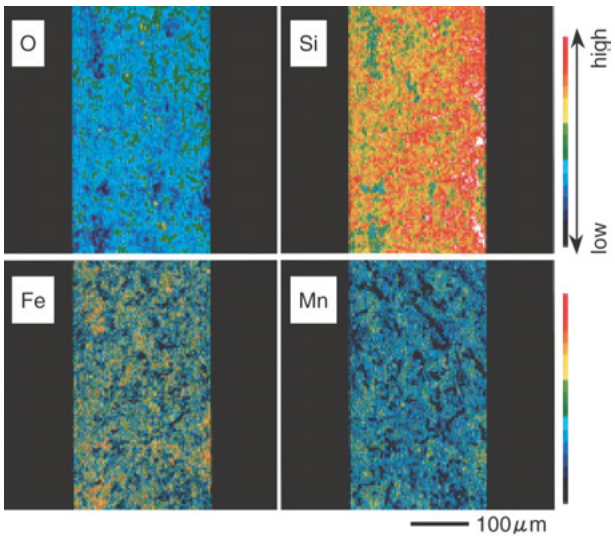


Fig. 8 Surface analysis (EPMA)

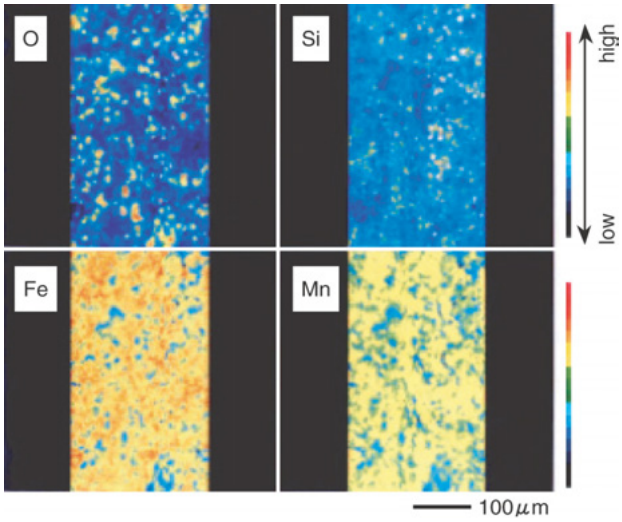


Fig. 10 Surface analysis (EPMA post countermeasure)

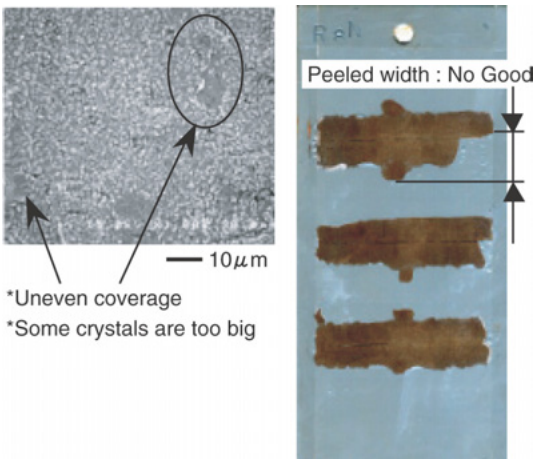


Fig. 9 Phosphatability and E-coat adhesion

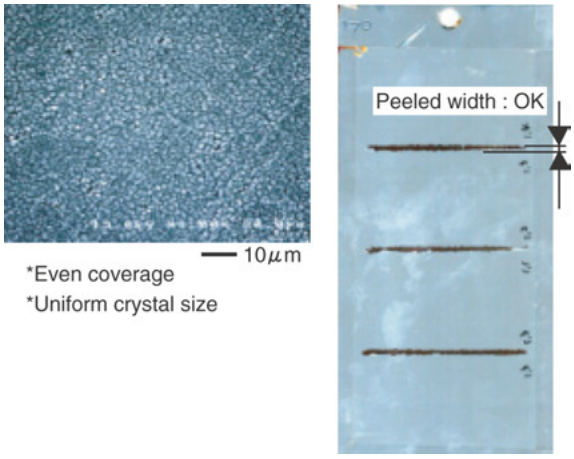


Fig. 11 Phosphatability and E-coat adhesion (post countermeasure)

4. Test Results

Tests were conducted to compare the newly developed TRIP steels to the conventional steels.

4.1. Formability

4.1.1. Limiting dome height tests

Figure 7 shows comparisons of the tensile strength and elongation of the newly developed TRIP steels and the conventional HSS. As the Figure shows, the TRIP steels have a better balance of strength and ductility than the other steels, and this can be interpreted as representing higher formability. However, elongation is not a sufficiently rigorous measure to enable comparison of formability, and limiting dome height tests were therefore conducted. These tests enable comparisons of formability under conditions closer to actual pressing than those of tensile tests. The tests measured the maximum height of deformation and the strain generated when rectangular test pieces were pressed by a punch with a fixed curvature or when bulging was conducted by fluid pressure until breaking, as shown in Fig. 12(a). Varying the dimensions of the short edge of the test piece enabled the



Fig. 12(a) Forming test method

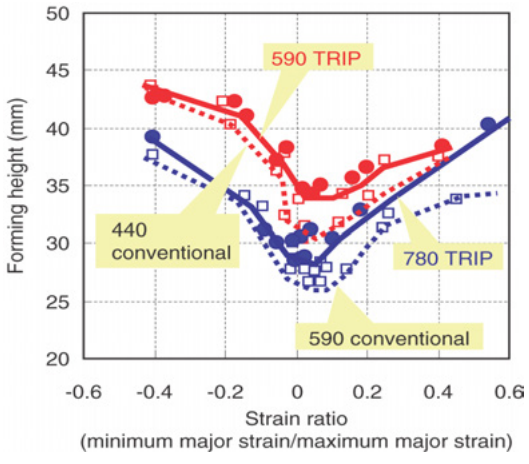


Fig. 12(b) Comparison of formability

ratio between the maximum major strain and the minimum major strain which is generated perpendicular to it to be varied.

The results of these tests are shown in Fig. 12(b). Comparison of the position of each of the steels on the graph indicates that the 590 and 780 MPa class TRIP steels have equivalent or superior formability to the conventional 440 and 590 MPa class HSS. This demonstrates that initial development targets have been achieved, and that the 590 and 780 MPa class steels can be used to replace, respectively, 440 and 590 MPa class steels in automobile body framework parts.

4.1.2. Prototype stamping trials

Trial stampings of prototype shapes were conducted to compare the formability of the steels for actual vehicle parts. As shown in Fig. 13(a), a test piece with a pouched edge was produced, and the height to which it was possible to form the pouched section was compared. Figure 13(b) shows the results. Under conditions closer to those of actual production, the new 590 and 780 MPa class TRIP steels demonstrate equivalent or higher levels of formability to the conventional 440 and 590 MPa class HSS, as they did in the limiting dome height tests.



Fig. 13(a) Appearance of prototype die

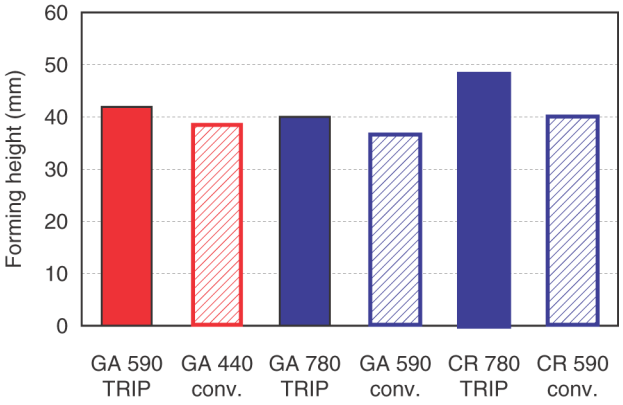


Fig. 13(b) Comparison of formability

4.2. Spot Welding Performance

In addition to formability, another important property for automotive steel sheets is good spot welding performance, and tests were conducted to verify this for the new steels. Tensile shearing tests and cross tension tests were conducted to measure static strength and fatigue strength in order to evaluate spot welding performance. Figure 14 shows the results of static tensile shearing strength tests as an example. When the results are organized in terms of sheet thickness (t), nugget diameter (N.D.) and the tensile strength of the steels (TS), the parameters that determine spot welding strength, it is clear that the spot welding strengths of the TRIP steels are within the range of distribution for the conventional materials which have been successfully employed in mass production, and strength can be assured with standard control of nugget diameter. The results of other tests of spot welding strength also showed that the performance of the new steels equaled that of the conventional steels.

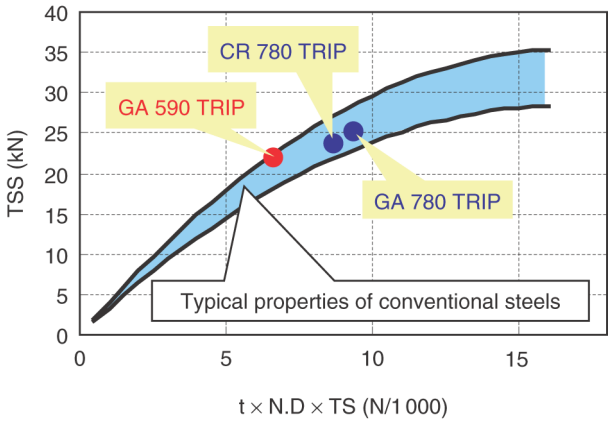


Fig. 14 Strength of spot-welded joint

4.3. Energy Absorption Properties

Given that the main purpose of applying HSS in framework parts is to balance increased collision safety performance with weight reductions, the energy absorption properties of the steels, which relate directly to collision performance, are extremely important factors. Tests of crushing deformation, an important mode of deformation in front and rear collisions, were therefore conducted to compare the energy absorption of the TRIP steels with that of the conventional HSS. Test samples were constructed by bending 1.6 mm thick sheets of 590 and 780 MPa class TRIP steel, 440 MPa solid solution strengthened HSS and 590 MPa precipitation hardened HSS and spot welding them to form hat-shaped quadratic prisms. The samples were subjected to bake-hardening (BH) treatment at 170 °C for 20 mins, after which they were subjected to the test procedures shown in Fig. 15. In the tests, a 160 kg weight was dropped on the test pieces from a height of 12 m, and the energy absorbed until deformations of 50, 100 and 150 mm were produced, was determined. The results of these tests are shown in Fig. 16, and show an increase of approximately 30% in energy absorption in the new 590 MPa and 780 MPa class TRIP steels against the conventional 440 MPa and 590 MPa class

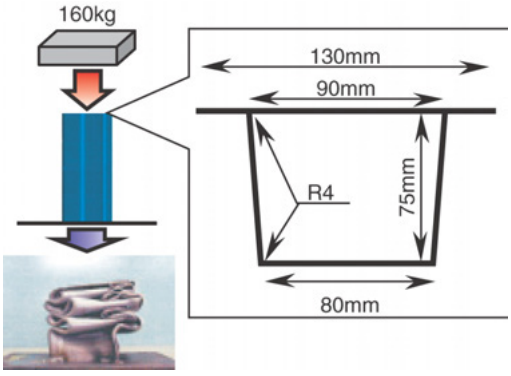


Fig. 15 Test method

HSS respectively.

The weight reduction effect of the TRIP steels was estimated on the basis of these results. The equation below, which shows the relationship between the thickness and shape of the materials on energy absorption in a quadratic prism, was used in the estimates[7]:

$$E_{ab} = C\ \delta\ L^{1/3} t^{3/5} \quad (1)$$

E_{ab} : Amount of energy absorbed
C : Constant
δ : Amount of deformation
L : Length of side
t : Sheet thickness

Equation (1) was used to find the relationship between energy absorption and thickness for steel sheets of identical side length (cross-sectional shape) for a deformation of 100 mm. The results of these calculations are shown in Fig. 17. The calculation results show that the energy absorption of a TRIP steel sheet of 1.4 mm is identical to the energy absorption of a conventional HSS sheet of 1.6 mm. The weight reduction benefit in this case is 12.5%, the difference between the thicknesses of the two sheets. The weight reduction benefit will increase or decrease depending on the thickness of the original sheet to be replaced, but with a range of thicknesses between 1.0 and 2.0 mm, which are the most widely used in automobile bodies, weight reductions of more than 10% can be expected.

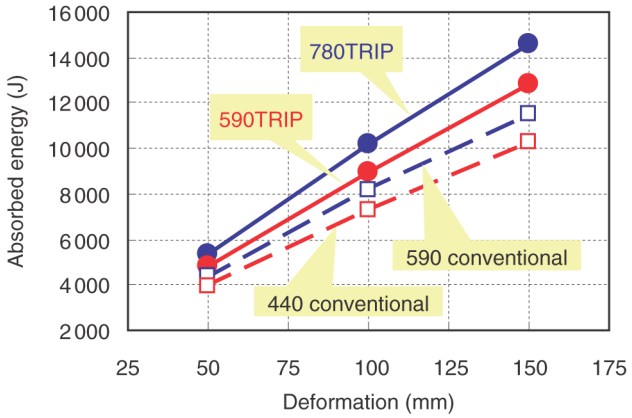


Fig. 16 Comparison of absorbed energy

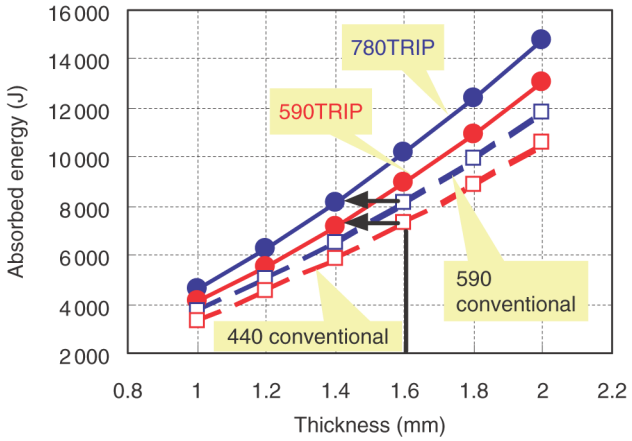


Fig. 17 Estimation of thickness

5. Effect in Vehicle Use

The effect of the new steels in vehicle use was verified using simulations of a rear collision with the TRIP steel sheets applied to the rear framework. The 440 MPa solid solution strengthened steel and the 590 MPa precipitation hardened steel, which currently are the most widely used at Honda, were used for comparison. The results of these simulations are shown in Fig. 18. The thickness of both the 590 MPa and 780 MPa TRIP steels was calculated as 0.2 mm thinner than that of the conventional 440 and 590 MPa class HSS. The results show almost identical deformation in the conventional HSS and the new TRIP steels, indicating that an equivalent level of collision safety performance can be achieved with a weight reduction of approximately 10% in the rear frame.

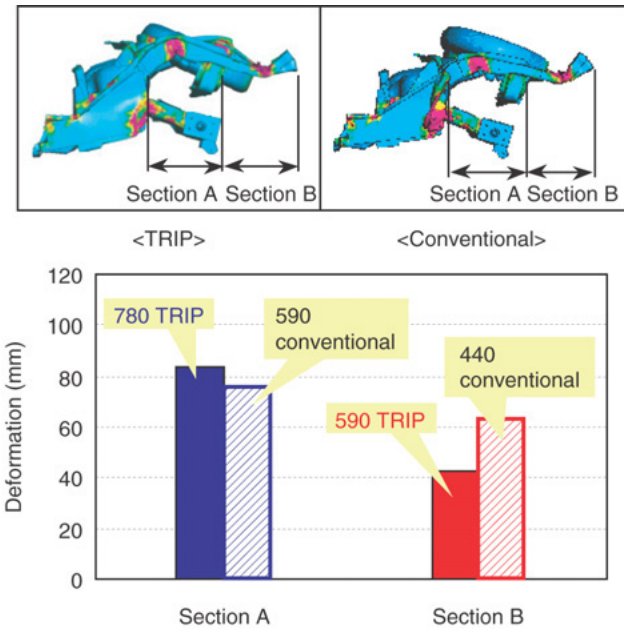


Fig. 18 Comparison of deformation (simulation)

6. Conclusion

590 and 780 MPa class TRIP steels have been developed to enable weight reductions to be achieved in automobile bodies. The results of the development project are as follows:

(1) Elements which control the concentration of Si were added to the basic composition of C-Si-Mn system to enable the achievement of a balance between the coating performance required for a GA steel and the required mechanical properties.
(2) Removal of the concentration of Si on the surface of CR TRIP steel sheets with the basic composition of C-Si-Mn ensured the level of e-coat performance for automotive use.
(3) An identical level of formability has been achieved in the 590 and 780 MPa class TRIP steels as that demonstrated by the conventional 440 and 590 MPa class HSS.
(4) Spot welding strength was also verified as equivalent in the TRIP steels to the conventional steels.
(5) The TRIP steels display excellent energy absorption properties, with an identical level of energy absorption to the conventional HSS at 10% lower weight.

(6) The TRIP steels have been applied to the 2004 model year Odyssey, and will continue to be used in future Honda models. On average their use enables a reduction of 10 kg or more in weight per vehicle.

Acknowledgments

The authors wish to take this opportunity to thank all concerned at Nippon Steel Corporation, who were jointly involved in this project with Honda, the many individuals at Takao Kinzoku Kogyo Co., Ltd. who generously assisted in the project, and everyone at Honda and other companies who offered advice and assistance.

References

(1) D&M Nikkei Mechanical, No. 586, p. 60-61 (2003)

(2) Yokota, C., Nakamura, Y., Yada, S., Funatsu, K., Kubo, F., Ohkubo, T., Watanabe, T.: Development of the 2001 Year Model CIVIC, Honda R&D Technical Review, Vol. 13, No. 1, p. 17-28

(3) Itami, A., Takahashi, M., Ushioda, K.: Plastic Stability of Retained Austenite in the Cold-rolled TRIP Sheet Steel, Tetsu-to-Hagane, Vol. 81, No. 6, p. 67-72 (1995)

(4) Takahashi, M., Yoshida, H., Hiwatashi, S.: Properties of TRIP type high strength steels, International Conference on TRIP-Aided High Strength Ferrous Alloys, 2002, p. 103-111

(5) Nishimura, K., Morimoto, Y.: Effect of Si-added steel surface condition on galvanealing reaction, CAMP-ISIJ, Vol. 10, p. 1389 (1997)

(6) Kimura, Y., Okamoto, S., Komatsu, N., Aiba, M., Nakamura, F.: Koucyugenso no hyoumen-nouka ni oyobosu syoudon-jyouken no eikyou, The Japan Institute of Metals Syuuki-taikai Symposium Kouen Gaiyou, p. 96 (1993) (in Japanese)

(7) Uenishi, A., Kuriyama, Y., Takahashi, M.: High-strength Steel Sheets Offering High Impact Energy-absorbing Capability, Nippon Steel Technical Report, No. 317, p. 18-22 (1999)

■ Authors ■



Takahiro TANAE



Katsuyoshi KANEKO

Development of Pb-free Free-cutting Microalloyed Steel with High Toughness for Crankshafts of Small Multipurpose Engines

Yuzuru TAHARA* Shingo SHIMIZU**

ABSTRACT

A ferrite-pearlite type microalloyed steel has been developed for use in the crankshafts of small multipurpose engines. Although the thermal refining process after hot forging has been eliminated, this steel possesses equivalent strength and toughness to thermally refined steel, and can also be induction hardened. The design of the alloy sought to ensure toughness by increasing the ratio of ferrite in the structure of the steel and refining the structure through the use of intragranular ferrite and, at the same time, to ensure strength by strengthening of solid solution and precipitation strengthening and increasing hardenability while still employing a carbon content within the range enabling induction hardening. In addition, conditions for the temperature of heating during hot forging and for cooling after hot forging were established to control coarsening of the structure and optimize the characteristics of the alloy. At the same time, the design ensured that while no lead was added, a level of machinability equivalent to that conventional free-cutting steel with added lead was achieved. This has reduced the cost of crankshaft manufacture by eliminating the thermal refining process and done away with the necessity of adding lead, an environmentally harmful substance.

1. Introduction

Steel that provides the required strength even when the quenching and tempering process (thermal refining process) after hot forging has been eliminated is called microalloyed steel. The basic microalloying method is to add trace amounts of vanadium (V) or other elements to normal structural steel and perform precipitation strengthening using carbonitrides to obtain a strength equivalent to thermal refined steel[(1) - (6)]. Steel produced using only this mechanism is called basic (ordinary) microalloyed steel.

However, the structure of this steel is the coarse ferrite-pearlite structure after hot forging, so the toughness is much lower than thermal refined steel which has a fine structure. For this reason application is limited to the connecting rods within engines and other locations that do not require high toughness.

High-toughness microalloyed steel is applied to automotive suspension components and other locations that require high toughness. In this case the toughness is increased by methods such as reducing the carbon content and increasing the alloy content[(1),(3) - (6)], suppressing structural coarsening during hot forging through the use of precipitated particles[(1),(4)], and refining the structure by precipitation of intragranular ferrite[(1),(3) - (5),(7)]. In addition, high-strength, high-toughness microalloyed steel has also been developed by adding the appropriate amounts of various alloy elements to steel with an extremely low to medium carbon content and then performing only natural cooling after hot forging to obtain a bainite structure[(1),(4),(8) - (11)].

In this manner, microalloyed steel with various characteristics has been developed thus far, and are being used in a wide range of fields from the perspective of reducing costs, shortening lead times and conserving energy, etc[(2),(12)].

* Honda Motor Co.,Ltd.
** Asakahigashi R&D Center

2. Using Microalloyed Steel for the Crankshafts of Small Multipurpose Engines

Unlike motorcycle and automobile engines, the crankshafts of small engines mounted in power products (hereafter, multipurpose engines) require not only strength but also high toughness. In power products such as the lawn mower shown in Fig. 1, the working part is sometimes connected directly to the crankshaft without a belt, clutch or other buffer mechanism, so a large impact load may be applied directly to the output shaft. In addition, induction hardening is generally performed on the pin, journal and other parts of multipurpose engine crankshafts in order to increase the wear resistance and the fatigue strength. For these reasons, the crankshafts used for these types of applications have thus far used S48C or other structural carbon steel that has been thermally refined after hot forging to provide the required strength and toughness.

When thinking of changing these parts to microalloyed steel, induction hardening can be performed on basic microalloyed steel, but as mentioned above this steel has lower toughness which makes it unsuitable. Conversely, the composition of high-toughness microalloyed steel is adjusted from low to medium carbon content to ensure toughness, so sufficient hardness of induction hardened parts cannot be obtained. Thus, existing microalloyed steels cannot be applied.

Therefore, this research not only designed new alloy contents, but also comprehensively studied the various process control conditions during hot forging. This resulted in the development of a new microalloyed steel that has the strength and toughness required for the crankshafts of multipurpose engines, and which also allows induction hardening.

In addition, the environmentally harmful substance lead was added to conventional structural steel to enhance machinability, but this research succeeded in eliminating the need for lead without deterioration of characteristics. These details are described below.

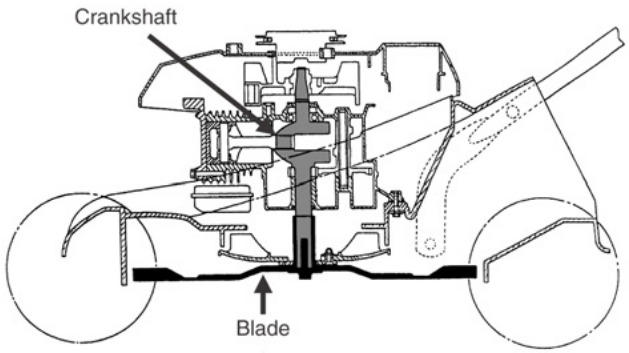


Fig. 1 Layout of lawn mower

3. Methods for Achieving Targets

3.1. Alloy Design

The hardness and tensile strength and the hardness of induction hardened parts of ferrite-pearlite steel are proportional, and the toughness is inversely proportional mainly to the carbon content. The induction hardened parts of multipurpose engine crankshafts require a hardness of HRC50 or more, so the lowest possible carbon content within the range that satisfies this hardness was used.

In addition, methods that refine the structure are effective for ensuring toughness. Therefore, the above-mentioned method of refining the structure by precipitation of intragranular ferrite was employed for the newly developed steel. This method refines the structure and thus increases toughness by precipitating ferrite around a core of MnS that is finely dispersed in large quantities throughout the structure even within the former austenite grains during cooling after hot forging. For this reason, the Mn and S contents were increased compared to basic steel.

On the other hand, reducing the carbon content lowers the steel strength, but this can be compensated by strengthening the steel. This was done by increasing the Si which strengthens the ferrite by solid solution, adding a trace amount of V for precipitation strengthening, and also enhancing the hardenability with Mn and Cr. The hardness and tensile strength of ferrite-pearlite microalloyed steel that contains these elements is known to correlate with the carbon equivalent Ceq expressed by the following equation[12].

$$Ceq = C + \frac{1}{10}Si + \frac{1}{5}Mn + \frac{5}{22}Cr + 1.65V - \frac{5}{7}S$$

A stable tensile strength equivalent or greater than that of S48C thermal refined steel, which was used as the comparison material, can be obtained by adjusting the Ceq value to 0.73 or more.

The above-mentioned MnS exhibits the same machinability effects as the lead in free-cutting steel with added lead[13) - (16)], so it was decided to use MnS.

Table 1 shows the chemical composition of the newly developed steel.

Table 1 Chemical composition of newly developed steel

(Wt.%)

C	Si	Mn	P	S	Cr	V	Pb	Ceq
0.33	0.68	1.33	≦ 0.020	0.055	0.20	0.08	–	0.80

3.2. Forging Process Conditions

The carbon content of the newly developed steel is slightly higher than that of existing high-toughness microalloyed steel in order to ensure induction hardening performance. However, this is disadvantageous for ensuring toughness, so in addition to refining the structure by designing the alloy as mentioned above, it was also necessary to prevent coarsening of the structure by controlling the process conditions during hot forging.

The first condition is the material heating temperature. Here, a lower heating temperature is better to prevent coarsening of the austenite grains. The structure of normal thermal refined steel can be adjusted in a later process, so a temperature of around 1 250 °C is often used in consideration of forgeability, die life and other factors. However, the structure of microalloyed steel is determined in the forging process, so a temperature of 1 150 to 1 200 °C is set, which is the lowest possible within the range that does not have a significant effect on the die life.

Next, after forging, the residual heat of the work causes the austenite to recrystallize and promotes grain growth, so it is necessary to cool the material quickly through the temperature range to transformation temperature to prevent coarsening of the structure. For this reason, forced (fan) cooling was introduced. Figure 2 shows the fan cooling conditions on a conveyor after hot forging. The cooling speed was investigated and determined as follows.

Of the various uses for multipurpose engines, the one with the potential to apply the harshest impact load to the crankshaft is that of the previously shown lawn mower. Based on the results of low-temperature blade-hit tests using an actual lawn mower as described hereafter, the shape specifications of the crankshaft output shaft that is directly connected to the lawn mower blade, and other factors, the impact value required for the crankshaft of a multipurpose engine was set at 40 J/cm^2 or more at –40 °C. On the other hand, the pearlite grain size and the impact value of the newly developed steel have the relationship shown in Fig. 3. This shows that the required impact value can be satisfied with sufficient margin by ensuring a pearlite grain size of No. 5 or more. Various cooling tests were conducted in the actual processes based on these observations, and the results showed that a cooling speed setting of 50 to 80 °C/minute between 800 °C and 550 °C is optimum for obtaining the above impact value.

These results are summarized in Fig. 4.



Fig. 2 Fan cooling after hot forging

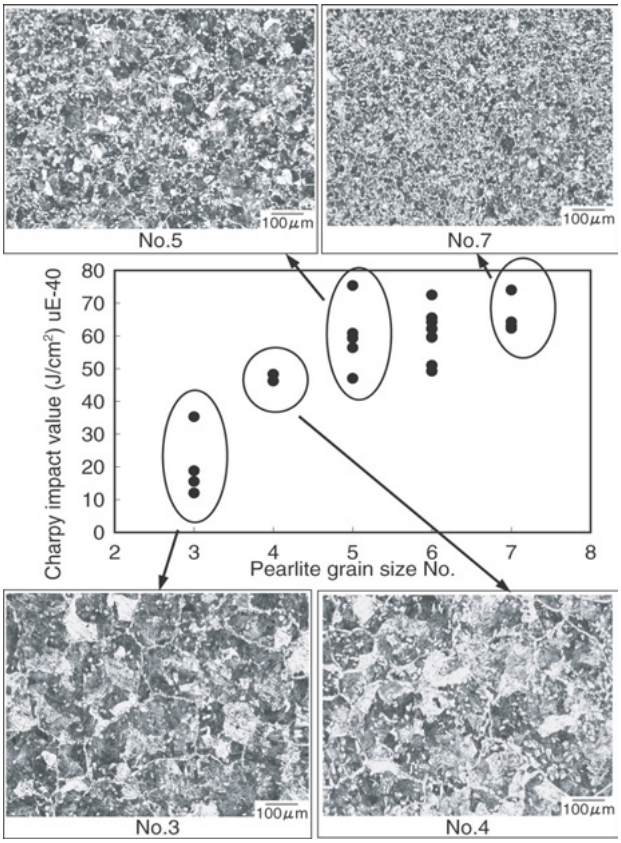


Fig. 3 Relation between pearlite grain size and charpy impact value

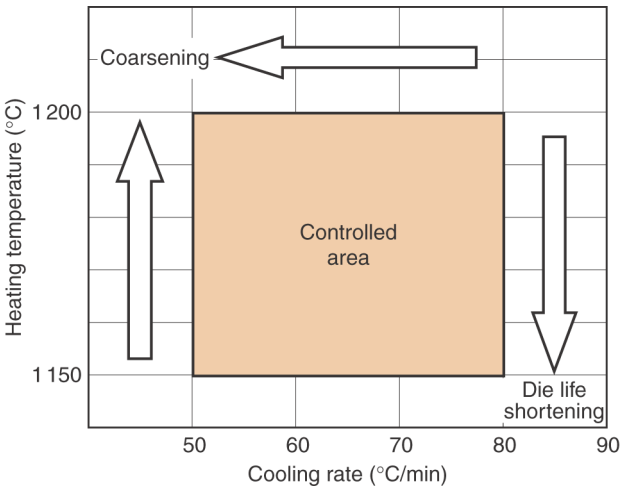


Fig. 4 Hot forging conditions

4. Test Results

4.1. Material Test Results

4.1.1. Charpy impact test

Figure 5 shows the results of Charpy impact tests conducted at various temperatures using JIS type 3 test pieces cut from actual crankshafts. This shows that the newly developed steel provides an impact value of 40 J/cm^2 or more even at –40 °C. In addition, when the test pieces were induction hardened to a depth of 1 to 3 mm in the U-notch portion, the results for the newly developed steel exceeded the impact value of the comparison material S48C thermal refined steel in all temperature areas. This is thought to be because the newly developed steel has a lower carbon content and thus a lower quenching hardness than the comparison material.

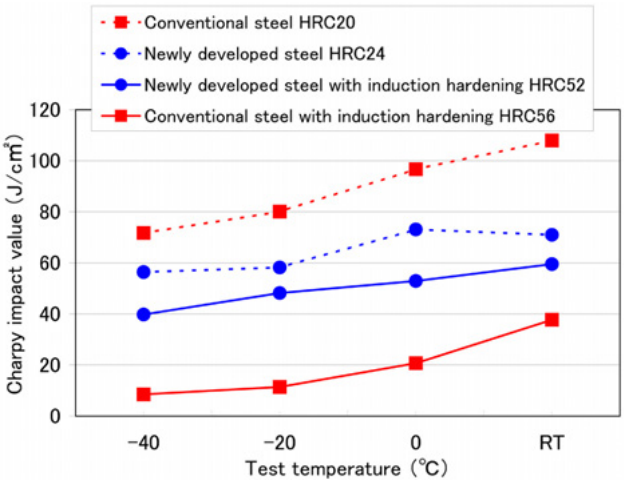


Fig. 5 Charpy impact value of newly developed and conventional steels

4.1.2. Other mechanical properties

Table 2 shows the results of material tests of other properties such as tensile strength and fatigue strength for the newly developed steel and the comparison material. Values equivalent to those for the comparison material were obtained for all items. In addition, the newly developed steel exhibited roughly the same amount of wear as the conventional steel in pin-on-disk type wear tests.

Table 2 Mechanical properties of newly developed and conventional steels

	Newly developed	Conventional
Hardness (HRC)	20	20
Tensile strength (MPa)	813	764
Yield point (MPa)	549	549
Elongation (%)	19	23
Rotating-bending fatigue strength (MPa)	412	372

4.2. Crankshaft Test Results

4.2.1. Low-temperature blade-hit tests

Impact tests were performed by assembling crankshafts into actual lawn mowers, and having a steel rod sprung up from the ground surface to collide with the lawn mower blade in an operating condition at –15 °C. Figure 6 shows an example of the results. Like the comparison material, the newly developed steel experienced no output shaft breakage, and the bending amount was also similar. These could be considered excellent results.



Fig. 6 Result of low temperature blade-hit test for crankshaft

4.2.2. Induction hardening ability

The pin portion of a crankshaft was induction hardened using actual mass production facilities, and the hardness at different depths was measured. Figure 7 shows the results, and confirms that the newly developed steel satisfies the quenching surface hardness of HRC50 or more required by the crankshafts of multipurpose engines, and that the hardening depth was also equivalent to the comparison material. Thus, there are no concerns with the hardening ability.

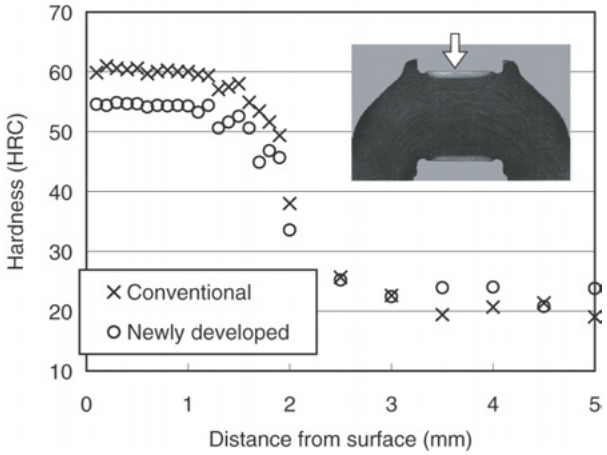


Fig. 7 Hardness of crank pin surface after induction hardening

4.2.3. Other tests

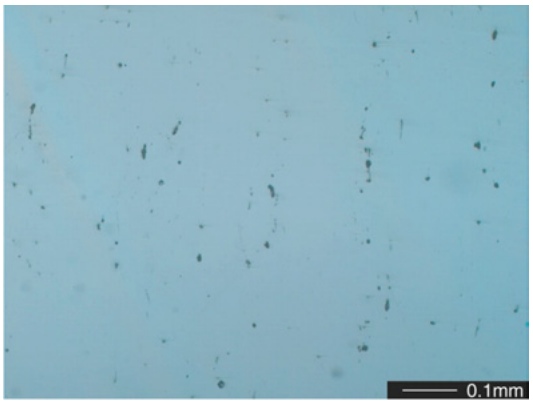
Table 3 shows the results of crankshaft fatigue tests. Both the bending fatigue tests and the torsion fatigue tests are completely reversed stress tests. Like the material test results, results roughly equivalent to those for the comparison material were obtained for each item. In addition, the newly developed steel was confirmed to satisfy the standard values of all confirmation items in the same manner as the conventional steel in various durability tests using actual engines.

Table 3 Result of various fatigue tests for crankshaft

		Newly developed	Conventional
Bending fatigue strength of crank pin (MPa)	Without induction hardening for fillet	402 (HRC24)	402 (HRC20)
	With induction hardening for fillet	647 (HRC52)	666 (HRC60)
Torsion fatigue strength of power take-off shaft (MPa)		182 (HRC20)	106 (HRC20)

4.3. Machinability

Figure 8 shows the free-cutting structure distribution formats for the newly developed steel and the comparison material. This shows that the MnS in the newly developed steel is distributed in a similar format as the Pb in the comparison material.



(a) Newly developed steel (MnS)



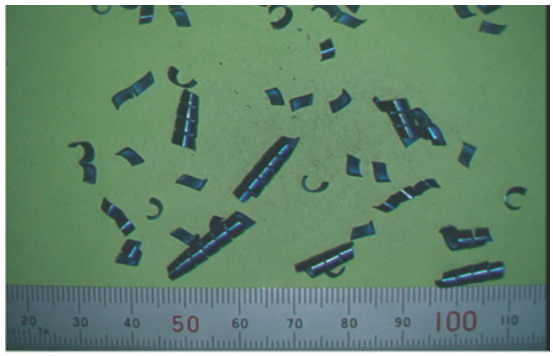
(b) Conventional steel (Pb)

Fig. 8 Distribution of inclusions

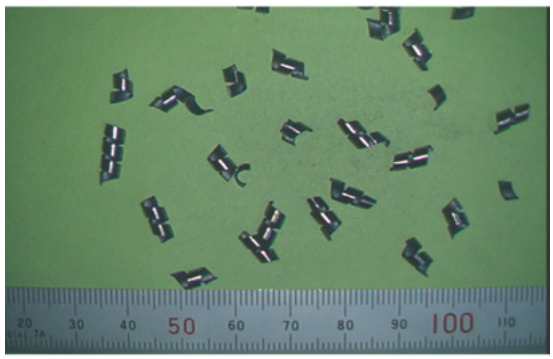
Tests were conducted to confirm the bite machinability and drill machinability of both steels under the same conditions. Table 4 shows the amount of tool wear, and Figs. 9 and 10 show the respective lathe turning and drilling chip shapes at that time. The newly developed steel showed a lower amount of tool wear than the comparison material, which is advantageous. The chips produced from the newly developed steel had a shape that was slightly more difficult to handle than the comparison material, but this difference was not of a degree that would be of any concern in an actual mass production machining line.

Table 4 Comparison of amount of tool wear between newly developed and conventional steels

	Newly developed	Conventional
Amount of wear of tip flank after 30 min. turning (mm)	0.07 (HRC19.4)	0.18 (HRC21.2)
Amount of wear of drill flank after drilling 200 holes (mm)	0.08 (HRC22.6)	0.09 (HRC20.1)

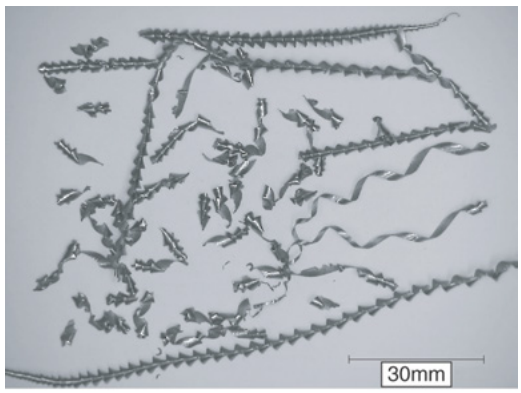


(a) Newly developed steel

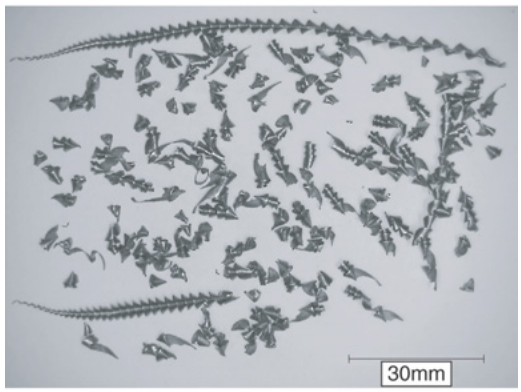


(b) Conventional steel

Fig. 9 Chips of newly developed and conventional steels produced by 30 min. of lathe turning



(a) Newly developed steel



(b) Conventional steel

Fig. 10 Chips of newly developed and conventional steels produced by drilling 200 holes

5. Conclusion

(1) A microalloyed steel was developed by comprehensively studying the alloy content and the forging conditions. This new microalloyed steel provides the same strength and toughness as conventional thermal refined steel even though the thermal refining process after hot forging has been eliminated, and it can also be induction hardened.
(2) The need to add lead, which is an environmentally harmful substance, has been eliminated while still maintaining a level of machinability equivalent to conventional free-cutting steel with added lead.

This newly developed steel is currently being applied to mass production as the crankshaft material for professional use multipurpose engines with a displacement of 160 to 390 cm^3.

Acknowledgements

The authors wish to take this opportunity to express their deep thanks to Sumitomo Metals (Kokura), Ltd. and all other related parties for their immense cooperation with this development.

References

(1) Nomura, I.: Metallurgical Technology in Microalloyed Steels for Automotive Parts, Materia Japan, Vol. 34, No. 6, p. 705 (1995)

(2) Hosono, A., Fujita, K.: Current Status of Microalloyed Steel, Isuzu Technical Journal, Vol. 90, p. 90

(3) Ikeda, M., Anan, G.: High Strength Microalloyed Steels, R&D Kobe Steel Engineering Reports, Vol.52, No. 3, p. 47 (2002)

(4) Takada, H., Koyasu, Y.: The Present and the Future of Forging Steel Free of Quenching and Tempering, Shinnittetsu Giho, Vol. 354, p. 6 (1994)

(5) Satoh, T., Kurita, M.: Saikin no Hityoushitsukou ni Tsuite, Tanzou Gihou, Vol. 83, p. 16 (2000) (in Japanese)

(6) Inoue, K., Nakamura, S.: High Strength and High Toughness Microalloyed Steels, Denki-Seiko (Electric Furnace Steel), Vol. 67, No. 1, p. 56 (1996)

(7) Ochi, T., Takahashi, T., Takada, H. : Improvement of the Toughness of Hot Forged Products Through Intragranular Ferrite Formation, Iron & Steel Maker, 16-2, p. 21-28 (1989)

(8) Katsumata, M., Matsushima, Y., Yamamoto, Y.: Newly Developed Low Carbon Martensite-Bainite Type High Strength High Toughness Steel Used in As-Hot Forged Condition, Bulletin of The Japan Institute of Metals, Vol. 31, No. 6, p. 547 (1992)

(9) Okatsu, M., Hayashi, T., Amano, K.: Weldability of Advanced Extremely-low Carbon Bainitic Steels for Thick Plate of 570 MPa Grade through As-rolled Process, Kawasaki Steel Giho, Vol. 30, No. 3, p. 131 (1998)

(10) Inoue, K., Nakamura, S.: Influence of Alloying Elements on Mechanical Properties and Fatigue Strength in Notched Specimens of Bainitic Microalloyed Steels, Denki-Seiko (Electric Furnace Steel), Vol. 69, No. 1, p. 27 (1998)

(11) Fukuzumi, T.: Development of Microalloyed Steels with Bainitic Microstructure for Hot-Forgings, Mitsubishi Steel Technical Review, Vol. 19, No. 1, 2, p. 33 (1985)

(12) Satoh, T.: Micro-alloyed High-strength Steel, Sumitomo Metals, Vol. 45, No. 4, p. 120 (1993)

(13) Ono, T.: A Review of Recent Studies for Machinability of Steel, Sumitomo Metals, Vol. 48, No. 1, p. 4 (1996)

(14) Hashimura, M., et al.: Development of Lead Free Micro Alloyed Steel for Crank Shafts, Shinnittetsu Giho, Vol. 378, p. 68 (2003)

(15) Tsunekage, N., et al.: Effect of Mg and Ca Addition on Toughness and Machinability of Resulfurized Free-cutting Steel (Development of New Resulfurized Free-cutting Steel - 1), CAMP-ISIJ, Vol. 14, No. 6, p. 1233 (2001)

(16) Sato, K., et al.: Effect of S Content and Mg and Ca Addition on the Machinability and Strength of Steels (Development of New Resulfurized Free-cutting Steel - 2), CAMP-ISIJ, Vol. 14, No. 6, p. 1234 (2001)

■ Authors ■



Yuzuru TAHARA



Shingo SHIMIZU

Development of Universal Solver for Incompressible and Compressible Flow Simulation

Yoshihiro YAMAGUCHI*

ABSTRACT

A numerical methodology that decomposes a fluid motion into the convection due to the flow material velocity and the transportation of the sound wave was newly developed and then a unified flow solver for all-speed flow regime was conducted. The developed flow solver has been validated using bench mark problems. Furthermore, the solver has been extended to practical one for an engineering purpose, such as three-dimensional turbulent flow, by implementing an unstructured grid method, a parallel computation technique, and a turbulence model. Availability as a unified flow solver in practical use has been confirmed by solving a flow field around three-dimensional wing.

1. Introduction

Until recently, advances in Computational Fluid Dynamics (CFD) have mainly proceeded along two tracks—solutions for incompressible problems and solutions for compressible problems—in terms both of the analytical methods developed and of the groups of researchers developing them. The reasons for this are not simply the difference between the two research objects. As shown in Fig. 1, the different methods of solution must be used for different conditions, determined by fluid thermal properties; it is simply not valid to use one method in a region that requires the other method. The border between the compressible and the weakly compressible regions is called the "low Mach number limit." Still, every fluid, whether liquid or gas, is actually compressible to at least some degree. Therefore, the term "incompressible flow" has been used to signify a fluid that is modeled with incompressible solution methods under the condition of zero changes in density. The researcher must bear in mind that this is only an approximation of the actual fluid. For the discussion in the present study, fluids with compressibilities or heat-expansion ratios of less than 5% were defined as weakly compressible.

As stated above, so far, designers have used different solution methods as appropriate to the flow phenomena under consideration. When handling conditions that extend across the low Mach number limit, however, they have had to make special assumptions, construct special models, or endure difficulties of convergence and questionable reliability in existing models.

Recent developments in computation capabilities have enabled solution of large and complicated systems. For example, complete simulations of gas turbine engines and reciprocating engines, from inlet to exhaust, have been constructed. Inside, slow- and high-speed flows intermix, and even the low-speed flows see density fluctuations due to combustion-caused temperature differentials. Previous

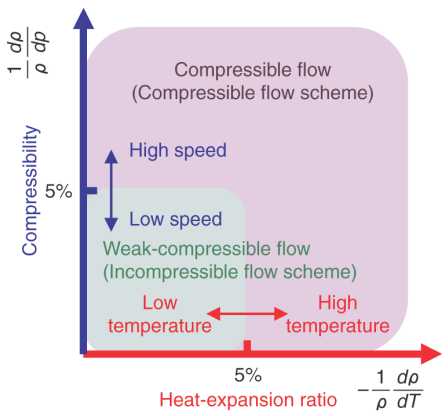


Fig. 1 Schematic of relation between flow phenomena and numerical method

* Wako Research Center

methods had to divide the models into distinct mechanical components and employ different analytical methods appropriate to each component. However, it is difficult to distinguish each component's interference with adjoining components, and boundary conditions are vague and contradictory; consequently, the precision of conventional models has been pretty low.

A simulation method that joins all the components of a system and allows large and complicated problems to be solved would constitute a powerful tool that also eliminates all of the problems described above. It would allow selection of specific inlet and outlet atmospheric conditions and other boundary conditions, without the introduction of models or assumptions. Such a method would also provide highly reliable solutions for the capabilities of every component and of the entire system.

The object of this research was to construct a CFD scheme with a unified algorithm capable of handling mixed flows of weakly compressible and compressible fluids and the flow phenomena occurring around the low Mach number limit. The following three topics were addressed, with the aim of applying this scheme to complex and large-scale problems: (1) employing of a turbulence model; (2) adaptability to hybrid grids to accommodate complicated shapes; and (3) capability for parallel computation to reduce the calculation load of large-scale problems. A code with all these capabilities was developed. This report describes validation of the code and the good results obtained when it was applied to a practical problem.

2. Comparison with Conventional Method

The following summarizes why methods for incompressible problems and methods for compressible problems may not be applied to each other's situations and describes the advantages of the present solver.

(1) Reasons incompressible solutions are unsuitable for compressible flows:
A simplified governing equation (conservation of mass, conservation of momentum) is derived from the complete Navier-Stokes (NS) equations and solved under the assumption of constant density. Because energy-conservation equations are not treated as simultaneous equations, compressibility cannot be considered.

(2) Reasons compressible solutions are unsuitable for weakly compressible flows:
The full NS equations are used as the governing equations. These are composed of the continuity equation, the momentum equation, and the energy equation, and account for weakly compressive phenomena. They describe macroscopic flow phenomena such as density and momentum and regard fluid materials as continuous body for microscopic phenomena of advection or pressure wave propagation of the fluid molecules and heat generation due to molecule confliction. It can be comprehended by eigenvalue analysis of NS equations proving that the advection of physical quantities of fluid is due both to the flow velocity and to acoustic waves (pressure waves). However, compressible solutions require simultaneous solution of advection equations for flow velocity and the speed of sound. In analysis of flows whose velocity scales are much less than the speed of sound, numerical errors build up due to scale differences. These can delay or even prevent convergence of calculations in such slow, weakly compressible flows.

(3) Characteristics of this solution:
Handling differences in scale between flow velocity and the speed of sound is the key to development of a universal solver. Preconditioning methods[1],[2],[3] have been proposed by inserting a preconditioning matrix for accommodating all scales into the equations. It has also been suggested to separate the calculations for advection and acoustics[4],[5]. Both of these approaches are still under study, and almost no techniques are presently in use for general problems.

The method described here employs the full NS equations as the constitutive equations and represents a new viewpoint of the properties of the full NS equations. The following two sentences discuss the two roles of flow velocity and acoustic waves are decomposed in the weakly compressive regime, as described above. Advection due to flow velocity can be expressed with a unidirectional, upstream-to-downstream hyperbolic equation. In contrast, since acoustic waves have the characteristics of a standing wave with a pressure-wave source and boundaries, they can be expressed using elliptic equations.

This analysis will separate the flow velocity-based effects from the acoustic wave-based effects to utilize the characteristics of each type of equation in the universal solver constructed here. In the first state, advection due to flow velocity is evaluated to exploit current knowledge from compressible-flow solutions. Next, propagation effects due to acoustic waves are provisionally used to approach the boundary value problem. It can be proven that the contribution of the pressure in the momentum equation is due both to flow velocity and to acoustic waves[6], so the contribution by pressure is separated, and high-precision calculations for pressure are performed.

3. Governing Equations

Nonconservative forms of the full equation (1), the momentum equation (2), and the temperature equation (3) were derived from the complete NS equations to form the governing equations. Here, the temperature equation is derived by substituting the continuity equation and the momentum equation into the energy equation:

$$\frac{\partial \rho}{\partial t} + \mathbf{u} \cdot \nabla \rho = -\rho \nabla \cdot \mathbf{u} \tag{1}$$

$$\frac{\partial \mathbf{u}}{\partial t} + \mathbf{u} \cdot \nabla \mathbf{u} = \frac{1}{\rho} \nabla \cdot (-p\mathbf{I} + \prod) \tag{2}$$

$$\frac{\partial T}{\partial t} + \mathbf{u} \cdot \nabla T = \frac{1}{C_v \rho} \{-p(\nabla \cdot \mathbf{u}) - \nabla \cdot k \nabla T + \prod : \nabla \mathbf{u}\} \tag{3}$$

Here, ρ, $\mathbf{u}$, p, and T represent density, velocity vector, pressure, and temperature, respectively. c_v, Π, and k represent the constant-volume specific heat, the viscosity tensor, and the thermal conductivity. $\mathbf{I}$ is the identity matrix.

In addition, the k-ω turbulence model[7],[8] is used for practical calculations. Here, k is the turbulent energy.

4. Separation of Variables

Equations (1) – (3) were solved in a multistage sequence with time steps proceeding as n → n + 1. The initial stage was called the advection stage (time step n → *), in which

physical quantities of the flow translated under the influence of the flow velocity only. The second stage is called the quasi-isentropic stage (time step * → **), in which small physical quantities were subjected to small disturbances under pressure waves according to the equation governing sound waves. Viscosity and heat flux were evaluated in the third stage, the viscid stage (time step ** → n + 1). The pressure equation was derived to evaluate the boundary value problems in the quasi-isentropic stage. Here, the time fluctuations in the pressure gradient term in the (n → **) time step for the momentum equation are separated using $\nabla p^{**} = \nabla(p^n + \phi)$. Here, ϕ was the value $\phi = p^{**} - p^*$, and a small disturbance of the pressure. The following two results of separation were observed. First, when the pressure equation was solved, the fact that pressure was not a direct variable moderated the accumulation of numerical errors. Second, the contribution of the pressure gradient term in the flow speed time scale was separated from its contribution in the acoustic speed time scale; this allowed calculations of each to be done in an appropriate manner[9].

The decomposition in the three stages are shown in Equations (4) — (6).

Advection stage:

$$\frac{\partial}{\partial t}\begin{pmatrix}\rho\\ \mathbf{u}\\ T\end{pmatrix}^{*} + (\mathbf{u}^n\cdot\nabla)\begin{pmatrix}\rho\\ \mathbf{u}\\ T\end{pmatrix}^{*} = \begin{pmatrix}0\\ -\nabla p^n\mathbf{I}/\rho^*\\ 0\end{pmatrix} \tag{4}$$

Adiabatic stage:

$$\frac{\partial}{\partial t}\begin{pmatrix}\rho\\ \mathbf{u}\\ T\end{pmatrix}^{**} = \begin{pmatrix}-\rho^*\nabla\cdot\mathbf{u}^{**}\\ -\dfrac{\nabla\phi\mathbf{I}}{\rho^*}\\ -\dfrac{p^*\nabla\cdot\mathbf{u}^{**}}{C_v\rho^*}\end{pmatrix} \tag{5}$$

Viscid Stage:

$$\frac{\partial}{\partial t}\begin{pmatrix}\rho\\ \mathbf{u}\\ T\end{pmatrix}^{n+1} = \begin{pmatrix}0\\ \dfrac{\nabla\cdot\prod^{n+1}}{\rho^*}\\ \dfrac{\nabla k\cdot\nabla T^{n+1} + \prod^{**}:\nabla\mathbf{u}^{**}}{C_v\rho^{**}}\end{pmatrix} \tag{6}$$

The next sections describe the solutions in each stage.

4.1. Advection Stage

The methods for solving advection calculations has developed with the methods for solution of compressible flows, where advection effects are dominant. This is called the approximate Reimann problem and features the capability to capture shock waves, which are physically discontinuous, in a sharp manner and without oscillation. The present method exploits the advantages of the approximate Riemann problem, since it involves flows in which shock waves occur. As shown in Eq. (4), the variable is not a conservative one but a primitive one which also is nonconservative; the approximate Riemann problem cannot be applied here. In addition, strict mathematical principles interfere with handling of shock waves[10]. Therefore, the key to these analyses is how to make an upwinding scheme for a wide range of flow speeds, from low to high. Equation (4) shows that the motion of physical quantities depends only on flow speed **u**. Nonetheless, the pressure gradient term remains on the right side of the momentum equation, as a term independent of the flow velocity. The Advection Upstream Splitting Method (AUSM)[11], an approximate Riemann problem, was used for obtaining flow velocity flux and pressure gradient terms in the upwinding scheme. The upwinding scheme contributed greatly to the precision of pressure calculations.

4.2. Quasi-isentropic Stage, Viscid Stage

Here, the authors take an asymptotic solution for the effects of advection due to acoustic waves, as boundary values problem. Equation (5) was substituted into the total time differential of the equation of state to derive the pressure equation:

$$\nabla\cdot\left(\frac{1}{\rho^*}\nabla\phi\right) - \frac{\phi}{\gamma\Delta t^2 p^*} = \frac{\nabla\cdot\mathbf{u}^*}{\Delta t} \tag{7}$$

Equation (7) can be solved with SOR, the residual cutting method[12], or other general matrix solution methods. Once the pressure is determined, the density, velocity, and temperature are calculated.

In the viscosity stage, the time step is advanced by one after the calculations have been completed using the values found in the quasi-isentropic stage.

5. Discretization

5.1. Spatial Discretization

Two methods can be considered for locating physical amounts of fluid on the calculation grid. One is to collocate all mass properties at each grid point, and the other is staggering, in which the density, pressure, temperature, and other mass properties are located in the center of a cell while the velocities are located at the grid surfaces. Considering the process of deriving the pressure equation, the staggered approach seemed preferable for this method. Nevertheless, collocation was used, because other objectives were to maintain the conservative properties of the discretization and to avoid complications during development of the program. A hybrid grid of two- and three-dimensional elements was used for flexibility in calculations for complex shapes. It was based on the finite volume method (FVM). The spatial resolution of the grid used in the advection stage greatly affects the sharpness of the calculations of shock waves. Still, since it is not possible to make stencils of wide areas in FVM, a Monotone Upstream-centered Scheme for Conservation Laws (MUSCL) was employed to improve second-order spatial accuracy.

5.2. Time Discretization

To shorten calculation time for steady-state calculations, local time stepping was performed with first-order time accuracy. For stability of calculations with progress of time, the lower–upper symmetric Gauss-Seidel (LU-SGS)[13] method with implicit calculations was employed in the advection and viscid stages. Meanwhile, for unsteady flow calculations, time accuracy was improved to second-accuracy with the Crank-Nicolson method. LU-SGS was combined with the Newton-Raphson method in the advection and viscid stages and accuracy of time was maintained using dual-time stepping[14].

6. Parallel Computations

This solver poses about the same calculation load as AUSM for compressive flow solutions in the advection stage; since the compressive equations were added in the quasi-

isentropic stage, the calculation load was higher than for the compressive solution. Parallel computation was employed to spread the considerable calculation load and to shorten the turnaround time.

Domain decomposition with memory allocation of the variables was used as the parallel computation method. This allows large-scale processing since the demanded memory can be distributed among all the nodes in shared-memory parallel processing. METIS[15] was used to code the domain decomposition, balancing the memory load in each node. Data exchange between adjacent regions was carried out only for physical quantities in dummy cells located on region boundaries. This method minimized the volume of data exchanged among nodes and the data communication time. Figure 2 shows the measured and theoretical dimensionless calculation times for a single CPU. About 1.1 million nodes were used for measurements; it was seen that the parallel processing approach was effective, with the actual calculation time approaching the theoretical time for the actual number of nodes.

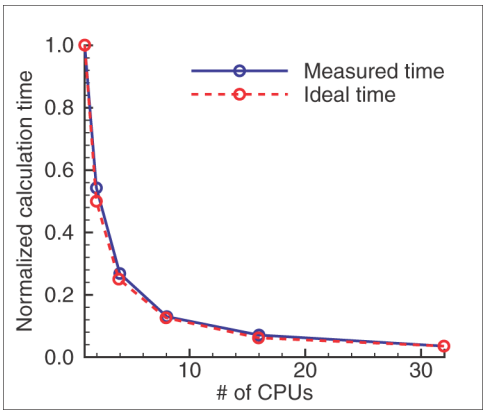


Fig. 2 Normalized calculation time between measured and ideal time

7. Validation

This solver was validated using typical problems in weak-compressible and compressible flow.

7.1. Validation of Weak-compressible Flow Solution

The weak-compressible flow model was validated by analyzing an incompressible, viscid cavity flow. The Reynolds number of the flow was 1 000 and the inlet Mach number was 0.01. Figure 3(a) is the analytical image. Figure 3(b) shows the calculated streamlines, Fig. 3(c) the distribution of velocity v at y = 0, and Fig. 3(d) the distribution of velocity u at x = 0. These velocity distributions are compared with the velocity profile validation data reported by Ghia et al.[16].

The velocity distribution in the primary vortex matches the validation results quite well. The secondary vortices were well captured, as they were in Ghia's results. These findings indicate that this method is appropriate for analysis of weak-compressible flow regions.

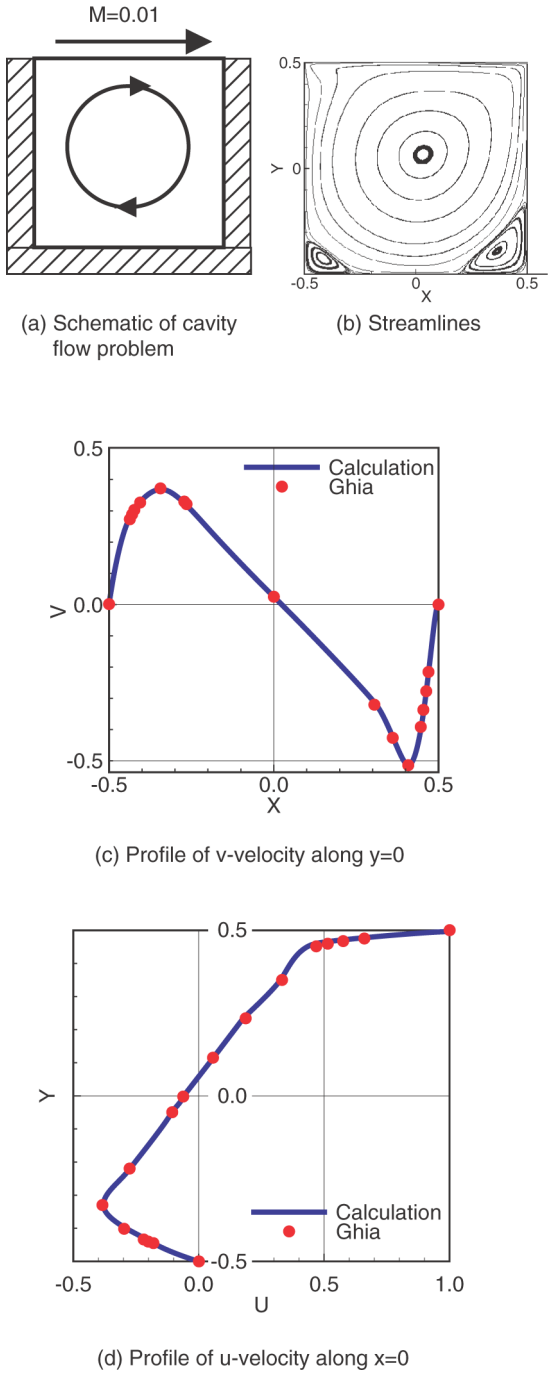
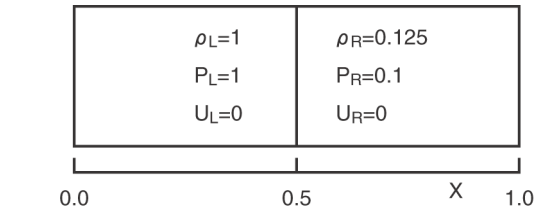


Fig. 3 Validation results for cavity flow at Re=1 000, Min=0.01

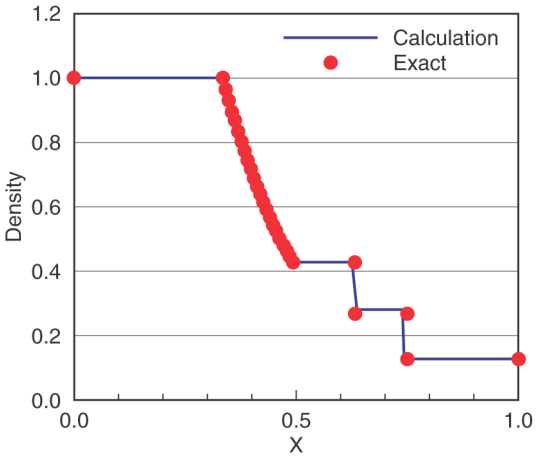
7.2. Validation of Compressible Flow Solution

The method was verified in a compressible flow by analyzing Sod's one-dimensional shock tube problem[17]. In this problem, the initial conditions are static with a 10:1 pressure ratio across the partition between the left and right sides of the tube and a density ratio of 8:1 in the same orientation for the gas densities. The test was carried out by comparing the model-calculated results with the exact solutions for the unsteady supersonic flow occurring after removal of the partition. Figure 4(a) diagrams the initial values in the shock tube, and (b) and (c) present the distribution of pressure and velocity, respectively, 0.14154 s after removal of the partition.

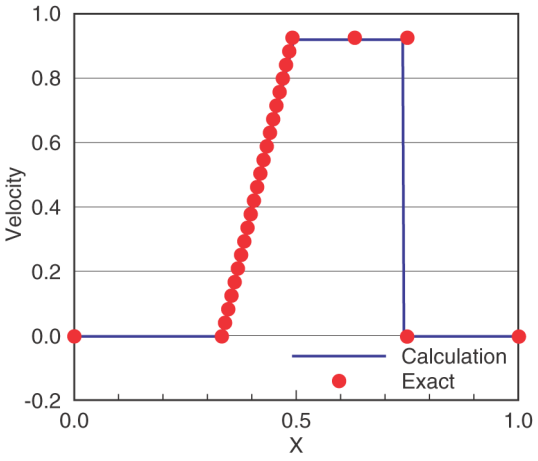
When nonconservative governing equations are used, the weak solution is incapable of recognizing the entropy jump in the shock wave, so it predicts the wave position somewhat later than the theoretical model does[10]. Almost no delay is seen by this solver, however; good results were obtained.



(a) Initial conditions



(b) Density : ρ profile

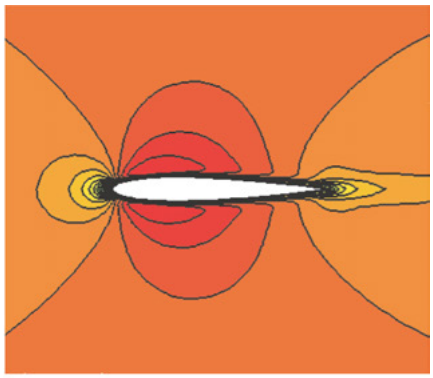


(c) Velocity : u profile

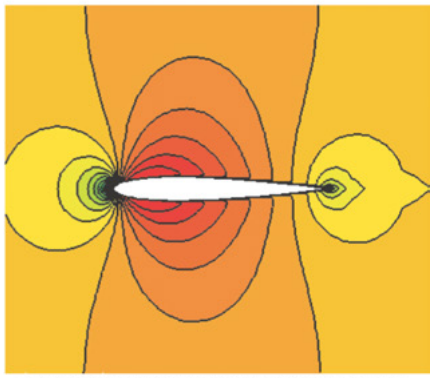
Fig. 4 Validation results for the Sod's problem

7.3. Validation of Flow around a Two-Dimensional Airfoil

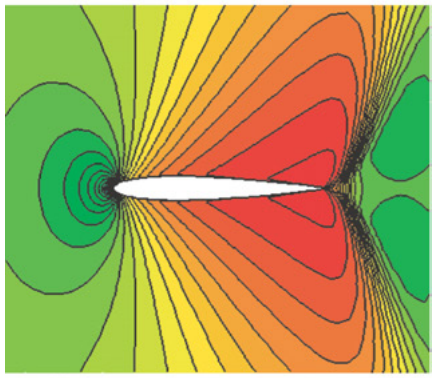
The two tests described above showed that the present method is usable for both weakly compressible and compressible internal flows. Next, a simulation of inviscid flow around a two-dimensional NACA0012 airfoil was performed as an example of external flow. Another type of universal solver, local preconditioning, requires some handling by the operators, because of its dependence on certain parameters at stagnation points[1] – [3]. Therefore, solutions from weakly compressible and compressible flows were sought in the vicinity of stagnation points to check for predictions of physically impossible behavior. The main flow speeds observed were weakly compressible flow at $M_\infty = 0.005$ [Fig. 5(a)], high subsonic flow at $M_\infty = 0.6$ [Fig. 5(b)], and transonic flow at $M_\infty = 0.9$ [Fig. 5(c)]. The angle of attack in all simulations was 0°. The contours in the figures are absolute flow speed values normalized to M_∞; consequently, the colors of the contours in Figs. (a) – (c) cannot be compared directly.



(a) Contour of velocity magnitude in weak compressible flow regime at M_∞=0.005



(b) Contour of velocity magnitude in high subsonic flow regime at M_∞=0.6



(c) Contour of velocity magnitude in transonic flow regime at M_∞=0.9

Fig. 5 Contours of velocity magnitude around NACA0012 airfoil

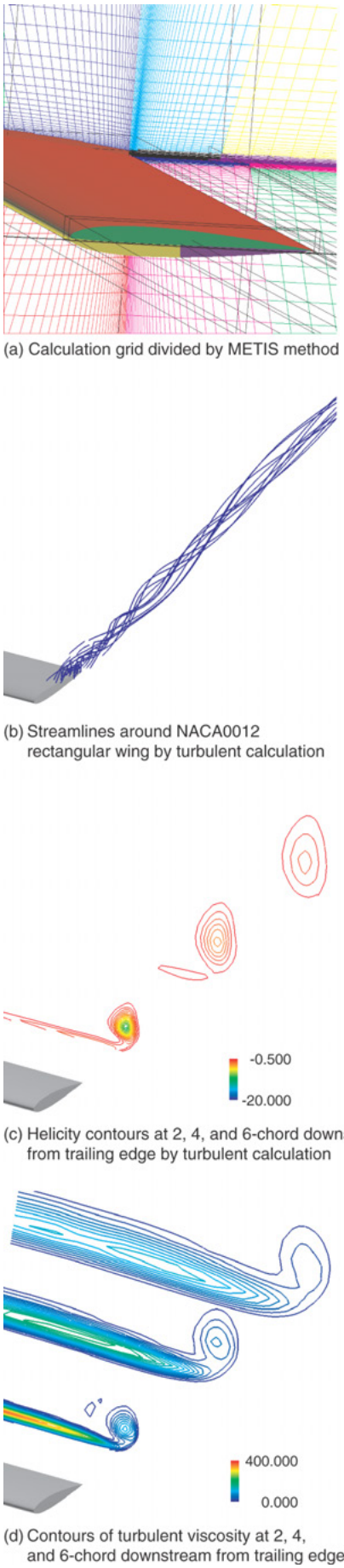
In the incompressible case, the same calculation results were found as in the weakly compressible case in Fig. 5(a), whereas this was not possible in the cases shown in Figs. (b) and (c), where compressibility effects were present. At the same time, although conventional compressive flow analysis shows the same results as in Figs. (b) and (c), it fails to converge in the case of Fig. (a), weakly compressible flow, a physically impossible "solution". In contrast, this method provided convergent solutions for a reasonable flow velocity distribution, from low speeds to shock wave speeds, in weakly compressible flows. These results indicate that the solver may also be applied to flows at a broad range of speeds around physical objects at which stagnation points form.

8. Analysis around a Three-dimensional Wing Flow

An analysis of turbulent flows around a three-dimensional NACA0012 airfoil was carried out to test this solver with a practical problem. The analytical conditions were low speed and high angles of attack, reflecting conditions at takeoff or landing. The reason for selecting high angles of attack was to raise the wing loading at low speed. The pressure difference across the upper and lower wing surfaces causes intense wingtip vortex and become wake vortex above an airport are an important reason for the delay between takeoffs and landings, as they interfere with the flight of planes passing through them. Thus, the safety issue and the desire to increase the volume of planes using an airport have inspired a large number of attempts to predict wingtip vortices using CFD. Since previous analyses have addressed speed regimes in the vicinity of the low Mach number limit, however, they have had problems with convergence, and the solutions have not been very reliable. It has been suggested that the influence of physically impossible viscosities in numerical treatment (numerical viscosity) causes the predicted wake vortex diffusing earlier than they actually do, with some dependence on the calculation method and the grid[18]. Accordingly, an analysis was performed, exploiting the present method's universal solver and high-precision approach to calculating pressure.

The total number of nodes in the grid was 1 157 856; all cells were hexahedral to reduce influences from numerical diffusion. The calculation domain was divided into 16 regions for parallel processing. Figure 6(a) shows the regions in color coding. The wing aspect ratio was 3, the flow Mach number was 0.12, the angle of attack was 10° and the Reynolds number was 0.9×10^6.

Figure 6(b) shows the streamlines of a wingtip vortex. This vortex is seen to arise on the upper surface of the wing and gradually diffuse due to viscosity effects, but it extends over 10 chord lengths downstream from the wing. This indicates that numerical diffusion was low. Next, Fig. 6(c) shows helicity contours. The contour locations correspond to 2, 4 and 6 chord lengths downstream. The helicity h is defined $h = \mathbf{u}\ curl(\mathbf{u})$; the maximum absolute value defines the center of the vortex, and the sign indicates the direction of vortex rotation. A negative sign means counterclockwise rotation, looking from upstream, and vice versa. Since the helicity is nearly zero in all locations other than wingtip vortices and downstream, the figure has been scaled for greater legibility. The vortices were negative at locations corresponding to wingtip vortices, and as in the previous streamline diagrams, counterclockwise vortices were clearly



(a) Calculation grid divided by METIS method

(b) Streamlines around NACA0012 rectangular wing by turbulent calculation

(c) Helicity contours at 2, 4, and 6-chord downstream from trailing edge by turbulent calculation

(d) Contours of turbulent viscosity at 2, 4, and 6-chord downstream from trailing edge

Fig. 6 Results of a wingtip vortex calculation around NACA0012 rectangular wing

occurring. Contours of turbulent flow viscosity ratio in the same locations as those for helicity are shown in Fig. 6(d). Turbulence models cannot be avoided, if the researcher wishes to obtain analytical results closely resembling real phenomena, at realistic calculation loads. Turbulent viscosity was clearly affecting this flow in the proper manner, judging from the flow cross sections at the wingtip and the downstream locations. This universal solver code was thus found to be useful for analyzing large-scale, complicated, three-dimensional phenomena.

9. Conclusion

A universal solver for numerical analysis of incompressible and compressible flows was constructed. Basic validation tests confirmed that this solver predicts both internal and external flows in the weakly compressible and compressible regimes. Capabilities for turbulent flow analysis and flow around complicated shapes were then shown, and finally the more realistic problem of flow around a three-dimensional airfoil was examined. This solver was shown to be useful for examining practical problems. The capability for parallel processing was also added, enabling efficient distribution of the calculation load, which nearly equaled the theoretical value. This solver should be fully developed in the future. It can be applied to analysis of flows in a gas turbine and a reciprocating engine and also used for studies of phenomena influenced by pressure fluctuations, such as combustion and environmental noise.

References

(1) Turkel, E.: Preconditioned Methods for Solving the Incompressible and Low Speed Compressible Equations, J. Comput. Phys., Vol.72, No. 2, p. 227-298 (1987)

(2) Choi, Y. H., Merkle, C. L.: The Application of Preconditioning in Viscous Flows, J. Compt. Phys., Vol. 105, p. 207-223 (1993)

(3) Turkel, E., Vatsa, V. N., Radespiel, R.: Preconditioning Methods for Low-Speed Flows, AIAA paper, 96-2460 (1996)

(4) Hah, C.: Navier-Stokes Calculation of Three-Dimensional Compressible Flow Across a Cascade of Airfoils with an Implicit Relaxation Method, AIAA paper, 86-0555 (1986)

(5) Yabe, T., Wang, P. Y.: Unified Numerical Procedure for Compressible and Incompressible Fluid, J. Phys. Soc. Japan, Vol. 60, No. 7, p. 2105-2108 (1991)

(6) Rehm, R, G., Baum, H. R.: The Equation of Motion for Thermally Driven Buoyant flows, J. of Research of the National Bureau of Standards, Vol. 83, p. 297 (1978)

(7) Wilcox, D. C.: Simulation of Transition with a Two-Equation Turbulence Model, AIAA Journal, Vol. 32, No. 2, p. 247-255 (1994)

(8) Wilcox, D. C.: Reassessment of the Scale-Determining Equation for Advanced Turbulence Models, AIAA Journal, Vol. 26, No. 11, p. 1299-1310 (1988)

(9) Yamaguchi, Y., Arima, T., Obayashi, S., Nakahashi, K.: Simulation of Aircraft Wake Vortex Using Pressure-based Unified Numerical Approach for Incompressible and Compressible Flows, AIAA Paper, 04-0077 (2004)

(10) Leveque, R. J.: Finite Volume Methods for Hyperbolic Problem, CAMBRIDGE TEXTS IN APPLIED MATHEMATICS (2002)

(11) Liou, M.–S.: Progress Towards An Improved CFD Method: AUSM+, AIAA Paper, 95-1701-CP (1995)

(12) Tamura, A., Kikuchi, K., Takahashi, T.: Residual Cutting Method for Elliptic Boundary Value Problems: Application to Poisson's Equation, J. Comput. Phys. No. 137, p. 247-264 (1997)

(13) Jameson, A., Yoon, S.: Lower-Upper Implicit Schemes with Multiple Grid for the Euler Equations, AIAA Journal, 30, No. 11 (1992)

(14) Pulliam, T. H.: Time Accuracy and the Use of Implicit Methods, AIAA paper, 93-3360 (1993)

(15) http://www-users.cs.umn.edu/~kaypis/metis/

(16) Ghia, U., Ghia, K. N., Shin, C. T.: High Re Solutions for Incompressible Flow Using the Navier-Stokes Equations and a Multigrid Method, J. Compt. Phys., No. 48, p. 387-411 (1982)

(17) Sod, G. A.: A Survey of Several Fluid Difference Methods for System of Nonlinear Hyperfsonic Conservation Laws, J. Comput. Phys, No. 27, p. 1-31 (1978)

(18) Murayama, M., Nakahashi, K., Obayashi, S., Kato, T.,: Numerical Simulation of Vortical Flows Using Vorticity Confinement Coupled with Unstructured Adaptive Grid Refinement, Computational Fluid Dynamics Journal, Vol. 10, p. 28-36 (2001)

■ Authors ■



Yoshihiro YAMAGUCHI

Development of Computational Fluid/Aeroacoustic Coupling Code

Toshihiro KAMATSUCHI*

ABSTRACT

A rather novel coupling method is developed for predictions of aerodynamic sound fields. The flow fields are predicted by Reynolds Averaged Navier-Stokes (RANS) and the sound propagations are computed by Linearized Euler Equations (LEE). This method enables wide range aeroacoustic analyses with the lower computational cost. All simulations are performed using unstructured grid methods because of their flexibility to fit complex geometries. To validate this method in the present work computational aeroacoustic analysis around an airfoil was carried out. Sound sources are treated universally by using turbulent vortex fluctuations which induce aeroacoustic phenomena, not by the secondary pressure fluctuations on the body surfaces. This suggests a new guidance in computational aeroacoustics.

1. Introduction

The term “aerodynamic sound” refers to the acoustic fields caused by air flows. The noise from home air conditioners, computer cooling fans, and exterior mirrors and sun roofs on automobiles are everyday examples of this; noise from engine compressors, turbines, engine jet mixing, and wing flaps are examples in aircraft. Because aerodynamic sound increases sharply with flow speed, it is of growing interest to be able to predict noise levels. Recently, aerodynamic noise has become the dominant factor in the noise emitted by automobiles, aircraft, and other vehicles as operating speeds increase. There is heightening demand from society to reduce such noise so as to preserve physical comfort and the livability of the environment.

Conventionally, predictions of aerodynamic noise levels have relied mainly on experiments and theory, but the recent advances in the techniques of Computational Fluid Dynamics (CFD) have allowed researchers to publish many numerical studies on prediction of the noise[(1)]. However, the conventional methods of aeroacoustic simulation have been hindered by the following issues:

(1) Precise simulation of time-dependent components of flow fluctuations require costly numerical approaches such as Direct Numerical Simulation (DNS) or Large Eddy Simulation (LES).
(2) Methods employing acoustic analogies, such as that of Lighthill, are limited to sources and propagation in homogeneous media with no velocity gradients.
(3) Analytical objects must have simple shapes.

The above issues were successfully solved with the Reynolds Averaged Navier-Stokes (RANS) and Stochastic Noise Generation and Radiation (SNGR) models, which were used to extract sound sources while suppressing computational costs. Linearized Euler equations (LEE) were used to handle acoustic simulation of various applications including non-homogeneous media. For the third concern, a new code for the coupled solution of flow and acoustic fields was developed exploiting the possibilities of an unstructured grid method, due to its superior adaptability to shapes and ability to analyze both fluids and acoustic fields. These methods together have enabled to carry out the numerical simulation of several aerodynamic noise issues in practical time frames and in several computation environments.

* Wako Research Center

2. Computational Method

2.1. Computational Procedure

Figure 1 diagrams the computational method used in this research. The procedure was as follows:

Step 1. The flow in the vicinity of the sound sources was analyzed using RANS and a turbulence model.

Step 2. The SNGR model was used to calculate the instantaneous turbulent flow velocity field from the turbulent kinetic energy and its dissipation rate obtained in Step 1.

Step 3. The turbulent flow velocity field obtained in Step 2 was treated as the sound source and combined with the flow field found in Step 1 for simulation by LEE.

If the RANS solution at the boundary of propagation space can be considered to be uniform, an integral equation based on theoretical analysis is solved to obtain the far-field solution.

This procedure can be broadly divided into the flow simulation by RANS and the turbulence model and the acoustic simulation with the SNGR model and LEE.

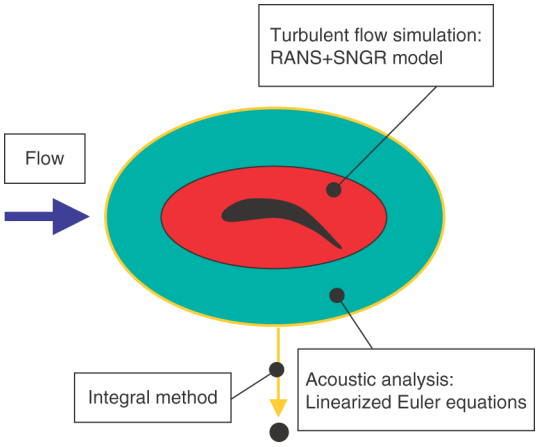


Fig. 1 Aeroacoustic simulation methods in different domains

2.2. Flow Simulation

The compressible Navier-Stokes equation is the governing equation for this flow field:

$$\frac{\partial \mathbf{Q}}{\partial t} + \frac{\partial (\mathbf{F}_j - \mathbf{G}_j)}{\partial x_j} = 0 \tag{1}$$

Here, t is time and xj are the coordinate axes. The vector of conservative variables $\mathbf{Q}$, inviscid flux vector $\mathbf{F}_j$, and viscid flux vector $\mathbf{G}_j$ are defined as follows:

$$\mathbf{Q} = [\rho \ \rho u_i \ \rho E]^T \tag{2}$$

$$\mathbf{F}_j = \begin{bmatrix} \rho u_j \\ \rho u_j u_i + p\delta_{ij} \\ \rho H u_j \end{bmatrix} \tag{3}$$

$$\mathbf{G}_j = \begin{bmatrix} 0 \\ \tau_{ji} \\ u_i \tau_{ij} - q_j + (\mu + \sigma\mu_T)\frac{\partial k}{\partial x_j} \end{bmatrix} \tag{4}$$

where ρ is density, u_i are the velocity components in the x_i directions, p is pressure, μ is the coefficient of viscosity in laminar flow, τ_{ij} is the viscous stress tensor, and q_j are the heat flux components. E and H are the total energy and total enthalpy per unit mass, respectively.

The turbulent kinetic energy k and coefficient of viscosity in turbulent flow μ_T are found using the turbulence model. Here, the distance from the wall is unnecessary; Wilcox's low Reynolds number k-ω model[2] was used due to its convenience for the storage of unstructured data. The turbulent model constant is σ.

2.3. Acoustic Simulation

LEE simulation with sound source terms is not limited by any assumptions of homogeneous media; it can also handle diffraction and wall reflection. In comparison to scalar wave equation, which can only handle acoustic waves, LEE may be used for examining entropy and vorticity waves.

The LEE is derived from the compressible Euler equation, and is shown in Eq. (5):

$$\frac{\partial \mathbf{Q}_a}{\partial t} + \frac{\partial \mathbf{F}_{aj}}{\partial x_j} = \mathbf{S}_a \tag{5}$$

where the vector of conservative variables $\mathbf{Q}_a$ and the inviscid flow velocity vector $\mathbf{F}_{aj}$ are as follows:

$$\mathbf{Q}_a = [\rho' \ (\rho u_i)' \ (\rho E)']^T \tag{6}$$

$$\mathbf{F}_{aj} = \begin{bmatrix} (\rho u_j)' \\ u_j(\rho u_i)' + u_i(\rho u_j)' - \rho' u_i u_j + p'\delta_{ij} \\ u_j(\rho H)' + H(\rho u_j)' - \rho' H u_j \end{bmatrix} \tag{7}$$

The primed quantities ( )' are the fluctuating components; here, they are acoustic components. The quantities u_i and H are values intrinsic to the flow field and were obtained with RANS in this study.

The noise arising from interference with the turbulent flow is expressed by the sound source term $\mathbf{S}_a$ below. It is employed as the formation term on the right side of the LEE equation.

$$\mathbf{S}_a = \begin{bmatrix} 0 \\ -\frac{\partial}{\partial x_j}(\rho u_i' u_j' + \overline{\rho u_i' u_j'}) \\ -\frac{\partial}{\partial x_j}(\rho H u_i' u_j' - \overline{\rho H u_i' u_j'}) \end{bmatrix} \tag{8}$$

When a flow field is simulated with RANS, the obtained solution is the time average of the turbulent flow field; it contains no information about the unsteady components of the sound source. The SNGR model proposed by Bechara et al[3]. was used here to extract the sound source from the turbulent flow field. In this model, the instantaneous turbulent velocity $\mathbf{u}_t$ at location $\mathbf{x}$ was found using the expression below, based on the random Fourier mode.

$$\mathbf{u}_t(\mathbf{x}) = 2\sum_{n=1}^{N} \hat{u}_n \cos(\mathbf{k}_n \cdot \mathbf{x} + \psi_n)\sigma_n \tag{9}$$

Here, $\hat{u}_n$, Ψ_n, $\boldsymbol{\sigma}_n$, and $\mathbf{k}_n$ mean the amplitude, phase angle, directional vector, and wave number vector of the nth Fourier

mode, respectively, and N is the total number of modes. Figure 2 shows the relations between these quantities in the wave number space for the nth mode. $\hat{u}_n$ was found from the turbulent kinetic energy spectrum of the von Karman-Pao spectrum[4]. The SNGR model requires input of the turbulent kinetic energy, integral length scale, and time scale. The turbulent kinetic energy is obtained from RANS, and the integral length scale and time scale are found from the turbulent kinetic energy and the dissipation rate. Once the turbulent shear stress has been calculated using the results from the SNGR model, the propagation calculations are carried out by inputting this into LEE as the sound source term.

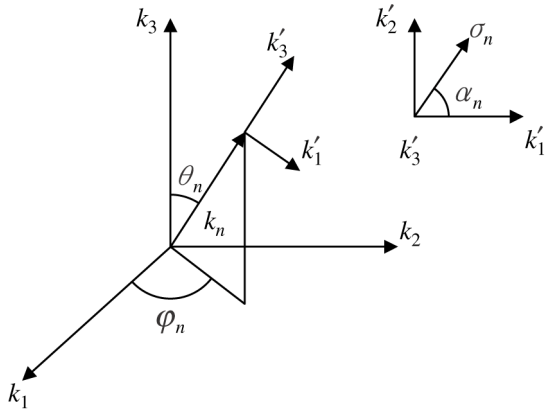


Fig. 2 Wave vector geometry for the nth Fourier velocity mode (φ_n, θ_n, and α_n : random functions)

3. Validation of Simulation Code

The acoustic simulation code developed in this study was tested to verify its accuracy. The LEE code was examined in a prediction of acoustic pulse propagation in a uniform flow field[5] as shown in Fig. 3. The initial conditions were as follows:

$$\begin{bmatrix} p' \\ u_i' \\ p' \end{bmatrix} = \begin{bmatrix} 0.03\exp[-(\ln 2)(x_1^2+x_2^2)]/5^2 \\ 0 \\ 0.03\exp[-(\ln 2)(x_1^2+x_2^2)]/5^2 \end{bmatrix} \quad (10)$$

Here, the Mach number of the uniform flow was 0.5. Figure 4(a) shows the calculation results for the acoustic pulse. The pulse diffuses through the space with the passage of time while transported downstream by the uniform flow. These results compare well with the analytical solution, as shown in Fig. 4(b). Thus, the LEE code developed in this research correctly describes the propagation of pulses in a uniform flow.

A turbulent velocity field solution[3] was sought to verify the results of SNGR. Figure 5 presents the calculated instantaneous turbulent flow field. This is dimensionless; the axes have been normalized to the turbulence scale. Some vortices with a size of approximately 1 are outlined in the figure, indicating that these results are reasonable. Figure 6 presents the spatial correlation of velocities in the turbulent flow field. The calculated results indicated that the correlation between any two points diminished with the distance between the points; this agreed with the analytical prediction. Figure 7 shows autocorrelation; this also diminished with the passage of time, in agreement with analytical predictions. The above results show that this SNGR simulation has a good correlation in both the time and space domains.

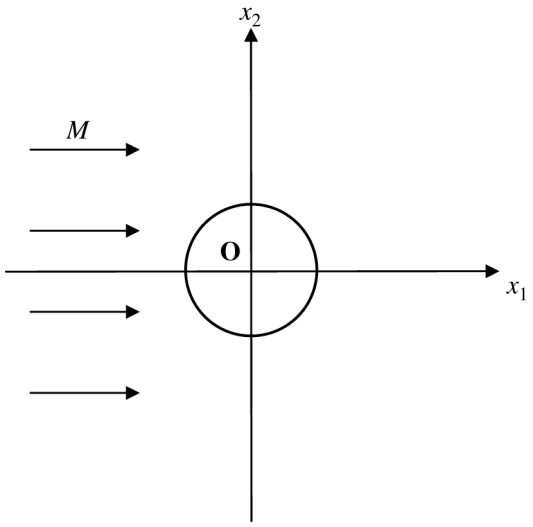


Fig. 3 Two-dimensional acoustic pulse in a uniform flow. The sound source is located at (0,0). The circle indicates the “edge” of the pulse.

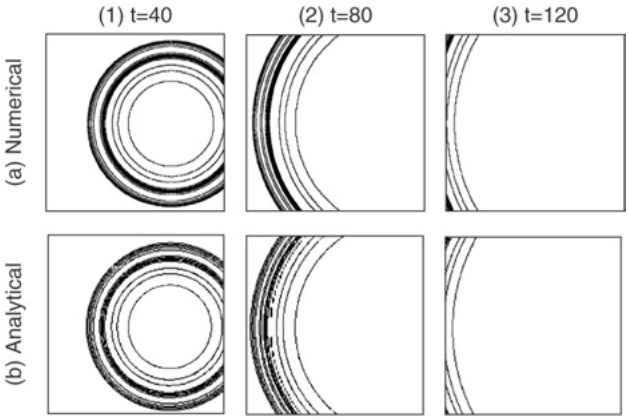


Fig. 4 Pressure fluctuation of acoustic pulse in a two-dimensional uniform flow

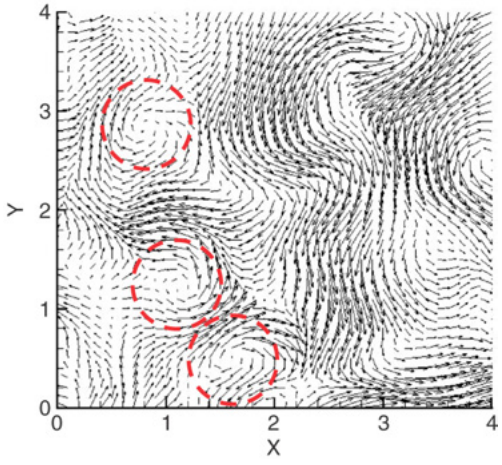


Fig. 5 Spatial distribution of the simulated turbulent velocity field (k=1714m^2/s^2, ε=44.8 × 10^{6}m^2/s^3, N=200). Several eddies are visible in the spots of red circles.

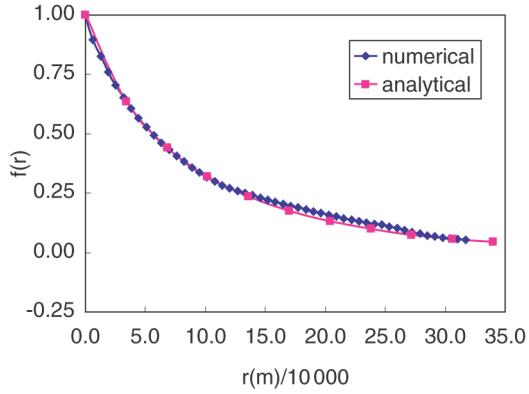


Fig. 6 Spatial two-point correlation function f(r) with a distance variable

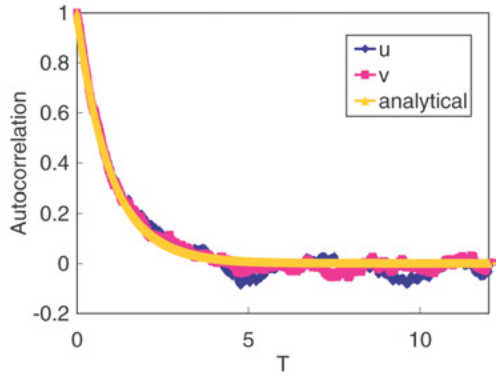


Fig. 7 Autocorrelation for generated turbulence as a function of normalized time separation

4. Coupled Aeroacoustic Simulation around an Airfoil

An aeroacoustic simulation of the flow around an airfoil was carried out to show the effectiveness of this simulation code. The object was an NACA0012 wing section with a thickened trailing edge, from which the noise has already been experimentally observed[6]. The inflow Mach number was $M_\infty = 0.205$ and the Reynolds number was $Re = 2.86 \times 10^6$. Turbulent flow was assumed over the whole region. Inflow turbulence intensity at the entrance portion of the boundary was set at Ti = 0.3%, turbulent flow length scale at 0.2% chord, and angle of attack at 5º. An unstructured hybrid grid was used for the simulation (Fig. 8).

Figure 9 presents the results of the simulation. Figure 9(a) is the Mach number distribution, Fig. 9(b) the turbulent kinetic energy distribution. High turbulent kinetic energies were generated by the thickened portion of the trailing edge.

Figure 10 shows the instantaneous velocity vectors, excluding the time average component, obtained by the SNGR model. Many large and small vortices were generated downstream. All in all, the figure indicates a very complicated flow situation. Notable is the turbulent boundary layer's interferes with the trailing edge, which gives rise to high turbulence. This agrees with the high turbulent kinetic energy predicted by fluid mechanics.

Figure 11 depicts the results of the LEE acoustic simulation [(a) through (d) occur simultaneously with the conditions shown in the corresponding parts of Fig. 10]. The propagation of small pressure fluctuations away from the vicinity of the airfoil trailing edge is clearly shown here. This shows the unique dipolar character of the dispersion of acoustic waves from the interface with a solid body. The Doppler effect of a shorter wavelength on the upstream side also appears.

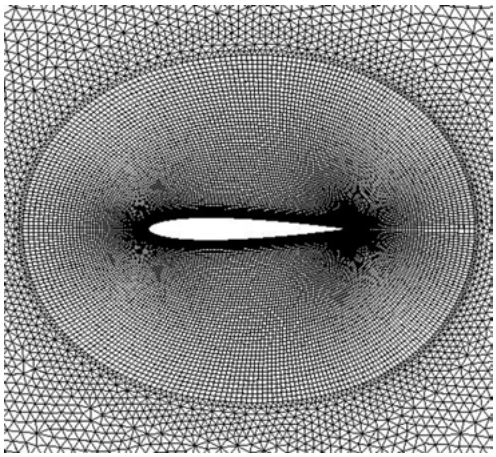
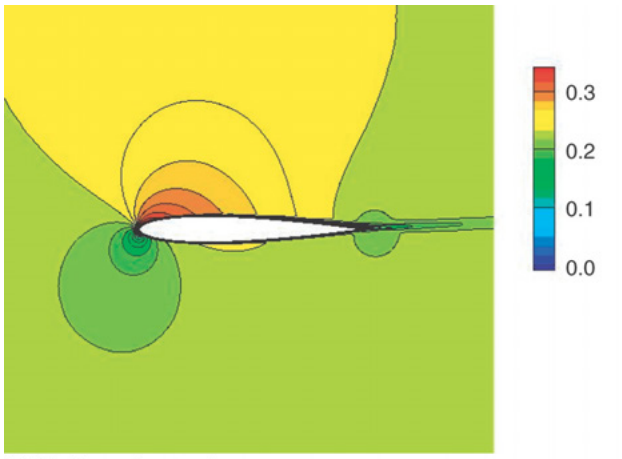
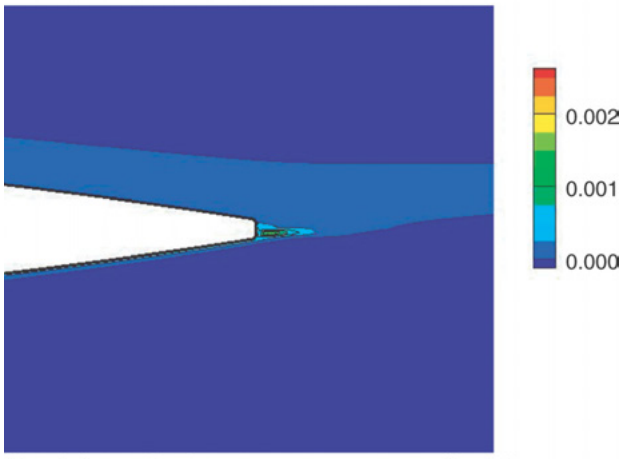


Fig. 8 Unstructured hybrid mesh around NACA0012 airfoil with the blunt trailing edge. Structured mesh are generated around the solid surface, surrounded by unstructured triangular mesh.



(a) Mach number contours



(b) turbulence kinetic energy contours near trailing edge

Fig. 9 Results of flow simulation around NACA0012 airfoil (M_∞ =0.205, Re=2.86 × 10^6, Ti=0.3%,

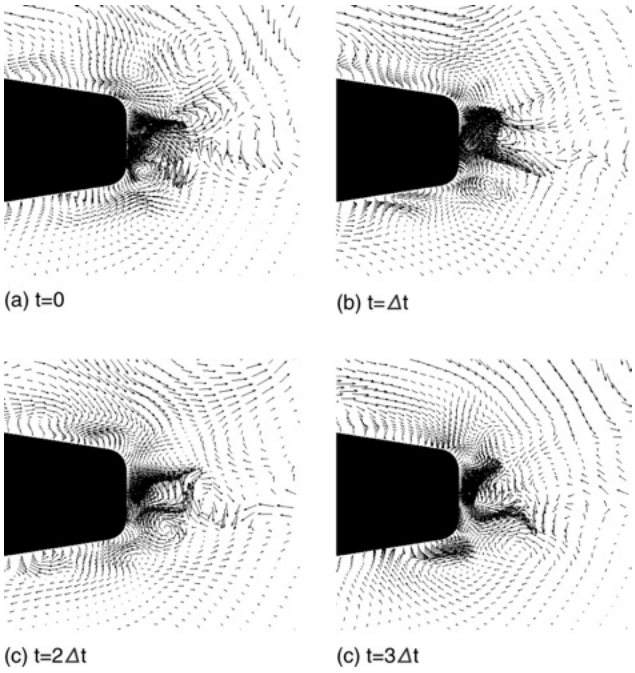


Fig. 10 Distributions of instantaneous velocity fluctuation near trailing edge (Δt: time increment)

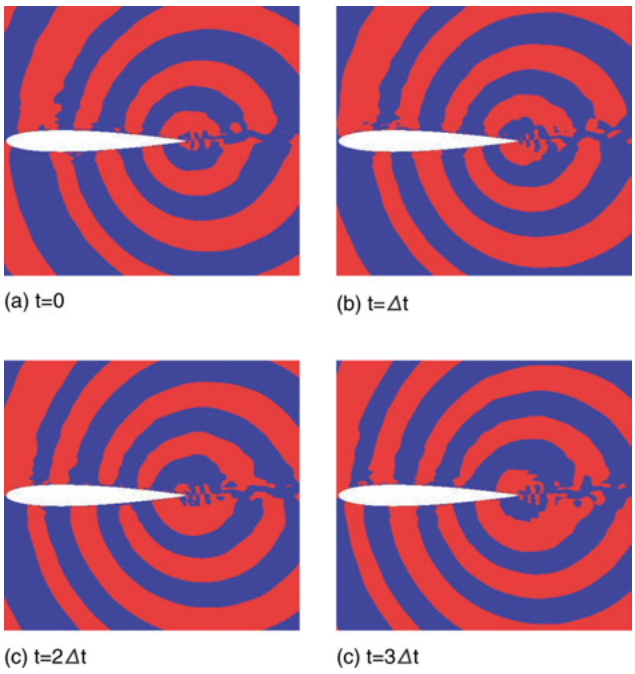


Fig. 11 Sound pressure field around NACA0012 airfoil (red: p'>0, blue: p'<0, Δt: time increment)

Figure 12 shows the large fluctuations in density in the vicinity of the trailing edge. Density showed periodic positive and negative fluctuations near the corners of the trailing edge. The greater tendency to occurrence at the bottom of the airfoil was considered to be due to the angle of attack. This study confirmed the generation of acoustic waves throughout the turbulent boundary layer, but most of the waves were generated at the trailing edge, and these often cancelled out the other waves.

The results of simulation described herein indicate that airfoil-generated noise is caused by fluctuations in density and pressure due to complex interference among trailing-edge vortices, and propagates into the surroundings as acoustic waves. RANS was used for this research because of its low cost, but this study confirmed that the same results are obtained by LES and other methods (Fig. 13). The new simulation code has been shown to be effective.

Previous research methods have shown that surface pressure fluctuations are the main sound source when a wing or other physical object is exposed to a fluid flow. In this study, turbulence fluctuations were used as the direct inputs, and the simulation correctly predicted the resulting dipole sound. This is due to the excitation of surface pressure fluctuations by fluctuations in the turbulent flow field, which shows that this approach makes more accurate assumptions about the mechanisms of these phenomena. It is, therefore, clear that the application of this method to acoustic simulation, in which the secondary surface pressure fluctuations are the main sound source, allows a better grasp of the mechanisms of sound from airfoils. In addition to the considerations of surface pressure fluctuations, using this technique enables simulation of the turbulence fluctuations themselves, and the proper model for sound sources. Sound sources can now be handled in general simulations.

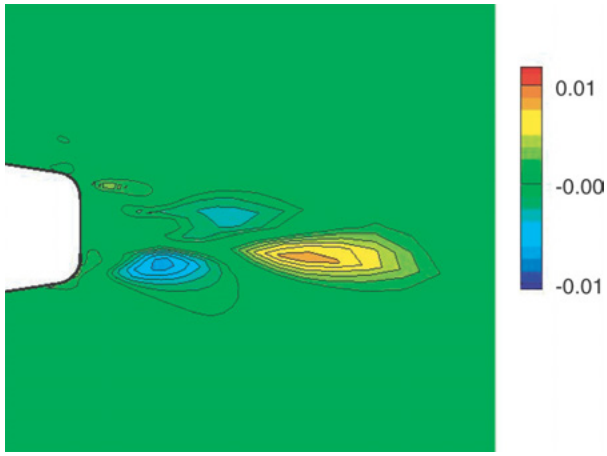


Fig. 12 Density fluctuation near trailing edge

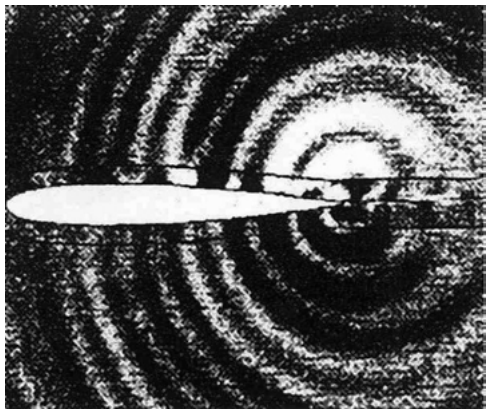


Fig. 13 Instantaneous pressure fluctuation field using LES data taken from the computational result by Manoha E. et al.[7]

5. Conclusion

A code has been developed for simulation of aerodynamic sound to overcome the longstanding shortcomings of high cost and limited applications of previous models. The following results were obtained:

(1) A combination of RANS and LEE was used to solve the flow field and the acoustic field, respectively, in a newly developed coupled method for aeroacoustic simulation. This method enables simulation of aerodynamic sound over a wide range of variables at low cost. An unstructured grid was used in all simulations and successfully accommodated complicated shapes.

(2) The validity of the code was verified by simulation of acoustic pulse propagation and turbulent velocity field solution.

(3) The code was applied to simulation of the flow around an airfoil. Results indicated that acoustic waves are generated at the trailing edge and propagate away to the surroundings. This result verified the effectiveness of this method. In addition, the direct use of turbulence fluctuations themselves, rather than of the secondary fluctuations in surface pressure, allows general handling of sound sources. This method points to a productive new direction in simulation of aerodynamic sound.

References

(1) Tam, C. K. W.: Computational aeroacoustics: Issues and Methods, AIAA Journal, Vol. 33, No. 10, p. 1788-1796 (1995)

(2) Wilcox, D. C.: Simulation of Transition with a Two-Equation Turbulence Model, AIAA Journal, Vol. 32, No. 2, p. 247-255 (1994)

(3) Bechara, W., Bailly, C., Lafon, P.: Stochastic Approach to Noise Modeling for Free Turbulent Flows, AIAA Journal, Vol. 32, No. 3, p. 455-463 (1994)

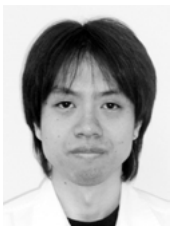
(4) Pao, Y. H.: Structure of turbulent velocity and scalar fields at large wave numbers, Phys. Fluids, Vol. 8, p. 1063-1075 (1965)

(5) http://www.codiciel.fr/database/acoustic/acoustic.html

(6) Brooks, T. F., Hodgson, T. H.: Trailing Edge Noise Prediction from Measured Surface Pressures, Journal of Sound and Vibration, Vol. 78(1), p. 69-117 (1981)

(7) Manoha, E., Herrero, C., Sagaut, P., Redonnet, S.: Numerical Prediction of Airfoil Aerodynamic Noise, AIAA paper, 2002-2573, p. 1730-1742 (2002)

■ Authors ■



Toshihiro KAMATSUCHI

Research on Technique for Identification of Sound Source of Pass-by Noise Using Matrix Inversion Method

Shinichi NISHIMURA* Yukihiko HANZAWA* Jyun KITAHARA*
Hiroshi NAKAGAWA** Hirofumi NAKAJIMA**

ABSTRACT

Identification of the contribution of individual sound sources is an essential step in attempting to reduce vehicle pass-by noise. This paper discusses a technique of source identification which utilizes the matrix inversion method. In this technique, multiple observation points are established around a sound source, and the source is identified using the observed sound pressures and a matrix of the acoustic transfer functions. The stability of the inverse matrix of the acoustic transfer function has a significant effect on the accuracy of sound source identification. An index expressing the stability of the inverse matrix of the transfer was therefore devised. The use of this index has made it possible to determine optimum observation points. The capability of this method to predict far-field sound pressures with a high degree of accuracy has been confirmed by actual vehicle tests.

1. Introduction

Sound sources of vehicle pass-by noise include engine noise, noise from the air intake system and exhaust system, and tire noise. Many components are responsible for this noise. For this reason, it is important to perform a factor analysis in order to know the contribution of each individual noise path.

One method conventionally used to identify a sound source is contribution analysis by masking[1]. However, this method necessitates much preparation time and also is unsuitable for pinpointing detailed parts. Other sound source location methods include acoustic intensity[2], acoustic holography, and the beam forming method[3]. These methods are superior in that they enable the condition of the acoustic field to be represented visually. However, they are unsuitable for cases in which the sound source is covered by the body such as the engine mounted in an actual vehicle. Research is being carried out for these methods with a view to realizing a more detailed analysis of the contribution of the sound source to by-pass noise[4, 5]. However, there are not many cases in which these methods are used for the actual analysis.

In this research, attention was focused on a method of calculating the intensity of a sound source by the acoustic transfer function matrix inversion method. To this end, empirical analysis methods that could be applied to source identification of vehicle pass-by noise, were studied.

2. Identifying a Sound Source Using Matrix Inversion Method

2.1. Outline

In the analysis of pass-by noise, it is important to obtain a grasp not only of the intensity of the sound source itself, but

* Tochigi R&D Center
** Nittobo Acoustic Engineering Co., Ltd.

also of the acoustic transfer characteristics from the vehicle. As shown in Fig. 1, it is possible to express the acoustic pressure P_F at a far field evaluation point 7.5 m from the vehicle, as the product of the volume velocity, Q_i at the source location and H_i, the acoustic transfer function from the source to the far acoustic field evaluation point, using Eq. (1).

$$P_F = \sum_i H_i Q_i \tag{1}$$

Where,
H_i: Acoustic transfer function [Pa/(m^3/s)]
Q_i: Volume velocity [m^3/s]
i: Number of sound sources

Examples of volume velocity (Q_i) identification methods include calculating volume velocity from the vibration acceleration of the radiation surface[6] and calculating the volume velocity using an acoustic tube[7]. In this research, however, the volume velocity was identified by the matrix inversion method using transfer functions obtained by empirical measurements using the reciprocity principle[8].

Here, a description is given of the principle of sound source identification using the matrix inversion method. It is assumed that there are M non-directional point sound sources, and that the sound sources are identified using N proximity observation points (Fig. 2). Here, if it is assumed that the volume velocity of the sound sources is Q_{Sm} (m-1, …, M), the acoustic pressure at the observation points is P_{Rn}(n=1, …, N), and the transfer function from point sound source m to observation point n is H_{SmRn} (m=1, …, M, n=1, …, N), these relational expressions can be expressed as Eq. (2).

$$\left.\begin{aligned} P_{R1} &= H_{S1R1}Q_{S1} + \ldots + H_{SMR1}Q_{SM} \\ P_{R2} &= H_{S1R2}Q_{S1} + \ldots + H_{SMR2}Q_{SM} \\ &\vdots \\ P_{RN} &= H_{S1RN}Q_{S1} + \ldots + H_{SMRN}Q_{SM} \end{aligned}\right\} \tag{2}$$

It is also possible to express these relationships as a matrix, as shown in Eq. (3).

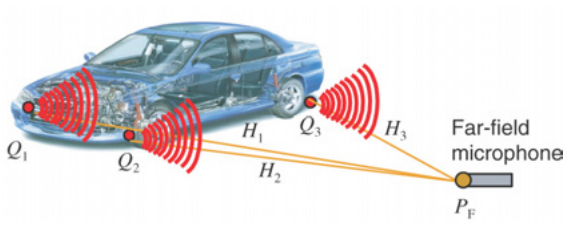


Fig. 1 Far-field sound pressure

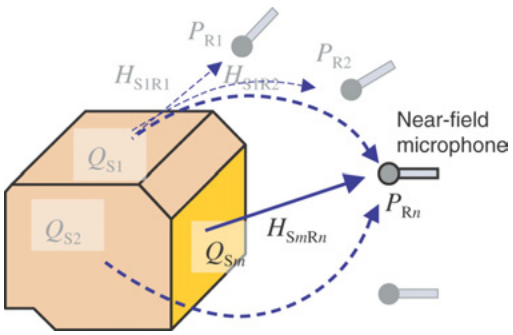


Fig. 2 Inverse matrix method

$$\mathbf{P} = \mathbf{HQ} \tag{3}$$

Consequently, it can be seen that the volume velocity of each of M sound sources can be identified by obtaining the acoustic pressure at the N observation points and also the inverse matrix of the $M \times N$ transfer function matrix. This is expressed in the form of Eq. (4).

$$\mathbf{Q} = \mathbf{H}^{+}\mathbf{P} = \mathbf{GP} \tag{4}$$

Where,

$$\mathbf{G} = \begin{pmatrix} G_{R1S1} & G_{R2S1} & \ldots & G_{RNS1} \\ G_{R1S2} & G_{R2S2} & \ldots & G_{RNS2} \\ \vdots & \vdots & \ldots & \vdots \\ G_{RNS1} & G_{RNS2} & \ldots & G_{RNSM} \end{pmatrix} \tag{5}$$

The + sign in this equation indicate that the matrix is a Moore-Penrose general inverse matrix. The actual matrix takes the form of Eq. (5). A general inverse matrix is an expanded matrix of an ordinary inverse matrix, and can also be applied to matrixes other than regular matrixes of the form $M = N$. In this paper, this general inverse matrix is hereafter referred to simply as an inverse matrix.

2.2. Features and Issues

As mentioned in sub-section 2.1, the volume velocity of each sound source can be determined by obtaining the inversion of the transfer function matrix. Consequently, the stability of an inverse matrix significantly affects the accuracy of the sound source volume velocity identification. In order to perform highly accurate sound source identification, the following conditions must be satisfied.

(1) $M \leq N$. In other words, the number of observation points N must be greater than the number of sound sources M.
(2) The transfer function vectors must intersection each other orthogonally.
(3) A highly accurate transfer function must be measured.

(1) means that if $M > N$, it will not be possible to obtain a solution to the inverse matrix of the transfer function.

(2) means that the location of the observation points has a large effect on the sound source identification accuracy. For example, even if many observation points are set in order to satisfy condition (1), if the observation points are very close to each other, the transfer function vectors from each of the sound sources will be similar. As a result, they will fail by a long way to intersect each other orthogonally, bringing about the possibility of divergence of the matrix. Also, even if the matrix does not diverge, this may result in increased errors during sound source identification.

A description of this is given using the two sound sources and two observation points shown in Fig. 3.

Here, each transfer function is shown below.

$$\begin{aligned} H_{S1R1} &= a, \quad H_{S2R1} = b \\ H_{S1R2} &= c, \quad H_{S2R2} = d \end{aligned} \tag{6}$$

The transfer function inverse matrix in this case is shown in Fig. 4.

$$D = ad - bc \tag{7}$$

$$H_{R1S1} = d/D, \quad H_{R2S1} = -b/D$$
$$H_{R1S2} = -c/D, \quad H_{R2S2} = a/D \tag{8}$$

D is the determinant of the transfer function matrix, and is a coefficient that is equivalent to the denominator of the transfer function inverse matrix. Consequently, in the case where D is near 0, the measured acoustic pressure increases. If there is no error, the reason for the volume velocity identification value under-estimating the source is that the direct paths, a and d are cancelled by the indirect paths b and c. In other words, if the transfer coefficient of the cross path is over estimated, the coefficient of those paths will also increase and thereby cancel the volume velocity components of the direct paths.

Next, a theoretical explanation is given concerning the fact that if an error is included in the observation point acoustic pressure, the error will increase. Assuming that error **E** is added to the observed acoustic pressure vector **P**, resulting in **P'**, and the volume velocity is identified in this state, the identification value **Q'** of the volume velocity in the state that includes the error will be as follows.

$$\begin{aligned} \mathbf{Q'} &= \mathbf{H}^{-1}\mathbf{P'} \\ &= \mathbf{H}^{-1}(\mathbf{P}+\mathbf{E}) \\ &= \mathbf{H}^{-1}\mathbf{P}+\mathbf{H}^{-1}\mathbf{E} \\ &= \mathbf{Q}+\mathbf{H}^{-1}\mathbf{E} \end{aligned} \tag{9}$$

The resulting error in the volume velocity identification value is the error E when the acoustic pressure is measured multiplied by the inverse matrix. This means that the magnitude of the inverse transfer function determines the increase in the error. In the case of a 2 × 2 matrix, the nature of the increase in the coefficient of the inverse transfer function is determined by matrix D, and becomes greater the closer the magnitude of the cross path approaches the magnitude of the direct path. Thus, in the case of a 2 × 2 matrix, it is possible to analyze the amplification ratio of an error relatively easily. However, if there are many points (including a non-square matrix), the coefficient of the inverse matrix will be represented by a complex equation, the number of terms of which is proportional to the exponential of the size of the matrix. This makes it difficult to perform an evaluation using an equation that includes the original coefficient.

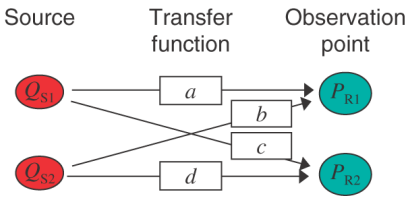


Fig. 3 Transfer function

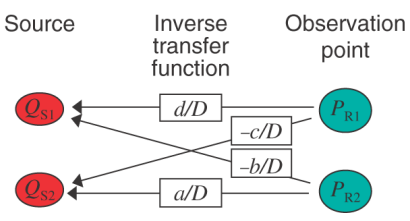


Fig. 4 Inverse transfer function

(3) means that the error included during measurement of the transfer function or the acoustic pressure at the observation point is a factor that produces an error in the sound source identification value. This particularly effects the transfer function measurement, since the reciprocity principle is applied, which means that the measurement is performed using microphones located near the sound sources and speakers located near the observation points. Which, in other words, is in the opposite location to that of actual sound propagation during operation. Consequently, an error occurs in the measured transfer function due to the location of the speakers and the difference in directionality. This is also one of the factors that degrade the sound source identification accuracy. Therefore, a transfer function identification method that is relatively unaffected by measurement errors is necessary.

Accordingly, in order to satisfy (2) and (3), the following were studied.

- Use of an energy transfer rate based on a 1/3 octave band conversion
- Application of an index for evaluating whether or not the transfer function is stable.

2.3. Reduction of Measuring Errors by Using 1/3 Octave Band Conversion

A measurement error due to a misalignment in the measurement position mentioned in (3) of sub-section 2.2 is likely to occur as a general phase error. In order to carry out robust sound source identification that is relatively unaffected by phase errors, the 1/3 octave band-converted energy transfer rate was used. In contrast to Eq. (4), the calculation equation is as shown in Eq. (10).

$$\begin{pmatrix} Q_{S1}^2 \\ Q_{S2}^2 \\ \vdots \\ Q_{M2}^2 \end{pmatrix} = \begin{pmatrix} \overline{H}_{S1R1}^2 & \overline{H}_{S2R1}^2 & \cdots & \overline{H}_{SNR1}^2 \\ \overline{H}_{S1R2}^2 & \overline{H}_{S2R2}^2 & \cdots & \overline{H}_{SNR2}^2 \\ \vdots & \vdots & \cdots & \vdots \\ \overline{H}_{S1RM}^2 & \overline{H}_{S2RM}^2 & \cdots & \overline{H}_{SNRM}^2 \end{pmatrix}^{+} \begin{pmatrix} P_{R1}^2 \\ P_{R2}^2 \\ \vdots \\ P_{RN}^2 \end{pmatrix} \tag{10}$$

Here, $\overline{H}_{SnRm}^2$ is the value of the energy transfer rate $|H_{SnRm}|^2$ averaged over a 1/3 octave band. Consequently, the error resulting from fluctuations and differences in measuring conditions of both the transfer function and acoustic pressure is reduced. However, there is a possibility of a new error occurring as a result of failure of the interference effect due to phase to be taken into account. It is considered, however, that this error can be reduced by increasing the number of measurement points, for example, and also that the effect of interference due to phase on pass-by noise is small. Consequently, it is important to improve the stability of the inverse matrix by using 1/3 octave band conversion.

2.4. Use of an Index of Stability of a Transfer Function Matrix

In order to obtain a stable transfer function matrix, it is necessary to ensure that the location of the sound source points and observation points is appropriate. Taking the engine as an example, an appropriate location of sound source points is equivalent to dividing of the engine, which is a plane sound source, into "appropriate" sound source elements. Regarding the observation points, this is equivalent to the laying out of microphones around the engine. However, an "appropriate" location depends greatly on the sound source and the sound profile in the vicinity. Generally, the observation points should be arranged at equal intervals from each other and equidistant from the sound sources and

surrounding them. However, it is sometimes difficult in practice to arrange the observation points at equal intervals in the case of an actual engine mounted in the engine compartment. Consequently, it is necessary to judge whether or not the microphone positions as observation point are appropriate. As an index for obtaining this appropriateness, instability I was defined as shown in Eq. (11), and studied.

$$\mathrm{I} = \mathrm{Max}\{|\mathbf{g}_n| \cdot \mathrm{Max}\{\mathbf{h}_n\}\} \tag{11}$$

Here, $\mathbf{g}_n$ is the vector of the nth row of the inverse transfer function matrix, $\mathbf{h}_n$ is the vector of the nth column of the transfer function matrix and Max {} is the maximum value inside {}. The instability is expressed as the degree to which the error increases when identification of volume velocity using multiple points is compared to the case where there is one sound source and one observation point.

First, consider the identification of volume velocity Q_n by conventional 1-point estimation, using transfer functions recorded at multiple points. In the conventional 1-point estimation, there is a degree of freedom regarding what observation points to use as the basis for identification. When performing identification based on acoustic pressure P_m at observation point m, the identification value is as follows.

$$Q_n = P_m / H_{SnRm} \tag{12}$$

Here, like in the case of 2-point estimation mentioned above, the error contained in the acoustic pressure P_m is multiplied by $1/H_{SnRm}$. If the magnitude of the measurement error in all channels is assumed to be the same, the error will be minimum in the case where the volume velocity is estimated based on the observation point at which the transfer rate from Q_n will be largest, that is, on the measurement point m where H_{SnRm} is greatest. The amplification ratio R_1 of the error in this case can be expressed as follows.

$$\begin{aligned} R_1 &= 1/\mathrm{Max}\{H_{S1R1}, H_{S1R2}, ..., H_{S1RN}\} \\ &= 1/\mathrm{Max}\{\mathbf{h}_n\} \end{aligned} \tag{13}$$

On the other hand, when volume velocity is identified using inverse transfer functions at multiple points, the identification equation will be as follows.

$$Q_n = G_{R1Sn}P_1 + G_{R2Sn}P_2 + ... + G_{RMSn}P_M \tag{14}$$

Here, if the errors contained in the measured acoustic pressure P_1 to P_M are defined as E_1 to E_M, the estimated error in the volume velocity E_q can be expressed according to the following equation.

$$E_q = G_{R1Sn}E_1 + G_{R2Sn}E_2 + ... + G_{RMSn}E_M \tag{15}$$

From this equation, it can be seen that the amplification ratio of the error differs depending upon the channel, and its value is assigned by G_{RmSn}. Here, if it is assumed that the magnitude of each error from E_1 to E_M is the same, and there is no correlation between the errors, the expected value $\overline{|E_q|^2}$ of the square of the estimated error will be as follows.

$$\begin{aligned} \overline{|E_q|^2} &= \overline{|G_{R1Sn}E_1 + G_{R2Sn}E_2 + ... + G_{RMSn}E_M|^2} \\ &= \overline{|G_{R1Sn}E_1|^2} + \overline{|G_{R2Sn}E_2|^2} + ... + \overline{|G_{RMSn}E_M|^2} \\ &= (G_{R1Sn}^2 + G_{R2Sn}^2 + ... + G_{RMSn}^2) \cdot \overline{|E_1|^2} \end{aligned} \tag{16}$$

Consequently, the amplification ratio R_2 of the magnitude of the estimated error when an inverse matrix is calculated from the expected value is as follows.

$$R_2 = \sqrt{G_{R1Sn}^2 + G_{R2Sn}^2 + ... + G_{RMSn}^2} = |\mathbf{g}_n| \tag{17}$$

The ratio I_n of the amplification ratios of the two errors obtained using Eqs. (12) and (16) is shown in Eq. (18).

$$I_n = R_2 / R_1 = |\mathbf{g}_n| \cdot \mathrm{Max}\{\mathbf{h}_n\} \tag{18}$$

This I_n indicates the degree to which the error is increased when the matrix inversion method is used to calculate the volume velocity Q_n compared to a single point based estimation. It can be used as an index that expresses the instability during inversion. The value of the instability I that corresponds to the most unstable calculation is used as a representative value, when all of the volume velocity values of Q_1 to Q_N have been identified. In other words, it is defined as follows.

$$I = \mathrm{Max}\{[I_1, I_2, ..., I_N]\} = \mathrm{Max}\{|\mathbf{g}_n| \cdot \mathrm{Max}\{\mathbf{h}_n\}\} \tag{19}$$

As an index of the stability of a matrix, the condition number is generally used. However, this poses issues, namely that it is difficult to obtain coherence with physical meaning and also when the dimensions of the matrix are different it is not possible to make a direct comparison. The instability is used to overcome this issue. This index enables the effectiveness of increasing the number of observation points in reducing the error, for example, to be judged.

3. Basic Verification Using a Speaker Sound Source

3.1. Speaker Experiment

An engine-like unit consisting of six speakers (Fig. 5) was used as a sound source, and the effectiveness of the index of the instability was confirmed. Mutually independent noise (white noise) was emitted simultaneously from the six (top, bottom, left, right, front, rear) speakers. Twenty four observation points were set in the vicinity of this unit, and the acoustic pressure at each point was measured. Also, 6 × 24 = 144 transfer functions between the sound source and the observation points were measured using the reciprocity principle. The matrix inversion method was used to identify the volume velocity of each speaker by means of the observation point acoustic pressure and the transfer function. Also, in order to confirm the relationship between the instability due to the layout and the sound source identification accuracy, an experiment using two layouts in which the observation positions were changed was carried out (Fig. 6).

Figure 7 shows the instability of each location. The solid line in the figure applies for the case where the distance between the sound source and the observation point is 20 cm

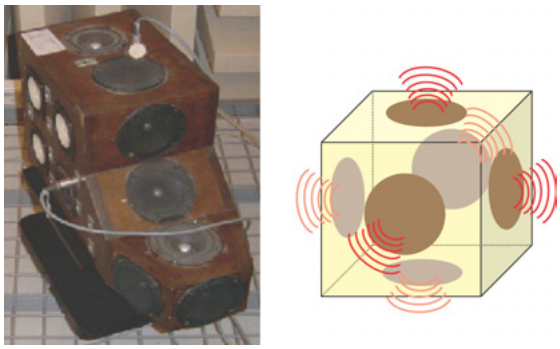


Fig. 5 Dummy noise source with loud speakers

(layout 2), and the broken line is for the case where this distance is 1 m (layout 1). When the frequency is higher than 500 Hz, the instability values for both distances were roughly equal. However, for 500 Hz or below, a distance of 20 cm resulted in lower instability. Figure 8 shows one of the volume velocities for the six identified sound sources. Here, only one sound source was driven, and the volume velocity that was identified using one sound source and one observation point was defined to be the true value. The observation point used here was located 20 cm in front of the sound source. Regarding the types of lines in the figure, the broken line was the true value, the long and short dash line was the identification value for layout 1, and the solid line was the identification value for layout 2. At a frequency of more than 500 Hz, both identification values agreed roughly with the true value. However, at 500 Hz or below, the sound source was not correctly identified in the case of layout 1, whereas the sound source could be identified with an error of about 3 dB in the case of layout 2. This agrees roughly with the trend indicated by the instability. As a result, it was possible to quantitatively judge the appropriateness of the observation point location for obtaining high sound source identification accuracy.

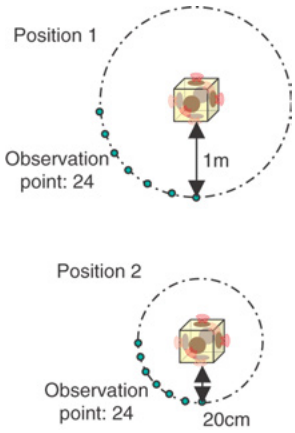


Fig. 6 Measurement conditions

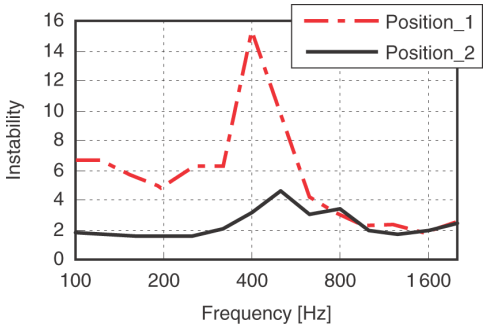


Fig. 7 Instability

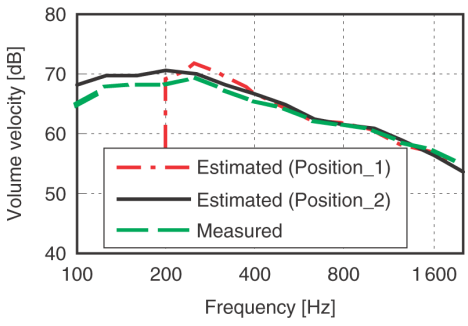


Fig. 8 Volume velocity

4. Example of Application to Actual Vehicle

4.1. Outline of Measurement

Shown below is an example of the application of the sound source identification method of this research to an actual vehicle. The vehicle used contained a 2.4L in-line 4-cylinder engine and a manual transmission.

As shown Fig. 9, the vehicle was placed on a chassis dynamometer in a semi-anechoic room, and the dynamometer was rotated by running resistance control operation that simulated actual running of the vehicle.

The acoustic pressure on the observation points in the vicinity of the sound source and also the far acoustic field acoustic pressure were measured in 3rd gear when the engine was running at 3 000 rpm. The far acoustic field was set at a point 7.5 m in the lateral direction from the front edge of the vehicle, and 5 m to the rear of it.

The sound sources were broadly divided into four areas, engine radiation noise, intake orifice noise, exhaust radiation noise, and exhaust orifice noise. The number of each type of sound source was, engine radiation noise: 6 points, intake orifice noise: 1 point, exhaust radiation noise: 5 points, and exhaust orifice noise: 2 points. Regarding the tires, slick tires were used to ensure that the contribution of the tires to the far acoustic field was as small as possible.

The number observation points for each area was, engine radiation noise: 42 points, intake orifice noise: 6 points, exhaust radiation noise: 30 points, and exhaust orifice noise: 12 points.

Table 1 shows the number of sound sources, observation points and transfer function in each area. A transfer function matrix was formed for each area, and the instability was calculated. The result is shown in Fig. 10. From this, it was confirmed that a stable transfer function matrix was obtained.

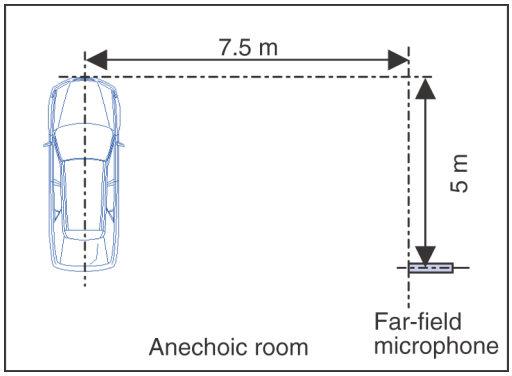


Fig. 9 Measurement conditions

Table 1 Measurement point readings

Area	Source	Observation point	Transfer function
Engine noise	6	42	252
Intake orifice noise	1	6	6
Exhaust radiation noise	5	30	150
Exhaust orifice noise	2	12	24
Total	14	90	432

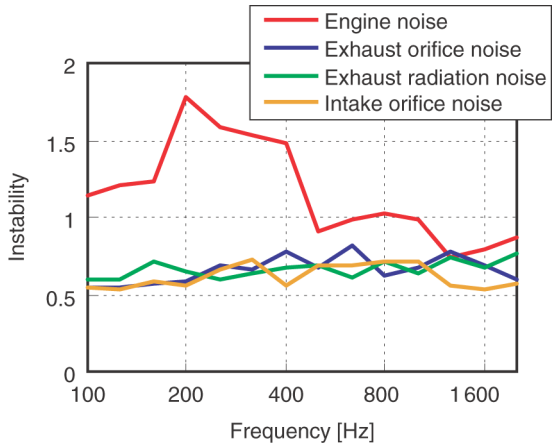


Fig. 10 Result of instability

4.2. Far Acoustic Field Prediction Results

The far acoustic field acoustic pressure was predicted by means of the volume velocity of each identified sound source and the transfer function to the far acoustic field. The results are shown in Fig. 11.

From this, it was confirmed possible to predict the far acoustic field acoustic pressure level to an accuracy of within ± 3 dB.

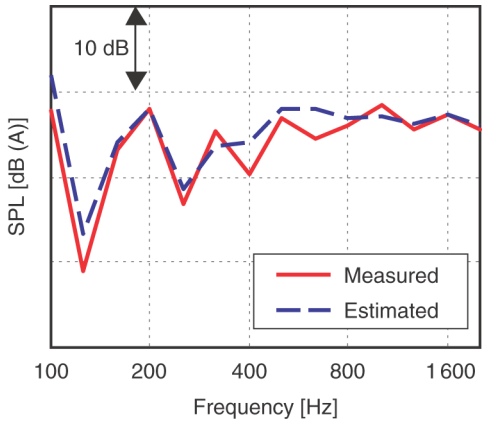


Fig. 11 Result of far-field SPL

5. Conclusion

A matrix inversion method was used to identify a sound source for use in contribution analysis of pass-by noise.

Here, an index of stability of a transfer function matrix that affects the sound source identification accuracy (instability) was used and studied. As a result, it was possible to quantitatively indicate the appropriateness of the locations of the observation points that affect the accuracy of sound source identification by means of instability.

Also, in verification using an actual vehicle, the far acoustic field acoustic pressure could be predicted to an accuracy of within ± 3% of the measured value.

Acknowledgments

The authors would like to express their sincere gratitude to the staff of Sankei Giken Kougyou Co., Ltd. for their cooperation in this research.

References

(1) Sawai: Measurement method for contribution of pass-by noise, JSAE, Vol. 35, No. 12, p. 1428-1432 (1981)

(2) Kashiwagi, H., Shimizu, S., Shimokobe, K., Sekita, M.: Development of Noise Measurement System Using Microphones Array in Anechoic Chamber, 1993 JSAE Annual Congress Proceedings, No. 936, p. 281-284 (1993)

(3) Hanzawa, Y., Kitahara, J., Nishimura, S.: Locating Source of Vehicle Pass-by Noise Using Beamforming Method, Honda R&D Technical Review, Vol. 16, No. 1, p. 179-184

(4) A. R. Fleszar, P. J. G. Linden, J. R. Johnson, M.J. Grimmer: Combining Vehicle and Test-Bed Diagnosis Information to Guide Vehicle Development for Pass-by Noise, SAE 2001-10-1565 (2001)

(5) Biermayer, W., Brandl, F., Shirahashi, Y., Nishimaru, H.: Development of a Software Tool for the Analysis and Optimization of Passenger Car Pass-by Noise, 2003 JSAE Annual Congress Proceedings No. 40-03, p. 13-16(2003)

(6) Nakamura, M.: Principles of Estimating Sound Radiation Level at a Far Point Based on the Reciprocity Theorem, Transactions of The Japan Society of Mechanical Engineers (C), Vol. 63, No. 616, p. 76-81 (1997)

(7) Nakamura, M., Nakano, M.: Exterior Engine Noise Prediction Utilizing an Acoustic Tube by the Volume Velocity Measurement Method, Transactions of The Japan Society of Mechanical Engineers (C), Vol. 63, No. 667, p. 68-73 (2002)

(8) Maruyama, S., Furuyama, M., Aoki, J.: A Reciprocity Technique of Acoustic Transfer Functions for Sound Radiation from Vibrating Components, 1996 JSAE Annual Congress Proceedings, No. 963, p. 185-188 (1996)

■ Authors ■


Shinichi NISHIMURA


Yukihiko HANZAWA


Jyun KITAHARA


Hiroshi NAKAGAWA


Hirofumi NAKAJIMA

Establishment of Analysis Method for Pulse Feeling of Four-stroke, V-twin Engine, American-type Motorcycles

Kunihiro OSADA* Ryuta NIIMURA*
Keikichi SHIMOKOBE* Goro YAMASAKI*

ABSTRACT

Pulse feeling is an important factor of ride comfort for V-twin engine, American-type motorcycles. Depending on sensory evaluation, the pulse feeling varies widely among estimators. Therefore, it takes a large amount of time to determine specifications. To solve this problem, a quantitative evaluation method was developed. In the development process, sensory evaluation testing using Japanese and American riders was conducted to verify how they feel the pulse. There was no significant difference between both sets of riders. Both sets of riders felt that seat vibration made the largest contribution to the pulse feeling. In order to quantify the seat vibration pulse, a pulse intensity indicator was added to the previous sensory vibration indicator. Furthermore, time domain response analysis was applied to a complete motorcycle analysis model. The output showed good correlation with the actual data. The pulse feeling indicator was obtained from the analysis results. Consequently, the established method has allowed early prediction of the pulse intensity at the design stage.

1. Introduction

Pulse feeling is a performance characteristic of American-type motorcycles. It contributes to the rider's comfort and to his/her impression of the ride. However, this evaluation is a sensory evaluation of the actual ride, and there is large variation in judgment among in-house evaluation experts. Additionally, a large amount of time is required to determine specifications using a trial and error approach. Evaluations before and after countermeasures cannot be quantified. Therefore, an index to quantitatively evaluate pulse feeling at the development stage was desired. In this research project, sensory evaluation tests were conducted using Japanese and American riders. The purpose was to clarify differences in how pulse is perceived, and to clarify the component factors of pulse. Sensory evaluations were carried out with the test subjects seated on a vibration generator. The aim was to determine body sensory characteristics related to pulse, and to create a quantitative evaluation index. Furthermore, in order to establish a method for prediction at the design stage, body, engine and drivetrain models were created for the purpose of conducting time domain response analysis. This paper reports on the correlation to the actual measured data, and on development tools.

* Asaka R&D Center

2. Creating a Pulse Feeling Index

2.1. Pulse Feeling Component Factors

When quantifying pulse intensity, it is first necessary to clarify characteristics that people feel as pulse. Japanese and American subjects were surveyed to determine how they feel the pulse. Riding on a number of different types of American-type motorcycles, the subjects were asked to answer questions concerning where pulse feeling originates and how each location contributes to the overall feeling. Figure 1 shows the results with two American-type motorcycles. It is clear in Fig. 1 that both Japanese and American riders agree that the greatest pulse feeling comes from seat vibration.

Additionally, along with this survey, another survey was conducted. The second survey was related to how they want to feel pulse feeling. The results in Fig. 2 clearly show that both Japanese and American riders said that seat vibration was desired as pulse feeling.

For both Japanese and American riders, seat vibration was the major element contributing to pulse feeling. It was clear that this was desirable. Therefore, it was decided to quantify pulse intensity using seat vibration.

Here, if sensations concerning pulse intensity are different between Japanese and American riders, it is necessary to carry out tests for each country. In order to confirm whether or not there are differences, a survey was conducted to determine the level of intensity at which pulse feeling is felt. The Japanese and American riders assigned scores to the level of pulse feeling intensity when driving the same motorcycle at the same speed under the same conditions. The results are shown in Fig. 3. It was determined that there is no significant difference between Japanese and American riders, in the way in which pulse intensity is felt. Accordingly, with Japanese riders as the test subjects, an attempt was made to quantify pulse intensity using seat vibration.

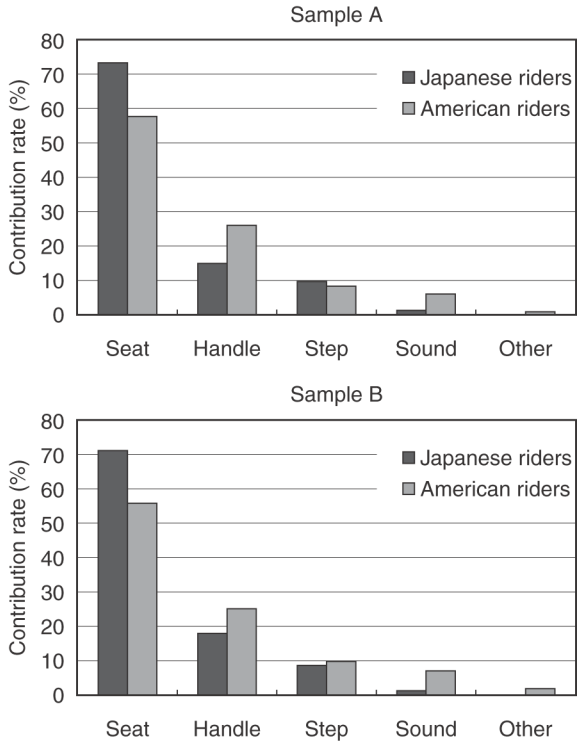


Fig. 1 Contribution to pulse feeling

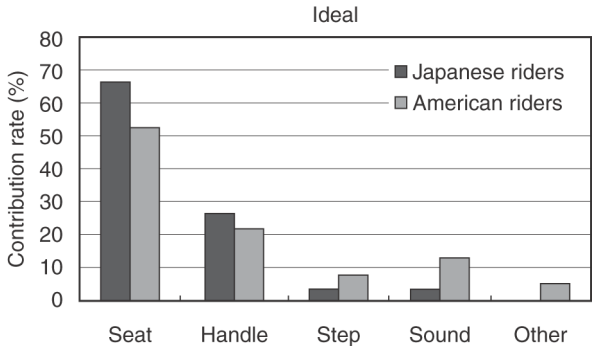


Fig. 2 Ideal contribution to pulse feeling

2.2. Process of Creating Index

2.2.1. Quantification of seat vibration intensity

Pulse intensity quantification was carried out using seat vibration. A previous in-house method was used in quantifying seat vibration intensity.

The following is an explanation of seat vibration intensity quantification. Seat vibration intensity is the level of intensity of seat vibration that is felt. In the field of acoustics, the level of sound felt by people is defined as "loudness", in contrast to the physical property of sound pressure. In the same way, the intensity of vibration felt by people is defined as the "Vibration Intensity Index" using the physical property of vibration acceleration.

The values of sensation of vibration intensity are known to differ according to frequency and direction. As a method for correcting values of sensation of vibration acceleration, ISO2631-1 defines the weighting curve according to whole-body vibration frequency and direction. This is similar to A-weighting in the field of acoustics[1]. Figure 4 shows the whole-body vibration weighting curve at the seated position according to ISO definition.

However, experiments have shown the vibration acceleration with this ISO weighting added uniformly to be different from the intensity of seat vibration sensation. It is believed that a major cause is that the frequency weighting is different according to vibration acceleration[2]. It was decided to create a curved surface that can define seat vibration intensity according to frequency and vibration acceleration in each direction (back/forth, right/left and up/down). The vibrations created by a vibration generator were applied to the human body in a riding position on the motorcycle. The sensory evaluation tests[3] were repeated. Sensory evaluations were carried out for the following four items.

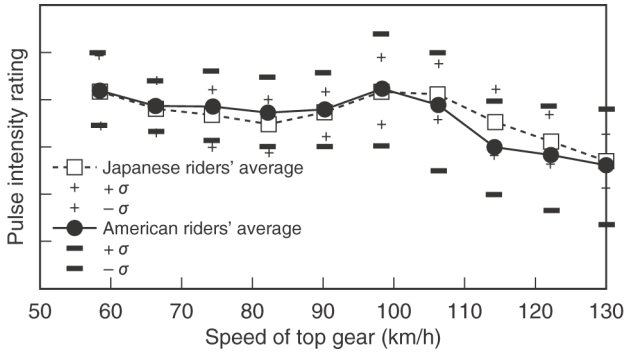


Fig. 3 Difference in pulse feeling rating

(1) Threshold investigation
An investigation of vibration acceleration threshold values, according to each direction, frequency.
(2) Investigation of equal sensation acceleration cause by vibration frequency
Using the paired comparison method, an investigation was made of vibration acceleration that was felt as the same vibration intensity, in the same direction at various frequencies.
(3) Investigation of equal sensation acceleration caused by vibration direction
Using the paired comparison method, an investigation was made of vibration acceleration that was felt as the same vibration intensity, in different directions but at the same frequency.
(4) Investigation of subjective feeling
Investigation of the relationship between sensory vibration intensity and vibration acceleration

As a result of these investigations, the curved surface of up and down direction (Z-axis) obtained are shown in Fig. 5.

Using these curves, it was possible to evaluate seat vibration intensity by measuring vibration acceleration for three axes and carrying out frequency analysis. Figure 6 shows the concept diagram outlining the calculation of the "Vibration Intensity Index" from the results of the frequency analysis of vibration acceleration measured on an actual motorcycle. By correcting vibration accelerations according to the sensory value curves for each direction, it is possible to combine 3 directions and obtain a single "vibration intensity value".

2.2.2. Difference between vibration and pulse feeling

Using the method described in Section 2.2.1, it has become possible to quantify a sensory level of vibration. Figure 7 shows the changes in "Vibration Intensity Index" due to certain American-type motorcycle engine speeds. Here, particularly in the high rpm range, the "Vibration Intensity Index" is large. The issue arises that this is not

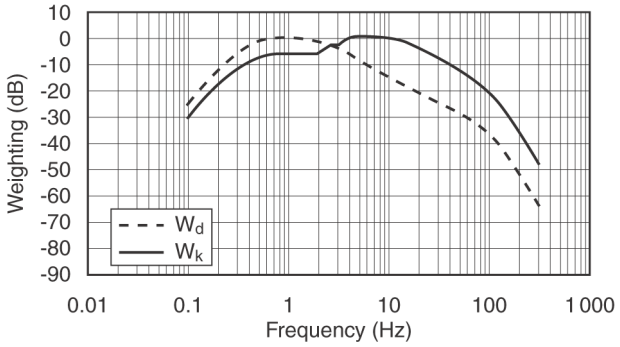


Fig. 4 Frequency weighting curves

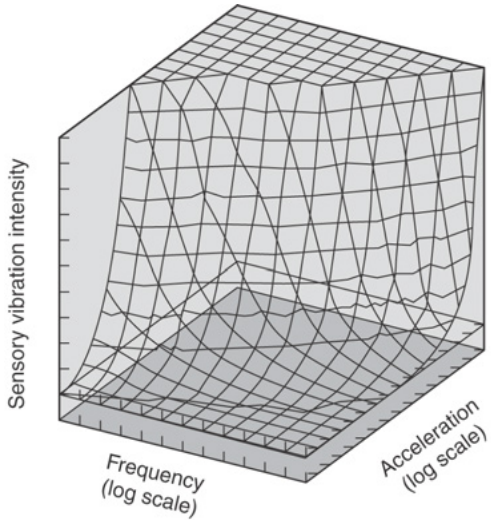


Fig. 5 Sensory vibration intensity curved surface for Z-axis

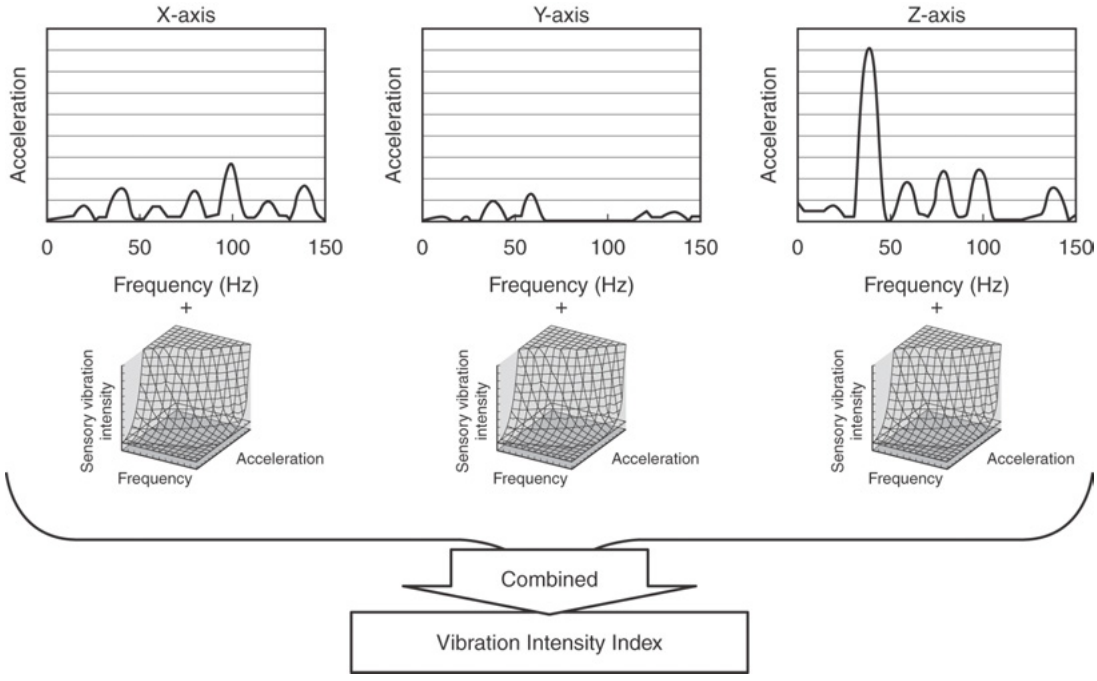


Fig. 6 Notion of "Vibration Annoyance Index" calculation method

perceived as pulse feeling. When an interview was made, it was determined that pulse feeling was an evaluation related to beating vibration. High frequency vibration was not evaluated as pulse feeling. Additionally, from the results of the tests using vibration generators, the question of whether or not something is perceived as pulse feeling does not depend on the level of the vibration acceleration, but on the frequency (that is to say, on engine speed in an actual motorcycle).

Therefore, a new index was developed that differentiates between vibration and pulse feeling. An investigation related to the level of engine speed up to which vibration is taken as pulse feeling was completed. Vibrations produced by several V-type 2-cylinder engines, common on American-type motorcycles, were selected at each engine speed and applied to the test subjects using a vibration generator. The results are shown in Fig. 8.

As clearly shown in Fig. 8, with a V-type 2-cylinder engine, when 4 000 r/min is exceeded, almost none of the test subjects perceived vibration as pulse feeling. The reciprocal number of the cumulative frequency of replies of perception as pulse feeling was adopted as the representative pulse feeling filter for V-type 2-cylinder engines. This filter was applied to the "Vibration Intensity Index", and with the high frequency vibration excluded, a pulse intensity "Pulse Beat Index" was created.

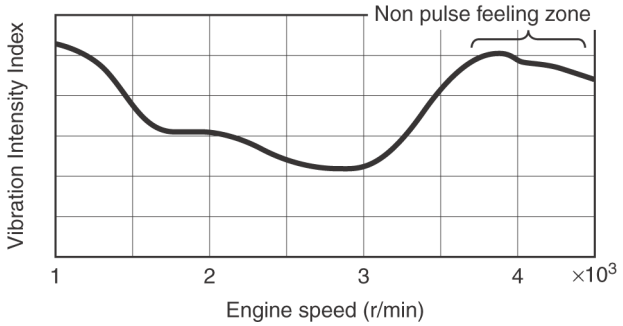


Fig. 7 "Vibration Intensity Index" alteration

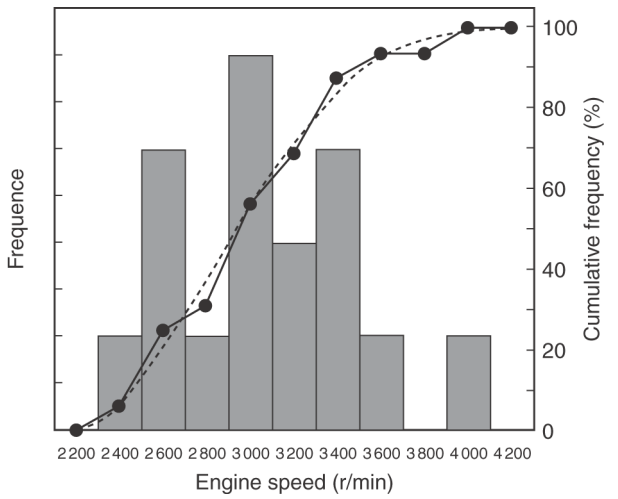


Fig. 8 Consciousness of pulse feeling

2.2.3. Verification of the index

Figures 9 and 10 show the evaluation scores according to the "Pulse Beat Index" calculated from the measured acceleration, and the sensory evaluations. The calculated pulse feeling "Pulse Beat Index" show good conformity with the sensory evaluation scores, including motorcycle model differences (Motorcycle A/ Motorcycle B) and different driving conditions (full load, partial load). This confirms the effectiveness of the index.

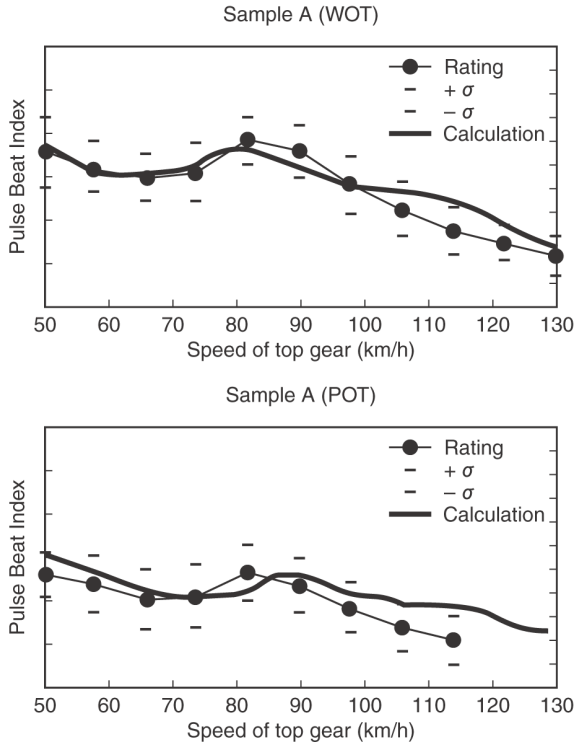


Fig. 9 "Pulse Beat Index" of sample A

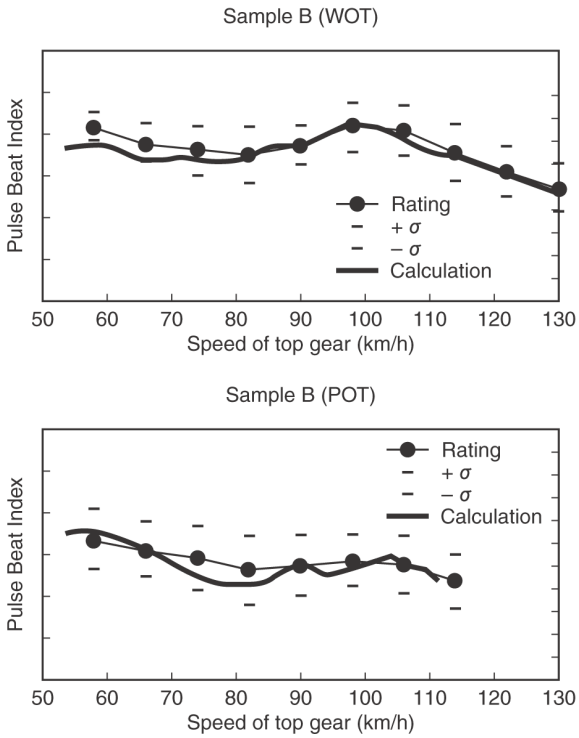


Fig. 10 "Pulse Beat Index" of sample B

3. Application of Time Domain Response Analysis

3.1. Overview of Analysis

A method of predicting vibration from the engine caused by the inertia force of reciprocating parts was established, and has become an effective development tool[4]. However, related to pulse, torque fluctuation components due to combustion are important. Therefore, it is not possible to reproduce this using conventional frequency response analysis, and it cannot be predicted at the design stage. Using mechanical analysis software (ADAMS), time domain response analysis[5] was carried out by integrating the Craig-Bampton model determined from the results of eigen value analysis and static rigidity analysis with the engine and drivetrain model. The correlation with the test data was then verified. Combustion pressure data determined from testing was used as input.

3.2. Analysis Procedure

Figure 11 shows the procedure for time domain response analysis.

3.3. Results of Analysis

3.3.1. Results of eigen value analysis model and frequency response calculations

In order to carry out time domain response analysis, a precise FE model of a completed motorcycle is necessary. Figure 12 shows the analysis model, and Fig. 13 gives the frequency response calculations. Figure 13 shows the results of frequency response calculations in the case when actual engine inertia force of reciprocating parts is added to the eigen value analysis results. The frequency analysis results are from an actual motorcycle. For modeling accuracy verification, a comparison in the motorcycle driving state is best, and as a time domain response analysis model, it is judged sufficiently accurate.



Fig. 12 Complete motorcycle FE model

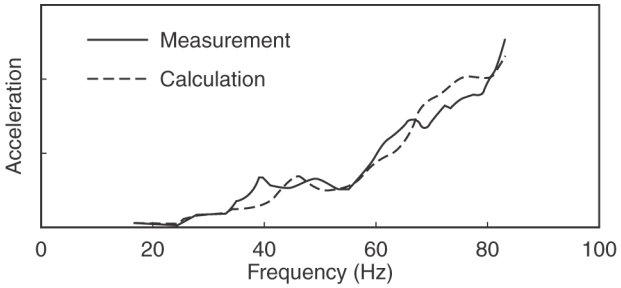


Fig. 13 Acceleration responses of complete motorcycle

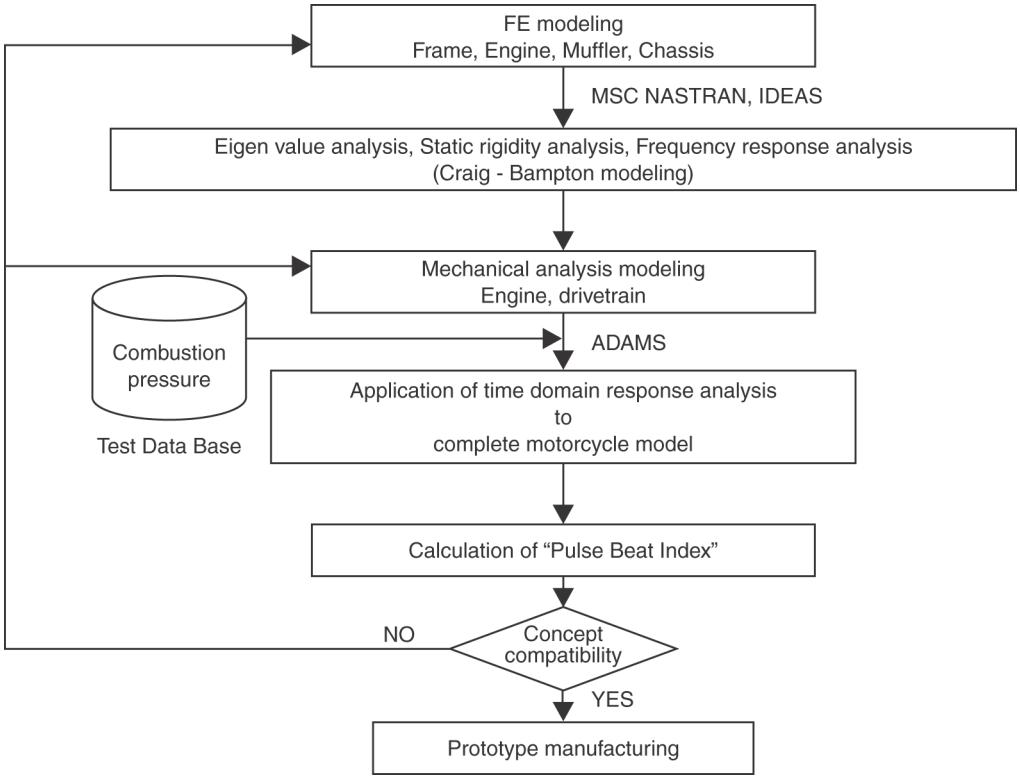


Fig. 11 Flowchart of time domain response analysis system

3.3.2. Time domain response analysis model

A mechanical analysis model was created, for the engine and drivetrain. Concerning the drive system, modeling was carried out of each detailed part, such as damper, drive shaft, etc. These models were combined with the Craig-Bampton model determined from the results of the eigen value and static rigidity analysis obtained in Section 3.3.1, creating a completed motorcycle model. Figure 14 shows the engine and drivetrain model, while Fig. 15 shows the time domain response analysis of the complete motorcycle.



Fig. 14 Engine drivetrain mode

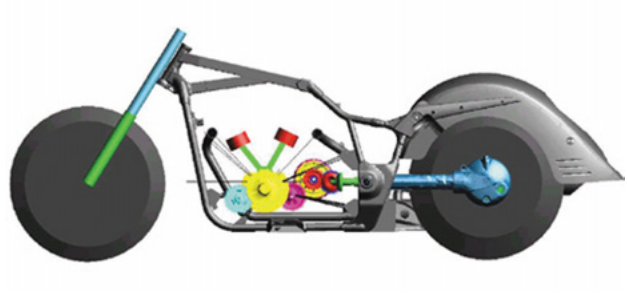


Fig. 15 Complete motorcycle time domain analysis model

3.3.3. Results of time domain response analysis

Figure 16 shows the input data (motorcycle combustion pressure), and Figs. 17 and 18 show the results of time domain response analysis and of frequency analysis. As shown in Figs. 17 and 18, there is a favorable correlation between time domain measurement data and calculation results. The same is true of frequency analysis results. From these results, "Pulse Beat Index" is determined, and it is possible to judge pulse intensity. This is effective as a pulse analysis tool. Figure 19 shows the changes in development procedure.

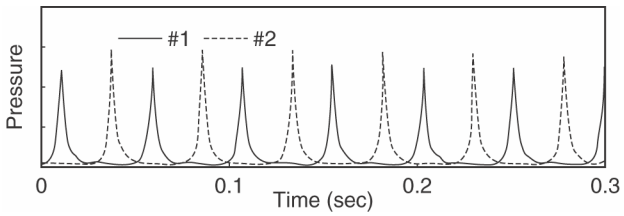


Fig. 16 Input data (Combustion pressure)

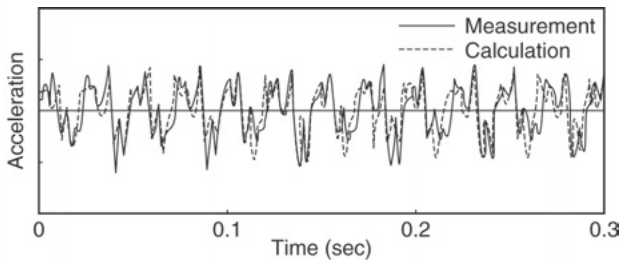


Fig. 17 Result of time domain response analysis

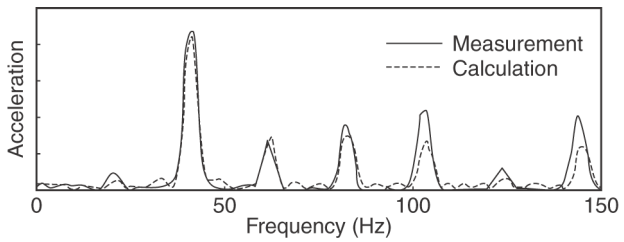


Fig. 18 Result of frequency response analysis

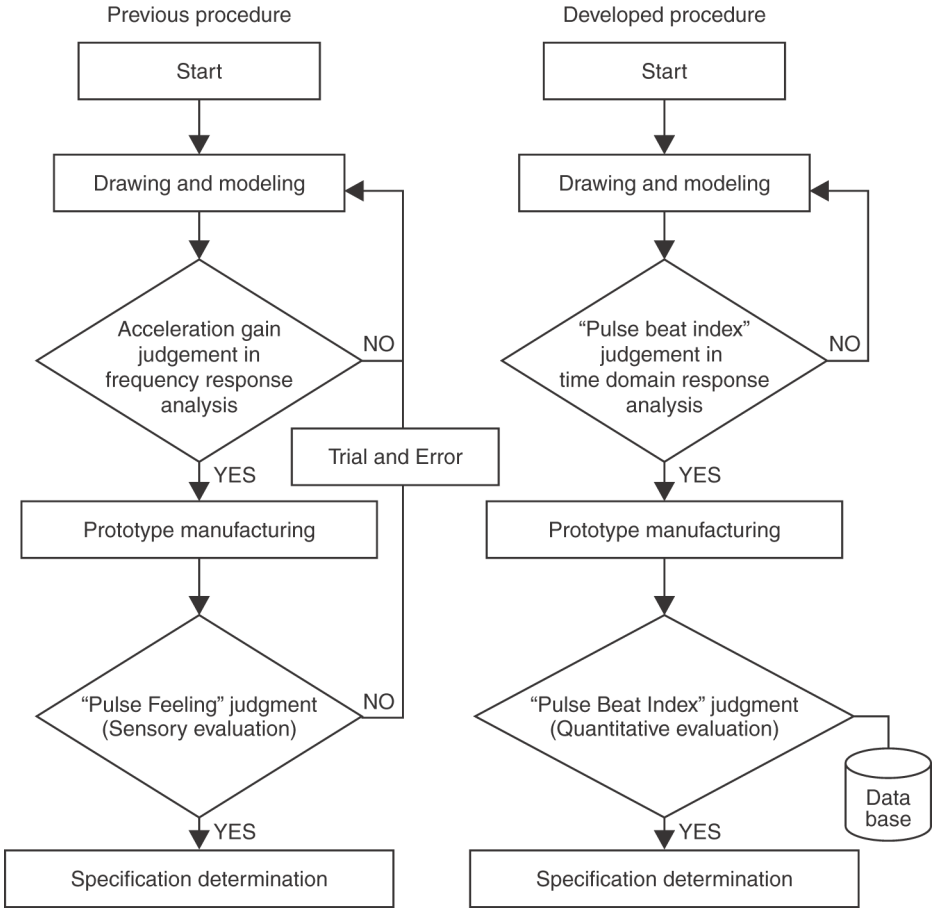


Fig. 19 Flowchart of development procedure

4. Conclusion

(1) Through the development of the "Pulse Beat Index", pulse feeling, which has conventionally been a qualitative evaluation, has now become a quantitative evaluation. This makes it easier to judge test motorcycles and confirm the effectiveness of countermeasures.
(2) Through time domain response analysis of the complete motorcycle, clarification was made of each part's contribution to pulse. It is now possible to predict "Pulse Beat Index" at the design stage. It was also possible to reduce test time and the time for determining specifications.

The focus of this project was quantification of pulse intensity, but there are some cases where "pulse quality" is an issue in the evaluation of pulse feeling. In the future, research will be carried out into how people perceive "pulse quality".

References

(1) ISO2631-1 Mechanical vibration and shock - Evaluation of human exposure to whole-body vibration - Part 1: General requirements (1997)

(2) Miwa, T.: Evaluation method for vibration effect, The National Institute of Industrial Health (1962)

(3) ISO13090-1 Mechanical vibration and shock - Guidance on safety aspects of tests and experiments with people - Part 1: Exposure to whole-body mechanical vibration and repeated shock (1998)

(4) Kuwahara, H., et al.: Virtual assessment of motorcycle vibrations, SETC 2001-01-1849

(5) Yamazaki, K., et al.: The development of a method for modeling ADAMS flexible body using residual vectors, MSC Software Solution Forum 2000

■ Authors ■



Kunihiro OSADA



Ryuta NIIMURA



Keikichi SHIMOKOBE



Goro YAMASAKI

Prediction of Fit Feeling of Motorcycle Seats Using Body Pressure Distribution Simulation

Toshinori NAKAMURA* Mitsue KOYANO* Takashi SUNAGA*

ABSTRACT

A measurement standard model of the buttocks shape was made. This model represented the average body pressure distribution of Japanese. The distribution data of Japanese, American, and European were measured and compared by using Buttocks Characteristic Index. The pressure body distributions for each category of motorcycle seats were measured using the measurement standard model of hip shape. Correlation between the measured distribution data and the fit feeling evaluation was analyzed. Based on the analysis, a prediction equation of fit feeling was devised. A simulation model of body pressure distribution was created using Finite Element Method. The simulation model was substituted for the measured distribution data in the prediction equation. A prediction method of fit feeling has been established. The established method has allowed early prediction of the fit feeling for motorcycle seats during the design stage.

1. Introduction

Motorcycle seat performance specifications can be broadly categorized as static seating comfort, dynamic ride comfort, and long-term fatigue level. In evaluating these performances, great differences may be evident, depending on the physique of the person carrying out the testing, especially their buttocks characteristics. Therefore, the authors have established a buttocks characteristic index, an index that expresses the differences in human buttocks characteristics, and have categorized people making the tests according to this index. In addition, a formula to predict static fit feeling was created, using the buttocks characteristic index and data concerning body pressure distribution when the test subject is seated[(1)]. However, human buttocks change over time, and so it is necessary to confirm the characteristics of buttocks periodically.

To create a method for predicting the fit feeling at the design stage, it is necessary find the correlation between seat design parameters (hardness, shape, material, etc.) and the fit feeling evaluation. In order to carry out this analysis, the focus was placed on body pressure distribution, which is a characteristic value between design parameters and fit feeling. Human body pressure distribution shows the results of design parameter changes, and is thought to be closely linked to fit feeling.

In order to create a standard model, data concerning the buttocks of people in various countries was collected. Simulations were carried out, and finite element models were created of the standard buttocks model and of the motorcycle seat. By determining body pressure distribution, trial predictions were made of fit feeling, at the design stage.

* Asaka R&D Center

2. Measurements of Buttocks Area Body Pressure Distribution

In order to create the standard buttocks model, body pressure distribution was measured when the subjects were seated on a reference seat (500 mm × 500 mm × 50 mm urethane). An example of these body pressure distribution measurements is given in Fig. 1. Measurements were made of men and women between the ages of 25 and 50 from various countries; Table 1 shows the number of sample and average age of subjects by country.

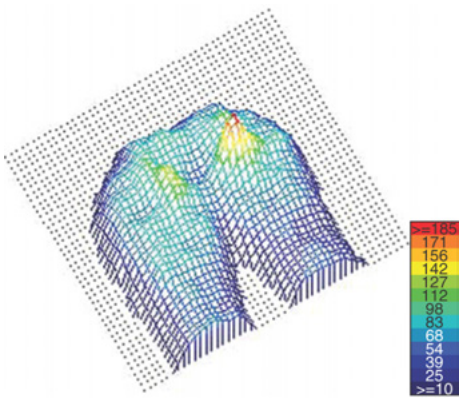


Fig. 1 Sample of measued body pressure distribution

Table 1 Sample number by country

	Number of sample		Average age	
	Males	Females	Males	Females
Japan	100	100	38.8	31.5
France	80	60	41.4	38.1
Italy	110	100	33.2	28
Germany	80	60	38.3	39.1
U.S.A	150	115	41.4	38.1

3. Establishing the Standard Model

3.1. Model Categorization

From the buttocks area body pressure distribution data, contact area was established as the parameter expressing the size of the buttocks area; contact surface pressure variation and kurtosis were established as the parameters expressing load on the buttocks, shape of the buttocks, and fleshiness. In order to bring out the buttocks characteristics for the men and women of each country, principal component analysis was implemented. The results are given in Tables 2, 3 and 4. As a result, the focus was placed on contact area, which has a high cumulative contribution and which is thought to express the size of the buttocks. Verification was made of average value difference of buttocks contact area. These results are shown in Table 5. There were four categories of models having a significant difference of 5% or more: the Japanese model, German Model, Italian and French model, and American model. Figure 2 shows their characteristic body pressure distribution.

Table 2 Results of principal component analysis (Eigen vector)

Variable name	Principal component 1	Principal component 2
Contact area	0.662	0.158
Total load	0.665	0.124
Variations of surface pressure	-0.1	0.938
Kurtosis	-0.331	0.282

Table 3 Results of principal component analysis (Eigen value)

	Eigen value	Contribution rate
Primary principal component	2.033	0.508
Second principal component	1.006	0.252

Table 4 Results of principal component analysis (Factor loading)

Variable name	Principal component 1	Principal component 2
Contact area	0.944	0.158
Total load	0.948	0.125
Variations of surface pressure	-0.142	0.941
Kurtosis	-0.473	0.283

Table 5 Verification results of difference of mean value

**1% significance
*5% significance

Males	US	Germany	France	Italy
Japan	**	**	**	**
U.S		**	**	**
Germany			———	———
France				———

Females	US	Germany	France	Italy
Japan	**	**	———	———
U.S		**	**	**
Germany			———	*
France				———

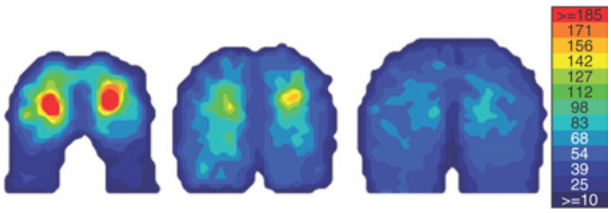


Fig. 2 Characteristics body pressure distribution

3.2. Buttocks Characteristics by Country

To confirm trend differences between countries, principal component analysis was carried out using all data for the four models. Figures 3 through 7 show the stratified distribution for each model. From the results of the principal component analysis in section 3.1, it was thought that the factor loading principal component 1 shown in Table 4 would express overall characteristics, representing size and that principal component 2 would express shape of the buttocks and its fleshiness. A characteristic of Japanese people's buttocks is that there is little variation in size, while there is large variation in shape and fleshiness of the buttocks.

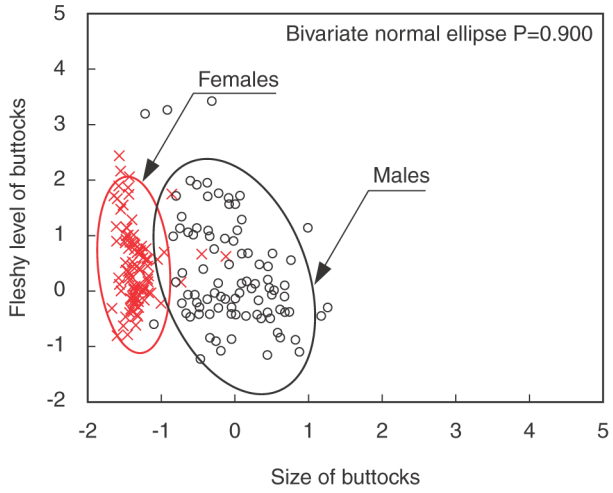


Fig. 3 Body pressure distribution of Japanese

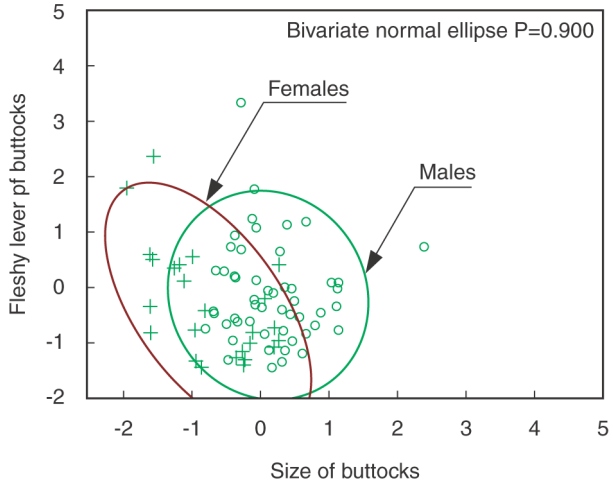


Fig. 4 Body pressure distribution of French

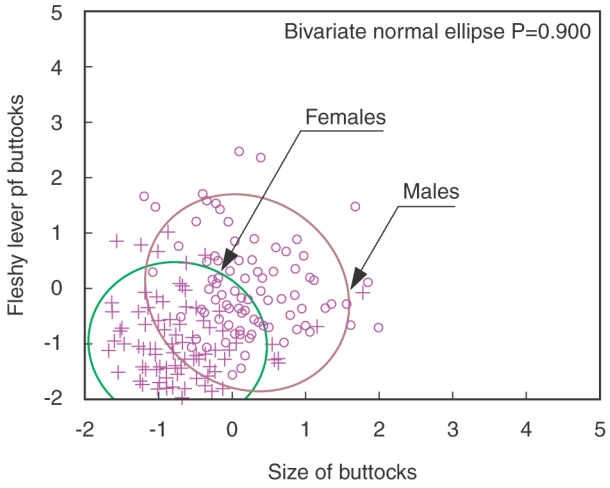


Fig. 5 Body pressure distribution of Italian

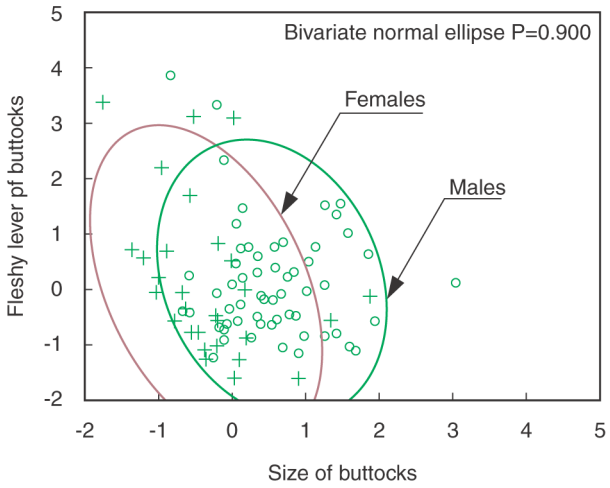


Fig. 6 Body pressure distribution of German

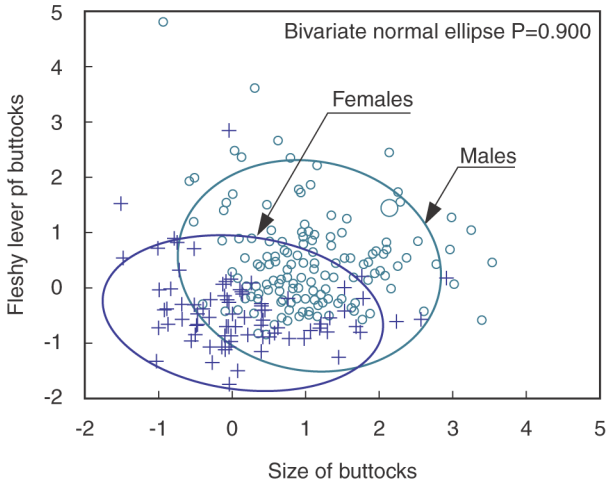


Fig. 7 Body pressure distribution of American

3.3. Creating a Standard Model for Measurements

From the fact described in section 3.2, the buttocks distribution and the average body pressure distribution are different by country, it is necessary to have a standard model for each country. In addition, because it cannot be said that the fit feeling evaluation is the same evaluation in each country, it is necessary to have a fit feeling prediction formula for each country. In this project, a model was created for standard measurement for an average Japanese male, in order to create a Japanese fit feeling prediction formula. Five test subjects were selected, close to the average of principal component 1 and principal component 2, as determined in section 3.2. Sizes of each part of their buttocks shown in Fig. 8 were compared with the average value, and the body pressure distribution closest to the average value shown in Fig. 9 was established as the target value for the standard measurement model. This model is shown in Fig. 10. It is composed of the pelvis and flesh. The hardness of the flesh was determined by measuring the buttocks hardness of ten Japanese males, selected at random, using a hardness gage.

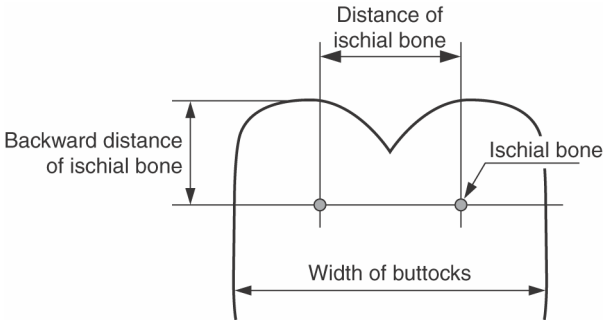


Fig. 8 Sizes of buttocks

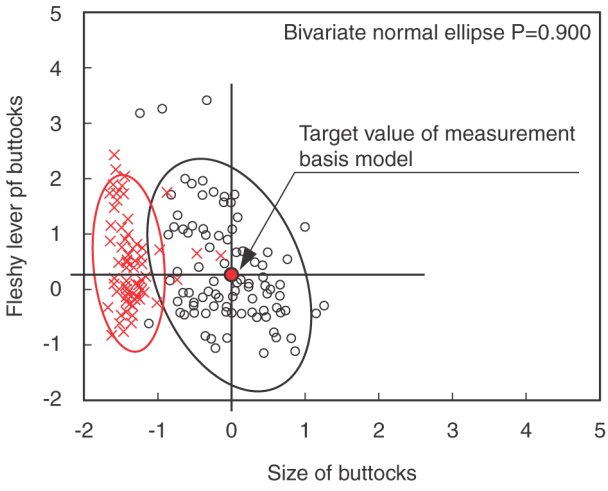


Fig. 9 Targeted value of measurement standard model

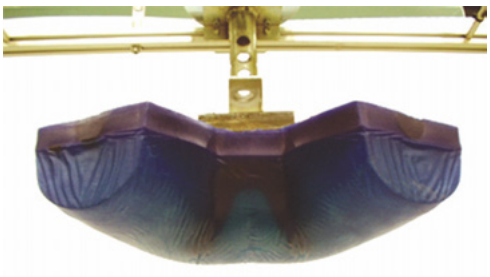


Fig. 10 Measurement standard model

Figure 11 shows the body pressure distribution of the test subjects when seated on the reference seat, and that of the standard measurement model. The contact area, the ischial bone peak value, distance of ischial bones, and backward distance of the ischial bone indicated by body pressure distribution are basically the same value.

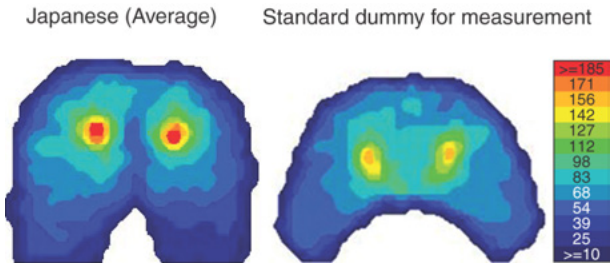


Fig. 11 Body pressure distribution at seated on reference seat

4. Formula to Predict Fit Feeling

4.1. Evaluation of Fit Feeling

The five test subjects, close to the average, determined in section 3.3 evaluated eight sample seats in different categories of motorcycle. They made a sensory evaluation of the fit feeling when in the static rider position, using the nine-point method as shown in Fig. 12. The results are given in Table 6. The sensory evaluation has a minimum score of 0.5 points, and from the analysis of variance shown in Table 7, variation of test subject scores were sufficiently small.

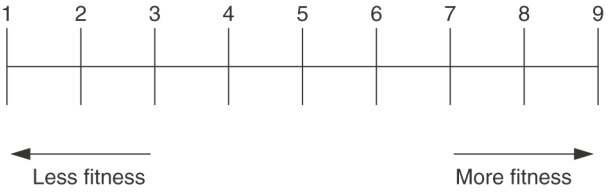


Fig. 12 Rating scale (Nine points method)

Table 6 Sensory evaluation results

Types of motorcycle	Score (Average)	Standard deviation
Touring	6.5	0.6
ATV	3	0.4
Large scooter	5.5	0.4
American	5	0.6
European “A”	3.75	0.6
European “B”	3.5	0.6
Small scooter	3	0.3
Off road	1.5	0.2

Table 7 Results of variance analysis

Factors	Sum of squares	Degree of freedom	Unbiased variance	Variance ratio	Verification
Test subject	3.78	4	0.94	2.29	
Sample	130.19	7	18.60	45.19	**
Error	11.53	28	0.41	–	
Summation	145.49	39	–	–	

**1% significance

4.2. Formula to Predict Fit Feeling

Using the standard measurement model, body pressure distribution for the eight sample seats were measured. Three body pressure distributions having different characteristics are shown in Fig. 13. The relationship between the results of the sensory evaluation in section 4.1 and the body pressure distribution data measured with the standard measurement model was subject to a multiple regression analysis, resulting in the fit feeling prediction formula (1). The relationship between the values predicted with this formula and the actual measurements is shown in Fig. 14. By substituting the measured values, it is now possible to predict fit feeling.

Fit Feeling = $\alpha_0 + \alpha_1 \times$ Contact Area $- \alpha_2 \times$ Ischial bone Peak Average (1)

α_0: Constant term

α_1: Contact area coefficient

α_2: Ischial bone peak average coefficient

($R^2 = 0.93$, Standard deviation of residual 0.4)

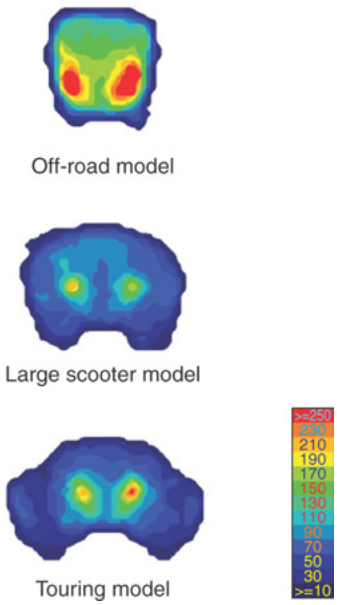


Fig. 13 Measured body pressure with measurement standard model

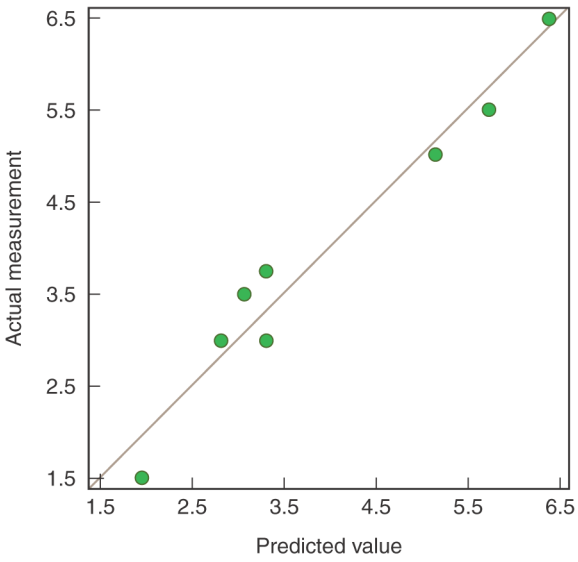


Fig. 14 Correlation between prediction score and sensory evaluation score

5. Creating a Body Pressure Distribution Simulation Method

The purpose of simulations is to make possible evaluations of the seat fit feeling at the design stage, thus enhancing the accuracy of the initial design. In order to make evaluations using the fit feeling prediction formula at the design stage, it is necessary to reproduce standard measurement model pressure distribution and contact area, at the same level as in the actual vehicle tests. As a method for actualizing this, a static implicit method that uses the finite element method was selected.

5.1. Analysis Software

In order to efficiently use the body pressure distribution simulation for standard measurement model, a general-purpose, nonlinear analysis software was selected, which serves the following functions.

- It must be able to accurately analyze the nonlinear characteristics of standard measurement model and seat contact area changes, major deformation of the buttocks, and material properties.
- Assuming an engineer with limited experience in analysis carries out this analysis as part of his/her routine work, it must have pre and post processor that makes possible easy creation of analysis data and processing of the necessary analysis results.

5.2. Mesh and Mesher Used

In this analysis, it is very important that contact and major deformation are able to be measured stably, and that the results obtained be the same as actual measurements. Considering this, the mesh consists of hexahedron elements. The mesher selected was one that can make highly accurate mesh, and for which one can freely specify the mesh size.

5.3. Analysis Model

In this analysis, the model is composed of the buttocks finite element model that can reproduce body pressure distribution equivalent to the standard measurement model, and the finite element model of the seat subject to analysis. To shorten the measurement period, half models were analyzed (Fig. 15).

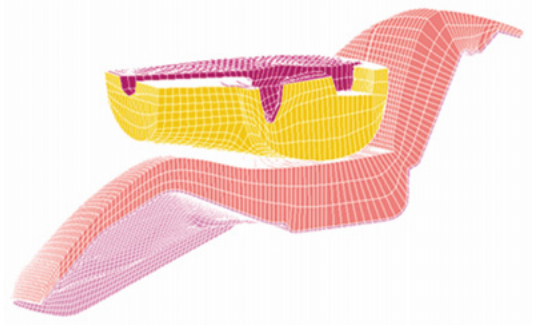


Fig. 15 Structure of analysis model

5.3.1. Buttocks finite element model

The pelvis and buttocks shape was made into 3D data through reverse engineering of the standard model shape, and the finite element model created (Fig. 16). This model is composed of muscle and fat, pelvis and thighbones. The detailed pelvis shape is reproduced using a surface. Deformation of the pelvis is not thought to be a large influence in this analysis, and was made rigid. The muscle and fat are given homogeneous characteristics, and the Mooney (binary format) Constitutive Material Law[(2)] was applied to the extremely soft elastomer. The Mooney energy function is estimated by simulating a tensile test of the material making up the standard model (Fig. 17).

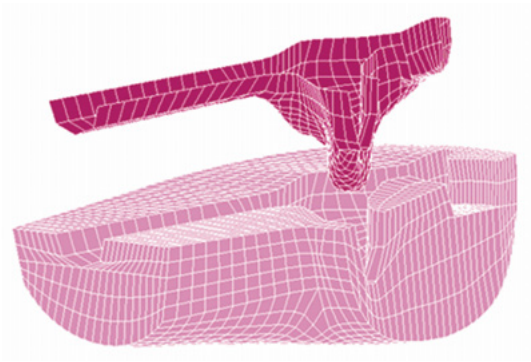


Fig. 16 FE model of buttocks

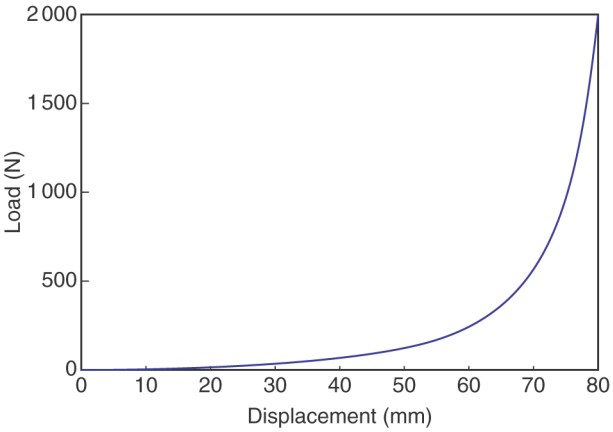


Fig. 17 Load-displacement charactoristic of Mooney

5.3.2. Seat finite element model

For external data, the 3D model created for use in design is used, and it is composed of urethane parts and plastic seat bottom (Fig. 18). The urethane parts are modeled from the form material. The required material constant was determined by measuring the "stress-strain curve", as shown in Fig. 19, in a single axis compression test. The seat bottom's material characteristics are obtained based on measuring the "stress-strain curve", as shown in Fig. 20, in the material tensile test using elastic-plastic material.

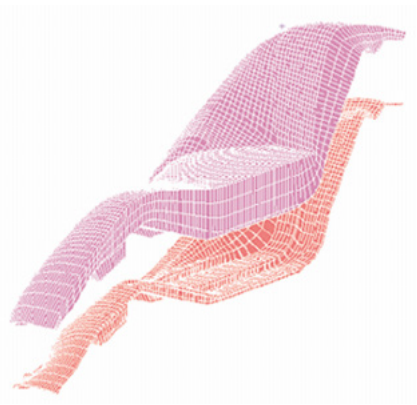


Fig. 18 FE model of seat

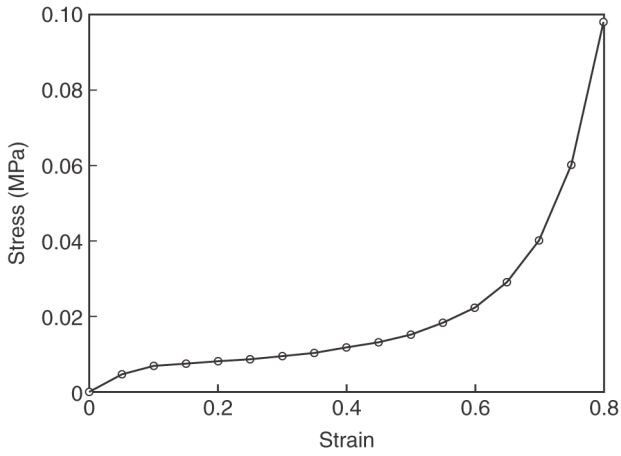


Fig. 19 Stress-strain curve of urethane

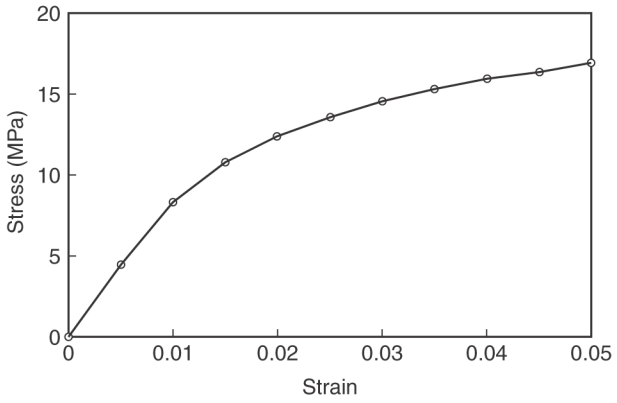


Fig. 20 Stress-strain curve of plastic

5.4. Analysis Results and Verification

5.4.1. Reference seat body pressure distribution simulation

The results of a simulation of sitting on the reference seat (500 mm × 500 mm × 50 mm urethane) confirmed that it is possible to reproduce well the standard measurement model contact surface shape and the pressure distribution (Fig. 21).

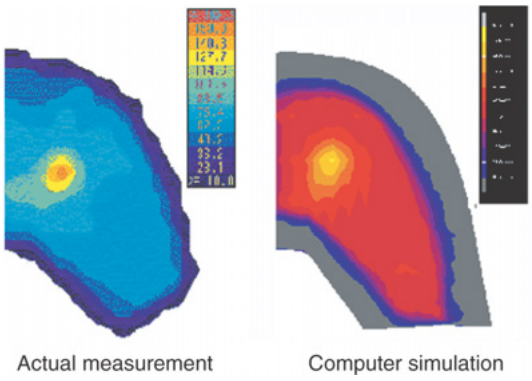


Fig. 21 Surface pressure distribution

5.4.2. Seat body pressure distribution simulation and fit feeling prediction

Simulations were carried out using motorcycle seats, with specifications that were changed in terms of urethane thickness, urethane hardness, and seat width. The results, as shown in Figs. 22, 23, and 24, confirmed a high correlation between simulated contact area, peak surface pressure, and fit feeling and the actual measurements of the above using the standard measurement model.

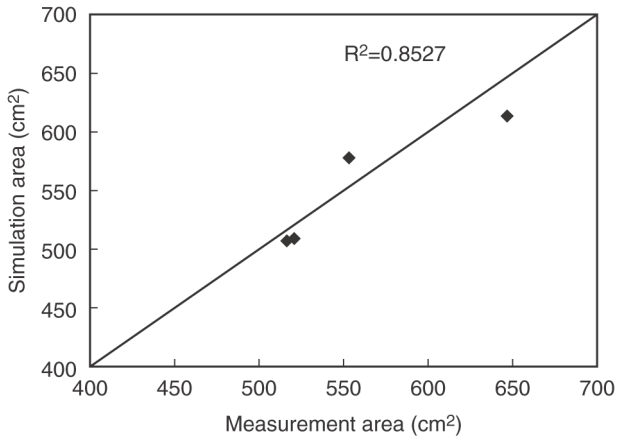


Fig. 22 Comparison of contact area between measurement and simulation

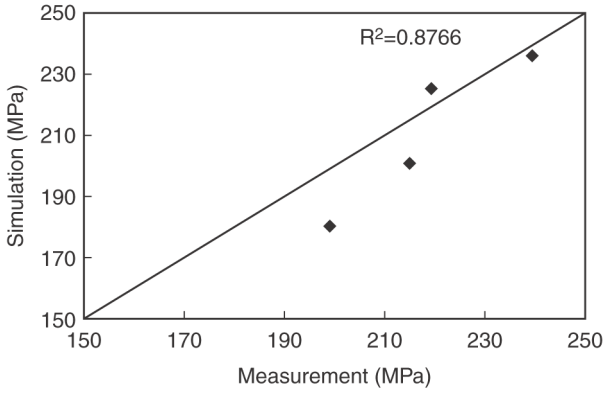


Fig. 23 Comparison of sarface pressure of ischial bone peak between measurement and simulation

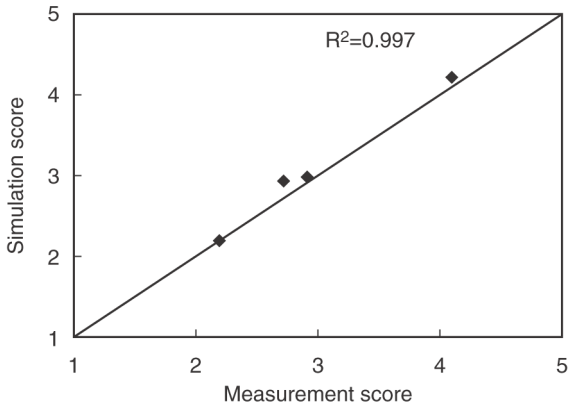


Fig. 24 Comparison of fitness feeling between measurement and simulation

6. Conclusion

(1) From data concerning body pressure distribution when seated on a reference seat, it was possible to categorize a Japanese, German, Italian, French, and American model using the average size for each area, and to clarify the characteristics.
(2) In order to accurately measure body pressure distribution data, a standard measurement model was created that is close to the average buttocks of Japanese males. Using the measurement data from this model, and the results of evaluation by average Japanese males, a fit feeling prediction formula was obtained.
(3) To use the fit feeling prediction formula as a tool in the design stage, a simulation was established that uses the finite element method, and it is now possible to predict fit feeling at the design stage.

References

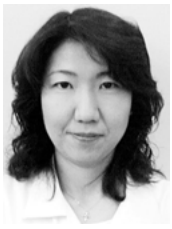
(1) Koyano. M., Nakayama, S., Kimishima, T.: Quantification of Static Seating Comfort of Motorcycle Seats, HONDA R&D Technical Review, Vol. 12, No. 2, p. 113-118

(2) Maekawa, Y., Kato, E., Kawasaki, R.: Virtual Human Who Estimates a Feeling of Seating by MARC 19th Users Conference, p. 189-193 (1998)

■ Authors ■



Toshinori NAKAMURA



Mitsue KOYANO



Takashi SUNAGA

Exploratory Study of Airbag for Large Scooter-type Motorcycle

Takeshi KUROE* Satoshi IIJIMA* Hideo NAMIKI*

ABSTRACT

The concept of Honda airbags for a large touring motorcycle is "to reduce the injuries to a rider when impacting with an opposing vehicle and/or opposing object in frontal collisions by absorbing rider kinetic energy and by reducing rider separation velocity from the motorcycle in the forward direction". In order to verify whether this concept is applicable to a large scooter-type motorcycle, an exploratory study was conducted. First, airbag positioning and supporting structure of the airbag was examined. Then, a prototype airbag system for a large scooter-type motorcycle was produced and tested by utilizing a part of ISO 13232: "Test and analysis procedures for research evaluation of rider crash protective devices fitted to motorcycles". As a result, it was recognized that an airbag with the same concept as a large touring motorcycle could also be applicable to a large scooter-type motorcycle.

1. Introduction

Honda began its research on motorcycle rider protection in the 1960s[1]. Recently, Honda has been researching the feasibility of reducing injuries with a motorcycle mounted airbag system as one of the alternative means of rider protection in the event of a frontal collision. The research results using the GL1500, a large touring motorcycle, was reported at the 16th ESV conference in 1998[2] and the 17th ESV conference in 2001[3]. In these previous investigations, the need for a feasibility study with other types of motorcycles was proposed.

In this research, a large scooter-type motorcycle (hereafter large scooter) was selected, and the applicability of an airbag was studied. Compared to the GL1500 large touring motorcycle, the large scooter had half the weight, step-through-type mainframe and smaller wheels. Using the airbag system established in the previous study with a large touring motorcycle, the preliminary study of an impact sensing system and the installation of an airbag considering a large scooter structure was conducted, and then a prototype large scooter with an airbag system was fabricated.

The basic evaluation criterion of this study was how much the airbag absorbed rider kinetic energy in the event of a frontal collision. Though the evaluation procedures of this study were based in part on ISO 13232: "Test and analysis procedures for research evaluation of rider crash protective devices fitted to motorcycles" [4], the evaluation concept was different from that of ISO 13232. The concept of ISO 13232 is to verify the injury reducing effects of a protective device by comparing the results of vehicles with and without rider protective devices. In this study, comparison tests of a large scooter with and without an airbag were not conducted. Also, test configurations that were not relevant to airbags in frontal collisions were not conducted.

The prototype large scooter was evaluated in four collision configurations. Three out of the four were selected from the seven test configurations provided by ISO 13232. The other one was developed by Honda.

In these previous investigations, the need for studies with other types of collisions was proposed. One of those studies

* Asaka R&D Center

was a collision configuration in which the front wheel does not hit the opposing subject first (hereafter called an under-ride collision).

This paper provides an outline of an airbag system for a large scooter and the results of the full-scale collision tests.

2. Investigation of Impact Sensing System

The impact sensing system on the large touring motorcycle used the acceleration data of the front fork near the front axle (hereafter front axle G). One issue for the large scooter was whether this same sensing system was also applicable to it. In order to establish a method to give a trigger signal for an airbag deployment, a series of tests, including circumstances in which the airbag must not deploy, were conducted, and the front axle G were recorded during these tests.

2.1. Collision Condition of "Must Deploy"

This airbag system for the large scooter is intended "To activate in the event of a frontal collision when the rider separates from the motorcycle in the forward direction". In order to investigate collision conditions to cause the forward separation of riders, actual collision tests were conducted. The 1998 to 2001 Japanese Model Honda Accord four-door sedan, was selected as the opposing vehicle. The major specifications are shown in Table 1. A Hybrid II AM50th percentile pedestrian type dummy was used.

Table 2 shows the test results. In the case of a collision against both the front and side of the opposing vehicle, the criteria for collision conditions were determined to be that the airbag "must deploy" at speeds of 30 km/h and higher.

Table 1 Opposing vehicle (Honda Accord) specifications

Length	(m)	4.635
Width	(m)	1.695
Height	(m)	1.420
Wheel base	(m)	2.665
Mass	(kg)	1 300
Displacement	(cm^3)	1 997

Table 2 Collision test results for operational setting

Impact conditions		Dummy motion	Deploy or not
Accord front	20 (km/h)	No separation from MC	Not necessary
	25 (km/h)	No separation from MC	Not necessary
	30 (km/h)	Just before separation from MC	Necessary
Accord side	25 (km/h)	No separation from MC	Not necessary
	30 (km/h)	Just before separation from MC	Necessary
	35 (km/h)	Separated from MC	Necessary

MC: Motorcycle

2.2. Collision Condition of "Must Not Deploy"

Except for special conditions in which continuing to ride is impossible, the airbag system "must not deploy" under defined road conditions such as rough road or irregularities during operation. In order to examine the effect of road impact on riding continuity and to monitor the front axle G data, the curb over ride test was conducted as shown in Fig. 1.

The wrists of the dummy were modified to be detached by specified tension in excess of that called for in ISO 13232 and were fixed on the handlebar grips.

The resulting dummy condition and driving continuity are shown in Table 3. The front axle G data was measured and collected. The conditions of the dummy and the motorcycle in this test are shown in Fig. 2. From the test results, when at least one hand remained on the handlebar, it was decided that riding can be continued and an airbag system "must not deploy."

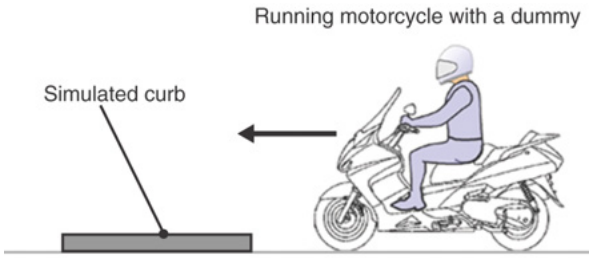


Fig. 1 Simulated curb ride over test

Table 3 Simulated curb ride over test results

Running condition	Dummy conditions /Continuous ride possibility	Deployment
A	No hands separation, possible	Not allowed
B	Single hand detached, critical	Not allowed
C	Hand detached, not possible	Allowed



Fig. 2 Motorcycle and dummy in simulated curb ride over test

2.3. Method to Determine the Operation Status

The logic of the method is "to start integration upon exceeding a certain acceleration value" and then "to activate air bag deployment when the integrated value reaches a given level (hereafter referred to as the threshold)". The certain acceleration value and the threshold were both examined using front axle G data from crash tests described in section 2.1, and curb ride over tests described in section 2.2. As a

result of the appropriate selection of the two values, the method to determine the operation status was obtained as shown in Fig. 3. Figure 4 shows the sensing decision flow.

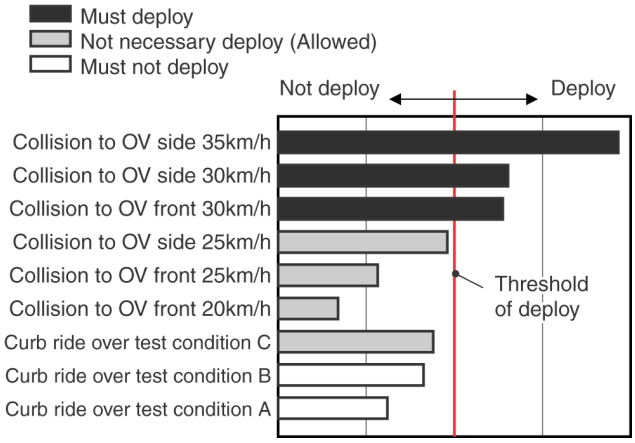


Fig. 3 Decision of deployment by integrated impact decelaration

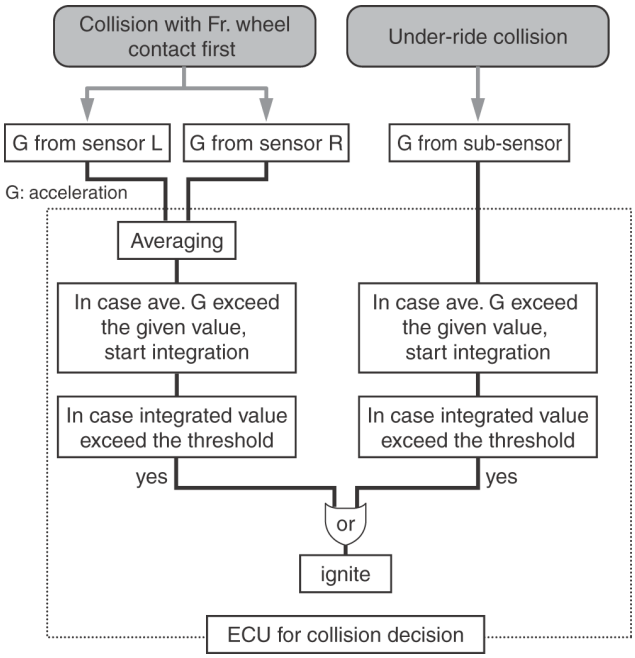


Fig. 4 Decision flow for deployment

3. Outline of a Large Scooter with a Prototype Airbag System

3.1. Overall Structure

Table 4 shows the specifications of a large scooter, a Silver Wing, which was selected as the test subject for this airbag feasibility study, and it has a different design from that of the large touring motorcycle, the GL1500. Figure 5 shows the large scooter with the prototype airbag.

Table 4 Large scooter (Silver Wing) specifications

Length	(m)	2.275
Width	(m)	0.070
Height	(m)	1.430
Wheel base	(m)	1.595
Mass	(kg)	224
Displacement	(cm^3)	582



Fig. 5 Large scooter with prototype airbag system

3.2. Airbag and Inflator

Knowledge gained from the study of an airbag for a large touring motorcycle was reflected in the prototype airbag specifications, such as the size of the airbag, the rear V-shaped airbag panel and the straps connecting the airbag to the frame. Figure 6 shows a prototype airbag system for a large scooter. The deployed volume of the airbag is approximately 150 liters. Deployment characteristics were verified through static deployment tests. This airbag needs about 40 msec to deploy. Airbag performance of rider kinetic energy absorption was proved to be equivalent to the airbag performance for a large touring motorcycle, GL1500, through sled tests.



Fig. 6 Prototype airbag system for large scooter

4. Full-scale Collision Tests

4.1. Test Procedure

The question "whether a similar airbag system that was mounted and studied on a large touring motorcycle can show the same kinetic energy absorbing performance for a large scooter" was evaluated through full-scale collision tests. The airbag system was evaluated in six collision configurations. Five were selected out of the seven collision configurations of full-scale tests provided by ISO 13232. A sixth was added by Honda. However, only four collision configuration tests were conducted, because the airbag effects in two collision configurations were estimated from the other test results as described in section 5.

Figure 7 shows the notation system of the collision configurations based on ISO 13232. Figure 8 shows the collision configurations for the evaluation. Here, a mark of "*" represents the ISO configuration, and a mark of "**" represents the Honda configuration, and a mark of "***" represents the configuration not tested. The collision speed (indicated by km/h) was set to be a little faster than indicated in ISO.

The ISO/CD 13232 (under discussion in ISO/TC22/SC22)-MATD (Motorcyclist Anthropometric Test Device) dummy was used for the full-scale collision tests. The 1998 to 2001 Japanese Model Honda Accord four-door sedan (shown in Table 1) was used as the opposing vehicle. Table 5 shows the measuring items on collision tests.

Table 5 Measuring items on collision tests

Head	Head maximum GAMBIT Head injury criterion (HIC)
Neck	Neck injury index (NII)
Chest	Sternum maximum normalized compression (C) Sternum maximum velocity-compression (VC)
Abdomen	Abdomen maximum residual penetration (pA)
Lower extremities	Damage of frangible component of lower extremities (IE)

4.2. Results of Full-scale Collision Tests

4.2.1. Determination of impact sensing system

Figure 9 shows the results of the impact sensing system for the four configurations of full-scale tests. In this figure, TTF (Time to fire) represents the time between the first contact of the large scooter and the opposing vehicle and the time of collision determination by the sensing system, deployment time represents the time for the airbag deploying, and rider encounter time represents the time between the first contact and the rider reaching the deployed airbag. In all four configurations, the airbag was fully deployed before the dummy reached the deployed airbag surface area.

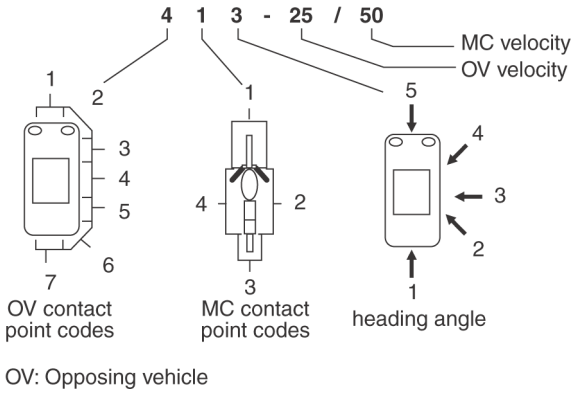


Fig. 7 Indication of impact configuration (ISO13232)

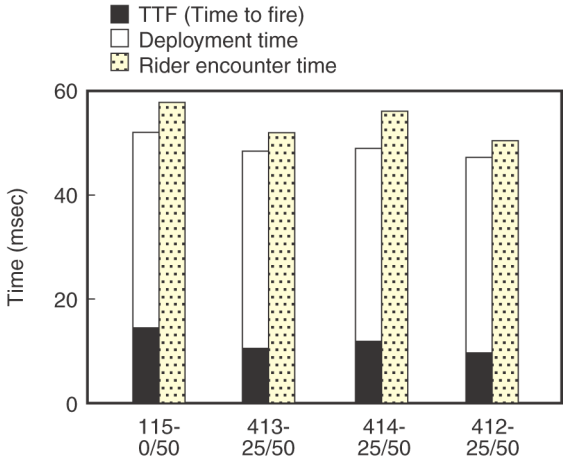


Fig. 9 Comparison of airbag deployment time and rider encounter time

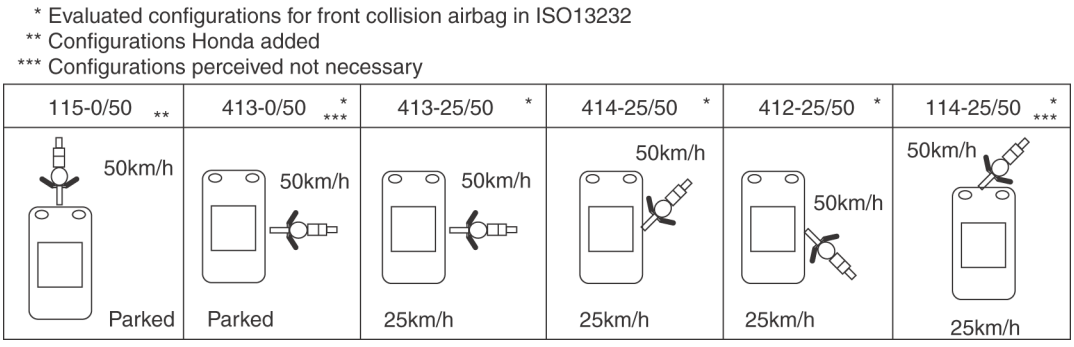


Fig. 8 Impact configurations for evaluation

4.2.2. Injury evaluation for each collision configuration

In the full-scale collision tests, the injury assessment values shown in Table 5 were evaluated using MATD dummy and injury evaluations defined in ISO/CD 13232.

Figure 10 shows the injury evaluation of each relevant area obtained from measured data of the dummy for the four test configurations. The primary impact injury in the figure represents the maximum injury value within 500 msec from the beginning of the collision. The secondary impact injury represents the maximum injury value after 500 msec, which most likely is the dummy's contact with the ground.

Figure 11 shows the condition of the large scooter and the dummy in the [115-0/50]-collision configuration. In this configuration, even though the motorcycle showed a significant vertical pitching motion, the airbag absorbed the kinetic energy of the dummy without forward separation. The primary impact injuries show that HIC = 15.4, GAMBIT = 0.08 and Chest deflection = 25 mm. Serious injury values were not observed.

Figure 12 shows the motion of the large scooter and the dummy in the [413-25/50]- collision configuration. Although the large scooter showed yawing motion after the initial impact, the airbag absorbed the kinetic energy of the dummy and prevented the contact of the dummy with the opposing vehicle. The primary impact injuries show that HIC = 28, GAMBIT = 0.1 and Chest deflection = 15 mm. Serious injury values were not observed.

Figure 13 shows the motion of the large scooter and the dummy in the [414-25/50]-collision configuration. The large scooter showed yawing motion after the collision. The different direction of movement of the dummy and the large scooter decreased the absorbing effect of the airbag. The dummy separated from the large scooter scraping the C-pillar of the opposing vehicle and contacted the ground. The primary impact injury caused by the impact between the dummy's head and the opposing vehicle showed that HIC =



Fig. 11 Dummy and motorcycle in configuration [115-0/50]

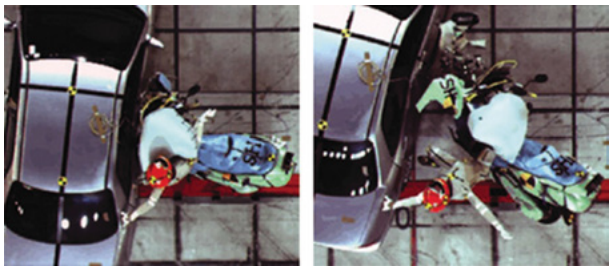


Fig. 12 Dummy and motorcycle in configuration [413-25/50]

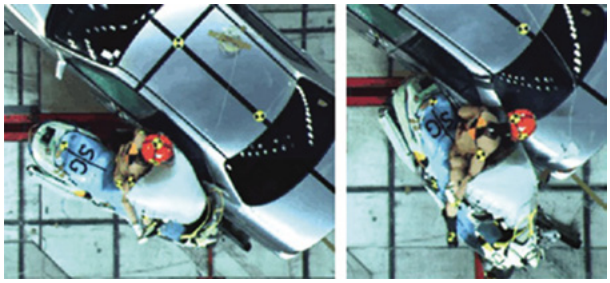


Fig. 13 Dummy and motorcycle in configuration [414-25/50]

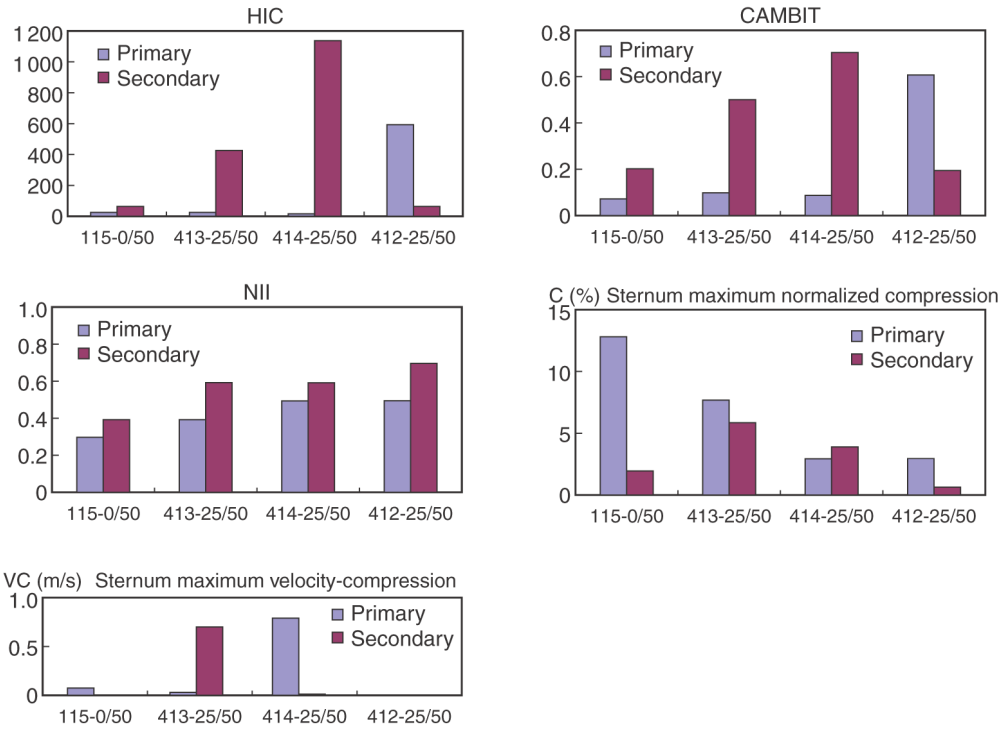


Fig. 10 Measured dummy injuries in collision tests

14 and GAMBIT = 0.09. Serious injury values were not observed. But for the secondary impact sequence, significant dummy injury was caused by ground impact, and injury evaluation values of HIC = 1138 and GAMBIT = 0.73 were observed. It was important to investigate whether or not the airbag contributed to these serious injury values. As shown in Fig. 14, the scenario of this serious injury was different from the harmful phenomenon of the head's first contact with the ground in the previous investigation by Iijima et al (1998) for the large touring motorcycle.

Figure 15 shows the motion of the large scooter and the dummy in the [412-25/50]-collision configuration. The large scooter started yawing just after the collision. The large scooter and the dummy moved in different directions. The dummy barely contacted the airbag and the dummy's head contacted the roof-edge of the opposing vehicle. But injury evaluation value showed that HIC = 600 and GAMBIT = 0.6, so the injury likelihood was low. It was determined the airbag did not contribute to the serious injury measured during the ground contact.



Fig. 14 Dummy contact ground in configuration [414-25/50]

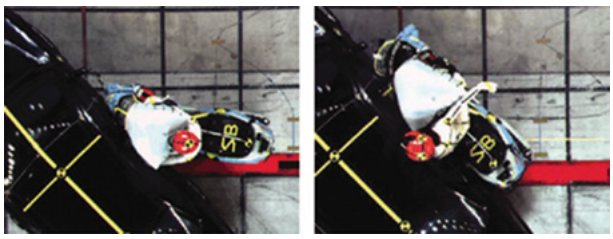


Fig. 15 Dummy and motorcycle in configuration [412-25/50]

Except for the case of ground impact in [414-25/50]-collision configuration, serious injury values were not measured in the four test configurations throughout all measured events including contact with the airbag, contact with the opposing vehicle and contact with the ground.

5. Rider Kinetic Energy Absorbing Performance of Airbag

The energy absorbing performance of the airbag was evaluated under the concept of the following goal:

" To reduce the injuries to a rider when impacting with an opposing vehicle and/ or opposing object in frontal collisions by absorbing rider kinetic energy and by reducing rider separation velocity from the large scooter in the forward direction".

From this viewpoint, the energy absorbing effect was evaluated in six collision configurations. Five were configurations of frontal collision specified in ISO 13232. The remaining configuration was uniquely examined by Honda. The effects of the airbag were classified as follows:

- Effective: The airbag effectively absorbs the kinetic energy of the dummy's upper body so that contact against the opposing vehicle does not occur.
- Slightly effective: The airbag absorbs some kinetic energy of the dummy's upper body so that only some contact against the opposing vehicle occurs.
- Not effective: The airbag does not absorb any kinetic energy of the dummy's upper body such that contact against the opposing vehicle occurs without sufficient impact reduction.

The energy absorption performance was decided from measured chest deflection data and the degree of contact between the dummy and the airbag observed in video review. The occurrence of contact of the dummy's upper body against the opposing vehicle was judged by contact marks, video review and the recorded acceleration of the dummy's head.

Table 6 shows the result. The full-scale collision test of [413-0/50] and [114-25/50] were not conducted and the absorption performance of the airbag was estimated by the following logic.

The yawing motion of the motorcycle affected the absorbing energy performance of the air bag. Greater yaw-motion caused lower absorbing performance of the airbag. As shown in Fig. 16, the magnitude of the yawing motion of a large touring motorcycle during the effective time period of airbag energy absorption in 6 configurations were ranked as [115-0/48] (=) [413-0/48] < [413-24/48] < [414-24/48] < [412-24/48] < [114-24/48].

Also as shown in Fig. 17, the magnitude of yawing motions of a large scooter were ranked as [413-25/50] < [414-25/50] < [412-25/50]. So in these three configurations,

Table 6 Rider kinetic energy absorbing effectiveness of airbag

	115-0/50	413-0/50	413-25/50	414-25/50	412-25/50	114-25/50
Large scooter (Silver Wing)	Effective	Effective*	Effective	Slightly effective	Not effective	Not effective*
Large motorcycle (GL1500)	Effective	Effective	Effective	Effective	Effective	Slightly effective

* Estimated result

the yawing trend of a large scooter is the same as a large touring motorcycle. From these results, it can be concluded that both motorcycle types had the same trend of yaw motion in the six collision configurations used for evaluation. Therefore in the collision of a large scooter, it was determined to be reasonable that the yawing motion of [413-0/50], which was not tested, should be smaller than that of [413-25/50], and the yawing motion of [114-25/50], which was also not tested, should be larger than that of [412-25/50]. Therefore, [413-0/50] with smaller yawing than [413-25/50] was expected to show a larger absorbing effect than [413-25/50]. That meant "Effective" because the judgment of [413-25/50] was "Effective." In the same way, [114-25/50], in which yawing is larger than [412-25/50], was expected to be "Not effective" because [412-25/50] was "Not effective."

As shown in Table 6, the airbag on a large scooter scored 3 "Effective" configurations, 1 "Slightly effective" configuration and 2 "Not effective" configurations out of the 6 collision configurations. On the other hand, a large touring motorcycle scored 5 "Effective" configurations, 1 "Slightly effective" configuration and zero "Not effective" configurations. Although the airbag energy absorbing effect for a large scooter was limited and smaller compared to that of a large touring motorcycle, the concept to absorb rider kinetic energy and to reduce rider separation velocity with an airbag attached to a motorcycle was observed to potentially be applicable to a large scooter.

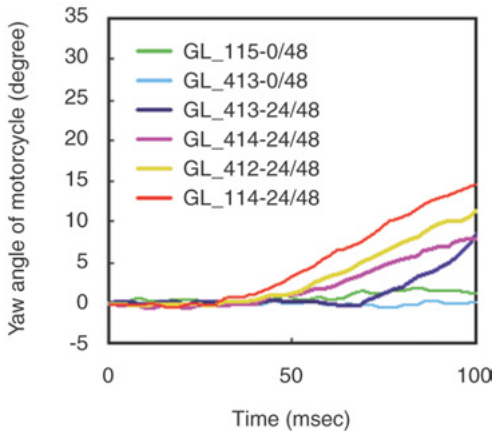


Fig. 16 Yaw motion of large touring motorcycle

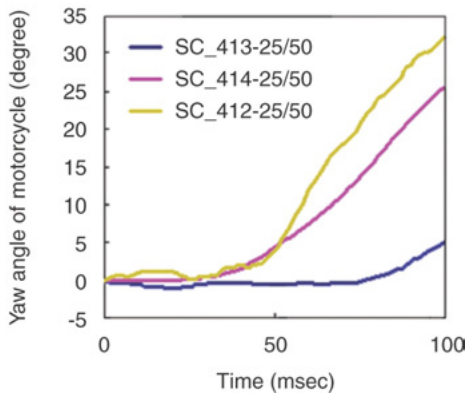


Fig. 17 Yaw motion of large scooter

6. Examination of Under-ride Collision

A collision pattern where the front wheel does not collide first (hereafter under-ride collision) is a potential collision scenario. This pattern occurs, for example, when a large scooter collides with a truck trailer. In this collision, the space between the rider and the opposing object surface (hereafter rider protective space) can be too small for the timing to begin deployment by the impact sensing system using front axle G. As shown in Fig. 18, the following three events are evaluated to be the cause of this:

(1) The front upper portion of the large scooter behind the front end of the front wheel collides first. So the rider protective space becomes smaller than that of the direct front wheel collision.
(2) The collision impact is transmitted from the impacted front upper portion to the front axle via the mainframe and the steering system structure affecting the timing of deployment.
(3) The large scooter has a step-though-type mainframe that results in greater bending due to external front forces as compared with conventional motorcycles.

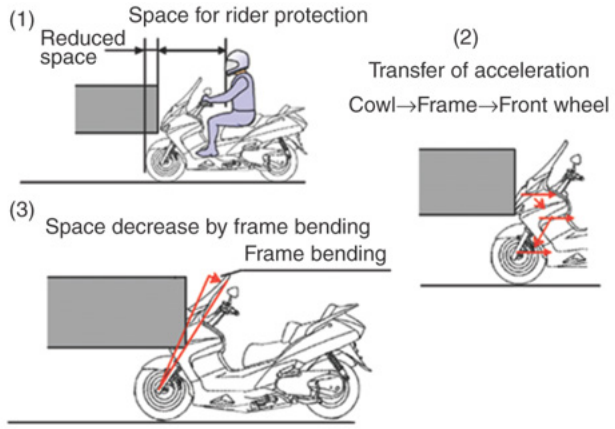


Fig. 18 Cause of protection space reduction in under-ride collision

6.1. Verification of Characteristics of a Baseline Scooter

Tests for the under-ride collision were carried out with a baseline scooter. The tested scooter collided with a stationary trolley that applied the parking brake at 50 km/h. The sensing system timing, the motion of the scooter and the dummy were recorded. The trolley used is shown in Fig. 19. A Hybrid Ⅱ AM50th percentile pedestrian type dummy was used.

Figure 20 shows the conditions of the dummy and the tested scooter at the beginning of the collision (t = 0 msec); the completion point of the collision determination by the sensing system (23 msec); the theoretical completion of the airbag deployment (63 msec), and the dummy contacting with the surface of the opposing object (82 msec).

These results show that the impact sensing system that

was used from the study of an airbag system for a large touring motorcycle did not adequately function for the large scooter. Thus, additional research was required.

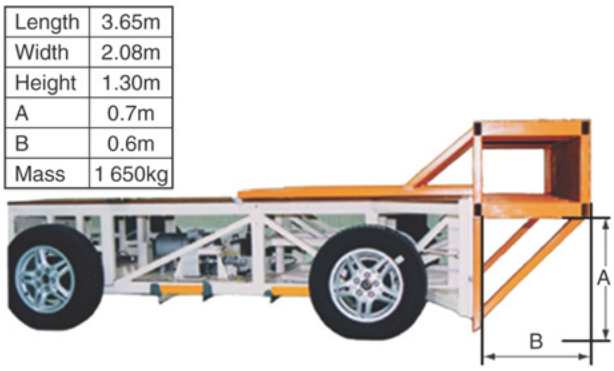


Fig. 19 Opposing trolley used in under-ride collision test

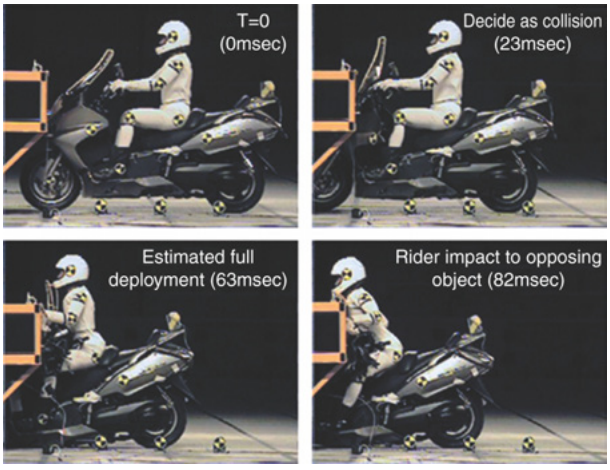


Fig. 20 Dummy and motorcycle in under-ride collision without airbag

6.2. Conceivable Methods for Further Development

The following three methods and their combinations were proposed for further development of the air bag system.

(1) To strengthen the front upper frame member against a collision. This would help reduce the loss of the rider's protective space and simultaneously increase the impact acceleration of the scooter body and front axle. This would lead to a quicker determination for deployment.

(2) To install an additional sensor on the front upper portion of the scooter body in order to advance the deployment determination timing.

(3) To strengthen the mainframe in order to help prevent the reduction of the rider protective space due to mainframe bending.

Those elements were examined by utilizing computer simulation.

6.3. Examination of Improvement Methods by Computer Simulation

Honda had proposed a need for computer simulation technology to estimate injury level of the dummy, prior to ground contact. That was presented in "Exploratory Study of Airbag Concept for a large Touring Motorcycle" unveiled at the 16th ESV Meeting in 1998[2]. As unveiled at the SETC conference in 2003[5], Honda introduced computer simulation technology that allowed for the precise estimation of the dummy's motion in the event of a collision. By using this technology, the proposed elements were examined.

First, the above mentioned under-ride collision with the baseline scooter was simulated by computer. Figures 21 and 22 show the comparison of vehicle deformation and mainframe acceleration between an actual test and a simulation.

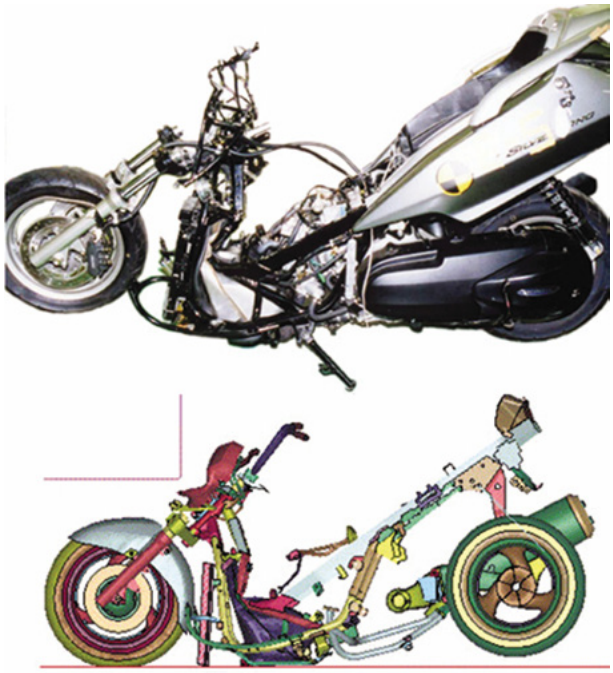


Fig. 21 Comparison of frame damage result between full scale test (FST) and computer simulation (CS)

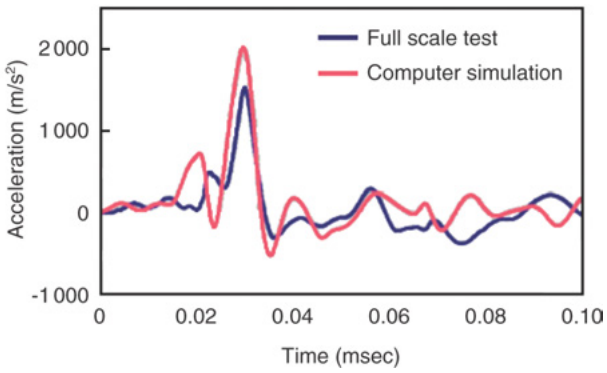


Fig. 22 Comparison of acceleration on frame between full scale test (FST) and computer simulation (CS)

6.4. Examination Result of Improvement Elements by Computer Simulation

The investigation with computer simulation provided output including the collision determination timing of the sensing system, rider protective space, and injury level of the rider's head, chest and so on with a deployed airbag. Through the examination of outputs, two practical countermeasures were proposed to achieve rider protection. One was to strengthen the cowl stay and the other was to attach a sub-sensor on the cowl stay. Figure 23 shows the modifications. Figure 24 shows the simulation results for the modified model. The determination flow for airbag deployment by the sensing system with the added sub-sensor is shown in Fig. 4.

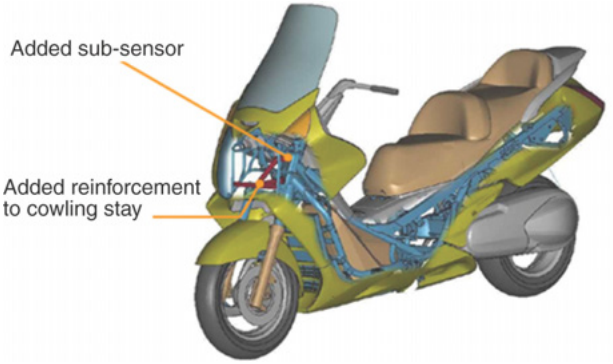


Fig. 23 Modification for under-ride collision analyzed by computer simulation

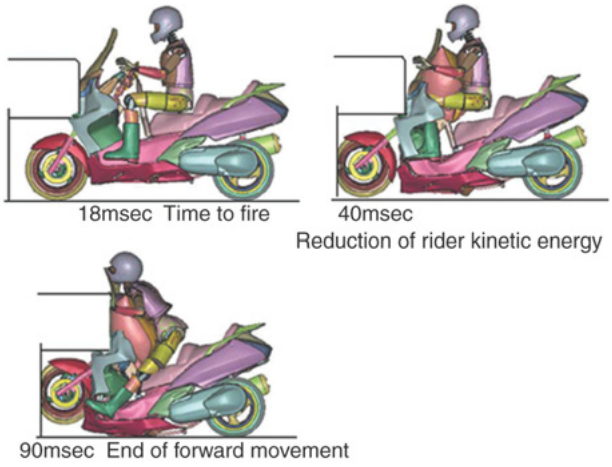


Fig. 24 Dummy and motorcycle movement with modification

6.5. Results of Under-ride Collision Test of Modified System for Large Scooter

The large scooter under-ride test was conducted with the modified airbag system. A Hybrid III AM50th percentile pedestrian type dummy was used and the measurement of the injury data as described in Table 7. Other test conditions were the same as the baseline scooter under-ride collision test mentioned at section 6.1.

The results were as follows.

Decision for deployment was made by the signal of the sub-sensor that came earlier than the signal of the main-sensor.

As shown in Fig. 25, the dummy encountered the airbag still deploying in this configuration. The primary impact injuries show that HIC = 221, neck tension = 45 Nm and chest deflection = 56 mm. Serious injury values were not observed.

It was confirmed that the airbag for a large scooter can maintain its protective capability for riders in an under ride collision.

Table 7 Measuring items on under-ride collision test

Head	Head injury criterion (HIC)
Neck	Tension, compression, flexion, extension
Chest	Chest deflection

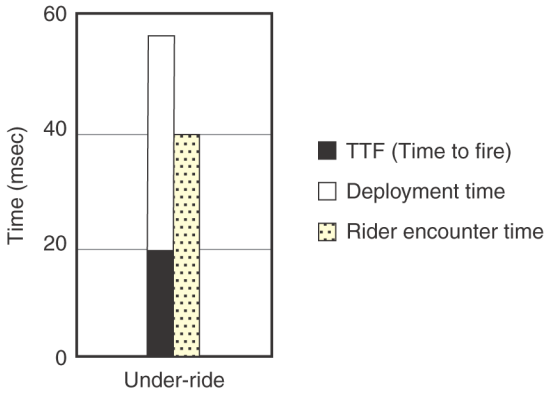


Fig. 25 Comparison of airbag deployment time and rider encounter time in under-ride condition

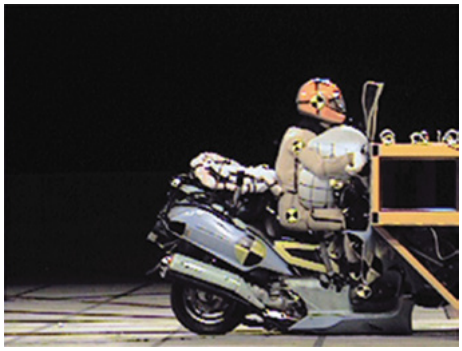


Fig. 26 Dummy and motorcycle in under-ride collision configuration

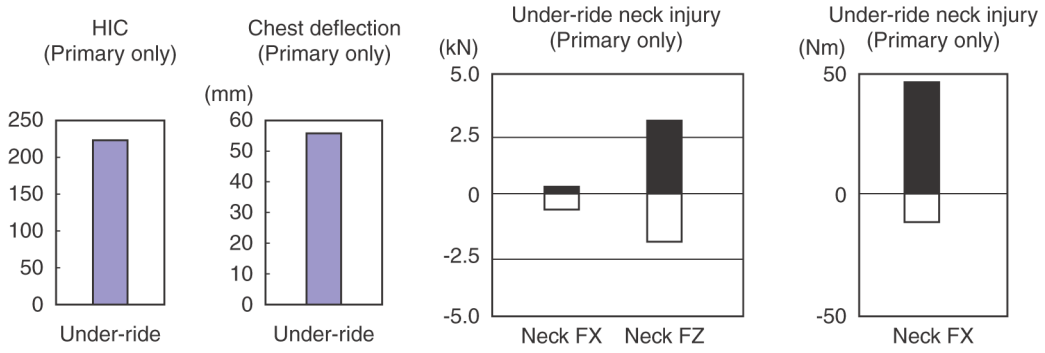


Fig. 27 Measured dummy injuries in under-ride collisions

7. Conclusion

(1) By detecting and calculating the impact acceleration of the front fork near the front axle, a large scooter sensing system:
- could properly determine operation status representing collision/ non collision conditions, and
- could properly deploy the airbag before the rider has reached the deployed area in four cases of collision configuration with an Accord at the speed of 50 km/h.

(2) Although the absorption performance of an airbag system fitted to a large scooter was limited to fewer collision configurations as compared to the large touring motorcycle, the concept of absorbing rider kinetic energy and reducing rider separation velocity with an airbag might be feasible for a large scooter.

(3) For an under-ride collision, the air bag for a large scooter might maintain a protective effect for riders if the large scooter has a sub-sensor on the front upper portion and a main sensor at the front fork near the front axle.

(4) Computer simulation proved to be effective for the examination of the crash characteristics of the motorcycle and for the investigation of modifications to the sensing system.

8. Future Issues

It has been proven through this study that an airbag may be effective when applied to a large scooter. Additional research needs to be done. The following items are listed as future issues: verification of applicability to other types of motorcycles; verification of effectiveness with different postures or sizes of a rider; risk-benefit analysis based on full-scale collision tests defined by ISO/CD 13232; and, injury evaluation until the rider contacts the ground through the use of computer simulation.

References

(1) Inoue, T., et al.: Experimental Collision Test on Motorcycles with Passenger Cars, JSAE, October 1969

(2) Iijima, S., et al.: Exploratory Study of an airbag Concept for a Large Touring Motorcycle, Sixteenth International Technical Conference on the Enhanced Safety of Vehicles, Paper No. 98-S10-O-14 (1998)

(3) Yamazaki, T., et al.: Exploratory Study of an airbag Concept for a Large Touring Motorcycle: Further Research, Seventeenth International Technical Conference on the Enhanced Safety of Vehicles, Paper No. 01-S9-O-240 (2001)

(4) International Standard ISO 13232: 1996(E), Motorcycles-Test and analysis procedures for research evaluation of rider crash protective devices fitted to motorcycles, Parts 1 to 8, International Standards Organization, Geneva, December 1996

(5) Namiki, H., et al.: A Computer Simulation for Motorcycle Rider-Motion in Collision, Small Engine Technology Conference, Paper 2003-32-0044 (2003)

■ Authors ■


Takeshi KUROE


Satoshi IIJIMA


Hideo NAMIKI

Technical Papers Submitted to Out-of-company: January, 2004 to June, 2004

(English Papers only)

Date	Conference	Title	Author	Organization
2004.1.1	JSAE/JSAE Review Vol.25, No.1	Advanced Technology for Pedestrian Protection	Masayoshi Okamoto Akihiko Akiyama	Tochigi R&D Center Tochigi R&D Center
2004.1.5-8	AIAA (The American Institute of Aeronautics and Astronautics)/42nd AIAA Aerospace Sciences Meeting and Exhibit (Reno, USA)	Simulation of Aircraft Wake Vortex Using Pressure-based Unified Numerical Approach for Incompressible and Compressible Flows	Yoshihiro Yamaguchi Toshiyuki Arima Shigeru Obayashi Kazuhiro Nakahashi	Wako Research Center Wako Research Center Tohoku University Tohoku University
2004.1.28	IIR (Institute for International Research) /AutoTech technology congress 2004 (BadenBaden, Germany)	Development of Collision Mitigation Brake System	Kenji Kodaka Jens Gayko	Tochigi R&D Center Honda R&D Europe (Deutschland) GmbH
2004.1.28-29	SAE/TOPTEC (San Diego, USA)	A Technical Description for Motor Assisted Hybrid Vehicle	Kunio Hasegawa	Tochigi R&D Center
2004.1.31	AIAA(The American Institute of Aeronautics and Astronautics)/Journal of Propulsion and Power Vol.20, No.1	Approach to High-performance Transonic Compressor Design	Mineyasu Oana Osamu Kawamoto Hideo Ohtani Yoshifumi Yamamoto	Wako Research Center Wako Research Center Wako Research Center Wako Research Center
2004.3.8-11	SAE/2004 SAE World Congress (Detroit, USA)	Development of Fuel Economy Measurement Method for Fuel Cell Vehicle	Satoshi Aoyagi Takuya Shirasaka Osamu Sukagawa Naoki Yoshizawa	Wako Research Center Wako Research Center Honda Motor Co.,Ltd. Honda Motor Co.,Ltd.
		Application Studies of Electric Double Layer Capacitor System for Fuel Cell Vehicle	Akihiro Anekawa Koji Tamenori Shinji Kato Koichi Yamamoto Naohiko Oki Minoru Noguchi	Wako Research Center Wako Research Center Wako Research Center Wako Research Center Wako Research Center Wako Research Center
		Development of Traction Motor for Fuel Cell Vehicle	Hiroyuki Sato Shigemitsu Akutsu Tomoya Miyamura Hiroaki Shinoki	Tochigi R&D Center Tochigi R&D Center Tochigi R&D Center Tochigi R&D Center
		Electric Power Control System for a Fuel Cell Vehicle Employing Electric Double-layer Capacitor	Hidekazu Takenaka Akira Ohkawa	Tochigi R&D Center Tochigi R&D Center
		Method of Heat Reduction for Vehicle Traction Motor Inverter Locked at Standstill on a Climbing Slope	Hiroaki Takanohashi Satoru Adachi Takuya Shirasaka	Tochigi R&D Center Tochigi R&D Center Wako Research Center
		Development of New Diesel Engine to Meet EURO-IV	Tomoya Abe Takatoshi Aoki Masahiro Kikuchi Ikuro Hara Seiichi Hosogai Hideki Minami	Tochigi R&D Center Tochigi R&D Center Tochigi R&D Center Tochigi R&D Center Tochigi R&D Center Tochigi R&D Center

2004.3.8-11	SAE/2004 SAE World Congress (Detroit, USA)	Development of a High-strength Aluminum Cylinder Block for Diesel Engine Employing a New Production Process	Masakazu Yamazaki Osamu Murakami Mitsuhiko Kawabata Atsushi Takai Hitoshi Tanikawa Osamu Ito	Tochigi R&D Center Tochigi R&D Center Tochigi R&D Center Tochigi R&D Center Honda Engineering Co.,Ltd. Honda Engineering Co.,Ltd.
		Study on Euro IV Combustion Technologies for Direct Injection Diesel Engine	Tomohiro Kanda Shinichi Kobayashi Ryuta Matsui Hiroshi Sono	Tochigi R&D Center Tochigi R&D Center Tochigi R&D Center Tochigi R&D Center
		Study on Engine Management System Using In-cylinder Pressure Sensor	Yuichi Shimasaki Makoto Kobayashi Hideki Sakamoto Masaki Ueno Mamoru Hasegawa Satoshi Yamaguchi	Tochigi R&D Center Tochigi R&D Center Tochigi R&D Center Tochigi R&D Center Tochigi R&D Center Tochigi R&D Center
		Research on HC Adsorption Emission System	Hideharu Yamazaki Masaki Ueno Tetsuo Endo Satoshi Sugaya	Tochigi R&D Center Tochigi R&D Center Tochigi R&D Center NTK/R&D Center
		In-situ Fuel Concentration Measurement near Spark Plug by 3.392 μm Infrared Absorption Method -Application to a Port Injected Lean-burn Engine	Atsushi Nishiyama Nobuyuki Kawahara Eiji Tomita Masahiro Fujiwara Naohiro Ishikawa Kazuhiro Kamei Keiichi Nagashima	Okayama University Okayama University Okayama University Okayama University Tochigi R&D Center Tochigi R&D Center Tochigi R&D Center
		Development of a Simulation Technique for CVT Metal Pushing V-Belt with Feedback Control	Toshihiro Saito Alan D. Lewis	Tochigi R&D Center LMS International
		Practical Examples for CAE-based Development for Automobile Transmissions by Designers	Shigeru Koyama Shigeru Nagai Takanao Uchida	Tochigi R&D Center Tochigi R&D Center Tochigi R&D Center
		Large-scale Electromagnetic Simulation of a Full Automobile Model Using the FDTD Method and Measurement	Hiroshi Kuribayashi Satoru Komatsu Tomoyuki Fukumaru Tatsuya Kashiwa Kenji Taguchi	Tochigi R&D Center Tochigi R&D Center Tochigi R&D Center Kitami Institute of Technology Kitami Institute of Technology
		Development of FIPG for Magnesium Alloys	Masayasu Sakata Satoshi Hosogi	Tochigi R&D Center Three Bond Co., Ltd.
		Development of High Heat Resistance High Nitrogen Containing Austenitic Stainless Steel for Exhaust Gasket	Takashi Katsurai Tadao Nishiyama Syuji Hamano	Tochigi R&D Center Tochigi R&D Center Daido Steel Co., Ltd.
		Application of Shape-controlled-sulfide Free Machining Steel for Automotive Component	Katsuaki Shiiki Takashi Kano	Tochigi R&D Center Daido Steel Co., Ltd.
		On Methods of Analysis of the Generation Mechanism of Radiation Noise in Exhaust Pulsating Flow	Masato Sakurai	Tochigi R&D Center

2004.3.8-11	SAE/2004 SAE World Congress (Detroit, USA)	Fast Crash Analysis of 3D Beam Structures Subjected to Crash Loading	Kenji Takada Wlodek Abramowicz	Tochigi R&D Center Impact Design EUROPE
		Analysis of Buckling Behavior of Aluminum Structures for Crash Absorbing	Takayuki Yamada Yusuke Takayama Daisei Abe Tetsu Nishimura	Tochigi R&D Center Tochigi R&D Center Tochigi R&D Center Nihon University
		Experimental Evaluation of Test Procedures for Frontal Collision Compatibility	Satoshi Takizawa Tomiji Sugimoto Eisei Higuchi Tatsuo Iwabe Takayuki Kisai Takayuki Suzuki	Tochigi R&D Center Tochigi R&D Center Tochigi R&D Center Tochigi R&D Center PSG Co., Ltd. PSG Co., Ltd.
		Development of Active Control System for Engine Booming Noise Applying Adaptive Notch Filter	Toshiro Inoue Akira Takahashi Satoru Minowa	Tochigi R&D Center Tochigi R&D Center Tochigi R&D Center
		Development of Active Control Engine Mount	Hideki Matsuoka Hirotomi Nemoto Tetsuo Mikasa	Tochigi R&D Center Tochigi R&D Center Tochigi R&D Center
		Prediction of Valve Train Motion by Virtual Diesel Engine	Hiroshi Takagishi Kazuaki Shimoyama Masaru Asari	Tochigi R&D Center Tochigi R&D Center Tochigi R&D Center
		Paradoxical Approach to Improve Fuel Economy for Small Motorcycles	Masatoshi Suzuki Yoichi Ishibashi Rumi Ando	Asaka R&D Center Asaka R&D Center Asaka R&D Center
		Control Device of Electronically Controlled Fuel Injection System of Air-cooled Engines for Small Motorcycles	Kenji Tamaki Shiro Kokubu Shunji Akamatsu	Asaka R&D Center Asaka R&D Center Asaka R&D Center
2004.3.11	National Institute for Materials Science/ The Second Japan-China Workshop on Automobile Materials for Environment and Safety (Tsukuba, Japan)	Activities for Reducing Environmental Impacts Substances in Production of Two-wheeled Vehicles	Tsutomu Tomizawa	Asaka R&D Center
		The Trend of Regulation about Car Recycling and Hazardous Substance -Expectation for China-	Akihiro Kotani	Tochigi R&D Center
2004.3.14-18	SPIE (Society of Photo-Optical Instrumentation Engineers) /SPIE 11th Annual International Symposium on Smart Structures and Materials (San Diego, USA)	Energy Absorption Material Using Buckling Strength of Shape Memory Alloy Plate	Shunji Suzuki Yuta Urushiyama Minoru Taya	Tochigi R&D Center Tochigi R&D Center University of Washington
2004.3.15	The official Journal of the Japan Society for Composite Materials Vol.30 No.2	Automotive Composites, Industrial Application	Nobuo Matsui	Wako Research Center

2004.3.29	The Thai Automotive Industry Association/The Next Generation of Low Emission Vehicle & Technology (Thai, Bangkok)	Challenges for Next-generation Vehicle & Technology	Masami Ogura	Tochigi R&D Center
2004.4.1	JSAE/JSAE Review Vol.25, No.2	Intelligent Vehicle and Advanced Safety Technology	Makoto Kawai Shinnnosuke Ishida Takayuki Tsuji	Wako Research Center Tochigi R&D Center Tochigi R&D Center
2004.4.1-3	John Wiley & Sons/International Journal of RF and Microwave Computer-Aided Engineering	FDTD Large-scale Parallel Supercomputing and Its Application to the Analysis of Radiation Characteristics of an Antenna Mounted on a Vehicle	Tatsuya Kashiwa Koichi Hirayama Kenji Taguchi Masashi Utiya Hiroshi Kuribayashi Satoru Komatsu	Kitami Institute of Technology Kitami Institute of Technology Kitami Institute of Technology Kitami Institute of Technology Tochigi R&D Center Tochigi R&D Center
2004.4.4-9	Acoustical Society of Japan/Proceedings of ICA2004, The 18th International Congress on Acoustics (Kyoto, Japan)	Modelling of Floor Carpet on Vibration and Structure-borne Noise Transmission	Toru Yamazaki Takashi Ono Satoshi Utsumi Kazuhito Misaji Minoru Kamata	Kanagawa University Kanagawa University The University of Tokyo Tochigi R&D Center The University of Tokyo
2004.4.19-23	IFAC (International Federation of Automatic Control) /Advances in Automotive Control (Salerno, Italy)	Progress and Future Direction of Chassis Control Technology	Yasuji Shibahata	Tochigi R&D Center
2004.4.28	Journal of the American Chemical Society Vol.126, No.16	Large-scale Synthesis of Perpendicularly Aligned Helical Carbon Nanotubes	Liming Dai Vardhan Bajpai Toshiyuki Ohashi	The University of Akron The University of Akron Wako Research Center
2004.5.13	IMechE (Institution of Mechanical Engineers)/Fuel Economy and Engine Downsizing (London, UK)	Development of the Engine and IMA System for the New Honda Civic	Kenji Nakano	Tochigi R&D Center
2004.5.23-27	FISITA2004 World Automotive Congress (Barcelona, Spain)	Improvement of Thermal Stability for NOx Adsorbents in Lean Nox Catalyst	Masato Kaneeda Hidehiro Iizuka Yuuichi Kitahara Hiroshi Ohno Toshikatsu Takanohashi Naohiro Satoh	Hitachi, Ltd. Hitachi, Ltd. Hitachi, Ltd. Tochigi R&D Center Tochigi R&D Center Tochigi R&D Center
		Development of a High Performance and High Fuel Economy Four-valve Direct-injection Engine with i-VTEC Mechanism	Kaoru Horie Yutaka Kohda Hiroyuki Goto Ken Ogawa	Tochigi R&D Center Tochigi R&D Center Tochigi R&D Center Tochigi R&D Center
		Countermeasure against Noise and Vibration of Direct Injection Diesel Engine for New Honda Accord	Hajime Igami Shigeji Nonaka Masao Hiruma Yuji Katoh	Tochigi R&D Center Tochigi R&D Center Tochigi R&D Center Tochigi R&D Center
		Prediction of Transmitted Load by Virtual Diesel Engine	Hiroshi Takagishi Masayuki Katsuki Yasuhiro Kawamura	Tochigi R&D Center Tochigi R&D Center Tochigi R&D Center

2004.5.23-27	FISITA2004 World Automotive Congress (Barcelona, Spain)	Application of Metal Pushing V-belt Stress Simulation for Prediction of Fatigue Strength	Toshihiro Saito	Tochigi R&D Center
		On the Grid System to Calculate Crash Worthiness Using Clusters of Engineering Workstations in Idle Periods	Yoshihiro Yamamoto	Tochigi R&D Center
		Development of a High-strength Aluminum Cylinder Block for Diesel Engine Employing a New Production Process	Masakazu Yamazaki Osamu Murakami Atsushi Takai Takahiro Suenaga	Tochigi R&D Center Tochigi R&D Center Tochigi R&D Center Honda Engineering Co.,Ltd.
		Development of Metal Pushing V-belt for Continuously Variable Transmission (Investigation for Clearance between Elements, Strength of Element Material and Ring Material)	Toru Yagasaki Shigeru Kanehara Kazuo Ishii Hideaki Aoyama Yoshinari Okada	Tochigi R&D Center Tochigi R&D Center Tochigi R&D Center Tochigi R&D Center Tochigi R&D Center
2004.5.31	Elsevier B.V./Solid State Ionics Volume 170, Issues 3-4	Effects of cation- or Oxide Ion-defect on Conductivities of Apatite-type La-Ge-O System Ceramics	Susumu Nakayama Yoshikatsu Higuchi	Niihama National College of Technology Wako Research Center
2004.6.1-4	AAB (Advanced Automotive Batteries)/The 4th International Advanced Automotive Battery Conference (San Francisco, USA)	Overview of Battery Technology for Advanced Vehicles	Noboru Sato	Tochigi R&D Center
2004.6.8-10	SAE/SAE Spring Fuels & Lubricants Meeting & Exhibition (Toulouse, France)	A Study of Gasoline-fuelled HCCI Engine Equipped with an Electromagnetic Valve Train	Yasuhiro Urata Moriyoshi Awasaka Junichi Takanashi Takashi Kakinuma Takazou Hakozaki Atsushi Umemoto	Tochigi R&D Center Tochigi R&D Center Tochigi R&D Center Tochigi R&D Center Tochigi R&D Center Tochigi R&D Center
		Study on Variable Valve Timing System Using Electomagnetic Mechanism	Chihaya Sugimoto Hisao Sakai Atsushi Umemoto Yasuo Shimizu Hidetaka Ozawa	Tochigi R&D Center Tochigi R&D Center Tochigi R&D Center Tochigi R&D Center Tochigi R&D Center
		Study on Combustion Monitoring System for Formula One Engines Using Ionic Current Measurement	Yuuichi Shimasaki Hidetaka Maki Junko Sakaguchi Hiroaki Suzuki Akira Kato Kazutoshi Nishizawa Noriaki Kondo Tatsunori Yamada	Tochigi R&D Center Tochigi R&D Center Tochigi R&D Center Tochigi R&D Center Tochigi R&D Center Honda R&D Europe (Deutschland) GmbH NGK SPARK PLUG CO.,LTD. NGK SPARK PLUG CO.,LTD.
		An Application Study of the Pneumatic Direct Injection Activated Radical Combustion Two-stroke Engine to Scooter	Yoichi Ishibashi Takashi Sakuyama	Asaka R&D Center Asaka R&D Center

2004.6.14-17	ASME (The American Society of Mechanical Engineers) & IGTI(The International Gas Turbine Institute)/ASME Turbo Expo 2004 (Vienna, Austria)	A Study of Advanced High Loaded Transonic Turbine Airfoils	Toyotaka Sonoda Toshiyuki Arima Markus Olhofer Bernhard Sendhoff Friedrich Kost Peter-Anton Giess	Wako Research Center Wako Research Center Honda Research Institute Europe GmbH Honda Research Institute Europe GmbH German Aerospace Center (DLR) German Aerospace Center (DLR)
2004.6.16-18	IEEE (Institute of Electrical and Electronics Engineers)/12th International Symposium ATA EL 2004 (Parma, Italy)	Development, Evaluation and Introduction of a Lane Keeping Assistance System	Shinnosuke Ishida Jens Gayko	Tochigi R&D Center Honda R&D Europe (Deutschland) GmbH
		Intelligent Systems for Active and Passive Safety - Collision Mitigation Brake System	Jens Gayko Kenji Kodaka	Honda R&D Europe (Deutschland) GmbH Tochigi R&D Center

Editor’s Postscript

Of late, we have been having a string of extremely hot days. The heat this summer seems to be gaining force, as though to break the high temperature records at every location. Probably some areas have already set new local records for high temperatures. This heat situation is part of the abnormal weather resulting from the global warming phenomenon. This warming seems to be advancing across the globe, and as such, it appears to signify a level of change in world climates that would have been unimaginable a decade or so ago.

The rate of this change also seems to be accelerating year by year. When we see temperatures higher than 39°C recorded during Tokyo summers, it makes us realize that abnormal weather is not just something in news reports from distant parts of the globe, and that it ourselves as well as other people. This is more than enough to make us truly feel climate change is a problem in our own familiar environment, the one in which we lead our own lives. The global warming phenomenon, and particularly the causal factors that are accelerating it, appear to involve the negative impact results of human activities.

If we assume that human activities are part and parcel of the causal factors for this kind of climate change, and the weather phenomena that is continuing to exert a negative influence on the global environment, then we start wanting to know specifically what those activities are. As can be learned from news reports, newspapers, and other information sources, activities result in increasing emissions of carbon dioxide and other gases, known as greenhouse gases, have a causative connection. Massive amounts of carbon dioxide are said to have been released into the atmosphere since the beginning of the industrial revolution in the late 18th century. We are now being told that the concentration of carbon dioxide in the atmosphere has increased by some 30% or more since that time.

These are the kinds of thoughts that have come to us during these days of unbearable heat, and said days have coincided with the editorial deadline for the current issue of the *Honda R&D Technical Review* (Vol. 16, No. 2). Surely it is essential that we give serious thought to how nations, governments, and people around the world should deal with these kinds of globally advancing changes and take action accordingly. The *Honda R&D Technical Review* is already accessible in bilingual format, being published in English as well as Japanese, on our intranet. In a sense, we can see this as an advance in our own globalization. This gives us the hope that the day is no longer distant when the *Honda R&D Technical Review* will fulfill a more global role as a tool to pass on technical and engineering expertise as well as still being an in-house technical bulletin. That can only be made possible, however, by massive, sustained efforts and activities on the part of the researchers who submit articles, the peer reviewers, the people who take part in the editing, and all of the people involved in doing the translating, printing, binding, and other support tasks.

It is our continuing hope that the *Honda R&D Technical Review*, which is produced as the result of such activities and efforts, will serve a growing number of researchers and engineers both as a tool for communication and also as a tool for passing on technical and engineering expertise. This journal is also unlike Honda's other technical publications in that it makes the most of the synergetic effect among automobile, motorcycle, power products, and general technology research, as well as taking advantage of our global perspective. Therefore, we further hope that our journal will be used to its fullest potential because of these qualities and that it will become an evolutionary tool for passing on Honda's corporate DNA into the future.

(Tanaka)

Honda R&D Technical Review English Version Vol.16 No.2

The following associates provided us with their cooperation and expertise:

Matt	Alexander	Honda R&D Americas, Inc. Ohio Center
Karen	Arneson	American Honda Motor Co., Inc.
David	Bates	Honda R&D Americas, Inc. Ohio Center
Bill	Bezilla	Honda R&D Americas, Inc. North Carolina Center
Jayme	Birken	Honda R&D Americas, Inc. Ohio Center
Scott	Blanford	Honda R&D Americas, Inc. Ohio Center
Matt	Chany	Honda R&D Americas, Inc. Ohio Center
Mary	Christopherson	Honda North America, Inc.
Dan	Croasman	Honda R&D Americas, Inc. Ohio Center
Brian	Doklovic	Honda R&D Americas, Inc. North Carolina Center
Charles	Gagliano	Honda R&D Americas, Inc. Ohio Center
Lee	Goldring	Honda North America, Inc.
Hiroshi	Inutsuka	Honda R&D Americas, Inc. Ohio Center
Dan	Leibovitz	Honda R&D Americas, Inc. Ohio Center
Todd	Luken	Honda R&D Americas, Inc. Ohio Center
Ashley	Nichols	Honda R&D Americas, Inc. Ohio Center
Tad	Nishimura	Honda R&D Americas, Inc. Ohio Center
Daryl	Nolt	Honda R&D Americas, Inc. Ohio Center
Ronald	Petrus	Honda R&D Americas, Inc. Ohio Center
Jason	Schmidt	Honda R&D Americas, Inc. Ohio Center
Steve	Shih	Honda R&D Americas, Inc. Ohio Center
Joshua	Sigmund	Honda R&D Americas, Inc. Ohio Center
Garrett	Stockburger	Honda R&D Americas, Inc. Ohio Center
Charles	Thomas	Honda R&D Americas, Inc. Ohio Center
Philip	Vais	Honda R&D Americas, Inc. Ohio Center
Mark	Wenden	Honda R&D Americas, Inc. Ohio Center
Randy	Wieland	Honda R&D Americas, Inc. Ohio Center (now on assignment at Honda R&D Co., Ltd. Tochigi Center)
William	Willen	American Honda Motor Co., Inc.
Daniel	Wilson	Honda R&D Americas, Inc. Ohio Center
Jun	Xin	Honda R&D Americas, Inc. Ohio Center


HONDA
HONDA
HONDA
T.KOSHIISHI 2004